

nature

QUANTUM COMPASS

A magnetically sensitive protein that could aid navigation in migratory birds



Coronavirus
Do breastfeeding mothers pass vaccine benefits to their babies?

Rapid response
Imaging technique captures real-time ion dynamics in batteries

Cellular growth
A roadmap for the development of hair follicles

Nature.2021.06.26

[Sat, 26 Jun 2021]

- [This Week](#)
- [News in Focus](#)
- [Opinion](#)
- [Work](#)
- [Research](#)

| [Next section](#) | [Main menu](#) |

Donation

| [Next section](#) | [Main menu](#) |

This Week

- **[Confronting gender bias in Nature's journalism](#)** [22 June 2021]
Editorial • An external analysis of 15 years of stories finds men quoted more than twice as often as women.
- **[A 21st-birthday wish for Young Academies of science](#)** [23 June 2021]
Editorial • A global movement of younger researchers is making its mark. Science must listen and learn from its next generation.
- **[World Bank grants for global vaccination — why so slow?](#)** [22 June 2021]
World View • International financial institutions say that vaccines are the highest-return investment on Earth — it is past time for them to pay up.
- **[Iran is draining its aquifers dry](#)** [16 June 2021]
Research Highlight • Wells are proliferating, but data from across the country show that groundwater extraction is falling.
- **[Humanity's fast-food habit is filling the ocean with plastic](#)** [10 June 2021]
Research Highlight • Food bags, drink bottles and similar items account for the biggest share of plastic waste near the shore.
- **[Amphibious fish get smart — by working out on land](#)** [15 June 2021]
Research Highlight • Fish navigate mazes more quickly and efficiently after a regimen of jumping about on a solid surface.
- **[How the brain makes us go ‘Achoo!’](#)** [16 June 2021]
Research Highlight • Researchers track down a signalling molecule and brain cells involved in generating a sneeze.
- **[Why a gargantuan star blinked](#)** [16 June 2021]
Research Highlight • Astronomers watch as a star is nearly totally blotted out, perhaps by a disk of material surrounding another star.
- **[Snap and trap: DNA panels click together to form tiny virus catchers](#)** [14 June 2021]

Research Highlight • Modular materials can be programmed to self-assemble into hollow shells with a wide variety of shapes.

- **A bark in the dark reveals a hidden hyrax** [14 June 2021]
Research Highlight • Its neighbours scream, but a new species of tree hyrax — a cousin of the elephant — unleashes a rattling bark.

- EDITORIAL
- 22 June 2021

Confronting gender bias in *Nature's* journalism

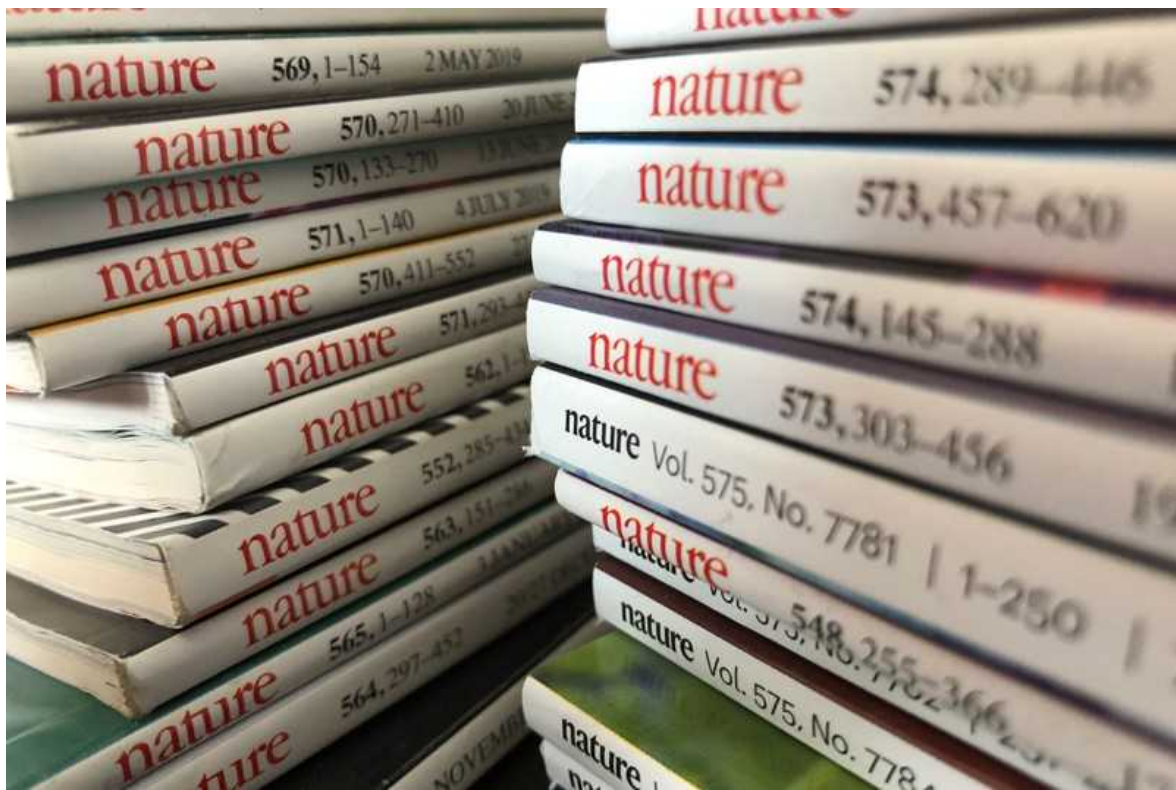
An external analysis of 15 years of stories finds men quoted more than twice as often as women.





•

[Download PDF](#)



At *Nature*, we need to work harder to eliminate biases in our journalism. Credit: *Nature*

A consistent finding of researchers studying the news media is that women are quoted much less often than men. The Gender Gap Tracker (GGT), an automated system created by a team at Simon Fraser University in Burnaby, Canada, has tracked seven Canadian news sites since October 2018 and found that 71% of interviewees quoted in articles were men ([F. T. Asr et al. PLoS ONE 16, e0245533; 2021](#)).

[Four other media agencies](#) around the world worked with the GGT to follow 5 days of their own news coverage last November, and found that 73% of quotes were from men. And the [Global Media Monitoring Project](#) reported in March that in 2020, just 25% of news sources and subjects were women — although this was an increase from 17% in 1995, when the project began its work.

Two researchers in the United States have now analysed *Nature*'s journalism — and found similarly sobering results.

The researchers estimate that, in 2020, some 69% of the direct quotes (not including paraphrased comments) in *Nature*'s journalistic articles were from men. This is according to a software analysis of the gender of people quoted in more than 16,000 *Nature* News, Features and Careers articles between 2005 and 2020. Overall, the proportion of men being quoted in *Nature*'s journalism has been falling. It was around 80% before 2017, and 87% in 2005.

These findings are an important and welcome reminder of gender bias in journalism — a problem that *Nature*'s editors are striving to address. The numbers also show how software can be used by writers and editors to recognize biases, and that at *Nature* we need to work harder to eliminate them.

The analysis, posted before peer review (N. R. Davidson and C. S. Greene Preprint at bioRxiv <https://doi.org/10.1101/2021.06.21.449261>; 2021), was automated with software. The researchers first scraped articles written by journalists and published on nature.com. They then wrote code to pick out the names of people quoted by reporters, counting those whose quotes are enclosed in speech marks. Another algorithm called genderize.io was used to assign gender, a standard approach for large bibliometric studies.

The idea for the study was developed in consultation with *Nature*, but the authors, Natalie Davidson and Casey Greene, both computational biologists at the University of Colorado School of Medicine in Aurora, worked independently to design and conduct the study.

The duo found one exception to the main finding on gender bias — in *Nature*'s Careers features articles. Quotes from men and women appear in equal numbers in this section, which comprises reporting from journalists on different aspects of research careers.

The study does not assess all of *Nature*'s non-primary-research output; for example, content written by invited expert authors is not included. This category of content tends not to directly quote other individuals.

But over the past five years, *Nature* has started collecting data on gender diversity among the authors of such commissioned content. For example,

last year, women comprised 58% of authors in *Nature*'s World View column — up from 35% in 2017, and from 18% in 2016. And, in 2020, women accounted for 34% of authors of News and Views articles — which explain and analyse new research — compared with 26% in 2017 and 12% in 2012. Another example of journalism is our photo-essay section, Where I Work, which profiles researchers in places where they study. This has featured 56% female scientists since its introduction in 2019.

Caveats and limitations

As with all studies, there are some caveats. Not all names could be analysed, and Davidson and Greene note that their software has a slight male bias when it comes to assigning gender to names. For instance, in a sample of articles from 2005 to 2015, it assigned 78% of quoted speakers as male, but the true number, when the authors checked, was 75%. It also cannot estimate non-binary gender.

To help contextualize their findings, the researchers consider various ways of measuring the overall proportion of women in academic research. The [global science report by UNESCO](#), the United Nations science and education organization, was published earlier this month and puts this at 33% in 2018. By comparison, Davidson and Greene found that women made up around 20% of last-author and 25% of first-author positions on *Nature* papers; the ratios are about 25% and 37% in a wider selection of papers in Springer Nature journals.

Davidson and Greene also analysed what they call the ‘name origins’ of quoted interviewees in *Nature*'s journalism — a linguistic analysis that assigns names to broad regions of the world where a particular name is over-represented. The authors use an algorithm called NamePrism that excludes the United States, Canada and Australia because of the diversity of names in these countries.

This analysis suggests that *Nature*'s journalists tend to quote more researchers with names commonly used in English-speaking cultures, and fewer with names that the algorithm classifies as being of East Asian origin (including China, Singapore, Vietnam and other southeast Asian countries).

It also indicates that this imbalance in name origins is greater than that seen in the names of last authors in Springer Nature research papers.

Nature's journalism team has been making efforts to track and improve its representation of all under-represented groups, but previously this has not been a centralized effort. In the past year, however, the team has been developing and trialling a prototype system, with the goal — while abiding by data-privacy regulations — of collecting information on the gender, career stage and location of journalistic sources, expert authors and other contributors. We hope to be able to use this to establish and report a set of baseline figures, and then to improve on them. We are also working hard to include more voices from all groups that are under-represented in research.

More than half of *Nature*'s journalism team is female, but the overwhelming majority of its members are in Europe, the United States and Australia. We recognize that we need to strive harder to find diverse sources across the world.

Journalists, non-profit organizations and scientists have written excellent guides to diversifying sources, such as [at the Open Notebook](#). They have also produced [databases of diverse experts](#) in [many scientific fields](#). And, as [personal testimonies](#) from [science reporters](#) and [other journalists attest](#), keeping track of the numbers, as Davidson and Greene are doing, is an essential part of this process, so we can be reminded of just how much more we need to do.

Nature **594**, 473-474 (2021)

doi: <https://doi.org/10.1038/d41586-021-01676-7>

Related Articles

- [Analysis of scientific journalism in Nature reveals gender and regional disparities in coverage](#)



- [Nature's under-representation of women](#)



- [Science benefits from diversity](#)



- [Women from some under-represented minorities are given too few talks at world's largest Earth-science conference](#)



- [Publishers: let transgender scholars correct their names](#)

Subjects

- [Authorship](#)
- [Careers](#)
- [Lab life](#)
- [Research management](#)

[Jobs from Nature Careers](#)

- - - [All jobs](#)
 - - [Laboratory Research Scientist](#)

[Francis Crick Institute](#)

[London, United Kingdom](#)

[JOB POST](#)

- [Bachelor of Science in Computer Engineering \(f/m/d\)](#)

[Helmholtz-Zentrum Berlin for Materials and Energy \(HZB\)](#)

[Berlin, Germany](#)

[JOB POST](#)

- [Laboratory Engineer / Scientific and Technical Head of Reactor Technology \(f/m/x\)](#)

[Helmholtz Centre for Environmental Research \(UFZ\)](#)

[Leipzig, Germany](#)

[JOB POST](#)

- [Administrative Assistant/Internal Event Coordinator](#)

[Oklahoma Medical Research Foundation \(OMRF\)](#)

[Oklahoma City, United States](#)

[JOB POST](#)

[Download PDF](#)

Related Articles

- [Analysis of scientific journalism in Nature reveals gender and regional disparities in coverage](#)



- [Nature's under-representation of women](#)



- [Science benefits from diversity](#)



- [Women from some under-represented minorities are given too few talks at world's largest Earth-science conference](#)



- [Publishers: let transgender scholars correct their names](#)

Subjects

- [Authorship](#)
- [Careers](#)
- [Lab life](#)
- [Research management](#)

- EDITORIAL
- 23 June 2021

A 21st-birthday wish for Young Academies of science

A global movement of younger researchers is making its mark. Science must listen and learn from its next generation.





•

[Download PDF](#)



As Young Academies celebrate their 21st birthday, science must let young researchers lead the way. Credit: Franki Simonds/Shutterstock

The new millennium coincided with the start of an important new movement in research. In June 2000, early-career researchers in Germany established the first in a wave of national Young Academies, organizations dedicated to looking after the needs — and advancing the aspirations — of researchers at the start of their careers. Twenty-one years later, there are Young Academies in 45 countries, as well as international ones such as the Global Young Academy and the Young Academy of Europe. And the wave is growing: 2020 saw Young Academies launch in the Democratic Republic of the Congo, Nepal and Romania.

Young Academies are a necessary development in international science, as the founders of Hungary's Young Academy, which launched in 2019, [explain](#). Most early-career researchers are in a much more precarious position than were previous generations — a situation worsened by the COVID-19 pandemic and a year of financial losses for universities. [As we have reported](#), funding agencies are not doing enough to support these

scientists. By organizing and collaborating on a larger scale, young researchers are making themselves heard.



[Six reasons to launch a Young Academy](#)

One of the aims of the Hungarian academy's founders is to encourage the formation of more Young Academies, and to show their peers how this can be achieved. It's timely advice: there are still plenty of places where Young Academies do not exist, including China, England, the United States and most of the Middle East, where only Egypt and Israel have Young Academies.

There's no one model for a Young Academy — their structure and funding will depend on national circumstances. Some are independent non-governmental organizations; others have a formal relationship with a country's national science academy. Regardless of the model, it's essential that they are a platform for researchers to have a voice on the issues that matter to their careers and to society.

Young Academies offer a range of activities. In the past year, they have run events and workshops on such diverse topics as working during the pandemic, grant-writing, responsible research, and supporting refugee and at-risk scholars. They also provide research-informed advice for decision-makers. For example, Young Academy members have been urging funding

agencies to ensure that research-evaluation systems incorporate credit for parental leave.

The academies' advice to decision-makers is often on the topics that are front and centre for young people — such as open science and open data, climate change and biodiversity loss. Last November, members of the Netherlands Young Academy published a study, *[Flying High But Flying Less](#)*, on how researchers could reduce carbon emissions from work-related air travel.

Despite the pressures that early-career researchers experience — Young Academy members and office-holders are often carers and parents of young children — members are committed to carrying out public-engagement activities to encourage younger generations to get into science.



[Postdocs need urgent financial support amid COVID conditions](#)

It takes time for the seeds of new institutions to bear fruit, but the Young Academy movement is already having an impact on scientific advice, for example. Last month, the European Commission included representatives from the 14 European Young Academies in the latest meeting of its official Group of Chief Scientific Advisors. The group advises Europe's leaders on science-policy questions, such as those related to cleaner energy or dealing with future pandemics. It's a rare example of how younger people's voices

are being incorporated into official scientific advice — yet it shouldn't be a rarity. More science-advice systems need to be doing the same. This message is now more important than ever. But even before the pandemic, younger people's voices struggled to be heard in science's established institutions — especially by the leadership of funding agencies, universities and national academies.

Just as climate-change policy has been electrified by the activism of younger people, science, too, needs to hear — and act on — the voices of the next generation, as it did in earlier times. Remember that it was younger scientists — several in their thirties — who founded the Royal Society of London.

Happy 21st birthday to all Young Academies. May there be many more to come.

Nature **594**, 474 (2021)

doi: <https://doi.org/10.1038/d41586-021-01677-6>

Related Articles

-  [Six reasons to launch a Young Academy](#)
-  [Postdocs need urgent financial support amid COVID conditions](#)
-  [Postdocs in crisis: science cannot risk losing the next generation](#)



- **'I'll work on it over the weekend': high workload and other pressures faced by early-career researchers**

Subjects

- Careers
- Policy
- Research management

Jobs from Nature Careers

- - - All jobs
 - - Laboratory Research Scientist
Francis Crick Institute
London, United Kingdom
JOB POST
 - Bachelor of Science in Computer Engineering (f/m/d)
Helmholtz-Zentrum Berlin for Materials and Energy (HZB)
Berlin, Germany
JOB POST

- **Laboratory Engineer / Scientific and Technical Head of Reactor Technology (f/m/x)**

Helmholtz Centre for Environmental Research (UFZ).

Leipzig, Germany.

JOB POST

- **Administrative Assistant/Internal Event Coordinator**

Oklahoma Medical Research Foundation (OMRF).

Oklahoma City, United States

JOB POST

Download PDF

Related Articles

-  **Six reasons to launch a Young Academy**
-  **Postdocs need urgent financial support amid COVID conditions**
-  **Postdocs in crisis: science cannot risk losing the next generation**



- **'I'll work on it over the weekend': high workload and other pressures faced by early-career researchers**

Subjects

- [Careers](#)
- [Policy](#)
- [Research management](#)

This article was downloaded by **calibre** from <https://www.nature.com/articles/d41586-021-01677-6>

| [Section menu](#) | [Main menu](#) |

- WORLD VIEW
- 22 June 2021

World Bank grants for global vaccination — why so slow?



International financial institutions say that vaccines are the highest-return investment on Earth — it is past time for them to pay up.

- [Justin Sandefur](#) 0

1. [Justin Sandefur](#)

1. Justin Sandefur is a senior fellow at the Center for Global Development in Washington DC, USA.

[View author publications](#)

You can also search for this author in [PubMed](#) [Google Scholar](#)





•

[Download PDF](#)

Some day, my grandchildren will read how teams of scientists around the world developed vaccines against COVID-19 within a year. They will also read a sadder history: how millions of people in low- and middle-income countries (LMICs) died after those vaccines came to market. Part of the reason, they'll learn, was the lack of financing to buy vaccines.

Earlier this month, leaders of the G7 group of rich countries cobbled together a plan to donate one billion vaccine doses to LMICs, but the head scratcher remains: why didn't the World Bank do this months ago?

The bank entered the pandemic with both the money and the mandate to quickly finance a global vaccination drive. It had roughly US\$50 billion available in grants, and a further \$100 billion in lending capacity. But it has lacked leadership and flexibility. In October, the bank pledged \$12 billion in loans to purchase and distribute vaccines, tests and treatments. Eight months later, it had lent just \$3.6 billion. Poor countries, mired in debt, are wary to take on more. The bank is supposed to be a fast, flexible, smart multilateral organization that can act in a crisis. But it has taken months to do so, sacrificing people's lives and its own relevance.

More than a year ago, the World Health Organization (WHO) and other global health organizations launched the COVAX initiative, part of its broader Access to COVID-19 Tools Accelerator (ACT-A) programme to provide testing, treatment and vaccines to rich and poor countries alike. But COVAX and ACT-A are receptacles for donor money, not sources of finance. This month, ACT-A announced that it still needs \$21 billion.



Rich countries should tithe their vaccines

Meanwhile, the World Bank has seemed reluctant to release money for vaccines. For months, it imposed hurdles beyond the standards of any single stringent regulatory authority or the WHO prequalification system for health products. The procurement process for the Oxford–AstraZeneca vaccine, for instance, was not eligible for World Bank support until nearly

two months after the United Kingdom had begun rolling out the vaccine in January, wasting precious time. (The bank relaxed its requirements after a review in April.)

These failures squander the fruits of research. The enormous contributions that science can make to public health, poverty reduction and development come largely in the form of public goods. These are ideas and technologies that have big global benefits, but which any single country — especially poor ones — might be reluctant to pay for alone. The COVID-19 pandemic is revealing the World Bank's inability, or unwillingness, to invest in these goods.

The bank took until last month to issue a plan to set things right. On 31 May, its president, David Malpass, penned a joint statement with the heads of the International Monetary Fund (IMF), the World Trade Organization and the WHO. It called for \$50 billion in new public spending to accelerate COVID-19 vaccination in LMICs, with at least \$35 billion to come as grants to those countries to purchase vaccines and build up their health systems. In a background paper, the IMF's chief economist, Gita Gopinath, called this plan "[possibly the highest-return public investment ever](#)", with the potential to generate \$9 trillion in other outputs, on top of the direct health benefits.

But the proposal had one glaring weakness: none of these institutions volunteered to pay for it.

To be fair, the World Bank president can't just give away \$50 billion. That would limit the bank's ability to keep lending in 2022 and beyond, possibly angering LMICs as well. And its biggest shareholders, including the United States and other rich countries, would have to be on board. In that case, faced with a World Bank leadership that is dragging its feet, they might just as well buy the vaccines directly, as per the G7's latest plan.



National COVID debts: climate change imperils countries' ability to repay

So what now? The bank must soften the terms of its loans for health systems and unleash more of its \$12 billion pledge as grants for vaccine procurement. The longer it waits, the less good its money will do.

The fate of the world shouldn't rest on, say, Kenya's willingness to take on more debt. Unchecked outbreaks kill and disable, and they are breeding grounds for new variants, which do not respect national borders. Even in the narrowest economic terms, the IMF estimates that its \$50-billion proposal to increase the target vaccination rate for LMICs from 30% to 40% by the end of 2021 would boost global economic activity, generating \$1 trillion for advanced economies in extra tax revenue alone. It's unrealistic, not to mention unfair, to expect low-income countries to pay for that.

Achieving the highest possible take-up of vaccines requires that they are free to individuals. The same logic applies to countries, at least to some degree. Myriad other constraints — supply limitations, export bans and weak national health systems — will continue to limit access to COVID-19 vaccines in LMICs well into 2022. The World Bank should ensure that finance isn't one of them.

The bank says it is doing all it can. Perhaps so, for normal times. But other sectors have been able to innovate and push their capacities during this

extraordinary challenge. If there was ever a time to break the bank, this is it.

Nature **594**, 475 (2021)

doi: <https://doi.org/10.1038/d41586-021-01678-5>

Competing Interests

J.S. is principal investigator on a randomized control trial of remote learning techniques during school closures in Sierra Leone, funded by the World Bank, for which he receives reimbursement for his time. He is also contracted by the World Bank as a paid member of an External Review Panel tasked with writing a report.

Related Articles



- [**National COVID debts: climate change imperils countries' ability to repay**](#)



- [**Rich countries should tithe their vaccines**](#)



- [**The world must learn from COVID before diving into a pandemic treaty**](#)



- [**The United States can help the IMF to rethink how it lends**](#)

Subjects

- [SARS-CoV-2](#)
- [Vaccines](#)
- [Institutions](#)

Jobs from Nature Careers

- - - [All jobs](#)
 -
 - [Laboratory Research Scientist](#)

[Francis Crick Institute](#)

[London, United Kingdom](#)

[JOB POST](#)

- [Bachelor of Science in Computer Engineering \(f/m/d\)](#)

[Helmholtz-Zentrum Berlin for Materials and Energy \(HZB\)](#)

[Berlin, Germany](#)

[JOB POST](#)

- [Laboratory Engineer / Scientific and Technical Head of Reactor Technology \(f/m/x\)](#)

[Helmholtz Centre for Environmental Research \(UFZ\)](#)

[Leipzig, Germany](#)

JOB POST

- **Administrative Assistant/Internal Event Coordinator**

Oklahoma Medical Research Foundation (OMRF)

Oklahoma City, United States

JOB POST

[Download PDF](#)

Related Articles



- **National COVID debts: climate change imperils countries' ability to repay**



- **Rich countries should tithe their vaccines**



- **The world must learn from COVID before diving into a pandemic treaty**



- **The United States can help the IMF to rethink how it lends**

Subjects

- [SARS-CoV-2](#)
 - [Vaccines](#)
 - [Institutions](#)
-

This article was downloaded by **calibre** from <https://www.nature.com/articles/d41586-021-01678-5>

| [Section menu](#) | [Main menu](#) |



Many communities in Iran depend on wells for water, and are threatened by the rapid fall in the nation's groundwater table. Credit: Mohsen Maghrebi

Water resources

16 June 2021

Iran is draining its aquifers dry

Wells are proliferating, but data from across the country show that groundwater extraction is falling.





•

Iran is using more groundwater than can be naturally recharged, according to an analysis of national data. And even as more wells are tapped into the ground each year, their overall output keeps dropping.

Iran's sources of groundwater include wells, springs and underground aqueducts known as qanats. Groundwater amounts to 60% of the country's total supply and is consumed almost entirely by agriculture.

Roohollah Noori at the University of Oulu in Finland and his colleagues studied data from Iran's national groundwater-monitoring system from between 2002 and 2015. During that period, the number of wells and other locations that tap into groundwater nearly doubled. Yet the amount of

groundwater extracted declined by 18%. Nationwide, the groundwater table dropped by an average of almost half a metre per year.

In many wells, the water also became significantly saltier, to the point that only salt-tolerant plants would thrive if irrigated with it. Groundwater quality improved in only a few wet regions.

Water scarcity threatens the livelihoods of people across Iran as the land becomes drier.

[Proc. Natl Acad. Sci. USA \(2021\)](#)

- [Water resources](#)

This article was downloaded by **calibre** from <https://www.nature.com/articles/d41586-021-01604-9>

| [Section menu](#) | [Main menu](#) |



Plastic detritus from snacks and meals floats in the Red Sea. Marine sampling shows that food waste accounts for nearly 90% of plastic pollution at some locales. Credit: Andrey Nekrasov/Barcroft Media/Getty

Ocean sciences

10 June 2021

Humanity's fast-food habit is filling the ocean with plastic

Food bags, drink bottles and similar items account for the biggest share of plastic waste near the shore.





•

Takeaway food and beverage packaging is the main source of plastic litter accumulating along many coasts.

Around 8 million metric tons of plastic waste ended up in the ocean in 2010. Using data from scientific surveys and community waste inventories, Carmen Morales-Caselles and Andrés Cózar, at the University of Cadiz in Puerto Real, Spain, and their colleagues classified more than 12 million items of litter found worldwide according to product type, material composition and probable origin.

Takeaway items discarded shortly after use, including plastic bags, wrappers, food containers, bottles, cans and cutlery, accounted for the largest

share — up to 88% — of waste accumulating along shorelines and in near-shore waters. Waste resulting from fishing activities, including synthetic ropes, strings and nets, is the dominant source of litter in the open ocean, the researchers found.

Understanding the products that account for the biggest share of marine litter is crucial to reducing pollution, the authors say. Such knowledge is also needed to ensure responsible production and consumption patterns, they add.

[Nature Sustain. \(2021\)](#)

- [Ocean sciences](#)

This article was downloaded by **calibre** from <https://www.nature.com/articles/d41586-021-01563-1>

| [Section menu](#) | [Main menu](#) |



The mangrove killifish is a quicker study after spending bouts of time in air, experiments show. Credit: Pally/Alamy

Physiology

15 June 2021

Amphibious fish get smart — by working out on land

Fish navigate mazes more quickly and efficiently after a regimen of jumping about on a solid surface.





•

Experiments on amphibious fish have shown that those that dwell in both air and water become smarter than those that reside only in water. Fish that exercise on land experience a similar brain boost.

Giulia Rossi and Patricia Wright at the University of Guelph in Canada placed mangrove killifish (*Kryptolebias marmoratus*), a species that thrives both on land and in water, in small containers. The authors exposed some of the fish to periodic drops in water levels, and so to the air, over a period of eight weeks. Other fish were placed in a terrarium every few days and spurred to jump for three minutes. Control fish were left to swim about undisturbed.

The trained jumpers and fish that had been exposed to air navigated a maze and found the meal at the end more quickly, and covered a shorter distance to do so, than did control fish. They also had more cell proliferation in a brain area that is linked to spatial learning.

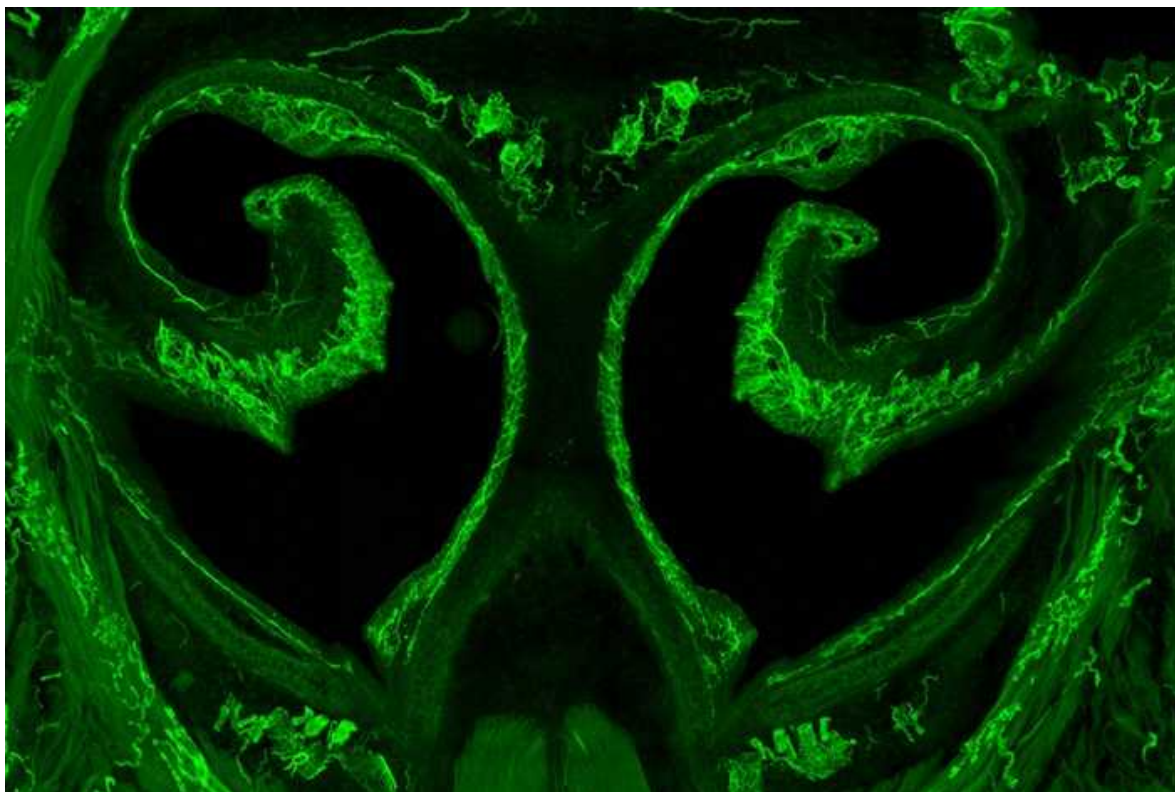
The authors say the work is a step towards showing how ancient fish evolved and adapted while making the move from water onto land.

[Proc. R. Soc. B \(2021\)](#)

- [Physiology](#)

This article was downloaded by **calibre** from <https://www.nature.com/articles/d41586-021-01593-9>

| [Section menu](#) | [Main menu](#) |



The inside of a mouse's nose is rich in nerve fibres (green) that carry sensory information. Credit: F. Li *et al./Cell*

Neuroscience

16 June 2021

How the brain makes us go ‘Achoo!’

Researchers track down a signalling molecule and brain cells involved in generating a sneeze.





•

Scientists have pinpointed the precise populations of neurons that produce the sneeze — a crucial reflex that enables us to remove pathogens and irritants from our airways.

Researchers had previously identified a sneeze-evoking region in part of the brainstem known as the ventromedial spinal trigeminal nucleus (SpV). But the specific cells responsible for sneezing were unknown.

To find those neurons, Qin Liu at the Washington University School of Medicine in St Louis, Missouri, and her colleagues made mice sneeze by getting them to inhale droplets of sneeze-inducing compounds such as capsaicin, which gives chilli peppers their kick. The team then screened the

signalling molecules released by the sensory neurons of the nose and zeroed in on one that was essential for sneezing, called neuromedin B. The authors also located the neurons in the SpV that received this molecular messenger.

The team identified a set of neurons that receives sneeze-eliciting signals from the SpV. These neurons lie in a brain region that controls exhalation, an action required for sneezing. Injecting neuromedin B into this region made mice go ‘achoo! ’ — thus revealing a nose-to-brainstem pathway behind sneezes.

[Cell \(2021\)](#)

- [Neuroscience](#)

This article was downloaded by **calibre** from <https://www.nature.com/articles/d41586-021-01605-8>

| [Section menu](#) | [Main menu](#) |



An enormous star's drastic dimming might have been caused by a yet-undetected object that blocked its light (artist's impression). Credit: Amanda Smith, University of Cambridge

Astronomy and astrophysics

16 June 2021

Why a gargantuan star blinked

Astronomers watch as a star is nearly totally blotted out, perhaps by a disk of material surrounding another star.





•

An enormous blinking star has been spotted at the heart of our Galaxy.

Many stars dim and brighten regularly because they pulsate or are eclipsed by a companion star. Even the Sun varies in luminosity by about 0.1% over an 11-year cycle. But it is extremely unusual for a star to become fainter over several months before slowly recovering.

Leigh Smith at the University of Cambridge, UK, and his colleagues unexpectedly discovered such a blinking star in data collected by the VISTA telescope in Chile. The star is roughly 100 times bigger than the Sun and resides on the opposite side of the Galactic Centre, relative to the Solar

System. Over a few hundred days, the huge star dimmed by 97% and then gradually returned to its former brightness.

The team hypothesizes that an object, such as an orbiting planet or a companion star, passes in front of the star once every few decades, and that this object is circled by material that forms an opaque disk. The disk is much larger than the giant star, which therefore dims when blocked by the disk.

[Mon. Not. R. Astron. Soc. \(2021\)](#)

- [Astronomy and astrophysics](#)

This article was downloaded by **calibre** from <https://www.nature.com/articles/d41586-021-01607-6>

| [Section menu](#) | [Main menu](#) |



Scientists have made virus-trapping shells from as few as 8 DNA panels (left) and as many as 180 (right). Credit: C. Sigl *et al./Nature Mater.*

Materials science

14 June 2021

Snap and trap: DNA panels click together to form tiny virus catchers

Modular materials can be programmed to self-assemble into hollow shells with a wide variety of shapes.





•

Scientists have designed DNA panels that can recognize specific viruses and clamp together around the pathogens, trapping the viral particles inside an impregnable DNA shell.

Antibiotics can kill bacteria, but medicine has no such weapon against viruses. Hendrik Dietz at the Technical University of Munich in Germany and his colleagues have come up with an alternative: quarantining viruses inside traps to stop them interacting with cells.

The researchers first designed triangular panels that self-assembled from DNA strands and had patterns of knobs and hollows on their edges. This

meant that panels could click together like puzzle pieces, forming a range of 3D shapes, or shells.

Shells of different shapes had internal cavities of different sizes and as a result could accommodate viruses big and small. The inner side of the panels carried antibodies to allow them to target specific viruses.

When combined with human cells and live virus, the shells prevented the viral particles from infecting most of the cells.

Nature Mater. (2021)

- [Materials science](#)

This article was downloaded by **calibre** from <https://www.nature.com/articles/d41586-021-01608-5>

| [Section menu](#) | [Main menu](#) |



Some tree hyraxes scream in the night, but the newly identified *Dendrohyrax interfluvialis* (above, camera-trap image) utters a complex series of squawks, rattles and barks. Credit: J. F. Oates *et al./Zool. J. Linn. Soc.*

Zoology

14 June 2021

A bark in the dark reveals a hidden hyrax

Its neighbours scream, but a new species of tree hyrax — a cousin of the elephant — unleashes a rattling bark.





•

Tree hyraxes don't look like elephants. They are furry, they can climb trees and they weigh only around 3 kilograms. Yet these mammals, which live in African tropical forests, are among the closest contemporary relatives of the great grey beasts with swinging trunks.

Now, John Oates at the City University of New York and his colleagues have identified a new species of tree hyrax living in southeastern Ghana, southern Togo and Benin, and southwestern Nigeria, between the Volta and Niger rivers. Scientists knew these animals existed, but didn't realize that they are a separate species from tree hyraxes in other parts of the region.

The first clue was their distinctive call — more of a bark than the shrieks of the hyraxes across the rivers. The team analysed hyrax mitochondrial genomes, fur colour and other traits. They concluded that the barking creature, which has a short, broad head and dark fur, is a new species, which they dubbed *Dendrohyrax interfluvialis*.

The area inhabited by the new hyrax deserves more conservation and scientific attention, the authors say.

[Zool. J. Linn. Soc. \(2021\)](#)

- [Zoology](#)

This article was downloaded by **calibre** from <https://www.nature.com/articles/d41586-021-01606-7>

| [Section menu](#) | [Main menu](#) |

News in Focus

- **[Mars selfie, Betelgeuse mystery and the impact of journal closure](#)** [23 June 2021]
News Round-Up • The latest science news, in brief.
- **[How scientists are embracing NFTs](#)** [18 June 2021]
News • Is a trend of auctioning non-fungible tokens based on scientific data a fascinating art fad, an environmental disaster or the future of monetized genomics?
- **[CureVac COVID vaccine let-down spotlights mRNA design challenges](#)** [18 June 2021]
News • Scientists are searching for explanations to disappointing final-stage trial results. These insights could help guide the future development of mRNA vaccines.
- **[Mars helicopter kicks up ‘cool’ dust clouds — and unexpected science](#)** [16 June 2021]
News • Videos of the surprising phenomenon could help researchers to better understand natural ‘dust devils’ blowing across the red planet.
- **[Massive science-funding bill passes US Senate — but China focus worries researchers](#)** [11 June 2021]
News • Scientists praise the budget boost slated for the National Science Foundation, but worry the legislation could dampen international collaborations.
- **[How three missions to Venus could solve the planet’s biggest mysteries](#)** [17 June 2021]
News Explainer • A renewed focus on our planetary neighbour could help to answer major questions about its atmosphere and geology.
- **[How ancient people fell in love with bread, beer and other carbs](#)** [22 June 2021]
News Feature • Well before people domesticated crops, they were grinding grains for hearty stews and other starchy dishes.
- **[COVID vaccines and breastfeeding: what the data say](#)** [23 June 2021]
News Feature • The vaccines do not pass through breast milk, but antibodies do — providing hope that breastfed babies might have some level of protection.

| [Next section](#) | [Main menu](#) | [Previous section](#) |

- NEWS ROUND-UP
- 23 June 2021

Mars selfie, Betelgeuse mystery and the impact of journal closure

The latest science news, in brief.





•

[Download PDF](#)



Zhurong took this selfie using a detachable camera it released onto the ground. Credit: Jin Liwang/CNSA/Xinhua/ZUMA Press

China's Zhurong Mars rover snaps self-portrait

The Chinese rover Zhurong landed on the red planet on 15 May. Now, a [flurry of images](#) taken by the rover itself and from spacecraft in Mars's orbit are capturing its activities. This shot — released by the China National Space Administration (CNSA) on 11 June — was taken by a detachable camera that Zhurong dropped ten metres away before returning to the lander.

A scientifically important image was a high-resolution colour shot taken by NASA's Mars Reconnaissance Orbiter (MRO), which offers scientists an extremely detailed view of the landing site.

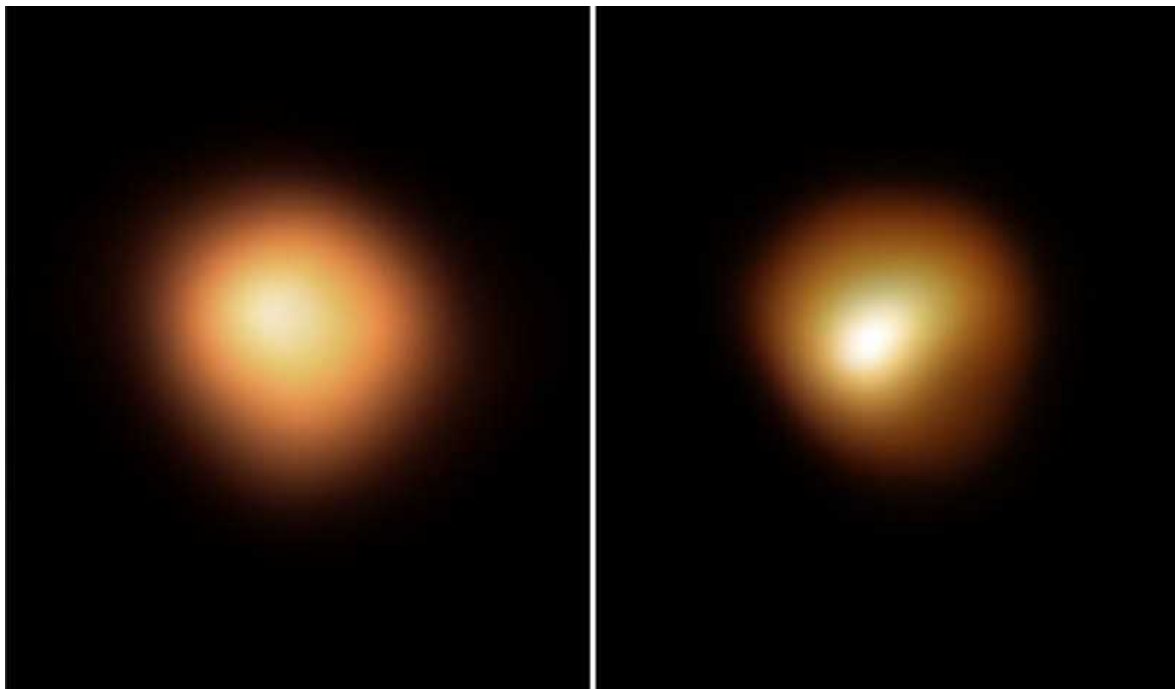
"It's incredible!" says Peter Grindrod, a planetary scientist at the Natural History Museum in London, who confirmed that the 6 June image revealed Zhurong had by then made reasonable headway, travelling 22 metres from the lander.

NASA and the CNSA are not collaborating on this mission, but Alfred McEwen, a planetary scientist at the University of Arizona in Tucson, and

principal investigator for the HiRISE camera on the MRO, suggests the image could be used by Chinese researchers to help plot Zhurong's route.

"Maybe they will see something of interest," he says.

Further images in black and white, released by the CNSA and taken by the Tianwen-1 spacecraft that carried Zhurong to Mars, show the rover's landing site, both before and after it arrived.



Betelgeuse spewed out so much dust that its brightness dropped by two-thirds in 2020.Credit: ESO/M. Montargès *et al.*

Why Betelgeuse went mysteriously dim last year

Normally, Betelgeuse is one of the ten brightest stars in the night sky. In February 2020, however, astronomers noticed that the star's brightness had dropped by an unprecedented two-thirds.

The dimming fuelled speculation that Betelgeuse could be about to explode, but many astrophysicists pointed out that it was likely to be caused by more mundane mechanisms, such as a blob of unusually cold matter appearing on

the star's surface in what's known as a convective cell, or a cloud of dust crossing our line of sight to it.

Now, researchers have found that the dimming was probably caused by a combination of both of those factors ([M. Montargès et al. *Nature* 594, 365–368; 2021](#)).

A series of high-resolution images of the star using the Very Large Telescope in Chile's Atacama Desert showed that the position of the darker region did not change substantially over the imaging period. This indicated that the dim spot was [caused by a cloud of dust that had come from the star itself](#).

The researchers think that an unusually cool convective cell led to a temperature drop in Betelgeuse's atmosphere. This enabled gas that the star had spewed out in the previous year to condense quickly into dust, blocking out light from the star.

Journal closure leads to dip in papers' citations

Papers published in a now-defunct business journal get 20% fewer citations than do similar articles published in titles that are still running, according to an [analysis of finance scholars' citing behaviour](#).

The findings suggest that researchers are “fixated” on the prestige of the journal that a paper is published in, the study's authors conclude ([A. Rubin and E. Rubin *J. Polit. Econ.* <https://doi.org/10.1086/715021>; 2021](#)).

The *Journal of Business* was once considered one of the top five finance-research journals. In 2004, its publisher, Chicago University Press in Illinois, decided to discontinue the title for administrative reasons. The journal officially closed in 2006 and published no new research from that point on. To see how the closure affected citations of the journal's papers, researchers matched articles published in the *Journal of Business* between 1995 and 2006 with articles published in one of the other four top-tier finance journals. They then tracked the citations of almost 3,000 articles over the following 10 years.

Articles published in the now-defunct title received 20% fewer citations than did those in journals that are still operating. Even when matched articles had similar topics or findings, those published in the *Journal of Business* got fewer citations.

The study is a “provocative contribution” to our understanding of how scientists work, says Flaminio Squazzoni, a social scientist at the University of Milan, Italy. But he adds that when a journal is discontinued, the attention of researchers and scientific debate will inevitably go elsewhere.

Nature **594**, 479 (2021)

doi: <https://doi.org/10.1038/d41586-021-01679-4>

Subjects

- [Publishing](#)
- [Astronomy and astrophysics](#)
- [Imaging](#)
- [Planetary science](#)

[Jobs from Nature Careers](#)

- - - [All jobs](#)
 - - [Laboratory Research Scientist](#)

[Francis Crick Institute](#)

[London, United Kingdom](#)

[JOB POST](#)



Bachelor of Science in Computer Engineering (f/m/d)

Helmholtz-Zentrum Berlin for Materials and Energy (HZB)

Berlin, Germany

JOB POST

- **Laboratory Engineer / Scientific and Technical Head of Reactor Technology (f/m/x)**

Helmholtz Centre for Environmental Research (UFZ)

Leipzig, Germany

JOB POST

- **Administrative Assistant/Internal Event Coordinator**

Oklahoma Medical Research Foundation (OMRF)

Oklahoma City, United States

JOB POST

Download PDF

Subjects

- Publishing
- Astronomy and astrophysics
- Imaging
- Planetary science

This article was downloaded by **calibre** from <https://www.nature.com/articles/d41586-021-01679-4>

| [Section menu](#) | [Main menu](#) |

- NEWS
- 18 June 2021

How scientists are embracing NFTs

Is a trend of auctioning non-fungible tokens based on scientific data a fascinating art fad, an environmental disaster or the future of monetized genomics?

- [Nicola Jones](#) ⁰

1. Nicola Jones

1. Nicola Jones is a science journalist based in Pemberton, British Columbia

[View author publications](#)

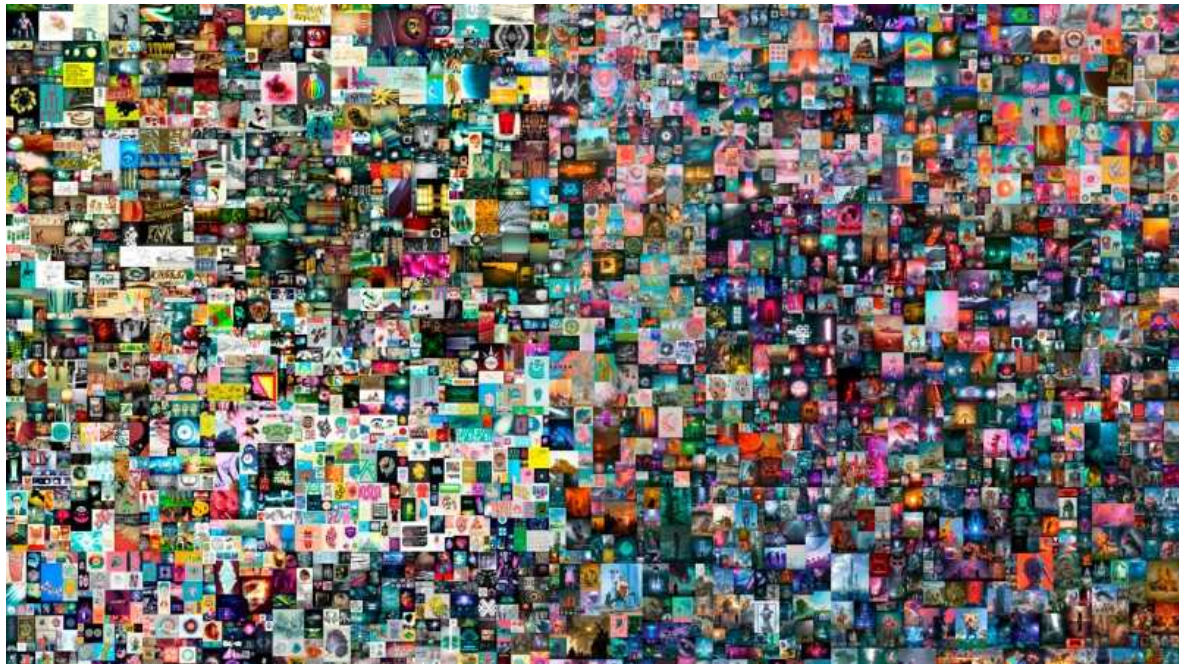
You can also search for this author in [PubMed](#) [Google Scholar](#)





•

[Download PDF](#)



The NFT for a digital collage called *Everydays: The first 5000 days* by US artist Beeple (pictured) sold for US\$69.3 million in March. Credit: Christie's Images Limited 2021

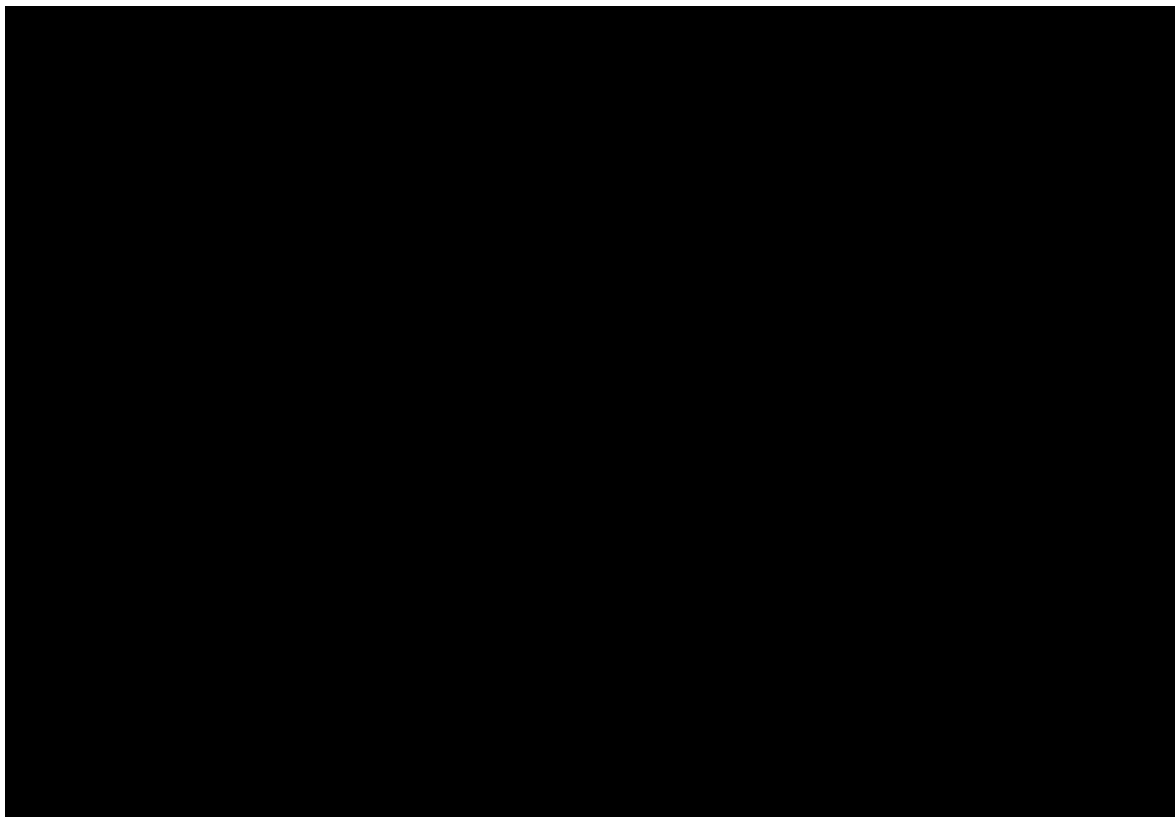
From cat memes and music tracks to all manner of digital art, the bizarre, often quirky market for non-fungible tokens (NFTs) is booming. And now, science is hopping on the bandwagon for these receipts of ownership of digital files that are bought and sold online.

On 8 June, the University of California, Berkeley, auctioned off an NFT based on documents relating to the work of Nobel-prizewinning cancer researcher James Allison for more than US\$50,000. On 17 June, the US Space Force — a branch of the US Armed Forces — started selling a series of NFTs featuring augmented-reality images of satellites and space iconography.

And, from 23 to 30 June, computer scientist Tim Berners-Lee, who invented the World Wide Web, is auctioning an NFT featuring the source code of the original web browser, along with a silent video of the code being typed out.

Meanwhile, biology pioneer George Church and a company he co-founded, Nebula Genomics in San Francisco, California, have advertised their intention to sell an NFT of Church's genome. Church, a geneticist at

Harvard University in Cambridge, Massachusetts, who helped to launch the Human Genome Project, is well known for controversial proposals, including resurrecting the woolly mammoth and creating a dating app based on DNA.



An animated visualization of the source code for the World Wide Web is part of an NFT being auctioned by Internet pioneer Tim Berners-Lee in late June. Credit: Sotheby's

The fad for NFTs has been celebrated online for elevating digital art — and simultaneously derided as meaningless and for having a huge carbon footprint because of the massive computing power required to sustain it.

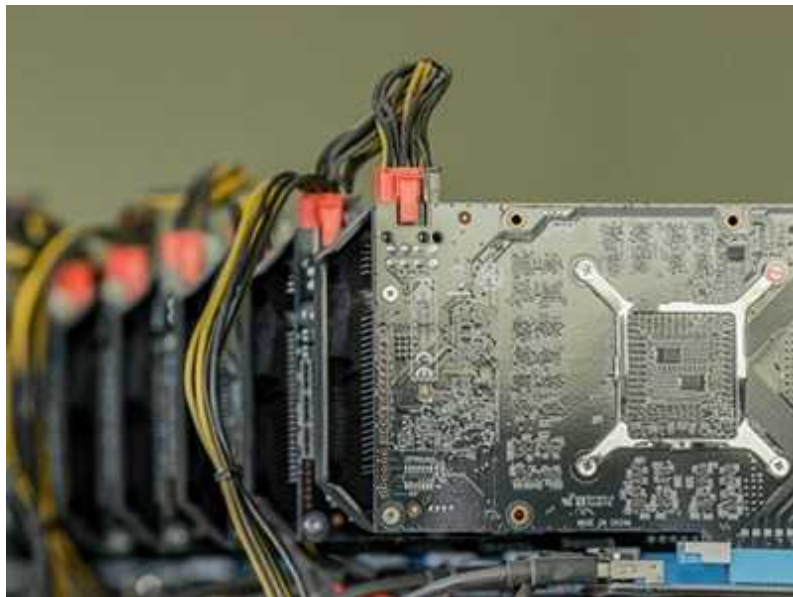
The arguments over NFTs in science are similarly heated, with some saying they provide an incentive to showcase science to the public; a new method of fundraising; and even a way for people to earn royalties when pharmaceutical companies buy access to their genomic data. Others say that NFTs — which operate in a similar way to digital cryptocurrencies — are just needless energy pouring into a market bubble that's sure to burst.

“The more you look at it, the more you realize how bonkers it is,” says Nicholas Weaver, who studies cryptocurrency at the International Computer Science Institute in Berkeley.

NFT bubble

NFTs use the [blockchain technology](#) that underlies cryptocurrencies such as Bitcoin to certify ownership of a file. NFTs are ‘minted’ in the same way as cryptocurrency — using one of many online platforms to add them to a tamper-proof blockchain ledger, typically at a cost of tens or hundreds of dollars — and then sold online. People can buy and trade these certificates in the same way as physical collectibles, such as baseball cards. The art or data can be freely viewed online and downloaded in their original form; the NFT buyer simply has a verifiable receipt of ownership.

The NFT concept was born in the early 2010s but exploded this year: in March, for example, an NFT for a digital artwork by a US artist nicknamed Beeple sold for nearly \$70 million. The NFT market hit a 30-day sales record of \$325 billion in early May. In June, it cooled significantly, but it is still seeing more than \$10 million in sales per week.



[Could Bitcoin technology help science?](#)

Michael Alvarez Cohen, director of innovation ecosystem development in the intellectual-property office at the University of California, Berkeley, decided to try to use NFTs to raise funds for the university. A team of designers scanned legal papers filed with the university, along with handwritten notes and faxes relating to Allison's valuable discoveries. This artwork, called *The Fourth Pillar*, is available for all to see online, and the team minted an NFT for ownership of the work.

After a short bidding war, the NFT sold on 8 June for 22 ether (around US\$54,000). The buyer was a Berkeley alumni group called FiatLux DAO, founded days before by the same blockchain experts who had advised Berkeley on how to create the NFT in the first place. The money will be split between NFT auction site Foundation, a Berkeley research fund and carbon offsets.

"It's an interesting combination of showing the world these historic documents, and also creating art and sponsoring research and education," says Cohen. "It's kind of a beautiful circle."



An artwork including patent disclosures for the Nobel-prizewinning work of Jim Allison is part of an NFT sold by the University of California, Berkeley. Credit: UC Berkeley

But others counter that selling NFTs is a waste, because blockchains rely on energy-hungry computational crunching to prevent data corruption. Digital-currency operator Ethereum, for example, currently has about the same energy usage as the whole of Zimbabwe.

That makes NFTs “really a criminal amount of waste for something that doesn’t do anything valuable other than act as a database for receipts for ugly cats”, says Weaver. Auctioning off the physical papers would make more sense, he says.

Genome gold rush

The Berkeley team is also creating a digital artwork from documents relating to Nobel laureate Jennifer Doudna, one of the pioneers of CRISPR gene-editing, for a future NFT auction. That is being slowed by the need to make sure that her patent — which is still active — isn’t infringed by the art.

Meanwhile, on 10 June, Church and Nebula Genomics put up for sale [20 NFTs](#), each featuring an artwork based on Church’s likeness and a special, limited edition discount on Nebula’s whole-genome sequencing service. Money raised will be split between an unnamed charity, Church, blockchain company Oasis Labs, Nebula Genomics and the sales platform AkoinNFT.

That offering is a surprising step back from what was originally advertised: the group said it would be selling an NFT including Church’s genome in a 10 June auction. But that plan was put on the back burner at the last minute, Nebula Genomics told *Nature*, “because the NFT and crypto markets have declined over the past week”.

“Our plan is to continue to wait for market conditions to improve before launching the entire auction,” says Nebula co-founder Kamal Obbad. It is unclear when that might be.

The idea of selling an NFT of Church’s genome had provoked both excitement and bemusement online. As one scientist [joked on Twitter](#), given that Church’s genome has long been [freely available](#) online: “By a weird coincidence, I’m also selling George Church’s genome! No auction or NFT

or anything though,” they quipped, offering to send the link in exchange for \$5.



Harvard University geneticist George Church plans to auction an NFT for his genome. Credit: Gretchen Ertl/The New York Times/Redux/eyevine

Ethical issues

But for Church’s company, this NFT has a more serious purpose: a trial run. Nebula Genomics already uses blockchain technology to allow 15,000 people whose entire genomes it has sequenced to grant temporary access to their data to specific users (such as pharmaceutical companies searching for links between genes and diseases). NFTs could in future provide a handy system to let customers make money from those exchanges, says Obbad.

A few other companies are [similarly experimenting](#) with ways for customers to sell genomic data on blockchain marketplaces. The idea is to give users more control of their data and to direct profits straight to the individuals, thereby encouraging more people to get their genomes sequenced.



AI researchers embrace Bitcoin technology to share medical data

But some note that these goals can be achieved without NFTs. The plan to auction an NFT for Church's genome "is a PR stunt", says Yaniv Erlich, a computer scientist at Columbia University in New York City and chief science officer of MyHeritage, a genome-sequencing and genealogy company based in Or Yehuda, Israel.

Selling personal genomes opens up ethical issues, says bioethicist Vardit Ravitsky at the University of Montreal in Canada, such as whether any individual truly owns their genome, given that much of it is shared with family members. She also notes there are already debates about whether people should be allowed to make money from their biological resources, for example through sperm donation. The problem of selling data, she says, "will be the next generation of these issues".

There are plenty of "open questions", agrees Obbad, who says that the proposal to sell an NFT featuring Church's genome had been "a good conversation starter".

Nature **594**, 481-482 (2021)

doi: <https://doi.org/10.1038/d41586-021-01642-3>

Related Articles

-  [Could Bitcoin technology help science?](#)
-  [Quantum computers put blockchain security at risk](#)
- [The future of cryptocurrencies: Bitcoin and beyond](#)

Subjects

- [Computer science](#)
- [Genomics](#)
- [Technology](#)

Jobs from Nature Careers

- - - [All jobs](#)
 - - [Laboratory Research Scientist](#)
 - [Francis Crick Institute](#)
 - [London, United Kingdom](#)
 - [JOB POST](#)

Bachelor of Science in Computer Engineering (f/m/d)

Helmholtz-Zentrum Berlin for Materials and Energy (HZB)

Berlin, Germany

JOB POST

- **Laboratory Engineer / Scientific and Technical Head of Reactor Technology (f/m/x)**

Helmholtz Centre for Environmental Research (UFZ)

Leipzig, Germany

JOB POST

- **Administrative Assistant/Internal Event Coordinator**

Oklahoma Medical Research Foundation (OMRF)

Oklahoma City, United States

JOB POST

Download PDF

Related Articles

- **Could Bitcoin technology help science?**



- [Quantum computers put blockchain security at risk](#)
- [The future of cryptocurrencies: Bitcoin and beyond](#)

Subjects

- [Computer science](#)
- [Genomics](#)
- [Technology](#)

This article was downloaded by **calibre** from <https://www.nature.com/articles/d41586-021-01642-3>

| [Section menu](#) | [Main menu](#) |

- NEWS
- 18 June 2021

CureVac COVID vaccine let-down spotlights mRNA design challenges

Scientists are searching for explanations to disappointing final-stage trial results. These insights could help guide the future development of mRNA vaccines.

- [Elie Dolgin](#)
 1. Elie Dolgin
[View author publications](#)

You can also search for this author in [PubMed](#) [Google Scholar](#)





•

[Download PDF](#)



A trial volunteer in Belgium receives a dose of CureVac's vaccine.Credit: Yves Herman/Reuters/Alamy

Two vaccines made using messenger RNA (mRNA) have proved spectacularly successful at warding off COVID-19, but a third mRNA-based candidate has flopped in a final-stage trial, according to an initial report released this week. Researchers are now asking why — and some think that choices about the type of mRNA chemistry used might be to blame. Any insight could help to guide the future design of mRNA vaccines against COVID-19 or other diseases.

The company behind the beleaguered trial, CureVac, based in Tübingen, Germany, announced preliminary data on 16 June from a 40,000-person trial, which showed that its two-dose vaccine was just 47% effective at preventing disease.



Six months of COVID vaccines: what 1.7 billion doses have taught scientists

CureVac's mRNA vaccine was expected to be cheaper and to last longer in refrigerated storage than the earlier mRNA vaccines made by Pfizer–BioNTech and Moderna. Many had hoped that it could help to expand the reach of mRNA-based vaccines in lower-income countries, and European countries were expecting to order hundreds of millions of doses.

“I’m definitely surprised — and also disappointed,” says Philip Santangelo, a biomedical engineer at the Georgia Institute of Technology in Atlanta who has worked with many mRNA-focused companies, including CureVac.

He and others suspect that CureVac’s decision not to tweak the biochemical make-up of its mRNA, as Pfizer–BioNTech and Moderna did, might be behind its poor performance — although it is too early to know for sure.

Variant problem

CureVac executives put the poor results down to the high number of coronavirus variants — including emerging ones such as the Lambda variant first detected in Peru — circulating in the ten countries across Europe and Latin America where the company is running its trial. Of 124 COVID-19 cases for which scientists obtained a genetic sequence, only one was caused by the original version of SARS-CoV-2.

But the other mRNA vaccines have fared much better in the face of variants.

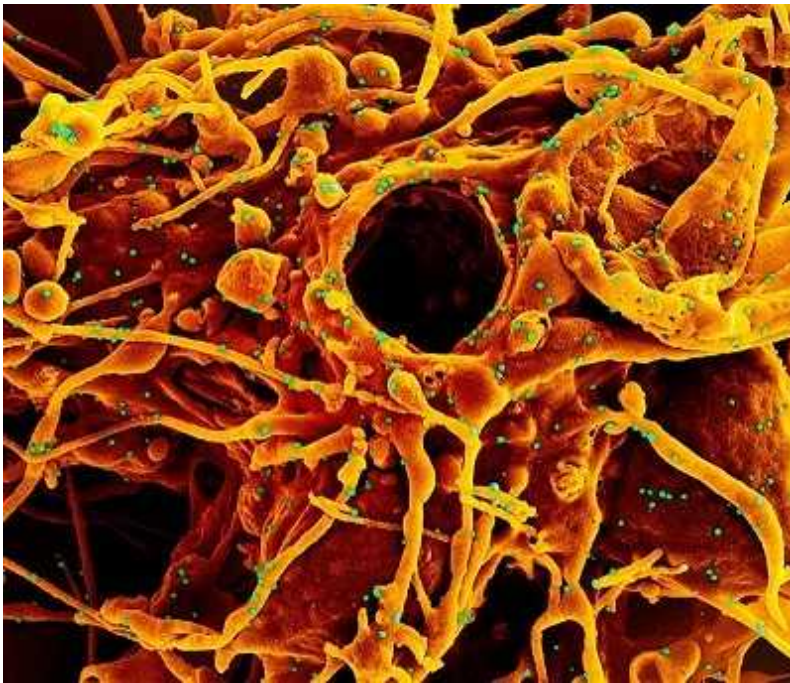
Researchers in the United Kingdom have reported, for instance, that the Pfizer–BioNTech shot offered 92% protection against symptomatic cases of COVID-19 caused by the Alpha variant (first identified in the United Kingdom) and 83% protection against the Delta variant (initially reported in India)¹. A study in Qatar similarly found the vaccine to be around 90% effective against the Alpha strain and 75% effective against the Beta variant that emerged in South Africa².

Those differences in efficacy have led trial investigators and other scientists to suggest that the problem is with the vaccine itself.

Dose of reality

“My best take is that the dose is the culprit,” says Peter Kremsner, an infectious-disease specialist at Tübingen University Hospital who is leading CureVac’s clinical studies.

In phase I testing, Kremsner and his colleagues evaluated doses ranging from 2 to 20 micrograms of mRNA per injection. At the higher dose levels, the vaccine caused too many side effects, with trial participants frequently complaining of problems such as severe headaches, fatigue, chills and injection-site pain.



Scientists zero in on long-sought marker of COVID-vaccine efficacy

At 12 micrograms, the vaccine proved more tolerable, and all recipients developed antibodies that blocked the virus from entering cells³. But the levels of those ‘neutralizing’ antibodies were relatively low — on a par with the amounts found in people who have recovered from SARS-CoV-2 infections, but well below the levels seen in recipients of the Moderna and Pfizer–BioNTech vaccines, which are both given at higher doses.

Perhaps it’s no surprise, then, that CureVac’s shot came up short, says Nathaniel Wang, the chief executive of Replicate Bioscience, an RNA-focused biotech start-up based in San Diego, California. Those low antibody titres in early testing were “already a red flag”, he says.

Some researchers wonder why the vaccine couldn’t be administered at higher doses without inducing side effects.

The tiny bubbles made of lipids that mRNA vaccines are encapsulated in — to help deliver their genetic payloads into cells — can trigger side effects such as those documented by the CureVac trial. But Santangelo says that the CureVac and the Pfizer–BioNTech vaccines use practically indistinguishable, if not identical, lipid bubbles.

He and others think that the problem might lie in the mRNA sequence.

Modified RNA

All three mRNA vaccines encode a form of the coronavirus spike protein, which helps virus particles to penetrate human cells. But the Moderna and Pfizer–BioNTech vaccines use modified RNA, incorporating an mRNA nucleotide called pseudouridine — which is similar to uridine but contains a natural modification — in place of uridine itself. This is thought to circumvent the body's inflammatory reactions to foreign mRNA. CureVac's vaccine uses normal uridine and relies on altering the sequence of RNA letters in a way that does not affect the protein it codes for, but helps the vaccine to evade immune detection.



Mix-and-match COVID vaccines trigger potent immune response

Proponents of modified mRNA have long argued that the chemical adjustment is integral to the success of the vaccine technology. Drew Weissman, an immunologist at the University of Pennsylvania in Philadelphia who co-discovered the importance of pseudouridine in this context in the mid-2000s⁴, describes it as the “best platform for antibody and neutralization levels”. In light of the new CureVac data, many scientists who spoke to *Nature* agree.

“Modified mRNA has won this game,” says Rein Verbeke, an mRNA-vaccine researcher at Ghent University in Belgium.

There are a few other possible explanations for CureVac’s tolerability problems. Structural differences in the non-coding regions of the CureVac sequence could play a part. Alternatively, the higher storage temperature of CureVac’s jab might have accelerated the breakdown of mRNA in the vial, yielding pieces of genetic code that would raise immune hackles. And if any impurities were introduced during the company’s manufacturing process, these would, in principle, have the same effect.

So for some scientists it remains too early to draw conclusions. “The jury is still out on which of these is a better technology,” says Jeffrey Ulmer, a former pharmaceutical executive who now consults on vaccine research issues. He predicts that both modified and unmodified mRNA will be useful in different contexts. “It could be that there’s not a one-size-fits-all solution to everything.”

CureVac hopes that its vaccine — or at least its unmodified mRNA technology — might yet deliver. The company is continuing its trial and expects a final analysis in the next few weeks. On a public health level, even if the vaccine fails, “I don’t think it’s going to set the world back much”, says Jacob Kirkegaard, a vaccine-supply expert at the Peterson Institute for International Economics, a think-tank in Washington DC.



Why COVID vaccines are so difficult to compare

He points out that another second-generation vaccine that offers many of the same logistical selling points as CureVac's, such as long-term refrigerator storage, has stood up to the variant challenge well. Earlier this week, Novavax in Gaithersburg, Maryland, reported that its protein-based vaccine was more than 90% effective at preventing COVID-19 in a large US trial, run at a time that the Alpha variant was prevalent.

The scale of production of other vaccines more than makes up for the lack of CureVac's product, Kirkegaard says.

CureVac, in collaboration with London-based GlaxoSmithKline, also has a second-generation COVID-19 vaccine in the works that, like its predecessor, uses unmodified mRNA, but has been fine-tuned so that it elicits levels of neutralizing antibodies that are around ten times higher, according to data from rat and monkey studies. "Our optimization has never stopped," says CureVac's chief technology officer Mariola Fotin-Mleczek. "It's too early to say unmodified, natural messenger RNA is not an option." Human trials are due to launch later this year.

Nature **594**, 483 (2021)

doi: <https://doi.org/10.1038/d41586-021-01661-0>

References

1. 1.

Sheikh, A., McMenamin, J., Taylor, R. & Robertson, C. *Lancet* [https://doi.org/10.1016/S0140-6736\(21\)01358-1](https://doi.org/10.1016/S0140-6736(21)01358-1) (2021).

[Article](#) [Google Scholar](#)

2. 2.

Abu-Raddad, L. J., Chemaitelly, H. & Butt, A. A. *N. Engl. J. Med.* <https://doi.org/10.1056/NEJMc2104974> (2021).

[PubMed](#) [Google Scholar](#)

3. 3.

Kremsner, P. *et al.* Preprint at MedRxiv
<https://doi.org/10.1101/2020.11.09.20228551> (2020).

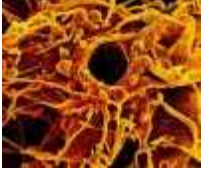
4. 4.

Karikó, K., Buckstein, M., Ni, H. & Weissman, D. *Immunity* **23**, 165–175 (2005).

[PubMed](#) [Article](#) [Google Scholar](#)

[Download references](#)

Related Articles

-  [Six months of COVID vaccines: what 1.7 billion doses have taught scientists](#)
-  [Scientists zero in on long-sought marker of COVID-vaccine efficacy](#)
-  [Mix-and-match COVID vaccines trigger potent immune response](#)



- [**COVID vaccines and blood clots: five key questions**](#)



- [**WHO approval of Chinese CoronaVac COVID vaccine will be crucial to curbing pandemic**](#)



- [**Why COVID vaccines are so difficult to compare**](#)



- [**Rare COVID reactions might hold key to variant-proof vaccines**](#)

Subjects

- [SARS-CoV-2](#)
- [Vaccines](#)

Jobs from Nature Careers

- - - [All jobs](#)
 - - [Laboratory Research Scientist](#)

[Francis Crick Institute](#)

[London, United Kingdom](#)

[JOB POST](#)

- [**Bachelor of Science in Computer Engineering \(f/m/d\)**](#)

[Helmholtz-Zentrum Berlin for Materials and Energy \(HZB\)](#)

[Berlin, Germany](#)

[JOB POST](#)

- [**Laboratory Engineer / Scientific and Technical Head of Reactor Technology \(f/m/x\)**](#)

[Helmholtz Centre for Environmental Research \(UFZ\)](#)

[Leipzig, Germany](#)

[JOB POST](#)

- [**Administrative Assistant/Internal Event Coordinator**](#)

[Oklahoma Medical Research Foundation \(OMRF\)](#)

[Oklahoma City, United States](#)

[JOB POST](#)

[Download PDF](#)

Related Articles



- Six months of COVID vaccines: what 1.7 billion doses have taught scientists



- Scientists zero in on long-sought marker of COVID-vaccine efficacy



- Mix-and-match COVID vaccines trigger potent immune response



- COVID vaccines and blood clots: five key questions



- WHO approval of Chinese CoronaVac COVID vaccine will be crucial to curbing pandemic



- Why COVID vaccines are so difficult to compare



- Rare COVID reactions might hold key to variant-proof vaccines

Subjects

- [SARS-CoV-2](#)
 - [Vaccines](#)
-

This article was downloaded by **calibre** from <https://www.nature.com/articles/d41586-021-01661-0>

| [Section menu](#) | [Main menu](#) |

- NEWS
- 16 June 2021

Mars helicopter kicks up ‘cool’ dust clouds — and unexpected science

Videos of the surprising phenomenon could help researchers to better understand natural ‘dust devils’ blowing across the red planet.

- [Alexandra Witze](#)
 1. Alexandra Witze
[View author publications](#)

You can also search for this author in [PubMed](#) [Google Scholar](#)





•

[Download PDF](#)

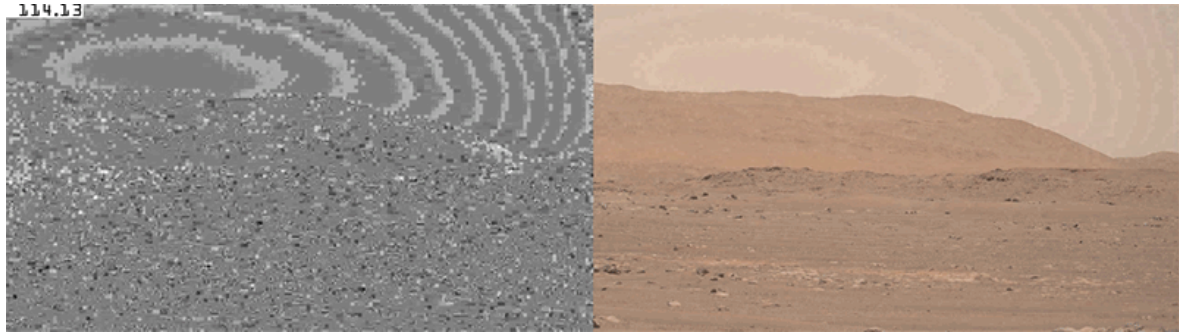


NASA's Ingenuity helicopter is the first spacecraft to successfully achieve controlled flight on another planet. Credit: NASA/JPL-Caltech/ASU/MSSS

Ingenuity, NASA's pint-sized Mars helicopter, has kicked up some surprising science on its flights over the red planet. When whizzing through the Martian air, its blades sometimes stir up a dust cloud that envelops and travels along with the tiny chopper.

In several videos of Ingenuity's flights, planetary scientists have seen dust whirling beneath the helicopter's rotors — even when Ingenuity is flying as high as 5 metres above the Martian surface. That suggests that dust can get lifted and transported in the thin Martian air more easily than researchers had suspected.

"It's really cool," says Mark Lemmon, a planetary scientist at the Space Science Institute in Boulder, Colorado.



On its fourth flight, on 30 April, Ingenuity kicked up a large bolus of dust that travelled along with the helicopter as it flew, as shown in this video taken by Perseverance. Credit: NASA/JPL-Caltech/ASU/MSSS/SSI

Mars is a dusty planet, so it's not surprising that the helicopter kicks up dust during takeoff and landing, much as helicopters on Earth do when operating in the desert. Engineers designed Ingenuity to operate with a lot of dust blowing around as it takes off and lands. But scientists are surprised by how the dust interacts with the drone during flight. By watching how Ingenuity entrains dust as it flies, researchers can better understand the dynamics of Mars's thin atmosphere, where tornado-like 'dust devils' often form when the Sun heats the air and afternoon winds begin to blow.

"There's an unanticipated atmospheric science experiment coming out of this," says Jim Bell, a planetary scientist at Arizona State University in Tempe.

Ingenuity is what NASA calls a technology demonstration, whose only goal is to show that flight on Mars is possible. So "anything we can learn from it scientifically is icing on the cake", says Brian Jackson, a physicist at Boise State University in Idaho who studies Martian dust.

Bizarre dust clouds

Space scientists and amateur image processors have been analysing images and videos of the helicopter that NASA has posted online.

The agency's Perseverance rover [carried Ingenuity to the surface of Mars](#) in February. Its job is to roll around Jezero Crater and [explore the rocks](#) that

were once part of an ancient lake, to look for signs of past life. In April, Ingenuity [became the first machine](#) to achieve powered flight on another planet. It has made seven flights so far.



Dust devils like this one, 20 kilometres high and captured by NASA's Mars Reconnaissance Orbiter, regularly swirl across the Martian surface. Credit: NASA/JPL-Caltech/UA

On the first two flights, Ingenuity [kicked up a fair amount of dust](#) as it rose 3 to 5 metres above the surface, but it didn't travel far from its takeoff point and the dust cloud phenomenon wasn't pronounced. On its third flight, the helicopter rose 5 metres and then flew north from its takeoff point, kicking up a cloud from several light-coloured patches it flew over on the Martian surface. Those patches might be small hollows where dust has collected in the Martian landscape, says Lemmon. "A lot more dust comes up at that moment" when the helicopter flies over them, he says.

Ingenuity's blades spin at more than 2,400 revolutions per minute — a dizzying rate necessary for the helicopter to achieve lift in the Martian

atmosphere, which is just 1% the density of Earth's.



Lift off! First flight on Mars launches new way to explore worlds

It was Ingenuity's fourth flight, on 30 April, that really intrigued scientists. A video, recorded by Perseverance from a vantage point nearby, shows the helicopter rise, disappear from view, and then re-appear while enveloped in an enormous cloud of dust following a 133-metre flight.

The video confirms that Ingenuity was flying along with the 3.5-metre-per-second wind, says Håvard Grip, the helicopter's chief pilot at the Jet Propulsion Laboratory in Pasadena, California. "The dust was getting carried beneath us," he says.

Lemmon plans to compare tracks on the Martian surface left behind by natural dust devils with those where the helicopter kicked up the most dust. That will help researchers to better understand how winds blowing across Mars can lift dust and spin it into dust devils. The Martian atmosphere is so thin that scientists have had a hard time explaining how so much dust gets aloft, says Jackson. "We have to know how that first step in the process works," he says.



Mars video reveals Perseverance rover's daring touchdown

Ingenuity ran into some trouble on its sixth flight, on 22 May; it began wobbling because of a glitch in its navigation system, but managed to land safely. On its seventh flight, on 8 June, it flew 106 metres with no problem.

The helicopter has been wildly successful in demonstrating flight on other worlds, says Grip. In the future, bigger helicopters could travel long distances and scout out areas where wheeled vehicles cannot travel. "It's just so clear that this is definitely a way that could be used to explore Mars," he says.

Ingenuity will now tag along as Perseverance begins to roll south from its landing site. The helicopter will probably make additional flights every two weeks or so from now until the end of August, when operations are expected to draw to a close.

Perseverance has been exploring the rocks that make up Jezero Crater's ancient lake bed. Team scientists are in the process of deciding where to drill to collect their first geological sample — either from the fractured rock that makes up the crater floor, or from a dune-laden region nearby. It will be the first in a collection of rock cores that are destined for pickup by future spacecraft, which will fly the material back to Earth — in the first-ever sample return from Mars.

Nature **594**, 484 (2021)

doi: <https://doi.org/10.1038/d41586-021-01537-3>

Related Articles



- [Lift off! First flight on Mars launches new way to explore worlds](#)



- [Mars video reveals Perseverance rover's daring touchdown](#)



- [A month on Mars: what NASA's Perseverance rover has found so far](#)



- [The hunt for life on Mars: A visual guide to NASA's latest mission](#)

Subjects

- [Planetary science](#)
- [Atmospheric science](#)

[Jobs from Nature Careers](#)

-

- - [All jobs](#)
- - **[Laboratory Research Scientist](#)**
[Francis Crick Institute](#)
[London, United Kingdom](#)
[JOB POST](#)
 - **[Bachelor of Science in Computer Engineering \(f/m/d\)](#)**
[Helmholtz-Zentrum Berlin for Materials and Energy \(HZB\)](#)
[Berlin, Germany](#)
[JOB POST](#)
 - **[Laboratory Engineer / Scientific and Technical Head of Reactor Technology \(f/m/x\)](#)**
[Helmholtz Centre for Environmental Research \(UFZ\)](#)
[Leipzig, Germany](#)
[JOB POST](#)
 - **[Administrative Assistant/Internal Event Coordinator](#)**
[Oklahoma Medical Research Foundation \(OMRF\)](#)
[Oklahoma City, United States](#)

JOB POST

[Download PDF](#)

Related Articles



- [Lift off! First flight on Mars launches new way to explore worlds](#)



- [Mars video reveals Perseverance rover's daring touchdown](#)



- [A month on Mars: what NASA's Perseverance rover has found so far](#)



- [The hunt for life on Mars: A visual guide to NASA's latest mission](#)

Subjects

- [Planetary science](#)
- [Atmospheric science](#)

| [Section menu](#) | [Main menu](#) |

- NEWS
- 11 June 2021

Massive science-funding bill passes US Senate — but China focus worries researchers

Scientists praise the budget boost slated for the National Science Foundation, but worry the legislation could dampen international collaborations.

- [Ariana Remmel](#)
 1. Ariana Remmel
[View author publications](#)

You can also search for this author in [PubMed](#) [Google Scholar](#)





•

[Download PDF](#)



Senator Chuck Schumer, who has championed the Innovation and Competition Act, speaking at a press conference. Credit: Michael Brochstein/ZUMA/Alamy

The US Senate has voted overwhelmingly in favour of legislation that invests heavily in the US National Science Foundation (NSF). But the bill, once aimed primarily at helping the United States to maintain its status as a global leader through direct funding for research and development, now includes amendments aimed at preventing China from stealing or benefitting from US intellectual property — a development that scientists fear could threaten international collaborations.

In another major revision, Senate advocates for other US agencies that conduct research, such as the Department of Energy (DOE), have chipped away at the funding allotment originally intended for the NSF, arguing that they also deserve some of the money.

But if the legislation passes the US House of Representatives, the NSF could still see a doubling of its budget over five years. Given the agency's large role in funding basic research, science-policy researchers are praising this outcome.



[How a historic funding boom might transform the US National Science Foundation](#)

Although they have concerns, researchers agree that an investment of this size in US scientific research is long overdue: funding of US scientific research has not kept pace with the nation's economic growth. "Even if it weren't for the competition with China, the American people deserve the benefits that come from these kinds of investments of taxpayer money," says Neal Lane, a science-policy researcher with the Baker Institute for Public Policy at Rice University in Houston, who is a former NSF director.

The bill "will jump-start American competitiveness, and make one of the most significant government investments in American innovation and manufacturing in generations", said Senate majority leader Chuck Schumer, who co-sponsored the legislation, which passed on 8 June.

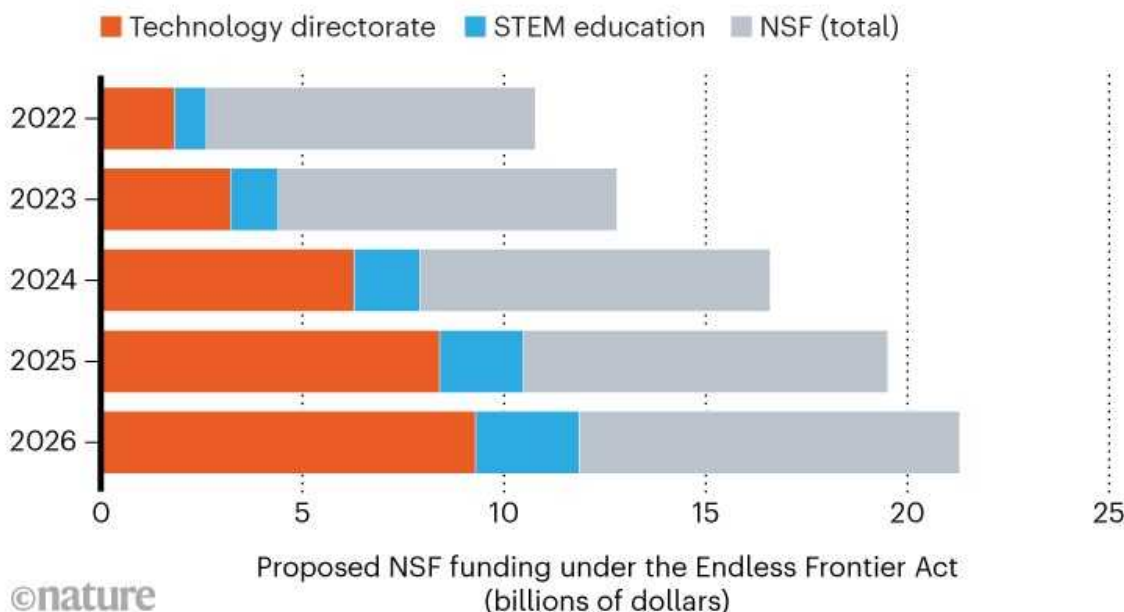
Windfall downsized

The legislation began in 2020 as the Endless Frontier Act (EFA), which proposed investing US\$100 billion to create a technology directorate at the NSF, an agency that funds almost a quarter of all federally backed basic research at US universities. The directorate would act as a hub for translating fundamental scientific discoveries into commercial technologies.

Because the NSF's budget had risen only incrementally since the agency's inception 70 years ago, many researchers and policy experts were elated to see [renewed interest in the agency](#). But the focus on the NSF was quickly overshadowed during early debates in Congress, when senators of states with national laboratories, and those who were members of committees representing agencies such as the DOE, began vying for a slice of the multibillion-dollar pie. At the same time, US lawmakers questioned whether the legislation included adequate security measures to protect against espionage from global competitors, such as China.

BUDGET BREAKDOWN

The US National Science Foundation is poised to receive US\$81 billion over 5 years, with designated funding for a technology directorate and science workforce education and development. This would more than double the agency's current budget.



Source: Endless Frontier Act (2021)

Eventually, the Senate incorporated a revised version of the EFA into a much larger legislative package called the US Innovation and Competition Act (I&CA), which includes the provisions that curtail — and increase scrutiny of — Chinese involvement in government-funded research. The EFA now authorizes a \$120-billion cash infusion to multiple US science agencies. The NSF would receive \$81 billion of that amount over 5 years; 36% of that

would be designated for the technology directorate and 10% for science, technology, engineering and mathematics (STEM) education and workforce development (see ‘Budget breakdown’). The remaining research funding would go to NASA, the DOE and the Department of Commerce.

Some are disheartened by the downsizing of the investment in an NSF technology directorate. But others who had worried that an intense focus on the directorate would give short shrift to basic research and therefore undercut the central mission of the NSF see advantages in the new form of the bill. For instance, Lane says the decreased allotment for the directorate gives the agency more discretion and flexibility to fund projects that could lead to innovative technologies both through basic science and applied-research initiatives.

Staying competitive

Increased funding to the NSF is an important investment for the United States, especially as China continues its own strong investment in infrastructure for research and development, says Lane. China awards more bachelor’s degrees in science and engineering than do the United States, the European Union and Japan combined. And [researchers in China publish more articles](#) than do those in the United States, increasingly in high-impact journals.



China is closing gap with United States on research spending

But lawmakers reviewing the EFA say that a huge boost in funding for the NSF might end up benefiting China, too — and this concerns them. Over the past few years, [the United States](#) and [countries such as Australia](#) have taken [steps to safeguard technology and intellectual property](#) that has been developed through international collaborations with China. The actions have come partly in response to cases of alleged intellectual-property theft and concern regarding Chinese President Xi Jinping's '[military–civil’ fusion strategy](#)', which aims to co-opt university research in China for military use.

"I don't want the taxpayer funds to go in the front door and then to have the research go out the back door to China or other adversaries," said senator Rob Portman, a ranking member on the Senate Committee for Homeland Security and Government Affairs, in a recent Senate floor proceeding. His additions to the I&CA include the Safeguarding American Innovation Act, which would establish a Federal Research Security Council in the Office of Management and Budget to develop policies governing grants for research and development.

Many university officials support the funding increase for US science, but they're keeping a close eye on provisions in the legislation aimed at curbing foreign influence on research. This includes a ban on federally funded researchers participating in foreign talent-recruitment programs, such as China's Thousand Talents Plan, which recruits researchers to share their expertise and knowledge.

The Association of Public and Land-Grant Universities (APLU) in Washington DC, an advocacy group for university research, is particularly concerned about a requirement that foreign gifts to universities of \$1 million or more be reviewed by a committee that normally scrutinizes massive business investments from foreign sources. "It's not designed to look at short-term contracts or gifts to universities," says Deborah Altenburg, associate vice-president for research policy and government affairs at APLU. She worries that, if the amendment becomes law, the review process for universities could be prohibitively expensive and time-consuming.



Biden pursues giant boost for science spending

Multiple congressional investigations have highlighted the need for increased awareness of national security concerns in partnerships with China and other foreign nations. But Denis Simon, executive director of the Center for Innovation Policy at the Duke University School of Law in Durham, North Carolina, cautions that being too reactive to China's investment strategies could distract legislators from setting their own agenda for the future of research in the country. The United States is at the forefront of international efforts to tackle global challenges — including climate change and the COVID-19 pandemic — and it is to the country's benefit to collaborate with international partners such as China to find sustainable solutions, he says. Simon, who once served as the executive vice-chancellor of Duke Kunshan University in China, says that increased scrutiny on Chinese scientists who collaborate with US research projects is already sending "tremors through the system".

A long road lies ahead before the I&CA might become law, including reconciliation proceedings with similar legislation proposed in the House of Representatives. Also uncertain at this stage is how the \$120-billion boost to US agencies will be paid for, which Congress will decide.

Nature **594**, 485 (2021)

doi: <https://doi.org/10.1038/d41586-021-01559-x>

Related Articles

-  [How a historic funding boom might transform the US National Science Foundation](#)
-  [NSF grant changes raise alarm about commitment to basic research](#)
-  [Biden pursues giant boost for science spending](#)
-  [China is closing gap with United States on research spending](#)

Subjects

- [Scientific community](#)
- [Politics](#)
- [Policy](#)
- [Funding](#)

[Jobs from Nature Careers](#)

- - - [All jobs](#)

o

- **Laboratory Research Scientist**

Francis Crick Institute

London, United Kingdom

JOB POST

- **Bachelor of Science in Computer Engineering (f/m/d)**

Helmholtz-Zentrum Berlin for Materials and Energy (HZB)

Berlin, Germany

JOB POST

- **Laboratory Engineer / Scientific and Technical Head of Reactor Technology (f/m/x)**

Helmholtz Centre for Environmental Research (UFZ)

Leipzig, Germany

JOB POST

- **Administrative Assistant/Internal Event Coordinator**

Oklahoma Medical Research Foundation (OMRF)

Oklahoma City, United States

JOB POST

Download PDF

Related Articles

-  [How a historic funding boom might transform the US National Science Foundation](#)
-  [NSF grant changes raise alarm about commitment to basic research](#)
-  [Biden pursues giant boost for science spending](#)
-  [China is closing gap with United States on research spending](#)

Subjects

- [Scientific community](#)
- [Politics](#)
- [Policy](#)
- [Funding](#)

This article was downloaded by **calibre** from <https://www.nature.com/articles/d41586-021-01559-x>

- NEWS EXPLAINER
- 17 June 2021

How three missions to Venus could solve the planet's biggest mysteries

A renewed focus on our planetary neighbour could help to answer major questions about its atmosphere and geology.

- [Jonathan O'Callaghan](#)
 1. Jonathan O'Callaghan
[View author publications](#)

You can also search for this author in [PubMed](#) [Google Scholar](#)





•

[Download PDF](#)



In three newly-approved missions to Venus, scientists will probe the planet's atmosphere and geology. Credit: JSC/NASA

After years of waiting, an armada of spacecraft are headed to Venus. US scientists were thrilled earlier this month when NASA approved not one, but [two new missions](#) to our closest planetary neighbour. Now, Europe has followed suit and approved its own mission. The explorations raise the prospect that major questions about this planet — from whether it once had oceans and was therefore habitable to whether it still has active volcanoes — could finally be answered.

On 2 June, NASA announced it would send two spacecraft to Venus this decade: VERITAS, an orbiter that will map the planet's surface, and DAVINCI+, which includes a probe that will dive into Venus's atmosphere. On 10 June, the European Space Agency (ESA) [announced its own orbiter](#), EnVision, that would launch in the early 2030s to take high-resolution radar images of the planet's surface.



Venus is Earth’s evil twin — and space agencies can no longer resist its pull

“We’re delighted that all our hard work has paid off,” says planetary scientist Colin Wilson at the University of Oxford, UK, one of the deputy lead scientists on EnVision.

NASA’s pair of spacecraft will be its first missions to Venus since its Magellan orbiter in 1989; EnVision is ESA’s first since [Venus Express in 2005](#). Only one probe currently orbits the planet: Japan’s Akatsuki spacecraft, which arrived in 2015 and is studying the planet’s atmosphere. “Venus has been a forgotten planet for too long,” says ESA’s Håkan Svedhem, the former project scientist on Venus Express.

As the planetary-science community celebrates the approvals, *Nature* explores the questions that scientists hope these missions might answer.

Why are Venus and Earth so different?

One of the major questions about Venus is why, despite being a similar size to Earth and a similar distance from the Sun, is it a [hellish locale](#) with a poisonous atmosphere composed mostly of carbon dioxide and surface temperatures that are hot enough to melt lead, rather than a pleasant oasis for life.

“Why is Venus, our sibling planet, not our twin planet?” says Paul Byrne, a planetary scientist at North Carolina State University in Raleigh. “How is it

you can have a world that's functionally the same as Earth, but with a vastly different history?"

To find out, scientists will use the missions to probe the planet's geological past to see how it evolved. VERITAS and EnVision will both be crucial in that aim — each will study the geological record of the planet by imaging its surface with their radar instruments.

The DAVINCI+ mission, meanwhile, will include an orbiter that images the planet using ultraviolet and infrared light. It will also drop a small spherical probe into the atmosphere. This will sample the atmosphere, including looking for unreactive noble gases such as helium and xenon, which persist for a long time. "They are clues as to the early formation and evolution of the planet," says Wilson. "Do they come from magma in the interior, were they there from formation, were they brought by comets?"

Did Venus once have oceans?

Working out whether Venus ever had bodies of liquid water on its surface is crucial to understanding why Venus and Earth are different. Astronomers can see [hints of past water](#) in the planet's atmosphere, but it's unclear whether this water comes from ancient oceans on the surface that were lost as the planet warmed, or whether water existed only as vapour early in the planet's history. The former would suggest the planet was once habitable, like Earth.



Prospects for life on Venus fade — but aren't dead yet

DAVINCI+ will be useful in answering this question when it studies the planet's atmosphere. Its probe will descend for about an hour, sampling the atmosphere up to every 100 metres at lower altitudes and making high-precision measurements to reveal which gases are present, says James Garvin, chief scientist for NASA's Goddard Space Flight Center in Greenbelt, Maryland, and mission lead for DAVINCI+. This will surpass data on Venus's atmosphere taken by the Soviet Union's [Venera probes](#) in the 1960s, 1970s and 1980s.

“The chemical signatures will tell us the history, permanence and nature of past oceans,” he says. “Those will provide boundary conditions for everyone. Then we can tailor the big climate models, and ask questions with other missions like VERITAS and EnVision, with their global mapping.”

Did Venus have continents?

About 7% of Venus is covered in [highland regions](#) known as tesserae, plateaus that rise above the surrounding surface. These “might be the equivalent of continents on Earth”, says Byrne.

To find out, VERITAS will study the composition of the tesserae, including comparing their content of the volcanic rock basalt with regions at lower elevation. “On Earth when continents form, the massive amounts of basalt in the oceanic crust melt in the presence of water,” says Suzanne Smrekar, the mission lead for VERITAS at NASA’s Jet Propulsion Laboratory in Pasadena, California. “If we can test this hypothesis, we can show that these huge plateaus are effectively fingerprints of a time when water was present,” with the tesserae being the continental landmasses that were once surrounded by water.

The DAVINCI+ probe will also descend over a tessera called Alpha Regio, taking up to 500 images as it falls to the surface. Although the spacecraft will eventually be destroyed, there is a small chance that it could survive on the surface for several minutes before it is wiped out by the intense pressure and temperature. These pictures of the tessera could be enlightening. “Our final images should have a resolution of tens of centimetres,” says Garvin.



An artist's impression of the ESA mission EnVision, which will take high-resolution radar images of Venus's surface. Credit: ESA/VR2Planets/DamiaBouic

Is Venus still volcanically active?

Earlier probes have shown that volcanoes are present on Venus, but it's unclear whether any have been geologically active in the past few thousand years — or whether they are [still active today](#). Both VERITAS and EnVision will help to answer this question by mapping the surface. EnVision's high-resolution images in particular are expected to reveal previously unseen surface features.

The mapping will include looking for volcanic features such as lava flows, and the amount of weathering they have encountered could reveal when they erupted. "Fresh lava flows may appear particularly dark or black," says Wilson.

The Akatsuki spacecraft has seen recent changes in the amount of ultraviolet light absorbed by Venus's atmosphere, which could be an indicator of recent volcanic activity. "The changing climate of Venus [today] may depend on volcanic activity," says Masato Nakamura at the Institute of Space and Astronautical Science in Sagamihara, Japan, who is the project manager for Akatsuki.

Is there phosphine on Venus?

Last year, scientists announced that they had [detected phosphine — a compound of phosphorus and a possible signature of life — on Venus](#). How this would have been produced was unclear, but there was a tantalizing possibility that it could have been made by microbial life in the atmosphere.

The result has since been [called into question](#), and the presence of phosphine has been hotly debated. The argument might ultimately be put to rest with DAVINCI+, which might detect phosphine when it samples the atmosphere.

"If there's a ton of phosphine, we'll be able to measure it," says Garvin.

Is there 'snow' on Venus?

The planet's mountaintops above 2.6 kilometres look strangely reflective, like those on Earth do, "where you have snow and frost deposited above a certain altitude", says Wilson. But Venus is much too hot for water to exist,

leading scientists to wonder whether the reflective regions might be something else.

One possibility is a substance called semiconductor snow — a mix of exotic metals such as bismuth tellurium and sulfur, which can condense at these higher altitudes and are all known to be produced by volcanic activity. DAVINCI+ might detect these materials in the atmosphere, whereas VERITAS and EnVision will search for deposits near any volcanic vents.

Perhaps one day, researchers will sample these mountaintops directly, with a lander. “It’s certainly something which is technically possible,” says Wilson.

Nature **594**, 486-487 (2021)

doi: <https://doi.org/10.1038/d41586-021-01634-3>

Related Articles

-  [Prospects for life on Venus fade — but aren't dead yet](#)
-  [Venus is Earth's evil twin — and space agencies can no longer resist its pull](#)
-  [Life on Venus? Scientists hunt for the truth](#)

Subjects

- [Astronomy and astrophysics](#)
- [Planetary science](#)

Jobs from Nature Careers

- - - [All jobs](#)
 - - [Laboratory Research Scientist](#)
[Francis Crick Institute](#)
[London, United Kingdom](#)
[JOB POST](#)
 - [Bachelor of Science in Computer Engineering \(f/m/d\)](#)
[Helmholtz-Zentrum Berlin for Materials and Energy \(HZB\)](#)
[Berlin, Germany](#)
[JOB POST](#)
 - [Laboratory Engineer / Scientific and Technical Head of Reactor Technology \(f/m/x\)](#)
[Helmholtz Centre for Environmental Research \(UFZ\)](#)
[Leipzig, Germany](#)
[JOB POST](#)
 - [Administrative Assistant/Internal Event Coordinator](#)
[Oklahoma Medical Research Foundation \(OMRF\)](#)

[Oklahoma City, United States](#)

[JOB POST](#)

[Download PDF](#)

Related Articles



- [Prospects for life on Venus fade — but aren't dead yet](#)



- [Venus is Earth's evil twin — and space agencies can no longer resist its pull](#)



- [Life on Venus? Scientists hunt for the truth](#)

Subjects

- [Astronomy and astrophysics](#)
- [Planetary science](#)

This article was downloaded by **calibre** from <https://www.nature.com/articles/d41586-021-01634-3>

- NEWS FEATURE
- 22 June 2021

How ancient people fell in love with bread, beer and other carbs

Well before people domesticated crops, they were grinding grains for hearty stews and other starchy dishes.

- [Andrew Curry](#) ⁰

1. Andrew Curry

1. Andrew Curry is a science journalist in Berlin.

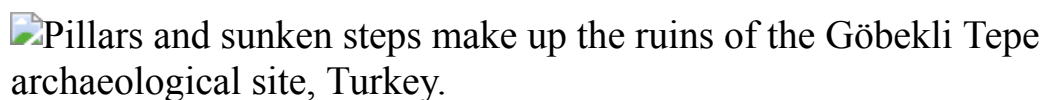
[View author publications](#)

You can also search for this author in [PubMed](#) [Google Scholar](#)





•



Grains were on the menu at feasts that took place more than 11,000 years ago at Göbekli Tepe in Turkey — one of the world's oldest temples. Credit: Vincent J. Musi

[Download PDF](#)

On a clear day, the view from the ruins of Göbekli Tepe stretches across southern Turkey all the way to the Syrian border some 50 kilometres away. At 11,600 years old, this mountaintop archaeological site has been described

as the world's oldest temple — so ancient, in fact, that its T-shaped pillars and circular enclosures pre-date pottery in the Middle East.

The people who built these monumental structures were living just before a major transition in human history: the Neolithic revolution, when humans began farming and domesticating crops and animals. But there are no signs of domesticated grain at Göbekli Tepe, suggesting that its residents hadn't yet made the leap to farming. The ample animal bones found in the ruins prove that the people living there were accomplished hunters, and there are signs of massive feasts. Archaeologists have suggested that mobile bands of hunter-gatherers from all across the region came together at times for huge barbecues, and that these meaty feasts led them to build the impressive stone structures.

Now that view is changing, thanks to researchers such as Laura Dietrich at the German Archaeological Institute in Berlin. Over the past four years, Dietrich has discovered that the people who built these ancient structures were fuelled by vat-fulls of porridge and stew, made from grain that the ancient residents had ground and processed on an almost industrial scale¹. The clues from Göbekli Tepe reveal that ancient humans relied on grains much earlier than was previously thought — even before there is evidence that these plants were domesticated. And Dietrich's work is part of a growing movement to take a closer look at the role that grains and other starches had in the diet of people in the past.

The researchers are using a wide range of techniques — from examining microscopic marks on ancient tools to analysing DNA residues inside pots. Some investigators are even experimentally recreating 12,000-year-old meals using methods from that time. Looking even further back, evidence suggests that some people ate starchy plants more than 100,000 years ago. Taken together, these discoveries shred the long-standing idea that early people subsisted mainly on meat — a view that has fuelled support for the palaeo diet, popular in the United States and elsewhere, which recommends avoiding grains and other starches.

The new work fills a big hole in the understanding of the types of food that made up ancient diets. “We’re reaching a critical mass of material to realize

there's a new category we've been missing," says Dorian Fuller, an archaeobotanist at University College London.

A garden of grinding stones

Dietrich's discoveries about the feasts at Göbekli Tepe started in the site's 'rock garden'. That's the name archaeologists dismissively gave a nearby field where they dumped basalt grinding stones, limestone troughs and other large pieces of worked stone found amid the rubble.

As excavations continued over the past two decades, the collection of grinding stones quietly grew, says Dietrich. "Nobody thought about them." When she started cataloguing them in 2016, she was stunned at the sheer numbers. The 'garden' covered an area the size of a football field, and contained more than 10,000 grinding stones and nearly 650 carved stone platters and vessels, some big enough to hold up to 200 litres of liquid.



Amaia Arranz-Otaegui (right) examines grain growing in northeastern Jordan, near the Shubayqa 1 archaeological site where she and her

colleagues found evidence that bread had been baked there some 14,000 years ago, several millennia before domestication of grains. Credit: Joe Roe

“No other settlement in the Near East has so many grinding stones, even in the late Neolithic, when agriculture was already well-established,” Dietrich says. “And they have a whole spectrum of stone pots, in every thinkable size. Why so many stone vessels?” She suspected that they were for grinding grain to produce porridge and beer. Archaeologists had long argued that stone vats at the site were evidence of occasional ceremonial beer consumption at Göbekli Tepe, but thought of it as a rare treat.

Teasing answers from the stones there and at other sites is not a simple process. In archaeology, it is much easier to spot evidence of meat meals than ones based on grains or other plants. That’s because the bones of butchered animals fossilize much more readily than do the remains of a vegetarian feast. The fragile nature of ancient plant remains makes archaeobotany — the study of how ancient people used plants — tricky, time-consuming work. Researchers use sieves, fine mesh and buckets to wash and separate debris from archaeological sites. Tiny bits of organic material such as seeds, charred wood and burnt food float to the top, while heavier dirt and rocks sink.

The vast majority of what emerges amounts to the raw ingredients, the bits that never made it into a pot. By identifying and counting grass seeds, grain kernels and grape pips mixed into the soil, archaeobotanists can tell what was growing in the area around the settlement. Unusual amounts of any given species offer circumstantial evidence that those plants might have been used, and perhaps cultivated, by people in the past.



Move over, DNA: ancient proteins are starting to reveal humanity's history

Some of the earliest evidence for plant domestication, for example, comes from einkorn wheat grains recovered from a site near Göbekli Tepe that are subtly different in shape and genetics from wild varieties². At Göbekli Tepe itself, the grains look wild, suggesting that domestication hadn't taken place or was in its earliest stages. (Archaeologists suspect that it might have taken centuries for domestication to alter the shape of grains.)

Direct proof that plants landed in cooking pots is harder to come by. To work out what people were eating, archaeologists are turning to previously ignored sources of evidence, such as charred bits of food. They're the mistakes of the past: stews and porridge left on the fire for too long, or bits of bread dropped in the hearth or burnt in the oven. “Anyone who’s cooked a meal knows sometimes it burns,” says Lucy Kubiak-Martens, an archaeobotanist working for BIAX Consult Biological Archaeology & Environmental Reconstruction in Zaandam, the Netherlands.

Until the past few years, these hard-to-analyse remnants of ruined meals were rarely given a second look. “It’s just a difficult material. It’s fragile, ugly stuff,” says Andreas Heiss, an archaeobotanist at the Austrian Academy of Sciences in Vienna. “Most researchers just shied away.” Pottery sherds encrusted with food remains were cleaned off or discarded as ‘crud ware’,

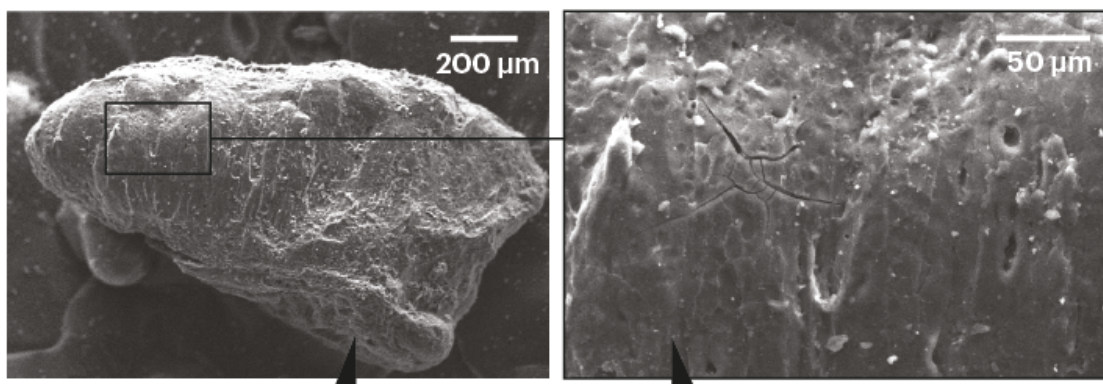
and charred bits of food were dismissed as unanalysable ‘probable food’ and shelved or thrown out.

The first step towards changing that perception was to go back to the kitchen. That was the inspiration of Soultana Valamoti, an archaeobotanist at the Aristotle University of Thessaloniki in Greece who, not coincidentally, is also a passionate home cook. Valamoti spent the early years of her career toting buckets and sieves from one excavation site to another across Greece, all while combing museum storerooms for ancient plant remains to analyse. The work convinced her there was an untapped wealth of evidence in burnt food remains — if she could find a way to identify what she was looking at.

More than 20 years ago, Valamoti decided to turn her lab into an experimental kitchen. She ground and boiled wheat to make bulgur, and then charred it in an oven to simulate a long-ago cooking accident (see ‘Fast food of the Bronze Age’). By comparing the burnt remains to 4,000-year-old samples from a site in northern Greece, she was able to show that the ancient and modern versions matched, and that this way of preparing grain had its roots in the Bronze Age³.

FAST FOOD OF THE BRONZE AGE

Bulgur-like grain fragments found at a roughly 4,000-year-old site in northern Greece have microscopic features resembling those of modern samples that had been parboiled and charred in experiments. The ancient grain was apparently boiled then dried to speed up later cooking.



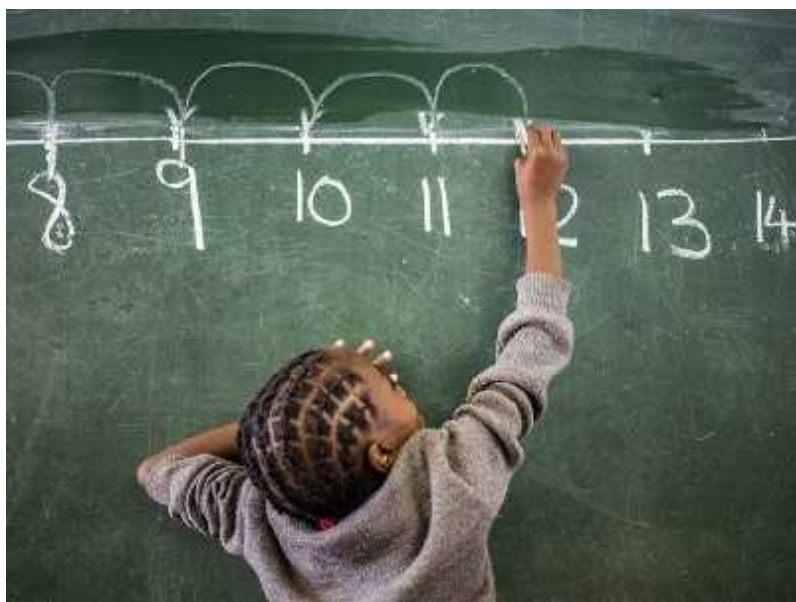
Scanning electron microscope reveals surface textures of grain fragment.

Smooth, almost glassy, surface indicates that the grain gelatinized, perhaps from parboiling.

Credit: Soultana Maria Valamoti *et al./J. Archaeol. Sci.*

Over the decade that followed, she continued experimenting. Beginning in 2016, a European Research Council grant allowed her to create a crusty, charred reference collection of more than 300 types of ancient and experimental samples. After making bread dough, baked bread, porridge, bulgur and a traditional food called trachana from heirloom wheat and barley, Valamoti chars each sample in an oven under controlled conditions.

She then magnifies the crispy results by 750 to 1,000 times to identify the tell-tale changes in cell structure caused by different cooking processes. Whether boiled or fresh, ground or whole, dried or soaked, the grains all look different at high magnification. Baking bread leaves tell-tale bubbles behind, for example, whereas boiling grain before charring it gelatinizes the starch, Valamoti says. “And we can see all that under the scanning electron microscope.”



How did Neanderthals and other ancient humans learn to count?

Comparing the ancient samples with her modern experiments, Valamoti has been able to go beyond identifying plant species to reconstruct the cooking methods and dishes of ancient Greece. There is evidence that people in the region have been eating bulgur for at least 4,000 years⁴. By boiling barley or wheat and then drying it for storage and quick rehydration later, “you could

process the harvest in bulk and take advantage of the hot sun”, Valamoti says. “Then you can use it throughout the year. It was the fast food of the past.”

Other researchers are also pursuing ancient cooking mistakes. Charred food remains “are providing us with direct evidence of food”, says Amaia Arranz-Otaegui, an archaeobotanist at the Paris Museum of Natural History. “That’s revolutionary. It’s an unprecedented source of information.”

In the past, it has been difficult for researchers to find hard evidence that our distant ancestors ate plants. “We’ve always suspected starch was in the diet of early hominins and early *Homo sapiens*, but we didn’t have the evidence,” says Kubiak-Martens.

Genetic data support the idea that people were eating starch. In 2016, for example, geneticists reported⁵ that humans have more copies of the gene that produces enzymes to digest starch than do any of our primate relatives. “Humans have up to 20 copies, and chimpanzees have 2,” says Cynthia Larbey, an archaeobotanist at the University of Cambridge, UK. That genetic change in the human lineage helped to shape the diet of our ancestors, and now us. “That suggests there’s a selective advantage to higher-starch diets for *Homo sapiens*. ”



Food remnants resembling bread were found in a hearth at the Shubayqa 1 site in Jordan. Credit: Alexis Pantos

To find supporting evidence in the archaeological record, Larbey turned to cooking hearths at sites in South Africa dating back 120,000 years, picking out chunks of charred plant material — some the size of a peanut. Under the scanning electron microscope, she identified cellular tissue from starchy plants⁶ — the earliest evidence of ancient people cooking starch. “Right through from 120,000 to 65,000 years ago, they’re cooking roots and tubers,” Larbey says. The evidence is remarkably consistent, she adds, particularly compared with animal remains from the same site. “Over time they change hunting techniques and strategies, but still continue to cook and eat plants.”

Early humans probably ate a balanced diet, leaning on starchy plants for calories when game was scarce or hard to hunt. “And being able to find carbohydrates as they moved into new ecologies would have provided important staple foods,” Larbey adds.

Evidence suggests that plants were popular among Neanderthals, too. In 2011, Amanda Henry, a palaeoanthropologist now at Leiden University in the Netherlands, published her findings from dental plaque picked from the teeth of Neanderthals who were buried in Iran and Belgium between 46,000 and 40,000 years ago. Plant microfossils trapped and preserved in the hardened plaque showed that they were cooking and eating starchy foods including tubers, grains and dates⁷. “Plants are ubiquitous in our environment,” Henry says, “and it’s no surprise we put them to use.”



Indigenous groups look to ancient DNA to bring their ancestors home

In May, Christina Warinner, a palaeogeneticist at Harvard University in Cambridge, Massachusetts, and her colleagues reported the extraction of bacterial DNA from the dental plaque of Neanderthals, including a 100,000-year-old individual from what is now Serbia. The species they found included some that specialized in breaking down starch into sugars, supporting the idea that Neanderthals had already adapted to a plant-rich diet⁸. Plaque on the teeth of early modern humans shared a similar bacterial profile, providing more evidence to suggest that they were eating starchy plants.

The finds push back against the idea that our ancestors spent their time sitting around campfires mostly chewing on mammoth steaks. It's an idea that has penetrated popular culture, with proponents of the palaeo diet

arguing that grains, potatoes and other starchy foods have no place on our plates because our hunter-gatherer ancestors didn't evolve to eat them.

But it has become clear that early humans were cooking and eating carbs almost as soon as they could light fires. "The old-fashioned idea that hunter-gatherers didn't eat starch is nonsense," says Fuller.

Invisible cooks

The push to better understand how people were cooking in the past also means paying more attention to the cooks themselves. It's part of a larger trend in archaeology to look at household activities and daily lives.

"Essentially, we're trying to figure out what kind of information you can find out about people who have never had histories written about them," says Sarah Graff, an archaeologist at Arizona State University in Tempe.

In the past, when researchers found plant remains at archaeological sites, they often considered them as accidental 'ecofacts' — natural objects, such as seeds, pollen and burnt wood, that offer evidence for what kind of plants grew in a region. But there has been a shift towards treating food remains as evidence of an activity that required craft, intent and skill. "Prepared food needs to be looked at as an artefact first and a species second," Fuller says. "Heated, fermented, soaked — making food is akin to making a ceramic vessel."



Archaeologist Laura Dietrich at work at Göbekli Tepe, where she has documented extensive operations for grinding grain. Credit: Hassan Yıldız

And, as researchers increasingly collaborate to compare ancient remains, they're finding remarkable similarities across time and cultures. At Neolithic sites in Austria dating back more than 5,000 years, for example, archaeologists found unusually shaped charred crusts. It was as though the contents of a large jar or pot had been heated until the liquid burned off, and the dried crust inside began to burn. The team's first guess was that the crusts were from grain storage jars destroyed in a fire. But under the scanning electron microscope, the cell walls of individual grains looked unusually thin — a sign, Heiss says, that something else was going on.

After comparing the Austrian finds to similar crusts found in Egyptian breweries from around the same time, Heiss and Valamoti concluded that the thin cell walls were the result of germination, or malting, a crucial step in the brewing process. These early Austrian farmers were brewing beer⁹. “We

ended up with something completely different” from the earlier hypotheses, Heiss says. “Several lines of evidence really interlocked and fell into place.”

Bread, it seems, goes even further back. Arranz-Otaegui was working at a 14,500-year-old site in Jordan when she found charred bits of ‘probable food’ in the hearths of long-ago hunter-gatherers. When she showed scanning electron microscope images of the stuff to Lara González Carretero, an archaeobotanist at the Museum of London Archaeology who works on evidence of bread baking at a Neolithic site in Turkey called Çatalhöyük, both researchers were shocked. The charred crusts from Jordan had tell-tale bubbles, showing they were burnt pieces of bread¹⁰.



Hundreds of Israel's archaeological sites are vanishing under concrete

Most archaeologists have assumed that bread didn’t appear on the menu until after grain had been domesticated — 5,000 years after the cooking accident in question. So it seems that the early bakers in Jordan used wild wheat.

The evidence provides crucial clues to the origins of the Neolithic revolution, when people began to settle down and domesticate grain and animals, which happened at different times in various parts of the world. Before farming began, a loaf of bread would have been a luxury product that

required time-consuming and tedious work gathering the wild grain needed for baking. That hurdle could have helped to spur crucial changes.

Arranz-Otaegui's research suggests that — at least in the Near East — demand for bread might have been a factor in driving people to attempt to domesticate wheat, as they looked for ways to ensure a steady supply of baked goods. "What we are seeing in Jordan has implications for bigger processes. What drove the transition to agriculture is one of the fundamental questions in archaeology," Arranz-Otaegui says. "This shows hunter-gatherers were using cereals."

The next frontier for archaeobotanists is prehistoric salad bars. Researchers are working on ways to look for the remains of food that wasn't cooked, such as leafy greens, another overlooked part of the ancient diet. Because raw greens and vegetables are even harder to find in the archaeological record than cooked seeds and grains, Kubiak-Martens calls them the "missing link" in knowledge about ancient diets. "There's no way to prove green leaves were eaten from charred remains," Kubiak-Martens says. "But you would be surprised at how much green vegetables are in human coprolites", or preserved faeces. Kubiak-Martens got a grant in 2019 to look at 6,300-year-old palaeofaeces preserved at wetland sites in the Netherlands, which she hopes will reveal everything prehistoric farmers there had on their dinner tables.

Recreating ancient meals

The quest to understand ancient diets has led some researchers to take extreme measures. That's the case with Göbekli Tepe, which has yielded very few organic remains that could provide clues to the prehistoric plant-based meals there. So Dietrich has tried innovative thinking — and a lot of elbow grease. Her approach has been to recreate the tools people used to make food, not the dishes themselves.

In her airy lab on a tree-lined street in Berlin, Dietrich explains her time-consuming and physically demanding process. Starting with a replica grindstone — a block of black basalt the size of a bread roll that fits neatly in the palm of her hand — she photographs it from 144 different angles.

After spending eight hours grinding four kilograms of heirloom einkorn wheat kernels, Dietrich photographs the stone again. A software program then produces 3D models from the two sets of pictures. Her experiments have shown that grinding fine flour for baking bread leaves a different finish on the stones from producing coarsely ground grain that is ideal for boiling as porridge or brewing beer.

And after handling thousands of grindstones, she is often able to identify what they were used for by touch. “I touch the stones to feel for flattening,” she says. “Fingers can feel changes at the nano level.” By comparing the wear patterns on her modern replicas to the stones piled in Göbekli Tepe’s rock garden, Dietrich could show that fine-ground bread flour was the exception. In a 2020 study¹¹, she argues people there were mostly grinding grain coarsely, just enough to break up its tough outer layer of bran and make it easy to boil and eat as porridge or ferment into beer.

To test the theory, Dietrich commissioned a stonemason to carve a replica of a 30-litre stone vat from Göbekli Tepe. In 2019, she and her team successfully cooked porridge using heated stones, carefully recording and timing each step of the process. They also brewed a Neolithic beer from hand-ground germinated grain, or malt, in the open vessel. The results were “a bit bitter, but drinkable”, Dietrich says. “If you’re thirsty in the Neolithic.”

From the grind stones and other plant-processing tools at Göbekli Tepe, a picture is now emerging for what was going on there 12,000 years ago. Rather than just starting to experiment with wild grains, the monument builders were apparently proto-farmers, already familiar with the cooking possibilities grain offered despite having no domesticated crops. “These are the best grinding tools ever, and I’ve seen a lot of grindstones,” Dietrich says. “People at Göbekli Tepe knew what they were doing, and what could be done with cereals. They’re beyond the experimentation phase.”

Her experiments are shifting the way archaeologists understand the site — and the period when it was built. Their initial interpretations made the site sound a bit like a US college fraternity house: lots of male hunters on a hilltop, washing down barbecued antelope with vats of lukewarm beer at

occasional celebrations. “Nobody really thought of the possibility of plant consumption” on a large scale, Dietrich says.

In a study late last year¹², Dietrich argues the ‘barbecue and beer’ interpretation is way off. The sheer number of grain-processing tools at Göbekli Tepe suggest that even before farming took hold, cereals were a daily staple, not just part of an occasional fermented treat.

Nature **594**, 488-491 (2021)

doi: <https://doi.org/10.1038/d41586-021-01681-w>

References

1. 1.

Dietrich, L. *et al.* *PLoS ONE* **14**, e0215214 (2019).

[PubMed](#) [Article](#) [Google Scholar](#)

2. 2.

Heun, M. *et al.* *Science* **278**, 1312–1314 (1997).

[Article](#) [Google Scholar](#)

3. 3.

Valamoti, S. M. *Veget. Hist. Archaeobot.* **11**, 17–22 (2002).

[Article](#) [Google Scholar](#)

4. 4.

Valamoti, S. M. *et al.* *J. Archaeol. Sci.* **128**, 105347 (2021).

[Article](#) [Google Scholar](#)

5. 5.

Inchley, C. E. *et al.* *Sci. Rep.* **6**, 37198 (2016).

[PubMed](#) [Article](#) [Google Scholar](#)

6. 6.

Larbey, C., Mentzer, S. M., Ligouis, B., Wurz, S. & Jones, M. K. *J. Hum. Evol.* **131**, 210–227 (2019).

[PubMed](#) [Article](#) [Google Scholar](#)

7. 7.

Henry, A. G., Brooks, A. S. & Piperno, D. R. *Proc. Natl Acad. Sci. USA* **108**, 486–491 (2011).

[PubMed](#) [Article](#) [Google Scholar](#)

8. 8.

Fellows Yates, J. A. *et al.* *Proc. Natl Acad. Sci. USA* **118**, e2021655118 (2021).

[PubMed](#) [Article](#) [Google Scholar](#)

9. 9.

Heiss, A. G. *et al.* *PLoS ONE* **15**, e0231696 (2020).

[PubMed](#) [Article](#) [Google Scholar](#)

10. 10.

Arranz-Otaegui, A., Gonzalez Carretero, L., Ramsey, M. N., Fuller, D. Q. & Richter, T. *Proc. Natl Acad. Sci. USA* **115**, 7925–7930 (2018).

[PubMed](#) [Article](#) [Google Scholar](#)

11. 11.

Dietrich, L. & Haibt, M. *J. Archaeol. Sci. Rep.* **33**, 102525 (2020).

[Article](#) [Google Scholar](#)

12. 12.

Dietrich, L. *et al. J. Archaeol. Sci. Rep.* **34**, 102618 (2020).

[Article](#) [Google Scholar](#)

[Download references](#)

Related Articles



- [**How did Neanderthals and other ancient humans learn to count?**](#)



- [**Hundreds of Israel's archaeological sites are vanishing under concrete**](#)



- [**Move over, DNA: ancient proteins are starting to reveal humanity's history**](#)



- [**Indigenous groups look to ancient DNA to bring their ancestors home**](#)

Subjects

- [Archaeology](#)
- [Agriculture](#)
- [Anthropology](#)
- [History](#)

[Jobs from Nature Careers](#)

- - - [All jobs](#)
 - - **[Laboratory Research Scientist](#)**
[Francis Crick Institute](#)
[London, United Kingdom](#)
[JOB POST](#)
 - **[Bachelor of Science in Computer Engineering \(f/m/d\)](#)**
[Helmholtz-Zentrum Berlin for Materials and Energy \(HZB\)](#)
[Berlin, Germany](#)
[JOB POST](#)
 - **[Laboratory Engineer / Scientific and Technical Head of Reactor Technology \(f/m/x\)](#)**
[Helmholtz Centre for Environmental Research \(UFZ\)](#)

[Leipzig, Germany](#)

[JOB POST](#)

- [Administrative Assistant/Internal Event Coordinator](#)

[Oklahoma Medical Research Foundation \(OMRF\)](#)

[Oklahoma City, United States](#)

[JOB POST](#)

[Download PDF](#)

Related Articles



- [How did Neanderthals and other ancient humans learn to count?](#)



- [Hundreds of Israel's archaeological sites are vanishing under concrete](#)



- [Move over, DNA: ancient proteins are starting to reveal humanity's history](#)



- [Indigenous groups look to ancient DNA to bring their ancestors home](#)

Subjects

- [Archaeology](#)
- [Agriculture](#)
- [Anthropology](#)
- [History](#)

This article was downloaded by **calibre** from <https://www.nature.com/articles/d41586-021-01681-w>

| [Section menu](#) | [Main menu](#) |

- NEWS FEATURE
- 23 June 2021

COVID vaccines and breastfeeding: what the data say

The vaccines do not pass through breast milk, but antibodies do — providing hope that breastfed babies might have some level of protection.

- [Shannon Hall](#) 0

1. Shannon Hall

1. Shannon Hall is a freelance science journalist in Colorado.

[View author publications](#)

You can also search for this author in [PubMed](#) [Google Scholar](#)





•

[Download PDF](#)



A mother breastfeeds her newborn at a hospital in Belgium. Credit: Francisco Seco/AP/Shutterstock

Molly Siegel had long awaited a COVID-19 vaccine. As an obstetrician at Massachusetts General Hospital in Boston, she regularly saw pregnant people with COVID-19, and knew that the vaccine was the best way to protect herself, her family and others in her workplace. But with a seven-month-old baby at home who was still breastfeeding, she felt hesitant.

Understandably so. Following established norms for clinical trials, pregnant and breastfeeding people were not included in any of the trials for COVID-19 vaccines. So, as health systems around the world began to vaccinate eligible adults, scores of lactating people were left to make their decision in the dark.

“I certainly was frustrated that there weren’t studies on the vaccine in pregnant and lactating women — that as a group, they were excluded from the research,” Siegel says. “It made it really hard to know, as both the patient and the provider, how to think about the vaccine.”

Still, Siegel could not see any plausible risk to her breast milk (she knew that COVID-19 vaccines contain no live virus, for instance), and focused on the benefit of protecting herself and everyone around her. So she got the shot. Then, she donated samples of her breast milk to researchers who would analyse its contents in one of the first such studies.

Now, thanks to Siegel and other participants, scientists are beginning to understand the effects of COVID-19 vaccines on breast milk, and their preliminary results should come as welcome news to the more than 100 million lactating people across the world.

Scientists have so far looked only at the vaccines made by Pfizer–BioNTech and Moderna, and have not detected the vaccines in breast milk. What they have found are antibodies, produced by mothers in response to inoculations, to the coronavirus SARS-CoV-2.

“We’re really happy to have something good to hang our hat on,” says Stephanie Gaw, a perinatologist at the University of California, San Francisco. “The studies are small, they’re still early, but very positive.” Now, researchers want to know whether those antibodies can provide babies with at least partial protection against COVID-19.

Vaccine questions

Throughout the pandemic, pregnant people and new mothers have been faced with a slew of concerns and questions about the coronavirus.

One trend that became clear early on is that pregnant people diagnosed with COVID-19 are more likely to be hospitalized than are those of the same age who are not pregnant. That could be because the body is already working hard — the growing uterus pushes upwards, reducing lung capacity, and the immune system is suppressed so as not to harm the baby. Those factors don’t disappear the day a baby is born. As such, some obstetricians suspect that lactating individuals are also susceptible to severe COVID-19.

That conclusion might encourage breastfeeding mothers to get vaccinated, but scientists weren’t sure how they would respond to the vaccines, because little is known about the period of lactation.

So Kathryn Gray, a maternal–fetal medicine specialist at Brigham and Women’s Hospital in Boston, Massachusetts, and her colleagues decided to test how well the Pfizer–BioNTech and Moderna vaccines work in this group. They recruited 131 participants who were about to receive either vaccine and who were lactating, pregnant or neither, and found that the lactating individuals (which included Siegel and 30 others) generated the same robust antibody response as did those who were not lactating¹. In other words: the vaccine is just as beneficial for breastfeeding mums.



Scientists studying breast milk samples have discovered that they carry antibodies from vaccination. Credit: Remko de Waal/ANP/AFP via Getty Images

A second study by Gaw and her team, posted on the preprint server medRxiv, agrees². The team drew blood from 23 lactating participants and found that antibodies to SARS-CoV-2 increased after their second dose.

But for many parents, the looming question — as Siegel asked herself — was whether a COVID-19 vaccine would harm a nursing infant. After all,

some medications are not recommended during lactation because they pass through breast milk to infants. Nursing mothers are advised against taking high doses of aspirin, for example; even after low doses, mothers are warned to monitor the infant for signs of bruising and bleeding. Some vaccines are off limits, too. The US Centers for Disease Control and Prevention (CDC) advises nursing mothers against receiving the yellow-fever vaccine, which involves a live, weakened form of the virus, on the off-chance that an infection passes to the infant.

Because of such cases, some pharmacists and vaccine administrators have been urging nursing mothers to discard their breast milk after they are vaccinated.



Pregnancy and COVID: what the data say

“I think that clearly shows ignorance and a lack of understanding,” says Kirsi Jarvinen-Seppo, an immunologist at the University of Rochester Medical Center in Rochester, New York. “There seems to be an awful amount of misinformation out there on all levels.”

Unlike the yellow-fever vaccine, COVID-19 vaccines do not carry a risk of igniting an active infection. In addition, COVID-19 vaccines are extremely unlikely to cross into breast milk. The fragile messenger RNA used in the Pfizer–BioNTech and Moderna vaccines, for example, is designed to break

down so quickly that it should never leave the cells where it was injected — let alone get into the bloodstream and then the breast. In fact, researchers don't expect that any of the current vaccines will be excreted into breast milk.

To that end, the World Health Organization recommends that mothers continue to breastfeed after vaccination. In addition, the CDC and the UK Joint Committee on Vaccination and Immunisation issued statements shortly after the first vaccines were authorized in both countries. These noted that no safety concerns had been identified from the available data, so lactating people could choose to be vaccinated.

"It's sort of a backwards way of recommending it," argues Christina Chambers, a paediatrician at the University of California, San Diego, and the Rady Children's Hospital. "The foundation is that there's no reason to avoid it, which is a dilemma."

So Gaw and her colleagues ran a safety check. In a small study³, her team looked at breast milk samples from six participants up to two days after they received the Pfizer–BioNTech or Moderna vaccine, and found no trace of the mRNA in either case. (The group is now scouring a larger number of milk samples for different components of the vaccine, and expanding their study to include all the available COVID-19 vaccines in the United States.)

Liquid gold

There is one type of particle that scientists are eager to see in breast milk following a vaccine: COVID-19 antibodies.

Researchers have long known that newborn babies don't effectively produce antibodies against harmful bacteria and viruses; and it can take three to six months for this kind of protection to kick in. To help in those early days, a mother's breast milk overflows with antibodies capable of staving off potential threats.

"It's specifically designed by the mother, and by Mother Nature, to provide the child with the child's first vaccine," says Hedvig Nordeng at the

University of Oslo, who specializes in medication use and safety in pregnancy and lactation. “Breast milk by itself is more than nutrition, breast milk is medicine.”



[The lightning-fast quest for COVID vaccines — and what it means for other diseases](#)

In the mother, immune cells called B lymphocytes (or B cells) constantly produce antibodies. Then, once lactation begins, the mammary glands send out a chemical signal that draws these B cells to the breast — where they park in the glands and produce thousands of antibodies per second, ready to move into the breast milk in huge quantities. But unlike molecules from medications, coffee and alcoholic drinks, which are so small they can pass into the breast milk on their own (although at diluted levels), antibodies are too large to do so. Instead, receptors on the surface of the milk ducts grab the antibodies and package them in protective, fluid-filled bubbles that allow them to pass safely through the milk-duct cells and into the milk on the other side⁴.

“This process is so magical,” says Galit Alter, an immunologist and virologist at Harvard Medical School in Boston, who worked on Gray’s study.

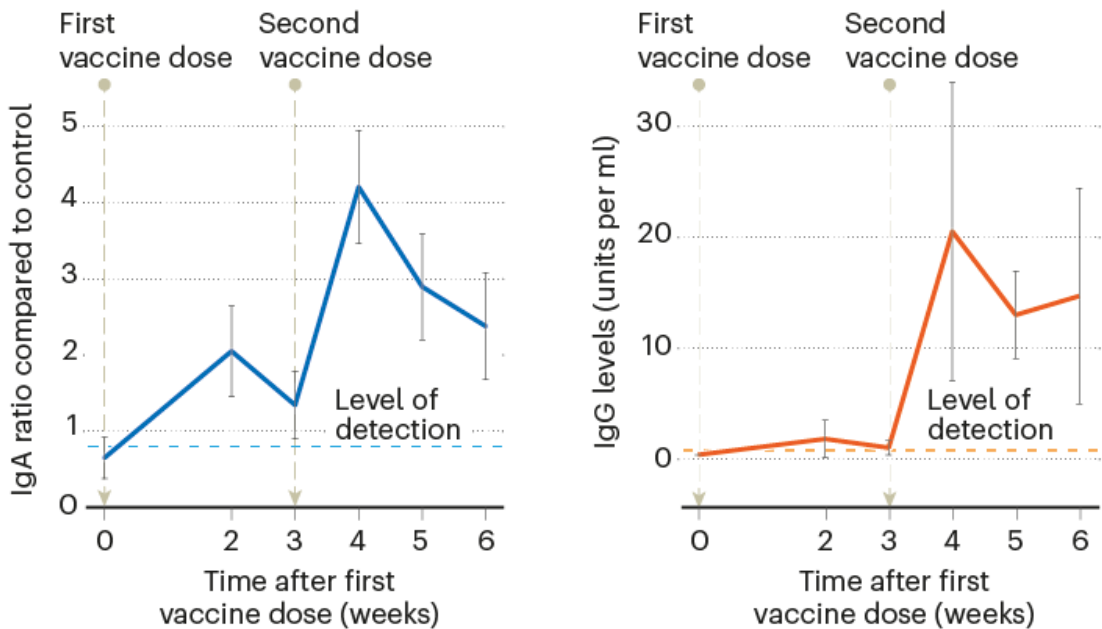
What happens once antibodies reach the baby, however, is more mysterious. Antibodies in the breast milk do not make it into a baby's bloodstream, but coat the mouth, throat and gut before they're ultimately digested⁴. Nonetheless, these antibodies seem to provide protection. It could be that they work at the body's entrances to fend off infection before it takes root.

Not all babies are raised on breast milk, but studies have shown that babies who exclusively breastfeed for their first six months have far fewer middle-ear infections than those who are breastfed for a shorter time, or not at all⁵. They also have a lower risk of respiratory-tract infections⁶. And lactating mothers who receive the influenza vaccine (and therefore transmit those protective antibodies to their infant through breast milk) provide some protection to babies who are too young to receive the shot⁷.

The same could be true for COVID-19 antibodies. Early this year, researchers found that breast milk from people who recover from the virus similarly oozes with antibodies⁸. And a smattering of small studies, many not yet peer reviewed, have found antibodies in breast milk from people who received the vaccine^{1,2,9–12} (see 'Breast-milk benefits').

BREAST-MILK BENEFITS

A study of 84 lactating health-care workers found that their breast milk contains substantial levels of antibodies to the coronavirus SARS-CoV-2 for several weeks after they were vaccinated. The study looked at two antibodies, immunoglobulin A (IgA, also found in the linings of the gut and respiratory tract) and immunoglobulin G (IgG, also found in the blood).



©nature

Source: Ref. 12

When Gray and her colleagues, for example, checked the blood and the breast milk of lactating mothers who had received a COVID-19 vaccine, they found high levels of COVID-19 antibodies in every sample¹.

“It’s very nice after this past year to have a tiny bit of good news,” says paediatric immunologist Bridget Young at the University of Rochester Medical Center.

And it’s a particularly exciting finding given that babies are not currently eligible to receive any of the available vaccines (although both Pfizer–BioNTech and Moderna have started trials of their COVID-19 vaccines in children as young as six months).

Whereas COVID-19 is often mild in younger populations, babies less than two years of age who contract the disease are more likely to be hospitalized than older children are⁸. That's thought to be because the bronchioles, the passageways that deliver air to the lungs, are much smaller in babies. In addition, babies and children can develop a severe illness known as MIS-C (multisystem inflammatory syndrome in children), in which different parts of the body become inflamed after the child contracts COVID-19.

Milk mysteries

One of the big unknowns now is how much protection babies receive from breast milk.

To begin, scientists aren't sure whether these antibodies are actually functional — meaning that they would kill the virus that causes COVID-19 if they came into contact with it. But early research is promising. Last year, a team in the Netherlands collected antibodies from the breast milk of people with a previous SARS-CoV-2 infection and found that the samples could neutralize the virus in the laboratory¹³. A month later, Young, Jarvinen-Seppo and their colleagues posted similar findings, which were subsequently published¹⁴.

Both teams are currently conducting the same experiment with vaccine-induced antibodies, following a study by scientists in Israel¹⁰ suggesting that antibodies created after vaccination could stop the virus infecting cells. The authors of that study predict that these antibodies should protect the baby, says Yariv Wine, an immunologist at Tel Aviv University and a co-author of the paper.

But this can happen only if the antibodies persist. Scientists don't yet know how long vaccinated people will continue to make COVID-19 antibodies, but evidence indicates they do so for a considerable time; one study of 33 people¹⁵ suggests that antibody production in adults given the Moderna vaccine continues for at least 6 months. That could mean that babies will continue to receive some protection from their mothers, as long as they continue nursing — although antibody concentrations in breast milk do drop over time⁴.

And that constant replenishment is key. Scientists suspect that antibodies are digested in the baby's gut after hours to days. That means their partial immunity will probably disappear once breastfeeding has ceased. It also suggests that giving breast milk to older children (as many vaccinated mothers have discussed in online forums) probably won't give them partial immunity — at least not for long.

But even for babies who are exclusively breastfed, clinicians urge mothers to continue to follow public-health strategies when they have visitors. "Anyone who's handling the baby in close contact really should be vaccinated and should be masked," says Andrea Edlow, a maternal-fetal medicine specialist at Harvard Medical School and Massachusetts General Hospital, who worked on the study with Gray.

Luckily, more data are on the way. Gray and her team will be tracking their participants, including Siegel and others, for a full year (although the details are still being discussed). Gaw's team at the University of California, San Francisco, is planning to assess the overall health and rate of infections of babies while they're being breastfed — the million-dollar question at the moment. The two studies pitting vaccine-induced antibodies against the virus in a Petri dish should offer another answer to this question.

Scientists are also working to analyse the antibodies in further detail. Chambers and her colleagues at the University of California, San Diego, for example, currently receive milk samples from roughly 40 participants per day; they also plan to follow the babies' growth and development.

Nonetheless, the results so far are promising enough that most experts would urge nursing mothers to get their shots. "If I had an itty-bitty baby right now, I would not take the risk — I would not wait," Alter says. "If you can empower your kid with immunity, I wouldn't even question it."

Nature **594**, 492-494 (2021)

doi: <https://doi.org/10.1038/d41586-021-01680-x>

References

1. 1.

Gray, K. J. *et al.* Preprint at medRxiv
<https://doi.org/10.1101/2021.03.07.21253094> (2021).

2. 2.

Golan, Y. *et al.* Preprint at medRxiv
<https://doi.org/10.1101/2021.03.09.21253241v2> (2021).

3. 3.

Golan, Y. *et al.* Preprint at medRxiv
<https://doi.org/10.1101/2021.03.05.21252998v1> (2021).

4. 4.

Atyeo, C. & Alter, G. *Cell* **184**, 1486–1499 (2021).

[PubMed](#) [Article](#) [Google Scholar](#)

5. 5.

Bowatte, G. *et al.* *Acta Paediatr.* **104**, 85–95 (2015).

[PubMed](#) [Article](#) [Google Scholar](#)

6. 6.

Tromp, I. *et al.* *PLoS ONE* **12**, e0172763 (2017).

[PubMed](#) [Article](#) [Google Scholar](#)

7. 7.

Zaman, K. *et al.* *N. Engl. J. Med.* **359**, 1555–1564 (2008).

[PubMed](#) [Article](#) [Google Scholar](#)

8. 8.

Kim, L. *et al.* *Morb. Mortal. Wkly Rep.* **69**, 1081–1088 (2020).

[PubMed](#) [Article](#) [Google Scholar](#)

9. 9.

Baird, J. K., Jensen, S. M., Urba, W. J., Fox, B. A. & Baird, J. R. Preprint at medRxiv <https://doi.org/10.1101/2021.02.23.21252328> (2021).

10. 10.

Rosenberg Friedman, M. *et al.* Preprint at medRxiv <https://doi.org/10.1101/2021.03.06.21252603> (2021).

11. 11.

Kelly, J. C. *et al.* *Am. J. Obstet. Gynecol.* <https://doi.org/10.1016/j.ajog.2021.03.031> (2021).

[Article](#) [Google Scholar](#)

12. 12.

Haia Perl, S. *et al.* *JAMA* **325**, 2013–2014 (2021).

[PubMed](#) [Article](#) [Google Scholar](#)

13. 13.

van Keulen, B. *et al.* Preprint at medRxiv <https://doi.org/10.1101/2020.08.18.20176743> (2020).

14. 14.

Pace, R. M. *et al.* *mBio* **12**, e03192-20 (2021).

[PubMed](#) [Article](#) [Google Scholar](#)

15. 15.

Doria-Rose, N. *et al.* *N. Engl. J. Med.* **384**, 2259–2261 (2021).

[PubMed](#) [Article](#) [Google Scholar](#)

[Download references](#)

Related Articles



- [Pregnancy and COVID: what the data say](#)



- [The lightning-fast quest for COVID vaccines — and what it means for other diseases](#)
- [Are COVID-19 vaccines safe in pregnancy?](#)

Subjects

- [SARS-CoV-2](#)
- [Epidemiology](#)
- [Vaccines](#)
- [Infection](#)

[Jobs from Nature Careers](#)

- - - [All jobs](#)
 - - [Laboratory Research Scientist](#)

[Francis Crick Institute](#)

[London, United Kingdom](#)

[JOB POST](#)

- [Bachelor of Science in Computer Engineering \(f/m/d\)](#)

[Helmholtz-Zentrum Berlin for Materials and Energy \(HZB\)](#)

[Berlin, Germany](#)

[JOB POST](#)

- [Laboratory Engineer / Scientific and Technical Head of Reactor Technology \(f/m/x\)](#)

[Helmholtz Centre for Environmental Research \(UFZ\)](#)

[Leipzig, Germany](#)

[JOB POST](#)

- [Administrative Assistant/Internal Event Coordinator](#)

[Oklahoma Medical Research Foundation \(OMRF\)](#)

[Oklahoma City, United States](#)

[JOB POST](#)

[Download PDF](#)

Related Articles



- [Pregnancy and COVID: what the data say](#)



- [The lightning-fast quest for COVID vaccines — and what it means for other diseases](#)
- [Are COVID-19 vaccines safe in pregnancy?](#)

Subjects

- [SARS-CoV-2](#)
- [Epidemiology](#)
- [Vaccines](#)
- [Infection](#)

This article was downloaded by **calibre** from <https://www.nature.com/articles/d41586-021-01680-x>

Opinion

- **[ISSCR: grave omission of age limit for embryo research](#)** [22 June 2021]
Correspondence •
- **[Fairer taxation to curb inequality and boost health](#)** [22 June 2021]
Correspondence •
- **[Ancient oaks of Europe are archives — protect them](#)** [22 June 2021]
Correspondence •
- **[United States: invest infrastructure stimulus in astronomy facilities](#)** [22 June 2021]
Correspondence •
- **[Europe's pandemic recovery: embed resilience](#)** [22 June 2021]
Correspondence •
- **[Canada is right to classify single-use plastics as toxic](#)** [22 June 2021]
Correspondence •
- **[A dangerous, wrong or unneeded experiment? Don't do it](#)** [22 June 2021]
Correspondence •

- CORRESPONDENCE
- 22 June 2021

ISSCR: grave omission of age limit for embryo research

- [Josephine Johnston](#) ORCID: http://orcid.org/0000-0002-7411-6992_0,
- [Françoise Baylis](#) ORCID: <http://orcid.org/0000-0003-2961-5802>¹ &
- [Henry T. Greely](#) ORCID: <http://orcid.org/0000-0002-1105-6734>²

1. [Josephine Johnston](#)

1. The Hastings Center, Garrison, New York, USA.

[View author publications](#)

You can also search for this author in [PubMed](#) [Google Scholar](#)

2. Françoise Baylis

1. Dalhousie University, Halifax, Canada.

[View author publications](#)

You can also search for this author in [PubMed](#) [Google Scholar](#)

3. Henry T. Greely

1. Stanford Law School, Stanford, California, USA.

[View author publications](#)

You can also search for this author in [PubMed](#) [Google Scholar](#)





•

[Download PDF](#)

We are researchers with differing views on the ethics of stem-cell and embryo research who nonetheless share deep concerns about the latest guidelines from the International Society for Stem Cell Research (ISSCR; see [R. Lovell-Badge *Nature* 593, 479; 2021](#)).

The 2016 ISSCR guidelines ruled out experiments on human embryos beyond 14 days, citing broad international consensus that these lacked “a compelling scientific rationale, raise substantial ethical concerns, and/or are illegal in many jurisdictions” (see [go.nature.com/3cqc4bw](#)). The latest

guidelines drop this prohibition (see go.nature.com/3gfk8) and do not propose any alternative.

At some point, the developing human embryo reaches a stage at which it should not be used for research. There is disagreement about when that happens, but scientists need to acknowledge that it does, and reassure the public that they accept limits. The latest guidelines do not prohibit the development or research use of *ex vivo* embryos at any stage.

Defining and defending a new limit, and possible constraints within it, will be hard. This was the case for the 14-day cut-off, selected some 40 years ago. But setting no limit is a grave omission.

Nature **594**, 495 (2021)

doi: <https://doi.org/10.1038/d41586-021-01697-2>

Competing Interests

The authors declare no competing interests.

Related Articles

- [See more letters to the editor](#)

Subjects

- [Stem cells](#)
- [Research management](#)
- [Society](#)

[Jobs from Nature Careers](#)

- - - [All jobs](#)

o

- **Laboratory Research Scientist**

Francis Crick Institute

London, United Kingdom

JOB POST

- **Bachelor of Science in Computer Engineering (f/m/d)**

Helmholtz-Zentrum Berlin for Materials and Energy (HZB)

Berlin, Germany

JOB POST

- **Laboratory Engineer / Scientific and Technical Head of Reactor Technology (f/m/x)**

Helmholtz Centre for Environmental Research (UFZ)

Leipzig, Germany

JOB POST

- **Administrative Assistant/Internal Event Coordinator**

Oklahoma Medical Research Foundation (OMRF)

Oklahoma City, United States

JOB POST

[Download PDF](#)

Related Articles

- [See more letters to the editor](#)

Subjects

- [Stem cells](#)
- [Research management](#)
- [Society](#)

This article was downloaded by **calibre** from <https://www.nature.com/articles/d41586-021-01697-2>

| [Section menu](#) | [Main menu](#) |

- CORRESPONDENCE
- 22 June 2021

Fairer taxation to curb inequality and boost health

- [Barry Bogin](#) ✉
 1. [Barry Bogin](#)
 1. Loughborough University, Barrow upon Soar, UK.

[View author publications](#)

You can also search for this author in [PubMed](#) [Google Scholar](#)





•

[Download PDF](#)

A century's research has shown that inequality in society makes everyone less healthy, including rich people. Despite this, almost nothing has been done to address the problem (see [Nature 592, 674–680; 2021](#)). Inequality increases every year in most nations, and affects every aspect of our lives.

Early-twentieth-century biocultural anthropologists found that average height reflects the “material and moral conditions of that society” ([J. M. Tanner Acta Paediatr. Jpn 29, 96–103; 1987](#)). My own research has found that more income equality predicts greater average height (and, by

extension, better health) for women and men. Having more money has a small effect on height but there is no association with national gross domestic product ([B. Bogin et al. Am. J. Hum. Biol. 29, e22980; 2017](#)).

When I talk to politicians about the suffering that inequality creates for all citizens, especially poor people, they say it's complicated. No, it is clear. To tackle inequality, we must encourage partnerships with groups that advocate on behalf of marginalized people. We must elect decision makers who will ensure that the super-rich pay their fair share in taxes, who will impose fairer corporate taxes and who will use the money to benefit the most deprived 20% of the population.

Nature **594**, 495 (2021)

doi: <https://doi.org/10.1038/d41586-021-01698-1>

Competing Interests

The author declares no competing interests.

Related Articles

- [See more letters to the editor](#)

Subjects

- [Anthropology](#)
- [Society](#)
- [Health care](#)

[Jobs from Nature Careers](#)

- - - [All jobs](#)

- **Laboratory Research Scientist**

Francis Crick Institute

London, United Kingdom

JOB POST

- **Bachelor of Science in Computer Engineering (f/m/d)**

Helmholtz-Zentrum Berlin for Materials and Energy (HZB)

Berlin, Germany

JOB POST

- **Laboratory Engineer / Scientific and Technical Head of Reactor Technology (f/m/x)**

Helmholtz Centre for Environmental Research (UFZ)

Leipzig, Germany

JOB POST

- **Administrative Assistant/Internal Event Coordinator**

Oklahoma Medical Research Foundation (OMRF)

Oklahoma City, United States

JOB POST

Download PDF

Related Articles

- [See more letters to the editor](#)

Subjects

- [Anthropology](#)
- [Society](#)
- [Health care](#)

This article was downloaded by **calibre** from <https://www.nature.com/articles/d41586-021-01698-1>

| [Section menu](#) | [Main menu](#) |

- CORRESPONDENCE
- 22 June 2021

Ancient oaks of Europe are archives — protect them

- [Christian Sonne](#)⁰,
- [Changlei Xia](#)¹ &
- [Su Shiung Lam](#)²

1. [Christian Sonne](#)

1. Aarhus University, Roskilde, Denmark.

[View author publications](#)

You can also search for this author in [PubMed](#) [Google Scholar](#)

2. Changlei Xia

1. Nanjing Forestry University, Nanjing, China.

[View author publications](#)

You can also search for this author in [PubMed](#) [Google Scholar](#)

3. Su Shiung Lam

1. University Malaysia Terengganu, Terengganu, Malaysia.

[View author publications](#)

You can also search for this author in [PubMed](#) [Google Scholar](#)





•

[Download PDF](#)



Kongeegen, the King Oak, in Denmark could be up to 2,000 years old. Credit: Andreas Altenburger/Alamy

Some of the oldest trees in Europe are in danger because they are not being given the necessary level of protection. Oak trees (*Quercus robur*) that are more than 1,000 years old are found in the United Kingdom and in Fennoscandia, which includes Denmark, Sweden and Norway.

For example, Denmark's King Oak (pictured) is one of the world's oldest living trees, dating to around 1,900 years of age. The United Kingdom has the largest collection of ancient oaks, reflecting 1,500 years of ship-building.

The trees contain rings that represent archives of historical climate fluctuations and levels of atmospheric gases, so they can help to answer pressing questions about climate change and ecosystem dynamics ([P. M. Kelly et al. *Nature* 340, 57–60; 1989](#)).

Fennoscandia and the United Kingdom could better safeguard their oaks using mechanisms such as those offered by the European Union's Natura 2000 network of protected areas, or the protections conferred by UNESCO

World Heritage sites in the United Kingdom. Otherwise, unsustainable management practices, deforestation, air pollution and climate change could leave these ancient species vulnerable to disease and extinction, with the loss of irreplaceable scientific information and cultural heritage.

Nature **594**, 495 (2021)

doi: <https://doi.org/10.1038/d41586-021-01699-0>

Competing Interests

The authors declare no competing interests.

Related Articles

- [See more letters to the editor](#)

Subjects

- [Conservation biology](#)
- [Environmental sciences](#)
- [Forestry](#)

[Jobs from Nature Careers](#)

- - - [All jobs](#)
 -
 - [Laboratory Research Scientist](#)
 - [Francis Crick Institute](#)
 - [London, United Kingdom](#)

JOB POST

- **Bachelor of Science in Computer Engineering (f/m/d)**

Helmholtz-Zentrum Berlin for Materials and Energy (HZB)

Berlin, Germany

JOB POST

- **Laboratory Engineer / Scientific and Technical Head of Reactor Technology (f/m/x)**

Helmholtz Centre for Environmental Research (UFZ)

Leipzig, Germany

JOB POST

- **Administrative Assistant/Internal Event Coordinator**

Oklahoma Medical Research Foundation (OMRF)

Oklahoma City, United States

JOB POST

Download PDF

Related Articles

- **See more letters to the editor**

Subjects

- [Conservation biology](#)
 - [Environmental sciences](#)
 - [Forestry](#)
-

This article was downloaded by **calibre** from <https://www.nature.com/articles/d41586-021-01699-0>

| [Section menu](#) | [Main menu](#) |

- CORRESPONDENCE
- 22 June 2021

United States: invest infrastructure stimulus in astronomy facilities

- [Adam Cohen](#)⁰,
- [Matt Mountain](#)¹ &
- [David Reitze](#)²

1. [Adam Cohen](#)

1. Associated Universities Incorporated, Washington DC, USA.

[View author publications](#)

You can also search for this author in [PubMed](#) [Google Scholar](#)

2. Matt Mountain

1. Association of Universities for Research in Astronomy,
Washington DC, USA.

[View author publications](#)

You can also search for this author in [PubMed](#) [Google Scholar](#)

3. David Reitze

1. California Institute of Technology, Pasadena, California, USA.

[View author publications](#)

You can also search for this author in [PubMed](#) [Google Scholar](#)





•

[Download PDF](#)

We argue that US President Joe Biden's planned investment in national infrastructure (see [Nature 593, 19–20; 2021](#)) should include the next generation of astronomy facilities. Priorities for these will be identified by the Astronomy and Astrophysics Decadal Survey, expected in July. They will be crucial to US research, development and diplomacy.

For example, the speedy development of vaccines against COVID-19 relied on previous big investments in scientific infrastructure, such as synchrotron X-ray sources and computational power. And remote working is predicated

on Wi-Fi technologies that were a by-product of research in radio-astronomy facilities.

US leadership in science rests in part on the facilities we operate. These have generated international collaborations to provide insight into how the Universe is structured and have contributed to Nobel prizes.

However, this leadership is jeopardized by our ageing observatory infrastructure. The 2018 US National Academy of Sciences report ‘Exoplanet Science Strategy’ concluded that progress requires substantial investment in extremely large telescopes on the ground, and ambitious space-based capabilities (see go.nature.com/3wsmzi2). These can take decades to put in place, and cost billions of dollars. Let’s start now.

Nature **594**, 496 (2021)

doi: <https://doi.org/10.1038/d41586-021-01691-8>

Competing Interests

A.C. is president and chief executive for Associated Universities, Inc. (AUI), which manages the National Radio Astronomy Observatory (NRAO) and the Green Bank Observatory (GBO) for the US National Science Foundation (NSF).

Related Articles

- [See more letters to the editor](#)

Subjects

- [Astronomy and astrophysics](#)
- [Physics](#)
- [Research management](#)
- [Policy](#)

Jobs from Nature Careers

- - - [All jobs](#)
 - - [Laboratory Research Scientist](#)
[Francis Crick Institute](#)
[London, United Kingdom](#)
[JOB POST](#)
 - [Bachelor of Science in Computer Engineering \(f/m/d\)](#)
[Helmholtz-Zentrum Berlin for Materials and Energy \(HZB\)](#)
[Berlin, Germany](#)
[JOB POST](#)
 - [Laboratory Engineer / Scientific and Technical Head of Reactor Technology \(f/m/x\)](#)
[Helmholtz Centre for Environmental Research \(UFZ\)](#)
[Leipzig, Germany](#)
[JOB POST](#)
 - [Administrative Assistant/Internal Event Coordinator](#)

[Oklahoma Medical Research Foundation \(OMRF\)](#)

[Oklahoma City, United States](#)

[JOB POST](#)

[Download PDF](#)

Related Articles

- [See more letters to the editor](#)

Subjects

- [Astronomy and astrophysics](#)
- [Physics](#)
- [Research management](#)
- [Policy](#)

This article was downloaded by **calibre** from <https://www.nature.com/articles/d41586-021-01691-8>

| [Section menu](#) | [Main menu](#) |

- CORRESPONDENCE
- 22 June 2021

Europe's pandemic recovery: embed resilience

- [Mariya Gabriel](#) ⁰ &
- [Sandrine Dixson-Declève](#) ¹

1. [Mariya Gabriel](#)

1. Brussels, Belgium.

[View author publications](#)

You can also search for this author in [PubMed](#) [Google Scholar](#)

2. Sandrine Dixson-Declève

1. Brussels, Belgium.

[View author publications](#)

You can also search for this author in [PubMed](#) [Google Scholar](#)





•

[Download PDF](#)

More than a year into the COVID-19 pandemic, the European Union is mobilizing extraordinary financial and human resources to foster the recovery and resilience of member states. This is a huge responsibility for policymakers at all levels. As EU commissioner for Innovation, Research, Culture, Education and Youth and chair of the ESIR expert group on the economic and societal impact of research and innovation, respectively, we contend that these EU and national programmes should be reinforced and coordinated to account for the needs of all Europeans.

The temporary recovery instrument NextGenerationEU will provide €750 billion (US\$913 billion). Horizon Europe will initially invest €123 million from a budget of €95.5 billion to fund research into viral variants.

Sustainable social recovery must leave no one behind, otherwise social, political and economic instability could stem from disenfranchisement and inequity.

Resilience must increase by design, not disaster. The EU’s “protect, prepare and transform” approach will ready our communities for future health and environmental shocks (see go.nature.com/352gb2s). Policy initiatives such as the European Research Area, the European Education Area, the Digital Education Action Plan, the New European Bauhaus and Horizon Europe aim for such resilience. This will involve collaboration across government, finance and industry.

Nature **594**, 496 (2021)

doi: <https://doi.org/10.1038/d41586-021-01700-w>

Competing Interests

The authors declare no competing interests.

Related Articles

- [See more letters to the editor](#)

Subjects

- [Policy](#)
- [Research management](#)
- [Education](#)

[Jobs from Nature Careers](#)

-

- - [All jobs](#)
 - - **[Laboratory Research Scientist](#)**
[Francis Crick Institute](#)
[London, United Kingdom](#)
[JOB POST](#)
 - **[Bachelor of Science in Computer Engineering \(f/m/d\)](#)**
[Helmholtz-Zentrum Berlin for Materials and Energy \(HZB\)](#)
[Berlin, Germany](#)
[JOB POST](#)
 - **[Laboratory Engineer / Scientific and Technical Head of Reactor Technology \(f/m/x\)](#)**
[Helmholtz Centre for Environmental Research \(UFZ\)](#)
[Leipzig, Germany](#)
[JOB POST](#)
 - **[Administrative Assistant/Internal Event Coordinator](#)**
[Oklahoma Medical Research Foundation \(OMRF\)](#)
[Oklahoma City, United States](#)

JOB POST

[Download PDF](#)

Related Articles

- [See more letters to the editor](#)

Subjects

- [Policy](#)
- [Research management](#)
- [Education](#)

This article was downloaded by **calibre** from <https://www.nature.com/articles/d41586-021-01700-w>

| [Section menu](#) | [Main menu](#) |

- CORRESPONDENCE
- 22 June 2021

Canada is right to classify single-use plastics as toxic

- [Tony R. Walker](#) 0

1. [Tony R. Walker](#)

1. Dalhousie University, Halifax, Canada.

[View author publications](#)

You can also search for this author in [PubMed](#) [Google Scholar](#)





•

[Download PDF](#)

Last month, the Canadian government added manufactured plastic items to the list of toxic substances under Schedule 1 of the Canadian Environmental Protection Act. A group of Canadian industry leaders has launched the Responsible Plastic Use Coalition to pursue legal action against the move.

The legislation change will pave the way for a ban on single-use plastic items that the government considers harmful, such as bags, straws, stirring sticks, six-pack rings, cutlery and hard-to-recycle food containers.

In my view, this bold move should be applauded.

The continued production, use and disposal of single-use plastics is unsustainable and prevents Canada from meeting its commitments under the Federal Sustainable Development Strategy, the Canada-wide Strategy on Zero Plastic Waste and the Ocean Plastics Charter adopted by the G7 group of countries ([T. R. Walker and D. Xanthos *Resour. Conserv. Recycl.* 133, 99–100; 2018](#)).

Cooperation from all stakeholders, including the plastics industry, is urgently required to address the rapidly growing menace of plastic pollution.

Nature **594**, 496 (2021)

doi: <https://doi.org/10.1038/d41586-021-01701-9>

Competing Interests

The author declares no competing interests.

Related Articles

- [See more letters to the editor](#)

Subjects

- [Environmental sciences](#)
- [Sustainability](#)
- [Toxicology](#)

[Jobs from Nature Careers](#)

- - - [All jobs](#)
 -

- **Laboratory Research Scientist**

Francis Crick Institute

London, United Kingdom

JOB POST

- **Bachelor of Science in Computer Engineering (f/m/d)**

Helmholtz-Zentrum Berlin for Materials and Energy (HZB)

Berlin, Germany

JOB POST

- **Laboratory Engineer / Scientific and Technical Head of Reactor Technology (f/m/x)**

Helmholtz Centre for Environmental Research (UFZ)

Leipzig, Germany

JOB POST

- **Administrative Assistant/Internal Event Coordinator**

Oklahoma Medical Research Foundation (OMRF)

Oklahoma City, United States

JOB POST

Download PDF

Related Articles

- [See more letters to the editor](#)

Subjects

- [Environmental sciences](#)
- [Sustainability](#)
- [Toxicology](#)

This article was downloaded by **calibre** from <https://www.nature.com/articles/d41586-021-01701-9>

| [Section menu](#) | [Main menu](#) |

- CORRESPONDENCE
- 22 June 2021

A dangerous, wrong or unneeded experiment? Don't do it

- [Matthew Cobb](#) ORCID: <http://orcid.org/0000-0002-8258-4913> ⁰ &
- [Robert Pollack](#) ¹

1. Matthew Cobb

1. University of Manchester, UK.

[View author publications](#)

You can also search for this author in [PubMed](#) [Google Scholar](#)

2. [Robert Pollack](#)

1. New York, New York, USA.

[View author publications](#)

You can also search for this author in [PubMed](#) [Google Scholar](#)





•

[Download PDF](#)

While making a BBC radio documentary together about the history of genetic engineering, one of us (R. P.) was reminded of an unsent letter to *Nature* and *Science*, drafted 50 years ago with molecular biologist Joe Sambrook, in response to the first proposed recombinant DNA experiment.

Four years later, in 1975, the Asilomar Conference — a meeting of biologists, lawyers and even physicians — rescinded a temporary moratorium on recombinant DNA research.

Amid today's debates about heritable gene editing, viral gain-of-function research and embryo experiments beyond 14 days, these words from the letter resonate: "We ought to ask ourselves whether the experimental results are worth the calculable and unknown dangers to ourselves and to the general population ... we are obliged to ask ourselves whether the experiment needs to be done, rather than if it ought to be done, or if it can be done."

The letter by R. P. and Sambrook (now deceased) was never sent. As early-career researchers, they decided not to risk antagonizing senior colleagues who might be hostile to the idea of limiting research.

The letter concluded: "If it is dangerous, or wrong, or both, and if it doesn't need to be done, we just ought not to do it." Then, as now, what is the right experiment to do should not be determined by scientists alone.

Nature **594**, 496 (2021)

doi: <https://doi.org/10.1038/d41586-021-01702-8>

Competing Interests

The authors declare no competing interests.

Related Articles

- [See more letters to the editor](#)

Subjects

- [History](#)
- [Genetics](#)
- [Conferences and meetings](#)

[Jobs from Nature Careers](#)

- - - [All jobs](#)
 - - **[Laboratory Research Scientist](#)**
[Francis Crick Institute](#)
[London, United Kingdom](#)
[JOB POST](#)
 - **[Bachelor of Science in Computer Engineering \(f/m/d\)](#)**
[Helmholtz-Zentrum Berlin for Materials and Energy \(HZB\)](#)
[Berlin, Germany](#)
[JOB POST](#)
 - **[Laboratory Engineer / Scientific and Technical Head of Reactor Technology \(f/m/x\)](#)**
[Helmholtz Centre for Environmental Research \(UFZ\)](#)
[Leipzig, Germany](#)
[JOB POST](#)
 - **[Administrative Assistant/Internal Event Coordinator](#)**
[Oklahoma Medical Research Foundation \(OMRF\)](#)
[Oklahoma City, United States](#)

JOB POST

[Download PDF](#)

Related Articles

- [See more letters to the editor](#)

Subjects

- [History](#)
- [Genetics](#)
- [Conferences and meetings](#)

This article was downloaded by **calibre** from <https://www.nature.com/articles/d41586-021-01702-8>

| [Section menu](#) | [Main menu](#) |

Work

- **[Six reasons to launch a Young Academy](#)** [21 June 2021]
Career Column • As the first national network of early-career researchers marks its 21st birthday, the founders of Hungary's describe how and why they set up theirs in 2019.
- **[Five trendy technologies: where are they now?](#)** [21 June 2021]
Technology Feature • A look at notable research tools and projects that have rocketed to prominence reveals some common routes to success.
- **[Shell shock: a biologist's quest to save the endangered painted snail](#)** [21 June 2021]
Where I Work • Bernardo Reyes-Tur aims to unravel the mating mysteries of Cuba's imperilled Polymita.

- CAREER COLUMN
- 21 June 2021

Six reasons to launch a Young Academy

As the first national network of early-career researchers marks its 21st birthday, the founders of Hungary's describe how and why they set up theirs in 2019.

- [Erika Bálint](#)⁰,
- [Dorottya Csuka](#)¹,
- [Viktória Venglovecz](#)²,
- [Gitta Schlosser](#)³,
- [Zsófia Lázár](#)⁴,
- [Eszter Gselmann](#)⁵,
- [Donát Alpár](#)⁶ &
- [Katalin Solymosi](#)⁷

1. Erika Bálint

1. Erika Bálint is an assistant professor at the Department of Organic Chemistry and Technology, Budapest University of Technology and Economics, Budapest, Hungary.

[View author publications](#)

You can also search for this author in [PubMed](#) [Google Scholar](#)

2. Dorottya Csuka

1. Dorottya Csuka is a senior research fellow at the Department of Internal Medicine and Haematology, Semmelweis University,

Budapest, Hungary.

[View author publications](#)

You can also search for this author in [PubMed](#) [Google Scholar](#)

3. Viktória Venglovecz

1. Viktória Venglovecz is an associate professor at the Department of Pharmacology and Pharmacotherapy, University of Szeged, Szeged, Hungary.

[View author publications](#)

You can also search for this author in [PubMed](#) [Google Scholar](#)

4. Gitta Schlosser

1. Gitta Schlosser is an assistant professor at the Department of Analytical Chemistry, Institute of Chemistry, ELTE Eötvös Loránd University, Budapest, Hungary.

[View author publications](#)

You can also search for this author in [PubMed](#) [Google Scholar](#)

5. Zsófia Lázár

1. Zsófia Lázár is assistant professor at the Department of Pulmonology, Semmelweis University, Budapest, Hungary.

[View author publications](#)

You can also search for this author in [PubMed](#) [Google Scholar](#)

6. Eszter Gselmann

1. Eszter Gselmann is an associate professor at the Department of Analysis, Institute of Mathematics, University of Debrecen, Debrecen, Hungary.

[View author publications](#)

You can also search for this author in [PubMed](#) [Google Scholar](#)

7. Donát Alpár

1. Donát Alpár is a senior research fellow in the 1st Department of Pathology and Experimental Cancer Research, Semmelweis University, Budapest, Hungary.

[View author publications](#)

You can also search for this author in [PubMed](#) [Google Scholar](#)

8. Katalin Solymosi

1. Katalin Solymosi is an assistant professor at the Department of Plant Anatomy, Institute of Biology, ELTE Eötvös Loránd University, Budapest, Hungary.

[View author publications](#)

You can also search for this author in [PubMed](#) [Google Scholar](#)





•

[Download PDF](#)



Science leadership training was organized for early-career researchers by the Global Young Academy in 2019. Credit: Tamás Szigeti/Hungarian Academy of Sciences

Twenty-one years ago this month, Germany became the first country to launch a national Young Academy of early-career researchers. This spawned a movement that now straddles 45 countries, from Albania to Zimbabwe, including 14 in Africa and 13 in Asia. Such academies now exist in countries that score well in academic-freedom indices, and in some that don't.

Alongside these national bodies, which usually have between 25 and 60 individual members, there are 16 similar bodies around the world (see 'A step beyond'), including 5 transnational organizations (such as the Global Young Academy, founded in 2010, and the Young Academy of Europe, founded in 2012). Their financial and legal status, as well as their relation to senior academies and governments, greatly varies—which strongly

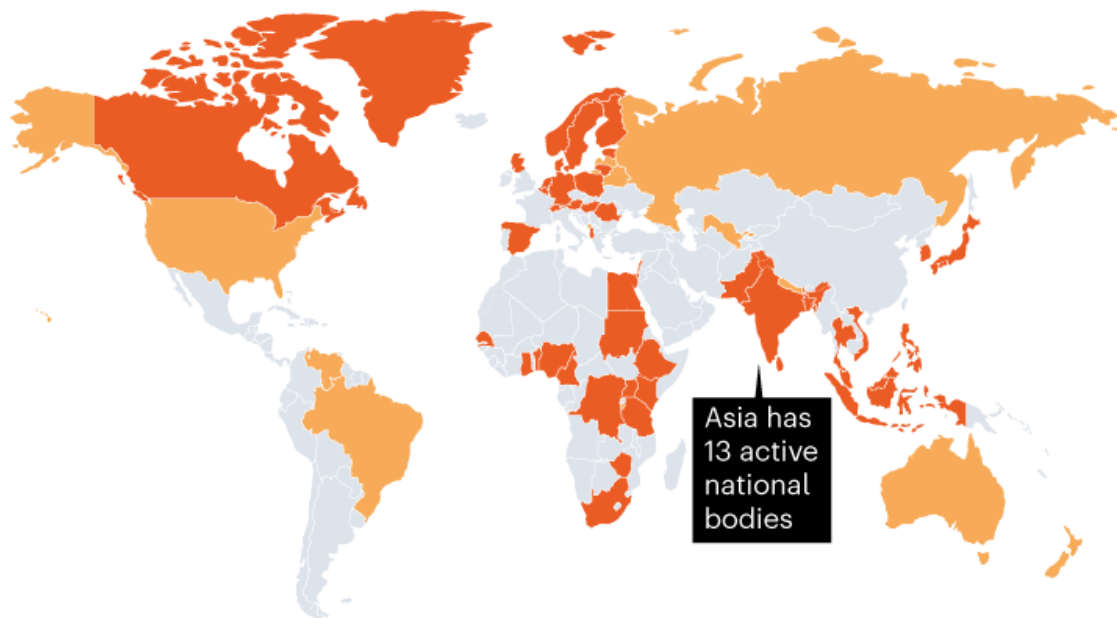
influences the possibilities and potential impacts of each of these organizations.

Young Academies aim to support junior scientists and to get their voices heard by decision-makers as they race to produce academic knowledge and meet ever-evolving research-evaluation procedures. They also advocate science's role in helping to meet societal challenges, and provide authentic, trustworthy information in an era of misinformation, disinformation and fake news. Many early-career researchers juggle these demands alongside precarious positions and caring responsibilities.

A STEP BEYOND

Young Academies and other organizations that support junior researchers and aim to get their voices heard by stakeholders number more than 60 worldwide across upwards of 50 nations. They also work to improve public understanding of how research works and its societal benefits.

■ With Young Academies ■ With similar bodies*



*'Similar bodies' are organizations with missions similar to those of Young Academies.
Nature publications remain neutral with regard to contested jurisdictional claims in published maps.

[Hungary's Young Academy](#) was launched in 2019. As founding members, we wanted to share how we went about getting it live. We hope our experience will be useful to early-career researchers who are keen to set up a

Young Academy in their country, and to raise awareness about the types of activity that Young Academies get involved in.

In 2018, the Hungarian Young Academy's founding members conducted a survey on the situation of young researchers in the country. The goal was to identify major life- and career-related challenges — such as job precarity, access to funding, work–life balance, gender equality, diversity and inclusion, working-environment conditions and international competitiveness — and to gather information for quantitative arguments that we can use in discussions about these issues with decision makers, and to prioritize the Hungarian Young Academy's future activities.

Alongside the survey, we reviewed the activities of existing academies. We found that Young Academies offer a wide variety of services and initiatives, as well as benefits to local scientific communities and society.

Outreach

Young Academies help to improve public understanding of how research works, and the societal benefits that scientific achievements can bring. They organize workshops that are open to members of the general public on hot topics, such as alternative medicine, COVID-19 and climate change. These workshops aim to make citizens aware of recent scientific results and evidence, or to raise public awareness of the importance of vaccination, for example.



Collection: Diversity and scientific careers

Young Academies can also promote scientific careers to the next generations of scholars. Some, such as those in Finland and Norway, run ‘Meet a Researcher’ or ‘Book a Researcher’ events, often at a scholar’s alma mater, where both early-career and senior scholars can talk about their everyday research tasks and career development. In 2020, along with the Hungarian Academy of Sciences, we launched a similar motivational programme, which helps secondary schools contact and invite their former students who now work in academia to participate in similar programmes.

Our audit also revealed how Young Academies encourage younger generations, from preschoolers to undergraduates, to develop investigative attitudes and critical-thinking skills. In 2011, the Dutch Young Academy, for example, devised the enquiry-based science-education game called Expedition Mundus for students aged 8 and older. This game simulates landing and exploration on an unknown planet by using various scientific-research methods, and has been translated into multiple languages and advertised in several Asian and African countries by the Global Young Academy.

Several Young Academies run scientific-communication talks by junior researchers that can attract a wide and an especially young audience, thanks

in large part to digital platforms, including social media and podcasts, and to the often informal communication style of younger people.

Open science

Many Young Academies are strongly promoting and supporting open science and open data — the legal removal of access barriers from peer-reviewed scientific research outputs around the world. In 2018, the Young Academy of Utrecht University in the Netherlands produced *The Road to Open Science* podcast. It explores the philosophy and history of open science and how it can benefit research. In April 2021, the Young Academy of Europe teamed up with other Young Academies and the open-access initiative cOAlition S for a webinar to discuss the Rights Retention Strategy, which aims to offer researchers the freedom to submit manuscripts to a journal of their choice while remaining fully compliant with Plan S. This requires researchers who benefit from state funding to publish their work in open repositories and journals.

Science policy

Some Young Academies publish articles in national and international journals to raise awareness of various issues of concern from a young researcher's perspective. One such initiative is the June 2019 survey led by the Young Academy of Europe, which illustrated that early-career researchers often work beyond a standard work week, juggling administrative and educational tasks alongside research.



Career resources for postdoctoral researchers

These publications are read not only by members of the scientific community, but also by policymakers, legislators, funding agencies, business leaders, journalists and members of the public. These articles can lead to Young Academies or early-career researchers getting involved in national — or global — decision-making. In April 2020, for instance, the Global Young Academy, together with 14 national academies, published a statement on the dire need for international cooperation among different sectors during the COVID-19 pandemic. In December 2020, 14 European Young Academies set up the Young Academies Science Advice Structure (YASAS). YASAS will soon become involved in the European Commission's Scientific Advice Mechanism, which was set up in 2016 to provide independent scientific advice to members of the European Commission.

Networking

Young Academies provide a multidisciplinary platform that allows their members to exchange diverse views and experiences to broaden their intellectual horizon. They also promote interdisciplinary research, and collaborations at both the national and international level. One such project is the Global Young Academy's cross-disciplinary biodiversity project Bio2Bio (Biodiversity for Survival via Biomedicine), which aims to

preserve knowledge about the medicinal properties of different species and develop pharmaceuticals from nature while protecting biodiversity.

Mentoring and advocacy

Mentoring offered by Young Academies might represent various opportunities to support the career development of young scientists, including science-communication, scientific-writing or grant-writing workshops and seminars for individual advice, counselling or mentoring schemes. Several Young Academies propose principles and guidelines for young scholars to achieve a sustainable academic career. These types of mentoring can help early-career researchers to choose an independent career path, regardless of discipline-specific convention, by generating, gathering and sharing knowledge on responsible research practices across all disciplines. And junior researchers who participate in Young Academy workshops might receive advice on how to preserve research integrity even in the face of scientific misconduct.



The executive committee of the Global Young Academy.Credit: Robert Lepenies/Jim Curtiss

Some Young Academies provide up-to-date information on available domestic and international grant applications, funding opportunities and resources, as well as potentially exciting scientific events. In September 2020, the Young Academy of Europe organized a European Research Council Starting Grant mentoring event involving almost 500 participants across European countries, with a follow-up one-to-one mentoring programme. In Hungary, we launched a similar initiative focused on major national grants and scholarships. This led to constructive discussion and jointly organized workshops with the country's major national funding agency about eligibility, grant and report evaluation criteria, discipline-specific aspects and administrative burdens.

We think these efforts all represent important milestones in establishing a sustainable career model in science. Doing so will certainly also require regular exchange with leaders of governmental organizations, funding agencies, research institutes and universities.

Equality, diversity and inclusion

Starting a family has a huge impact on the career development of young researchers. This usually coincides with the first decade(s) of their career, when their positions are often precarious and they are just starting to achieve professional recognition and success. Parental leave affects mainly women — especially in countries with traditional family models, such as Hungary — so it places a heavy burden on young female scientists, and many talents remain untapped or simply get lost along the leaky pipeline.



Beating the odds to secure a permanent contract

Young Academies make recommendations and provide advice to support early-career researchers' work-life balance and parental leave, and to help them find childcare facilities, and to develop strategies and initiatives that can reduce gender inequalities. These include new funding mechanisms to compensate for career responsibilities, and measures to achieve a more-even gender balance across panels, committees and other leadership and decision-making positions. The Hungarian Young Academy's founding members, for example, worked with a trade union in 2018 to boost awareness of the importance of increasing the eligibility window for grants to accommodate childcare activities. We also proposed a specific grant type to our country's funding agency and government to support reintegration of early-career researchers into science after a parental career break. We strongly feel that, to avoid losing junior talent and diversity in science, new measures that allow scientists to build successful careers alongside raising a family must be introduced.

These organizations can also promote successful, diverse role models and increase the visibility of research done by under-represented groups to make science more inclusive and more attractive to the public. The Women in Science working group of the Global Young Academy was among the first teams to publish inspiring experiences and advice for early-career researchers working in home offices during COVID-19 lockdowns. At the

same time, the members of the Hungarian Young Academy and the Young Academy of Europe tried to raise decision-makers' and grant agencies' awareness of the difficulties faced by young scientists, especially those with caring responsibilities, during the pandemic.

When recognized as independent, diverse actors in the local, national, regional and global science-policy systems, Young Academies can have a significant role as authentic and trusted mediators between society, the research community and decision-makers. This is a win-win situation for all.

However, these organizations rely on voluntary work and usually have a limited number of members — and it is crucial to not encourage junior researchers' tendencies to work themselves to exhaustion. Instead, Young Academies need to optimize their members' workload, energy, time and financial investment by strengthening existing collaborations, networking and synergies among similar organizations, as well as among senior academies and national and international bodies. Together, we can go further.

Nature **594**, 599-601 (2021)

doi: <https://doi.org/10.1038/d41586-021-01682-9>

This is an article from the Nature Careers Community, a place for Nature readers to share their professional experiences and advice. [Guest posts are encouraged.](#)

Competing Interests

The authors declare no competing interests.

Related Articles



- [How new principal investigators tackled a tumultuous year](#)



- ['I'll work on it over the weekend': high workload and other pressures faced by early-career researchers](#)



- [Beating the odds to secure a permanent contract](#)



- [Collection: Diversity and scientific careers](#)



- [Career resources for postdoctoral researchers](#)

Subjects

- [Careers](#)
- [Society](#)
- [Institutions](#)
- [Lab life](#)

[Jobs from Nature Careers](#)

- - - [All jobs](#)
 - - **[Laboratory Research Scientist](#)**
[Francis Crick Institute](#)
[London, United Kingdom](#)
[JOB POST](#)
 - **[Bachelor of Science in Computer Engineering \(f/m/d\)](#)**
[Helmholtz-Zentrum Berlin for Materials and Energy \(HZB\)](#)
[Berlin, Germany](#)
[JOB POST](#)
 - **[Laboratory Engineer / Scientific and Technical Head of Reactor Technology \(f/m/x\)](#)**
[Helmholtz Centre for Environmental Research \(UFZ\)](#)
[Leipzig, Germany](#)
[JOB POST](#)
 - **[Administrative Assistant/Internal Event Coordinator](#)**
[Oklahoma Medical Research Foundation \(OMRF\)](#)
[Oklahoma City, United States](#)

JOB POST

[Download PDF](#)

Related Articles



- [How new principal investigators tackled a tumultuous year](#)



- [‘I’ll work on it over the weekend’: high workload and other pressures faced by early-career researchers](#)



- [Beating the odds to secure a permanent contract](#)



- [Collection: Diversity and scientific careers](#)



- [Career resources for postdoctoral researchers](#)

Subjects

- [Careers](#)
 - [Society](#)
 - [Institutions](#)
 - [Lab life](#)
-

This article was downloaded by **calibre** from <https://www.nature.com/articles/d41586-021-01682-9>

| [Section menu](#) | [Main menu](#) |

- TECHNOLOGY FEATURE
- 21 June 2021

Five trendy technologies: where are they now?

A look at notable research tools and projects that have rocketed to prominence reveals some common routes to success.

- [Jyoti Madhusoodanan](#) ⁰

1. Jyoti Madhusoodanan

1. Jyoti Madhusoodanan is a freelance writer based in Portland, Oregon, and was a Knight Science Journalism project fellow at the Massachusetts Institute of Technology in autumn 2020.

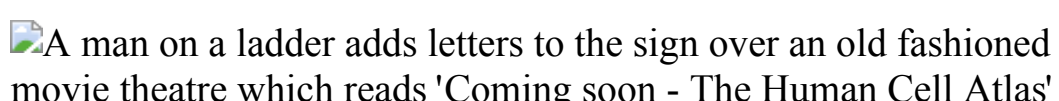
[View author publications](#)

You can also search for this author in [PubMed](#) [Google Scholar](#)





•



Credit: Adapted from Getty

[Download PDF](#)

When asked to describe his speciality, Kaihang Wang's answer is immediate: "handyman". After all, much of his work at the California Institute of Technology in Pasadena involves building things, albeit not with a hammer and nails. Wang and his team develop molecular tools, including a system that biologists can program to introduce a long, synthetic strand of DNA into

a bacterial cell¹. After further thought, Wang offers more-scientific alternatives: synthetic biology or genome engineering. “All our efforts are fundamentally driven by the goal to make a living thing,” he says.

Like Wang, many biologists reach across disciplines for materials, collaborators or different approaches when the tools at hand fall short. That can lead to methods or consortia that require new descriptors, such as ‘expansion microscopy’ or ‘Genome Project-write’. Some of these create a buzz among scientists through a combination of technical capability and good branding.

Coining a catchy name for a field or tool creates a conceptual infrastructure that researchers can use to frame enquiry, says Erika Szymanski, who studies the rhetoric of science at Colorado State University in Fort Collins. “Just as the constraints of a microscope determine what you can see with it, we can only ‘see’ things when we have names for them,” she says. “Sometimes, trying on a new frame for thinking about the work we do is productive, because it opens up space for imagining new possibilities.”

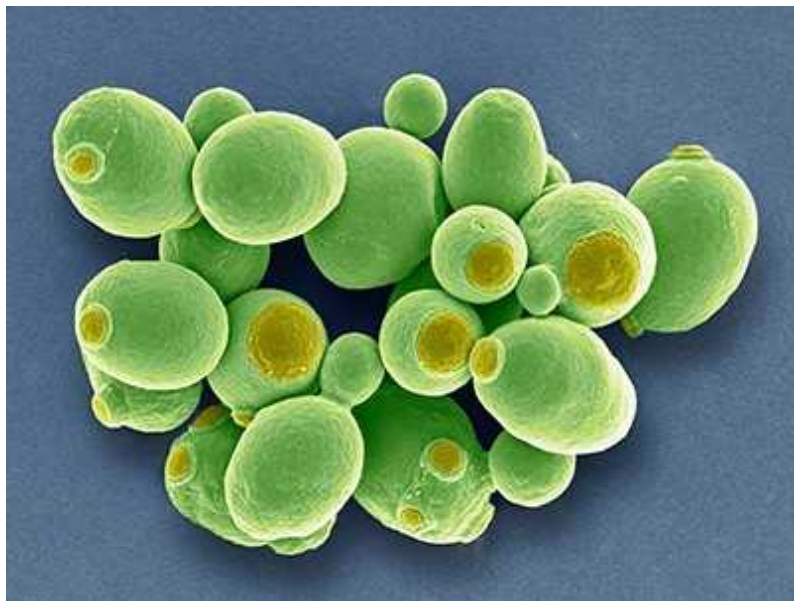
Here, *Nature* explores 5 noteworthy technologies from the past 15 years. Some have spawned fields of study or garnered funding; others have increased global collaboration or found fresh purpose in studies far from their original aim. But all have left their mark on science, whether by revealing cell functions, giving rise to companies and therapies or informing public-health policy during a pandemic.

Epitranscriptomics

Like genomic DNA, messenger RNA can carry chemical tags such as methyl or sugar groups that alter its function or fate. Such modifications are not uniform, and the discovery that some mRNAs are highly methylated and others are not hinted at a biological role for the tags. In 2012, RNA biologist Samie Jaffrey at Weill Cornell Medical College in New York City and his colleagues developed a method to identify a specific mRNA methylation mark, named m6A, across the transcriptome (the full complement of RNAs in a cell or organism)².

Study co-author Christopher Mason, also at Weill Cornell, coined the term epitranscriptomics to explain the team's hypothesis that the methyl tags regulate the activity of mRNA transcripts, thereby suggesting why protein levels don't always match the abundances of the transcripts that encode them. "The idea that this might be another layer of the genetic code was very appealing," Jaffrey says. The new name made it easier for others to grasp the concept.

Over the years, epitranscriptomics has grown into its own field, with specific calls for funding, meetings and collaborations. "In some ways, the fact that a new word was created led to this community," says RNA biologist Eva Maria Novoa Pardo at the Centre for Genomic Regulation (CRG) in Barcelona, Spain.



How to build a genome

Jaffrey and Mason's original method used an antibody to m6A to isolate fragments of modified RNA that were 100–200 nucleotides long, which they then identified by sequencing. Later, the team cross-linked the antibodies to a substrate, then precipitated the antibody-bound RNA fragments to pinpoint methylated sites, allowing them to generate the first single-nucleotide-level map of methylated mRNA. This helped to identify another class of molecules that carried the modification, called small nucleolar RNAs³. "We're now starting to coalesce around the idea that a major function of

m6A is to mark RNA for quick turnover,” Jaffrey says — which is crucial to a cell’s ability to change and respond to its environment.

Subsequent developments exploited enzymes that could cut non-methylated RNAs at specific sequences. That tool allowed its developer, RNA biologist Schraga Schwartz at the Weizmann Institute of Science in Rehovot, Israel, to detect not just whether a particular site was modified, but also what percentage of transcripts carried the methylated motif. When Schwartz and his colleagues applied this to the entire transcriptome, they found that nearly 75% of modified sites were missed by antibody-based technology, suggesting its sensitivity was limited⁴. “It was a big surprise to see,” he says. “Having two methods instead of just one allows us to get a more holistic view of the problem.”

Today, epitranscriptomics researchers can read modified RNA directly using nanopore sequencing machines. Unlike conventional sequencers, which require RNA to first be converted to DNA using reverse transcription, these instruments pass RNA molecules through protein nanopores, producing distinctive electrical currents that are then decoded to provide the RNA sequence. Methylated m6A nucleotides are often misread by the sequencing algorithm used to decode the currents. So in 2019, Novoa and her colleagues designed an algorithm (updated earlier this year⁵) that uses these errors to predict which of those sites carries a methylated nucleotide. “The possibility of sequencing native RNA” — without needing to reverse-transcribe it into DNA first — “opens up a completely unbiased view of the transcriptome,” she says.

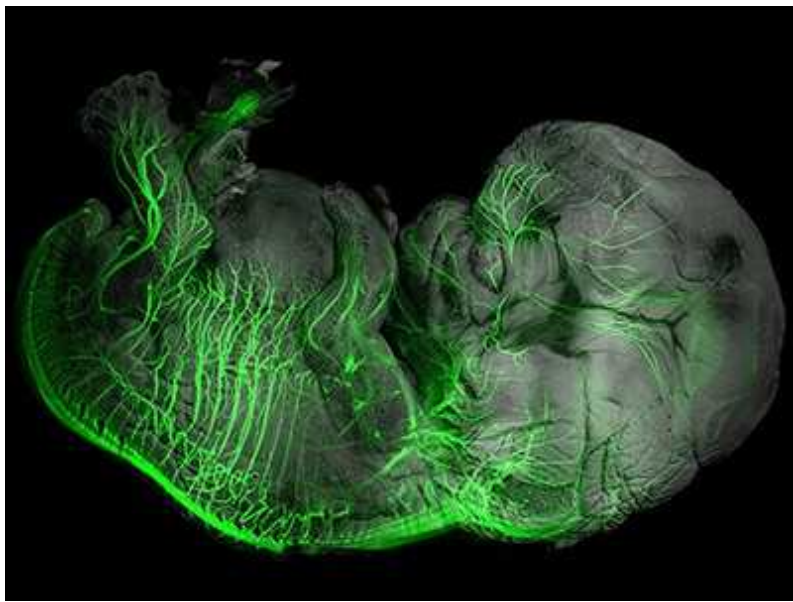
The Human Cell Atlas

The completion of sequencing of the human genome in 2003, together with the arrival of new tools to study single cells, led many to wonder whether they could map every human cell’s unique location, behaviour and development. Sarah Teichmann, a geneticist at the Wellcome Sanger Institute in Hinxton, UK, and Aviv Regev, a computational biologist who is now at Genentech in South San Francisco, California, were among them.

In late 2016, Teichmann, Regev and others convened to discuss the idea. The result was the Human Cell Atlas, a project that uses single-cell approaches to chart the organization, genetics and biology of every human cell, tissue and organ. The group emphasizes an open, collaborative approach: anyone can participate, and the consortium collects information using a wide array of molecular and computational methods.

“There’s no gold-standard technology that can do everything,” says Holger Heyn, who studies single-cell sequencing technologies at the CRG and leads the consortium’s standards and technologies working group. “Every method has biases. The more we integrate diverse technologies, the fewer biases we’ll have.”

In one 2020 study, Heyn and his collaborators compared 13 single-cell RNA sequencing technologies across a common reference set of samples, judging them on their ability to spot cell-specific markers⁶. One major source of variation in the results, they found, turned out to be the size of cells in a sample. “The goal was not to find a winner or loser, just to define what you might expect to get with each technology,” Heyn says.



[Transparent tissues bring cells into focus for microscopy](#)

The Human Cell Atlas consortium now has almost 2,200 members in 77 countries, who collectively have analysed some 39 million cells from 14

major organs and produced nearly 80 publications, and counting.

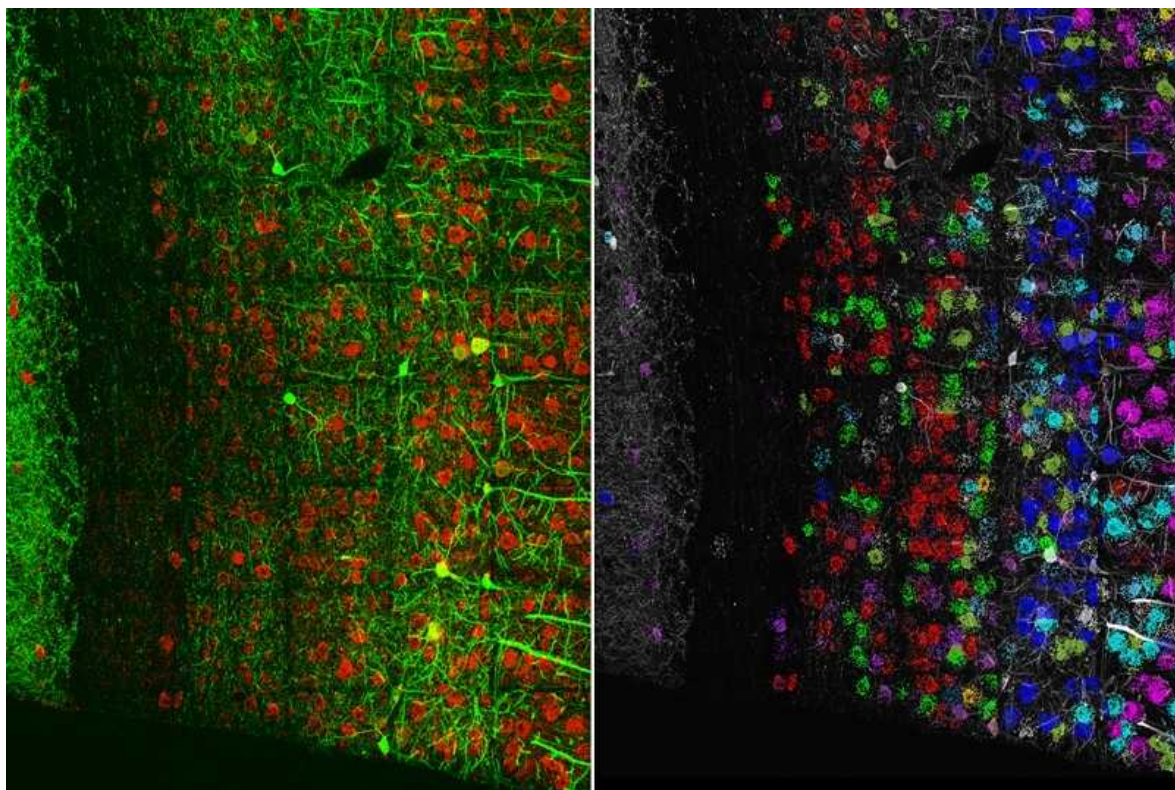
Among other things, those data have helped to unlock the mysteries of COVID-19. In early 2020, consortium members pooled 26 published and unpublished data sets to understand how the coronavirus SARS-CoV-2 invades lung tissues. They mapped the cell-surface receptors that the virus uses to enter tissues, including those of the nose, mouth, eyes and more⁷. Researchers around the world have since used that map to understand the process of infection. It has even helped to inform public-health policies, such as those requiring people to wear face masks, Teichmann says. “The pandemic was really transformative for the Human Cell Atlas project,” she says. “It shows you the value of a cell atlas — even an early, incomplete one.”

Expansion microscopy

Although many researchers obsessed with microscopy resolution have focused on building better hardware, neuroscientist Ed Boyden took a different tack. Together with colleagues at the Massachusetts Institute of Technology in Cambridge, he devised a technique called expansion microscopy, which enlarges cells and tissues like inflating a balloon.

The method infuses a sample with a monomer called acrylate. Adding water causes that monomer to polymerize and swell, pushing cellular components apart as it grows. In early attempts, the cells cracked or swelled unevenly. But adding enzymes to soften tissues before polymerization allowed the researchers to expand mouse brain tissues to 4.5 times their original size⁸. Two years later, the team extended the method to a dozen tissue types, some of which could be expanded 16-fold⁹. “Making sure the physical magnification is scaled correctly was essential to making the technique worthwhile,” Boyden says.

This year, Boyden and his team used the concept to locate specific RNAs in tissues, a subfield called spatial transcriptomics. They first expanded a section of mouse brain tissue and then sequenced the embedded RNAs *in situ*¹⁰.



Combining expansion microscopy with RNA sequencing (left) reveals the organization of neurons in the mouse visual cortex (right). Credit: S. Alon *et al./Science*

Neuroscientist Erin Schuman at the Max Planck Institute for Brain Research in Frankfurt, Germany, who studies how proteins are formed at nerve-cell junctions called synapses, has long relied on indirect methods such as silver staining to visualize this process. Schuman wanted to see newly made proteins in synapses directly. But the synapses are formed by long, thin fibres known as axons that lack good molecular markers. “They’re actually one of the most elusive things to study,” she says.

Using expansion microscopy, Schuman and her team were able to see, for the first time, that almost all axon terminals had the machinery to synthesize new proteins¹¹. “It really helped us access the synapse with a high degree of confidence, and do high-throughput analysis,” she says.

And at Stanford University in California, bioengineer Bo Wang has used the tool to create a high-resolution image of how the common gut pathogen *Salmonella* interacts with human cells. In optimizing the ‘softening’ step of

the process, Wang and his colleagues found that the method could be used to measure the stiffness of the bacterial cell wall. That tough layer is crucial to the pathogen's resistance to antibiotics and host defences, for instance. Gauging the mechanical properties of microscale objects is difficult, but expansion microscopy helped the team to measure the strength of thousands of cell walls in a single batch, to understand how the bacteria reacted to host-defence mechanisms¹². "Similar strategies can help answer physiological questions in plants, fungi and many different species," Wang says.

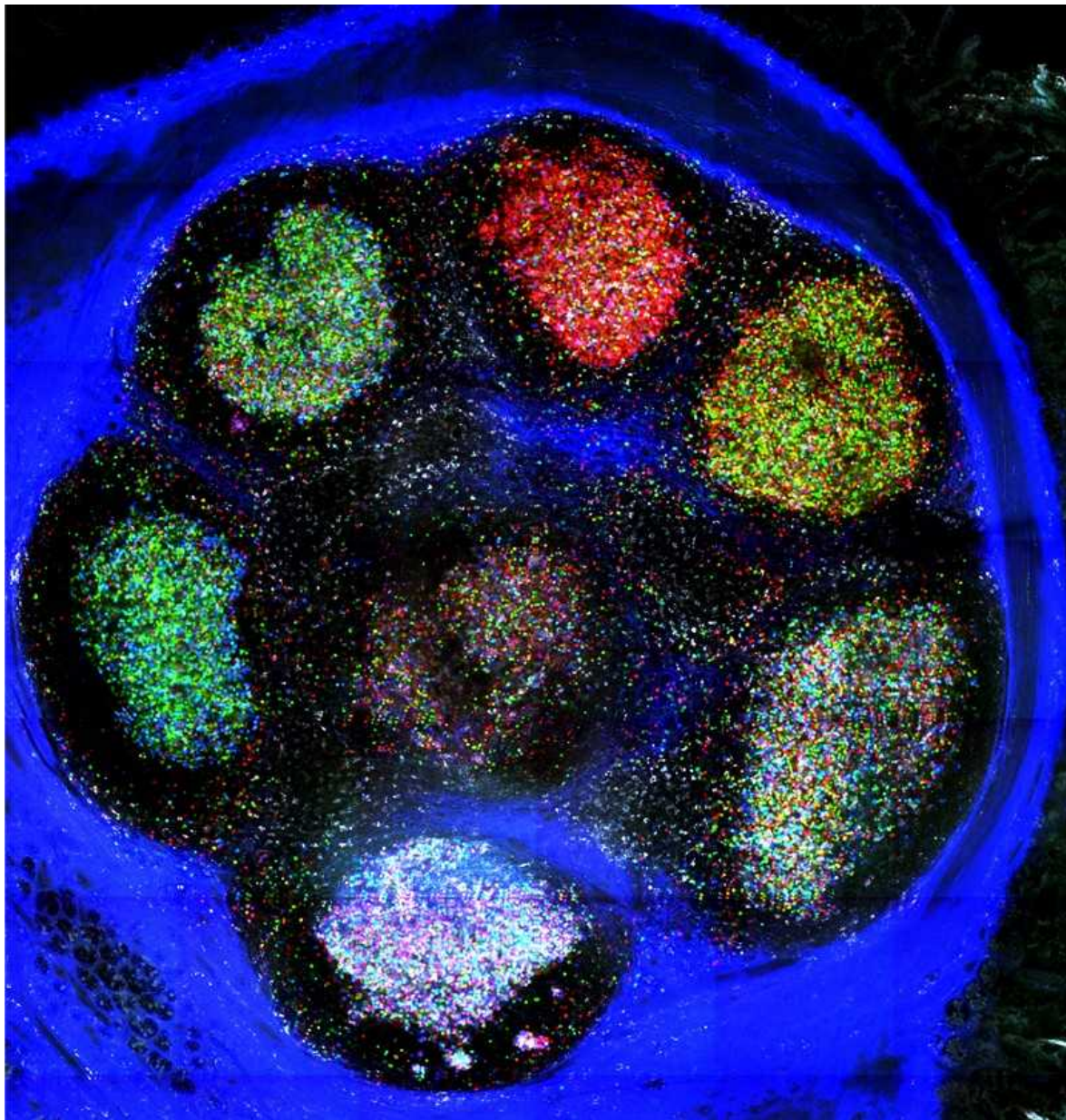
Brainbow

In 2007, a team led by neuroscientists Jeff Lichtman and Joshua Sanes at Harvard University in Cambridge, Massachusetts, developed a way to distinguish the tangled skeins of neurons in the mouse brain¹³. The researchers constructed a system in which genes for a few fluorescent proteins were controlled by regulatory sequences specific to neurons, and flanked by tags that would mark the fluorescent genes to be shuffled in an enzyme-catalysed process called recombination. Cells were given multiple copies of these gene 'cassettes', so when the researchers activated a protein that recognized the recombination tags, it shuffled the genes into various, random combinations, expressed as a rainbow of fluorescence. They called their tool Brainbow.

As a graduate student at New York University, Gabriel Victora recalls being awestruck by those kaleidoscopic pictures of the brain, each cell a different hue. But Victora's studies focused on germinal centres, microstructures in lymph nodes where immune cells divide and grow. "We didn't immediately think to use this technology," says Victora, now an immunologist at The Rockefeller University in New York City. "I remember thinking, 'pity that's in the brain'."

Lichtman hoped that the ability to label individual cells would help to resolve fine-scale details such as synaptic connections in the brain. But small cellular structures have fewer fluorescent molecules, making them dimmer — often too dim to be useful. Disappointed with the results, Lichtman says he has since turned to techniques such as serial block-face scanning electron

microscopy, in which a block of tissue is repeatedly imaged, peeled back and imaged again to map neural connections. “You have to find the right tool for the job, and in this case, Brainbow wasn’t quite adequate,” he says.



Brainbow-labelled germinal centres.Credit: Carla Nowosad

Lichtman does use Brainbow for experiments in the peripheral nervous system, where cells are farther apart so even dim fluorescence can be observed. And other groups have adapted the tool for different organisms — Flybow for *Drosophila* brains and Zebrabow for zebrafish tissues, for

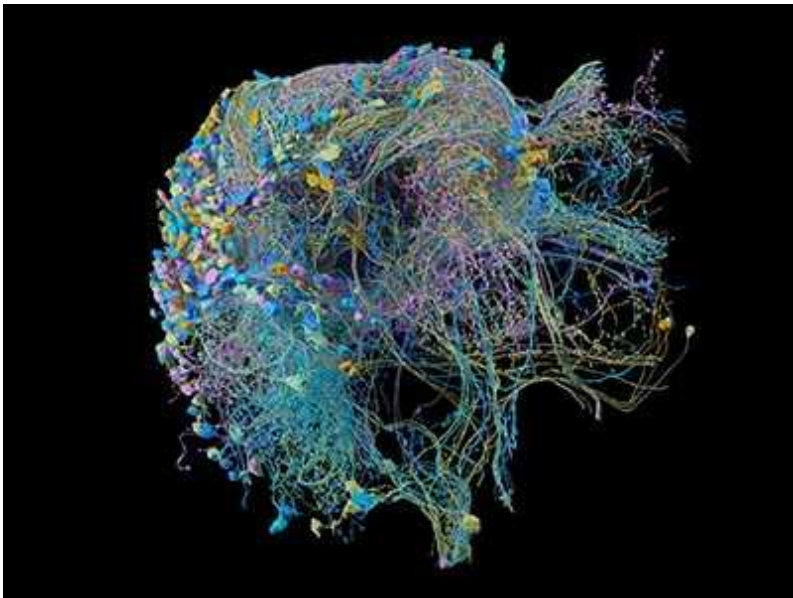
instance. Combining Brainbow with expansion microscopy has allowed researchers to examine cellular shapes and connectivity in mammalian tissue^{[14](#)}.

For Victora, it was a mouse model called Confetti, which extends the technology to non-neuronal cells, that reignited his interest in Brainbow. Inside the germinal centres of lymph nodes, clusters of B cells produce different antibodies and compete to thrive. Most germinal centres maintain a diversity of antibody molecules. But in 5–10% of these structures, Victora and his team found that cells that produce high-affinity antibodies can quickly outcompete other B cells and take over a germinal centre^{[15](#)}. Researchers tracking these ‘clonal bursts’ with Brainbow see all the cells in a germinal centre in different colours when they first label cells. Then, as one dominant clone takes over, its progeny — all of which bear the same colour as the parent cell — turn the structure from technicolour to monochrome. “Brainbow shows this division of labour [between B cells] very clearly,” he says.

Genome Project-write

If scientists could make complete synthetic chromosomes, they could confer new functions on cells, swap out disease-causing genetic pathways or design new experimental systems for research. But synthetic chromosomes cannot be built in one go.

In 2010, researchers pieced together the first synthetic bacterial genome^{[16](#)}. They remade the organism’s DNA in short chunks, stitched these together, then swapped portions of the chromosome one piece at a time until the native DNA was entirely replaced by its synthetic counterpart. The process has remained largely unchanged since this first attempt, says Wang at the California Institute of Technology. Despite remarkable progress in bacteria and yeast, the technique had never been extended to organisms with more complex genomes. Then, in 2016, researchers announced Genome Project-write, which aimed to synthesize complicated genomes, including that of humans.



Probing fine-scale connections in the brain

Launched with great excitement, the project had to scale back its aspirations — owing to both funding and technical challenges (see *Nature* **557**, 16–17; 2018) — to focus on engineering a human cell line that is resistant to viruses. But DNA synthesis on that scale remains a challenge, as does the design of genetic circuits that encode new functions. For the moment, such work largely remains the purview of individual researchers or small teams, says Christopher Voigt, a synthetic biologist at the Massachusetts Institute of Technology. That process that must shift if larger-scale genome synthesis is to become viable. “It’s something like a single person building an airplane, doing everything from designing it to gluing parts together,” he says. “It shows how far we are from being able to design something at the scale of a genome.”

Still, that lofty goal can spur the field forwards, Wang says. “The motivation to make a whole genome drives the development of technology. It’s a loop: once we have the tools, it makes genome synthesis more realistic and people pour more resources into the field.”

Nature **594**, 602–604 (2021)

doi: <https://doi.org/10.1038/d41586-021-01684-7>

References

1. 1.

Fredens, J. *et al.* *Nature* **569**, 514–518 (2019).

[PubMed](#) [Article](#) [Google Scholar](#)

2. 2.

Meyer, K. D. *et al.* *Cell* **149**, 1635–1646 (2012).

[PubMed](#) [Article](#) [Google Scholar](#)

3. 3.

Linder, B. *et al.* *Nature Methods* **12**, 767–772 (2015).

[PubMed](#) [Article](#) [Google Scholar](#)

4. 4.

Garcia-Campos, M. A. *et al.* *Cell* **178**, 731–747 (2019).

[PubMed](#) [Article](#) [Google Scholar](#)

5. 5.

Begik, O. *et al.* Preprint at bioRxiv
<https://doi.org/10.1101/2020.07.06.189969> (2021).

6. 6.

Mereu, E. *et al.* *Nature Biotechnol.* **38**, 747–755 (2020).

[PubMed](#) [Article](#) [Google Scholar](#)

7. 7.

Sungnak, W. *et al.* *Nature Med.* **26**, 681–687 (2020).

[PubMed](#) [Article](#) [Google Scholar](#)

8. 8.

Chen, C., Tillberg, P. W. & Boyden, E. S. *Science* **347**, 543–548 (2015).

[PubMed](#) [Article](#) [Google Scholar](#)

9. 9.

Chang, J.-B. *et al.* *Nature Methods* **14**, 593–599 (2017).

[PubMed](#) [Article](#) [Google Scholar](#)

10. 10.

Alon, S. *et al.* *Science* **371**, eaax2656 (2021).

[PubMed](#) [Article](#) [Google Scholar](#)

11. 11.

Hafner, A.-S., Donlin-Asp, P. G., Leitch, B., Herzog, E. & Schuman, E. M. *Science* **364**, eaau3644 (2019).

[PubMed](#) [Article](#) [Google Scholar](#)

12. 12.

Lim, Y. *et al.* *PLoS Biol.* **17**, e3000268 (2019).

[PubMed](#) [Article](#) [Google Scholar](#)

13. 13.

Livet, J. *et al.* *Nature* **450**, 56–62 (2007).

[PubMed](#) [Article](#) [Google Scholar](#)

14. 14.

Shen, F. Y. *et al. Nature Commun.* **11**, 4632 (2020).

[PubMed](#) [Article](#) [Google Scholar](#)

15. 15.

Nowosad, C. R. *et al. Nature* **588**, 321–326 (2020).

[PubMed](#) [Article](#) [Google Scholar](#)

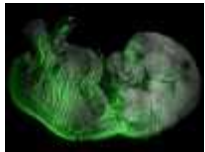
16. 16.

Gibson, D. G. *et al. Science* **329**, 52–56 (2010).

[PubMed](#) [Article](#) [Google Scholar](#)

[Download references](#)

Related Articles



- [Transparent tissues bring cells into focus for microscopy](#)



- [Probing fine-scale connections in the brain](#)



- [How to build a genome](#)



- [NatureTech hub](#)

Subjects

- [Biological techniques](#)
- [Microscopy](#)
- [Neuroscience](#)
- [Genomics](#)

[Jobs from Nature Careers](#)

- - - [All jobs](#)
 - - [Laboratory Research Scientist](#)
[Francis Crick Institute](#)
[London, United Kingdom](#)
[JOB POST](#)
 - [Bachelor of Science in Computer Engineering \(f/m/d\)](#)
[Helmholtz-Zentrum Berlin for Materials and Energy \(HZB\)](#)
[Berlin, Germany](#)
[JOB POST](#)
 -

Laboratory Engineer / Scientific and Technical Head of Reactor Technology (f/m/x)

Helmholtz Centre for Environmental Research (UFZ).

Leipzig, Germany

JOB POST

- Administrative Assistant/Internal Event Coordinator

Oklahoma Medical Research Foundation (OMRF)

Oklahoma City, United States

JOB POST

Download PDF

Related Articles

-  Transparent tissues bring cells into focus for microscopy
-  Probing fine-scale connections in the brain
-  How to build a genome



- [**NatureTech hub**](#)

Subjects

- [Biological techniques](#)
- [Microscopy](#)
- [Neuroscience](#)
- [Genomics](#)

This article was downloaded by **calibre** from <https://www.nature.com/articles/d41586-021-01684-7>

| [Section menu](#) | [Main menu](#) |

- WHERE I WORK
- 21 June 2021

Shell shock: a biologist's quest to save the endangered painted snail

Bernardo Reyes-Tur aims to unravel the mating mysteries of Cuba's imperilled *Polymita*.

- [Kendall Powell](#) 0

1. Kendall Powell

1. Kendall Powell is a freelance writer in Boulder, Colorado.

[View author publications](#)

You can also search for this author in [PubMed](#) [Google Scholar](#)





•



Bernardo Reyes-Tur is a professor of conservation biology at University Oriente in Santiago de Cuba, Cuba. Credit: Bruno D'Amicis

[Download PDF](#)

In my laboratory at the University of Oriente, in Santiago de Cuba, we study the six species of *Polymita*, known as painted snails, which are endemic to eastern Cuba and are in danger of extinction. The shells' vibrant swirls and stripes look as if they've been painted by hand. Unfortunately, you can find

their shells for sale on eBay, and many are exported to places such as the United States, China and Spain for use in art and jewellery — despite laws banning such trade.

Painted snails live in mangrove forests, in sandy and rocky coastal areas and in rainforests. Some species are important parts of agro-ecosystems, such as coffee and coconut plantations. In 1995, my team began a breeding laboratory. We needed a way to isolate individual snails in containers, and to provide them with food, such as a fig-tree branch covered with moss, lichens and sooty mould fungus. But getting enough of the right containers was a problem because the nation was in an economic depression then.

My students realized that when tourists visited Cuba, they left behind plastic one-litre water bottles. Since then we've been using them as living spaces for the snails.

We study the breeding behaviour, nesting, hatching and growth of these hermaphrodites. If we want to save *Polymita*, we need to know more about their reproduction patterns — why one species hatches only between July and December, for instance.

When mating, *Polymita* use a protrusion called a dart to transfer hormones, but we know very little about it. We are studying how these hormones affect the reproductive tract and influence fertilization success.

In Cuba, there is more support for medical research than for biodiversity research. So we look for collaborations around the world. My motto is a Cuban saying: “We have the ‘no’, and therefore always have to look for the ‘yes’.” In other words, there is always another way, if you keep looking.



Polymita's vibrant swirls and stripes make the endangered snails valuable for illegal trade.Credit: Bruno D'Amicis/NPL

Nature **594**, 606 (2021)

doi: <https://doi.org/10.1038/d41586-021-01683-8>

Related Articles

-  [My race against time to capture the sounds of ancient rainforests](#)
-  [Fighting fires to save a natural reserve in Brazil](#)



- [Catching a wave to study coral](#)

Subjects

- [Careers](#)
- [Conservation biology](#)
- [Developing world](#)

[Jobs from Nature Careers](#)

- - - [All jobs](#)
 -
 - [Laboratory Research Scientist](#)
 - [Francis Crick Institute](#)
 - [London, United Kingdom](#)
 - [JOB POST](#)
 - [Bachelor of Science in Computer Engineering \(f/m/d\)](#)
 - [Helmholtz-Zentrum Berlin for Materials and Energy \(HZB\)](#)
 - [Berlin, Germany](#)
 - [JOB POST](#)
 - [Laboratory Engineer / Scientific and Technical Head of Reactor Technology \(f/m/x\)](#)

[Helmholtz Centre for Environmental Research \(UFZ\)](#)

[Leipzig, Germany](#)

[JOB POST](#)

- [Administrative Assistant/Internal Event Coordinator](#)

[Oklahoma Medical Research Foundation \(OMRF\)](#)

[Oklahoma City, United States](#)

[JOB POST](#)

[Download PDF](#)

Related Articles



- [My race against time to capture the sounds of ancient rainforests](#)



- [Fighting fires to save a natural reserve in Brazil](#)



- [Catching a wave to study coral](#)

Subjects

- [Careers](#)
 - [Conservation biology](#)
 - [Developing world](#)
-

This article was downloaded by **calibre** from <https://www.nature.com/articles/d41586-021-01683-8>

| [Section menu](#) | [Main menu](#) |

Research

- **[Unravelling the enigma of bird magnetoreception](#)** [23 June 2021]

News & Views • How animals sense Earth's magnetic field is an enduring mystery. The protein cryptochrome ErCRY4, found in the eyes of migratory European robins, has the right physical properties to be the elusive magnetosensor.

- **[Plasmons dragged by drifting electrons](#)** [23 June 2021]

News & Views • Plasmons are combinations of light and collective electron oscillations. The demonstration that plasmons can be dragged by drifting electrons in the 2D material graphene could lead to advances in optical physics.

- **[A 4D road map for the formation of hair follicles](#)** [09 June 2021]

News & Views • Combined imaging and gene-expression analyses reveal that the arrangement of cells in concentric rings in the disc-like structures that give rise to hair follicles predetermines their eventual fate and location in mature follicles.

- **[Natural killer cells lull tumours into dormancy](#)** [02 June 2021]

News & Views • Natural killer cells can drive spreading cancer cells to enter a state of dormancy. That finding, together with the discovery of a pathway that hinders this antitumour function, could spur the development of new treatments.

- **[Ion dynamics in battery materials imaged rapidly](#)** [23 June 2021]

News & Views • An imaging method has been developed that tracks ion transport in functioning battery materials in real time, at submicrometre scales — offering insights into how to design batteries that charge in minutes.

- **[Past, present and future stars that can see Earth as a transiting exoplanet](#)** [23 June 2021]

Article • The Gaia database is used to identify stars from which astronomers on orbiting planets could see Earth transiting the Sun in the past, present and future.

- **[Accurately computing the electronic properties of a quantum ring](#)** [23 June 2021]

Article • As a blueprint for high-precision quantum simulation, an 18-qubit algorithm that consists of more than 1,400 two-qubit gates is demonstrated, and reconstructs the energy eigenvalues of the simulated one-dimensional wire to a precision of 1 per cent.

- **Fizeau drag in graphene plasmonics** [23 June 2021]
Article • Direct infrared nano-imaging of plasmonic waves in graphene carrying high current density reveals the Fizeau drag of plasmon polaritons by fast-moving quasi-relativistic electrons.
- **Efficient Fizeau drag from Dirac electrons in monolayer graphene** [23 June 2021]
Article • Fizeau drag of plasmon polaritons by an electron flow in strongly biased monolayer graphene is directly observed by exploiting the high electron mobility and slow plasmon propagation of Dirac electrons.
- **Operando optical tracking of single-particle ion dynamics in batteries** [23 June 2021]
Article • The dynamics of ions within a working lithium-ion battery are examined using optical interferometric scattering microscopy, which allows ion transport to be related to phase transitions and microstructural features.
- **A catalysis-driven artificial molecular pump** [23 June 2021]
Article • A molecular-scale pump whose operation is driven by a catalytic process when in the presence of chemical fuel is autonomous, within an operating window, as long as the fuel lasts.
- **Magnetic sensitivity of cryptochrome 4 from a migratory songbird** [23 June 2021]
Article • Cryptochrome 4 from the night-migratory European robin displays magnetically sensitive photochemistry in vitro, in which four successive flavin–tryptophan radical pairs generate magnetic-field effects and stabilize potential signalling states.
- **Representational drift in primary olfactory cortex** [09 June 2021]
Article • All odours elicit a unique pattern of neuronal activity in primary olfactory cortex but these patterns drift over time, posing a problem for the perceptual constancy of odours.
- **Tracing the origin of hair follicle stem cells** [09 June 2021]
Article • Live imaging and single-cell transcriptomics of mouse hair follicles reveal their development from 2D concentric zones in the placode to 3D longitudinal compartments, one of which is a stem cell compartment.
- **Neutralizing antibody vaccine for pandemic and pre-emergent coronaviruses** [10 May 2021]
Article • Immunization of macaques with nanoparticle-conjugated receptor-binding domain of SARS-CoV-2 adjuvanted with 3M-052 and alum results in cross-neutralizing antibodies against bat coronaviruses, SARS-CoV and SARS-CoV-2 variants, and may provide a platform for developing pan-coronavirus vaccines.

- **MARK4 controls ischaemic heart failure through microtubule detyrosination** [26 May 2021]
Article • MARK4 regulates cardiomyocyte contractility by promoting MAP4 phosphorylation, which facilitates the access of VASH2 to microtubules for the detyrosination of α -tubulin; MARK4 deficiency after acute myocardial infarction limits the reduction in the left ventricular ejection fraction.
- **Hepatic stellate cells suppress NK cell-sustained breast cancer dormancy** [02 June 2021]
Article • Liver-resident natural killer (NK) cells sustain the dormancy of disseminated breast cancer cells, and a decrease in NK cells and increase in activated hepatic stellate cells is associated with the formation of liver metastases.
- **Concerted cutting by Spo11 illuminates meiotic DNA break mechanics** [09 June 2021]
Article • A small proportion of Spo11-dependent DNA double-strand breaks are ‘double cuts’—adjacent breaks that occur in concert—revealing that gap repair during meiosis includes that of DNA gaps generated by Spo11 itself.
- **Spo11 generates gaps through concerted cuts at sites of topological stress** [09 June 2021]
Article • Meiotic recombination in yeast is not only initiated by single break sites, but also caused by closely spaced Spo11-dependent double-stranded DNA breaks that create chromosomal gaps.
- **Structures of Gi-bound metabotropic glutamate receptors mGlu2 and mGlu4** [16 June 2021]
Article • Cryo-electron microscopy structures of mGlu2 and mGlu4 bound to heterotrimeric Gi protein shed light on the molecular basis of asymmetric signal transduction by metabotropic glutamate receptors.
- **Structures of human mGlu2 and mGlu7 homo- and heterodimers** [16 June 2021]
Article • Cryo-electron microscopy structures of homo- and heterodimers of mGlu2 and mGlu7 provide insights into their dimerization modes and the subunit conformational changes that characterize the activation of these class C G-protein-coupled receptors.
- **Structural basis of GABAB receptor–Gi protein coupling**
[28 April 2021]
Article • Cryo-electron microscopy structure of heterodimeric GABAB receptor in complex with Gi1 protein reveals that the mode of G-protein binding in this class-C G-protein-coupled receptor differs from that of other classes.

- NEWS AND VIEWS
- 23 June 2021

Unravelling the enigma of bird magnetoreception

How animals sense Earth's magnetic field is an enduring mystery. The protein cryptochrome *ErCRY4*, found in the eyes of migratory European robins, has the right physical properties to be the elusive magnetosensor.

- [Eric J. Warrant](#) [ORCID: http://orcid.org/0000-0001-7480-7016](http://orcid.org/0000-0001-7480-7016) ⁰

1. [Eric J. Warrant](#)

1. Eric J. Warrant is in the Lund Vision Group and in the Department of Biology, University of Lund, S-22362 Lund, Sweden.

[View author publications](#)

You can also search for this author in [PubMed](#) [Google Scholar](#)



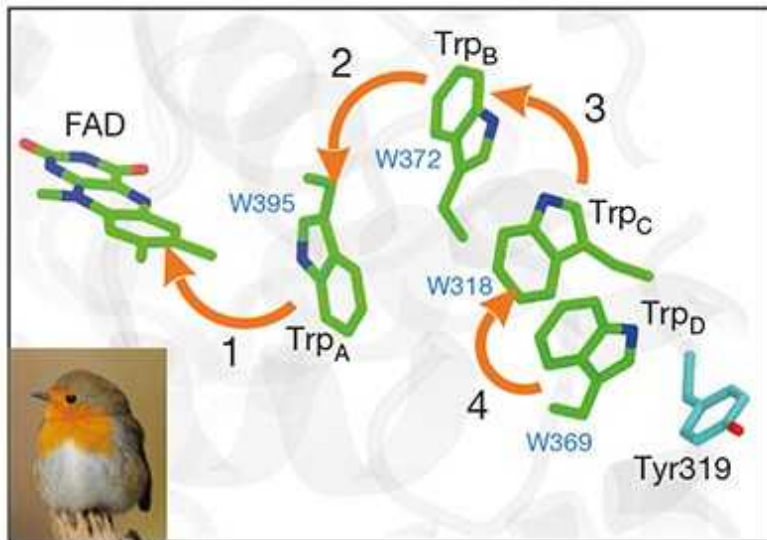


•

[Download PDF](#)

Arguably the greatest mystery in sensory biology is magnetoreception — how animals sense Earth's magnetic field and use it as a compass to determine their spatial orientation. Animals as varied as birds, sea turtles, fishes, crustaceans and insects depend on this field for both short- and long-range navigation¹. The identity of the biological tissue responsible for sensing the field's direction, and the sensory mechanism that underpins this type of navigation, have remained an enigma. In migratory birds, the main contenders are magnetically sensitive proteins called cryptochromes, which are located in the retina². However, proof has been lacking that these

proteins truly possess the magnetic sensitivity and physical properties needed to detect Earth's extremely weak magnetic field. [Writing in Nature](#), Xu *et al.*³ provide this proof *in vitro*, bringing us tantalizingly close to solving the mystery of magnetoreception.



[Read the paper: Magnetic sensitivity of cryptochrome 4 from a migratory songbird](#)

There are currently two main hypotheses for how animals sense Earth's magnetic field^{1,4} (as well as some alternative hypotheses put forward in the past few years^{5,6}). One proposes that, as an animal changes direction, crystals of the oxidized-iron compound magnetite (Fe_3O_4), located in its body and aligned with the field, exert a rotational force — called torque — on mechanoreceptors with which they are in physical contact. This might thereby signal changes in body alignment through the opening and closing of mechanoreceptor ion channels.

The other main hypothesis (Fig. 1) proposes that, when cryptochrome proteins absorb photons of light and become ‘photoexcited’, they form magnetically sensitive chemical intermediates known as radical pairs. Variations in the yield of their reaction product (the form of the cryptochrome that contains a radical molecule called FADH^\bullet) are thought to signal the animal’s direction with respect to Earth’s magnetic field^{7,8}. These

two proposed mechanisms are not mutually exclusive⁶ — indeed, migratory birds might possess both, using magnetite for their ‘magnetic-map’ sense (the ability to sense magnetic characteristics associated with a given location on Earth’s surface) and cryptochromes for their magnetic-compass sense (which offers the animal a way to sense its direction relative to magnetic north)^{1,2}.

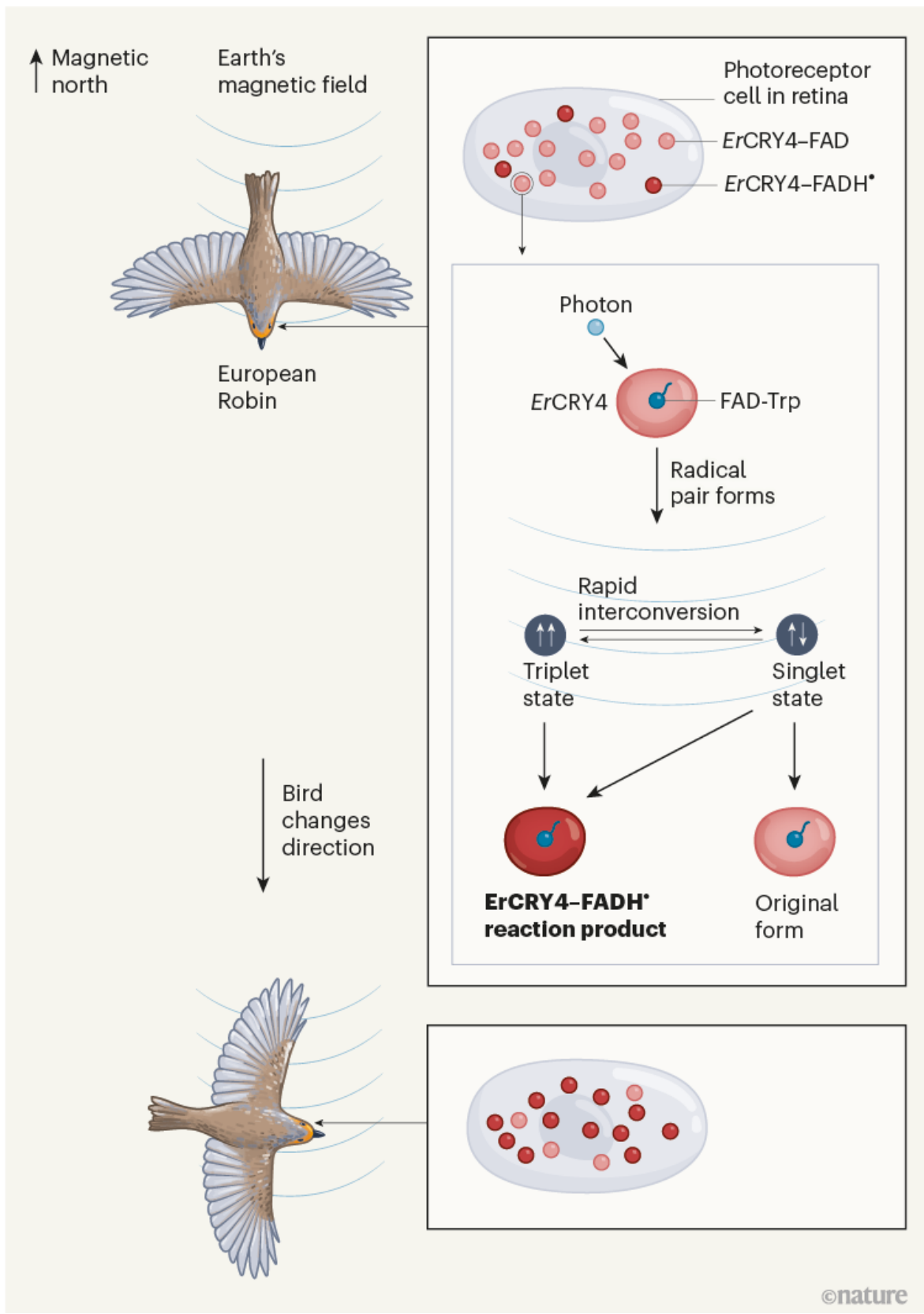


Figure 1 | A model for bird magnetoreception. Birds use Earth's magnetic field to aid their migration¹. Photoreceptor cells in the retina of the migratory European robin *Erithacus rubecula* contain a protein called ErCRY4, which binds to the molecule FAD. The resulting complex is ErCRY4–FAD (when FAD is in its ground state) or ErCRY4–FADH[•] when FAD is in its 'photoexcited' form (a radical, FADH[•]). When ErCRY4–FAD absorbs a photon of blue light, reactive molecules called radical pairs arise. These form through interactions between FAD and a tryptophan (Trp) amino-acid residue of ErCRY4, which supplies an electron. The radical pair is sensitive to Earth's magnetic field and oscillates rapidly between a singlet and a triplet state (which have different electron 'spin' states as indicated by the white arrows). The radical pair can generate ErCRY4–FADH[•] (which is a long-lived reaction product hypothesized to trigger a sensory signalling cascade). Alternatively, ErCRY4 might return to its original form (ErCRY4–FAD). Which outcome occurs is influenced by the state of the radical pair. If the bird changes direction, the change in the relative orientation of the magnetic field drives a shift in the proportions of the singlet and triplet states, potentially altering the yield of ErCRY4–FADH[•]. Xu *et al.*³ present data indicating that ErCRY4 fulfils the physical requirements needed for this magnetosensing mechanism.

Cryptochromes are found both in animals and in plants, and are a type of protein known as a flavoprotein. Cryptochromes bind non-covalently to a molecule called a chromophore, such as FAD, which absorbs photons of blue light when in its fully oxidized state. In animals, cryptochrome proteins termed CRY1 and CRY2 are involved in the regulation of daily (circadian) rhythms⁹, and their expression levels in tissue typically cycle over the course of 24 hours. By contrast, the cryptochrome CRY4 lacks such signs of circadian cycling, suggesting that it has a different biological role, possibly that of magnetoreception^{10,11}. CRY4 is found only in birds, fishes and amphibians, which are types of animal with well-documented magnetically guided behaviours. CRY4 has therefore emerged as the leading candidate for enabling cryptochrome-based magnetoreception in vertebrates.

Previous analysis¹⁰ of chickens (*Gallus gallus*) and migratory European robins (*Erithacus rubecula*) indicates that CRY4 is located in the outer segments of two types of photoreceptor cell in the retina — double cones

and long-wavelength single cones. This is an ideal location for receiving the light that would excite cryptochromes and thus aid magnetic sensing. Further evidence consistent with a possible role for CRY4 in magnetoreception is that its expression level in the robin retina rises as the migratory season approaches, whereas its level remains permanently low in non-migratory chickens¹⁰.



A bird's migration decoded

Xu and colleagues' major advance is the demonstration that the version of CRY4 (dubbed *ErCRY4*) in the migratory European robin has a crucial property needed to sense Earth's magnetic field: the ability to form radical pairs that have high magnetic sensitivity. Radical pairs arise when the FAD bound to *ErCRY4* is reduced (gains an electron) in the presence of light. Radicals contain an odd number of electrons, and a radical pair consists of two radicals that have been created simultaneously, usually by a chemical reaction. In *ErCRY4*, the radicals' odd electrons are supplied through sequential electron-hopping along a chain of three or four tryptophan amino-acid residues (termed Trp_A to Trp_D) that are located between FAD and the surface of the cryptochrome.

In the case of FAD, the odd electron that arises from reduction in the presence of light makes the radicals intrinsically magnetic. This is because electrons behave as microscopic magnets, with a property that physicists call

spin (typically symbolized by an arrow \uparrow). In a molecule with an even number of electrons, the spins of each electron pair exactly cancel each other out, rendering the molecule non-magnetic.

If the spins of the odd electrons in each of the two radicals in a radical pair are antiparallel ($\downarrow\uparrow$), the radical pair is said to occupy a singlet state, but when they are parallel ($\uparrow\uparrow$), the pair occupies a triplet state. When cryptochrome becomes photoexcited, it always forms a radical pair in the singlet state, but it doesn't stay that way for long. Owing to a quirk of quantum mechanics, the radical pair rapidly converts to the triplet state, and then continues to bounce between these two states millions of times per second. Each of these two states can produce a reaction product — the form of CRY4 that contains the radical FADH $^\bullet$, which is the proposed signalling molecule for magnetoreception (Fig. 1). But the singlet state can also revert to its oxidized, non-excited ground state, thereby reducing its relative contribution to the generation of reaction products. Thus, if the interconversion of the singlet and triplet states can be manipulated to change the relative amounts of time spent in each of the two states, so too can the yield of the reaction products be manipulated, because a greater fraction of time in the triplet state leads to a higher yield of reaction products.



[Foraging skills develop over generations in the wild](#)

Herein lies the heart of the proposed cryptochrome-based magnetosensor: the relative amounts of time spent in the singlet and triplet states and the yield of reaction products are directly manipulated by the direction of Earth's magnetic field. The interaction between a single *ErCRY4* molecule and the field is, on its own, at least one million times too weak to create the radicals and influence their stability², but the energy required is provided by the photon absorbed by FAD. However, for this to work at all, the radical pair must be sufficiently magnetically sensitive, and the reaction product must exist for long enough and have a sufficiently high yield to realistically act as a sensory signalling substance. In a tour de force of biophysical chemistry, Xu and colleagues used a wide range of techniques, such as spectroscopic methods and molecular-dynamics simulations, to show that all of these conditions are satisfied by *ErCRY4*, at least *in vitro*.

Not only does *ErCRY4* have a much higher magnetic sensitivity than do CRY4 proteins in non-migratory pigeons and chickens, but site-specific mutations of amino-acid residues in *ErCRY4* also reveal that its Trp_D is probably responsible for generating high and long-lasting (of greater-than-millisecond duration) yields of reaction products that would be needed for magnetosensory signalling. Although the evidence provided by Xu and colleagues is not definitive proof that *ErCRY4* is the elusive magnetoreceptor *in vivo*, the authors have brought us ever closer to solving this abiding mystery of sensory biology.

Nature **594**, 497–498 (2021)

doi: <https://doi.org/10.1038/d41586-021-01596-6>

References

1. 1.

Mouritsen, H. *Nature* **558**, 50–59 (2018).

[PubMed](#) [Article](#) [Google Scholar](#)

2. 2.

Hore, P. J. & Mouritsen, H. *Annu. Rev. Biophys.* **45**, 299–344 (2016).

[PubMed](#) [Article](#) [Google Scholar](#)

3. 3.

Xu, J. *et al.* *Nature* **594**, 535–540 (2021).

[Article](#) [Google Scholar](#)

4. 4.

Lohmann, K. J. *Nature* **464**, 1140–1142 (2010).

[PubMed](#) [Article](#) [Google Scholar](#)

5. 5.

Qin, S. *et al.* *Nature Mater.* **15**, 217–226 (2016).

[PubMed](#) [Article](#) [Google Scholar](#)

6. 6.

Nimpf, S. *et al.* *Curr. Biol.* **29**, 4052–4059 (2019).

[PubMed](#) [Article](#) [Google Scholar](#)

7. 7.

Schulten, K., Swenberg, C. E. & Weller, A. *Z. Phys. Chem.* **111**, 1–5 (1978).

[Article](#) [Google Scholar](#)

8. 8.

Ritz, T., Adem, S. & Schulten, K. *Biophys. J.* **78**, 707–718 (2000).

[PubMed](#) [Article](#) [Google Scholar](#)

9. 9.

Griffin, E. A., Staknis, D. & Weitz, C. J. *Science* **286**, 768–771 (1999).

[PubMed](#) [Article](#) [Google Scholar](#)

10. 10.

Günther, A. *et al.* *Curr. Biol.* **28**, 211–223 (2018).

[PubMed](#) [Article](#) [Google Scholar](#)

11. 11.

Pinzon-Rodriguez, A., Bensch, S. & Muheim, R. *J. R. Soc. Interface* **15**, 20180058 (2018).

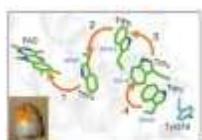
[PubMed](#) [Article](#) [Google Scholar](#)

[Download references](#)

Competing Interests

The author declares no competing interests.

Related Articles



- [Read the paper: Magnetic sensitivity of cryptochrome 4 from a migratory songbird](#)



- [A bird's migration decoded](#)



- [Foraging skills develop over generations in the wild](#)
- [See all News & Views](#)

Subjects

- [Evolution](#)
- [Animal behaviour](#)

[Jobs from Nature Careers](#)

- - - [All jobs](#)
 - - [Laboratory Research Scientist](#)

[Francis Crick Institute](#)

[London, United Kingdom](#)

[JOB POST](#)

- [Bachelor of Science in Computer Engineering \(f/m/d\)](#)

[Helmholtz-Zentrum Berlin for Materials and Energy \(HZB\)](#)

[Berlin, Germany](#)

[JOB POST](#)

- **Laboratory Engineer / Scientific and Technical Head of Reactor Technology (f/m/x)**

Helmholtz Centre for Environmental Research (UFZ).

Leipzig, Germany.

JOB POST

- **Administrative Assistant/Internal Event Coordinator**

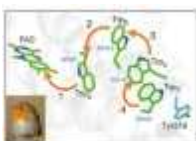
Oklahoma Medical Research Foundation (OMRF).

Oklahoma City, United States

JOB POST

Download PDF

Related Articles

-  **Read the paper: Magnetic sensitivity of cryptochrome 4 from a migratory songbird**
-  **A bird's migration decoded**
-  **Foraging skills develop over generations in the wild**

- [See all News & Views](#)

Subjects

- [Evolution](#)
- [Animal behaviour](#)

This article was downloaded by **calibre** from <https://www.nature.com/articles/d41586-021-01596-6>

| [Section menu](#) | [Main menu](#) |

- NEWS AND VIEWS
- 23 June 2021

Plasmons dragged by drifting electrons

Plasmons are combinations of light and collective electron oscillations. The demonstration that plasmons can be dragged by drifting electrons in the 2D material graphene could lead to advances in optical physics.

- [Hugen Yan](#) ⁰

1. [Hugen Yan](#)

1. Hugen Yan is at the State Key Laboratory of Surface Physics, the Key Laboratory of Micro- and Nano-Photonic Structures (Ministry of Education) and the Department of Physics, Fudan University, Shanghai 200433, China.

[View author publications](#)

You can also search for this author in [PubMed](#) [Google Scholar](#)



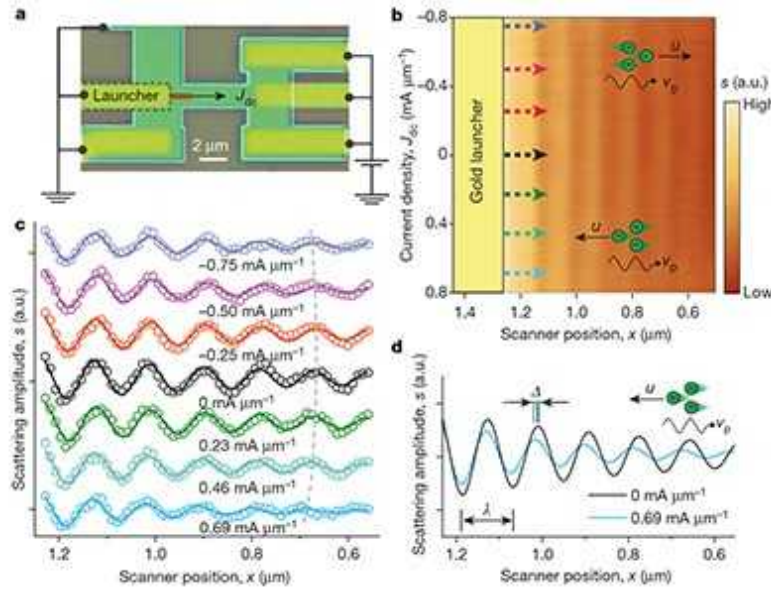


•

[Download PDF](#)

A wave passing through a moving medium can be dragged by that medium. Depending on the relative velocity directions of the wave and medium, this effect can either increase or decrease the wave's speed. For a light wave, which typically travels at an enormous speed, the drag effect of a moving medium is negligibly small. Only sensitive optical-interference techniques can detect such a speed change — as shown by a celebrated experiment performed by the French physicist Hippolyte Fizeau in 1851, in which light passes through moving water¹. Writing in *Nature*, [Dong et al.](#)² and [Zhao et al.](#)³ demonstrate an analogous effect in which plasmons (combinations of

light and collective electron oscillations) are dragged by drifting electrons in solids. The groups show that this effect is much more pronounced than that for light travelling through a moving medium.



[Read the paper: Fizeau drag in graphene plasmonics](#)

Waves are said to be transverse if they oscillate perpendicularly to their direction of propagation, and longitudinal if they oscillate parallel to that direction. Light is a transverse wave, whereas a plasmon is a longitudinal wave. In Fizeau's experiment, the light and the moving water are separate constituents, and the light can travel without a medium. However, for a plasmon, the light and the electrons are inseparable. As a result, a plasmon can be efficiently dragged by its constituent electrons if these electrons are drifting in an electric field. Crucially, this drag effect is easier to observe than that for light passing through a moving medium, because plasmons travel much slower than light.

Dong *et al.* and Zhao *et al.* fired a beam of infrared light at a gold bar, which launched plasmons in graphene⁴ — a single sheet of carbon atoms. They directly visualized the plasmons at cryogenic temperatures using an imaging method known as near-field infrared nanoscopy. The groups found that plasmons travelling in the opposite direction to the electron flow in the graphene had a shorter wavelength (and, therefore, a lower speed) than those propagating in the same direction (Fig. 1). They conclude that the drag effect

alters the plasmon wavelength by a few per cent. Such a change is remarkable because it can be directly measured without needing to resort to sensitive optical-interference techniques.

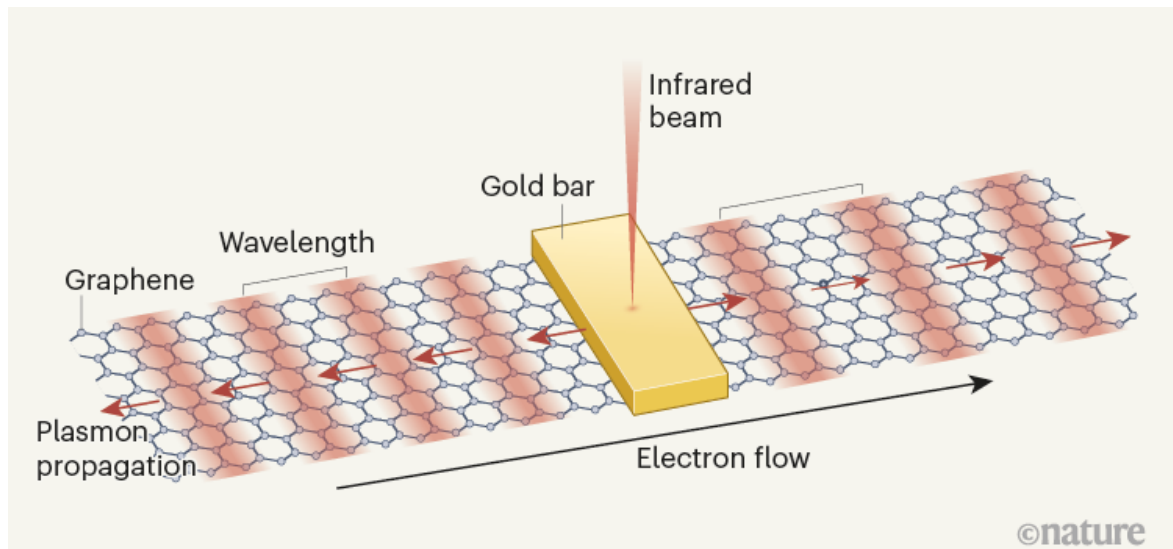
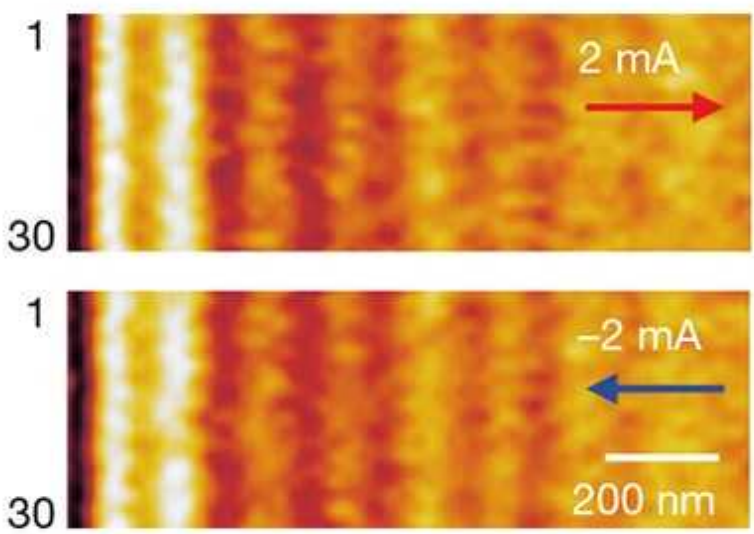


Figure 1 | Plasmons in graphene dragged by drifting electrons. Dong *et al.*² and Zhao *et al.*³ directed a beam of infrared light at a gold bar, which launched propagating waves called plasmons (shown by red shading) in a single sheet of carbon atoms, known as graphene. The two groups found that plasmons moving in the opposite direction to the flow of drifting electrons in the graphene had a shorter wavelength (and, thus, a lower speed) than those travelling in the same direction. This observation suggests that plasmons can be dragged by drifting electrons in solids.

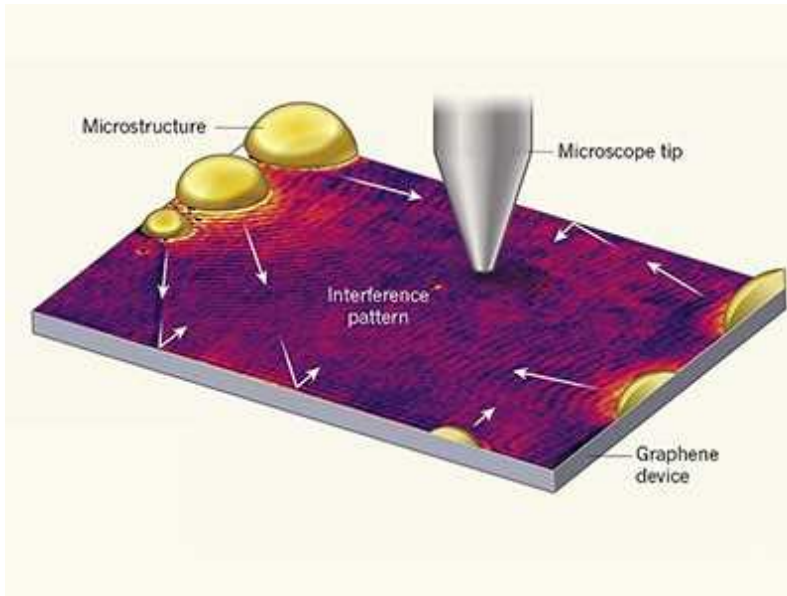
Plasmons exist in many materials, including noble metals (such as silver and gold), and the conventional 2D electron gas found in semiconductor stacks called heterostructures. However, plasmons in graphene have three distinctive attributes that are relevant to the drag effect. First, their drift velocity can be large — a few orders of magnitude larger than in noble metals. That's because electrons in graphene are highly mobile and relatively sparse. This feature allowed Dong and colleagues to observe the complex (nonlinear) drag effect in their experiments.



[Read the paper: Efficient Fizeau drag from Dirac electrons in monolayer graphene](#)

Second, the plasmon-drag effect in graphene is well described by Einstein's special theory of relativity and not by classical physics⁵. For the conventional 2D electron gas, the drag effect satisfies a classical relationship in which the plasmon's final velocity is simply the sum of its initial velocity and the electron drift velocity. However, for graphene, as for Fizeau's experiment on light passing through moving water, special relativity is needed to determine the final velocity, as shown by both groups of researchers. Third, electrons in graphene are highly mobile even at room temperature, suggesting that the drag effect might be observable under ambient conditions. For the conventional 2D electron gas, cryogenic temperatures are required before such an effect can be studied.

The two groups' plasmon-drag experiments provide insight into electron-electron scattering in graphene⁶. A measured quantity known as the drag coefficient reflects the scattering rate. If this rate (given in units of energy) is low compared with the plasmon energy, the drag coefficient is 0.25, as observed by Dong and colleagues. However, if the scattering rate is high relative to the plasmon energy, the drag coefficient is 0.5. Therefore, the plasmon-drag effect provides a measurement of the electron-electron scattering rate, which is particularly valuable for analysing interactions involving many electrons.



Plasmon propagation pushed to the limit

The progress made by these two groups has profound implications. The drag effect causes forwards- and backwards-propagating plasmons to have different wavelengths and speeds, introducing a property called non-reciprocity. As a result, time-reversal symmetry is broken: the physical characteristics of the system would change if the direction of time was reversed. Typically, an external magnetic field or a process known as chiral pumping⁷ is needed to break such symmetry. However, the first of these approaches would not be useful in the context of a plasmonic device, because a magnetic field strong enough to break time-reversal symmetry could not be applied to individual photonic components in the device: it would affect all of the components. The groups' results show that a current of drifting electrons can efficiently break time-reversal symmetry; this effect could be readily applied to a targeted photonic component, thereby improving the controllability and multifunctional capabilities of the device.

To fully unleash the potential of these non-reciprocal plasmons in graphene or other plasmonic systems, many further experimental studies would be needed. First, the difference in propagation length between forwards- and backwards-moving plasmons should be determined. Theoretical work⁸ suggests that forwards-moving plasmons have a much longer propagation length than do backwards-moving ones; and, in the extreme case, backwards-moving plasmons cannot propagate. Such unidirectional

plasmons are immune to being scattered back by material defects and obstacles. Second, with respect to the groups' experiments, achieving an even stronger drag effect requires a higher drift velocity, which would cause severe heating — a problem that might be alleviated using a pulsed current.

Third, the two groups studied only single-frequency plasmons. Measuring the drag coefficient for plasmons that range in frequency from the far- to the mid-infrared would provide a more complete picture of the plasmon-drag effect. Finally, the method of near-field infrared nanoscopy could be applied to the conventional 2D electron gas, which has been investigated using techniques based on infrared absorption⁹ and a process called Raman scattering¹⁰. A careful comparison of nanoscopy images for the conventional 2D electron gas and graphene would be rewarding, directly revealing the difference in drag coefficients.

Nature **594**, 498–499 (2021)

doi: <https://doi.org/10.1038/d41586-021-01599-3>

References

1. 1.

Fizeau, H. C. *R. Acad. Sci.* **33**, 349–355 (1851).

[Google Scholar](#)

2. 2.

Dong, Y. *et al.* *Nature* **594**, 513–516 (2021).

[Article](#) [Google Scholar](#)

3. 3.

Zhao, W. *et al.* *Nature* **594**, 517–521 (2021).

[Article](#) [Google Scholar](#)

4. 4.

Novoselov, K. S. *et al. Science* **306**, 666–669 (2004).

[PubMed](#) [Article](#) [Google Scholar](#)

5. 5.

Borgnia, D. S., Phan, T. V. & Levitov, L. S. Preprint at <https://arxiv.org/abs/1512.09044> (2015).

6. 6.

Sun, Z., Basov, D. N. & Fogler, M. M. *Proc. Natl Acad. Sci. USA* **115**, 3285–3289 (2018).

[PubMed](#) [Article](#) [Google Scholar](#)

7. 7.

Song, J. C. W. & Rudner, M. S. *Proc. Natl Acad. Sci. USA* **113**, 4658–4663 (2016).

[PubMed](#) [Article](#) [Google Scholar](#)

8. 8.

Morgado, T. A. & Silveirinha, M. G. *ACS Photonics* **5**, 4253–4258 (2018).

[Article](#) [Google Scholar](#)

9. 9.

Tyson, R. E. *et al. Int. J. Infrared Millim. Waves* **14**, 1237–1249 (1993).

[Article](#) [Google Scholar](#)

10. 10.

Súilleabhán, L. C. Ó. & Hughes, H. P. *J. Appl. Phys.* **76**, 1701 (1994).

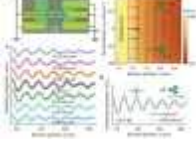
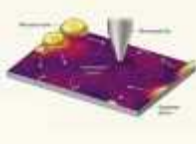
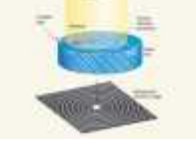
[Article](#) [Google Scholar](#)

[Download references](#)

Competing Interests

The author declares no competing interests.

Related Articles

-  [Read the paper: Efficient Fizeau drag from Dirac electrons in monolayer graphene](#)
-  [Read the paper: Fizeau drag in graphene plasmonics](#)
-  [Plasmon propagation pushed to the limit](#)
-  [Holograms from electrons scattered by light](#)
- [See all News & Views](#)

Subjects

- [Condensed-matter physics](#)
- [Materials science](#)
- [Optics and photonics](#)

Jobs from Nature Careers

- - - [All jobs](#)
 -
 - [Laboratory Research Scientist](#)
 - [Francis Crick Institute](#)
 - [London, United Kingdom](#)
 - [JOB POST](#)
 - [Bachelor of Science in Computer Engineering \(f/m/d\)](#)
 - [Helmholtz-Zentrum Berlin for Materials and Energy \(HZB\)](#)
 - [Berlin, Germany](#)
 - [JOB POST](#)
 - [Laboratory Engineer / Scientific and Technical Head of Reactor Technology \(f/m/x\)](#)
 - [Helmholtz Centre for Environmental Research \(UFZ\)](#)
 - [Leipzig, Germany](#)
 - [JOB POST](#)

- **Administrative Assistant/Internal Event Coordinator**

Oklahoma Medical Research Foundation (OMRF)

Oklahoma City, United States

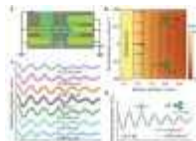
JOB POST

[Download PDF](#)

Related Articles



- [Read the paper: Efficient Fizeau drag from Dirac electrons in monolayer graphene](#)



- [Read the paper: Fizeau drag in graphene plasmonics](#)



- [Plasmon propagation pushed to the limit](#)



- [Holograms from electrons scattered by light](#)
- [See all News & Views](#)

Subjects

- [Condensed-matter physics](#)
 - [Materials science](#)
 - [Optics and photonics](#)
-

This article was downloaded by **calibre** from <https://www.nature.com/articles/d41586-021-01599-3>

| [Section menu](#) | [Main menu](#) |

- NEWS AND VIEWS
- 09 June 2021

A 4D road map for the formation of hair follicles

Combined imaging and gene-expression analyses reveal that the arrangement of cells in concentric rings in the disc-like structures that give rise to hair follicles predetermines their eventual fate and location in mature follicles.

- [Nivedita Saxena](#) ⁰ &
- [Michael Rendl](#) ¹

1. Nivedita Saxena

1. Nivedita Saxena is at the Black Family Stem Cell Institute and in the Department of Cell, Developmental and Regenerative Biology, Department of Dermatology and the Graduate School of Biomedical Sciences, Icahn School of Medicine at Mount Sinai, New York, New York 10029, USA.

[View author publications](#)

You can also search for this author in [PubMed](#) [Google Scholar](#)

2. [Michael Rendl](#)

1. Michael Rendl is at the Black Family Stem Cell Institute and in the Department of Cell, Developmental and Regenerative Biology, Department of Dermatology and the Graduate School of Biomedical Sciences, Icahn School of Medicine at Mount Sinai, New York, New York 10029, USA.

[View author publications](#)

You can also search for this author in [PubMed](#) [Google Scholar](#)

•

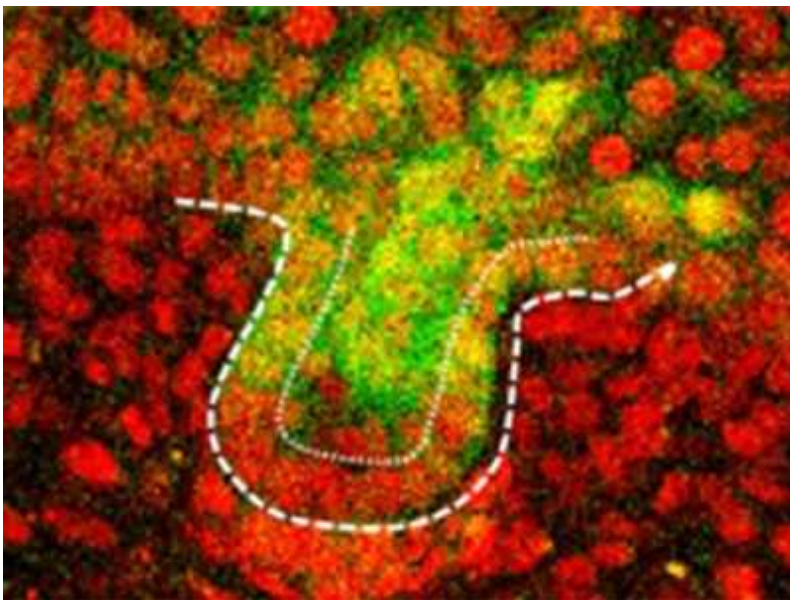


•

[Download PDF](#)

As a child, you might dream one day of becoming an astronaut and, the next day, of becoming a ballet dancer — the possibilities are endless. Eventually, this wealth of choice is whittled down by external circumstances and internal interests. Similarly, precursor cells in early embryos make a series of stepwise ‘decisions’ governed by external forces and internal factors to generate the diverse array of cell types present in adult organisms¹. [Writing in Nature](#), Morita *et al.*² show that the fate of cells that eventually make up mature hair follicles is determined by their positioning in concentric rings of nascent follicle structures during embryonic skin development. In this case,

how and where cells begin their developmental journey ultimately decides their destination.



[Read the paper: Tracing the origin of hair follicle stem cells](#)

Hair-follicle development begins with a clean slate. The skin comprises two major components: the epidermis, a layer of epithelial cells that form a protective barrier against external insults; and the dermis, which contains cells called fibroblasts that support the skin³. Epithelial cells and fibroblasts seem to be equally able to contribute to and regulate the formation of hair follicles. Dermal fibroblasts induce the formation of placodes — cellular thickenings in the epithelial layer that eventually give rise to hair follicles^{4,5}. Placodes develop as flat circles on the surface of the skin. How these flat disc structures eventually transform into a long, cylindrical 3D shape is a question of great interest not only to skin and hair researchers, but also to scientists investigating potential hair-replacement therapies that work through developmental mechanisms^{6,7}.

This is where Morita and colleagues step in. The authors optimized a technique called live imaging to record the movement of cells in cultured skin tissue taken from mouse embryos, beginning at 11.5 days after conception. They imaged the skin samples for three to five days, in three dimensions and at a microscopic level, to produce time-lapse videos of hair-follicle development⁸. By playing these videos in reverse, the authors traced

cells in fully grown hair follicles back to their embryonic placodal origins. They discovered that cells in early placode structures are organized into concentric zones, like the bullseye and surrounding rings of a target, such that the centre-most cells give rise to the bottom of the hair follicle, and cells at the outer edge of the placode remain at the surface of the skin, between follicles (Fig. 1). The downward growth from placode to fully developed hair follicle, which is enabled by the proliferation and movement of these cells over time, resembles the elongation of an extendable telescope; thus, the authors propose referring to this type of development as the “telescope model”.

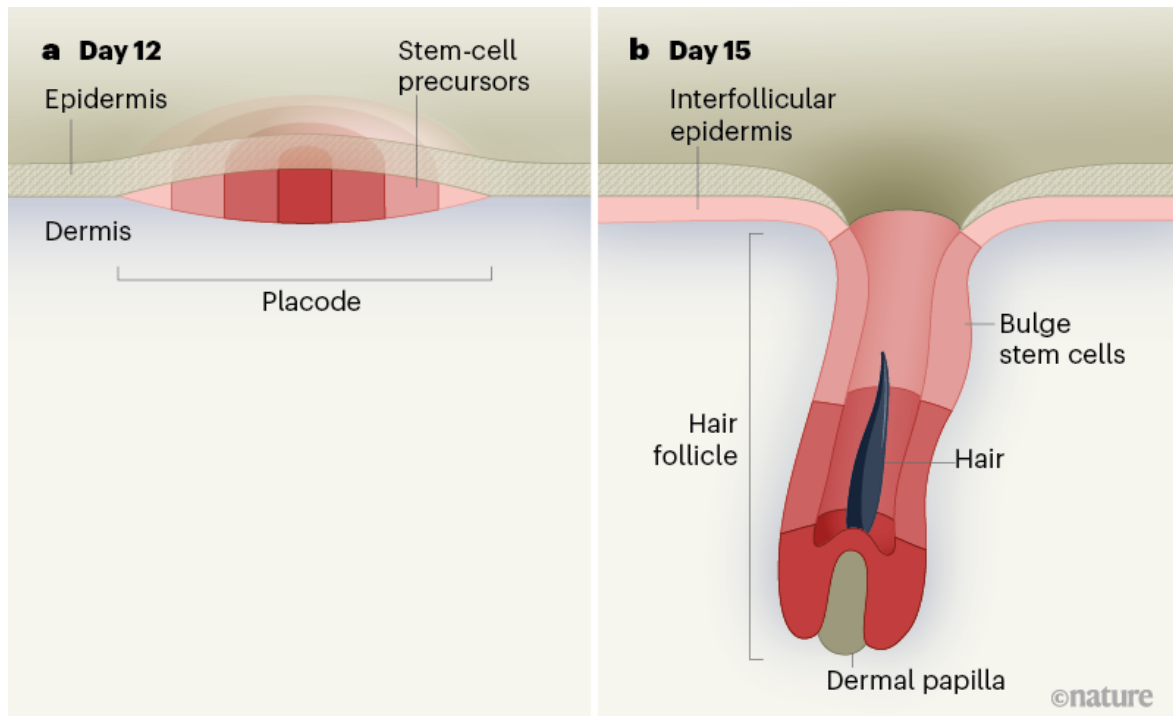
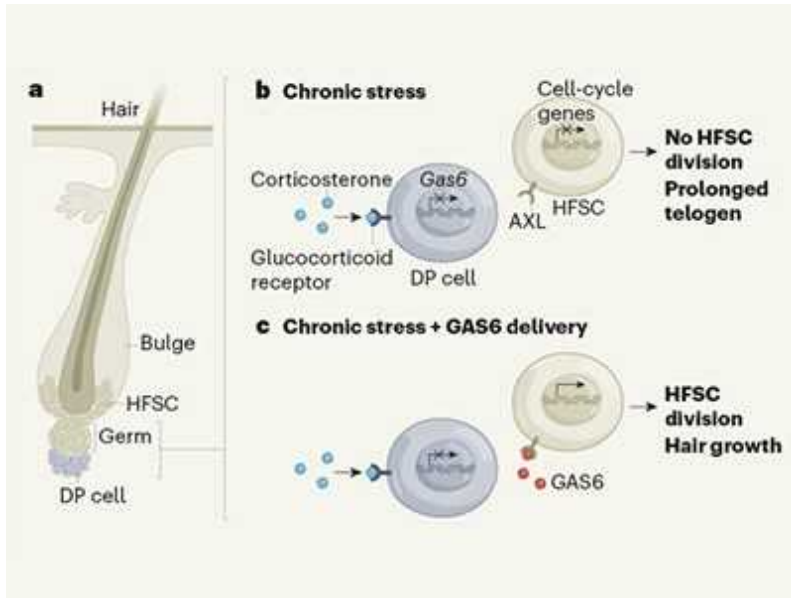


Figure 1 | Early placode arrangement determines final cell position in the hair follicle. Hair follicles develop from flat, disc-like structures called placodes in the epidermis — the surface layer of skin cells above the dermis. Morita *et al.*² used time-lapse live imaging and profiled the gene expression of cells in developing hair follicles from mouse embryos during days 12–15 after conception. Cells in the placodes were found to be arranged in concentric rings that define the final cell position in fully grown hair follicles. The innermost circle gives rise to the lowest portion of the hair follicle (adjacent to the dermal papilla, a cluster of specialized dermal cells), and the next ring out contributes to the next portion. Hair-follicle stem cells

born in the peripheral ring of the placode colonize the future bulge region of mature hair follicles, and the outermost area gives rise to interfollicular epidermal cells, which are not part of the hair follicle but form part of the epidermis between follicles.

Although this model is not familiar to hair biologists, the formation of cylindrical or other 3D-shaped appendages, such as legs and antennae, from flat surfaces was first described in the fruit fly *Drosophila melanogaster*⁹. Studies in flies have long informed biological principles in more-complex mammalian species; thus, although perhaps unsurprising, it is exciting that this telescope mechanism is evolutionarily conserved across species.

Adding further complexity to this system is the appearance of stem cells in the hair follicle as it develops. In adult animals, a reservoir of such cells resides in a part of the upper hair follicle called the bulge^{10,11} and is crucial for enabling the follicle to expand during the growth phase of the hair cycle, as part of normal tissue turnover throughout an animal's life¹². These stem cells can even repair injury to the rest of the epidermis¹². The hair-follicle placode harbours predecessors to bulge stem cells, and the stem cells' origin in the early placode was previously demonstrated by using protein markers expressed by the cells, such as the transcription factor SOX9, to track them. This approach suggested that, as the placode begins to extend downwards, bulge stem-cell precursors are born and remain superficial to the placode, before ultimately colonizing the bulge region¹³.



Relax to grow more hair

Morita and colleagues selectively labelled and isolated cells from early mouse hair follicles at the same time points as those analysed in their live-imaging experiments, to perform single-cell transcriptomics — gene-expression profiling of individual cells. Because single-cell transcriptomics allows a broad and unbiased survey of the genes and proteins expressed by each cell, it can be highly informative for ascribing cellular identity and for characterizing cellular dynamics during development^{2,8}. Using this approach, Morita and colleagues identified a population of cells expressing bulge stem-cell markers at the earliest stages of placode development. Through mathematical modelling of cells at all assessed time points, the authors determined that these marker-expressing cells differentiate into bulge stem cells in the early placode⁶, long before the time point at which such differentiation was previously reported to occur¹².

These stem-cell precursors expressed the gene that encodes SOX9, consistent with previous reports¹³. However, through further cell-lineage tracing and live imaging, these precursors were unequivocally demonstrated to originate from the previously unidentified peripheral ring zone of the early placode. This newly posited spatial localization will probably require a re-examination of previous findings related to bulge stem-cell precursors

and reopen questions of the regulatory conditions necessary for the induction of this cell population.

Although the authors' study makes huge strides in dissecting how different cell populations contribute to the mature hair follicle, it also invites many questions, the most compelling of which is how the concentric zones in the placode are established. It is likely that various elements contribute to the formation of these zones, such as diffusible factors secreted by other epidermal and dermal cells (including specialized dermal cells clustered directly below where placodes form¹⁴). By improving our understanding of hair-follicle development, future studies might unveil ways of generating hair follicles *de novo* that could eventually be used in hair-replacement therapies. However, unlike the routes taken by cells on their developmental journeys to their final destinations in the mature hair follicle, the pathway to such applications is still unclear.

Nature **594**, 500–501 (2021)

doi: <https://doi.org/10.1038/d41586-021-01482-1>

References

1. 1.

Hadjantonakis, K. & Solnica-Krezel, L. *Dev. Biol.* **341**, 2–4 (2010).

[PubMed](#) [Article](#) [Google Scholar](#)

2. 2.

Morita, R. *et al.* *Nature* **594**, 547–552 (2021).

[Article](#) [Google Scholar](#)

3. 3.

Saxena, N., Mok, K.-W. & Rendl, M. *Exp. Dermatol.* **28**, 332–344 (2019).

[PubMed](#) [Article](#) [Google Scholar](#)

4. 4.

Kollar, E. J. *J. Invest. Dermatol.* **55**, 374–378 (1970).

[PubMed](#) [Article](#) [Google Scholar](#)

5. 5.

Millar, S. E. *J. Invest. Dermatol.* **118**, 216–225 (2002).

[PubMed](#) [Article](#) [Google Scholar](#)

6. 6.

Ji, S., Zhu, Z., Sun, X. & Fu, X. *Signal Transduct. Target. Ther.* **6**, 66 (2021).

[PubMed](#) [Article](#) [Google Scholar](#)

7. 7.

Lee, J. *et al. Nature* **582**, 399–404 (2020).

[PubMed](#) [Article](#) [Google Scholar](#)

8. 8.

Heitman, N., Saxena, N. & Rendl, M. *Curr. Opin. Cell Biol.* **55**, 87–95 (2018).

[PubMed](#) [Article](#) [Google Scholar](#)

9. 9.

Ruiz-Losada, M., Blom-Dahl, D., Córdoba, S. & Estella, C. *J. Dev. Biol.* **6**, 17 (2018).

[Article](#) [Google Scholar](#)

10. 10.

Tumbar, T. *et al.* *Science* **303**, 359–363 (2004).

[PubMed](#) [Article](#) [Google Scholar](#)

11. 11.

Morris, R. J. *et al.* *Nature Biotechnol.* **22**, 411–417 (2004).

[PubMed](#) [Article](#) [Google Scholar](#)

12. 12.

Fuchs, E. & Blau, H. M. *Cell Stem Cell* **27**, 532–556 (2020).

[PubMed](#) [Article](#) [Google Scholar](#)

13. 13.

Ouspenskaia, T., Matos, I., Mertz, A. F., Fiore, V. F. & Fuchs, E. *Cell* **164**, 156–169 (2016).

[PubMed](#) [Article](#) [Google Scholar](#)

14. 14.

Mok, K.-W. *et al.* *Dev. Cell* **48**, 32–48 (2019).

[PubMed](#) [Article](#) [Google Scholar](#)

[Download references](#)

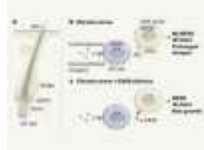
Competing Interests

The authors declare no competing interests.

Related Articles



- [Read the paper: Tracing the origin of hair follicle stem cells](#)



- [Relax to grow more hair](#)



- [Regenerative medicine could pave the way to treating baldness](#)
- [See all News & Views](#)

Subjects

- [Developmental biology](#)
- [Stem cells](#)

[Jobs from Nature Careers](#)

- - - [All jobs](#)
 -
 - [Laboratory Research Scientist](#)

[Francis Crick Institute](#)

[London, United Kingdom](#)

[JOB POST](#)

- **Bachelor of Science in Computer Engineering (f/m/d)**

Helmholtz-Zentrum Berlin for Materials and Energy (HZB)

Berlin, Germany

JOB POST

- **Laboratory Engineer / Scientific and Technical Head of Reactor Technology (f/m/x)**

Helmholtz Centre for Environmental Research (UFZ)

Leipzig, Germany

JOB POST

- **Administrative Assistant/Internal Event Coordinator**

Oklahoma Medical Research Foundation (OMRF)

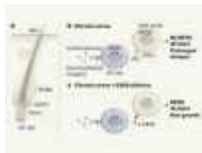
Oklahoma City, United States

JOB POST

Download PDF

Related Articles

-  **Read the paper: Tracing the origin of hair follicle stem cells**



-  [Relax to grow more hair](#)
 -  [Regenerative medicine could pave the way to treating baldness](#)
 - [See all News & Views](#)

Subjects

- Developmental biology
 - Stem cells

This article was downloaded by **calibre** from <https://www.nature.com/articles/d41586-021-01482-1>

- NEWS AND VIEWS
- 02 June 2021

Natural killer cells lull tumours into dormancy

Natural killer cells can drive spreading cancer cells to enter a state of dormancy. That finding, together with the discovery of a pathway that hinders this antitumour function, could spur the development of new treatments.

- [Noella Lopes](#)⁰ &
- [Eric Vivier](#)¹

1. Noella Lopes

1. Noella Lopes is at the Centre d'Immunologie de Marseille-Luminy, Aix Marseille University, Inserm, CNRS, 13288 Marseille, France.

[View author publications](#)

You can also search for this author in [PubMed](#) [Google Scholar](#)

2. Eric Vivier

1. Eric Vivier is at the Centre d'Immunologie de Marseille-Luminy, Aix Marseille University, Inserm, CNRS, 13288 Marseille, France, and at Marseille Immunopole, Hôpital de la Timone, Assistance Publique-Hôpitaux de Marseille and at Innate Pharma Research Laboratories, Innate Pharma, Marseille.

[View author publications](#)

You can also search for this author in [PubMed](#) [Google Scholar](#)

-

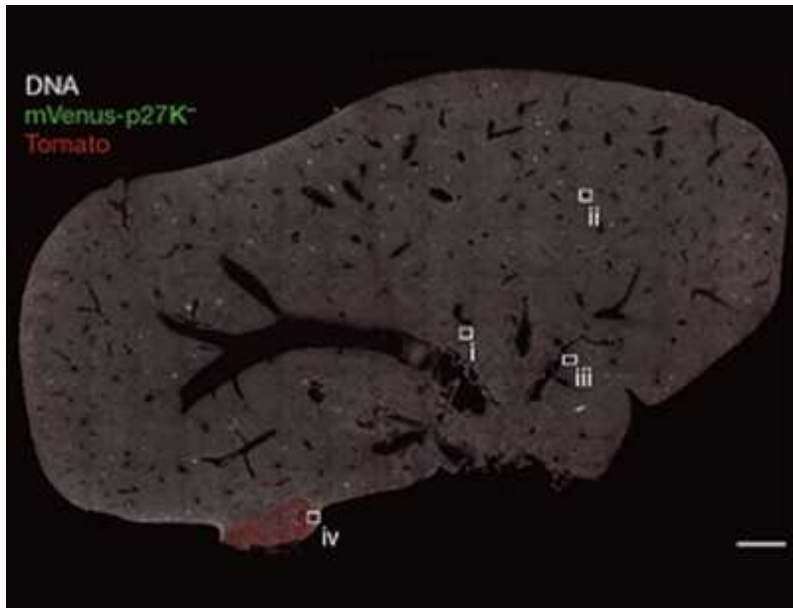


•

[Download PDF](#)

Efforts to treat tumours that have spread from their initial site in the body to grow elsewhere are often unsuccessful. Such tumours, called metastases, are the main cause of cancer-related deaths, so finding a way to control them is crucial to meeting this medical need. Before metastases begin to grow, cancer cells might have already migrated from the primary tumour to seed various other sites (a process called metastasis), where they can remain dormant for long periods of time. Surveillance by immune cells is known to help to maintain this dormancy¹, but the mechanisms involved in the switch from dormancy to the growth of metastases have been unclear — until now.

[Writing in Nature](#), Correia *et al.*² report the pivotal role of natural killer (NK) cells in controlling the development of liver metastases arising from breast cancer.



[Read the paper: Hepatic stellate cells suppress NK cell-sustained breast cancer dormancy](#)

NK cells are part of the innate branch of the immune system. They can kill other cells and produce soluble messenger molecules, called cytokines and chemokines, that regulate immune responses³. The ability of NK cells to detect and eliminate a wide array of tumour cells directly, and their capacity to shape antitumour immune responses by making cytokines or chemokines, have led to the development of clinical strategies that harness their anticancer functions^{3–5}.

Several studies have suggested that NK cells specialize in eliminating metastases rather than targeting tumour cells at their primary site of growth⁶. For some cancers, people who have more tumour-infiltrating NK cells seem to have fewer metastases, as seen in those with cancers such as gastrointestinal sarcoma, and gastric, colorectal, renal or prostate carcinoma^{3,6}. The depletion or dysfunction of NK cells in mice also results in an increase in metastases³. By contrast, when their normal regulation is removed, NK cells protect against the spread of tumours to the liver and

lungs⁷. Tumour cells entering dormancy downregulate their expression of ligand molecules that can activate NK cell receptors, and become resistant to killing mediated by NK cells⁸.

Correia and colleagues decided to further investigate the composition and dynamics of tumour cells in dormancy. One approach they took was to study the gene-expression profile of human and mouse breast cancer cells transplanted into mice. These cells underwent metastasis to reach sites such as the liver, where they became dormant tumour cells. The authors assessed genes expressed by cells in the vicinity of the dormant tumour cells in the surrounding stromal tissue. These data revealed a gene signature associated with responses mediated by NK cells. Furthermore, Correia *et al.* compared the areas around dormant tumour cells with those in tumour-free livers, and found that NK cells were the only type of immune cell to increase in number during dormancy. This suggests that NK cells have a crucial role in events that block the reawakening of dormant tumour cells (Fig. 1).

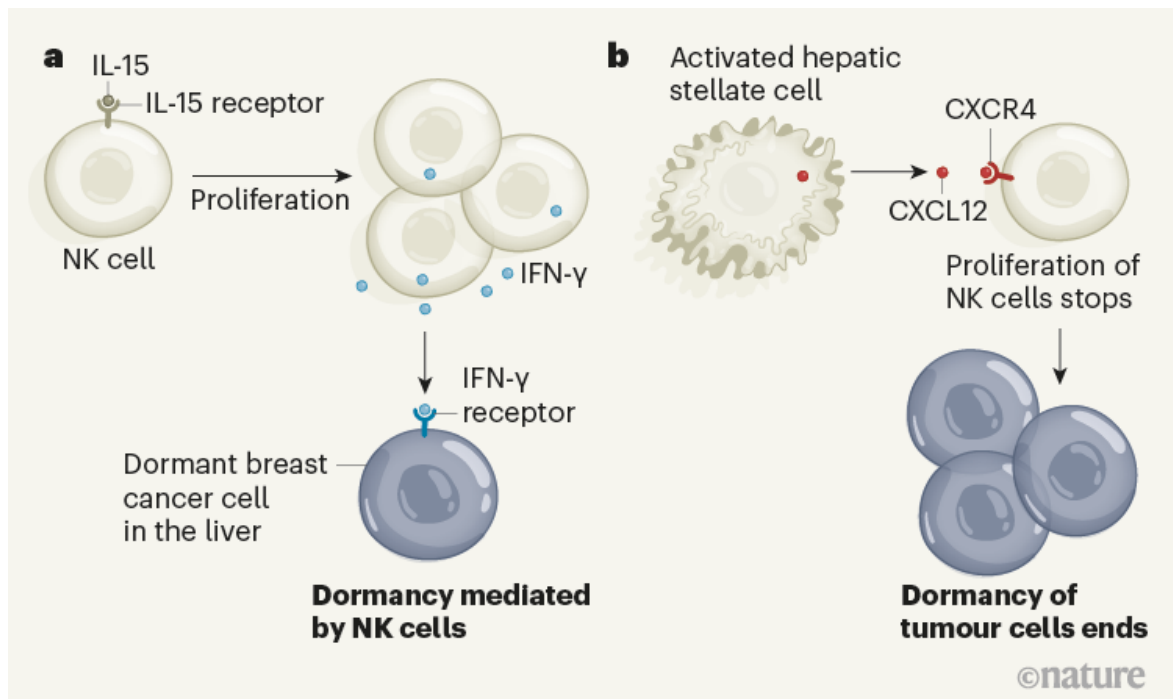


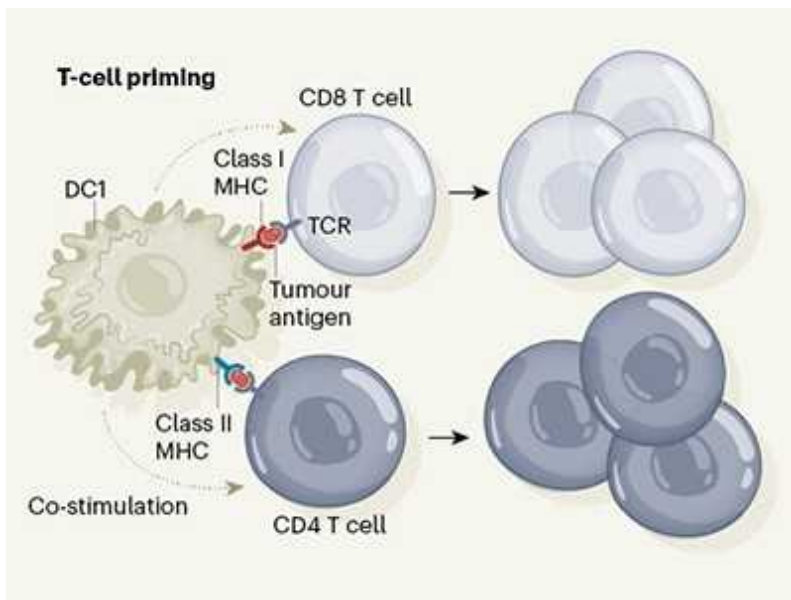
Figure 1 | Interactions that affect the dormancy of tumour cells. Correia *et al.*² report mouse and human evidence indicating that a type of immune cell called a natural killer (NK) cell has a key role in preventing the growth of spreading tumour cells, called metastases. **a**, The molecule IL-15 drives

NK cells to proliferate, and these cells secrete the protein IFN- γ , which keeps breast cancer cells that have migrated to the liver in a dormant state. **b**, Exit from this state of dormancy is associated with activated hepatic stellate cells, which secrete the molecule CXCL12. CXCL12 binds to the CXCR4 receptor on NK cells. This results in NK cells ceasing to divide and stops them from promoting tumour dormancy. The tumour cells proliferate as a consequence.

Consistent with this hypothesis, the authors report that depleting NK cells in a mouse tumour model then led to higher levels of metastases in the liver. However, if NK cells were boosted using the cytokine IL-15, this prevented the formation of liver metastases and tumour cells remained dormant. The authors' results demonstrate that the size of the pool of NK cells in the liver environment determines whether dormancy occurs or metastases form.

The liver environment associated with dormant tumour cells contained NK cells producing the cytokine interferon- γ (IFN- γ). Correia and colleagues report that, *in vitro*, adding IFN- γ can nudge cancer cells into dormancy — consistent with the idea that IFN- γ has a key role in controlling the cancer dormancy mediated by NK cells.

Might other factors disrupt NK cells and thereby promote the formation of metastases? A clue to this came from the authors' discovery that a pool of activated hepatic stellate cells found in the mouse liver increased when tumours switched from dormancy to forming metastases. Hepatic stellate cells have been identified as the main disease-driving population of cells for a condition called hepatic fibrosis⁹, in which the liver becomes damaged and scarred. These changes often precede tumour formation. The accumulation of activated hepatic stellate cells occurs at the same time as a decline in NK cells, owing to a decrease in NK-cell proliferation. The authors' results suggest that activated hepatic stellate cells promote metastases in the liver by inhibiting NK cells, thereby disrupting cancer dormancy.

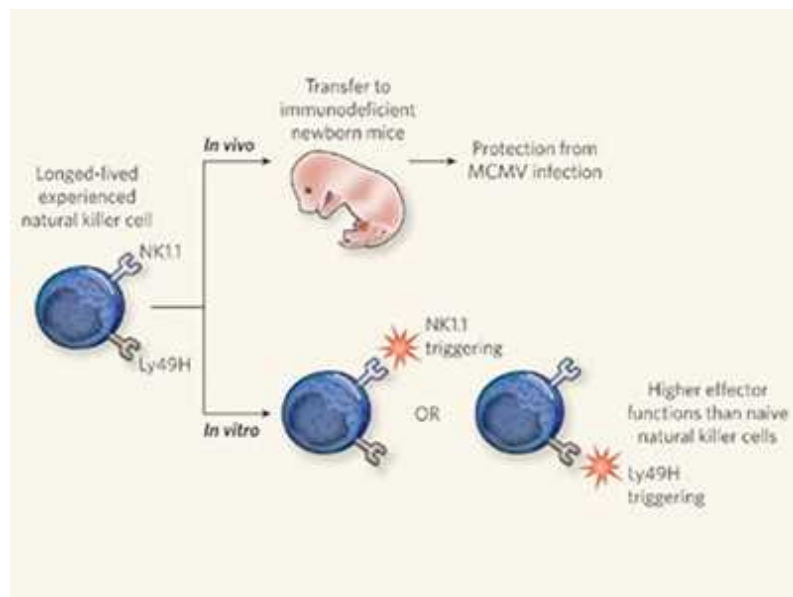


A dendritic cell multitasks to tackle cancer

Correia *et al.* found that hepatic stellate cells secrete the chemokine CXCL12, which has been implicated in aiding the directional migration of breast cancer cells¹⁰. Organs that express the highest levels of CXCL12 are the most common sites of metastasis in human breast cancer¹⁰. Human NK cells in the liver have a receptor, called CXCR4, that recognizes CXCL12. Correia and colleagues report that activated hepatic stellate cells hamper the function of NK cells in the liver through CXCL12–CXCR4 interactions that halt the proliferation of NK cells, thereby tipping the scales from tumour dormancy to the promotion of metastasis. This study thus reveals a previously unknown function of CXCL12 in altering NK-cell-mediated immunity, in addition to its known effects on tumour cells¹⁰.

The authors next examined pairs of human biopsy specimens from metastases and healthy adjacent liver tissue, taken from people with breast cancer. Consistent with the data from mice, the analysis showed that activated hepatic stellate cells accumulated in metastases, and that their abundance was inversely correlated with that of NK cells. The authors' analysis of published gene-expression data for colorectal cancer that has metastasized to the liver revealed the same association, suggesting that this cellular crosstalk might be relevant for the growth of other types of spreading cancer.

Several questions remain to be answered. For example, the mechanisms underlying the accumulation of NK cells associated with dormant tumour cells and the triggering of IFN- γ production in these circumstances remain to be fully determined. It is not completely clear how CXCL12 that is secreted by activated hepatic stellate cells hinders the function of NK cells. Furthermore, determining whether the CXCL12–CXRC4 axis awakens dormant tumour cells in humans is of utmost importance, and, if so, in which types of cancer.



Natural killer cells remember

Finally, the similarities between NK cells and another sort of immune cell called type 1 innate lymphoid cells (ILC1) should prompt further investigation of the role of ILC1 in controlling metastasis³. Indeed, these cells have a complex role in tumour responses^{11,12}. Correia *et al.* excluded ILC1 as having a role in controlling metastases, because they observed no notable changes in the level of these cells when comparing tumour dormancy and metastases in the liver. However, the lack of a specific ILC1-deficient mouse model means that it is not possible to precisely dissect the respective roles of NK cells and ILC1 in the control of metastasis, leaving a key question unresolved.

By showing that the IFN- γ -driven effects of NK cells maintain breast cancer cells in a dormant state, Correia and colleagues have revealed that NK cells

have other and previously unsuspected anticancer capacities. This finding paves the way for the development of cancer treatment strategies that prevent dormant reservoirs of tumour cells from awakening. For instance, molecules that strongly stimulate the IL-15 pathway in NK cells are already available. These IL-15 superagonists, such as ALT-803 or NKTR-255, are being tested in clinical trials^{3,5}, and the rationale for their use should now also take into account the role of NK cells in controlling dormant tumour cells.

Furthermore, drugs that inhibit CXCR4 are being developed. It would be interesting to determine whether these inhibitors could help to sustain the activity of NK cells in maintaining tumour dormancy. In addition, engineered antibodies called NK cell engagers, which can stimulate NK cells and form a bridge that connects them to tumour cells, offers another way to promote the function of NK cells¹³. Current clinical trials are also testing various approaches to manipulate NK cells for therapeutic benefit^{3–5}. Besides the well-characterized effects of NK cells in tumour immunity, Correia and colleagues' work further highlights the possible advantages of harnessing NK cells to target cancers.

Nature **594**, 501–502 (2021)

doi: <https://doi.org/10.1038/d41586-021-01381-5>

References

1. 1.

Mohme, M., Riethdorf, S. & Pantel, K. *Nature Rev. Clin. Oncol.* **14**, 155–167 (2017).

[PubMed](#) [Article](#) [Google Scholar](#)

2. 2.

Correia, A. *et al.* *Nature* **594**, 566–571 (2021).

[Article](#) [Google Scholar](#)

3. 3.

Chiassone, L., Dumas, P.-Y., Vienne, M. & Vivier, E. *Nature Rev. Immunol.* **18**, 671–688 (2018).

[PubMed](#) [Article](#) [Google Scholar](#)

4. 4.

Daher, M. & Rezvani, K. *Cancer Discov.* **11**, 45–58 (2021).

[PubMed](#) [Article](#) [Google Scholar](#)

5. 5.

Myers, J. A. & Miller, J. S. *Nature Rev. Clin. Oncol.* **18**, 85–100 (2021).

[PubMed](#) [Article](#) [Google Scholar](#)

6. 6.

López-Soto, A., Gonzalez, S., Smyth, M. J. & Galluzzi, L. *Cancer Cell* **32**, 135–154 (2017).

[PubMed](#) [Article](#) [Google Scholar](#)

7. 7.

Molgara, M. *et al.* *Nature* **551**, 110–114 (2017).

[PubMed](#) [Article](#) [Google Scholar](#)

8. 8.

Malladi, S. *et al.* *Cell* **165**, 45–60 (2016).

[PubMed](#) [Article](#) [Google Scholar](#)

9. 9.

Tsuchida, T. & Friedman, S. L. *Nature Rev. Gastroenterol. Hepatol.* **14**, 397–411 (2017).

[PubMed](#) [Article](#) [Google Scholar](#)

10. 10.

Shi, Y., Riese, D. J., 2nd & Shen, J. *Front. Pharmacol.* **11**, 574667 (2020).

[PubMed](#) [Article](#) [Google Scholar](#)

11. 11.

Dadi, S. *et al.* *Cell* **164**, 365–377 (2016).

[PubMed](#) [Article](#) [Google Scholar](#)

12. 12.

Gao, Y. *et al.* *Nature Immunol.* **18**, 1004–1015 (2017).

[PubMed](#) [Article](#) [Google Scholar](#)

13. 13.

Gauthier, L. *et al.* *Cell.* **177**, 1701–1713 (2019).

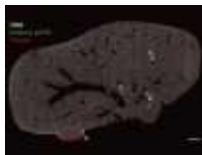
[PubMed](#) [Article](#) [Google Scholar](#)

[Download references](#)

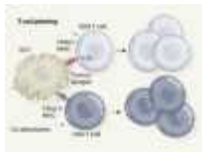
Competing Interests

E.V. is a shareholder and employee of Innate Pharma.

Related Articles



- [Read the paper: Hepatic stellate cells suppress NK cell-sustained breast cancer dormancy](#)



- [A dendritic cell multitasks to tackle cancer](#)
- [Natural killer cells remember](#)
- [See all News & Views](#)

Subjects

- [Cancer](#)
- [Immunology](#)

[Jobs from Nature Careers](#)

- - - [All jobs](#)
 - - [Laboratory Research Scientist](#)
[Francis Crick Institute](#)
[London, United Kingdom](#)
[JOB POST](#)

- **Bachelor of Science in Computer Engineering (f/m/d)**

Helmholtz-Zentrum Berlin for Materials and Energy (HZB)

Berlin, Germany

JOB POST

- **Laboratory Engineer / Scientific and Technical Head of Reactor Technology (f/m/x)**

Helmholtz Centre for Environmental Research (UFZ)

Leipzig, Germany

JOB POST

- **Administrative Assistant/Internal Event Coordinator**

Oklahoma Medical Research Foundation (OMRF)

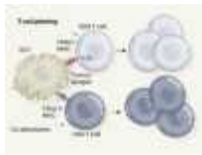
Oklahoma City, United States

JOB POST

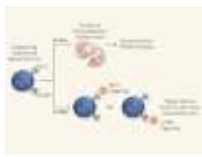
Download PDF

Related Articles

-  **Read the paper: Hepatic stellate cells suppress NK cell-sustained breast cancer dormancy**



- [A dendritic cell multitasks to tackle cancer](#)



- [Natural killer cells remember](#)

- [See all News & Views](#)

Subjects

- [Cancer](#)
- [Immunology](#)

This article was downloaded by **calibre** from <https://www.nature.com/articles/d41586-021-01381-5>

| [Section menu](#) | [Main menu](#) |

- NEWS AND VIEWS
- 23 June 2021

Ion dynamics in battery materials imaged rapidly

An imaging method has been developed that tracks ion transport in functioning battery materials in real time, at submicrometre scales — offering insights into how to design batteries that charge in minutes.

- [Aashutosh Mistry](#) ORCID: <http://orcid.org/0000-0002-4359-4975> 0
 1. [Aashutosh Mistry](#)

1. Aashutosh Mistry is in the Chemical Sciences and Engineering Division, Argonne National Laboratory, Lemont, Illinois 60439, USA.

[View author publications](#)

You can also search for this author in [PubMed](#) [Google Scholar](#)



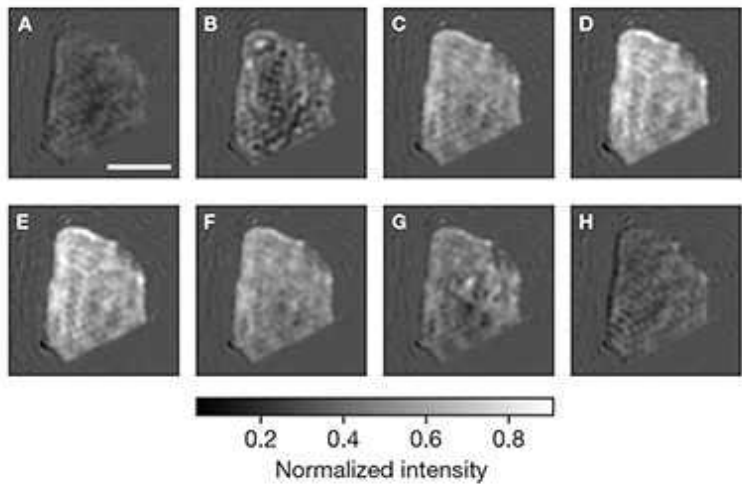


•

[Download PDF](#)

The most important materials in lithium-ion batteries are the ‘active’ particles that store and release lithium ions during charging and discharging, because they store the energy in these devices. To design batteries for any potential application, scientists need to understand the ion dynamics in the active particles. However, conventional methods for studying lithium-ion dynamics cannot track, at submicrometre resolution, the rapid changes occurring in batteries that charge in minutes. These are being developed for emerging applications such as fast-charging vehicles and flying taxis. In a

[paper in *Nature*](#), Merryweather *et al.*¹ report a technique that can visualize such fast dynamics.



[Read the paper: Operando optical tracking of single-particle ion dynamics in batteries](#)

Lithium-ion batteries consist of two porous electrodes (positive and negative), which are made up of active particles, carbon and a binder material. The carbon provides necessary electron conduction, and the binder holds the other materials together like a glue. The batteries also contain an electrolyte, which provides a conduit through which ions can move from one electrode to another.

Battery applications can be categorized in terms of their operation time — for example, portable electronics require batteries that last for 10 hours or more, and electric vehicles should be able to drive for 6–8 hours. To track the internal ion dynamics of batteries for each of these operations, researchers need to image the associated physical and chemical interactions at least ten times as fast as the operation time. This is analogous to selecting a camera shutter speed that is suitable for filming sport — if the shutter speed is too slow, the camera produces blurry pictures. In the context of batteries, the physical aspects of interest are the geometry of the active particles and the structure of the porous electrodes, whereas the key

chemical process is the evolution of ion concentrations in the active particles and the electrolyte.

Every battery-imaging technique has its own characteristic image-acquisition time — this determines which battery operations can be tracked accurately. Previously available techniques^{2–8} take a few minutes to acquire an image, and can therefore capture only processes that occur over several hours.

Merryweather *et al.* have customized an optical microscopy technique, previously used in biology⁹, to track the movement of lithium ions in the active materials of batteries. In this approach, a laser beam is shone at electrochemically operating battery particles as they store or release lithium ions, and the scattered light is analysed. The local concentration of electrons in these particles changes as more lithium is stored, which in turn alters the scattering pattern. Therefore, the time evolution of the scattering signals at each position on a particle correlates with the local change in lithium concentration (Fig. 1).

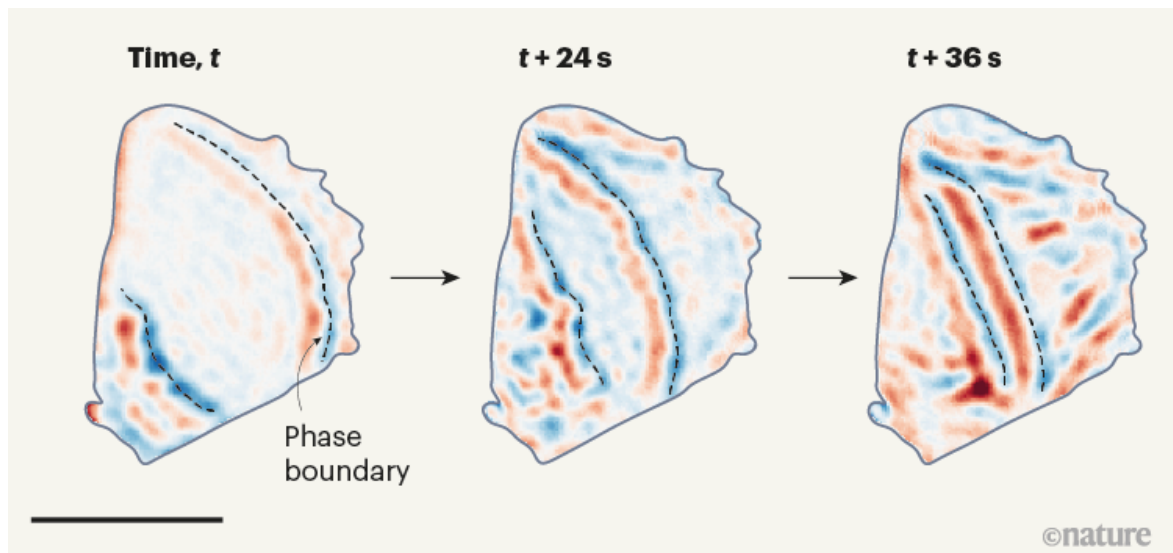
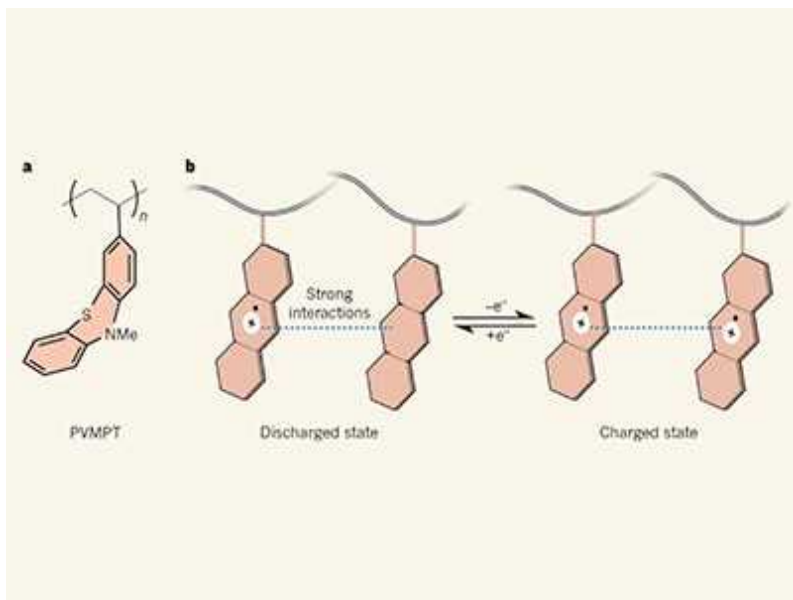


Figure 1 | Images of a functioning battery particle. ‘Active’ materials in battery electrodes store and release ions during charge–discharge cycles. Merryweather *et al.*¹ report an imaging technique that uses light scattered from functioning active particles to track changes in ion concentration in real time. In their approach, the scattering intensity changes with local ion concentration, and so the evolution of scattering patterns over time

represents the ion dynamics of the system. Here, the colours of the contours represent the change of scattering intensity over the previous 5-second period as more ions are stored in the particle: red indicates an increase in intensity; blue indicates a decrease. The changing patterns correlate with the transition of one phase of the material to another. Broken black lines indicate the boundaries between phases when a central domain consisting of one phase shrinks, and surrounding domains of another phase expand. Scale bar, 5 micrometres. Images from Fig. 5e of ref. 1.

Notably, the image-acquisition time for Merryweather and colleagues' technique is less than 1 second, which allows examination of much faster processes than was previously possible. However, having a short acquisition time is not the only requirement when studying battery function. Imaging techniques must also be able to study batteries during operation and have a reasonable spatial resolution — submicrometre resolution is needed to track what happens in an active particle. The authors' technique meets this requirement, too. Moreover, the technique can map ion dynamics at the electrode scale, by comparing the evolution of ion concentration in active particles that are spatially separated in the electrode.

Almost all active materials that store lithium or other ions undergo electronic changes as the ion concentration varies, and are therefore amenable to study by this technique. The time variation of ion concentration in active particles is poorly understood, because conventional techniques can not directly track changes in local concentration throughout a particle during fast operation. By solving this problem, Merryweather and co-workers' method will help researchers to validate the hypothesized mechanisms of ion transport in these materials (see ref. 10, for example).



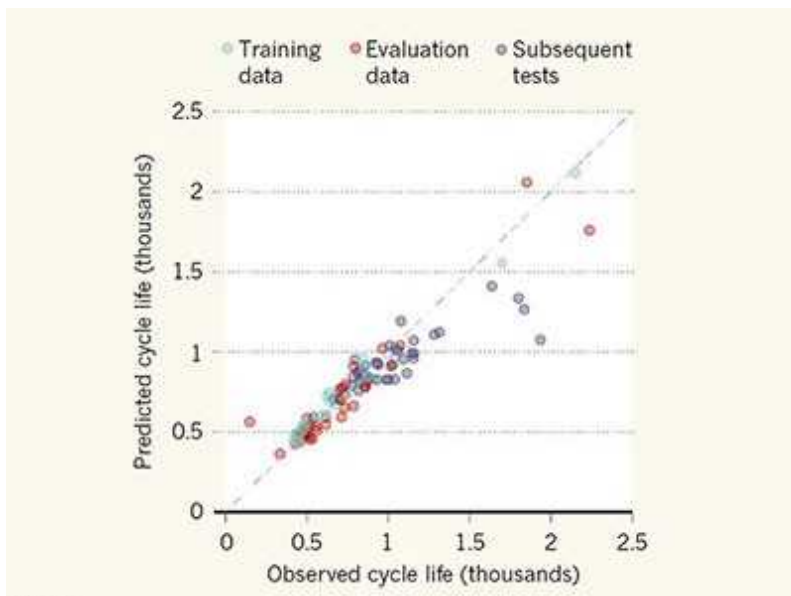
Long-lived electrodes for plastic batteries

It should be noted that the spatial resolution of the authors' imaging technique is constrained by a fundamental limit defined by the wavelength of the light used, which means that shorter wavelengths are needed to resolve smaller details. The resolution is about 300 nanometres in the current study. Another caveat is that scattering is the cumulative effect of light interacting with just the first couple of atomic layers of the particle. This approach therefore captures only the ion dynamics in the 2D plane associated with these atomic layers. By contrast, 3D information can be obtained using slower methods, such as X-ray tomography^{3,5}.

It will be exciting to take the authors' findings for individual particles further and study porous electrodes at the far-from-equilibrium conditions associated with rapid charging. For example, it was hypothesized¹¹ last year that inhomogeneous porous-electrode structures result in non-uniform distribution of lithium in electrodes when batteries are charged in minutes. Merryweather and colleagues' technique could act as a test for such predictions.

This method could also be used to examine solid electrolytes — battery materials that are interesting, but poorly understood. If light scattering from solid electrolytes changes with local ion concentration as it does in active materials, then the technique could be used to map how the ion distribution

in such electrolytes changes when an electric current passes through them. Optical scattering might be equally useful for studying other systems that involve coupled ion and electron transport, such as catalyst layers in fuel cells and electrochemical gas sensors.



Machine-learning techniques used to accurately predict battery life

In the future, it should be possible to quantify the relationship between the scattering response and lithium-ion concentration by conducting meticulous scattering experiments using active particles that are compositionally uniform. This correlation could then be used to convert scattering signals to local concentrations. However, the relationship will not necessarily be the same for different materials, and might be difficult to identify in each case. Machine-learning techniques could be used to streamline the determination of these relationships and to automate analysis of scattering responses¹².

The authors' imaging technique also opens up the prospect of simultaneously tracking the chemical and physical (geometric) changes that occur in active particles during battery operation. The time course of scattering in a particle would reveal local changes in lithium concentration, and the difference between the scattering from a particle and that from other materials in a battery (such as the binder or electrolyte) could be used to determine the particle shape and how it evolves with time. Such experiments would revolutionize the study of active materials (such as silicon) that

appreciably expand and contract as the lithium concentration changes within them. Materials of this type store much more energy than currently used active materials do, and their use might reduce battery weight. This would be particularly useful in electric vehicles, because it would enable longer driving ranges.

Merryweather and colleagues' research offers previously inaccessible insights into battery materials operating at far-from-equilibrium conditions. Their method for directly observing changes in active particles during operation will complement existing approaches, in which internal changes are inferred from destructive testing of batteries. It could therefore revolutionize the battery-design cycle.

Nature **594**, 503–504 (2021)

doi: <https://doi.org/10.1038/d41586-021-01600-z>

References

1. 1.

Merryweather, A. J., Schnedermann, C., Jacquet, Q., Grey, C. P. & Rao, A. *Nature* **594**, 522–528 (2021).

[Article](#) [Google Scholar](#)

2. 2.

Klett, M. *et al.* *J. Am. Chem. Soc.* **134**, 14654–14657 (2012).

[PubMed](#) [Article](#) [Google Scholar](#)

3. 3.

Ebner, M., Marone, F., Stampanoni, M. & Wood, V. *Science* **342**, 716–720 (2013).

[PubMed](#) [Article](#) [Google Scholar](#)

4. 4.

Ilott, A. J., Mohammadi, M., Chang, H. J., Grey, C. P. & Jerschow, A. *Proc. Natl Acad. Sci. USA* **113**, 10779–10784 (2016).

[PubMed](#) [Article](#) [Google Scholar](#)

5. 5.

Yermukhambetova, A. *et al. Sci. Rep.* **6**, 35291 (2016).

[PubMed](#) [Article](#) [Google Scholar](#)

6. 6.

Song, B. *et al. ACS Energy Lett.* **4**, 2402–2408 (2019).

[Article](#) [Google Scholar](#)

7. 7.

Steinruck, H.-G. *et al. Energy Environ. Sci.* **13**, 4312–4321 (2020).

[Article](#) [Google Scholar](#)

8. 8.

Gao, T. *et al. Joule* **5**, 393–414 (2021).

[Article](#) [Google Scholar](#)

9. 9.

Ortega-Arroyo, J. & Kukura, P. *Phys. Chem. Chem. Phys.* **14**, 15625–15636 (2012).

[PubMed](#) [Article](#) [Google Scholar](#)

10. 10.

Fraggedakis, D. *et al.* *Energy Environ. Sci.* **13**, 2142–2152 (2020).

[Article](#) [Google Scholar](#)

11. 11.

Mistry, A., Usseglio-Viretta, F. L. E., Colclasure, A., Smith, K. & Mukherjee, P. P. *J. Electrochem. Soc.* **167**, 090542 (2020).

[Article](#) [Google Scholar](#)

12. 12.

Mistry, A., Franco, A. A., Cooper, S. J., Roberts, S. A. & Viswanathan, V. *ACS Energy Letters* **6**, 1422–1431 (2021).

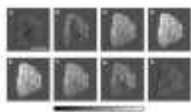
[PubMed](#) [Article](#) [Google Scholar](#)

[Download references](#)

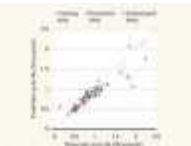
Competing Interests

The author declares no competing interests.

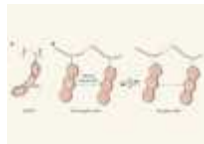
Related Articles



- [Read the paper: Operando optical tracking of single-particle ion dynamics in batteries](#)



- [Machine-learning techniques used to accurately predict battery life](#)



- [Long-lived electrodes for plastic batteries](#)
- [See all News & Views](#)

Subjects

- [Materials science](#)
- [Imaging](#)
- [Chemistry](#)

[Jobs from Nature Careers](#)

- - - [All jobs](#)
 - - [Laboratory Research Scientist](#)
[Francis Crick Institute](#)
[London, United Kingdom](#)
[JOB POST](#)
 - [Bachelor of Science in Computer Engineering \(f/m/d\)](#)
[Helmholtz-Zentrum Berlin for Materials and Energy \(HZB\)](#)
[Berlin, Germany](#)
[JOB POST](#)

- **Laboratory Engineer / Scientific and Technical Head of Reactor Technology (f/m/x)**

Helmholtz Centre for Environmental Research (UFZ).

Leipzig, Germany.

JOB POST

- **Administrative Assistant/Internal Event Coordinator**

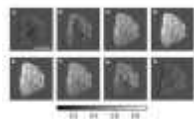
Oklahoma Medical Research Foundation (OMRF).

Oklahoma City, United States

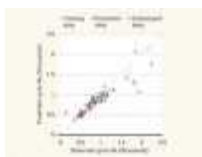
JOB POST

Download PDF

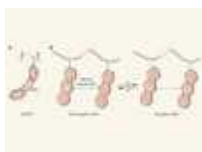
Related Articles



- **Read the paper: Operando optical tracking of single-particle ion dynamics in batteries**



- **Machine-learning techniques used to accurately predict battery life**



- **Long-lived electrodes for plastic batteries**

- [See all News & Views](#)

Subjects

- [Materials science](#)
- [Imaging](#)
- [Chemistry](#)

This article was downloaded by **calibre** from <https://www.nature.com/articles/d41586-021-01600-z>

| [Section menu](#) | [Main menu](#) |

- Article
- [Published: 23 June 2021](#)

Past, present and future stars that can see Earth as a transiting exoplanet

- [L. Kaltenegger](#) ORCID: orcid.org/0000-0002-0436-1802^{1,2} &
- [J. K. Faherty³](#)

[Nature](#) volume 594, pages 505–507 (2021)[Cite this article](#)

- 449 Accesses
- 2972 Altmetric
- [Metrics details](#)

Subjects

- [Astrobiology](#)
- [Communication](#)
- [Exoplanets](#)
- [Science in culture](#)

Abstract

In the search for life in the cosmos, transiting exoplanets are currently our best targets. With thousands already detected, our search is entering a new era of discovery with upcoming large telescopes that will look for signs of ‘life’ in the atmospheres of transiting worlds. Previous work has explored

the zone from which Earth would be visible while transiting the Sun^{1,2,3,4}. However, these studies considered only the current position of stars, and did not include their changing vantage point over time. Here we report that 1,715 stars within 100 parsecs from the Sun are in the right position to have spotted life on a transiting Earth since early human civilization (about 5,000 years ago), with an additional 319 stars entering this special vantage point in the next 5,000 years. Among these stars are seven known exoplanet hosts, including Ross-128, which saw Earth transit the Sun in the past, and Teegarden's Star and Trappist-1, which will start to see it in 29 and 1,642 years, respectively. We found that human-made radio waves have already swept over 75 of the closest stars on our list.

Access options

Subscribe to Journal

Get full journal access for 1 year

\$199.00

only \$3.90 per issue

[Subscribe](#)

All prices are NET prices.

VAT will be added later in the checkout.

Tax calculation will be finalised during checkout.

Rent or Buy article

Get time limited or full article access on ReadCube.

from \$8.99

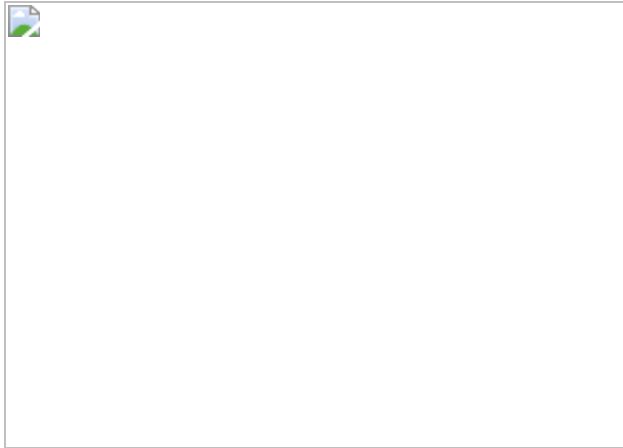
[Rent or Buy](#)

All prices are NET prices.

Additional access options:

- [Log in](#)
- [Access through your institution](#)
- [Learn about institutional subscriptions](#)

Fig. 1: Stars that can see Earth transit since early human civilization.



Data availability

All data are available in the [Supplementary Information](#) and at <https://github.com/jfaherty17/ETZ>.

Code availability

Code used in the analysis is available at <https://github.com/jfaherty17/ETZ>.

References

1. 1.

Shostak, S. & Villard, R. A Scheme for Targeting Optical SETI Observations. In *Symp. Int. Astron. Union* Vol. 213, 409–414 (Cambridge Univ. Press, 2004).

2. 2.

Filippova, L. N., Kardashev, N. S., Likhachev, S. F. & Strelnitskj, V. S. in *Bioastronomy: The Search for Extraterrestrial Life — The Exploration Broadens* 254–258 (Springer, 2008).

3. 3.

Heller, R. & Pudritz, R. E. The search for extraterrestrial intelligence in Earth's solar transit zone. *Astrobiology* **16**, 259–270 (2016).

[ADS](#) [PubMed](#) [PubMed Central](#) [Google Scholar](#)

4. 4.

Kaltenegger, L. & Pepper, J. Which stars can see Earth as a transiting exoplanet? *Mon. Not. R. Astron. Soc. Lett.* **499**, L111–L115 (2020).

[ADS](#) [Google Scholar](#)

5. 5.

Gaia Collaboration. Gaia Early Data Release 3. Summary of the contents and survey properties. *Astron. Astrophys.* **649**, 61 (2020).

[Google Scholar](#)

6. 6.

Gaia Collaboration. Gaia Early Data Release 3. The Gaia catalogue of nearby stars. *Astron. Astrophys.* **41**, 10 (2020).

[Google Scholar](#)

7. 7.

Marconi, S. G. Radio telegraphy. *J. Am. Inst. Electr. Eng.* **41**, 561–570 (1922).

[Google Scholar](#)

8. 8.

Gaia Collaboration. Gaia Data Release 2. *Astron. Astrophys.* **616**, A10 (2018).

[Google Scholar](#)

9. 9.

Kiman, R. et al. Exploring the age-dependent properties of M and L dwarfs using Gaia and SDSS. *Astron. J.* **157**, 231 (2019).

[ADS](#) [CAS](#) [Google Scholar](#)

10. 10.

Bochanski, J. J. et al. The luminosity and mass functions of low-mass stars in the galactic disk II. The field. *Astron. J.* **139**, 2679–2699 (2010).

[ADS](#) [CAS](#) [Google Scholar](#)

11. 11.

Sheikh, S. Z. et al. The breakthrough listen search for intelligent life: a 3.95–8.00 GHz search for radio technosignatures in the restricted Earth transit zone. *Astron. J.* **160**, 29 (2020).

[ADS](#) [Google Scholar](#)

12. 12.

Zhang, Z.-S. et al. First SETI observations with China’s Five-hundred-meter Aperture Spherical Radio Telescope (FAST). *Astrophys. J.* **891**, 174 (2020).

[ADS](#) [Google Scholar](#)

13. 13.

Zahnle, K. et al. Emergence of a habitable planet. *Space Sci. Rev.* **129**, 35–78 (2007).

[ADS](#) [CAS](#) [Google Scholar](#)

14. 14.

Lyons, T. W., Reinhard, C. T. & Planavsky, N. J. The rise of oxygen in Earth's early ocean and atmosphere. *Nature* **506**, 307–315 (2014).

[ADS](#) [CAS](#) [PubMed](#) [Google Scholar](#)

15. 15.

Mojzsis, S. J. et al. Evidence for life on Earth before 3,800 million years ago. *Nature* **384**, 55–59 (1996); correction **386**, 738 (1997).

[ADS](#) [CAS](#) [PubMed](#) [PubMed Central](#) [Google Scholar](#)

16. 16.

Agol, E. Transit survey for Earths in the habitable zone of white dwarfs. *Astrophys. J.* **731**, L31 (2011).

[ADS](#) [Google Scholar](#)

17. 17.

Ramirez, R. M. & Kaltenegger, L. Habitable zone of post-main sequence stars. *Astrophys. J.* **823**, 6 (2016).

[ADS](#) [Google Scholar](#)

18. 18.

Kozakis, T. & Kaltenegger, L. Atmospheres and UV environments of Earth-like planets throughout post-main-sequence evolution. *Astrophys. J.* **875**, 99 (2019).

[ADS](#) [CAS](#) [Google Scholar](#)

19. 19.

Vanderburg, A. et al. A giant planet candidate transiting a white dwarf. *Nature* **585**, 363–367 (2020).

[ADS](#) [CAS](#) [PubMed](#) [PubMed Central](#) [Google Scholar](#)

20. 20.

Kaltenegger, L. et al. The white dwarf opportunity: robust detections of molecules in Earth-like exoplanet atmospheres with the James Webb space telescope. *Astrophys. J.* **901**, L1 (2020).

[ADS](#) [CAS](#) [Google Scholar](#)

21. 21.

Zechmeister, M. et al. The CARMENES search for exoplanets around M dwarfs. *Astron. Astrophys.* **627**, A49 (2019).

[CAS](#) [Google Scholar](#)

22. 22.

Kasting, J. F., Whitmire, D. P. & Reynolds, R. T. Habitable zones around main sequence stars. *Icarus* **101**, 108–128 (1993).

[ADS](#) [CAS](#) [PubMed](#) [PubMed Central](#) [Google Scholar](#)

23. 23.

Kaltenegger, L. How to characterize habitable worlds and signs of life. *Annu. Rev. Astron. Astrophys.* **55**, 433–485 (2017).

[ADS](#) [Google Scholar](#)

24. 24.

Bryson, S. et al. A probabilistic approach to Kepler completeness and reliability for exoplanet occurrence rates. *Astron. J.* **159**, 279 (2020).

[ADS](#) [Google Scholar](#)

25. 25.

Crutzen, P. J. The “anthropocene”. *J. Phys. IV* **12**, 1–5 (2002).

[Google Scholar](#)

26. 26.

Frank, A., Carroll-Nellenback, J., Alberti, M. & Kleidon, A. The Anthropocene generalized: evolution of exo-civilizations and their planetary feedback. *Astrobiology* **18**, 503–518 (2018).

[ADS](#) [CAS](#) [PubMed](#) [PubMed Central](#) [Google Scholar](#)

27. 27.

Kipping, D. M. & Teachey, A. A cloaking device for transiting planets. *Mon. Not. R. Astron. Soc.* **459**, 1233–1241 (2016).

[ADS](#) [Google Scholar](#)

28. 28.

Kerins, E. Mutual detectability: a targeted SETI strategy that avoids the SETI paradox. *Astron. J.* **161**, 39 (2020).

[ADS](#) [Google Scholar](#)

29. 29.

Kaltenegger, L., Traub, W. A. & Jucks, K. W. Spectral evolution of an Earth-like planet. *Astron. J.* **658**, 598–616 (2007).

[CAS](#) [Google Scholar](#)

30. 30.

Kaltenegger, L., Lin, Z. & Madden, J. High-resolution transmission spectra of Earth through geological time. *Astrophys. J. Lett.* **892**, 17 (2020).

[ADS](#) [Google Scholar](#)

31. 31.

Kaltenegger, L., Lin, Z. & Rugheimer, S. Finding signs of life on transiting Earth-like planets: high-resolution transmission spectra of Earth through time around FGKM host stars. *Astrophys. J.* **904**, 10 (2020).

[ADS](#) [CAS](#) [Google Scholar](#)

32. 32.

Lovelock, J. E. A physical basis for life detection experiments. *Nature* **207**, 568–570 (1965).

[ADS](#) [CAS](#) [PubMed](#) [PubMed Central](#) [Google Scholar](#)

33. 33.

Lederberg, J. Signs of life: criterion-system of exobiology. *Nature* **207**, 9–13 (1965).

[ADS](#) [CAS](#) [PubMed](#) [PubMed Central](#) [Google Scholar](#)

34. 34.

Fujii, Y. et al. Exoplanet biosignatures: observational prospects. *Astrobiology* **18**, 739–778 (2018).

[ADS](#) [PubMed](#) [PubMed Central](#) [Google Scholar](#)

35. 35.

Catling, D. C. et al. Exoplanet biosignatures: a framework for their assessment. *Astrobiology* **18**, 709–738 (2018).

[ADS](#) [PubMed](#) [PubMed Central](#) [Google Scholar](#)

36. 36.

Kasting, J. F., Kopparapu, R., Ramirez, R. M. & Harman, C. E. Remote life-detection criteria, habitable zone boundaries, and the frequency of Earth-like planets around M and late K stars. *Proc. Natl Acad. Sci. USA* **111**, 12641–12646 (2014).

[ADS](#) [CAS](#) [PubMed](#) [PubMed Central](#) [Google Scholar](#)

37. 37.

Tarter, J. The search for extraterrestrial intelligence (SETI). *Annu. Rev. Astron. Astrophys.* **39**, 511–548 (2001).

[ADS](#) [Google Scholar](#)

38. 38.

Ricker, G. R. et al. Transiting Exoplanet Survey Satellite (TESS). In *Proc. SPIE, Space Telescopes and Instrumentation 2014: Optical, Infrared, and Millimeter Wave* Vol. 9143 (eds Oschmann Jr, J. M. et al.) 914320 (SPIE, 2014).

39. 39.

Stassun, K. G. et al. The revised TESS input catalog and candidate target list. *Astron. J.* **158**, 138 (2019).

[ADS](#) [Google Scholar](#)

40. 40.

Faherty, J. K. et al. A late-type L dwarf at 11 pc hiding in the Galactic plane characterized using Gaia DR2. *Astrophys. J.* **868**, 44 (2018).

[ADS](#) [Google Scholar](#)

41. 41.

Caselden, D. et al. WiseView: visualizing motion and variability of faint WISE sources. *Astrophysics Source Code Library* <https://ascl.net/1806.004> (2018).

42. 42.

Gagné, J. & Faherty, J. K. BANYAN. XIII. A first look at nearby young associations with Gaia Data Release 2. *Astrophys. J.* **862**, 138 (2018).

[ADS](#) [Google Scholar](#)

43. 43.

Smart, R. L. et al. The Gaia ultracool dwarf sample – II. Structure at the end of the main sequence. *Mon. Not. R. Astron. Soc.* **485**, 4423–4440 (2019).

[ADS](#) [CAS](#) [Google Scholar](#)

44. 44.

Muirhead, P. S. et al. A catalog of cool dwarf targets for the transiting exoplanet survey satellite. *Astron. J.* **155**, 180 (2018).

[ADS](#) [Google Scholar](#)

45. 45.

Anders, F. et al. Photo-astrometric distances, extinctions, and astrophysical parameters for Gaia DR2 stars brighter than $G = 18$. *Astron. Astrophys.* **628**, A94 (2019).

[Google Scholar](#)

46. 46.

Cifuentes, C. et al. CARMENES input catalogue of M dwarfs. *Astron. Astrophys.* **642**, A115 (2020).

[Google Scholar](#)

47. 47.

Malo, L. et al. Bayesian analysis to identify new star candidates in nearby young stellar kinematic groups. *Astrophys. J.* **762**, 88 (2013).

[ADS](#) [Google Scholar](#)

48. 48.

Bock, A. et al. OpenSpace: a system for astrographics. *IEEE Trans. Vis. Comput. Graph.* **26**, 633–642 (2019).

[PubMed](#) [PubMed Central](#) [Google Scholar](#)

49. 49.

Kozakis, T. & Kaltenegger, L. High-resolution spectra of Earth-like planets orbiting red giant host stars. *Astrophys. J.* **160**, 225 (2020).

[CAS](#) [Google Scholar](#)

50. 50.

O’Malley-James, J. T., Cockell, C. S., Greaves, J. S. & Raven, J. A. Swansong biospheres II: the final signs of life on terrestrial planets near the end of their habitable lifetimes. *Int. J. Astrobiol.* **13**, 229–243 (2014).

[ADS](#) [Google Scholar](#)

[Download references](#)

Acknowledgements

L.K. acknowledges support from the Carl Sagan Institute at Cornell and the Breakthrough Initiative. J.K.F. acknowledges support from the Heising Simons Foundation and the Research Corporation for Science Advancement (award 2019-1488). This work has made use of data from the European Space Agency (ESA) mission Gaia, processed by the Gaia Data Processing and Analysis Consortium DPAC20 (<https://www.cosmos.esa.int/gaia>, <https://www.cosmos.esa.int/web/gaia/dpac/consortium>). Funding for DPAC has been provided by national institutions, in particular the institutions participating in the Gaia Multilateral Agreement. This research also used NASA's Astrophysics Data System and the VizieR and SIMBAD databases operated at CDS, Strasbourg, France.

Author information

Affiliations

1. Carl Sagan Institute, Cornell University, Ithaca, NY, USA
L. Kaltenegger
2. Astronomy Department, Cornell University, Ithaca, NY, USA
L. Kaltenegger
3. Department of Astrophysics, American Museum of Natural History, New York, NY, USA
J. K. Faherty

Authors

1. L. Kaltenegger
[View author publications](#)

You can also search for this author in [PubMed](#) [Google Scholar](#)

2. J. K. Faherty

[View author publications](#)

You can also search for this author in [PubMed](#) [Google Scholar](#)

Contributions

L.K. conceived the idea of the study and J.K.F identified the ETZ stars. L.K. and J.K.F composed the manuscript, undertook the analysis and discussed the content of this manuscript.

Corresponding author

Correspondence to [L. Kaltenegger](#).

Ethics declarations

Competing interests

The authors declare no competing interests.

Additional information

Peer review information *Nature* thanks the anonymous reviewer(s) for their contribution to the peer review of this work.

Publisher's note Springer Nature remains neutral with regard to jurisdictional claims in published maps and institutional affiliations.

Supplementary information

[Supplementary Information](#)

A guide to Supplementary Tables 1 and 2.

Supplementary Table 1

Stars that can see Earth transit in the +/-5000-year period. This Table lists all characteristics for stars that can see Earth transit in the +/-5000-year period, sorted by distance from the Sun. The authors cross-matched their full sample against literature estimates of mass, effective temperature, radii, bolometric luminosity, metallicity, and log g for Gaia sources. Respective catalogue references for the parameter are noted in Table 1 and Table 2.

Supplementary Table 2

Exoplanet host stars that can see Earth transit in the +/-5000-year period. This table lists the characteristics of the seven known stars that can see Earth transit in the +/-5000-year period, that are known exoplanet host stars, sorted by distance from the Sun.

Rights and permissions

[Reprints and Permissions](#)

About this article



Check for
updates

Cite this article

Kaltenegger, L., Faherty, J.K. Past, present and future stars that can see Earth as a transiting exoplanet. *Nature* **594**, 505–507 (2021).
<https://doi.org/10.1038/s41586-021-03596-y>

[Download citation](#)

- Received: 17 February 2021
- Accepted: 29 April 2021
- Published: 23 June 2021
- Issue Date: 24 June 2021
- DOI: <https://doi.org/10.1038/s41586-021-03596-y>

Comments

By submitting a comment you agree to abide by our [Terms](#) and [Community Guidelines](#). If you find something abusive or that does not comply with our terms or guidelines please flag it as inappropriate.

[Access through your institution](#)

[Change institution](#)

[Buy or subscribe](#)

Advertisement

This article was downloaded by **calibre** from <https://www.nature.com/articles/s41586-021-03596-y>.

| [Section menu](#) | [Main menu](#) |

- Article
- [Published: 23 June 2021](#)

Accurately computing the electronic properties of a quantum ring

- [C. Neill](#) ORCID: orcid.org/0000-0001-8509-9836¹,
- [T. McCourt](#)¹,
- [X. Mi](#)¹,
- [Z. Jiang](#)¹,
- [M. Y. Niu](#)¹,
- [W. Mruczkiewicz](#) ORCID: orcid.org/0000-0002-8497-6363¹,
- [I. Aleiner](#)¹,
- [F. Arute](#)¹,
- [K. Arya](#)¹,
- [J. Atalaya](#)¹,
- [R. Babbush](#)¹,
- [J. C. Bardin](#) ORCID: orcid.org/0000-0002-6523-6730^{1,2},
- [R. Barends](#)¹,
- [A. Bengtsson](#)¹,
- [A. Bourassa](#)^{1,3},
- [M. Broughton](#)¹,
- [B. B. Buckley](#)¹,
- [D. A. Buell](#)¹,
- [B. Burkett](#) ORCID: orcid.org/0000-0001-8474-6317¹,
- [N. Bushnell](#)¹,
- [J. Campero](#)¹,
- [Z. Chen](#)¹,
- [B. Chiaro](#)¹,

- [R. Collins](#)¹,
- [W. Courtney](#)¹,
- [S. Demura](#) [ORCID: orcid.org/0000-0003-3727-7380](#)¹,
- [A. R. Derk](#)¹,
- [A. Dunsworth](#)¹,
- [D. Eppens](#)¹,
- [C. Erickson](#)¹,
- [E. Farhi](#)¹,
- [A. G. Fowler](#)¹,
- [B. Foxen](#)¹,
- [C. Gidney](#)¹,
- [M. Giustina](#)¹,
- [J. A. Gross](#)¹,
- [M. P. Harrigan](#) [ORCID: orcid.org/0000-0001-9412-0553](#)¹,
- [S. D. Harrington](#) [ORCID: orcid.org/0000-0003-0521-8378](#)¹,
- [J. Hilton](#)¹,
- [A. Ho](#)¹,
- [S. Hong](#)¹,
- [T. Huang](#)¹,
- [W. J. Huggins](#) [ORCID: orcid.org/0000-0003-2735-1380](#)¹,
- [S. V. Isakov](#)¹,
- [M. Jacob-Mitos](#)¹,
- [E. Jeffrey](#)¹,
- [C. Jones](#)¹,
- [D. Kafri](#)¹,
- [K. Kechedzhi](#)¹,
- [J. Kelly](#) [ORCID: orcid.org/0000-0002-2596-2121](#)¹,
- [S. Kim](#)¹,
- [P. V. Klimov](#)¹,
- [A. N. Korotkov](#)^{1,4},
- [F. Kostritsa](#)¹,
- [D. Landhuis](#) [ORCID: orcid.org/0000-0001-9804-2185](#)¹,
- [P. Laptev](#)¹,
- [E. Lucero](#)¹,

- [O. Martin](#)¹,
- [J. R. McClean](#) ORCID: orcid.org/0000-0002-2809-0509¹,
- [M. McEwen](#) ORCID: orcid.org/0000-0002-9544-141X^{1,5},
- [A. Megrant](#) ORCID: orcid.org/0000-0002-6371-6140¹,
- [K. C. Miao](#)¹,
- [M. Mohseni](#)¹,
- [J. Mutus](#)¹,
- [O. Naaman](#) ORCID: orcid.org/0000-0002-7760-9186¹,
- [M. Neeley](#) ORCID: orcid.org/0000-0002-5548-0051¹,
- [M. Newman](#)¹,
- [T. E. O'Brien](#)¹,
- [A. Opremcak](#)¹,
- [E. Ostby](#)¹,
- [B. Pató](#)¹,
- [A. Petukhov](#)¹,
- [C. Quintana](#)¹,
- [N. Redd](#) ORCID: orcid.org/0000-0002-6549-5441¹,
- [N. C. Rubin](#)¹,
- [D. Sank](#)¹,
- [K. J. Satzinger](#) ORCID: orcid.org/0000-0001-5865-0813¹,
- [V. Shvarts](#)¹,
- [D. Strain](#)¹,
- [M. Szalay](#)¹,
- [M. D. Trevithick](#)¹,
- [B. Villalonga](#)¹,
- [T. C. White](#)¹,
- [Z. Yao](#)¹,
- [P. Yeh](#) ORCID: orcid.org/0000-0003-0837-1028¹,
- [A. Zalcman](#) ORCID: orcid.org/0000-0002-2585-2424¹,
- [H. Neven](#)¹,
- [S. Boixo](#) ORCID: orcid.org/0000-0002-1090-7584¹,
- [L. B. Ioffe](#)¹,
- [P. Roushan](#)¹,
- [Y. Chen](#)¹ &

- [V. Smelyanskiy](#) ¹

[Nature volume 594](#), pages 508–512 (2021) [Cite this article](#)

- 433 Accesses
- 41 Altmetric
- [Metrics details](#)

Subjects

- [Quantum metrology](#)
- [Quantum simulation](#)

Abstract

A promising approach to study condensed-matter systems is to simulate them on an engineered quantum platform^{1,2,3,4}. However, the accuracy needed to outperform classical methods has not been achieved so far. Here, using 18 superconducting qubits, we provide an experimental blueprint for an accurate condensed-matter simulator and demonstrate how to investigate fundamental electronic properties. We benchmark the underlying method by reconstructing the single-particle band structure of a one-dimensional wire. We demonstrate nearly complete mitigation of decoherence and readout errors, and measure the energy eigenvalues of this wire with an error of approximately 0.01 rad, whereas typical energy scales are of the order of 1 rad. Insight into the fidelity of this algorithm is gained by highlighting the robust properties of a Fourier transform, including the ability to resolve eigenenergies with a statistical uncertainty of 10^{-4} rad. We also synthesize magnetic flux and disordered local potentials, which are two key tenets of a condensed-matter system. When sweeping the magnetic flux we observe avoided level crossings in the spectrum, providing a detailed fingerprint of the spatial distribution of local disorder. By combining these methods we reconstruct electronic properties of the eigenstates, observing persistent currents and a strong suppression of conductance with added disorder. Our

work describes an accurate method for quantum simulation^{5,6} and paves the way to study new quantum materials with superconducting qubits.

Access options

Subscribe to Journal

Get full journal access for 1 year

\$199.00

only \$3.90 per issue

[Subscribe](#)

All prices are NET prices.

VAT will be added later in the checkout.

Tax calculation will be finalised during checkout.

Rent or Buy article

Get time limited or full article access on ReadCube.

from \$8.99

[Rent or Buy](#)

All prices are NET prices.

Additional access options:

- [Log in](#)
- [Access through your institution](#)
- [Learn about institutional subscriptions](#)

Fig. 1: Engineering a one-dimensional system with energy, momentum and flux.

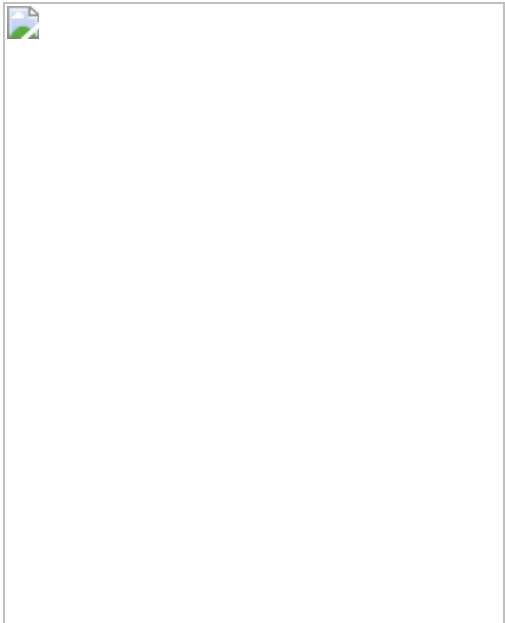


Fig. 2: Measuring the single-particle band structure.



Fig. 3: Synthetic flux as a probe of local disorder.



Fig. 4: Inferring current and conductance from avoided level crossings.

Data availability

The data presented in this study can be found in the Dryad repository located at <https://doi.org/10.5061/dryad.4f4qrfj9x>.

Code availability

The Python code for processing the data presented in this study can be found in the Dryad repository located at
<https://doi.org/10.5061/dryad.4f4qrfj9x>.

References

1. 1.

Feynman, R. P. Simulating physics with computers. *Int. J. Theor. Phys.* **21**, 467–488 (1982).

[MathSciNet](#) [Article](#) [Google Scholar](#)

2. 2.

Cirac, J. I. & Zoller, P. Quantum computations with cold trapped ions. *Phys. Rev. Lett.* **74**, 4091–4094 (1995).

[CAS](#) [Article](#) [ADS](#) [Google Scholar](#)

3. 3.

Bloch, I., Dalibard, J. & Zwerger, W. Many-body physics with ultracold gases. *Rev. Mod. Phys.* **80**, 885 (2008).

[CAS](#) [Article](#) [ADS](#) [Google Scholar](#)

4. 4.

Georgescu, I., Ashhab, S. & Nori, F. Quantum simulation. *Rev. Mod. Phys.* **86**, 153 (2014).

[Article](#) [ADS](#) [Google Scholar](#)

5. 5.

Polkovnikov, A., Sengupta, K., Silva, A. & Vengalatorre, M.
Nonequilibrium dynamics of closed interacting quantum systems. *Rev. Mod. Phys.*, **83**, 863 (2011).

[Article](#) [ADS](#) [Google Scholar](#)

6. 6.

Carusotto, I. et al. Photonic materials in circuit quantum electrodynamics. *Nat. Phys.* **16**, 268–279 (2020).

[CAS](#) [Article](#) [Google Scholar](#)

7. 7.

Qin, M. et al. Absence of superconductivity in the pure two-dimensional Hubbard model. *Phys. Rev. X* **10**, 031016 (2020).

[CAS](#) [Google Scholar](#)

8. 8.

Jiang, H. C. & Devereaux, T. P. Superconductivity in the doped Hubbard model and its interplay with next-nearest hopping t' . *Science* **365**, 1424–1428 (2019).

[MathSciNet](#) [CAS](#) [Article](#) [ADS](#) [Google Scholar](#)

9. 9.

Willett, R. et al. Observation of an even-denominator quantum number in the fractional quantum Hall effect. *Phys. Rev. Lett.* **59**, 1776–1779 (1987).

[CAS](#) [Article](#) [ADS](#) [Google Scholar](#)

10. 10.

Dolev, M., Heiblum, M., Umansky, V., Stern, A. & Mahalu, D. Observation of a quarter of an electron charge at the $\nu = 5/2$ quantum Hall state. *Nature* **452**, 829–834 (2008).

[CAS](#) [Article](#) [ADS](#) [Google Scholar](#)

11. 11.

Willett, R. et al. Interference measurements of non-abelian $e/4$ & abelian $e/2$ quasiparticle braiding. Preprint at <https://arxiv.org/abs/1905.10248> (2019).

12. 12.

Chen, Y. et al. Qubit architecture with high coherence and fast tunable coupling. *Phys. Rev. Lett.* **113**, 220502 (2014).

[Article](#) [ADS](#) [Google Scholar](#)

13. 13.

Neill, C. A Path Towards Quantum Supremacy with Superconducting Qubits. PhD Thesis, Univ. California, Santa Barbara (2017).

14. 14.

Arute, F. et al. Quantum supremacy using a programmable superconducting processor. *Nature* **574**, 505–510 (2019).

[CAS](#) [Article](#) [ADS](#) [Google Scholar](#)

15. 15.

Giamarchi, T. *Quantum Physics in One Dimension* Vol. 121 (Clarendon, 2003).

16. 16.

Jotzu, G. et al. Experimental realization of the topological Haldane model with ultracold fermions. *Nature* **515**, 237–240 (2014).

[CAS](#) [Article](#) [ADS](#) [Google Scholar](#)

17. 17.

Manovitz, T., Shapira, Y., Akerman, N., Stern, A. & Ozeri, R. Quantum simulations with complex geometries and synthetic gauge fields in a trapped ion chain. *PRX Quantum* **1**, 020303 (2020).

[Article](#) [Google Scholar](#)

18. 18.

Roushan, P. et al. Spectroscopic signatures of localization with interacting photons in superconducting qubits. *Science* **358**, 1175–1179 (2017).

[MathSciNet](#) [CAS](#) [Article](#) [ADS](#) [Google Scholar](#)

19. 19.

Aharonov, Y. & Bohm, D. Significance of electromagnetic potentials in the quantum theory. *Phys. Rev.* **115**, 485–491 (1959).

[MathSciNet](#) [Article](#) [ADS](#) [Google Scholar](#)

20. 20.

Pal, A. & Huse, D. Many-body localization phase transition. *Phys. Rev. B* **82**, 174411 (2010).

[Article](#) [ADS](#) [Google Scholar](#)

21. 21.

Ponte, P., Papić, Z., Huvveneers, F. & Abanin, D. A. Many-body localization in periodically driven systems. *Phys. Rev. Lett.* **114**,

140401 (2015).

[Article](#) [ADS](#) [Google Scholar](#)

22. 22.

Schreiber, M. et al. Observation of many-body localization of interacting fermions in a quasirandom optical lattice. *Science* **349**, 842–845 (2015).

[MathSciNet](#) [CAS](#) [Article](#) [ADS](#) [Google Scholar](#)

23. 23.

Kleemans, N. A. et al. Oscillatory persistent currents in self-assembled quantum rings. *Phys. Rev. Lett.* **99**, 146808 (2007).

[CAS](#) [Article](#) [ADS](#) [Google Scholar](#)

24. 24.

Bleszynski-Jayich, A. C. et al. Persistent currents in normal metal rings. *Science* **326**, 272–275 (2009).

[CAS](#) [Article](#) [ADS](#) [Google Scholar](#)

25. 25.

Thouless, D., Kohmoto, M., Nightingale, M. & den Nijs, M. Quantized Hall conductance in a two-dimensional periodic potential. *Phys. Rev. Lett.* **49**, 405–408 (1982).

[CAS](#) [Article](#) [ADS](#) [Google Scholar](#)

26. 26.

Braun, D., Hofstetter, E., MacKinnon, A. & Montambaux, G. Level curvatures and conductances: A numerical study of the thouless relation. *Phys. Rev. B* **55**, 7557 (1997).

[CAS](#) [Article](#) [ADS](#) [Google Scholar](#)

27. 27.

White, S. R. Density matrix formulation for quantum renormalization groups. *Phys. Rev. Lett.* **69**, 2863–2866 (1992).

[CAS](#) [Article](#) [ADS](#) [Google Scholar](#)

28. 28.

White, S. R. & Huse, D. A. Numerical renormalization-group study of low-lying eigenstates of the antiferromagnetic $S=1$ Heisenberg chain. *Phys. Rev. B* **48**, 3844–3852 (1993).

[CAS](#) [Article](#) [ADS](#) [Google Scholar](#)

29. 29.

Kelly, J., O’Malley, P., Neeley, M., Neven, H. & Martinis, J. Physical qubit calibration on a directed acyclic graph. Preprint at <https://arxiv.org/abs/1803.03226> (2018).

[Download references](#)

Acknowledgements

We acknowledge discussions with B. Altshuler and L. Faoro. We thank J. Platt, J. Dean and J. Yagnik for their executive sponsorship of the Google Quantum AI team, and for their continued engagement and support. We thank A. Brown and J. Platt for reviewing and providing advice on the draft of the manuscript.

Author information

Affiliations

1. Google Quantum AI, Mountain View, CA, USA

C. Neill, T. McCourt, X. Mi, Z. Jiang, M. Y. Niu, W. Mruczkiewicz, I. Aleiner, F. Arute, K. Arya, J. Atalaya, R. Babbush, J. C. Bardin, R. Barends, A. Bengtsson, A. Bourassa, M. Broughton, B. B. Buckley, D. A. Buell, B. Burkett, N. Bushnell, J. Campero, Z. Chen, B. Chiaro, R. Collins, W. Courtney, S. Demura, A. R. Derk, A. Dunsworth, D. Eppens, C. Erickson, E. Farhi, A. G. Fowler, B. Foxen, C. Gidney, M. Giustina, J. A. Gross, M. P. Harrigan, S. D. Harrington, J. Hilton, A. Ho, S. Hong, T. Huang, W. J. Huggins, S. V. Isakov, M. Jacob-Mitos, E. Jeffrey, C. Jones, D. Kafri, K. Kechedzhi, J. Kelly, S. Kim, P. V. Klimov, A. N. Korotkov, F. Kostritsa, D. Landhuis, P. Laptev, E. Lucero, O. Martin, J. R. McClean, M. McEwen, A. Megrant, K. C. Miao, M. Mohseni, J. Mutus, O. Naaman, M. Neeley, M. Newman, T. E. O'Brien, A. Opremcak, E. Ostby, B. Pató, A. Petukhov, C. Quintana, N. Redd, N. C. Rubin, D. Sank, K. J. Satzinger, V. Shvarts, D. Strain, M. Szalay, M. D. Trevithick, B. Villalonga, T. C. White, Z. Yao, P. Yeh, A. Zalcman, H. Neven, S. Boixo, L. B. Ioffe, P. Roushan, Y. Chen & V. Smelyanskiy

2. Department of Electrical and Computer Engineering, University of Massachusetts, Amherst, MA, USA

J. C. Bardin

3. Pritzker School of Molecular Engineering, University of Chicago, Chicago, IL, USA

A. Bourassa

4. Department of Electrical and Computer Engineering, University of California, Riverside, Riverside, CA, USA

A. N. Korotkov

5. Department of Physics, University of California, Santa Barbara, Santa Barbara, CA, USA

M. McEwen

Authors

1. C. Neill

[View author publications](#)

You can also search for this author in [PubMed](#) [Google Scholar](#)

2. T. McCourt

[View author publications](#)

You can also search for this author in [PubMed](#) [Google Scholar](#)

3. X. Mi

[View author publications](#)

You can also search for this author in [PubMed](#) [Google Scholar](#)

4. Z. Jiang

[View author publications](#)

You can also search for this author in [PubMed](#) [Google Scholar](#)

5. M. Y. Niu

[View author publications](#)

You can also search for this author in [PubMed](#) [Google Scholar](#)

6. W. Mruczkiewicz

[View author publications](#)

You can also search for this author in [PubMed](#) [Google Scholar](#)

7. I. Aleiner

[View author publications](#)

You can also search for this author in [PubMed](#) [Google Scholar](#)

8. F. Arute

[View author publications](#)

You can also search for this author in [PubMed](#) [Google Scholar](#)

9. K. Arya

[View author publications](#)

You can also search for this author in [PubMed](#) [Google Scholar](#)

10. J. Atalaya

[View author publications](#)

You can also search for this author in [PubMed](#) [Google Scholar](#)

11. R. Babbush

[View author publications](#)

You can also search for this author in [PubMed](#) [Google Scholar](#)

12. J. C. Bardin

[View author publications](#)

You can also search for this author in [PubMed](#) [Google Scholar](#)

13. R. Barends

[View author publications](#)

You can also search for this author in [PubMed](#) [Google Scholar](#)

14. A. Bengtsson

[View author publications](#)

You can also search for this author in [PubMed](#) [Google Scholar](#)

15. A. Bourassa

[View author publications](#)

You can also search for this author in [PubMed](#) [Google Scholar](#)

16. M. Broughton

[View author publications](#)

You can also search for this author in [PubMed](#) [Google Scholar](#)

17. B. B. Buckley

[View author publications](#)

You can also search for this author in [PubMed](#) [Google Scholar](#)

18. D. A. Buell

[View author publications](#)

You can also search for this author in [PubMed](#) [Google Scholar](#)

19. B. Burkett

[View author publications](#)

You can also search for this author in [PubMed](#) [Google Scholar](#)

20. N. Bushnell

[View author publications](#)

You can also search for this author in [PubMed](#) [Google Scholar](#)

21. J. Campero

[View author publications](#)

You can also search for this author in [PubMed](#) [Google Scholar](#)

22. Z. Chen

[View author publications](#)

You can also search for this author in [PubMed](#) [Google Scholar](#)

23. B. Chiaro

[View author publications](#)

You can also search for this author in [PubMed](#) [Google Scholar](#)

24. R. Collins

[View author publications](#)

You can also search for this author in [PubMed](#) [Google Scholar](#)

25. W. Courtney

[View author publications](#)

You can also search for this author in [PubMed](#) [Google Scholar](#)

26. S. Demura

[View author publications](#)

You can also search for this author in [PubMed](#) [Google Scholar](#)

27. A. R. Derk

[View author publications](#)

You can also search for this author in [PubMed](#) [Google Scholar](#)

28. A. Dunsworth

[View author publications](#)

You can also search for this author in [PubMed](#) [Google Scholar](#)

29. D. Eppens

[View author publications](#)

You can also search for this author in [PubMed](#) [Google Scholar](#)

30. C. Erickson

[View author publications](#)

You can also search for this author in [PubMed](#) [Google Scholar](#)

31. E. Farhi

[View author publications](#)

You can also search for this author in [PubMed](#) [Google Scholar](#)

32. A. G. Fowler

[View author publications](#)

You can also search for this author in [PubMed](#) [Google Scholar](#)

33. B. Foxen

[View author publications](#)

You can also search for this author in [PubMed](#) [Google Scholar](#)

34. C. Gidney

[View author publications](#)

You can also search for this author in [PubMed](#) [Google Scholar](#)

35. M. Giustina

[View author publications](#)

You can also search for this author in [PubMed](#) [Google Scholar](#)

36. J. A. Gross

[View author publications](#)

You can also search for this author in [PubMed](#) [Google Scholar](#)

37. M. P. Harrigan

[View author publications](#)

You can also search for this author in [PubMed](#) [Google Scholar](#)

38. S. D. Harrington

[View author publications](#)

You can also search for this author in [PubMed](#) [Google Scholar](#)

39. J. Hilton

[View author publications](#)

You can also search for this author in [PubMed](#) [Google Scholar](#)

40. A. Ho

[View author publications](#)

You can also search for this author in [PubMed](#) [Google Scholar](#)

41. S. Hong

[View author publications](#)

You can also search for this author in [PubMed](#) [Google Scholar](#)

42. T. Huang

[View author publications](#)

You can also search for this author in [PubMed](#) [Google Scholar](#)

43. W. J. Huggins

[View author publications](#)

You can also search for this author in [PubMed](#) [Google Scholar](#)

44. S. V. Isakov

[View author publications](#)

You can also search for this author in [PubMed](#) [Google Scholar](#)

45. M. Jacob-Mitos

[View author publications](#)

You can also search for this author in [PubMed](#) [Google Scholar](#)

46. E. Jeffrey

[View author publications](#)

You can also search for this author in [PubMed](#) [Google Scholar](#)

47. C. Jones

[View author publications](#)

You can also search for this author in [PubMed](#) [Google Scholar](#)

48. D. Kafri

[View author publications](#)

You can also search for this author in [PubMed](#) [Google Scholar](#)

49. K. Kechedzhi

[View author publications](#)

You can also search for this author in [PubMed](#) [Google Scholar](#)

50. J. Kelly

[View author publications](#)

You can also search for this author in [PubMed](#) [Google Scholar](#)

51. S. Kim

[View author publications](#)

You can also search for this author in [PubMed](#) [Google Scholar](#)

52. P. V. Klimov

[View author publications](#)

You can also search for this author in [PubMed](#) [Google Scholar](#)

53. A. N. Korotkov

[View author publications](#)

You can also search for this author in [PubMed](#) [Google Scholar](#)

54. F. Kostritsa

[View author publications](#)

You can also search for this author in [PubMed](#) [Google Scholar](#)

55. D. Landhuis

[View author publications](#)

You can also search for this author in [PubMed](#) [Google Scholar](#)

56. P. Laptev

[View author publications](#)

You can also search for this author in [PubMed](#) [Google Scholar](#)

57. E. Lucero

[View author publications](#)

You can also search for this author in [PubMed](#) [Google Scholar](#)

58. O. Martin

[View author publications](#)

You can also search for this author in [PubMed](#) [Google Scholar](#)

59. J. R. McClean

[View author publications](#)

You can also search for this author in [PubMed](#) [Google Scholar](#)

60. M. McEwen

[View author publications](#)

You can also search for this author in [PubMed](#) [Google Scholar](#)

61. A. Megrant

[View author publications](#)

You can also search for this author in [PubMed](#) [Google Scholar](#)

62. K. C. Miao

[View author publications](#)

You can also search for this author in [PubMed](#) [Google Scholar](#)

63. M. Mohseni

[View author publications](#)

You can also search for this author in [PubMed](#) [Google Scholar](#)

64. J. Mutus

[View author publications](#)

You can also search for this author in [PubMed](#) [Google Scholar](#)

65. O. Naaman

[View author publications](#)

You can also search for this author in [PubMed](#) [Google Scholar](#)

66. M. Neeley

[View author publications](#)

You can also search for this author in [PubMed](#) [Google Scholar](#)

67. M. Newman

[View author publications](#)

You can also search for this author in [PubMed](#) [Google Scholar](#)

68. T. E. O'Brien

[View author publications](#)

You can also search for this author in [PubMed](#) [Google Scholar](#)

69. A. Opremcak

[View author publications](#)

You can also search for this author in [PubMed](#) [Google Scholar](#)

70. E. Ostby

[View author publications](#)

You can also search for this author in [PubMed](#) [Google Scholar](#)

71. B. Pató

[View author publications](#)

You can also search for this author in [PubMed](#) [Google Scholar](#)

72. A. Petukhov

[View author publications](#)

You can also search for this author in [PubMed](#) [Google Scholar](#)

73. C. Quintana

[View author publications](#)

You can also search for this author in [PubMed](#) [Google Scholar](#)

74. N. Redd

[View author publications](#)

You can also search for this author in [PubMed](#) [Google Scholar](#)

75. N. C. Rubin

[View author publications](#)

You can also search for this author in [PubMed](#) [Google Scholar](#)

76. D. Sank

[View author publications](#)

You can also search for this author in [PubMed](#) [Google Scholar](#)

77. K. J. Satzinger

[View author publications](#)

You can also search for this author in [PubMed](#) [Google Scholar](#)

78. V. Shvarts

[View author publications](#)

You can also search for this author in [PubMed](#) [Google Scholar](#)

79. D. Strain

[View author publications](#)

You can also search for this author in [PubMed](#) [Google Scholar](#)

80. M. Szalay

[View author publications](#)

You can also search for this author in [PubMed](#) [Google Scholar](#)

81. M. D. Trevithick

[View author publications](#)

You can also search for this author in [PubMed](#) [Google Scholar](#)

82. B. Villalonga

[View author publications](#)

You can also search for this author in [PubMed](#) [Google Scholar](#)

83. T. C. White

[View author publications](#)

You can also search for this author in [PubMed](#) [Google Scholar](#)

84. Z. Yao

[View author publications](#)

You can also search for this author in [PubMed](#) [Google Scholar](#)

85. P. Yeh

[View author publications](#)

You can also search for this author in [PubMed](#) [Google Scholar](#)

86. A. Zalcman

[View author publications](#)

You can also search for this author in [PubMed](#) [Google Scholar](#)

87. H. Neven

[View author publications](#)

You can also search for this author in [PubMed](#) [Google Scholar](#)

88. S. Boixo

[View author publications](#)

You can also search for this author in [PubMed](#) [Google Scholar](#)

89. L. B. Ioffe

[View author publications](#)

You can also search for this author in [PubMed](#) [Google Scholar](#)

90. P. Roushan

[View author publications](#)

You can also search for this author in [PubMed](#) [Google Scholar](#)

91. Y. Chen

[View author publications](#)

You can also search for this author in [PubMed](#) [Google Scholar](#)

92. V. Smelyanskiy

[View author publications](#)

You can also search for this author in [PubMed](#) [Google Scholar](#)

Contributions

C.N. designed and executed the experiment. C.N. and P.R. wrote the manuscript. C.N., T.M. and V. Smelyanskiy wrote the Supplementary Information. V. Smelyanskiy, S.B., T.M., Z.J., X.M., L.B.I. and C.N. provided the theoretical support and analysis techniques, the theory of Floquet calibration and the open system model. Y.C., V. Smelyanskiy and H.N. led and coordinated the project. Infrastructure support was provided by the hardware team. All authors contributed to revising the manuscript and the Supplementary Information.

Corresponding authors

Correspondence to [P. Roushan](#) or [Y. Chen](#) or [V. Smelyanskiy](#).

Ethics declarations

Competing interests

The authors declare no competing interests.

Additional information

Peer review information *Nature* thanks Jonas Bylander, Frank Wilhelm and the other, anonymous, reviewer(s) for their contribution to the peer review of this work. Peer reviewer reports are available.

Publisher's note Springer Nature remains neutral with regard to jurisdictional claims in published maps and institutional affiliations.

Supplementary information

[Supplementary Information](#)

This file contains Supplementary Sections A-G, including Supplementary Figures 1-15 – see contents page for details.

[Peer Review File](#)

Rights and permissions

[Reprints and Permissions](#)

About this article



Check for
updates

Cite this article

Neill, C., McCourt, T., Mi, X. *et al.* Accurately computing the electronic properties of a quantum ring. *Nature* **594**, 508–512 (2021).
<https://doi.org/10.1038/s41586-021-03576-2>

[Download citation](#)

- Received: 28 November 2020
- Accepted: 22 April 2021
- Published: 23 June 2021
- Issue Date: 24 June 2021
- DOI: <https://doi.org/10.1038/s41586-021-03576-2>

Comments

By submitting a comment you agree to abide by our [Terms](#) and [Community Guidelines](#). If you find something abusive or that does not comply with our terms or guidelines please flag it as inappropriate.

[Access through your institution](#)

[Change institution](#)

[Buy or subscribe](#)

Advertisement

| [Section menu](#) | [Main menu](#) |

- Article
- [Published: 23 June 2021](#)

Fizeau drag in graphene plasmonics

- [Y. Dong^{1,2}](#) na1,
- [L. Xiong¹](#) na1,
- [I. Y. Phinney³](#),
- [Z. Sun](#) [ORCID: orcid.org/0000-0002-0342-6248¹](#),
- [R. Jing](#) [ORCID: orcid.org/0000-0002-0358-6831¹](#),
- [A. S. McLeod](#) [ORCID: orcid.org/0000-0002-5232-634X¹](#),
- [S. Zhang¹](#),
- [S. Liu](#) [ORCID: orcid.org/0000-0002-3046-3335⁴](#),
- [F. L. Ruta](#) [ORCID: orcid.org/0000-0002-8746-9420^{1,2}](#),
- [H. Gao³](#),
- [Z. Dong³](#),
- [R. Pan¹](#),
- [J. H. Edgar](#) [ORCID: orcid.org/0000-0003-0918-5964⁴](#),
- [P. Jarillo-Herrero](#) [ORCID: orcid.org/0000-0001-8217-8213³](#),
- [L. S. Levitov³](#),
- [A. J. Millis¹](#),
- [M. M. Fogler⁵](#),
- [D. A. Bandurin](#) ³ &
- [D. N. Basov](#) [ORCID: orcid.org/0000-0001-9785-5387¹](#)

[Nature](#) volume 594, pages 513–516 (2021) [Cite this article](#)

- 321 Accesses
- 19 Altmetric

- [Metrics details](#)

Subjects

- [Electronic devices](#)
- [Electronics, photonics and device physics](#)
- [Optical properties and devices](#)
- [Polaritons](#)
- [Surfaces, interfaces and thin films](#)

Abstract

Dragging of light by moving media was predicted by Fresnel¹ and verified by Fizeau's celebrated experiments² with flowing water. This momentous discovery is among the experimental cornerstones of Einstein's special relativity theory and is well understood^{3,4} in the context of relativistic kinematics. By contrast, experiments on dragging photons by an electron flow in solids are riddled with inconsistencies and have so far eluded agreement with the theory^{5,6,7}. Here we report on the electron flow dragging surface plasmon polaritons^{8,9} (SPPs): hybrid quasiparticles of infrared photons and electrons in graphene. The drag is visualized directly through infrared nano-imaging of propagating plasmonic waves in the presence of a high-density current. The polaritons in graphene shorten their wavelength when propagating against the drifting carriers. Unlike the Fizeau effect for light, the SPP drag by electrical currents defies explanation by simple kinematics and is linked to the nonlinear electrodynamics of Dirac electrons in graphene. The observed plasmonic Fizeau drag enables breaking of time-reversal symmetry and reciprocity¹⁰ at infrared frequencies without resorting to magnetic fields^{11,12} or chiral optical pumping^{13,14}. The Fizeau drag also provides a tool with which to study interactions and nonequilibrium effects in electron liquids.

Access options

Subscribe to Journal

Get full journal access for 1 year

\$199.00

only \$3.90 per issue

[Subscribe](#)

All prices are NET prices.

VAT will be added later in the checkout.

Tax calculation will be finalised during checkout.

Rent or Buy article

Get time limited or full article access on ReadCube.

from \$8.99

[Rent or Buy](#)

All prices are NET prices.

Additional access options:

- [Log in](#)
- [Access through your institution](#)
- [Learn about institutional subscriptions](#)

Fig. 1: Plasmonic Fizeau drag in graphene: theory and modelling.

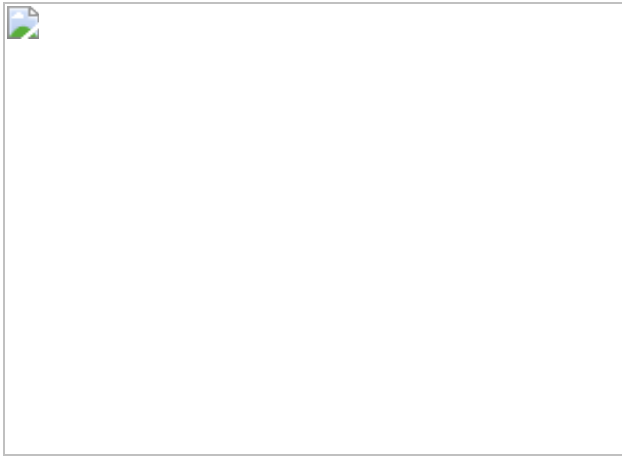


Fig. 2: Experimental demonstration of the plasmonic Fizeau drag.

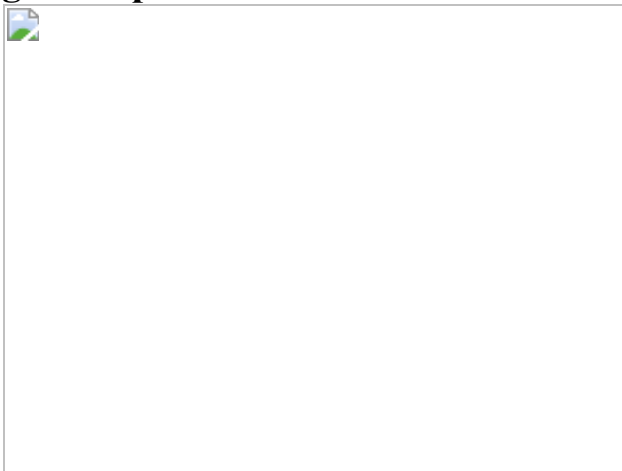


Fig. 3: Quantitative analysis of the plasmonic Fizeau drag.

Data availability

The data that support the findings of this study are available from the corresponding author upon reasonable request.

Code availability

The code used to analyse data are available from the corresponding author upon reasonable request.

References

1. 1.

Fresnel, A., Théorie de la lumière. Cinquième section: questions diverses d'optique [Theory of light. Fifth section: various questions of optics]. Letter to F. Arago, September 1818. In *Oeuvres complètes d'Augustin Fresnel* Vol. 2, 627–636 (Imprimerie Impériale, 1868).

2. 2.

Fizeau, H. Sur les hypothèses relativesal, áther lumineux, et sur une expérience qui paraît démontrer que le mouvement des corps change la vitesse avec laquelle la lumiere se propage dans leur intérieur [On the relative hypotheses, luminous ether, and on an experiment which seems to demonstrate that the movement of bodies changes the speed with which light propagates in their interior]. *CR Hebd. Acad. Sci.* **33**, 349–355 (1851).

[Google Scholar](#)

3. 3.

Landau, L. & Lifshitz, E. *The Classical Theory of Fields* Vol. 2 4th edn (Pergamon, 1975).

4. 4.

Lorentz, H. A. *The Theory of Electrons and Its Applications to the Phenomena of Light and Radiant Heat* (Teubner, 1916).

5. 5.

Unz, H. Relativistic magneto-ionic theory for drifting plasma in longitudinal direction. *Phys. Rev.* **146**, 92–95 (1966).

[ADS](#) [CAS](#) [Google Scholar](#)

6. 6.

Moss, T., Burrell, G. & Hetherington, A. Measurement of Fresnel drag produced by electron motion in semiconductors. *Proc. Roy. Soc. London Ser. A* **308**, 125–132 (1968).

[ADS](#) [Google Scholar](#)

7. 7.

Almazov, L., Vas'ko, F. & Dykman, I. Influence of carrier drift on the propagation of electromagnetic wave in a solid-state plasma. *JETP Lett.* **16**, 241–216 (1972).

[Google Scholar](#)

8. 8.

Basov, D. N., Fogler, M. M. & García de Abajo, F. J. Polaritons in van der Waals materials. *Science* **354**, aag1992 (2016).

[PubMed](#) [Google Scholar](#)

9. 9.

Low, T. et al. Polaritons in layered two-dimensional materials. *Nat. Mater.* **16**, 182–194 (2017).

[ADS](#) [CAS](#) [PubMed](#) [Google Scholar](#)

10. 10.

Caloz, C. et al. Electromagnetic nonreciprocity. *Phys. Rev. Appl.* **10**, 047001 (2018).

[ADS](#) [CAS](#) [Google Scholar](#)

11. 11.

Jin, D. et al. Infrared topological plasmons in graphene. *Phys. Rev. Lett.* **118**, 245301 (2017).

[ADS](#) [PubMed](#) [Google Scholar](#)

12. 12.

Tokura, Y. & Nagaosa, N. Nonreciprocal responses from non-centrosymmetric quantum materials. *Nat. Commun.* **9**, 3740 (2018).

[ADS](#) [PubMed](#) [PubMed Central](#) [Google Scholar](#)

13. 13.

Kumar, A. et al. Chiral plasmon in gapped Dirac systems. *Phys. Rev. B* **93**, 041413 (2016).

[ADS](#) [Google Scholar](#)

14. 14.

Song, J. C. W. & Rudner, M. S. Chiral plasmons without magnetic field. *Proc. Natl Acad. Sci. USA* **113**, 4658–4663 (2016).

[ADS](#) [CAS](#) [PubMed](#) [PubMed Central](#) [Google Scholar](#)

15. 15.

Jablan, M., Buljan, H. & Soljačić, M. Plasmonics in graphene at infrared frequencies. *Phys. Rev. B* **80**, 245435 (2009).

[ADS](#) [Google Scholar](#)

16. 16.

Woessner, A. et al. Highly confined low-loss plasmons in graphene–boron nitride heterostructures. *Nat. Mater.* **14**, 421 (2015).

[ADS](#) [CAS](#) [PubMed](#) [Google Scholar](#)

17. 17.

Dai, S. et al. Graphene on hexagonal boron nitride as a tunable hyperbolic metamaterial. *Nat. Nanotechnol.* **10**, 682–686 (2015).

[ADS](#) [CAS](#) [PubMed](#) [Google Scholar](#)

18. 18.

Ni, G. X. et al. Fundamental limits to graphene plasmonics. *Nature* **557**, 530–533 (2018).

[ADS](#) [CAS](#) [PubMed](#) [Google Scholar](#)

19. 19.

Son, S.-K. et al. Graphene hot-electron light bulb: incandescence from hBN-encapsulated graphene in air. *2D Mater.* **5**, 011006 (2017).

[Google Scholar](#)

20. 20.

Borgnia, D. S., Phan, T. V. & Levitov, L. S. Quasi-relativistic Doppler effect and non-reciprocal plasmons in graphene. Preprint at: <https://arxiv.org/abs/1512.09044> (2015).

21. 21.

Sabbagh, M., Lee, H.-W., Stauber, T. & Kim, K. S. Drift-induced modifications to the dynamical polarization of graphene. *Phys. Rev. B* **92**, 195429 (2015).

[ADS](#) [Google Scholar](#)

22. 22.

Duppen, B. V., Tomadin, A., Grigorenko, A. N. & Polini, M. Current-induced birefringent absorption and non-reciprocal plasmons in graphene. *2D Mater.* **3**, 015011 (2016).

[Google Scholar](#)

23. 23.

Bliokh, K., Rodríguez-Fortuño, F. J., Bekshaev, A., Kivshar, Y. & Nori, F. Electric-current-induced unidirectional propagation of surface plasmon-polaritons. *Opt. Lett.* **43**, 963–966 (2018).

[ADS](#) [CAS](#) [PubMed](#) [Google Scholar](#)

24. 24.

Sabbaghi, M., Lee, H.-W. & Stauber, T. Electro-optics of current-carrying graphene. *Phys. Rev. B* **98**, 075424 (2018).

[ADS](#) [CAS](#) [Google Scholar](#)

25. 25.

W. Zhao et. al, Efficient Fizeau drag from Dirac electrons in monolayer graphene. *Nature* <https://www.nature.com/articles/s41586-021-03574-4> (2021).

26. 26.

Yu, Y.-J. et al. Tuning the graphene work function by electric field effect. *Nano Lett.* **9**, 3430–3434 (2009).

[ADS](#) [CAS](#) [PubMed](#) [Google Scholar](#)

27. 27.

Svintsov, D., Vyurkov, V., Ryzhii, V. & Otsuji, T. Hydrodynamic electron transport and nonlinear waves in graphene. *Phys. Rev. B* **88**, 245444 (2013).

[ADS](#) [Google Scholar](#)

28. 28.

Lucas, A. & Fong, K. C. Hydrodynamics of electrons in graphene. *J. Phys. Condens. Matter* **30**, 053001 (2018).

[ADS](#) [PubMed](#) [Google Scholar](#)

29. 29.

Sun, Z., Basov, D. N. & Fogler, M. M. Universal linear and nonlinear electrodynamics of a Dirac fluid. *Proc. Natl Acad. Sci. USA* **115**, 3285–3289 (2018).

[ADS](#) [MathSciNet](#) [CAS](#) [PubMed](#) [PubMed Central](#) [MATH](#) [Google Scholar](#)

30. 30.

Gao, H., Dong, Z. & Levitov, L. Plasmonic drag in a flowing Fermi liquid. Preprint at <https://arxiv.org/abs/1912.13409> (2020).

31. 31.

Brower, D. L. et al. Fizeau interferometer for measurement of plasma electron current. *Rev. Sci. Instrum.* **75**, 3399–3401 (2004).

[ADS](#) [CAS](#) [Google Scholar](#)

32. 32.

Tyson, R. E. et al. Far-infrared studies of the plasmon resonance of a drifting 2DEG. *Superlattices Microstruct.* **12**, 371–374 (1992).

[ADS](#) [CAS](#) [Google Scholar](#)

33. 33.

Gramila, T. J., Eisenstein, J. P., MacDonald, A. H., Pfeiffer, L. N. & West, K. W. Mutual friction between parallel two-dimensional electron systems. *Phys. Rev. Lett.* **66**, 1216–1219 (1991).

[ADS](#) [CAS](#) [PubMed](#) [Google Scholar](#)

34. 34.

Gorbachev, R. V. et al. Strong Coulomb drag and broken symmetry in double-layer graphene. *Nat. Phys.* **8**, 896–901 (2012).

[CAS](#) [Google Scholar](#)

35. 35.

Gurevich, Y. G. & Mashkevich, O. L. The electron–phonon drag and transport phenomena in semiconductors. *Phys. Rep.* **181**, 327–394 (1989).

[ADS](#) [CAS](#) [Google Scholar](#)

36. 36.

Narozhny, B. N. & Levchenko, A. Coulomb drag. *Rev. Mod. Phys.* **88**, 025003 (2016).

[ADS](#) [Google Scholar](#)

37. 37.

Lundeberg, M. B. et al. Tuning quantum nonlocal effects in graphene plasmonics. *Science* **357**, 187–191 (2017).

[ADS](#) [CAS](#) [PubMed](#) [Google Scholar](#)

38. 38.

Morgado, T. A. & Silveirinha, M. G. Nonlocal effects and enhanced nonreciprocity in current-driven graphene systems. *Phys. Rev. B* **102**,

075102 (2020).

[ADS](#) [CAS](#) [Google Scholar](#)

39. 39.

Papaj, M. & Lewandowski, C. Plasmonic nonreciprocity driven by band hybridization in moiré materials. *Phys. Rev. Lett.* **125**, 066801 (2020).

[ADS](#) [CAS](#) [PubMed](#) [Google Scholar](#)

40. 40.

Bistritzer, R. & MacDonald, A. H. Moiré bands in twisted double-layer graphene. *Proc. Natl Acad. Sci. USA* **108**, 12233–12237 (2011).

[ADS](#) [CAS](#) [PubMed](#) [PubMed Central](#) [Google Scholar](#)

41. 41.

Cao, Y. et al. Correlated insulator behaviour at half-filling in magic-angle graphene superlattices. *Nature* **556**, 80–84 (2018).

[ADS](#) [CAS](#) [Google Scholar](#)

42. 42.

Dyakonov, M. & Shur, M. Shallow water analogy for a ballistic field effect transistor: new mechanism of plasma wave generation by dc current. *Phys. Rev. Lett.* **71**, 2465–2468 (1993).

[ADS](#) [CAS](#) [PubMed](#) [Google Scholar](#)

43. 43.

Gupta, R. & Ridley, B. Two-stream instability in two-dimensional degenerate systems. *Phys. Rev. B* **39**, 6208 (1989).

[ADS](#) [CAS](#) [Google Scholar](#)

44. 44.

Aizin, G. R., Mikalopas, J. & Shur, M. Current-driven plasmonic boom instability in three-dimensional gated periodic ballistic nanostructures. *Phys. Rev. B* **93**, 195315 (2016).

[ADS](#) [Google Scholar](#)

45. 45.

Zolotovskii, I. O. et al. Plasmon-polariton distributed-feedback laser pumped by a fast drift current in graphene. *Phys. Rev. A* **97**, 053828 (2018).

[ADS](#) [CAS](#) [Google Scholar](#)

46. 46.

Smetanin, I. V., Bouhelier, A. & Uskov, A. V. Coherent surface plasmon amplification through the dissipative instability of 2D direct current. *Nanophotonics* **8**, 135–143 (2018).

[Google Scholar](#)

47. 47.

Zhang, Y., Small, J. P., Pontius, W. V. & Kim, P. Fabrication and electric-field-dependent transport measurements of mesoscopic graphite devices. *Appl. Phys. Lett.* **86**, 073104 (2005).

[ADS](#) [Google Scholar](#)

48. 48.

Liu, S. et al. Single crystal growth of millimeter-sized monoisotopic hexagonal boron nitride. *Chem. Mater.* **30**, 6222–6225 (2018).

[CAS](#) [Google Scholar](#)

49. 49.

Dean, C. R. et al. Boron nitride substrates for high-quality graphene electronics. *Nat. Nanotechnol.* **5**, 722–726 (2010).

[ADS](#) [CAS](#) [PubMed](#) [Google Scholar](#)

50. 50.

Purdie, D. G. et al. Cleaning interfaces in layered materials heterostructures. *Nat. Commun.* **9**, 5387 (2018).

[ADS](#) [CAS](#) [PubMed](#) [PubMed Central](#) [Google Scholar](#)

51. 51.

Wang, L. et al. One-dimensional electrical contact to a two-dimensional material. *Science* **342**, 614–617 (2013).

[ADS](#) [CAS](#) [PubMed](#) [Google Scholar](#)

52. 52.

Ben Shalom, M. et al. Quantum oscillations of the critical current and high-field superconducting proximity in ballistic graphene. *Nat. Phys.* **12**, 318–322 (2016).

[Google Scholar](#)

53. 53.

Ocelic, N., Huber, A. & Hillenbrand, R. Pseudoheterodyne detection for background-free near-field spectroscopy. *Appl. Phys. Lett.* **89**, 101124 (2006).

[ADS](#) [Google Scholar](#)

54. 54.

Krishna Kumar, R. et al. Superballistic flow of viscous electron fluid through graphene constrictions. *Nat. Phys.* **13**, 1182 (2017).

[CAS](#) [Google Scholar](#)

55. 55.

Meeker, W. Q. & Escobar, L. A. Teaching about approximate confidence regions based on maximum likelihood estimation. *Am. Stat.* **49**, 48–53 (1995).

[Google Scholar](#)

56. 56.

Jiang, B.-Y., Zhang, L. M., Castro Neto, A. H., Basov, D. N. & Fogler, M. M. Generalized spectral method for near-field optical microscopy. *J. Appl. Phys.* **119**, 054305 (2016).

[ADS](#) [Google Scholar](#)

[Download references](#)

Acknowledgements

Research on the physics and imaging of the plasmonic Fizeau effect at Columbia was supported by the US Department of Energy (DOE), Office of Science, Basic Energy Sciences (BES), under award no. DE-SC0018426. D.A.B. acknowledges the support from MIT Pappalardo Fellowship.

M.M.F. is supported by the Office of Naval Research under grant ONR-N000014-18-1-2722. Work in the P.J.-H. group was supported by AFOSR grant FA9550-16-1-0382, the Gordon and Betty Moore Foundation’s EPiQS Initiative through grant GBMF9643, and Fundacion Ramon Areces. The development of new nanofabrication and characterization techniques enabling this work has been supported by the US DOE Office of Science, BES, under award DE-SC0019300. The development of the universal

cryogenic platform used for scanning probe measurements is supported as part of the Energy Frontier Research Center on Programmable Quantum Materials funded by the US Department of Energy (DOE), Office of Science, Basic Energy Sciences (BES), under award no. DE-SC0019443. The development of infrared nano-optics is supported by Vannevar Bush Faculty Fellowship to D.N.B., ONR-VB: N00014-19-1-2630. D.N.B. is Moore Investigator in Quantum Materials EPIQS #9455. This work also made use of the Materials Research Science and Engineering Center Shared Experimental Facilities supported by the National Science Foundation (NSF) (grant no. DMR-0819762). Support from the Materials Engineering and Processing programme of the National Science Foundation, award number CMMI 1538127 for hBN crystal growth is also greatly appreciated.

Author information

Author notes

1. These authors contributed equally: Y. Dong, L. Xiong

Affiliations

1. Department of Physics, Columbia University, New York, NY, USA

Y. Dong, L. Xiong, Z. Sun, R. Jing, A. S. McLeod, S. Zhang, F. L. Ruta, R. Pan, A. J. Millis & D. N. Basov

2. Department of Applied Physics and Applied Mathematics, Columbia University, New York, NY, USA

Y. Dong & F. L. Ruta

3. Department of Physics, Massachusetts Institute of Technology, Cambridge, MA, USA

I. Y. Phinney, H. Gao, Z. Dong, P. Jarillo-Herrero, L. S. Levitov & D. A. Bandurin

4. The Tim Taylor Department of Chemical Engineering, Kansas State University, Manhattan, KS, USA

S. Liu & J. H. Edgar

5. Department of Physics, University of California San Diego, La Jolla, CA, USA

M. M. Fogler

Authors

1. Y. Dong

[View author publications](#)

You can also search for this author in [PubMed](#) [Google Scholar](#)

2. L. Xiong

[View author publications](#)

You can also search for this author in [PubMed](#) [Google Scholar](#)

3. I. Y. Phinney

[View author publications](#)

You can also search for this author in [PubMed](#) [Google Scholar](#)

4. Z. Sun

[View author publications](#)

You can also search for this author in [PubMed](#) [Google Scholar](#)

5. R. Jing

[View author publications](#)

You can also search for this author in [PubMed](#) [Google Scholar](#)

6. A. S. McLeod

[View author publications](#)

You can also search for this author in [PubMed](#) [Google Scholar](#)

7. S. Zhang

[View author publications](#)

You can also search for this author in [PubMed](#) [Google Scholar](#)

8. S. Liu

[View author publications](#)

You can also search for this author in [PubMed](#) [Google Scholar](#)

9. F. L. Ruta

[View author publications](#)

You can also search for this author in [PubMed](#) [Google Scholar](#)

10. H. Gao

[View author publications](#)

You can also search for this author in [PubMed](#) [Google Scholar](#)

11. Z. Dong

[View author publications](#)

You can also search for this author in [PubMed](#) [Google Scholar](#)

12. R. Pan

[View author publications](#)

You can also search for this author in [PubMed](#) [Google Scholar](#)

13. J. H. Edgar

[View author publications](#)

You can also search for this author in [PubMed](#) [Google Scholar](#)

14. P. Jarillo-Herrero

[View author publications](#)

You can also search for this author in [PubMed](#) [Google Scholar](#)

15. L. S. Levitov

[View author publications](#)

You can also search for this author in [PubMed](#) [Google Scholar](#)

16. A. J. Millis

[View author publications](#)

You can also search for this author in [PubMed](#) [Google Scholar](#)

17. M. M. Fogler

[View author publications](#)

You can also search for this author in [PubMed](#) [Google Scholar](#)

18. D. A. Bandurin

[View author publications](#)

You can also search for this author in [PubMed](#) [Google Scholar](#)

19. D. N. Basov

[View author publications](#)

You can also search for this author in [PubMed](#) [Google Scholar](#)

Contributions

D.A.B. and D.N.B. conceived and supervised the project. Y.D., L.X., S.Z., D.A.B. and D.N.B. designed the experiments. I.Y.P. and D.A.B. fabricated the devices. S.L. and J.H.E. provided the isotopic hBN crystals. Y.D., L.X., A.S.M. and R.P. performed the experimental measurements. Y.D., L.X., R.J., F.L.R., D.A.B. and D.N.B. analysed the experimental data. Z.S., M.M.F., A.J.M. and L.S.L. developed the theoretical analysis of the experimental data with input from P.J.-H., H.G. and Z.D. Y.D., L.X., Z.S., M.M.F., D.A.B. and D.N.B. co-wrote the manuscript with input from all co-authors.

Corresponding authors

Correspondence to [D. A. Bandurin](#) or [D. N. Basov](#).

Ethics declarations

Competing interests

The authors declare no competing interests.

Additional information

Peer review information *Nature* thanks Joel Cox, Jiahua Duan and Hugen Yan for their contribution to the peer review of this work.

Publisher's note Springer Nature remains neutral with regard to jurisdictional claims in published maps and institutional affiliations.

Extended data figures and tables

[Extended Data Fig. 1 Gate-dependent transport of a typical device.](#)

Two-terminal resistance $R_{2\text{pt}}$ of a typical device as a function of the back-gate voltage V_g at $T = 170$ K. Inset shows the transport measurement configuration, where a source meter (Keithley 2450) was used to source gate voltage, and a lock-in amplifier (SR 830) was used to measure the resistance of the entire device.

[Extended Data Fig. 2 Experimental configuration for measuring current-gating effects.](#)

Voltage is applied across the source/drain electrode and SPP imaging is performed close to the drain. The black streamlines symbolize the d.c.

current. The voltmeter measures the electrostatic potential of the SPP launcher as a function of the biasing current.

Extended Data Fig. 3 Current–voltage characteristics of a typical device.

The black symbols represent the source–drain voltage while sourcing current through the device. The blue symbols represent the simultaneously measured voltage on the SPP launcher, representing the current-gating effect induced by the biasing current. Inset shows a magnified view of the low-voltage region.

Extended Data Fig. 4 Characteristic real-space nano-infrared and topography images.

a, Near-field image taken in the vicinity of a gold launcher at $T = 170$ K and $V_g = 50$ V. Gold-launched λ_p fringes and tip-launched $\lambda_p/2$ fringes near the graphene edge are clearly visible. Dashed rectangles mark the regions magnified in **c** and **d**. **b**, AFM topography image taken simultaneously with the near-field image in **a**. The graphene region is uniform with minimal topographic variations. **c**, **d**, Magnified near-field images near graphene edges, showing the tip-launched and edge-reflected SPP fringes with $\lambda_p/2$ periodicity.

Extended Data Fig. 5 Real-space nano-infrared and topography line profiles under current.

a–d, Representative results for simultaneously taken topography (**a**, **b**) and near-field (**c**, **d**) data as a function of current density at $T = 170$ K and $V_g = -50$ V. **a**, AFM topography collected in the vicinity of a gold launcher on the left of the field of view. The 2D plot is assembled from AFM line profiles measured at different current densities while scanning along the same line in real space. Red and black arrows and dashed lines indicate positions where the averaged line profiles in **b** are acquired. **b**, Averaged line profiles of AFM topography for current densities of ± 0.75 mA μm^{-1} , whose topography signals are essentially the same. One of the line profiles

is shifted vertically for clarity. **c**, Near-field data, taken simultaneously with **a**. A standard one-dimensional Fourier filter was applied here to reduce noise. **d**, Averaged line profiles of the near-field signal in **c** for the same current densities as the topography data in **b**. A Fizeau shift is clearly visible.

Extended Data Fig. 6 Uncertainty analysis for fitted SPP wavelength.

a, Distribution of the least-squares estimate of the SPP wavelength in equation (7) generated by Monte Carlo simulation. **b**, Examples of typical simulated SPP line profiles used for analysis in **a**. **c**, I: Dependence of variance (bright and dark red lines) and bias (blue line) of wavelength estimate on spatial resolution (SR). Bright red line corresponds to zero signal noise ($\sigma_y/A = 0$). Dark red and blue lines correspond to $\sigma_y/A = 10\%$; II: Dependence of bias and variance in wavelength estimate on pixel size in units of wavelength. The pixel size has minimal effect on σ_λ as long as one samples above the Nyquist rate, as indicated by the vertical green dashed line. **d**, I: Strong dependence of error in wavelength estimate on signal noise σ_y . The variance of the wavelength estimate (bright red, dark red and green lines) will increase roughly linearly with σ_y until about 25%, and the bias (bright and dark blue lines) is less than 1 nm for SR = 20 nm; II: Dependence of error in wavelength estimate on SPP propagation length $1/q_2$. Both the variance (bright and dark red lines) and the bias (blue line) of the wavelength estimate improve with $1/q_2$, even more so when there is positioning noise σ_x (dark red line). **e**, Assessing the statistical significance of the Fizeau shift using an F test. Solid red and purple lines represent the dependence of F statistics on the sample wavelength-shift standard deviation $s_{\Delta\lambda}$. Purple line assumes $\alpha = 0$ and red line assumes α is finite (see text). Cyan shaded region corresponds to F statistics that reject the null hypothesis of no Fizeau shift ($F > F_{\text{crit}} = 2.65$). Vertical dashed line corresponds to wavelength-shift standard deviation $s_{\Delta\lambda}$ estimated from data in Fig. 3a,b.

Extended Data Fig. 7 Additional datasets revealing plasmonic Fizeau drag in graphene.

Other representative data when scanning along the same line at different d.c. currents (averaged $\pm 25 \mu\text{A} \mu\text{m}^{-1}$ for each profile) for different gate voltages, temperatures and devices. Within a set of polariton line profiles, the first polariton fringes are aligned to enable better visual inspection of Fizeau shifts. Line profiles are shifted vertically for clarity. Within each panel, the fitted line profiles of the smallest and largest current densities are shown in the lower panel for visual comparison. The images of the devices are near-field scattering amplitude measured at 170 K without gating. **a**, Device 1, $T = 170 \text{ K}$, $V_g = -47 \text{ V}$; **b**, Device 1, $T = 170 \text{ K}$, $V_g = +47 \text{ V}$; **c**, Device 1, $T = 170 \text{ K}$, $V_g = -60 \text{ V}$; **d**, Device 1, $T = 60 \text{ K}$, $V_g = +60 \text{ V}$; **e**, Device 2, $T = 170 \text{ K}$, $V_g = +50 \text{ V}$; **f**, Device 3, $T = 60 \text{ K}$, $V_g = +60 \text{ V}$.

Supplementary information

Supplementary Information

This file contains a list of the notations, details regarding the theory of Fizeau plasmon drag in graphene (this section includes Supplementary Figures 1-4), Supplementary Table 1 and the Supplementary References.

Rights and permissions

Reprints and Permissions

About this article



Check for
updates

Cite this article

Dong, Y., Xiong, L., Phinney, I.Y. *et al.* Fizeau drag in graphene plasmonics. *Nature* **594**, 513–516 (2021). <https://doi.org/10.1038/s41586-021-03640-x>

[Download citation](#)

- Received: 06 October 2020
- Accepted: 12 May 2021
- Published: 23 June 2021
- Issue Date: 24 June 2021
- DOI: <https://doi.org/10.1038/s41586-021-03640-x>

Comments

By submitting a comment you agree to abide by our [Terms](#) and [Community Guidelines](#). If you find something abusive or that does not comply with our terms or guidelines please flag it as inappropriate.

[Access through your institution](#)

[Change institution](#)

[Buy or subscribe](#)

Associated Content

[Plasmons dragged by drifting electrons](#)

- Hugen Yan

Advertisement

| [Section menu](#) | [Main menu](#) |

- Article
- [Published: 23 June 2021](#)

Efficient Fizeau drag from Dirac electrons in monolayer graphene

- [Wenyu Zhao^{1,na1}](#),
- [Sihan Zhao](#) [ORCID: orcid.org/0000-0003-2162-734X^{1,na1}](#),
- [Hongyuan Li](#) [ORCID: orcid.org/0000-0001-9119-5592^{1,2,3}](#),
- [Sheng Wang](#) [ORCID: orcid.org/0000-0001-7923-478X^{1,3}](#),
- [Shaoxin Wang¹](#),
- [M. Iqbal Bakti Utama](#) [ORCID: orcid.org/0000-0002-4454-8348^{1,3,4}](#),
- [Salman Kahn](#) [ORCID: orcid.org/0000-0002-0012-3305^{1,3}](#),
- [Yue Jiang](#) [ORCID: orcid.org/0000-0003-1524-2654^{1,5}](#),
- [Xiao Xiao^{1,5}](#),
- [SeokJae Yoo](#) [ORCID: orcid.org/0000-0002-6438-7123¹](#),
- [Kenji Watanabe](#) [ORCID: orcid.org/0000-0003-3701-8119⁶](#),
- [Takashi Taniguchi](#) [ORCID: orcid.org/0000-0002-1467-3105⁷](#),
- [Alex Zettl^{1,3,8}](#) &
- [Feng Wang](#) [ORCID: orcid.org/0000-0001-8369-6194^{1,3,8}](#)

[Nature](#) volume **594**, pages 517–521 (2021) [Cite this article](#)

- 337 Accesses
- 17 Altmetric
- [Metrics details](#)

Subjects

- [Nanophotonics and plasmonics](#)

- [Quantum fluids and solids](#)
- [Two-dimensional materials](#)

Abstract

Fizeau demonstrated in 1850 that the speed of light can be modified when it is propagating in moving media¹. However, such control of the light speed has not been achieved efficiently with a fast-moving electron media by passing an electrical current. Because the strong electromagnetic coupling between the electron and light leads to the collective excitation of plasmon polaritons, it is hypothesized that Fizeau drag in electron flow systems manifests as a plasmonic Doppler effect. Experimental observation of the plasmonic Doppler effect in electronic systems has been challenge because the plasmon propagation speed is much faster than the electron drift velocity in conventional noble metals. Here we report direct observation of Fizeau drag of plasmon polaritons in strongly biased monolayer graphene by exploiting the high electron mobility and the slow plasmon propagation of massless Dirac electrons. The large bias current in graphene creates a fast-drifting Dirac electron medium hosting the plasmon polariton. This results in non-reciprocal plasmon propagation, where plasmons moving with the drifting electron media propagate at an enhanced speed. We measure the Doppler-shifted plasmon wavelength using cryogenic near-field infrared nanoscopy, which directly images the plasmon polariton mode in the biased graphene at low temperature. We observe a plasmon wavelength difference of up to 3.6 per cent between a plasmon moving with and a plasmon moving against the drifting electron media. Our findings on the plasmonic Doppler effect provide opportunities for electrical control of non-reciprocal surface plasmon polaritons in non-equilibrium systems.

Access options

Subscribe to Journal

Get full journal access for 1 year

\$199.00

only \$3.90 per issue

[Subscribe](#)

All prices are NET prices.

VAT will be added later in the checkout.

Tax calculation will be finalised during checkout.

Rent or Buy article

Get time limited or full article access on ReadCube.

from \$8.99

[Rent or Buy](#)

All prices are NET prices.

Additional access options:

- [Log in](#)
- [Access through your institution](#)
- [Learn about institutional subscriptions](#)

Fig. 1: Schematic view of the Doppler effect in a graphene device.

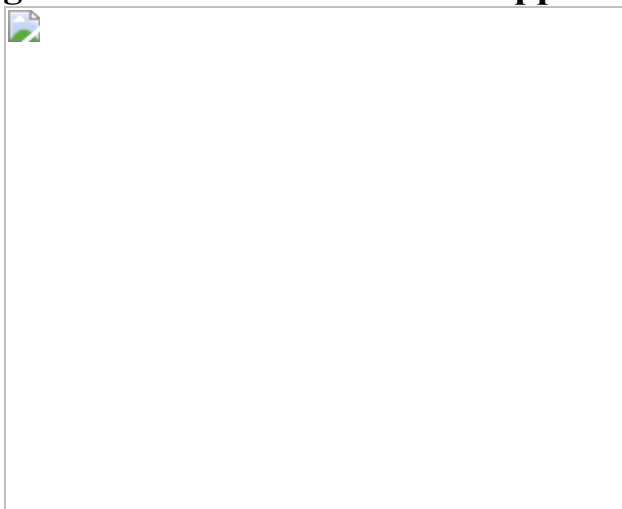


Fig. 2: Near-field signal of the propagating plasmons under different driving currents.

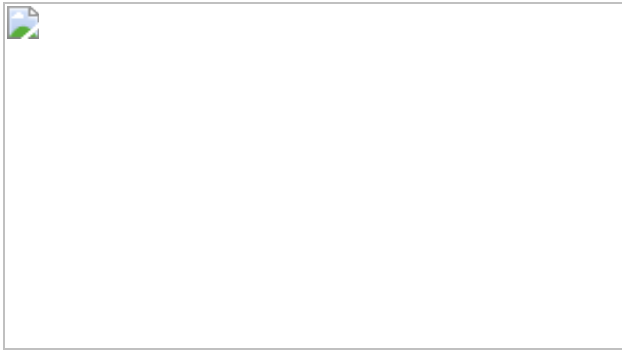


Fig. 3: Gating dependence of graphene plasmon wavelength.

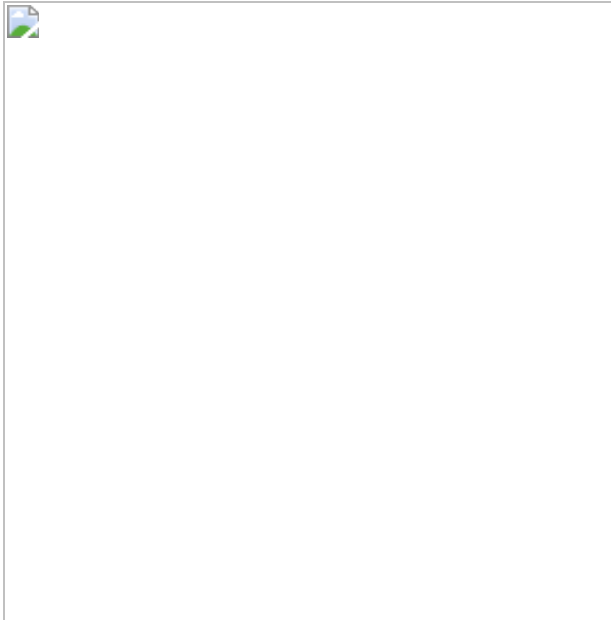
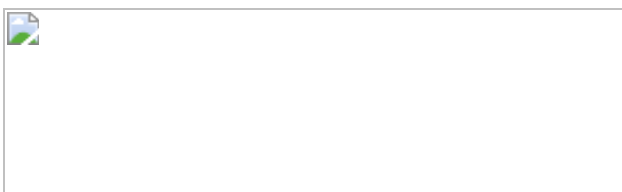


Fig. 4: Graphene plasmon dispersion and Doppler-induced wavelength shift.



Data availability

The data that support the findings of this study are available from the corresponding author upon reasonable request.

References

1. 1.

Foucault, L. Méthode générale pour mesurer la vitesse de la lumière dans l'air et les milieux transparents. Vitesses relatives de la lumière dans l'air et dans l'eau. Projet d'expérience sur la vitesse de propagation du calorique rayonnant. *C. R. Acad. Sci.* **30**, 551–560 (1850).

[Google Scholar](#)

2. 2.

Christensen, T. in *From Classical to Quantum Plasmonics in Three and Two Dimensions* 13–35 (Springer, 2017).

3. 3.

Maier, S. A. *Plasmonics: Fundamentals and Applications* (Springer Science & Business Media, 2007).

4. 4.

Jablan, M., Soljačić, M. & Buljan, H. Plasmons in graphene: fundamental properties and potential applications. *Proc. IEEE* **101**, 1689–1704 (2013).

[CAS Article](#) [Google Scholar](#)

5. 5.

Low, T. et al. Polaritons in layered two-dimensional materials. *Nat. Mater.* **16**, 182–194 (2017).

[ADS](#) [CAS Article](#) [Google Scholar](#)

6. 6.

Novotny, L. & Hecht, B. *Principles of Nano-optics* (Cambridge Univ. Press, 2012).

7. 7.

Kauranen, M. & Zayats, A. V. Nonlinear plasmonics. *Nat. Photon.* **6**, 737–748 (2012).

[ADS](#) [CAS](#) [Article](#) [Google Scholar](#)

8. 8.

Bozhevolnyi, S. I., Martin-Moreno, L. & Garcia-Vidal, F. *Quantum Plasmonics* (Springer, 2017).

9. 9.

Yu, N. & Capasso, F. Flat optics with designer metasurfaces. *Nat. Mater.* **13**, 139–150 (2014).

[ADS](#) [CAS](#) [Article](#) [Google Scholar](#)

10. 10.

Xia, F., Wang, H., Xiao, D., Dubey, M. & Ramasubramaniam, A. Two-dimensional material nanophotonics. *Nat. Photon.* **8**, 899–907 (2014).

[ADS](#) [CAS](#) [Article](#) [Google Scholar](#)

11. 11.

Castro Neto, A. H., Guinea, F., Peres, N. M., Novoselov, K. S. & Geim, A. K. The electronic properties of graphene. *Rev. Mod. Phys.* **81**, 109–162 (2009).

[ADS](#) [CAS](#) [Article](#) [Google Scholar](#)

12. 12.

Ni, G. et al. Fundamental limits to graphene plasmonics. *Nature* **557**, 530–533 (2018).

[ADS](#) [CAS](#) [Article](#) [Google Scholar](#)

13. 13.

Koppens, F. H., Chang, D. E. & Garcia de Abajo, F. J. Graphene plasmonics: a platform for strong light–matter interactions. *Nano Lett.* **11**, 3370–3377 (2011).

[ADS](#) [CAS](#) [Article](#) [Google Scholar](#)

14. 14.

Dean, C. R. et al. Boron nitride substrates for high-quality graphene electronics. *Nat. Nanotechnol.* **5**, 722–726 (2010).

[ADS](#) [CAS](#) [Article](#) [Google Scholar](#)

15. 15.

Mak, K. F. et al. Measurement of the optical conductivity of graphene. *Phys. Rev. Lett.* **101**, 196405 (2008).

[ADS](#) [Article](#) [Google Scholar](#)

16. 16.

Zhang, Y., Small, J. P., Pontius, W. V. & Kim, P. Fabrication and electric-field-dependent transport measurements of mesoscopic graphite devices. *Appl. Phys. Lett.* **86**, 073104 (2005).

[ADS](#) [Article](#) [Google Scholar](#)

17. 17.

Yu, Y.-J. et al. Tuning the graphene work function by electric field effect. *Nano Lett.* **9**, 3430–3434 (2009).

[ADS](#) [CAS](#) [Article](#) [Google Scholar](#)

18. 18.

Dorgan, V. E., Bae, M.-H. & Pop, E. Mobility and saturation velocity in graphene on SiO₂. *Appl. Phys. Lett.* **97**, 082112 (2010).

[ADS](#) [Article](#) [Google Scholar](#)

19. 19.

Woessner, A. et al. Highly confined low-loss plasmons in graphene–boron nitride heterostructures. *Nat. Mater.* **14**, 421–425 (2015).

[ADS](#) [CAS](#) [Article](#) [Google Scholar](#)

20. 20.

Fei, Z. et al. Gate-tuning of graphene plasmons revealed by infrared nano-imaging. *Nature* **487**, 82–85 (2012).

[ADS](#) [CAS](#) [Article](#) [Google Scholar](#)

21. 21.

Chen, J. et al. Optical nano-imaging of gate-tunable graphene plasmons. *Nature* **487**, 77–81 (2012).

[ADS](#) [CAS](#) [Article](#) [Google Scholar](#)

22. 22.

Jablan, M., Buljan, H. & Soljačić, M. Plasmonics in graphene at infrared frequencies. *Phys. Rev. B* **80**, 245435 (2009).

[ADS](#) [Article](#) [Google Scholar](#)

23. 23.

Ramamoorthy, H. et al. “Freeing” graphene from its substrate: observing intrinsic velocity saturation with rapid electrical pulsing.

Nano Lett. **16**, 399–403 (2016).

[ADS](#) [CAS](#) [Article](#) [Google Scholar](#)

24. 24.

Borgnia, D. S., Phan, T. V. & Levitov, L. S. Quasi-relativistic Doppler effect and non-reciprocal plasmons in graphene. Preprint at <https://arxiv.org/abs/1512.09044> (2015).

25. 25.

Correas-Serrano, D. & Gomez-Diaz, J. Non-reciprocal and collimated surface plasmons in drift-biased graphene metasurfaces. *Phys. Rev. B* **100**, 081410 (2019).

26. 26.

Morgado, T. A. & Silveirinha, M. G. Drift-induced unidirectional graphene plasmons. *ACS Photon.* **5**, 4253–4258 (2018).

[CAS](#) [Article](#) [Google Scholar](#)

27. 27.

Sabbaghi, M., Lee, H.-W. & Stauber, T. Electro-optics of current-carrying graphene. *Phys. Rev. B* **98**, 075424 (2018).

[ADS](#) [CAS](#) [Article](#) [Google Scholar](#)

28. 28.

Sabbaghi, M., Lee, H.-W., Stauber, T. & Kim, K. S. Drift-induced modifications to the dynamical polarization of graphene. *Phys. Rev. B* **92**, 195429 (2015).

[ADS](#) [Article](#) [Google Scholar](#)

29. 29.

Wenger, T., Viola, G., Kinaret, J., Fogelström, M. & Tassin, P. Current-controlled light scattering and asymmetric plasmon propagation in graphene. *Phys. Rev. B* **97**, 085419 (2018).

[ADS](#) [CAS](#) [Article](#) [Google Scholar](#)

30. 30.

Van Duppen, B., Tomadin, A., Grigorenko, A. N. & Polini, M. Current-induced birefringent absorption and non-reciprocal plasmons in graphene. *2D Mater.* **3**, 015011 (2016).

[Article](#) [Google Scholar](#)

31. 31.

Song, J. C. & Rudner, M. S. Chiral plasmons without magnetic field. *Proc. Natl Acad. Sci. USA* **113**, 4658–4663 (2016).

[ADS](#) [CAS](#) [Article](#) [Google Scholar](#)

32. 32.

Hamm, J. M., Page, A. F., Bravo-Abad, J., Garcia-Vidal, F. J. & Hess, O. Nonequilibrium plasmon emission drives ultrafast carrier relaxation dynamics in photoexcited graphene. *Phys. Rev. B* **93**, 041408 (2016).

[ADS](#) [Article](#) [Google Scholar](#)

33. 33.

Morgado, T. A. & Silveirinha, M. G. Negative Landau damping in bilayer graphene. *Phys. Rev. Lett.* **119**, 133901 (2017).

[ADS](#) [Article](#) [Google Scholar](#)

34. 34.

Ni, G. et al. Ultrafast optical switching of infrared plasmon polaritons in high-mobility graphene. *Nat. Photon.* **10**, 244–247 (2016).

[ADS](#) [CAS](#) [Article](#) [Google Scholar](#)

35. 35.

Page, A. F., Ballout, F., Hess, O. & Hamm, J. M. Nonequilibrium plasmons with gain in graphene. *Phys. Rev. B* **91**, 075404 (2015).

[ADS](#) [Article](#) [Google Scholar](#)

36. 36.

Lin, X. et al. Unidirectional surface plasmons in nonreciprocal graphene. *New J. Phys.* **15**, 113003 (2013).

[ADS](#) [Article](#) [Google Scholar](#)

37. 37.

Wang, Z., Chong, Y., Joannopoulos, J. D. & Soljačić, M. Reflection-free one-way edge modes in a gyromagnetic photonic crystal. *Phys. Rev. Lett.* **100**, 013905 (2008).

[ADS](#) [Article](#) [Google Scholar](#)

38. 38.

Yu, Z., Veronis, G., Wang, Z. & Fan, S. One-way electromagnetic waveguide formed at the interface between a plasmonic metal under a static magnetic field and a photonic crystal. *Phys. Rev. Lett.* **100**, 023902 (2008).

[ADS](#) [Article](#) [Google Scholar](#)

39. 39.

Wang, L. et al. One-dimensional electrical contact to a two-dimensional material. *Science* **342**, 614–617 (2013).

[ADS](#) [CAS](#) [Article](#) [Google Scholar](#)

40. 40.

Ocelic, N., Huber, A. & Hillenbrand, R. Pseudoheterodyne detection for background-free near-field spectroscopy. *Appl. Phys. Lett.* **89**, 101124 (2006).

[ADS](#) [Article](#) [Google Scholar](#)

41. 41.

Kotov, V. N., Uchoa, B., Pereira, V. M., Guinea, F. & Neto, A. C. Electron–electron interactions in graphene: current status and perspectives. *Rev. Mod. Phys.* **84**, 1067–1125 (2012).

[ADS](#) [CAS](#) [Article](#) [Google Scholar](#)

42. 42.

Morgado, T. A. & Silveirinha, M. G. Nonlocal effects and enhanced nonreciprocity in current-driven graphene systems. *Phys. Rev. B* **102**, 075102 (2020).

[ADS](#) [CAS](#) [Article](#) [Google Scholar](#)

43. 43.

Geick, R., Perry, C. & Rupprecht, G. Normal modes in hexagonal boron nitride. *Phys. Rev.* **146**, 543–547 (1966).

[ADS](#) [CAS](#) [Article](#) [Google Scholar](#)

44. 44.

Hwang, C. et al. Fermi velocity engineering in graphene by substrate modification. *Sci. Rep.* **2**, 590 (2012).

[Article](#) [Google Scholar](#)

45. 45.

Dong, Y. et al. Fizeau drag in graphene plasmonics. *Nature* <https://www.nature.com/articles/s41586-021-03640-x> (2021).

46. 46.

Ponomarenko, L. et al. Cloning of Dirac fermions in graphene superlattices. *Nature* **497**, 594–597 (2013).

[ADS](#) [CAS](#) [Article](#) [Google Scholar](#)

47. 47.

Yankowitz, M. et al. Emergence of superlattice Dirac points in graphene on hexagonal boron nitride. *Nat. Phys.* **8**, 382–386 (2012).

[CAS](#) [Article](#) [Google Scholar](#)

[Download references](#)

Acknowledgements

The device fabrication and characterization and theoretical analysis of the work is supported by the Director, Office of Science, Office of Basic Energy Sciences, Materials Sciences and Engineering Division of the US Department of Energy under contract number DE-AC02-05CH11231 (sp2-Bonded Materials Program KC2207). The cryogenic near-field nanoscopy measurement was supported by the NSF award 1808635. K.W. and T.T. acknowledge support from the Elemental Strategy Initiative conducted by the MEXT, Japan and the CREST (JPMJCR15F3), JST.

Author information

Author notes

1. These authors contributed equally: Wenyu Zhao, Sihan Zhao

Affiliations

1. Department of Physics, University of California, Berkeley, Berkeley, CA, USA

Wenyu Zhao, Sihan Zhao, Hongyuan Li, Sheng Wang, Shaoxin Wang, M. Iqbal Bakti Utama, Salman Kahn, Yue Jiang, Xiao Xiao, SeokJae Yoo, Alex Zettl & Feng Wang

2. Graduate Group in Applied Science and Technology, University of California, Berkeley, Berkeley, CA, USA

Hongyuan Li

3. Materials Science Division, Lawrence Berkeley National Laboratory, Berkeley, CA, USA

Hongyuan Li, Sheng Wang, M. Iqbal Bakti Utama, Salman Kahn, Alex Zettl & Feng Wang

4. Department of Materials Science and Engineering, University of California, Berkeley, Berkeley, CA, USA

M. Iqbal Bakti Utama

5. Department of Physics, Chinese University of Hong Kong, Hong Kong, China

Yue Jiang & Xiao Xiao

6. Research Center for Functional Materials, National Institute for Materials Science, Tsukuba, Japan

Kenji Watanabe

7. International Center for Materials Nanoarchitectonics, National Institute for Materials Science, Tsukuba, Japan

Takashi Taniguchi

8. Kavli Energy NanoSciences Institute at University of California Berkeley and Lawrence Berkeley National Laboratory, Berkeley, CA, USA

Alex Zettl & Feng Wang

Authors

1. Wenyu Zhao

[View author publications](#)

You can also search for this author in [PubMed](#) [Google Scholar](#)

2. Sihan Zhao

[View author publications](#)

You can also search for this author in [PubMed](#) [Google Scholar](#)

3. Hongyuan Li

[View author publications](#)

You can also search for this author in [PubMed](#) [Google Scholar](#)

4. Sheng Wang

[View author publications](#)

You can also search for this author in [PubMed](#) [Google Scholar](#)

5. Shaoxin Wang

[View author publications](#)

You can also search for this author in [PubMed](#) [Google Scholar](#)

6. M. Iqbal Bakti Utama

[View author publications](#)

You can also search for this author in [PubMed](#) [Google Scholar](#)

7. Salman Kahn

[View author publications](#)

You can also search for this author in [PubMed](#) [Google Scholar](#)

8. Yue Jiang

[View author publications](#)

You can also search for this author in [PubMed](#) [Google Scholar](#)

9. Xiao Xiao

[View author publications](#)

You can also search for this author in [PubMed](#) [Google Scholar](#)

10. SeokJae Yoo

[View author publications](#)

You can also search for this author in [PubMed](#) [Google Scholar](#)

11. Kenji Watanabe

[View author publications](#)

You can also search for this author in [PubMed](#) [Google Scholar](#)

12. Takashi Taniguchi

[View author publications](#)

You can also search for this author in [PubMed](#) [Google Scholar](#)

13. Alex Zettl

[View author publications](#)

You can also search for this author in [PubMed](#) [Google Scholar](#)

14. Feng Wang

[View author publications](#)

You can also search for this author in [PubMed](#) [Google Scholar](#)

Contributions

F.W. conceived the research. W.Z. and S.Z. carried out the near-field optical measurements. W.Z., S.Z., Sheng Wang, S.Y. and F.W. performed the data analysis. W.Z., S.Z., H.L., Shaoxin Wang, M.I.B.U, S.K., Y.J. and X.X. fabricated the graphene devices. K.W. and T.T. grew the hexagonal boron nitride crystals. All authors discussed the results and wrote the manuscript.

Corresponding author

Correspondence to [Feng Wang](#).

Ethics declarations

Competing interests

The authors declare no competing interests.

Additional information

Peer review information *Nature* thanks Jiahua Duan, Joel Cox and Hugen Yan for their contribution to the peer review of this work.

Publisher's note Springer Nature remains neutral with regard to jurisdictional claims in published maps and institutional affiliations.

Extended data figures and tables

[Extended Data Fig. 1 Graphene channel current at discrete bias voltages in the two-terminal device.](#)

Measurements taken at 25 K at a carrier density of $7.0 \times 10^{12} \text{ cm}^{-2}$.

Extended Data Fig. 2 Near-field signal of the propagating plasmon on the left side of the gold nanobar.

a, b, Illustration of plasmon propagation under negative (**a**) and positive (**b**) current flows. **c, e, g**, Near-field data at -0.4 mA and $+0.4 \text{ mA}$ (**c**), -1.2 mA and $+1.2 \text{ mA}$ (**e**) and -1.9 mA and $+1.7 \text{ mA}$ (**g**). **d, f, h**, The corresponding line profiles for **c, e, g**, respectively, averaged over the 30 scans. The gold nanobar is located on the right and the graphene plasmons propagate from the right to the left.

Extended Data Fig. 3 Near-field signal of the propagating plasmon on the right side of the gold nanobar.

a, b, Illustration of plasmon propagation under negative (**a**) and positive (**b**) current flows. **c, e**, Near-field data at -0.4 mA and $+0.4 \text{ mA}$ (**c**) and -1.2 mA and $+1.2 \text{ mA}$ (**e**). **d, f**, The corresponding line profiles **c, e**, respectively, averaged over the 30 scans. The gold nanobar is located on the left and the graphene plasmons propagate from the left to the right.

Extended Data Fig. 4 Comparison of the Doppler effect between theory and experiment at different carrier drift velocities in the second device.

The width of the graphene channel is $w = 2.5 \mu\text{m}$ and the carrier density is estimated to be $|n| = 7.0 \times 10^{12} \text{ cm}^{-2}$.

Extended Data Fig. 5 Breakdown of device under high positive backgate voltages.

The ultrahigh backgate voltage at the positive side triggers a series of gas ionization in high vacuum and damages the sample.

Extended Data Fig. 6 Filtered optical image to enhance the contrast between hBN and graphene.

The alignment angle between the hBN and graphene is around 0.93° and corresponds to a moiré period of around 10.3 nm, which is calculated from the carrier density ($n_s \approx 3.98 \times 10^{12} \text{ cm}^{-2}$) at the small resistance peak in our device. The white line indicates the straight graphene edge and the yellow line shows the top hBN edge.

Rights and permissions

Reprints and Permissions

About this article



Check for
updates

Cite this article

Zhao, W., Zhao, S., Li, H. *et al.* Efficient Fizeau drag from Dirac electrons in monolayer graphene. *Nature* **594**, 517–521 (2021).
<https://doi.org/10.1038/s41586-021-03574-4>

Download citation

- Received: 06 October 2020
- Accepted: 21 April 2021
- Published: 23 June 2021
- Issue Date: 24 June 2021
- DOI: <https://doi.org/10.1038/s41586-021-03574-4>

Comments

By submitting a comment you agree to abide by our [Terms](#) and [Community Guidelines](#). If you find something abusive or that does not comply with our terms or guidelines please flag it as inappropriate.

[Access through your institution](#)

[Change institution](#)

[Buy or subscribe](#)

Associated Content

[Plasmons dragged by drifting electrons](#)

- Hugen Yan

Advertisement

This article was downloaded by **calibre** from <https://www.nature.com/articles/s41586-021-03574-4>

| [Section menu](#) | [Main menu](#) |

- Article
- [Published: 23 June 2021](#)

Operando optical tracking of single-particle ion dynamics in batteries

- [Alice J. Merryweather](#) ORCID: [orcid.org/0000-0002-9386-1760^{1,2}](https://orcid.org/0000-0002-9386-1760),
- [Christoph Schnedermann](#) ORCID: [orcid.org/0000-0002-2841-8586¹](https://orcid.org/0000-0002-2841-8586),
- [Quentin Jacquet](#) ORCID: [orcid.org/0000-0002-3684-9423²](https://orcid.org/0000-0002-3684-9423),
- [Clare P. Grey](#) ORCID: [orcid.org/0000-0001-5572-192X²](https://orcid.org/0000-0001-5572-192X) &
- [Akshay Rao](#) ORCID: [orcid.org/0000-0003-4261-0766¹](https://orcid.org/0000-0003-4261-0766)

[Nature](#) volume 594, pages 522–528 (2021) [Cite this article](#)

- 391 Accesses
- 158 Altmetric
- [Metrics details](#)

Subjects

- [Batteries](#)
- [Energy](#)
- [Interference microscopy](#)
- [Materials chemistry](#)

Abstract

The key to advancing lithium-ion battery technology—in particular, fast charging—is the ability to follow and understand the dynamic processes occurring in functioning materials under realistic conditions, in real time and on the nano- to mesoscale. Imaging of lithium-ion dynamics during battery operation (operando imaging) at present requires sophisticated synchrotron X-ray^{1,2,3,4,5,6,7} or electron microscopy^{8,9} techniques, which do not lend themselves to high-throughput material screening. This limits rapid and rational materials improvements. Here we introduce a simple laboratory-based, optical interferometric scattering microscope^{10,11,12,13} to resolve nanoscopic lithium-ion dynamics in battery materials, and apply it to follow cycling of individual particles of the archetypal cathode material^{14,15}, Li_xCoO_2 , within an electrode matrix. We visualize the insulator-to-metal, solid solution and lithium ordering phase transitions directly and determine rates of lithium diffusion at the single-particle level, identifying different mechanisms on charge and discharge. Finally, we capture the dynamic formation of domain boundaries between different crystal orientations associated with the monoclinic lattice distortion at the $\text{Li}_{0.5}\text{CoO}_2$ composition¹⁶. The high-throughput nature of our methodology allows many particles to be sampled across the entire electrode and in future will enable exploration of the role of dislocations, morphologies and cycling rate on battery degradation. The generality of our imaging concept means that it can be applied to study any battery electrode, and more broadly, systems where the transport of ions is associated with electronic or structural changes. Such systems include nanoionic films, ionic conducting polymers, photocatalytic materials and memristors.

Access options

Subscribe to Journal

Get full journal access for 1 year

\$199.00

only \$3.90 per issue

Subscribe

All prices are NET prices.
VAT will be added later in the checkout.
Tax calculation will be finalised during checkout.

Rent or Buy article

Get time limited or full article access on ReadCube.

from \$8.99

Rent or Buy

All prices are NET prices.

Additional access options:

- [Log in](#)
- [Access through your institution](#)
- [Learn about institutional subscriptions](#)

Fig. 1: Electrochemical performance and interferometric scattering microscopy of an LCO electrode.

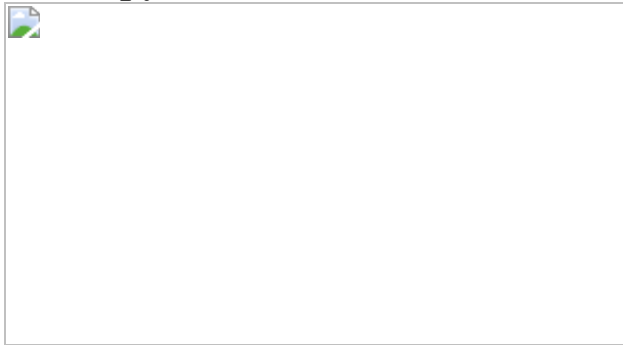


Fig. 2: Overview of the optical response of an active particle during battery operation.

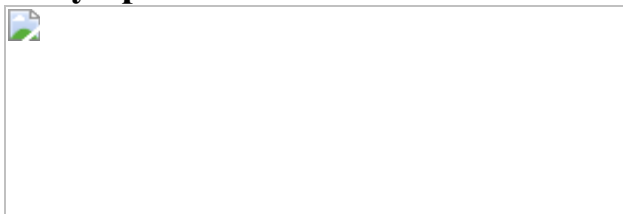


Fig. 3: Behaviour of biphasic phase transitions upon delithiation and lithiation.

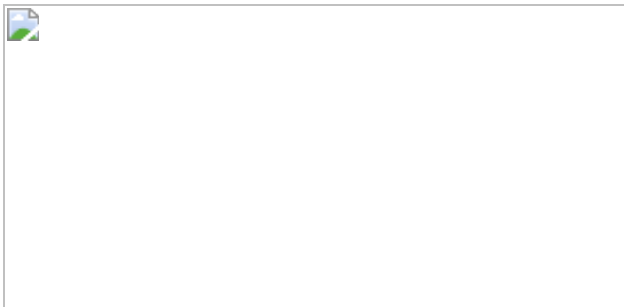


Fig. 4: Behaviour of biphasic phase transitions at various applied current densities.

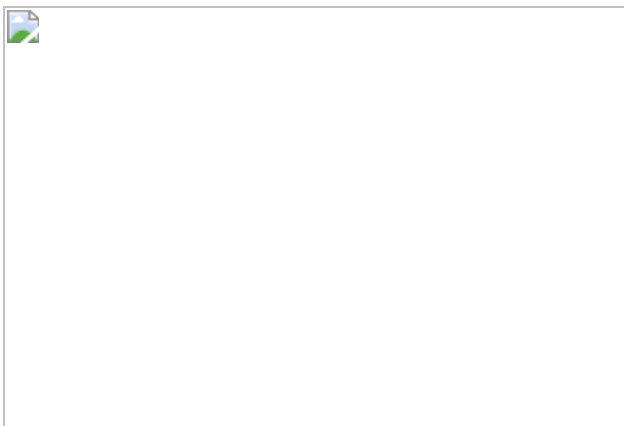
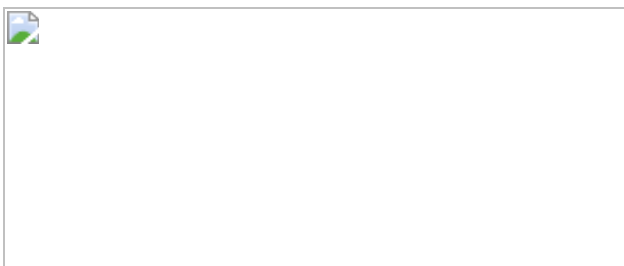


Fig. 5: Dynamics of the monoclinic distortion at a composition of $\text{Li}_{0.5}\text{CoO}_2$, with and without domain formation.



Data availability

The data underlying all figures in the main text and the Extended Data are publicly available from the University of Cambridge repository at <https://doi.org/10.17863/CAM.70023>.

Code availability

All code used in this work is available from the corresponding authors upon reasonable request.

References

1. 1.

Yu, Y.-S. et al. Three-dimensional localization of nanoscale battery reactions using soft X-ray tomography. *Nat. Commun.* **9**, 921 (2018).

[ADS](#) [PubMed](#) [PubMed Central](#) [Google Scholar](#)

2. 2.

Lim, J. et al. Origin and hysteresis of lithium compositional spatiodynamics within battery primary particles. *Science* **353**, 566–571 (2016).

[ADS](#) [CAS](#) [PubMed](#) [Google Scholar](#)

3. 3.

Li, S. et al. Mutual modulation between surface chemistry and bulk microstructure within secondary particles of nickel-rich layered oxides. *Nat. Commun.* **11**, 4433 (2020).

[ADS](#) [CAS](#) [PubMed](#) [PubMed Central](#) [Google Scholar](#)

4. 4.

Tsai, P.-C. et al. Single-particle measurements of electrochemical kinetics in NMC and NCA cathodes for Li-ion batteries. *Energy Environ. Sci.* **11**, 860–871 (2018).

[CAS](#) [Google Scholar](#)

5. 5.

Xu, Y. et al. In situ visualization of state-of-charge heterogeneity within a LiCoO₂ particle that evolves upon cycling at different rates. *ACS Energy Lett.* **2**, 1240–1245 (2017).

[CAS](#) [Google Scholar](#)

6. 6.

Singer, A. et al. Nucleation of dislocations and their dynamics in layered oxide cathode materials during battery charging. *Nat. Energy* **3**, 641–647 (2018).

[ADS](#) [CAS](#) [Google Scholar](#)

7. 7.

Zhang, X. et al. Direct view on the phase evolution in individual LiFePO₄ nanoparticles during Li-ion battery cycling. *Nat. Commun.* **6**, 8333 (2015).

[ADS](#) [CAS](#) [PubMed](#) [Google Scholar](#)

8. 8.

Holtz, M. E. et al. Nanoscale imaging of lithium ion distribution during in situ operation of battery electrode and electrolyte. *Nano Lett.* **14**, 1453–1459 (2014).

[ADS](#) [CAS](#) [PubMed](#) [Google Scholar](#)

9. 9.

He, K. et al. Operando liquid cell electron microscopy of discharge and charge kinetics in lithium-oxygen batteries. *Nano Energy* **49**, 338–345 (2018).

[CAS](#) [Google Scholar](#)

10. 10.

Lindfors, K., Kalkbrenner, T., Stoller, P. & Sandoghdar, V. Detection and spectroscopy of gold nanoparticles using supercontinuum white light confocal microscopy. *Phys. Rev. Lett.* **93**, 037401 (2004).

[ADS](#) [CAS](#) [PubMed](#) [Google Scholar](#)

11. 11.

Ortega-Arroyo, J. & Kukura, P. Interferometric scattering microscopy (iSCAT): new frontiers in ultrafast and ultrasensitive optical microscopy. *Phys. Chem. Chem. Phys.* **14**, 15625–15636 (2012).

[CAS](#) [Google Scholar](#)

12. 12.

Young, G. & Kukura, P. Interferometric scattering microscopy. *Annu. Rev. Phys. Chem.* **70**, 301–322 (2019).

[ADS](#) [CAS](#) [PubMed](#) [Google Scholar](#)

13. 13.

Taylor, R. W. & Sandoghdar, V. in *Label-free Super-resolution Microscopy* (ed. Astratov, V.) 25–65 (Springer, 2019).

14. 14.

Mizushima, K., Jones, P. C., Wiseman, P. J. & Goodenough, J. B. Li_xCoO_2 ($0 < x \leq 1$): a new cathode material for batteries of high energy density. *Mater. Res. Bull.* **15**, 783–789 (1980).

[CAS](#) [Google Scholar](#)

15. 15.

Amatucci, G. G., Tarascon, J. M. & Klein, L. C. CoO_2 , the end member of the Li_xCoO_2 solid solution. *J. Electrochem. Soc.* **143**,

1114–1123 (1996).

[ADS](#) [CAS](#) [Google Scholar](#)

16. 16.

Reimers, J. N. & Dahn, J. R. Electrochemical and in situ X-ray diffraction studies of lithium intercalation in Li_xCoO_2 . *J. Electrochem. Soc.* **139**, 2091–2097 (1992).

[ADS](#) [CAS](#) [Google Scholar](#)

17. 17.

Liu, H. et al. Capturing metastable structures during high-rate cycling of LiFePO_4 nanoparticle electrodes. *Science* **344**, 1252817 (2014).

[PubMed](#) [Google Scholar](#)

18. 18.

Zhang, Y., Yang, Z. & Tian, C. Probing and quantifying cathode charge heterogeneity in Li ion batteries. *J. Mater. Chem. A* **7**, 23628–23661 (2019).

[CAS](#) [Google Scholar](#)

19. 19.

Wu, Y. & Liu, N. Visualizing battery reactions and processes by using in situ and in operando microscopies. *Chem* **4**, 438–465 (2018).

[CAS](#) [Google Scholar](#)

20. 20.

Otoyama, M., Kowada, H., Sakuda, A., Tatsumisago, M. & Hayashi, A. Operando confocal microscopy for dynamic changes of Li^+ ion

conduction path in graphite electrode layers of all-solid-state batteries. *J. Phys. Chem. Lett.* **11**, 900–904 (2020).

[CAS](#) [PubMed](#) [Google Scholar](#)

21. 21.

Kazyak, E. et al. Li penetration in ceramic solid electrolytes: operando microscopy analysis of morphology, propagation, and reversibility. *Matter* **2**, 1025–1048 (2020).

[Google Scholar](#)

22. 22.

Wood, K. N. et al. Dendrites and pits: untangling the complex behavior of lithium metal anodes through operando video microscopy. *ACS Cent. Sci.* **2**, 790–801 (2016).

[CAS](#) [PubMed](#) [PubMed Central](#) [Google Scholar](#)

23. 23.

Namink, K., Meng, X., Koper, M. T. M., Kukura, P. & Faez, S. Electric-double-layer-modulation microscopy. *Phys. Rev. Appl.* **13**, 044065 (2020).

[ADS](#) [CAS](#) [Google Scholar](#)

24. 24.

Ortega Arroyo, J., Cole, D. & Kukura, P. Interferometric scattering microscopy and its combination with single-molecule fluorescence imaging. *Nat. Protocols* **11**, 617–633 (2016).

[CAS](#) [PubMed](#) [Google Scholar](#)

25. 25.

Piliarik, M. & Sandoghdar, V. Direct optical sensing of single unlabelled proteins and super-resolution imaging of their binding sites. *Nat. Commun.* **5**, 4495 (2014).

[ADS](#) [CAS](#) [PubMed](#) [Google Scholar](#)

26. 26.

Gholami Mahmoodabadi, R. et al. Point spread function in interferometric scattering microscopy (iSCAT). Part I: aberrations in defocusing and axial localization. *Opt. Express* **28**, 25969–25988 (2020).

[ADS](#) [PubMed](#) [Google Scholar](#)

27. 27.

Van der Ven, A. & Ceder, G. Lithium diffusion in layered Li_xCoO_2 . *Electrochem. Solid-State Lett.* **3**, 301–304 (2000).

[Google Scholar](#)

28. 28.

Sugiyama, J. et al. Li diffusion in Li_xCoO_2 probed by muon-spin spectroscopy. *Phys. Rev. Lett.* **103**, 147601 (2009).

[ADS](#) [PubMed](#) [Google Scholar](#)

29. 29.

Jang, Y.-I., Neudecker, B. J. & Dudney, N. J. Lithium diffusion in Li_xCoO_2 ($0.45 < x < 0.7$) intercalation cathodes. *Electrochem. Solid-State Lett.* **4**, A74–A77 (2001).

[CAS](#) [Google Scholar](#)

30. 30.

Xia, H., Lu, L. & Ceder, G. Li diffusion in LiCoO_2 thin films prepared by pulsed laser deposition. *J. Power Sources* **159**, 1422–1427 (2006).

[ADS](#) [CAS](#) [Google Scholar](#)

31. 31.

Xie, J. et al. Orientation dependence of Li–ion diffusion kinetics in LiCoO_2 thin films prepared by RF magnetron sputtering. *Solid State Ion.* **179**, 362–370 (2008).

[CAS](#) [Google Scholar](#)

32. 32.

Takeuchi, S. et al. Epitaxial LiCoO_2 films as a model system for fundamental electrochemical studies of positive electrodes. *ACS Appl. Mater. Interfaces* **7**, 7901–7911 (2015).

[CAS](#) [PubMed](#) [Google Scholar](#)

33. 33.

Dokko, K. et al. Kinetic characterization of single particles of LiCoO_2 by AC impedance and potential step methods. *J. Electrochem. Soc.* **148**, A422–A426 (2001).

[CAS](#) [Google Scholar](#)

34. 34.

Ménétrier, M., Saadoune, I., Levasseur, S. & Delmas, C. The insulator–metal transition upon lithium deintercalation from LiCoO_2 : electronic properties and ${}^7\text{Li}$ NMR study. *J. Mater. Chem.* **9**, 1135–1140 (1999).

[Google Scholar](#)

35. 35.

Ménétrier, M., Carlier, D., Blangero, M. & Delmas, C. On “really” stoichiometric LiCoO₂. *Electrochem. Solid-State Lett.* **11**, A179–A182 (2008).

[Google Scholar](#)

36. 36.

Liu, H. L. et al. Electronic structure and lattice dynamics of Li_xCoO₂ single crystals. *New J. Phys.* **17**, 103004 (2015).

[ADS](#) [Google Scholar](#)

37. 37.

Rubin, M., von Rottkay, K., Wen, S.-J., Özer, N. & Slack, J. Optical indices of lithiated electrochromic oxides. *Sol. Energy Mater. Sol. Cells* **54**, 49–57 (1998).

[CAS](#) [Google Scholar](#)

38. 38.

Sung, J. et al. Long-range ballistic propagation of carriers in methylammonium lead iodide perovskite thin films. *Nat. Phys.* **16**, 171–176 (2020).

[CAS](#) [Google Scholar](#)

39. 39.

Schnedermann, C. et al. Ultrafast tracking of exciton and charge carrier transport in optoelectronic materials on the nanometer scale. *J. Phys. Chem. Lett.* **10**, 6727–6733 (2019).

[CAS](#) [PubMed](#) [PubMed Central](#) [Google Scholar](#)

40. 40.

Evans, R. C., Nilsson, Z. N. & Sambur, J. B. High-throughput single-nanoparticle-level imaging of electrochemical ion insertion reactions. *Anal. Chem.* **91**, 14983–14991 (2019).

[CAS](#) [PubMed](#) [Google Scholar](#)

41. 41.

Fraggedakis, D. et al. A scaling law to determine phase morphologies during ion intercalation. *Energy Environ. Sci.* **13**, 2142–2152 (2020).

[CAS](#) [Google Scholar](#)

42. 42.

Zhang, W., Srinivasan, S. & Ploehn, H. J. Analysis of transient hydrogen uptake by metal alloy particles. *J. Electrochem. Soc.* **143**, 4039–4047 (1996).

[ADS](#) [CAS](#) [Google Scholar](#)

43. 43.

Singh, G. K., Ceder, G. & Bazant, M. Z. Intercalation dynamics in rechargeable battery materials: general theory and phase-transformation waves in LiFePO₄. *Electrochim. Acta* **53**, 7599–7613 (2008).

[CAS](#) [Google Scholar](#)

44. 44.

Li, Y. et al. Current-induced transition from particle-by-particle to concurrent intercalation in phase-separating battery electrodes. *Nat. Mater.* **13**, 1149–1156 (2014).

[ADS](#) [CAS](#) [PubMed](#) [Google Scholar](#)

45. 45.

Nadkarni, N., Zhou, T., Fraggedakis, D., Gao, T. & Bazant, M. Z. Modeling the metal–insulator phase transition in Li_xCoO_2 for energy and information storage. *Adv. Funct. Mater.* **29**, 1902821 (2019).

[Google Scholar](#)

46. 46.

Bazant, M. Z. Theory of chemical kinetics and charge transfer based on nonequilibrium thermodynamics. *Acc. Chem. Res.* **46**, 1144–1160 (2013).

[CAS](#) [PubMed](#) [Google Scholar](#)

47. 47.

Van der Ven, A., Bhattacharya, J. & Belak, A. A. Understanding Li diffusion in Li-intercalation compounds. *Acc. Chem. Res.* **46**, 1216–1225 (2013).

[PubMed](#) [Google Scholar](#)

48. 48.

Morcrette, M. et al. In situ X-ray diffraction techniques as a powerful tool to study battery electrode materials. *Electrochim. Acta* **47**, 3137–3149 (2002).

[CAS](#) [Google Scholar](#)

49. 49.

Shao-Horn, Y., Levasseur, S., Weill, F. & Delmas, C. Probing lithium and vacancy ordering in O₃ layered Li_xCoO_2 ($x \sim 0.5$): an electron diffraction study. *J. Electrochem. Soc.* **150**, A366–A373 (2003).

[CAS](#) [Google Scholar](#)

50. 50.

Delor, M., Weaver, H. L., Yu, Q. & Ginsberg, N. S. Imaging material functionality through three-dimensional nanoscale tracking of energy flow. *Nat. Mater.* **19**, 56–62 (2020).

[ADS](#) [CAS](#) [PubMed](#) [Google Scholar](#)

51. 51.

Folie, B. D. et al. Effect of anisotropic confinement on electronic structure and dynamics of band edge excitons in inorganic perovskite nanowires. *J. Phys. Chem. A* **124**, 1867–1876 (2020).

[CAS](#) [PubMed](#) [Google Scholar](#)

52. 52.

Chen, K.-H. et al. Dead lithium: mass transport effects on voltage, capacity, and failure of lithium metal anodes. *J. Mater. Chem. A* **5**, 11671–11681 (2017).

[CAS](#) [Google Scholar](#)

53. 53.

Spindler, S. et al. Visualization of lipids and proteins at high spatial and temporal resolution via interferometric scattering (iSCAT) microscopy. *J. Phys. D* **49**, 274002 (2016); erratum **49**, 349601 (2016).

[Google Scholar](#)

[Download references](#)

Acknowledgements

The authors acknowledge financial support from the Faraday Institution, Battery Characterisation Call. A.J.M. acknowledges support from the EPSRC Cambridge NanoDTC, EP/L015978/1. C.S. acknowledges financial support by the Royal Commission of the Exhibition of 1851. We

acknowledge financial support from the EPSRC and the Winton Program for the Physics of Sustainability. This project has received funding from the European Research Council (ERC) under the European Union’s Horizon 2020 research and innovation programme (grant agreement no. 758826). We thank P. Kukura, A. Fineberg and G. Young for helpful discussions during the initial phase of the project.

Author information

Affiliations

1. Cavendish Laboratory, University of Cambridge, Cambridge, UK
Alice J. Merryweather, Christoph Schnedermann & Akshay Rao
2. Yusuf Hamied Department of Chemistry, University of Cambridge, Cambridge, UK
Alice J. Merryweather, Quentin Jacquet & Clare P. Grey

Authors

1. Alice J. Merryweather
[View author publications](#)

You can also search for this author in [PubMed](#) [Google Scholar](#)

2. Christoph Schnedermann
[View author publications](#)

You can also search for this author in [PubMed](#) [Google Scholar](#)

3. Quentin Jacquet
[View author publications](#)

You can also search for this author in [PubMed](#) [Google Scholar](#)

4. Clare P. Grey

[View author publications](#)

You can also search for this author in [PubMed](#) [Google Scholar](#)

5. Akshay Rao

[View author publications](#)

You can also search for this author in [PubMed](#) [Google Scholar](#)

Contributions

A.R. conceived the idea. A.R. and C.P.G. planned and supervised the project. C.S. designed the optical setup. Q.J. and A.J.M. prepared samples. C.S., Q.J. and A.J.M. planned all experiments and A.J.M. carried out the measurements. Q.J. developed the phase field modelling. All authors discussed the results and contributed to writing the manuscript.

Corresponding authors

Correspondence to [Christoph Schnedermann](#) or [Clare P. Grey](#) or [Akshay Rao](#).

Ethics declarations

Competing interests

The authors declare no competing interests.

Additional information

Peer review information *Nature* thanks Aashutosh Mistry, Yan Hui Ying and the other, anonymous, reviewer(s) for their contribution to the peer review of this work.

Publisher's note Springer Nature remains neutral with regard to jurisdictional claims in published maps and institutional affiliations.

Extended data figures and tables

Extended Data Fig. 1 Structure and orientation of LCO particles, and comparison of iSCAT and SEM images.

a, Crystal structure of LiCoO₂. Top left, view down the *c* axis, showing edge-sharing CoO₆ octahedra. Right, angled view showing alternate layers of cobalt-centred and lithium-centred octahedra. Four unit cells are displayed (two repeats in the *a* and *b* directions). Lithium transport occurs in the *a*-*b* plane. **b**, X-ray diffraction patterns of the pristine LCO powder (black trace) and the self-standing electrode film (blue trace). The comparatively high intensities of the (001) reflections indicate that the LCO particles display a preferred orientation within the electrode film, with the [001] direction (that is, the *c* direction) normal to the electrode film. The peak marked * originates from the conductive carbon. **c**, Mass-weighted diameter distribution for LCO particles (based on 681 particles). **d**, SEM image of a dilute working electrode, showing two particles of LCO dispersed in a conductive matrix. Scale bar, 10 μm. **e**, iSCAT image of a single active LCO particle in the electrode (250 μs exposure time). Intensity values are normalized to a linear scale between 0 (black) and 1 (white). Scale bar, 5 μm. **f–i**, Left, iSCAT intensity image of an LCO particle, normalized between 0 (black) and 1 (white). Right, corresponding SEM image of the same LCO particle. The white dashed line represents the outline of the bright region in the iSCAT image. All scale bars, 2 μm. Comparisons of iSCAT and SEM images confirm that the bright regions observed by iSCAT correspond to relatively flat areas on the particle surface. The curved sides of each particle are out of focus, and do not contribute substantially to the iSCAT image (Supplementary Information section 2). The flat surfaces imply that, for these particles, the direction of observation is along the *c* axis of the crystal. This particle orientation is ideally suited to investigate the in-plane ion transport within the layered host lattice.

Extended Data Fig. 2 Galvanostatic cycling at 2C of LCO in an optical cell and in a coin cell.

a, Specific capacity plots for 5 cycles of LCO electrodes in the optical cell (blue trace, as shown in Fig. [1b, c](#)) and in a coin cell (grey trace), each cycled at a rate of 2C from 3.0 V to 4.2 V. **b**, Corresponding differential capacity plots. The positive absolute value of dQ/dV is displayed for delithiation, and the negative absolute value is displayed for lithiation. Peaks attributed to the biphasic transitions (I and IV) and lithium ordering (II and III) are indicated. Both cells were cycled about 20 times at 2C before obtaining the displayed data. The sets of results are in good agreement with each other and with previous reports^{[16](#)} for LCO. The slightly higher overpotentials and lower capacity seen in the optical cell compared to the coin cell were probably caused by a higher internal resistance in the optical cell, perhaps due to the lower stack pressure.

[Extended Data Fig. 3 Optical response of an LCO particle over five galvanostatic cycles at 2C.](#)

Top, cell voltage (versus Li/Li⁺) during five galvanostatic cycles at 2C (as plotted in Fig. [1b, c](#)), as a function of time. Bottom, normalized ('norm.') iSCAT intensity change averaged over the active particle shown in Extended Data Fig. [1e](#), during this galvanostatic cycling. White and blue vertical bars indicate delithiation (charging) and lithiation (discharging), respectively.

[Extended Data Fig. 4 Schematic showing biphasic mechanisms upon delithiation and lithiation.](#)

a, Shrinking core mechanism upon delithiation. **b**, Intercalation wave mechanism upon lithiation. Throughout, the lithium-rich phase ($\text{Li}_{0.95}\text{CoO}_2$) is represented in pink and the lithium-poor phase ($\text{Li}_{0.77}\text{CoO}_2$) in blue. Black arrows indicate the direction of lithium-ion transport at the particle surface (that is, charge transfer), and white arrows indicate lithium-ion diffusion in the bulk particle. Black dotted lines highlight the positions of the phase boundaries.

[Extended Data Fig. 5 Behaviour of biphasic transitions upon \(de\)lithiation for five cycles at 2C.](#)

a–j, Sequential differential images of the active particle upon delithiation (**a, c, e, g, i**) and lithiation (**b, d, f, h, j**) during the biphasic transition, for all five galvanostatic cycles at 2C (as plotted in Fig. [1b,c](#)). The black dashed lines are a guide for the eye, representing the phase boundary position. Sequential contrast (colour scale) represents the intensity changes over a 20 s timescale, and the colour scale is consistent throughout all images. Scale bar, 5 μm.

[Extended Data Fig. 6 Intensity changes caused by ordering transitions upon \(de\)lithiation for five cycles at 2C.](#)

a–e, Images showing the total contrast (colour scale) resulting from lithium ordering for delithiation and lithiation, for all five galvanostatic cycles at 2C (as plotted in Fig. [1b,c](#)). These represent the total intensity change caused by the transition, and the colour scale is consistent throughout all images. For cycles 3, 4 and 5, the formation of the ordered state produces bright lines at approximately 120°. Scale bar, 5 μm.

Supplementary information

[Supplementary Information](#)

This file contains Supplementary Discussions regarding iSCAT signal contributions, imaging depth, localisation precision, data analysis methods for determining phase boundary velocities, and details and determination of the miscibility gap compositions for LCO. The broad application scope for iSCAT in the field of battery research is elaborated and compared to other imaging methods. Additionally, the document contains Supplementary Methods and discussion of the phase field modelling, as referred to in the main text, Supplementary Figures 1–13, Supplementary Table 1 and a guide to Supplementary Videos 1–10.

[Video 1 Optical response of an active LCO particle during five galvanostatic cycles at 2C](#)

Top left: Cell voltage during five consecutive galvanostatic cycles at 2C (corresponding to the data displayed in Figure 1c). Bottom left: iSCAT intensity change averaged over the active particle during cycling. Right: Full background-subtracted iSCAT video of the active particle during cycling (corresponding to the selected snapshots displayed in Figure 2b). Background subtraction was achieved by subtracting reference values for each pixel at the beginning of the first cycle from the corresponding pixels in all subsequent images.

Video 2 Sequential differential images of an active LCO particle during the biphasic transition upon delithiation

Sequential differential images of the active particle during the insulator-metal biphasic transition upon delithiation, for all five cycles. (For cycle 4, this corresponds to the selected snapshots displayed in Figure 3a).

Sequential contrast is obtained by dividing pixel intensity values by those from 20 s earlier, then subtracting 1, to represent the intensity changes over this timescale. The ‘shrinking core’ mechanism is observable in all cycles.

Video 3 Sequential differential images of an active LCO particle during the biphasic transition upon lithiation

Sequential differential images of the active particle during the insulator-metal biphasic transition upon lithiation, for all five cycles. (For cycle 4, this corresponds to the selected snapshots displayed in Figure 3b).

Sequential contrast is obtained by dividing pixel intensity values by those from 20 s earlier, then subtracting 1, to represent the intensity changes over this timescale. The ‘intercalation wave’ mechanism is observable in all cycles.

Video 4 Sequential differential images of an active LCO particle during the lithium-ordering transition upon delithiation

Sequential differential images of the active particle during the lithium-ordering transition upon lithiation, for all five cycles. Sequential contrast is

obtained by dividing pixel intensity values by those from 5 s earlier, then subtracting 1, to represent the intensity changes over this timescale.

Video 5 Sequential differential images of an active LCO particle during the lithium-ordering transition upon lithiation

Sequential differential images of the active particle during the lithium-ordering transition upon lithiation, for all five cycles. (For cycles 1 and 4, this corresponds to the selected snapshots displayed in Figure 5e,f). Sequential contrast is obtained by dividing pixel intensity values by those from 5 s earlier, then subtracting 1, to represent the intensity changes over this timescale.

Video 6 Optical response of an active LCO particle during one galvanostatic cycle at C/2

Top left: Cell voltage during a galvanostatic cycle at C/2. Bottom left: iSCAT intensity change averaged over the active particle during cycling (corresponding to the data displayed in Figure 4a). Right: Full background-subtracted iSCAT video of the active particle during cycling. Background subtraction was achieved by subtracting reference values for each pixel at the beginning of the cycle from the corresponding pixels in all subsequent images.

Video 7 Optical response of an active LCO particle during two galvanostatic cycles at 1C

Top left: Cell voltage during two consecutive galvanostatic cycles at 1C. Bottom left: iSCAT intensity change averaged over the active particle during cycling (corresponding to the data displayed in Figure 4a). Right: Full background-subtracted iSCAT video of the active particle during cycling. Background subtraction was achieved by subtracting reference values for each pixel at the beginning of the first cycle from the corresponding pixels in all subsequent images.

[Video 8 Optical response of an active LCO particle during two galvanostatic cycles at 2C](#)

Top left: Cell voltage during two consecutive galvanostatic cycles at 2C.
Bottom left: iSCAT intensity change averaged over the active particle during cycling (corresponding to the data displayed in Figure 4a). Right: Full background-subtracted iSCAT video of the active particle during cycling. Background subtraction was achieved by subtracting reference values for each pixel at the beginning of the first cycle from the corresponding pixels in all subsequent images.

[Video 9 Optical response of an active LCO particle during two galvanostatic cycles at 4C](#)

Top left: Cell voltage during two consecutive galvanostatic cycles at 4C.
Bottom left: iSCAT intensity change averaged over the active particle during cycling (corresponding to the data displayed in Figure 4a). Right: Full background-subtracted iSCAT video of the active particle during cycling. Background subtraction was achieved by subtracting reference values for each pixel at the beginning of the first cycle from the corresponding pixels in all subsequent images.

[Video 10 Optical response of an active LCO particle during two galvanostatic cycles at 6C](#)

Top left: Cell voltage during two consecutive galvanostatic cycles at 6C.
Bottom left: iSCAT intensity change averaged over the active particle during cycling (corresponding to the data displayed in Figure 4a). Right: Full background-subtracted iSCAT video of the active particle during cycling. Background subtraction was achieved by subtracting reference values for each pixel at the beginning of the first cycle from the corresponding pixels in all subsequent images.

Rights and permissions

[Reprints and Permissions](#)

About this article



Cite this article

Merryweather, A.J., Schnedermann, C., Jacquet, Q. *et al.* Operando optical tracking of single-particle ion dynamics in batteries. *Nature* **594**, 522–528 (2021). <https://doi.org/10.1038/s41586-021-03584-2>

[Download citation](#)

- Received: 09 November 2020
- Accepted: 27 April 2021
- Published: 23 June 2021
- Issue Date: 24 June 2021
- DOI: <https://doi.org/10.1038/s41586-021-03584-2>

Comments

By submitting a comment you agree to abide by our [Terms](#) and [Community Guidelines](#). If you find something abusive or that does not comply with our terms or guidelines please flag it as inappropriate.

[Access through your institution](#)

[Change institution](#)

[Buy or subscribe](#)

Associated Content

Ion dynamics in battery materials imaged rapidly

- Aashutosh Mistry

Advertisement

This article was downloaded by **calibre** from <https://www.nature.com/articles/s41586-021-03584-2>

| [Section menu](#) | [Main menu](#) |

- Article
- [Published: 23 June 2021](#)

A catalysis-driven artificial molecular pump

- [Shuntaro Amano](#) ORCID: orcid.org/0000-0001-6017-6823¹,
- [Stephen D. P. Fielden](#) ORCID: orcid.org/0000-0001-7883-8135¹ &
- [David A. Leigh](#) ORCID: orcid.org/0000-0002-1202-4507^{1,2}

[Nature](#) volume **594**, pages 529–534 (2021) [Cite this article](#)

- 927 Accesses
- 195 Altmetric
- [Metrics details](#)

Subjects

- [Interlocked molecules](#)
- [Molecular machines and motors](#)
- [Supramolecular chemistry](#)

Abstract

All biological pumps are autonomous catalysts; they maintain the out-of-equilibrium conditions of the cell by harnessing the energy released from their catalytic decomposition of a chemical fuel^{1,2,3}. A number of artificial molecular pumps have been reported to date⁴, but they are all either fuelled by light^{5,6,7,8,9,10} or require repetitive sequential additions of reagents or varying of an electric potential during each cycle to operate^{11,12,13,14,15,16}.

Here we describe an autonomous chemically fuelled information ratchet^{[17,18,19,20](#)} that in the presence of fuel continuously pumps crown ether macrocycles from bulk solution onto a molecular axle without the need for further intervention. The mechanism uses the position of a crown ether on an axle both to promote barrier attachment behind it upon threading and to suppress subsequent barrier removal until the ring has migrated to a catchment region. Tuning the dynamics of both processes^{[20,21](#)} enables the molecular machine^{[22,23,24,25](#)} to pump macrocycles continuously from their lowest energy state in bulk solution to a higher energy state on the axle. The ratchet action is experimentally demonstrated by the progressive pumping of up to three macrocycles onto the axle from bulk solution under conditions where barrier formation and removal occur continuously. The out-of-equilibrium [n]rotaxanes (characterized with n up to 4) are maintained for as long as unreacted fuel is present, after which the rings slowly de-thread. The use of catalysis to drive artificial molecular pumps opens up new opportunities, insights and research directions at the interface of catalysis and molecular machinery.

Access options

Subscribe to Journal

Get full journal access for 1 year

\$199.00

only \$3.90 per issue

[Subscribe](#)

All prices are NET prices.

VAT will be added later in the checkout.

Tax calculation will be finalised during checkout.

Rent or Buy article

Get time limited or full article access on ReadCube.

from \$8.99

[Rent or Buy](#)

All prices are NET prices.

Additional access options:

- [Log in](#)
- [Access through your institution](#)
- [Learn about institutional subscriptions](#)

Fig. 1: Structure and operation of a catalysis-driven artificial molecular pump.

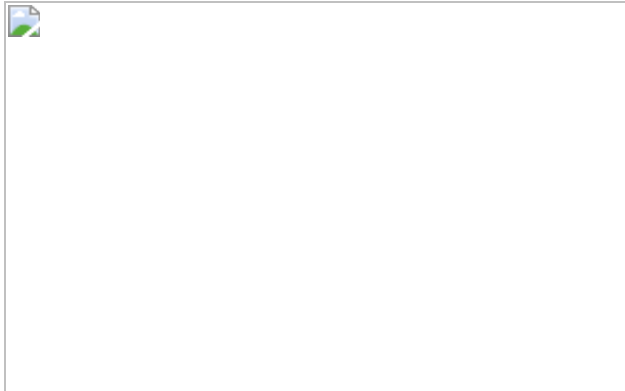


Fig. 2: Macrocycle distribution in [n]rotaxane co-conformers.

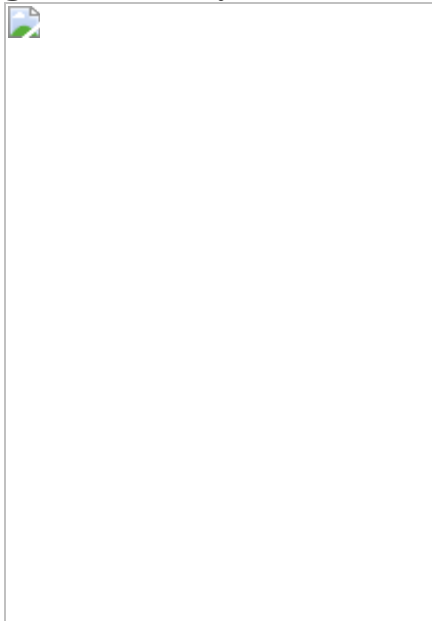


Fig. 3: Fmoc removal, pseudorotaxane dethreading, and irreversible rotaxane formation experiments.

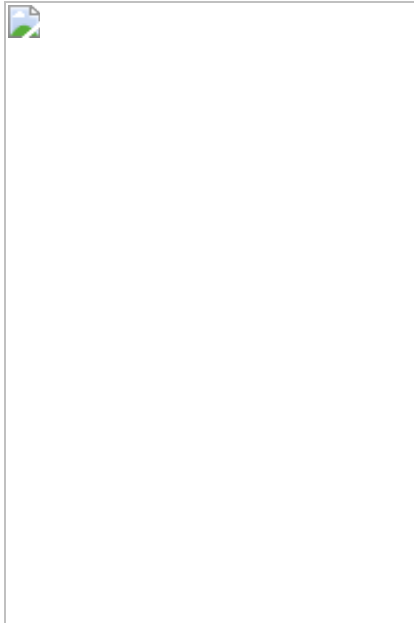


Fig. 4: Out-of-equilibrium state produced by the operation of pump 1.



Data availability

The data that support the findings of this study are available within the paper and its [Supplementary Information](#), or are available from the Mendeley data repository (<https://data.mendeley.com/>) at <https://doi.org/10.17632/r339vx45sz.1>.

References

1. 1.

Skou, J. C. The identification of the sodium–potassium pump (Nobel Lecture). *Angew. Chem. Int. Ed.* **37**, 2320–2328 (1998).

[CAS](#) [Google Scholar](#)

2. 2.

Lodish, H. et al. Transport across cell membranes. In *Molecular Cell Biology* Vol. 4, Ch. 15 (W. H. Freeman, 2000).

3. 3.

Du, D. et al. Multidrug efflux pumps: structure, function and regulation. *Nat. Rev. Microbiol.* **16**, 523–539 (2018).

[CAS](#) [PubMed](#) [Google Scholar](#)

4. 4.

Qiu, Y., Feng, Y., Guo, Q.-H., Astumian, R. D. & Stoddart, J. F. Pumps through the ages. *Chem* **6**, 1952–1977 (2020).

[CAS](#) [Google Scholar](#)

5. 5.

Steinberg-Yfrach, G. et al. Conversion of light energy to proton potential in liposomes by artificial photosynthetic reaction centres. *Nature* **385**, 239–241 (1997).

[ADS](#) [CAS](#) [Google Scholar](#)

6. 6.

Bennett, I. M. et al. Active transport of Ca^{2+} by an artificial photosynthetic membrane. *Nature* **420**, 398–401 (2002).

[ADS](#) [CAS](#) [Google Scholar](#)

7. 7.

Bhosale, S. et al. Photoproduction of proton gradients with π -stacked fluorophore scaffolds in lipid bilayers. *Science* **313**, 84–86 (2006).

[ADS](#) [CAS](#) [Google Scholar](#)

8. 8.

Serreli, V., Lee, C.-F., Kay, E. R. & Leigh, D. A. A molecular information ratchet. *Nature* **445**, 523–527 (2007).

[ADS](#) [CAS](#) [Google Scholar](#)

9. 9.

Baroncini, M., Silvi, S., Venturi, M. & Credi, A. Photoactivated directionally controlled transit of a non-symmetric molecular axle through a macrocycle. *Angew. Chem. Int. Ed.* **51**, 4223–4226 (2012).

[CAS](#) [Google Scholar](#)

10. 10.

Ragazzon, G., Baroncini, M., Silvi, S., Venturi, M. & Credi, A. Light-powered autonomous and directional molecular motion of a dissipative self-assembling system. *Nat. Nanotechnol.* **10**, 70–75 (2015).

[ADS](#) [CAS](#) [Google Scholar](#)

11. 11.

Cheng, C. et al. An artificial molecular pump. *Nat. Nanotechnol.* **10**, 547–553 (2015).

[ADS](#) [CAS](#) [Google Scholar](#)

12. 12.

Pezzato, C. et al. An efficient artificial molecular pump. *Tetrahedron* **73**, 4849–4857 (2017).

[CAS](#) [Google Scholar](#)

13. 13.

Erbas-Cakmak, S. et al. Rotary and linear molecular motors driven by pulses of a chemical fuel. *Science* **358**, 340–343 (2017).

[ADS](#) [CAS](#) [Google Scholar](#)

14. 14.

Pezzato, C. et al. Controlling dual molecular pumps electrochemically. *Angew. Chem. Int. Ed.* **57**, 9325–9329 (2018).

[CAS](#) [Google Scholar](#)

15. 15.

Qiu, Y. et al. A molecular dual pump. *J. Am. Chem. Soc.* **141**, 17472–17476 (2019).

[CAS](#) [Google Scholar](#)

16. 16.

Qiu, Y. et al. A precise polyrotaxane synthesizer. *Science* **368**, 1247–1253 (2020).

[ADS](#) [CAS](#) [PubMed](#) [PubMed Central](#) [Google Scholar](#)

17. 17.

Astumian, R. D. & Bier, M. Mechanochemical coupling of the motion of molecular motors to ATP hydrolysis. *Biophys. J.* **70**, 637–653 (1996).

[ADS](#) [CAS](#) [PubMed](#) [PubMed Central](#) [Google Scholar](#)

18. 18.

Kay, E. R., Leigh, D. A. & Zerbetto, F. Synthetic molecular motors and mechanical machines. *Angew. Chem. Int. Ed.* **46**, 72–191 (2007).

[CAS](#) [Google Scholar](#)

19. 19.

Astumian, R. D. Design principles for Brownian molecular machines: how to swim in molasses and walk in a hurricane. *Phys. Chem. Chem. Phys.* **9**, 5067–5083 (2007).

[CAS](#) [Google Scholar](#)

20. 20.

Astumian, R. D. Kinetic asymmetry allows macromolecular catalysts to drive an information ratchet. *Nat. Commun.* **10**, 3837 (2019).

[ADS](#) [PubMed](#) [PubMed Central](#) [Google Scholar](#)

21. 21.

Astumian, R. D. How molecular motors work—insights from the molecular machinist’s toolbox: the Nobel prize in Chemistry 2016. *Chem. Sci.* **8**, 840–845 (2017).

[CAS](#) [Google Scholar](#)

22. 22.

Pezzato, C., Cheng, C., Stoddart, J. F. & Astumian, R. D. Mastering the non-equilibrium assembly and operation of molecular machines. *Chem. Soc. Rev.* **46**, 5491–5507 (2017).

[CAS](#) [Google Scholar](#)

23. 23.

Kassem, S. et al. Artificial molecular motors. *Chem. Soc. Rev.* **46**, 2592–2621 (2017).

[CAS](#) [Google Scholar](#)

24. 24.

Wang, Q., Chen, D. & Tian, H. Artificial molecular machines that can perform work. *Sci. China Chem.* **61**, 1261–1273 (2018).

[CAS](#) [Google Scholar](#)

25. 25.

Findlay, J. A. & Crowley, J. D. Functional nanomachines: recent advances in synthetic molecular machinery. *Tetrahedron Lett.* **59**, 334–346 (2018).

[CAS](#) [Google Scholar](#)

26. 26.

Coutrot, F. A focus on triazolium as a multipurpose molecular station for pH-sensitive interlocked crown-ether-based molecular machines. *ChemistryOpen* **4**, 556–576 (2015).

[CAS](#) [PubMed](#) [PubMed Central](#) [Google Scholar](#)

27. 27.

Zheng, H. et al. A dual-response [2]rotaxane based on a 1,2,3-triazole ring as a novel recognition station. *Chem. Eur. J.* **15**, 13253–13262 (2009).

[CAS](#) [Google Scholar](#)

28. 28.

Fielden, S. D. P., Leigh, D. A., McTernan, C. T., Pérez-Saavedra, B. & Vitorica-Yrezabal, I. J. Spontaneous assembly of rotaxanes from a primary amine, crown ether and electrophile. *J. Am. Chem. Soc.* **140**, 6049–6052 (2018).

[CAS](#) [Google Scholar](#)

29. 29.

Tian, C., Fielden, S. D. P., Whitehead, G. F. S., Vitorica-Yrezabal, I. J. & Leigh, D. A. Weak functional group interactions revealed through metal-free active template rotaxane synthesis. *Nat. Commun.* **11**, 744 (2020).

[ADS](#) [CAS](#) [PubMed](#) [PubMed Central](#) [Google Scholar](#)

30. 30.

Tian, C., Fielden, S. D. P., Pérez-Saavedra, B., Vitorica-Yrezabal, I. J. & Leigh, D. A. Single-step enantioselective synthesis of mechanically planar chiral [2]rotaxanes using a chiral leaving group strategy. *J. Am. Chem. Soc.* **142**, 9803–9808 (2020).

[CAS](#) [PubMed](#) [PubMed Central](#) [Google Scholar](#)

31. 31.

Denis, M. & Goldup, S. M. The active template approach to interlocked molecules: Principles, progress and applications. *Nat. Rev. Chem.* **1**, 0061 (2017).

[CAS](#) [Google Scholar](#)

32. 32.

Wilson, M. R. et al. An autonomous chemically fuelled small-molecule motor. *Nature* **534**, 235–240 (2016).

[ADS](#) [CAS](#) [Google Scholar](#)

33. 33.

Fyfe, M. C. T. et al. Anion assisted self-assembly. *Angew. Chem. Int. Ed. Engl.* **36**, 2068–2070 (1997).

[CAS](#) [Google Scholar](#)

34. 34.

della Sala, F., Neri, S., Maiti, S., Chen, J. L.-Y. & Prins, L. J. Transient self-assembly of molecular nanostructures driven by chemical fuels. *Curr. Opin. Biotechnol.* **46**, 27–33 (2017).

[Google Scholar](#)

35. 35.

van Rossum, S. A. P., Tena-Solsona, M., van Esch, J. H., Eelkema, R. & Boekhoven, J. Dissipative out-of-equilibrium assembly of man-made supramolecular materials. *Chem. Soc. Rev.* **46**, 5519–5535 (2017).

[Google Scholar](#)

36. 36.

Ragazzon, G. & Prins, L. J. Energy consumption in chemical fuel-driven self-assembly. *Nat. Nanotechnol.* **13**, 882–889 (2018).

[ADS](#) [CAS](#) [Google Scholar](#)

37. 37.

Rieß, B., Grötsch, R. & Boekhoven, J. The design of dissipative molecular assemblies driven by chemical reaction cycles. *Chem* **6**, 552–578 (2020).

[Google Scholar](#)

38. 38.

Borsley, S., Leigh, D. A. & Roberts, B. M. W. A doubly kinetically-gated information ratchet autonomously driven by carbodiimide hydration. *J. Am. Chem. Soc.* **143**, 4414–4420 (2021).

[CAS](#) [Google Scholar](#)

39. 39.

Astumian, R. D. Irrelevance of the power stroke for the directionality, stopping force, and optimal efficiency of chemically driven molecular machines. *Biophys. J.* **108**, 291–303 (2015).

[ADS](#) [CAS](#) [PubMed](#) [PubMed Central](#) [Google Scholar](#)

40. 40.

Howard, J. Protein power strokes. *Curr. Biol.* **16**, R517–R519 (2006).

[CAS](#) [Google Scholar](#)

41. 41.

Hwang, W. & Karplus, M. Structural basis for power stroke vs. Brownian ratchet mechanisms of motor proteins. *Proc. Natl Acad. Sci. USA* **116**, 19777–19785 (2019).

[CAS](#) [PubMed](#) [PubMed Central](#) [Google Scholar](#)

42. 42.

van Dijk, L., Tilby, M. J., Szpera, R., Smith, O. A., Bunce, H. A. P. & Fletcher, S. P. Molecular machines for catalysis. *Nat. Rev. Chem.* **2**, 0117 (2018).

[Google Scholar](#)

43. 43.

Zhang, L., Marcos, V. & Leigh, D. A. Molecular machines with bio-inspired mechanisms. *Proc. Natl Acad. Sci. USA* **115**, 9397–9404 (2018).

[CAS](#) [PubMed](#) [PubMed Central](#) [Google Scholar](#)

44. 44.

Biagini, C. et al. Dissipative catalysis with a molecular machine. *Angew. Chem. Int. Ed.* **58**, 9876–9880 (2019).

[CAS](#) [Google Scholar](#)

45. 45.

Astumian, R. D. et al. Non-equilibrium kinetics and trajectory thermodynamics of synthetic molecular pumps. *Mater. Chem.* **4**, 1304–1314 (2020).

[CAS](#) [Google Scholar](#)

46. 46.

Heard, A. W. & Goldup, S. M. Simplicity in the design, operation and applications of mechanically interlocked molecular machines. *ACS Cent. Sci.* **6**, 117–128 (2020).

[CAS](#) [PubMed](#) [PubMed Central](#) [Google Scholar](#)

47. 47.

Aprahamian, I. The future of molecular machines. *ACS Cent. Sci.* **6**, 347–358 (2020).

[CAS](#) [PubMed](#) [PubMed Central](#) [Google Scholar](#)

48. 48.

Moulin, E., Faour, L., Carmona-Vargas, C. C. & Giuseppone, N. From molecular machines to stimuli-responsive materials. *Adv. Mater.* **32**, 1906036 (2020).

[CAS](#) [Google Scholar](#)

[Download references](#)

Acknowledgements

We thank the Engineering and Physical Sciences Research Council (EPSRC; grant number EP/P027067/1) and the European Research Council (ERC; Advanced Grant number 786630) for funding. We also thank the University of Manchester's Department of Chemistry Services for mass spectrometry. D.A.L. is a Royal Society Research Professor.

Author information

Affiliations

1. Department of Chemistry, University of Manchester, Manchester, UK

Shuntaro Amano, Stephen D. P. Fielden & David A. Leigh

2. School of Chemistry and Molecular Engineering, East China Normal University, Shanghai, China

David A. Leigh

Authors

1. Shuntaro Amano

[View author publications](#)

You can also search for this author in [PubMed](#) [Google Scholar](#)

2. Stephen D. P. Fielden

[View author publications](#)

You can also search for this author in [PubMed](#) [Google Scholar](#)

3. David A. Leigh

[View author publications](#)

You can also search for this author in [PubMed](#) [Google Scholar](#)

Contributions

S.A. and S.D.P.F. carried out the synthesis and characterization studies. D.A.L. directed the research. All authors contributed to the analysis of the results and the writing of the manuscript.

Corresponding author

Correspondence to [David A. Leigh](#).

Ethics declarations

Competing interests

The authors declare no competing interests.

Additional information

Peer review information *Nature* thanks R. Dean Astumian and the other, anonymous, reviewer(s) for their contribution to the peer review of this work. Peer reviewer reports are available.

Publisher's note Springer Nature remains neutral with regard to jurisdictional claims in published maps and institutional affiliations.

Supplementary information

Supplementary Information

This Supplementary Information file contains the following sections: Abbreviations; General Information. Experimental Data; NMR Spectra; Supplementary Text (Optimisation of pumping conditions); and Supplementary References.

Peer Review File

Rights and permissions

Reprints and Permissions

About this article



Check for
updates

Cite this article

Amano, S., Fielden, S.D.P. & Leigh, D.A. A catalysis-driven artificial molecular pump. *Nature* **594**, 529–534 (2021).
<https://doi.org/10.1038/s41586-021-03575-3>

Download citation

- Received: 23 February 2021
- Accepted: 22 April 2021
- Published: 23 June 2021
- Issue Date: 24 June 2021
- DOI: <https://doi.org/10.1038/s41586-021-03575-3>

Comments

By submitting a comment you agree to abide by our [Terms](#) and [Community Guidelines](#). If you find something abusive or that does not comply with our terms or guidelines please flag it as inappropriate.

[Access through your institution](#)

[Change institution](#)

[Buy or subscribe](#)

Advertisement

This article was downloaded by **calibre** from <https://www.nature.com/articles/s41586-021-03575-3>

| [Section menu](#) | [Main menu](#) |

- Article
- [Published: 23 June 2021](#)

Magnetic sensitivity of cryptochrome 4 from a migratory songbird

- [Jingjing Xu¹](#),
- [Lauren E. Jarocha](#) [ORCID: orcid.org/0000-0002-2448-8843²](#),
- [Tilo Zollitsch²](#),
- [Marcin Konowalczyk](#) [ORCID: orcid.org/0000-0003-0921-4278³](#),
- [Kevin B. Henbest^{2,3}](#),
- [Sabine Richert](#) [ORCID: orcid.org/0000-0002-2990-974X⁴](#),
- [Matthew J. Golesworthy](#) [ORCID: orcid.org/0000-0003-1265-5525³](#),
- [Jessica Schmidt¹](#),
- [Victoire Déjean](#) [ORCID: orcid.org/0000-0002-1306-8130³](#),
- [Daniel J. C. Sowood²](#),
- [Marco Bassetto^{1,2}](#),
- [Jiate Luo²](#),
- [Jessica R. Walton²](#),
- [Jessica Fleming²](#),
- [Yujing Wei](#) [ORCID: orcid.org/0000-0001-8913-9719²](#),
- [Tommy L. Pitcher³](#),
- [Gabriel Moise³](#),
- [Maike Herrmann¹](#),
- [Hang Yin⁵](#),
- [Haijia Wu⁶](#),
- [Rabea Bartölke](#) [ORCID: orcid.org/0000-0003-2531-747X¹](#),
- [Stefanie J. Käsehagen¹](#),
- [Simon Horst¹](#),

- [Glen Dautaj¹](#),
- [Patrick D. F. Murton²](#),
- [Angela S. Gehrckens²](#),
- [Yogarany Chelliah^{7,8}](#),
- [Joseph S. Takahashi](#) [ORCID: orcid.org/0000-0003-0384-8878^{7,8}](#),
- [Karl-Wilhelm Koch](#) [ORCID: orcid.org/0000-0003-1501-0044^{6,9}](#),
- [Stefan Weber](#) [ORCID: orcid.org/0000-0003-4090-7435⁴](#),
- [Ilia A. Solov'yov](#) [ORCID: orcid.org/0000-0002-8626-145X^{9,10}](#),
- [Can Xie](#) [ORCID: orcid.org/0000-0002-7412-3236^{11,12}](#),
- [Stuart R. Mackenzie](#) ²,
- [Christiane R. Timmel](#) [ORCID: orcid.org/0000-0003-1828-7700^{3,13}](#),
- [Henrik Mouritsen](#) [ORCID: orcid.org/0000-0001-7082-4839^{1,9}](#) &
- [P. J. Hore](#) [ORCID: orcid.org/0000-0002-8863-570X²](#)

[Nature](#) volume **594**, pages 535–540 (2021) [Cite this article](#)

- 1350 Accesses
- 656 Altmetric
- [Metrics details](#)

Subjects

- [Biophysics](#)
- [Chemistry](#)

Abstract

Night-migratory songbirds are remarkably proficient navigators¹. Flying alone and often over great distances, they use various directional cues including, crucially, a light-dependent magnetic compass^{2,3}. The mechanism of this compass has been suggested to rely on the quantum spin dynamics of photoinduced radical pairs in cryptochrome flavoproteins located in the retinas of the birds^{4,5,6,7}. Here we show that the photochemistry of cryptochrome 4 (CRY4) from the night-migratory

European robin (*Erithacus rubecula*) is magnetically sensitive in vitro, and more so than CRY4 from two non-migratory bird species, chicken (*Gallus gallus*) and pigeon (*Columba livia*). Site-specific mutations of *ErCRY4* reveal the roles of four successive flavin–tryptophan radical pairs in generating magnetic field effects and in stabilizing potential signalling states in a way that could enable sensing and signalling functions to be independently optimized in night-migratory birds.

Access options

Subscribe to Journal

Get full journal access for 1 year

\$199.00

only \$3.90 per issue

[Subscribe](#)

All prices are NET prices.

VAT will be added later in the checkout.

Tax calculation will be finalised during checkout.

Rent or Buy article

Get time limited or full article access on ReadCube.

from \$8.99

[Rent or Buy](#)

All prices are NET prices.

Additional access options:

- [Log in](#)
- [Access through your institution](#)

- [Learn about institutional subscriptions](#)

Fig. 1: Purification, electron transfer pathway and photoreduction of European robin CRY4.

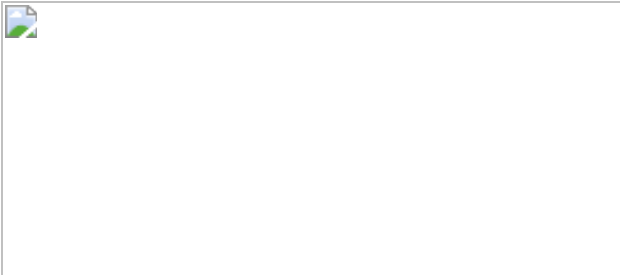


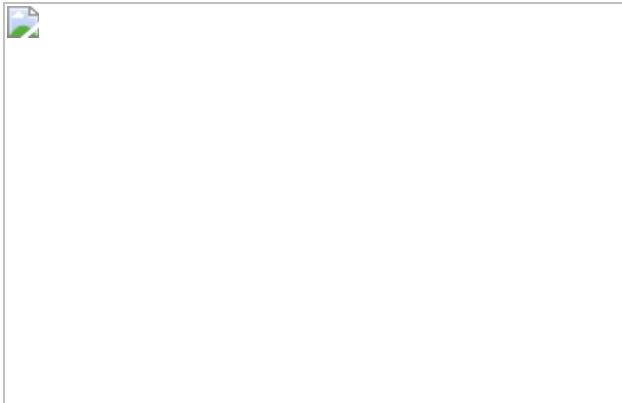
Fig. 2: Magnetic field effects on the yields of photoinduced radicals in CRY4 proteins.



Fig. 3: Electron paramagnetic resonance and optical spectroscopy of photoinduced FAD–Trp radical pairs in *ErCRY4*.



Fig. 4: Reaction scheme and simulated magnetic field effects for *ErCRY4*.



Data availability

The complete set of molecular dynamics simulation and quantum chemistry data (300 GB) can be downloaded from the University of Oldenburg repository: <https://cloud.uol.de/s/NrTYpoEzL6RbPq7>. Specific molecular dynamics data can also be obtained directly from I.A.S. on request. [Source data](#) are provided with this paper.

References

1. 1.

Mouritsen, H. Long-distance navigation and magnetoreception in migratory animals. *Nature* **558**, 50–59 (2018).

[ADS](#) [CAS](#) [PubMed](#) [PubMed Central](#) [Google Scholar](#)

2. 2.

Wiltschko, W., Munro, U., Ford, H. & Wiltschko, R. Red-light disrupts magnetic orientation of migratory birds. *Nature* **364**, 525–527 (1993).

[ADS](#) [Google Scholar](#)

3. 3.

Zapka, M. et al. Visual but not trigeminal mediation of magnetic compass information in a migratory bird. *Nature* **461**, 1274–1277 (2009).

[ADS](#) [CAS](#) [PubMed](#) [Google Scholar](#)

4. 4.

Hore, P. J. & Mouritsen, H. The radical-pair mechanism of magnetoreception. *Annu. Rev. Biophys.* **45**, 299–344 (2016).

[CAS](#) [PubMed](#) [PubMed Central](#) [Google Scholar](#)

5. 5.

Ritz, T., Adem, S. & Schulten, K. A model for photoreceptor-based magnetoreception in birds. *Biophys. J.* **78**, 707–718 (2000).

[CAS](#) [PubMed](#) [PubMed Central](#) [Google Scholar](#)

6. 6.

Ritz, T., Thalau, P., Phillips, J. B., Wiltschko, R. & Wiltschko, W. Resonance effects indicate a radical-pair mechanism for avian magnetic compass. *Nature* **429**, 177–180 (2004).

[ADS](#) [CAS](#) [PubMed](#) [PubMed Central](#) [Google Scholar](#)

7. 7.

Engels, S. et al. Anthropogenic electromagnetic noise disrupts magnetic compass orientation in a migratory bird. *Nature* **509**, 353–356 (2014).

[ADS](#) [CAS](#) [PubMed](#) [Google Scholar](#)

8. 8.

Steiner, U. E. & Ulrich, T. Magnetic field effects in chemical kinetics and related phenomena. *Chem. Rev.* **89**, 51–147 (1989).

[CAS](#) [Google Scholar](#)

9. 9.

Maeda, K. et al. Chemical compass model of avian magnetoreception. *Nature* **453**, 387–390 (2008).

[ADS](#) [CAS](#) [PubMed](#) [Google Scholar](#)

10. 10.

Kerpel, C. et al. Chemical compass behaviour at microtesla magnetic fields strengthens the radical pair hypothesis of avian magnetoreception. *Nat. Commun.* **10**, 3707 (2019).

[ADS](#) [PubMed](#) [PubMed Central](#) [Google Scholar](#)

11. 11.

Giovani, B., Byrdin, M., Ahmad, M. & Brettel, K. Light-induced electron transfer in a cryptochrome blue-light photoreceptor. *Nat. Struct. Biol.* **10**, 489–490 (2003).

[CAS](#) [PubMed](#) [Google Scholar](#)

12. 12.

Müller, P., Yamamoto, J., Martin, R., Iwai, S. & Brettel, K. Discovery and functional analysis of a 4th electron-transferring tryptophan conserved exclusively in animal cryptochromes and (6-4) photolyases. *Chem. Commun.* **51**, 15502–15505 (2015).

[Google Scholar](#)

13. 13.

Nohr, D. et al. Determination of radical–radical distances in light-active proteins and their implication for biological magnetoreception. *Angew. Chem. Int. Ed.* **56**, 8550–8554 (2017).

[CAS](#) [Google Scholar](#)

14. 14.

Nohr, D. et al. Extended electron-transfer pathways in animal cryptochromes mediated by a tetrad of aromatic amino acids. *Biophys. J.* **111**, 301–311 (2016).

[ADS](#) [CAS](#) [PubMed](#) [PubMed Central](#) [Google Scholar](#)

15. 15.

Zoltowski, B. D. et al. Chemical and structural analysis of a photoactive vertebrate cryptochrome from pigeon. *Proc. Natl Acad. Sci. USA* **116**, 19449–19457 (2019).

[CAS](#) [PubMed](#) [PubMed Central](#) [Google Scholar](#)

16. 16.

Sheppard, D. M. W. et al. Millitesla magnetic field effects on the photocycle of an animal cryptochrome. *Sci. Rep.* **7**, 42228 (2017).

[ADS](#) [CAS](#) [PubMed](#) [PubMed Central](#) [Google Scholar](#)

17. 17.

Maeda, K. et al. Magnetically sensitive light-induced reactions in cryptochrome are consistent with its proposed role as a magnetoreceptor. *Proc. Natl Acad. Sci. USA* **109**, 4774–4779 (2012).

[ADS](#) [CAS](#) [PubMed](#) [PubMed Central](#) [Google Scholar](#)

18. 18.

Fedele, G., Green, E. W., Rosato, E. & Kyriacou, C. P. An electromagnetic field disrupts negative geotaxis in *Drosophila* via a CRY-dependent pathway. *Nat. Commun.* **5**, 4391 (2014).

[ADS](#) [CAS](#) [PubMed](#) [Google Scholar](#)

19. 19.

Geegear, R. J., Casselman, A., Waddell, S. & Reppert, S. M. Cryptochrome mediates light-dependent magnetosensitivity in *Drosophila*. *Nature* **454**, 1014–1018 (2008).

[ADS](#) [CAS](#) [PubMed](#) [PubMed Central](#) [Google Scholar](#)

20. 20.

Hoang, N. et al. Human and *Drosophila* cryptochromes are light activated by flavin photoreduction in living cells. *PLoS Biol.* **6**, e160 (2008).

[PubMed](#) [PubMed Central](#) [Google Scholar](#)

21. 21.

Pooam, M. et al. Magnetic sensitivity mediated by the *Arabidopsis* blue-light receptor cryptochrome occurs during flavin reoxidation in the dark. *Planta* **249**, 319–332 (2019).

[CAS](#) [PubMed](#) [Google Scholar](#)

22. 22.

Xu, C. X., Lv, Y., Chen, C. F., Zhang, Y. X. & Wei, S. F. Blue light-dependent phosphorylations of cryptochromes are affected by magnetic fields in *Arabidopsis*. *Adv. Space Res.* **53**, 1118–1124 (2014).

[ADS](#) [CAS](#) [Google Scholar](#)

23. 23.

Giachello, C. N. G., Scrutton, N. S., Jones, A. R. & Baines, R. A. Magnetic fields modulate blue-light-dependent regulation of neuronal firing by cryptochrome. *J. Neurosci.* **36**, 10742–10749 (2016).

[CAS](#) [PubMed](#) [PubMed Central](#) [Google Scholar](#)

24. 24.

Watari, R. et al. Light-dependent structural change of chicken retinal cryptochrome4. *J. Biol. Chem.* **287**, 42634–42641 (2012).

[CAS](#) [PubMed](#) [PubMed Central](#) [Google Scholar](#)

25. 25.

Günther, A. et al. Double-cone localization and seasonal expression pattern suggest a role in magnetoreception for European robin cryptochrome 4. *Curr. Biol.* **28**, 211–223.e4 (2018).

[PubMed](#) [PubMed Central](#) [Google Scholar](#)

26. 26.

Nießner, C., Denzau, S., Peichl, L., Wiltschko, W. & Wiltschko, R. Magnetoreception in birds: I. Immunohistochemical studies concerning the cryptochrome cycle. *J. Exp. Biol.* **217**, 4221–4224 (2014).

[PubMed](#) [PubMed Central](#) [Google Scholar](#)

27. 27.

Nießner, C., Denzau, S., Peichl, L., Wiltschko, W. & Wiltschko, R. Magnetoreception: activation of avian cryptochrome 1a in various light conditions. *J. Comp. Physiol. A* **204**, 977–984 (2018).

[Google Scholar](#)

28. 28.

Wiltschko, R., Ahmad, M., Nießner, C., Gehring, D. & Wiltschko, W. Light-dependent magnetoreception in birds: the crucial step occurs in the dark. *J. R. Soc. Interface* **13**, 20151010 (2016).

[PubMed](#) [PubMed Central](#) [Google Scholar](#)

29. 29.

Player, T. C. & Hore, P. J. Viability of superoxide-containing radical pairs as magnetoreceptors. *J. Chem. Phys.* **151**, 225101 (2019).

[ADS](#) [PubMed](#) [Google Scholar](#)

30. 30.

Müller, P. & Ahmad, M. Light-activated cryptochrome reacts with molecular oxygen to form a flavin–superoxide radical pair consistent with magnetoreception. *J. Biol. Chem.* **286**, 21033–21040 (2011).

[PubMed](#) [PubMed Central](#) [Google Scholar](#)

31. 31.

Bolte, P. et al. Cryptochrome 1a localisation in light- and dark-adapted retinae of several migratory and non-migratory bird species: no signs of light-dependent activation. *Ethol. Ecol. Evol.* <https://doi.org/10.1080/03949370.2020.1870571> (2021).

32. 32.

Kutta, R. J., Archipowa, N., Johannissen, L. O., Jones, A. R. & Scrutton, N. S. Vertebrate cryptochromes are vestigial flavoproteins. *Sci. Rep.* **7**, 44906 (2017).

[ADS](#) [CAS](#) [PubMed](#) [PubMed Central](#) [Google Scholar](#)

33. 33.

Qin, S. et al. A magnetic protein biocompass. *Nat. Mater.* **15**, 217–226 (2016).

[ADS](#) [CAS](#) [PubMed](#) [Google Scholar](#)

34. 34.

Maeda, K. et al. Following radical pair reactions in solution: a step change in sensitivity using cavity ring-down detection. *J. Am. Chem. Soc.* **133**, 17807–17815 (2011).

[CAS](#) [PubMed](#) [Google Scholar](#)

35. 35.

Neil, S. R. T. et al. Broadband cavity-enhanced detection of magnetic field effects in chemical models of a cryptochrome magnetoreceptor. *J. Phys. Chem. B* **118**, 4177–4184 (2014).

[CAS](#) [PubMed](#) [Google Scholar](#)

36. 36.

Roos, A. & Boron, W. F. Intracellular pH. *Physiol. Rev.* **61**, 296–434 (1981).

[CAS](#) [PubMed](#) [Google Scholar](#)

37. 37.

Reeves, R. B. The interaction of body temperature and acid–base balance in ectothermic vertebrates. *Annu. Rev. Physiol.* **39**, 559–586 (1977).

[CAS](#) [PubMed](#) [Google Scholar](#)

38. 38.

Weber, S. et al. Origin of light-induced spin-correlated radical pairs in cryptochrome. *J. Phys. Chem. B* **114**, 14745–14754 (2010).

[CAS](#) [PubMed](#) [PubMed Central](#) [Google Scholar](#)

39. 39.

Hochstoeger, T. et al. The biophysical, molecular, and anatomical landscape of pigeon CRY4: a candidate light-based quantal magnetosensor. *Sci. Adv.* **6**, eabb9110 (2020).

[ADS](#) [CAS](#) [PubMed](#) [PubMed Central](#) [Google Scholar](#)

40. 40.

Kattnig, D. R., Solov'yov, I. A. & Hore, P. J. Electron spin relaxation in cryptochrome-based magnetoreception. *Phys. Chem. Chem. Phys.* **18**, 12443–12456 (2016).

[CAS](#) [PubMed](#) [Google Scholar](#)

41. 41.

Efimova, O. & Hore, P. J. Role of exchange and dipolar interactions in the radical pair model of the avian magnetic compass. *Biophys. J.* **94**, 1565–1574 (2008).

[CAS](#) [PubMed](#) [PubMed Central](#) [Google Scholar](#)

42. 42.

Timmel, C. R., Till, U., Brocklehurst, B., McLauchlan, K. A. & Hore, P. J. Effects of weak magnetic fields on free radical recombination reactions. *Mol. Phys.* **95**, 71–89 (1998).

[ADS](#) [CAS](#) [Google Scholar](#)

43. 43.

Worster, S., Mouritsen, H. & Hore, P. J. A light-dependent magnetoreception mechanism insensitive to light intensity and polarization. *J. R. Soc. Interface* **14**, 20170405 (2017).

[PubMed](#) [PubMed Central](#) [Google Scholar](#)

44. 44.

Kattnig, D. R., Sowa, J. K., Solov'yov, I. A. & Hore, P. J. Electron spin relaxation can enhance the performance of a cryptochrome-based magnetic compass sensor. *New J. Phys.* **18**, 063007 (2016).

[ADS](#) [Google Scholar](#)

45. 45.

Wu, H., Scholten, A., Einwich, A., Mouritsen, H. & Koch, K. W. Protein–protein interaction of the putative magnetoreceptor cryptochrome 4 expressed in the avian retina. *Sci. Rep.* **10**, 7364 (2020).

[ADS](#) [CAS](#) [PubMed](#) [PubMed Central](#) [Google Scholar](#)

[Download references](#)

Acknowledgements

This work was supported by the Air Force Office of Scientific Research (Air Force Materiel Command, USAF award no. FA9550-14-1-0095, to P.J.H., H.M., C.R.T., S.R.M. and K.-W.K.); by the European Research Council (under the European Union’s Horizon 2020 research and innovation programme, grant agreement no. 810002, Synergy Grant: ‘QuantumBirds’, awarded to P.J.H. and H.M.); by the Office of Naval Research Global, award no. N62909-19-1-2045, to P.J.H., C.R.T. and S.R.M.; by the Deutsche Forschungsgemeinschaft (SFB 1372, ‘Magnetoreception and navigation in vertebrates’, project number: 395940726 to H.M., K.-W.K., I.A.S. and P.J.H., and GRK 1885, ‘Molecular basis of sensory biology’ to K.-W.K., I.A.S. and H.M.); by a DAAD

(German Academic Exchange Service, Graduate School Scholarship Programme, ID 57395813) stipend to J.X.; by funding for G.M. from the SCG Innovation Fund; by the Electromagnetic Fields Biological Research Trust (to P.J.H., C.R.T. and S.R.M.); by the National Natural Science Foundation of China, grant no. 31640001, and the Presidential Foundation of Hefei Institutes of Physical Science, Chinese Academy of Sciences, grant no. BJZX201901 (to C.X.); and by the Lundbeck Foundation, the Danish Councils for Independent Research, and the Volkswagen Foundation (to I.A.S.). V.D. is grateful to the Clarendon Fund, University of Oxford. M.J.G. thanks the Biotechnology and Biological Sciences Research Council, grant number BB/M011224/1 and the Clarendon Fund. We acknowledge use of the Advanced Research Computing (ARC) facility of the University of Oxford. J.S.T. is an Investigator and Y.C. is a Research Specialist in the Howard Hughes Medical Institute. I.A.S. is grateful to the DeiC National HPC Center, University of Southern Denmark for computational resources. We thank B. Grünberg, I. Fomins, A. Günther and A. Einwich for laboratory assistance and for providing protein sequence information. J.X. thanks Y. Tan for training in protein expression and purification. We thank S. Chandler for mass spectrometry, S. Y. Wong for assistance with spin dynamics calculations, and W. Myers (CAESR, Engineering and Physical Sciences Research Council, grant no. EP/L011972/1) for obtaining a threefold improvement in the time-resolved electron paramagnetic resonance signal. We are grateful to the staff of the mechanical and electronic workshops in the Oxford Chemistry Department and at the University of Oldenburg.

Author information

Affiliations

1. AG Neurosensory Sciences/Animal Navigation, Institut für Biologie und Umweltwissenschaften, Carl-von-Ossietzky Universität Oldenburg, Oldenburg, Germany

Jingjing Xu, Jessica Schmidt, Marco Bassetto, Maike Herrmann, Rabea Bartölke, Stefanie J. Käsehagen, Simon Horst, Glen Dautaj & Henrik Mouritsen

2. Physical and Theoretical Chemistry Laboratory, Department of Chemistry, University of Oxford, Oxford, UK
- Lauren E. Jarocha, Tilo Zollitsch, Kevin B. Henbest, Daniel J. C. Sowood, Marco Bassetto, Jiate Luo, Jessica R. Walton, Jessica Fleming, Yujing Wei, Patrick D. F. Murton, Angela S. Gehrckens, Stuart R. Mackenzie & P. J. Hore
3. Inorganic Chemistry Laboratory, Department of Chemistry, University of Oxford, Oxford, UK
- Marcin Konowalczyk, Kevin B. Henbest, Matthew J. Golesworthy, Victoire Déjean, Tommy L. Pitcher, Gabriel Moise & Christiane R. Timmel
4. Institut für Physikalische Chemie, Albert-Ludwigs-Universität Freiburg, Freiburg, Germany
- Sabine Richert & Stefan Weber
5. Department of Medicinal Chemistry and Molecular Pharmacology, Purdue University, West Lafayette, IN, USA
- Hang Yin
6. Division of Biochemistry, Department of Neuroscience, Carl-von-Ossietzky-Universität Oldenburg, Oldenburg, Germany
- Haijia Wu & Karl-Wilhelm Koch
7. Department of Neuroscience, University of Texas Southwestern Medical Center, Dallas, TX, USA
- Yogarany Chelliah & Joseph S. Takahashi
8. Howard Hughes Medical Institute, University of Texas Southwestern Medical Center, Dallas, TX, USA
- Yogarany Chelliah & Joseph S. Takahashi

9. Research Centre for Neurosensory Science, University of Oldenburg,
Oldenburg, Germany

Karl-Wilhelm Koch, Ilia A. Solov'yov & Henrik Mouritsen

10. Department of Physics, Carl-von-Ossietzky Universität Oldenburg,
Oldenburg, Germany

Ilia A. Solov'yov

11. High Magnetic Field Laboratory, Key Laboratory of High Magnetic
Field and Ion Beam Physical Biology, Hefei Institutes of Physical
Science, Chinese Academy of Sciences, Hefei, PR China

Can Xie

12. International Magnetobiology Frontier Research Center, Hefei, PR
China

Can Xie

13. Centre for Advanced Electron Spin Resonance (CAESR), Department
of Chemistry, University of Oxford, Oxford, UK

Christiane R. Timmel

Authors

1. Jingjing Xu

[View author publications](#)

You can also search for this author in [PubMed](#) [Google Scholar](#)

2. Lauren E. Jarocha

[View author publications](#)

You can also search for this author in [PubMed](#) [Google Scholar](#)

3. Tilo Zollitsch

[View author publications](#)

You can also search for this author in [PubMed](#) [Google Scholar](#)

4. Marcin Konowalczyk

[View author publications](#)

You can also search for this author in [PubMed](#) [Google Scholar](#)

5. Kevin B. Henbest

[View author publications](#)

You can also search for this author in [PubMed](#) [Google Scholar](#)

6. Sabine Richert

[View author publications](#)

You can also search for this author in [PubMed](#) [Google Scholar](#)

7. Matthew J. Golesworthy

[View author publications](#)

You can also search for this author in [PubMed](#) [Google Scholar](#)

8. Jessica Schmidt

[View author publications](#)

You can also search for this author in [PubMed](#) [Google Scholar](#)

9. Victoire Déjean

[View author publications](#)

You can also search for this author in [PubMed](#) [Google Scholar](#)

10. Daniel J. C. Sowood

[View author publications](#)

You can also search for this author in [PubMed](#) [Google Scholar](#)

11. Marco Bassetto

[View author publications](#)

You can also search for this author in [PubMed](#) [Google Scholar](#)

12. Jiate Luo

[View author publications](#)

You can also search for this author in [PubMed](#) [Google Scholar](#)

13. Jessica R. Walton

[View author publications](#)

You can also search for this author in [PubMed](#) [Google Scholar](#)

14. Jessica Fleming

[View author publications](#)

You can also search for this author in [PubMed](#) [Google Scholar](#)

15. Yujing Wei

[View author publications](#)

You can also search for this author in [PubMed](#) [Google Scholar](#)

16. Tommy L. Pitcher

[View author publications](#)

You can also search for this author in [PubMed](#) [Google Scholar](#)

17. Gabriel Moise

[View author publications](#)

You can also search for this author in [PubMed](#) [Google Scholar](#)

18. Maike Herrmann

[View author publications](#)

You can also search for this author in [PubMed](#) [Google Scholar](#)

19. Hang Yin

[View author publications](#)

You can also search for this author in [PubMed](#) [Google Scholar](#)

20. Haijia Wu

[View author publications](#)

You can also search for this author in [PubMed](#) [Google Scholar](#)

21. Rabea Bartölke

[View author publications](#)

You can also search for this author in [PubMed](#) [Google Scholar](#)

22. Stefanie J. Käsehagen

[View author publications](#)

You can also search for this author in [PubMed](#) [Google Scholar](#)

23. Simon Horst

[View author publications](#)

You can also search for this author in [PubMed](#) [Google Scholar](#)

24. Glen Dautaj

[View author publications](#)

You can also search for this author in [PubMed](#) [Google Scholar](#)

25. Patrick D. F. Murton

[View author publications](#)

You can also search for this author in [PubMed](#) [Google Scholar](#)

26. Angela S. Gehrckens

[View author publications](#)

You can also search for this author in [PubMed](#) [Google Scholar](#)

27. Yogarany Chelliah

[View author publications](#)

You can also search for this author in [PubMed](#) [Google Scholar](#)

28. Joseph S. Takahashi

[View author publications](#)

You can also search for this author in [PubMed](#) [Google Scholar](#)

29. Karl-Wilhelm Koch

[View author publications](#)

You can also search for this author in [PubMed](#) [Google Scholar](#)

30. Stefan Weber

[View author publications](#)

You can also search for this author in [PubMed](#) [Google Scholar](#)

31. Ilia A. Solov'yov

[View author publications](#)

You can also search for this author in [PubMed](#) [Google Scholar](#)

32. Can Xie

[View author publications](#)

You can also search for this author in [PubMed](#) [Google Scholar](#)

33. Stuart R. Mackenzie

[View author publications](#)

You can also search for this author in [PubMed](#) [Google Scholar](#)

34. Christiane R. Timmel

[View author publications](#)

You can also search for this author in [PubMed](#) [Google Scholar](#)

35. Henrik Mouritsen

[View author publications](#)

You can also search for this author in [PubMed](#) [Google Scholar](#)

36. P. J. Hore

[View author publications](#)

You can also search for this author in [PubMed](#) [Google Scholar](#)

Contributions

J.X., L.E.J., T.Z., M.K., K.B.H., S.R. and M.J.G. made particularly important experimental contributions. J.X. cloned wild-type *ErCRY4* and all the mutants and developed the protocols for expression and purification of the proteins with FAD bound. J.X. and J.S. produced the protein samples. L.E.J. developed the continuous illumination experiment for studying photoreduction and the picosecond transient absorption experiment for measuring magnetic field effects, and recorded and interpreted data. T.Z. and M.J.G. developed the CRDS experiment for measuring magnetic field effects and recorded and interpreted data. M.K. developed the broadband cavity-enhanced absorption spectroscopy experiment for measuring magnetic field effects and recorded and interpreted data. S.R. and S.W. recorded and interpreted the EPR data. K.B.H. participated in all five of the above experiments and recorded and interpreted spectroscopic data. J.F., with K.B.H., recorded and interpreted some of the transient absorption data and all of the re-oxidation data. M.K. helped with the global analysis of the re-oxidation data. M.J.G., V.D., J.R.W. and P.D.F.M. made spectroscopic measurements of magnetic field effects. D.J.C.S. helped to develop the picosecond TA apparatus. J.L. and Y.W. performed spin dynamics calculations. T.L.P. and G.M. reproduced and helped to interpret the EPR data. A.S.G. recorded and interpreted mass spectra. M.B. expressed and purified chicken CRY4. M.H., S.H., G.D. and S.J.K. expressed and purified some of the *ErCRY4* protein samples. Y.C., J.S.T. and J.X. expressed and purified pigeon CRY4. H.Y., H.W., K.-W.K., R.B. and C.X. provided advice on protein expression. I.A.S. performed molecular dynamics simulations and provided advice on cryptochrome structure and dynamics. L.E.J. had

oversight of the organization and administration of the optical spectroscopy measurements. P.J.H., H.M., C.R.T. and S.R.M. conceived the study. P.J.H., H.M., C.R.T., S.R.M. and C.X. supervised the work. P.J.H. and H.M. wrote the manuscript, and all authors commented on the manuscript.

Corresponding authors

Correspondence to [Ilia A. Solov'yov](#) or [Can Xie](#) or [Stuart R. Mackenzie](#) or [Christiane R. Timmel](#) or [Henrik Mouritsen](#) or [P. J. Hore](#).

Ethics declarations

Competing interests

The authors declare no competing interests.

Additional information

Peer review information *Nature* thanks Aurelien de la Lande, Thorsten Ritz, Eric Warrant and the other, anonymous, reviewer(s) for their contribution to the peer review of this work.

Publisher's note Springer Nature remains neutral with regard to jurisdictional claims in published maps and institutional affiliations.

Supplementary information

[Supplementary Information](#)

This file contains Supplementary Methods, Supplementary Figures 1-19, Supplementary Tables 1-7, Supplementary Notes and Data – see contents pages for details.

[Reporting Summary](#)

Source data

[Source Data Fig. 1](#)

[Source Data Fig. 2](#)

[Source Data Fig. 3](#)

[Source Data Fig. 4](#)

Rights and permissions

[Reprints and Permissions](#)

About this article



Check for
updates

Cite this article

Xu, J., Jarocha, L.E., Zollitsch, T. *et al.* Magnetic sensitivity of cryptochrome 4 from a migratory songbird. *Nature* **594**, 535–540 (2021). <https://doi.org/10.1038/s41586-021-03618-9>

[Download citation](#)

- Received: 17 July 2019
- Accepted: 06 May 2021
- Published: 23 June 2021
- Issue Date: 24 June 2021

- DOI: <https://doi.org/10.1038/s41586-021-03618-9>

Comments

By submitting a comment you agree to abide by our [Terms](#) and [Community Guidelines](#). If you find something abusive or that does not comply with our terms or guidelines please flag it as inappropriate.

[Access through your institution](#)

[Change institution](#)

[Buy or subscribe](#)

Associated Content

[Unravelling the enigma of bird magnetoreception](#)

- Eric J. Warrant

Advertisement

This article was downloaded by **calibre** from <https://www.nature.com/articles/s41586-021-03618-9>

- Article
- [Published: 09 June 2021](#)

Representational drift in primary olfactory cortex

- [Carl E. Schoonover](#) [ORCID: orcid.org/0000-0002-6397-1010^{1 na1}](#),
- [Sarah N. Ohashi^{1 nAff2}](#),
- [Richard Axel](#) [ORCID: orcid.org/0000-0002-3141-4076¹](#) &
- [Andrew J. P. Fink](#) [ORCID: orcid.org/0000-0003-4191-3298^{1 na1}](#)

[Nature](#) volume **594**, pages 541–546 (2021) [Cite this article](#)

- 5967 Accesses
- 54 Altmetric
- [Metrics details](#)

Subjects

- [Cortex](#)
- [Olfactory cortex](#)
- [Sensory processing](#)

Abstract

Perceptual constancy requires the brain to maintain a stable representation of sensory input. In the olfactory system, activity in primary olfactory cortex (piriform cortex) is thought to determine odour identity^{1,2,3,4,5}. Here we present the results of electrophysiological recordings of single units maintained over weeks to examine the stability of odour-evoked responses

in mouse piriform cortex. Although activity in piriform cortex could be used to discriminate between odorants at any moment in time, odour-evoked responses drifted over periods of days to weeks. The performance of a linear classifier trained on the first recording day approached chance levels after 32 days. Fear conditioning did not stabilize odour-evoked responses. Daily exposure to the same odorant slowed the rate of drift, but when exposure was halted the rate increased again. This demonstration of continuous drift poses the question of the role of piriform cortex in odour perception. This instability might reflect the unstructured connectivity of piriform cortex^{[6](#),[7](#),[8](#),[9](#),[10](#),[11](#),[12](#)}, and may be a property of other unstructured cortices.

Access options

Subscribe to Journal

Get full journal access for 1 year

\$199.00

only \$3.90 per issue

[Subscribe](#)

All prices are NET prices.

VAT will be added later in the checkout.

Tax calculation will be finalised during checkout.

Rent or Buy article

Get time limited or full article access on ReadCube.

from \$8.99

[Rent or Buy](#)

All prices are NET prices.

Additional access options:

- [Log in](#)
- [Access through your institution](#)
- [Learn about institutional subscriptions](#)

Fig. 1: Odour-evoked activity in piriform cortex over 32 days.



Fig. 2: Drift of odour responses across days despite conserved statistics within each day.

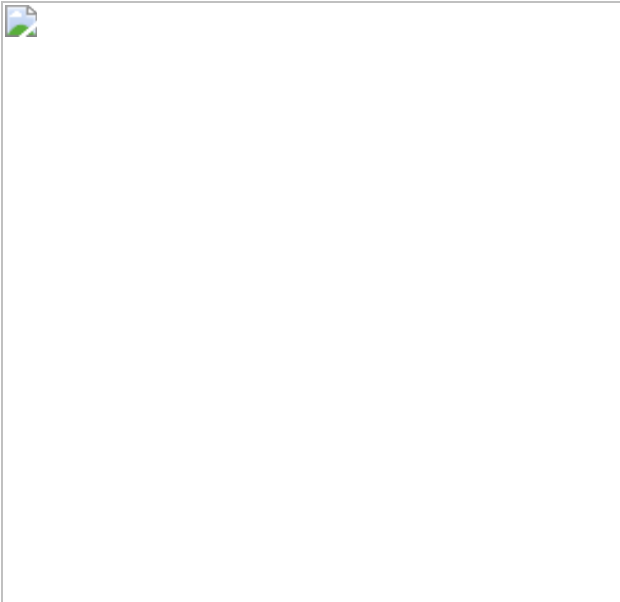


Fig. 3: Odour response geometry drifts over time.

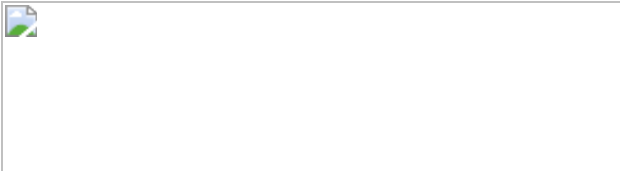
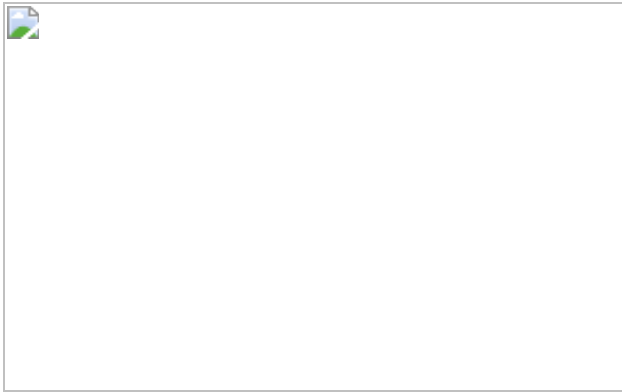


Fig. 4: Frequent experience, but not fear conditioning, reduces drift rate.



Data availability

Data will be made available upon reasonable request to the corresponding authors.

Code availability

Code will be made available upon reasonable request to the corresponding authors.

References

1. 1.

Haberly, L. B. Single unit responses to odor in the prepyriform cortex of the rat. *Brain Res.* **12**, 481–484 (1969).

[CAS](#) [PubMed](#) [Google Scholar](#)

2. 2.

Kadohisa, M. & Wilson, D. A. Separate encoding of identity and similarity of complex familiar odors in piriform cortex. *Proc. Natl Acad. Sci. USA* **103**, 15206–15211 (2006).

[ADS](#) [CAS](#) [PubMed](#) [PubMed Central](#) [Google Scholar](#)

3. 3.

Stettler, D. D. & Axel, R. Representations of odor in the piriform cortex. *Neuron* **63**, 854–864 (2009).

[CAS](#) [PubMed](#) [Google Scholar](#)

4. 4.

Miura, K., Mainen, Z. F. & Uchida, N. Odor representations in olfactory cortex: distributed rate coding and decorrelated population activity. *Neuron* **74**, 1087–1098 (2012).

[CAS](#) [PubMed](#) [PubMed Central](#) [Google Scholar](#)

5. 5.

Bolding, K. A. & Franks, K. M. Recurrent cortical circuits implement concentration-invariant odor coding. *Science* **361**, eaat6904 (2018).

[PubMed](#) [PubMed Central](#) [Google Scholar](#)

6. 6.

Haberly, L. B. & Price, J. L. The axonal projection patterns of the mitral and tufted cells of the olfactory bulb in the rat. *Brain Res.* **129**, 152–157 (1977).

[CAS](#) [PubMed](#) [Google Scholar](#)

7. 7.

Sosulski, D. L., Bloom, M. L., Cutforth, T., Axel, R. & Datta, S. R. Distinct representations of olfactory information in different cortical centres. *Nature* **472**, 213–216 (2011).

[ADS](#) [CAS](#) [PubMed](#) [PubMed Central](#) [Google Scholar](#)

8. 8.

Miyamichi, K. et al. Cortical representations of olfactory input by trans-synaptic tracing. *Nature* **472**, 191–196 (2011).

[ADS](#) [CAS](#) [PubMed](#) [Google Scholar](#)

9. 9.

Ghosh, S. et al. Sensory maps in the olfactory cortex defined by long-range viral tracing of single neurons. *Nature* **472**, 217–220 (2011).

[ADS](#) [CAS](#) [PubMed](#) [Google Scholar](#)

10. 10.

Davison, I. G. & Ehlers, M. D. Neural circuit mechanisms for pattern detection and feature combination in olfactory cortex. *Neuron* **70**, 82–94 (2011).

[CAS](#) [PubMed](#) [PubMed Central](#) [Google Scholar](#)

11. 11.

Johnson, D. M., Illig, K. R., Behan, M. & Haberly, L. B. New features of connectivity in piriform cortex visualized by intracellular injection of pyramidal cells suggest that “primary” olfactory cortex functions like “association” cortex in other sensory systems. *J. Neurosci.* **20**, 6974–6982 (2000).

[CAS](#) [PubMed](#) [PubMed Central](#) [Google Scholar](#)

12. 12.

Franks, K. M. et al. Recurrent circuitry dynamically shapes the activation of piriform cortex. *Neuron* **72**, 49–56 (2011).

[CAS](#) [PubMed](#) [PubMed Central](#) [Google Scholar](#)

13. 13.

Gilbert, C. D. & Wiesel, T. N. Receptive field dynamics in adult primary visual cortex. *Nature* **356**, 150–152 (1992).

[ADS](#) [CAS](#) [PubMed](#) [Google Scholar](#)

14. 14.

Rose, T., Jaepel, J., Hübener, M. & Bonhoeffer, T. Cell-specific restoration of stimulus preference after monocular deprivation in the visual cortex. *Science* **352**, 1319–1322 (2016).

[ADS](#) [CAS](#) [PubMed](#) [Google Scholar](#)

15. 15.

Clark, S. A., Allard, T., Jenkins, W. M. & Merzenich, M. M. Receptive fields in the body-surface map in adult cortex defined by temporally correlated inputs. *Nature* **332**, 444–445 (1988).

[ADS](#) [CAS](#) [PubMed](#) [Google Scholar](#)

16. 16.

Margolis, D. J. et al. Reorganization of cortical population activity imaged throughout long-term sensory deprivation. *Nat. Neurosci.* **15**, 1539–1546 (2012).

[CAS](#) [PubMed](#) [Google Scholar](#)

17. 17.

Mayrhofer, J. M., Haiss, F., Helmchen, F. & Weber, B. Sparse, reliable, and long-term stable representation of periodic whisker deflections in the mouse barrel cortex. *Neuroimage* **115**, 52–63 (2015).

[PubMed](#) [Google Scholar](#)

18. 18.

Weinberger, N. M., Javid, R. & Lepan, B. Long-term retention of learning-induced receptive-field plasticity in the auditory cortex. *Proc. Natl Acad. Sci. USA* **90**, 2394–2398 (1993).

[ADS](#) [CAS](#) [PubMed](#) [PubMed Central](#) [Google Scholar](#)

19. 19.

Kato, H. K., Gillet, S. N. & Isaacson, J. S. Flexible sensory representations in auditory cortex driven by behavioral relevance. *Neuron* **88**, 1027–1039 (2015).

[CAS](#) [PubMed](#) [PubMed Central](#) [Google Scholar](#)

20. 20.

Mombaerts, P. et al. Visualizing an olfactory sensory map. *Cell* **87**, 675–686 (1996).

[CAS](#) [PubMed](#) [Google Scholar](#)

21. 21.

Bhalla, U. S. & Bower, J. M. Multiday recordings from olfactory bulb neurons in awake freely moving rats: spatially and temporally organized variability in odorant response properties. *J. Comput. Neurosci.* **4**, 221–256 (1997).

[CAS](#) [PubMed](#) [MATH](#) [Google Scholar](#)

22. 22.

Kato, H. K., Chu, M. W., Isaacson, J. S. & Komiyama, T. Dynamic sensory representations in the olfactory bulb: modulation by wakefulness and experience. *Neuron* **76**, 962–975 (2012).

[CAS](#) [PubMed](#) [PubMed Central](#) [Google Scholar](#)

23. 23.

Poo, C. & Isaacson, J. S. Odor representations in olfactory cortex: “sparse” coding, global inhibition, and oscillations. *Neuron* **62**, 850–861 (2009).

[CAS](#) [PubMed](#) [PubMed Central](#) [Google Scholar](#)

24. 24.

Wilson, C. D., Serrano, G. O., Koulakov, A. A. & Rinberg, D. A primacy code for odor identity. *Nat. Commun.* **8**, 1477 (2017).

[ADS](#) [PubMed](#) [PubMed Central](#) [Google Scholar](#)

25. 25.

Chestek, C. A. et al. Single-neuron stability during repeated reaching in macaque premotor cortex. *J. Neurosci.* **27**, 10742–10750 (2007).

[CAS](#) [PubMed](#) [PubMed Central](#) [Google Scholar](#)

26. 26.

Flurkey, K., Currer, J. M. & Harrison, D. E. in *The Mouse in Biomedical Research* 637–672 (Elsevier, 2007).

27. 27.

Pashkovski, S. L. et al. Structure and flexibility in cortical representations of odour space. *Nature* **583**, 253–258 (2020).

28. 28.

Kobak, D. et al. Demixed principal component analysis of neural population data. *eLife* **5**, e10989 (2016).

[PubMed](#) [PubMed Central](#) [Google Scholar](#)

29. 29.

Fink, A. J., Axel, R. & Schoonover, C. E. A virtual burrow assay for head-fixed mice measures habituation, discrimination, exploration and avoidance without training. *eLife* **8**, e45658 (2019).

[PubMed](#) [PubMed Central](#) [Google Scholar](#)

30. 30.

Fusi, S., Drew, P. J. & Abbott, L. F. Cascade models of synaptically stored memories. *Neuron* **45**, 599–611 (2005).

[CAS](#) [PubMed](#) [Google Scholar](#)

31. 31.

Rule, M. E., O’Leary, T. & Harvey, C. D. Causes and consequences of representational drift. *Curr. Opin. Neurobiol.* **58**, 141–147 (2019).

[CAS](#) [PubMed](#) [PubMed Central](#) [Google Scholar](#)

32. 32.

Káli, S. & Dayan, P. Off-line replay maintains declarative memories in a model of hippocampal-neocortical interactions. *Nat. Neurosci.* **7**, 286–294 (2004).

[PubMed](#) [Google Scholar](#)

33. 33.

Gallego, J. A., Perich, M. G., Chowdhury, R. H., Solla, S. A. & Miller, L. E. Long-term stability of cortical population dynamics underlying consistent behavior. *Nat. Neurosci.* **23**, 260–270 (2020).

[CAS](#) [PubMed](#) [PubMed Central](#) [Google Scholar](#)

34. 34.

Brette, R. Is coding a relevant metaphor for the brain? *Behav. Brain Sci.* **42**, e215 (2018).

[PubMed](#) [Google Scholar](#)

35. 35.

Roxin, A. & Fusi, S. Efficient partitioning of memory systems and its importance for memory consolidation. *PLOS Comput. Biol.* **9**, e1003146 (2013).

[ADS](#) [CAS](#) [PubMed](#) [PubMed Central](#) [Google Scholar](#)

36. 36.

McClelland, J. L., McNaughton, B. L. & O'Reilly, R. C. Why there are complementary learning systems in the hippocampus and neocortex: insights from the successes and failures of connectionist models of learning and memory. *Psychol. Rev.* **102**, 419–457 (1995).

[PubMed](#) [Google Scholar](#)

37. 37.

Kentros, C. G., Agnihotri, N. T., Streater, S., Hawkins, R. D. & Kandel, E. R. Increased attention to spatial context increases both place field stability and spatial memory. *Neuron* **42**, 283–295 (2004).

[CAS](#) [PubMed](#) [Google Scholar](#)

38. 38.

Mankin, E. A. et al. Neuronal code for extended time in the hippocampus. *Proc. Natl Acad. Sci. USA* **109**, 19462–19467 (2012).

[ADS](#) [CAS](#) [PubMed](#) [PubMed Central](#) [Google Scholar](#)

39. 39.

Rubin, A., Geva, N., Sheintuch, L. & Ziv, Y. Hippocampal ensemble dynamics timestamp events in long-term memory. *eLife* **4**, e12247 (2015).

[PubMed](#) [PubMed Central](#) [Google Scholar](#)

40. 40.

Lee, J. S., Briguglio, J. J., Cohen, J. D., Romani, S. & Lee, A. K. The statistical structure of the hippocampal code for space as a function of time, context, and value. *Cell* **183**, 620–635.e22 (2020).

[CAS](#) [PubMed](#) [Google Scholar](#)

41. 41.

Rokni, U., Richardson, A. G., Bizzi, E. & Seung, H. S. Motor learning with unstable neural representations. *Neuron* **54**, 653–666 (2007).

[CAS](#) [PubMed](#) [Google Scholar](#)

42. 42.

Driscoll, L. N., Pettit, N. L., Minderer, M., Chettih, S. N. & Harvey, C. D. Dynamic reorganization of neuronal activity patterns in parietal cortex. *Cell* **170**, 986–999.e16 (2017).

[CAS](#) [PubMed](#) [PubMed Central](#) [Google Scholar](#)

43. 43.

Tolias, A. S. et al. Recording chronically from the same neurons in awake, behaving primates. *J. Neurophysiol.* **98**, 3780–3790 (2007).

[PubMed](#) [Google Scholar](#)

44. 44.

Mank, M. et al. A genetically encoded calcium indicator for chronic in vivo two-photon imaging. *Nat. Methods* **5**, 805–811 (2008).

[CAS](#) [PubMed](#) [Google Scholar](#)

45. 45.

Jeon, B. B., Swain, A. D., Good, J. T., Chase, S. M. & Kuhlman, S. J. Feature selectivity is stable in primary visual cortex across a range of spatial frequencies. *Sci. Rep.* **8**, 15288 (2018).

[ADS](#) [PubMed](#) [PubMed Central](#) [Google Scholar](#)

46. 46.

White, E. L. Thalamocortical synaptic relations: a review with emphasis on the projections of specific thalamic nuclei to the primary sensory areas of the neocortex. *Brain Res.* **180**, 275–311 (1979).

[ADS](#) [CAS](#) [PubMed](#) [Google Scholar](#)

47. 47.

Marks, T. D. & Goard, M. J. Stimulus-dependent representational drift in primary visual cortex. Preprint at <https://doi.org/10.1101/2020.12.10.420620> (2020).

48. 48.

Cui, X., Wiler, J., Dzaman, M., Altschuler, R. A. & Martin, D. C. In vivo studies of polypyrrole/peptide coated neural probes. *Biomaterials* **24**, 777–787 (2003).

[CAS](#) [PubMed](#) [Google Scholar](#)

49. 49.

Ludwig, K. A. et al. Poly(3,4-ethylenedioxythiophene) (PEDOT) polymer coatings facilitate smaller neural recording electrodes. *J.*

Neural Eng. **8**, 014001 (2011).

[ADS](#) [PubMed](#) [PubMed Central](#) [Google Scholar](#)

50. 50.

Okun, M., Lak, A., Carandini, M. & Harris, K. D. Long term recordings with immobile silicon probes in the mouse cortex. *PLoS ONE* **11**, e0151180 (2016).

[PubMed](#) [PubMed Central](#) [Google Scholar](#)

51. 51.

Steinmetz, N. A. et al. Neuropixels 2.0: A miniaturized high-density probe for stable, long-term brain recordings. *Science* **372**, eabf4588 (2021).

[CAS](#) [PubMed](#) [Google Scholar](#)

52. 52.

Cladé, P. *PyDAQmx: a Python Interface to the National Instruments DAQmx Driver* <http://pythonhosted.org/PyDAQmx/> (2010).

53. 53.

Pachitariu, M., Steinmetz, N. A., Kadir, S. N., Carandini, M. & Harris, K. D. in *Adv. Neural Information Processing Systems* 4448–4456 (NeurIPS, 2016).

54. 54.

Dickey, A. S., Suminski, A., Amit, Y. & Hatsopoulos, N. G. Single-unit stability using chronically implanted multielectrode arrays. *J. Neurophysiol.* **102**, 1331–1339 (2009).

[PubMed](#) [PubMed Central](#) [Google Scholar](#)

55. 55.

Dhawale, A. K. et al. Automated long-term recording and analysis of neural activity in behaving animals. *eLife* **6**, e27702 (2017).

[PubMed](#) [PubMed Central](#) [Google Scholar](#)

56. 56.

Fan, R.-E., Chang, K.-W., Hsieh, C.-J., Wang, X.-R. & Lin, C.-J. LIBLINEAR: A library for large linear classification. *J. Mach. Learn. Res.* **9**, 1871–1874 (2008).

[MATH](#) [Google Scholar](#)

57. 57.

Perez-Orive, J. et al. Oscillations and sparsening of odor representations in the mushroom body. *Science* **297**, 359–365 (2002).

[ADS](#) [CAS](#) [PubMed](#) [Google Scholar](#)

58. 58.

Rolls, E. T. & Tovee, M. J. Sparseness of the neuronal representation of stimuli in the primate temporal visual cortex. *J. Neurophysiol.* **73**, 713–726 (1995).

[CAS](#) [PubMed](#) [Google Scholar](#)

59. 59.

Willmore, B. & Tolhurst, D. J. Characterizing the sparseness of neural codes. *Network* **12**, 255–270 (2001).

[CAS](#) [PubMed](#) [Google Scholar](#)

60. 60.

Lein, E. S. et al. Genome-wide atlas of gene expression in the adult mouse brain. *Nature* **445**, 168–176 (2007).

[ADS](#) [CAS](#) [PubMed](#) [Google Scholar](#)

[Download references](#)

Acknowledgements

We thank L. F. Abbott, S. R. Datta, S. Fusi, J. W. Krakauer, A. Kumar, M. A. Long, A. M. Michaiel, and S. L. Pashkovski for comments on the manuscript; G. W. Johnson and T. Tabachnik for assistance with instrumentation; G. Buzsáki and members of the Buzsáki laboratory, D. A. Gutnisky, and C. C. Rodgers for experimental advice; the instructors of the 2015 Advanced Course in Computational Neuroscience at the Champalimaud Foundation for instruction; D. F. Albeanu and members of the Albeanu laboratory, D. Aronov, K. A. Bolding, R. Costa, J. P. Cunningham, J. T. Dudman, W. M. Fischler, K. M. Franks, M. E. Hasselmo, V. Jayaraman, A. Y. Karpova, E. Marder, J. A. Miri, C. Poo, D. Rinberg and members of the Rinberg laboratory, E. S. Schaffer, and D. D. Stettler for comments; M. Gutierrez, C. H. Eccard, P. J. Kisloff, and A. Nemes for general laboratory support; and the Howard Hughes Medical Institute and the Helen Hay Whitney Foundation for financial support.

Author information

Author notes

1. Sarah N. Ohashi

Present address: Immunobiology Graduate Program, Yale School of Medicine, New Haven, CT, USA

2. These authors contributed equally: Carl E. Schoonover, Andrew J. P. Fink

Affiliations

1. Howard Hughes Medical Institute, Mortimer B. Zuckerman Mind Brain Behavior Institute, Department of Neuroscience, Columbia University, New York, NY, USA

Carl E. Schoonover, Sarah N. Ohashi, Richard Axel & Andrew J. P. Fink

Authors

1. Carl E. Schoonover

[View author publications](#)

You can also search for this author in [PubMed](#) [Google Scholar](#)

2. Sarah N. Ohashi

[View author publications](#)

You can also search for this author in [PubMed](#) [Google Scholar](#)

3. Richard Axel

[View author publications](#)

You can also search for this author in [PubMed](#) [Google Scholar](#)

4. Andrew J. P. Fink

[View author publications](#)

You can also search for this author in [PubMed](#) [Google Scholar](#)

Contributions

This work is the result of a close collaboration between C.E.S. and A.J.P.F., who conceived the study and designed the experiments. Experiments were performed by C.E.S., S.N.O. and A.J.P.F. The data were analysed and the manuscript was written by C.E.S, R.A. and A.J.P.F.

Corresponding authors

Correspondence to [Carl E. Schoonover](#) or [Richard Axel](#) or [Andrew J. P. Fink](#).

Ethics declarations

Competing interests

The authors declare no competing interests.

Additional information

Peer review information *Nature* thanks the anonymous reviewers for their contribution to the peer review of this work. Peer reviewer reports are available.

Publisher's note Springer Nature remains neutral with regard to jurisdictional claims in published maps and institutional affiliations.

Extended data figures and tables

[Extended Data Fig. 1 Longitudinal tracking of single units in piriform cortex.](#)

a, Chronic silicon probe implantation in anterior piriform cortex (green). Anatomical image and structure designations from the Allen Mouse Brain Atlas⁶⁰ (<http://www.brain-map.org>). Inset, probe diagram with relative positions of the 32 recording electrodes; red, DiI marking probe position; black, cell bodies (NeuroTrace). Diagrams not to scale. **b**, Number of single units retained as a function of recording interval duration. Mean ± s.d. with individual data points; blue dotted line, linear regression; blue shading, 95% CI. $\rho = -0.41$, $P = 1.2 \times 10^{-3}$, $n = 24$ recordings across 8 days, $n = 18$ recordings across 16 days, $n = 12$ recordings across 24 days, $n = 6$ recordings across 32 days, all from 6 mice. **c**, Single-unit yield for single-day record sessions. Left, per recording session as a function of time since probe implantation. Blue dotted line, linear regression; blue shading, 95%

CI. $\rho = -0.12$, $P = 0.23$. Right, single-unit yields across all single-day recording sessions ($n = 97$ recording sessions in 16 mice). **d**, Left, probability density of waveform similarities for all pairs of single units simultaneously recorded within each day. Red dashed line indicates inclusion criterion (0.93, the distribution's 99th percentile) for rejection of candidate single units recorded across multiple days. Right, probability density of refractory period violations (refractory period is defined as an inter-spike interval <1.5 ms). **e**, Average waveforms for a representative single unit recorded at each of the recording sites of the silicon probe. Waveforms from all days (0–32) are superimposed with each day plotted as a separate colour (colour scheme maintained throughout). Inset **e,i**, mean waveforms for days 0, 8, 16, 24, and 32 for a subset of recording sites, indicated by the grey box. Inset **e,ii**, mean waveforms for days 0 to 32, superimposed for a single recording site (dashed grey box). **f**, Waveform correlations for each single unit across days 0 and 32 (red) and across all single units within-day (grey); within-unit, across-days versus within-day, across-units, $P = 4.8 \times 10^{-246}$, Wilcoxon rank-sum, $n = 379$ single units from 6 mice. The grey distribution is replotted from **d** (left). **g**, Single-unit waveform centroids across a 32-day interval from a representative mouse (centroid computed using spatial average across electrode positions weighted by the squared mean waveform amplitude at each electrode). Centroid for each single unit isolated on day 0 (blue circles) and days 8, 16, 24, and 32 (red circles, columns 1–4, respectively; days 0 versus 8, $n = 100$ single units; days 0 versus 16, $n = 94$ single units; days 0 versus 24, $n = 84$ single units; days 0 versus 32, $n = 77$ single units). Grey circles indicate the positions and sizes of the probe's 32 electrode sites. **h**, Mean displacement of single-unit centroids from this mouse between day 0 (blue circle, defined at origin) and days 8, 16, 24, and 32 (red circles, columns 1–4, respectively). Grey contours indicate quintile boundaries of the distribution of centroid position displacement for the population. **i**, Top, cumulative distribution of within-unit centroid displacement (red) between day 0 and days 8, 16, 24, and 32 (columns 1–4, respectively) and across-unit centroid displacement within day (black) for this mouse. Median on day 0 versus 8 within-unit = $1.8 \mu\text{m}$ ($Q_1 = 1.1 \mu\text{m}$, $Q_3 = 2.9 \mu\text{m}$), across-unit = $63.5 \mu\text{m}$ ($Q_1 = 31.5 \mu\text{m}$, $Q_3 = 107 \mu\text{m}$); day 0 versus 16 within-unit = $2.1 \mu\text{m}$ ($Q_1 = 1.3 \mu\text{m}$, $Q_3 = 3.2 \mu\text{m}$), across-unit = $64.2 \mu\text{m}$ ($Q_1 = 32.0 \mu\text{m}$, $Q_3 = 108 \mu\text{m}$); day 0 versus 24 within-unit = $2.6 \mu\text{m}$ ($Q_1 = 1.5 \mu\text{m}$,

$Q3 = 3.5 \mu\text{m}$), across-unit = $64.4 \mu\text{m}$ ($Q1 = 32.2 \mu\text{m}$, $Q3 = 108 \mu\text{m}$); day 0 versus 32 within-unit = $2.8 \mu\text{m}$ ($Q1 = 2.2 \mu\text{m}$, $Q3 = 4.2 \mu\text{m}$), across-unit = $64.5 \mu\text{m}$ ($Q1 = 32.1 \mu\text{m}$, $Q3 = 108 \mu\text{m}$); for all comparisons $P < 9.5 \times 10^{-51}$, Wilcoxon rank-sum, n as in **g**. Inset at bottom, x -axis 0 to $10 \mu\text{m}$.

Extended Data Fig. 2 Assessing the stability of single units recorded across multiple days.

a, b, Experiment time courses for 16-day (**a**) and 32-day (**b**) interval protocols. ‘Recovery’, period following headplate attachment and stereotactic targeting before silicon probe implantation to allow full recovery; ‘settling’, minimum five-week period after probe implantation to permit tissue settling and signal stabilization; ‘monitor’, minimum ten-day period during which neural signals were recorded daily to assess signal stability. Experiments began only once single units could be reliably tracked across days. ‘Record’, experiment protocol (Figs. **1a**, **4a, c**). ‘Familiarization’ (16-day interval experiments in **a** only), daily odorant presentation for experiments described in Fig. **4c, d** and Extended Data Fig. **10d–h**. **c**, For single units held during 16-day interval experiments, waveform similarity (left; Pearson’s correlation), centroid displacement (middle), and spike time ACG distance (right; Euclidean norm between normalized ACGs) measured between day 0 and subsequent days (red, ‘within-unit, across-day’) and across all single units within each day (black, ‘across-unit, within-day’). Dotted lines, median. Shading, boundaries of top and bottom quartiles ($n = 690$ single units from 7 mice). **d**, As in **c** but for single units held during 32-day interval experiments ($n = 379$ single units from 6 mice). **e**, Example spike–time autocorrelograms from two single units recorded in the same mouse on five separate days. **f**, Density heatmap showing ACG distance of pairs of simultaneously recorded single units plotted against waveform similarity (left) and distance between their centroids (right) for those pairs. Top, 16-day interval experiments ($n = 1,248,216$ pairs of single units from 7 mice on 17 days); bottom, 32-day interval experiments ($n = 841,138$ pairs of single units from 6 mice on 33 days). This shows that waveform-based features (waveform similarity and centroid distance) vary independently of the similarity of the spike–time ACGs. Thus, ACG distance is a measure of single-unit stability to which the spike-sorting pipeline is insensitive. **g**, Waveform similarity (top),

centroid distance (middle), and ACG distance (bottom) for a given single unit between days 0 and 32, plotted against the same metric applied to the same single unit versus the most similar other simultaneously recorded single unit. Dashed line, unity. **h**, Mean single unit spontaneous firing rate on an individual day (baseline firing rate) compared across intervals of 8 days ($\rho = 0.89$, $n = 2,177$ single units), 16 days ($\rho = 0.82$, $n = 1,412$ single units), 24 days ($\rho = 0.74$, $n = 816$ single units) and 32 days ($\rho = 0.68$, $n = 379$ single units) from 6 mice. For all correlations, $P < 4.0 \times 10^{-52}$. Each plot shows a random subset of 379 single units, to match the number of single units recorded across the 32-day interval (right). Black dashed line, unity; blue dotted line, linear regression; blue shading, 95% CI. **i**, Odour response similarity plotted against change in mean spontaneous firing rate on a symlog scale (left; $\rho = -0.041$, $P = 0.43$) and absolute spontaneous firing rate on a log scale (right; $\rho = 0.087$, $P = 0.09$) across a 32-day interval ($n = 379$ single units from 6 mice). Blue dotted line, linear regression; blue shading, 95% CI. **j**, For single units held during 16-day interval experiments, waveform similarity (left), centroid displacement (middle) and ACG distance (right) measured between days 0 and 16, plotted against odour response similarity of that same single unit (Pearson's correlation of pairs of vectors computed on the two days, consisting of the response magnitudes for each odorant of a panel); black circles, individual units; blue dotted line, linear regression; blue shading, 95% CI. **k**, As in **j** but for single units held during 32-day interval experiments, plotting these features measured between days 0 and 32.

Extended Data Fig. 3 A single unit is more similar to itself across days than to any other single unit on the probe.

a, Bottom, single unit recorded on day 32 (red, same as shown in Extended Data Fig. 1e) overlaid with the five most similar single units to it recorded on the same day (black), as measured by waveform similarity (Pearson's correlation between waveforms). Top, spike–time cross correlograms between the example single unit and each of the five most similar single units. The absence of a dip in cross correlogram amplitude at the 0-ms time lag (refractory period violations) indicates that the example single unit and each of the five most similar single units correspond to distinct neurons. **b**, Top, for single units held across days, waveform similarity measured on day

0 versus subsequent days (red; within-unit, across-days), and waveform similarity measured between a given single unit and the ten single units most similar to it within a given day (blue; across-units, within-day). Dotted line, median. Shading, top and bottom quartiles. Bottom, cumulative distributions (left, full distribution; inset at right, expanded *x*-axis) within-unit for day 0 versus day 16 (red), ten most similar single units within a day (blue), one most similar single unit within a day (cyan). Median within-unit waveform similarity between day 0 and day 16, 0.98 (Q1 = 0.97, Q3 = 0.99); median across-unit waveform similarity with the ten most similar, 0.86 (Q1 = 0.80, Q3 = 0.90); median across-unit waveform similarity with the one most similar, 0.94 (Q1 = 0.91, Q3 = 0.95). **c, d**, Same analysis as in **b** but for centroid displacement and spike–time ACG distance (Euclidean norm between normalized ACGs), respectively. **c**, Median within-unit displacement between day 0 and day 16, 2.9 μm (Q1 = 1.6 μm , Q3 = 5.0 μm); median across-unit distance from the ten most similar, 11.2 μm (Q1 = 6.9 μm , Q3 = 16.5 μm); median across-unit distance from the one most similar, 6.1 μm (Q1 = 3.6 μm , Q3 = 9.3 μm). **d**, Median within-unit ACG distance between day 0 and day 16, 0.018 (Q1 = 0.012, Q3 = 0.028); median across-unit ACG distance for the ten most similar, 0.047 (Q1 = 0.031, Q3 = 0.069); median across-unit ACG distance for the one most similar, 0.044 (Q1 = 0.030, Q3 = 0.064). **e–g**, As in **b–d** but for the experiments performed across a 32-day interval. **e**, Median within-unit waveform similarity between day 0 and day 32, 0.97 (Q1 = 0.96, Q3 = 0.98); median across-unit waveform similarity with the ten most similar, 0.87 (Q1 = 0.82, Q3 = 0.91); median across-unit waveform similarity with the one most similar, 0.93 (Q1 = 0.91, Q3 = 0.96). **f**, Median within-unit displacement between day 0 and day 32, 3.5 μm (Q1 = 2.1 μm , Q3 = 5.6 μm); median across-unit distance from ten most similar, 11.2 μm (Q1 = 6.9 μm , Q3 = 16.7 μm); median across-unit distance from one most similar, 7.3 μm (Q1 = 4.6 μm , Q3 = 10.7 μm). **g**, Median within-unit ACG distance between day 0 and day 32, 0.024 (Q1 = 0.016, Q3 = 0.038); median across-unit ACG distance for the ten most similar, 0.048 (Q1 = 0.032, Q3 = 0.072); median ACG distance for the one most similar, 0.050 (Q1 = 0.030, Q3 = 0.077). All within-unit metrics are significantly different from across-unit metrics ($P < 1.4 \times 10^{-60}$, Wilcoxon rank-sum), for both the one most and ten most similar comparisons, across both the 16-day ($n = 690$ single units from 7 mice) and 32-day ($n = 379$ single units

from 6 mice) interval experiments. Thus, a single unit is more similar to itself across days than it is even to those single units most similar to it recorded within a given day. **h–j**, Receiver operator characteristic (ROC) curves showing the true positive rate versus the false positive rate for waveform similarity (**h**), centroid displacement (**i**) and ACG distance (**j**) for both 16-day and 32-day intervals for the ten most (blue) and one most (cyan) similar units. When computing the ROC, ‘signal’ was defined as the distribution with the higher mean. Dashed line corresponds to unity.

Extended Data Fig. 4 Evoked responses in single units across days.

a, Activity of eight single units across a 32-day interval selected to illustrate the diversity of odour-evoked response profiles across single units within each day and within individual single units across days. Columns separate test odorants (chemical names, top). Spike rasters (rows: 7 trials per day) and PSTHs are coloured by day as indicated. Horizontal black bars, 4-s odourant stimulus epochs. The single-unit responses to individual stimuli shown in Fig. [1b](#) are replotted here alongside responses for those single units to the seven other stimuli in the panel: Fig. [1b](#), left: unit 1, stimulus 7 (linalool oxide); Fig. [1b](#), middle: unit 2, stimulus 5 (nerol); Fig. [1b](#), right: unit 3, stimulus 2 (geranyl nitrile). **b**, *z*-scored odour-evoked activity of 300 randomly selected odour–unit pairs during the 4-s odourant stimulus epoch (black bars), ordered differently in each panel. Left, ordered by odour response magnitude on day 0 (replotted from Fig. [1c](#)); middle, ordered by odour response magnitude on day 32; right, ordered by odour response magnitude individually on each day.

Extended Data Fig. 5 Selective odour responses with stable within-day statistics and across-day drift in piriform cortex.

a, b, Fraction of single units that exhibit a significant modulation (**a**) and an increase (red) or decrease (blue) (**b**) in firing rate during the odourant stimulus epoch in response to 0–8 odorants (Wilcoxon rank-sum on firing rate during the odourant stimulus epoch versus spontaneous baseline firing rate, $\alpha = 0.001$). **c**, Cumulative distributions (left) and mean coefficient of

variation (c_v ; right) of response magnitude computed on each odour test day across all trials for each odour–unit pair. Mean (95% CI) across days, $c_v = 0.88$ (0.87, 0.89), $n = 19,356$ odour–unit pairs. **d**, Cumulative distributions (left) and mean fraction of responses preserved per responsive single unit (right) across 8–32-day intervals (8 days: 35.0% (27.3%, 42.5%), 16 days: 19.8% (13.5%, 27.5%), 24 days: 16.9% (10.3%, 26.7%), 32 days: 6.6% (1.9%, 17.5%); $\rho = -0.25$, $P = 5 \times 10^{-6}$, $n = 318$ single units). Non-responsive and broadly responsive single units were excluded from the analysis by setting a threshold on lifetime sparseness (0.65). **e**, Left, fraction of preserved responses per single unit across 32 days versus lifetime sparseness threshold. Right, fraction of single units stable across 32 days versus lifetime sparseness threshold. A single unit was considered stable over 32 days if all significantly modulated responses to the odorant panel were preserved. These quantities do not depend on lifetime sparseness threshold (0.2–0.65, 40th–95th percentile across all single units). **f**, Classification accuracy (8-way, SVM, linear kernel, L2 regularization, trained and tested on data stitched across 3 mice, random draws of 231 single unit subsets from 286 total single units to avoid saturation, 1-s sliding window, 250-ms steps). Grey box, 4-s odorant stimulus epoch; vertical dotted line, onset of odour response at odour port (mean time across all stimuli at which the PID signal reached 5% of maximum); horizontal dashed line, chance performance for 8-way classification. **g**, Classification performance for fifteen temporal binnings of the odour response epoch, measured by maximum classification accuracy (top) and number of single units required to reach 50% of maximum accuracy (bottom) ($n = 286$ single units recorded within-day, stitched across 3 mice). Black shading, binning used for all subsequent classification and for computation of pairwise population vector correlations, angles and drift rate, unless otherwise indicated. For classification using single bins, the window start was set to 500 ms after stimulus initiation so the quantification windows did not begin before odorant stimulus onset as measured by the PID signal. **h**, Classification accuracy as a function of number of single units used, using the highest performance binning in **g** (four 2-s bins). Dashed arrow, number (21) of single units required to achieve >50% classification accuracy. **i**, Classification accuracy for a classifier trained on earlier days and tested on later days ('Forward', replotted from Fig. 2b) compared with a model trained on later days and tested on earlier day ('Reverse'). Dotted lines,

mean; shading, s.d.; limit of 41 single units per animal with 100 permutations. **j**, Classification accuracy of a classifier trained on responses on day 24 alone (all 56 trials) and tested on day 32 compared with a model trained on 75 random subsets of 56 trials drawn from days 0–24 and tested on day 32; $P = 2.6 \times 10^{-5}$, Wilcoxon rank-sum, 100 random subsets of 23 single units per mouse. A classifier trained on concatenated data from days 0–24 will assign high weights to single units with stable (less variable) responses across all days and low weights to single units whose responses varied. Thus, if there is a special population of neurons whose responses are informative about stimulus class and are more stable than others, a model trained on a concatenation of days 0 through 24 ought to perform better when tested on day 32 than a model trained on day 24 alone. However, we do not observe this: thus, it is not possible to establish single units that are most informative about odour identity on day 32 based on their responses across days 0–24. This finding argues against the presence of an informative stable subpopulation. **k**, Representational drift between a pair of days can be estimated by measuring the difference in odour-evoked population responses across days after correcting for within-day variability²⁵. Top left, variability across days (across-day drift + within-day variability), estimated by computing the angle ($\theta_{p,q}$) between trial-averaged population vectors \mathbf{u}_p and \mathbf{u}_q for each odour across each pair of days p and q . Bottom left, variability within a day (noise), estimated by measuring the mean of the angle between the trial-averaged population vectors ($\bar{\theta}$) for each odour within each day on odd trials versus even trials (θ_k , over all days k). Right, the drift rate ($r_{p,q}$) is the corrected angle ($\theta_{p,q} - \bar{\theta}$) divided by the time between days p and q ($\Delta t_{p,q}$). **l**, Cumulative distributions (left) and mean angles (right) between trial-averaged population vectors within-day and across 8–32-day intervals ($n = 180$, $n = 144$, $n = 108$, $n = 72$ and $n = 36$ pairs, respectively). Blue dotted line, exponential regression fit with $\theta = C - R e^{-t/\tau}$, where θ is the variability (angle), C the asymptote, R the intercept at $t = 0$ (within-day variability), and τ the time constant of the exponential in days. The mean rate of change of the exponential fit over the 32-day interval is 1.0 ° per day. **m**, Cumulative distributions (left) and mean within-day angles (right) between trial-averaged population vectors ($n = 72$ pairs per day). No pair of within-day

angles differs significantly ($P \geq 0.56$ for all pairs, Wilcoxon rank-sum). Black crosses, mean \pm 95% CI; blue dotted line, linear regression; blue shading, 95% CI. Classification performed on the three mice presented with an eight-odorant panel. Otherwise, $n = 6$ mice.

Extended Data Fig. 6 Odorant stimuli.

a, PID signals for an example odorant (anisole) across a 32-day interval from a single experiment. Black traces, individual trials; red traces, within-day mean ($n = 7$ trials). **b**, Example PID traces for all other odorant stimuli used in this study. Black traces, individual trials on one day; red, mean ($n = 7$ trials). **c**, Mean PID amplitude across all intervals for experiments in which odorants were presented every 8 days. PID amplitude for a given odorant stimulus is highly correlated across sessions (8-day interval, $\rho = 0.99$, $P = 6.9 \times 10^{-276}$, $n = 288$ comparisons; 16-day interval, $\rho = 0.99$, $P = 7.9 \times 10^{-166}$, $n = 208$ comparisons; 24-day interval, $\rho = 0.98$, $P = 6.2 \times 10^{-94}$, $n = 128$ comparisons; 32-day interval, $\rho = 0.98$, $P = 3.7 \times 10^{-46}$, $n = 64$ comparisons). **d**, Left, coefficient of variation of PID amplitude across all trials for each odorant for experiments in which odorants were presented every 8 days (median across all odorants: $c_v = 0.02$, (Q1 = 0.01, Q3 = 0.04), $n = 400$ mean odorant stimulus pulses computed across 2,800 individual trials for 12 distinct odorants). Middle, rise time (median across all odorants 0.47 s (Q1 = 0.21, Q3 = 1.0 s)). Right, decay time of PID signal (median across odorants 0.51 s (Q1 = 0.21 s, Q3 = 1.3 s)). PID signal onset was defined as the time required to reach 5% of maximum on each trial. PID rise time was defined as the time between onset and 66% of maximum on each trial; PID decay time was defined as the time between 95% and 33% of maximum after stimulus offset. Anisole $n = 350$ trials, 50 days; isopentyl acetate $n = 231$ trials, 33 days; ethyl *trans*-3-hexenoate $n = 350$ trials, 50 days; octanal $n = 245$ trials, 35 days; linalool oxide 231 trials, 33 days; *cis*-3-hexen-1-ol $n = 245$ trials, 35 days; geranyl nitrile $n = 168$ trials, 24 days; cuminaldehyde $n = 168$ trials, 24 days; R-($-$)-carvone $n = 63$ trials, 9 days; methyl salicylate $n = 63$ trials, 9 days; decanal $n = 231$ trials, 33 days; nerol $n = 231$ trials, 33 days. Grey bars, mean across all experiments by odorant; black bars, 95% CI. **e**, Corrected angle as a function of interval for each odorant stimulus used in 32-day interval experiments. Black crosses, mean \pm 95% CI. Decanal: corrected angle correlation across

intervals, $\rho = 0.63$, $P = 3.5 \times 10^{-6}$ and drift rate, $0.8 (0.5 - 1.1)^\circ$ per day ($n = 45$ population vector pairs from 3 mice). Isopentyl acetate: corrected angle correlation across intervals, $\rho = 0.63$, $P = 2.3 \times 10^{-11}$ and drift rate, $1.0 (0.8 - 1.3)^\circ$ per day ($n = 90$ population vector pairs from 6 mice). *cis*-3-Hexen-1-ol: corrected angle correlation across intervals, $\rho = 0.87$, $P = 1.7 \times 10^{-14}$ and drift rate, $1.0 (0.7 - 1.3)^\circ$ per day ($n = 45$ population vector pairs from 3 mice). Ethyl *trans*-3-hexenoate: corrected angle correlation across intervals, $\rho = 0.766$, $P = 1.3 \times 10^{-9}$ and drift rate, $1.3 (1.1 - 1.6)^\circ$ per day ($n = 45$ population vector pairs from 3 mice). Linalool oxide: corrected angle correlation across intervals, $\rho = 0.70$, $P = 1.7 \times 10^{-14}$ and drift rate, $1.5 (1.2 - 1.8)^\circ$ per day ($n = 90$ population vector pairs from 6 mice). Nerol: corrected angle correlation across intervals, $\rho = 0.78$, $P = 2.6 \times 10^{-10}$ and drift rate, $1.5 (1.1 - 1.9)^\circ$ per day ($n = 90$ population vector pairs from 6 mice). Cuminaldehyde: corrected angle correlation across intervals, $\rho = 0.57$, $P = 4.2 \times 10^{-5}$ and drift rate, $1.5 (1.1 - 2.2)^\circ$ per day ($n = 45$ population vector pairs from 3 mice). Octanal: corrected angle correlation across intervals, $\rho = 0.78$, $P = 2.6 \times 10^{-10}$ and drift rate, $1.6 (1.3 - 1.9)^\circ$ per day ($n = 45$ population vector pairs from 3 mice). Anisole: corrected angle correlation across intervals, $\rho = 0.69$, $P = 1.7 \times 10^{-7}$ and drift rate, $1.6 (1.2 - 2.1)^\circ$ per day ($n = 45$ population vector pairs from 3 mice). **f**, Drift rate for each odorant stimulus used in 32-day interval experiments. Red dotted line, mean drift rate across all experiments (from distribution in Fig. [2e](#)). **g**, Odorants used in this study. Numbers indicate the number of experimental replicates in which each odorant molecule was used for each experiment type. **h**, Mean, normalized PID signal recorded simultaneous to the neural signals that were used to classify odorant stimuli using a linear SVM (superimposed, reproduced from Extended Data Fig. [5f](#)).

Extended Data Fig. 7 Drift during the early phase of the odour response.

a, Mean local field potential over all 32 electrodes (filtered 0.1–20 Hz) from an example trial. We estimated the time of first sniff onset following stimulus onset by detecting the first peak of this oscillation on each trial. Only spikes that occurred within the 190 ms after and 10 ms before the detection of sniff onset were analysed (first sniff epoch). Arrowhead,

estimated sniff onset. Grey bar, 4-s odorant stimulus epoch. **b**, Red, classification accuracy (4-way, SVM, linear kernel, L2 regularization) of single-trial z -scored population vectors as a function of interval using only the 200-ms window during the first sniff (as estimated by the first peak in the local field potential) in this mouse ($n = 71$ single units). Classification performance on day 0 computed using leave-one-out cross-validation. For all other intervals the model was trained on all responses from the earlier day and tested on all responses from the later day, as in Fig. 2b. Black, performance with stimulus labels shuffled; mean \pm s.d. **c–e**, As in Fig. 2c–e, but for only the first sniff epoch in this mouse (8-day interval, $n = 32$ pairs of trial-averaged population vectors; 16-day interval, $n = 24$ pairs; 24-day interval, $n = 16$ pairs; 32-day interval, $n = 8$ pairs; within day, all days $n = 40$ pairs). **f**, Top, odour–odour correlation matrices computed on each day during the first sniff epoch in this mouse; middle, bottom, matrices computed using complementary splits of the trials recorded on each day. **g**, Correlation matrix dissimilarity (scaled Frobenius norm; see [Methods](#)). **h, i**, As in Fig. 3b, c but for only the first sniff epoch in this mouse. **h**, Edge angle matrices; **i**, edge angle matrix dissimilarity (scaled Frobenius norm; see [Methods](#)). Black crosses, mean \pm 95% CI; blue dotted line, linear regression; blue shading, 95% CI.

[Extended Data Fig. 8 Drift in response geometry under diverse similarity metrics and temporal binnings.](#)

a, Top, odour–odour correlation matrices computed within each odour test day using all trials (from same mouse as in Fig. 3b); middle, bottom, computed using splits of three trials per stimulus (middle) and the complementary four trials per stimulus (bottom) recorded on that day. Odour–odour correlation matrices were computed from trial-averaged population response vectors to eight odorant stimuli recorded on each of the five days. **b**, Correlation matrix dissimilarity (Frobenius norm; see [Methods](#)) from the same mouse as in **a** (mean \pm 95% CI). Grey dashed line, top, matrix dissimilarity computed using shuffled stimulus identities; bottom, matrix dissimilarity computed within all individual days; grey shading, 95% CI. $\rho = 0.43$, $P = 4.0 \times 10^{-25}$. Both within- and across-day matrix dissimilarity were calculated using odour–odour correlation matrices based on trial-averaged population vectors taken across all combinations of

3-trial/4-trial splits of the data for a given odorant on a given session. Within-day differences in odour response geometry measures (odour–odour correlation matrix dissimilarity) are significantly lower than differences measured across days ($P < 1.2 \times 10^{-34}$ for all measures and intervals from all three mice that were presented with a panel of eight stimuli). **c**, Correlation matrix dissimilarity averaged across all three mice, after scaling results from each subject between 0 (mean within-day matrix dissimilarity) and 1 (mean shuffle matrix dissimilarity). Blue dotted line, linear regression; blue shading, 95% CI. Within-day, 525 pairs; across days, 1,050 pairs. Correlation matrix dissimilarity increases significantly for: left, raw odour–odour correlations; second from left, odour–odour correlations computed using responses projected onto the data’s first six principal components (computed separately on each day); second from right, raw cosine distances; and right, cosine distances computed using responses projected onto the data’s first six principal components (computed separately on each day). **d**, Left, correlation coefficients of normalized matrix dissimilarity versus time interval (using odour–odour correlations measured in the full neural space; that is, Pearson’s correlation ρ such as that reported in **c**, left), computed at 250-ms steps using a 1-s sliding window along the odour response epoch. Grey box, 4-s odorant stimulus epoch; vertical dotted line, onset of odour response at odour port (mean time across all stimuli at which the PID signal reached 5% of max). Right, correlation coefficients for normalized matrix dissimilarity versus time interval computed using 15 temporal binnings of the odour response epoch. **e**, As in **d** but using edge angles rather than correlations. This effect also holds when using responses projected onto the data’s first six principal components, as well as using cosine distance rather than Pearson’s correlation (data not shown).

[Extended Data Fig. 9 Drift in response geometry in the odour coding subspace.](#)

a, Left, percentage of total variance explained by each demixed principal component (dPC)²⁸ from an example mouse; middle, fraction of total stimulus (red) and condition-independent (blue) variance explained for this example mouse; right, total variance explained by stimulus dPCs (red, 78.4% (95% CI 76.0%, 79.8%)) and condition-independent dPCs (blue,

21.6% (95% CI 20.2%, 23.7%) for the $n = 3$ mice shown a panel of 8 odorant stimuli. Dark red, variance explained by the first ten dPCs that were primarily stimulus coding (45% (41.8%, 48.6%)). Error bars, 95% CI. **b**, Odour–odour correlation matrices from the example mouse computed after projecting responses onto the data’s first ten stimulus-coding dPCs, computed separately on each day (top row) and then (bottom two rows) using complementary splits of the trials recorded on each day. **c**, Correlation matrix dissimilarity (scaled Frobenius norm; see [Methods](#)) for all mice, using responses projected onto the data’s first ten stimulus-coding dPCs. **d**, Edge angle matrices from the example mouse computed after projecting responses onto the data’s first ten stimulus-coding dPCs. **e**, Across-day edge angle matrix dissimilarity (scaled Frobenius norm; see [Methods](#)) for all mice, using responses projected onto the data’s first ten stimulus-coding dPCs. Black crosses, mean \pm 95% CI; blue dotted line, linear regression; blue shading, 95% CI.

[Extended Data Fig. 10 Effect of fear conditioning and familiarity on drift.](#)

a, Conditioning experiment. Day –1: present one odorant paired with shock (CS+) and a second without shock (CS–) in a conditioning chamber. Days 0 and 16: administer conditioned (CS+ and CS–) and four additional neutral odorants to head-fixed mouse while recording neural signals and measuring behavioural responses in a virtual burrow assay²⁹. Days 1–15: record neural signals in head-fixed mouse without test odorant administration. **b**, Behaviour. Left, trial-averaged ingress amplitude ($n = 5$ mice) across time on days 0 and 16 on trial blocks 2–7 (shading, 95% CI). Grey bar, 4-s odorant stimulus epoch. Right, mean \pm 95% CI ingress amplitude during the final second of the odorant epoch on blocks 2–7. For days 0 and 16, CS+ versus CS– and CS+ versus neutral, $P < 1.4 \times 10^{-3}$, Wilcoxon rank-sum. **c**, Neurophysiology. Left, scatter plots showing single-unit response magnitude for all three stimulus classes (mean spontaneous baseline-subtracted evoked responses computed during the odorant stimulus epoch) of odour–unit pairs on day 0 versus day 16 (CS+: $n = 148$ odour–unit pairs, CS–: $n = 129$ odour–unit pairs, neutral stimuli: $n = 482$ odour–unit pairs, data pooled across 5 mice). Black dashed line, unity; blue dotted line, linear regression; blue shading, 95% CI. Regression was performed across all

odour–unit pairs that showed a significantly modulated response on at least one of the two days (Wilcoxon rank-sum, $\alpha = 0.001$). Middle, cumulative distributions; right, mean \pm 95% CI ($n = 5$ mice) of corrected angles for all three classes of stimulus. For all comparisons, $P > 0.05$ (Wilcoxon rank-sum). We note that classical conditioning reduces within-day variability (unpublished observations). Thus, the odour–unit pair response correlations reported here, which are not corrected for within-day variability, are higher than in other experiments (for example, Fig. 2a), but measures that correct for within-day variability, such as corrected angle or drift rate, are comparable. **d**, Familiarity experiment. Mice were presented with a panel of four neutral odorants daily over a 32-day interval (days –16 to 16; familiar). Starting on day 0, a panel of unfamiliar odorants was presented at 8-day intervals. **e**, Mean odour-evoked response magnitude (spontaneous baseline-subtracted, computed during the odorant stimulus epoch) of odour–unit pairs across intervals of 8 days (left, familiar odorants: $n = 741$ odour–unit pairs, unfamiliar odorants: $n = 1,137$ odour–unit pairs) and 16 days (right, familiar odorants: $n = 371$ odour–unit pairs, unfamiliar odorants: $n = 570$ odour–unit pairs), data pooled across 5 mice. Black dashed line, unity; blue dotted line, linear regression; blue shading, 95% CI. Regression was performed across all odour–unit pairs that showed a significantly modulated response on at least one of the two days (Wilcoxon rank-sum, $\alpha = 0.001$). **f**, Across-day classification accuracy (4-way, SVM, linear kernel, L2 regularization, scaled between chance and maximum within-day performance to account for slight differences in within-day performance between the two conditions). Solid lines, mean; shading, 95% CI. **g, h**, Cumulative distribution (**g**) and mean \pm 95% CI (**h**) of corrected angles from $n = 5$ mice. Unfamiliar, $\rho = 0.48$, $P = 1.0 \times 10^{-4}$; familiar, $\rho = 0.23$, $P = 0.08$.

Supplementary information

Supplementary Information

This file contains a Supplementary Discussion and Supplementary References.

Reporting Summary

Peer Review File

Rights and permissions

Reprints and Permissions

About this article



Check for
updates

Cite this article

Schoonover, C.E., Ohashi, S.N., Axel, R. *et al.* Representational drift in primary olfactory cortex. *Nature* **594**, 541–546 (2021).
<https://doi.org/10.1038/s41586-021-03628-7>

Download citation

- Received: 02 September 2020
- Accepted: 11 May 2021
- Published: 09 June 2021
- Issue Date: 24 June 2021
- DOI: <https://doi.org/10.1038/s41586-021-03628-7>

Comments

By submitting a comment you agree to abide by our [Terms](#) and [Community Guidelines](#). If you find something abusive or that does not comply with our terms or guidelines please flag it as inappropriate.

[Access through your institution](#)

[Change institution](#)

[Buy or subscribe](#)

Advertisement

This article was downloaded by **calibre** from <https://www.nature.com/articles/s41586-021-03628-7>

| [Section menu](#) | [Main menu](#) |

- Article
- [Published: 09 June 2021](#)

Tracing the origin of hair follicle stem cells

- [Ritsuko Morita](#) ORCID: [orcid.org/0000-0001-6550-8778¹](https://orcid.org/0000-0001-6550-8778),
- [Noriko Sanzen](#) ORCID: [orcid.org/0000-0001-6518-403X¹](https://orcid.org/0000-0001-6518-403X),
- [Hiroko Sasaki](#) ORCID: [orcid.org/0000-0002-4216-6637¹](https://orcid.org/0000-0002-4216-6637),
- [Tetsutaro Hayashi](#) ORCID: [orcid.org/0000-0003-1679-5525²](https://orcid.org/0000-0003-1679-5525),
- [Mana Umeda](#)²,
- [Mika Yoshimura](#)²,
- [Takaki Yamamoto](#) ORCID: [orcid.org/0000-0002-4321-5269^{3,4}](https://orcid.org/0000-0002-4321-5269),
- [Tatsuo Shibata](#) ORCID: [orcid.org/0000-0002-9294-9998⁴](https://orcid.org/0000-0002-9294-9998),
- [Takaya Abe](#) ORCID: [orcid.org/0000-0001-5885-4875⁵](https://orcid.org/0000-0001-5885-4875),
- [Hiroshi Kiyonari](#) ORCID: [orcid.org/0000-0002-1509-8747⁵](https://orcid.org/0000-0002-1509-8747),
- [Yasuhide Furuta](#) ORCID: [orcid.org/0000-0002-2094-379X^{5,6}](https://orcid.org/0000-0002-2094-379X),
- [Itoshi Nikaido](#) ORCID: [orcid.org/0000-0002-7261-2570^{2,7,8}](https://orcid.org/0000-0002-7261-2570) &
- [Hironobu Fujiwara](#) ORCID: [orcid.org/0000-0003-0883-3384¹](https://orcid.org/0000-0003-0883-3384)

[Nature](#) volume 594, pages 547–552 (2021) [Cite this article](#)

- 8091 Accesses
- 130 Altmetric
- [Metrics details](#)

Subjects

- [Organogenesis](#)
- [Skin stem cells](#)

Abstract

Tissue stem cells are generated from a population of embryonic progenitors through organ-specific morphogenetic events^{1,2}. Although tissue stem cells are central to organ homeostasis and regeneration, it remains unclear how they are induced during development, mainly because of the lack of markers that exclusively label prospective stem cells. Here we combine marker-independent long-term 3D live imaging and single-cell transcriptomics to capture a dynamic lineage progression and transcriptome changes in the entire epithelium of the mouse hair follicle as it develops. We found that the precursors of different epithelial lineages were aligned in a 2D concentric manner in the basal layer of the hair placode. Each concentric ring acquired unique transcriptomes and extended to form longitudinally aligned, 3D cylindrical compartments. Prospective bulge stem cells were derived from the peripheral ring of the placode basal layer, but not from suprabasal cells (as was previously suggested³). The fate of placode cells is determined by the cell position, rather than by the orientation of cell division. We also identified 13 gene clusters: the ensemble expression dynamics of these clusters drew the entire transcriptional landscape of epithelial lineage diversification, consistent with cell lineage data. Combining these findings with previous work on the development of appendages in insects^{4,5}, we describe the ‘telescope model’, a generalized model for the development of ectodermal organs in which 2D concentric zones in the placode telescope out to form 3D longitudinally aligned cylindrical compartments.

Access options

Subscribe to Journal

Get full journal access for 1 year

\$199.00

only \$3.90 per issue

Subscribe

All prices are NET prices.

VAT will be added later in the checkout.

Tax calculation will be finalised during checkout.

Rent or Buy article

Get time limited or full article access on ReadCube.

from \$8.99

Rent or Buy

All prices are NET prices.

Additional access options:

- [Log in](#)
- [Access through your institution](#)
- [Learn about institutional subscriptions](#)

Fig. 1: Bulge stem cells are derived from the periphery of the placode basal layer.

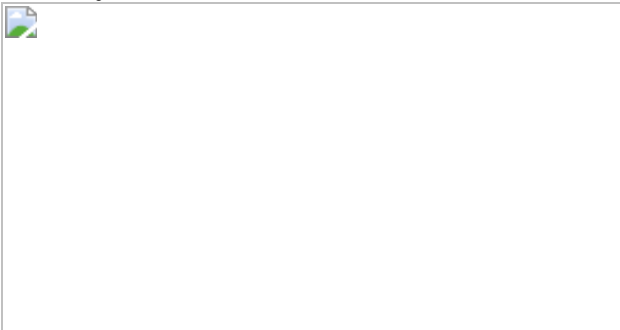


Fig. 2: Cell fate determination relies on cell position.

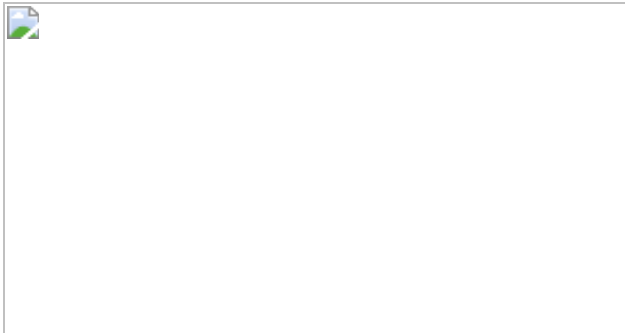


Fig. 3: Two-dimensional concentric transcriptional landscape characterizes stem cell origin.

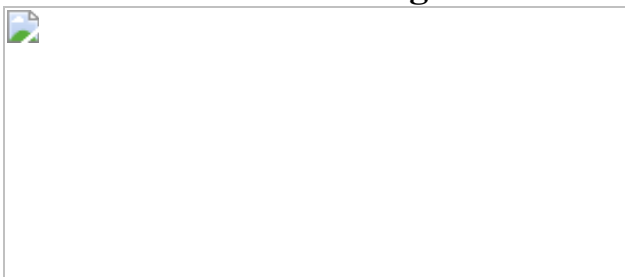
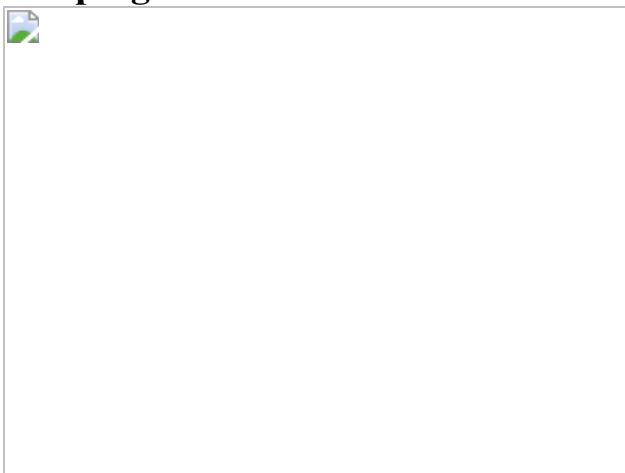


Fig. 4: Transcriptional landscape that underlies coordinated diversification of epithelial lineages and stem cell induction in the developing hair follicle.



Data availability

Live imaging data in this study have been deposited in the SSBD repository at <https://doi.org/10.24631/ssbd.repos.2020.06.002> and <http://ssbd.qbic.riken.jp/set/20200602/>. The scRNA-seq data in this study have been deposited in the Gene Expression Omnibus under accession code [GSE147372](#). The mouse genome (mm10) used in this study is available at

<https://genome.ucsc.edu/>. The web-based tool Enrichr is available at <https://maayanlab.cloud/Enrichr/>. The KEGG PATHWAY database is available at <https://www.genome.jp/kegg/>. Any other relevant data are available from the corresponding author upon reasonable request. [Source data](#) are provided with this paper.

Code availability

Scripts used for scRNA-seq analysis are available at https://github.com/FujiwaraLab/Morita_et_al_2021 and source code for analysis of the cell division orientation in live imaging data is available at <https://github.com/RIKEN-PHB/Morita-Paper-Spindle-Analysis>.

References

1. 1.

Xin, T., Greco, V. & Myung, P. Hardwiring stem cell communication through tissue structure. *Cell* **164**, 1212–1225 (2016).

[CAS](#) [Article](#) [Google Scholar](#)

2. 2.

Guiu, J. et al. Tracing the origin of adult intestinal stem cells. *Nature* **570**, 107–111 (2019).

[ADS](#) [CAS](#) [Article](#) [Google Scholar](#)

3. 3.

Ouspenskaia, T., Matos, I., Mertz, A. F., Fiore, V. F. & Fuchs, E. WNT–SHH antagonism specifies and expands stem cells prior to niche formation. *Cell* **164**, 156–169 (2016).

[Article](#) [Google Scholar](#)

4. 4.

Lecuit, T. & Cohen, S. M. Proximal–distal axis formation in the *Drosophila* leg. *Nature* **388**, 139–145 (1997).

[Article](#) [Google Scholar](#)

5. 5.

Ruiz-Losada, M., Blom-Dahl, D., Córdoba, S. & Estella, C. Specification and patterning of *Drosophila* appendages. *J. Dev. Biol.* **6**, E17 (2018).

[Article](#) [Google Scholar](#)

6. 6.

Pispa, J. & Thesleff, I. Mechanisms of ectodermal organogenesis. *Dev. Biol.* **262**, 195–205 (2003).

[CAS](#) [Article](#) [Google Scholar](#)

7. 7.

Fujiwara, H., Tsutsui, K. & Morita, R. Multi-tasking epidermal stem cells: beyond epidermal maintenance. *Dev. Growth Differ.* **60**, 531–541 (2018).

[Article](#) [Google Scholar](#)

8. 8.

Solanas, G. & Benitah, S. A. Regenerating the skin: a task for the heterogeneous stem cell pool and surrounding niche. *Nat. Rev. Mol. Cell Biol.* **14**, 737–748 (2013).

[CAS](#) [Article](#) [Google Scholar](#)

9. 9.

Nowak, J. A., Polak, L., Pasolli, H. A. & Fuchs, E. Hair follicle stem cells are specified and function in early skin morphogenesis. *Cell Stem Cell* **3**, 33–43 (2008).

[Article](#) [Google Scholar](#)

10. 10.

Liu, Y., Lyle, S., Yang, Z. & Cotsarelis, G. Keratin 15 promoter targets putative epithelial stem cells in the hair follicle bulge. *J. Invest. Dermatol.* **121**, 963–968 (2003).

[CAS](#) [Article](#) [Google Scholar](#)

11. 11.

Rhee, H., Polak, L. & Fuchs, E. Lhx2 maintains stem cell character in hair follicles. *Science* **312**, 1946–1949 (2006).

[ADS](#) [CAS](#) [Article](#) [Google Scholar](#)

12. 12.

Horsley, V., Aliprantis, A. O., Polak, L., Glimcher, L. H. & Fuchs, E. NFATc1 balances quiescence and proliferation of skin stem cells. *Cell* **132**, 299–310 (2008).

[CAS](#) [Article](#) [Google Scholar](#)

13. 13.

Xu, Z. et al. Embryonic attenuated Wnt/β-catenin signaling defines niche location and long-term stem cell fate in hair follicle. *eLife* **4**, e10567 (2015).

[Article](#) [Google Scholar](#)

14. 14.

Morita, R. et al. Coordination of cellular dynamics contributes to tooth epithelium deformations. *PLoS ONE* **11**, e0161336 (2016).

[Article](#) [Google Scholar](#)

15. 15.

Tsutsui, H., Karasawa, S., Shimizu, H., Nukina, N. & Miyawaki, A. Semi-rational engineering of a coral fluorescent protein into an efficient highlighter. *EMBO Rep.* **6**, 233–238 (2005).

[CAS](#) [Article](#) [Google Scholar](#)

16. 16.

Hayashi, T. et al. Single-cell full-length total RNA sequencing uncovers dynamics of recursive splicing and enhancer RNAs. *Nat. Commun.* **9**, 619 (2018).

[ADS](#) [Article](#) [Google Scholar](#)

17. 17.

Qiu, X. et al. Single-cell mRNA quantification and differential analysis with Census. *Nat. Methods* **14**, 309–315 (2017).

[CAS](#) [Article](#) [Google Scholar](#)

18. 18.

Qiu, X. et al. Reversed graph embedding resolves complex single-cell trajectories. *Nat. Methods* **14**, 979–982 (2017).

[CAS](#) [Article](#) [Google Scholar](#)

19. 19.

Huelsken, J., Vogel, R., Erdmann, B., Cotsarelis, G. & Birchmeier, W. β -Catenin controls hair follicle morphogenesis and stem cell

differentiation in the skin. *Cell* **105**, 533–545 (2001).

[CAS](#) [Article](#) [Google Scholar](#)

20. 20.

Närhi, K. et al. Sostdc1 defines the size and number of skin appendage placodes. *Dev. Biol.* **364**, 149–161 (2012).

[Article](#) [Google Scholar](#)

21. 21.

Kandyba, E. et al. Competitive balance of intrabulge BMP/Wnt signaling reveals a robust gene network ruling stem cell homeostasis and cyclic activation. *Proc. Natl Acad. Sci. USA* **110**, 1351–1356 (2013).

[ADS](#) [CAS](#) [Article](#) [Google Scholar](#)

22. 22.

Genander, M. et al. BMP signaling and its pSMAD1/5 target genes differentially regulate hair follicle stem cell lineages. *Cell Stem Cell* **15**, 619–633 (2014).

[CAS](#) [Article](#) [Google Scholar](#)

23. 23.

Joost, S. et al. Single-cell transcriptomics reveals that differentiation and spatial signatures shape epidermal and hair follicle heterogeneity. *Cell Syst.* **3**, 221–237 (2016).

[CAS](#) [Article](#) [Google Scholar](#)

24. 24.

Kandyba, E., Hazen, V. M., Kobielski, A., Butler, S. J. & Kobielski, K. Smad1 and 5 but not Smad8 establish stem cell quiescence which is critical to transform the premature hair follicle during morphogenesis toward the postnatal state. *Stem Cells* **32**, 534–547 (2014).

[CAS](#) [Article](#) [Google Scholar](#)

25. 25.

Saxena, N., Mok, K. W. & Rendl, M. An updated classification of hair follicle morphogenesis. *Exp. Dermatol.* **28**, 332–344 (2019).

[Article](#) [Google Scholar](#)

26. 26.

Maini, P. K., Baker, R. E. & Chuong, C. M. The Turing model comes of molecular age. *Science* **314**, 1397–1398 (2006).

[CAS](#) [Article](#) [Google Scholar](#)

27. 27.

Ahtiainen, L. et al. Directional cell migration, but not proliferation, drives hair placode morphogenesis. *Dev. Cell* **28**, 588–602 (2014).

[CAS](#) [Article](#) [Google Scholar](#)

28. 28.

Glover, J. D. et al. Hierarchical patterning modes orchestrate hair follicle morphogenesis. *PLoS Biol.* **15**, e2002117 (2017).

[Article](#) [Google Scholar](#)

29. 29.

Abe, T. et al. Establishment of conditional reporter mouse lines at ROSA26 locus for live cell imaging. *Genesis* **49**, 579–590 (2011).

[CAS](#) [Article](#) [Google Scholar](#)

30. 30.

Vassar, R., Rosenberg, M., Ross, S., Tyner, A. & Fuchs, E. Tissue-specific and differentiation-specific expression of a human K14 keratin gene in transgenic mice. *Proc. Natl Acad. Sci. USA* **86**, 1563–1567 (1989).

[ADS](#) [CAS](#) [Article](#) [Google Scholar](#)

31. 31.

Sakaue-Sawano, A. et al. Visualizing spatiotemporal dynamics of multicellular cell-cycle progression. *Cell* **132**, 487–498 (2008).

[CAS](#) [Article](#) [Google Scholar](#)

32. 32.

Biggs, L. C. et al. Hair follicle dermal condensation forms via Fgf20 primed cell cycle exit, cell motility, and aggregation. *eLife* **7**, e36468 (2018).

[Article](#) [Google Scholar](#)

33. 33.

Stuart, T. et al. Comprehensive integration of single-cell data. *Cell* **177**, 1888–1902 (2019).

[CAS](#) [Article](#) [Google Scholar](#)

34. 34.

La Manno, G. et al. RNA velocity of single cells. *Nature* **560**, 494–498 (2018).

[ADS](#) [Article](#) [Google Scholar](#)

35. 35.

Angerer, P. et al. destiny: diffusion maps for large-scale single-cell data in R. *Bioinformatics* **32**, 1241–1243 (2016).

[CAS](#) [Article](#) [Google Scholar](#)

36. 36.

Street, K. et al. Slingshot: cell lineage and pseudotime inference for single-cell transcriptomics. *BMC Genomics* **19**, 477 (2018).

[Article](#) [Google Scholar](#)

37. 37.

Yu, G., Wang, L. G., Han, Y. & He, Q. Y. clusterProfiler: an R package for comparing biological themes among gene clusters. *OMICS* **16**, 284–287 (2012).

[CAS](#) [Article](#) [Google Scholar](#)

38. 38.

Nakao, K. et al. The development of a bioengineered organ germ method. *Nat. Methods* **4**, 227–230 (2007).

[CAS](#) [Article](#) [Google Scholar](#)

[Download references](#)

Acknowledgements

We thank S. Kuraku and O. Nishimura for assistance with RNA sequencing and data processing; the RIKEN Genome Network Analysis Support Facility (GeNAS) for RNA sequencing; RIKEN Kobe Light Microscopy Facility, Laboratory for Animal Resources and Genetic Engineering and Unit for Four-Dimensional Tissue Analysis for technical assistance; F.

Matsuzaki for critical reading of the manuscript; T. Matsuzaki for an important suggestion related to the telescope model; S. Onami for discussions; M. Morimoto for providing a mouse line; A. Iijima for help with cell tracking analysis; and A. Matsushima and M. Ishii for their assistance with the infrastructure for the data analysis. This work was supported by a RIKEN intramural grant, the RIKEN Single Cell Project, the Platform Project for Supporting in Drug Discovery and Life Science Research from MEXT and AMED and the JST CREST program (JPMJCR1926) to H.F. and JSPS Grant-in-Aid for Young Scientists (B) (15K19709 and 17K16361), JSPS Grant-in-Aid for Scientific Research (C) (19K08763), the RIKEN BDR-Otsuka Pharmaceutical Collaboration Center (RBOC) founding program and a Shiseido Female Researcher Science Grant to R.M. This work was partially supported by JST CREST grant number JPMJCR16G3 to I.N.

Author information

Affiliations

1. Laboratory for Tissue Microenvironment, RIKEN Center for Biosystems Dynamics Research, Kobe, Japan

Ritsuko Morita, Noriko Sanzen, Hiroko Sasaki & Hironobu Fujiwara

2. Laboratory for Bioinformatics Research, RIKEN Center for Biosystems Dynamics Research, Kobe, Japan

Tetsutaro Hayashi, Mana Umeda, Mika Yoshimura & Itoshi Nikaido

3. Nonequilibrium Physics of Living Matter RIKEN Hakubi Research Team, RIKEN Center for Biosystems Dynamics Research, Kobe, Japan

Takaki Yamamoto

4. Laboratory for Physical Biology, RIKEN Center for Biosystems Dynamics Research, Kobe, Japan

Takaki Yamamoto & Tatsuo Shibata

5. Laboratory for Animal Resources and Genetic Engineering, RIKEN Center for Biosystems Dynamics Research, Kobe, Japan

Takaya Abe, Hiroshi Kiyonari & Yasuhide Furuta

6. Mouse Genetics Core Facility, Sloan Kettering Institute, Memorial Sloan Kettering Cancer Center, New York, NY, USA

Yasuhide Furuta

7. Master's and Doctoral Program in Life Science Innovation (Bioinformatics), Degree Programs in Systems and Information Engineering, Graduate School of Science and Technology, University of Tsukuba, Tsukuba, Japan

Itoshi Nikaido

8. Functional Genome Informatics, Medical Research Institute, Tokyo Medical and Dental University, Tokyo, Japan

Itoshi Nikaido

Authors

1. Ritsuko Morita

[View author publications](#)

You can also search for this author in [PubMed](#) [Google Scholar](#)

2. Noriko Sanzen

[View author publications](#)

You can also search for this author in [PubMed](#) [Google Scholar](#)

3. Hiroko Sasaki

[View author publications](#)

You can also search for this author in [PubMed](#) [Google Scholar](#)

4. Tetsutaro Hayashi

[View author publications](#)

You can also search for this author in [PubMed](#) [Google Scholar](#)

5. Mana Umeda

[View author publications](#)

You can also search for this author in [PubMed](#) [Google Scholar](#)

6. Mika Yoshimura

[View author publications](#)

You can also search for this author in [PubMed](#) [Google Scholar](#)

7. Takaki Yamamoto

[View author publications](#)

You can also search for this author in [PubMed](#) [Google Scholar](#)

8. Tatsuo Shibata

[View author publications](#)

You can also search for this author in [PubMed](#) [Google Scholar](#)

9. Takaya Abe

[View author publications](#)

You can also search for this author in [PubMed](#) [Google Scholar](#)

10. Hiroshi Kiyonari

[View author publications](#)

You can also search for this author in [PubMed](#) [Google Scholar](#)

11. Yasuhide Furuta

[View author publications](#)

You can also search for this author in [PubMed](#) [Google Scholar](#)

12. Itoshi Nikaido

[View author publications](#)

You can also search for this author in [PubMed](#) [Google Scholar](#)

13. Hironobu Fujiwara

[View author publications](#)

You can also search for this author in [PubMed](#) [Google Scholar](#)

Contributions

R.M. and H.F. conceived the project, designed experiments and wrote the manuscript. R.M. performed most of the experiments and bioinformatics and analysed the data. N.S. and H.S. assisted with cell tracking analysis and histological analysis. T.H. and M.U. performed the library preparation for the RamDA-seq. M.Y. and R.M. performed the bioinformatics analyses. I.N. supervised scRNA-seq experiments and bioinformatics analyses. T.Y. and T.S. provided the custom Python program to analyse the orientation of cell division. T.A., H.K. and Y.F. generated *R26-CAG-nKikGR*, *R26R-CAG-nKikGR* and *K14-H2B-eGFP* mice, and assisted with mouse experiments. H.F. supervised the project.

Corresponding author

Correspondence to [Hironobu Fujiwara](#).

Ethics declarations

Competing interests

The authors declare no competing interests.

Additional information

Peer review information *Nature* thanks Maria Kasper, Michael Rendl and the other, anonymous, reviewer(s) for their contribution to the peer review of this work. Peer reviewer reports are available.

Publisher's note Springer Nature remains neutral with regard to jurisdictional claims in published maps and institutional affiliations.

Extended data figures and tables

[Extended Data Fig. 1 Origin and early lineage of bulge stem cells cannot be traced by expression of known adult stem cell markers.](#)

a–g, Immunohistochemistry of developing whisker hair follicles (HFs) for known stem cell (SC) markers at E12.0 (**a**, early hair placode), E12.5 (**b**, late hair placode), E13.0 (**c**, hair germ), E14.0 (**d**), E15.0 (**e**), E17.0 (**f**) and post-natal day (P)5 (**g**). LHX2 was expressed in the basal cells of the placode, while K15 and SOX9 were detected in suprabasal and peripheral basal cells of the placode (**a**). At the late placode stage (E12.5), SOX9 was strongly expressed in the flat suprabasal cells of the placode (arrows in **b**) and also in some basal cells located near the placode periphery (arrowheads in **b**). NFATc1 was undetectable throughout these stages (**a, b**). Thus, at the onset of HF morphogenesis, the expression patterns of adult SC markers vary and there is no clear region in which all SC markers overlap. From the hair germ stage (E13.0) onward, NFATc1 appeared in whisker HFs, and its expression was always restricted to the upper region of the HF (**c–g**). NFATc1-positive epithelial cells formed a compartment with pseudo-stratified (see **h**) and bulge-like morphology (**d–g**) with gradual loss of the expression of mitotic marker Ki67 during follicle development (**a–g**), which are typical characteristics of adult bulge HFSCs. SOX9 and LHX2 expression also became restricted to the middle to upper part of the HF after E14.0 (**d–g**). The expression patterns of SC markers in E17.0 follicles were almost equivalent to those seen in the upper half of P5 mature follicles, in which a large bulge-like epithelial structure was evident (brackets in **f, g**). Taken together, these results indicate that basal epithelial cells acquire compartmentalized SC marker expression patterns of the mature bulge by

E17.0 in whisker HFs. The origin and early lineage of bulge SCs cannot be traced by following the expression of known adult SC markers because of their wide variation in expression patterns of the hair placode, hair germ and bulbous peg stages. Thus, at present, there is no marker that can exclusively label the origin and early lineage of prospective SCs from the placode stage. Scale bars, 100 μ m. **h**, Three-dimensional-reconstructed z -stack images from whisker HFs derived from *KRT5-cre;R26R-Lyn-Venus;R26-H2B-mCherry* at E14.0. Cell membranes were sparsely labelled by Venus. Arrowheads indicate the pseudo-stratified epithelium. Scale bar, 50 μ m. **i**, Summary of known SC marker expressions in the developing whisker HF. **j–n**, Immunohistochemistry of developing dorsal HFs for known SC markers at E14.5 (**j**, hair placode), E15.5 (**k**, hair germ), E16.5 (**l**), E17.5 (**m**) and E19.5 (**n**). SOX9-positive cells were localized in the suprabasal layer (arrows in **j**) and in the basal layer near the placode periphery (arrowheads in **j**) in the dorsal HF placode as observed in the whisker HF placode. Morphogenetic events and marker expression patterns closely resemble those of whisker HFs. Scale bars, 50 μ m.

Extended Data Fig. 2 Ex vivo culture system of developing whisker HFs.

a, Strategy to identify the origin and lineage dynamics of HF epithelial cells. **b**, Photographs of ex vivo cultured whisker pad derived from E11.5 *K14-rtTA;TetO-H2B-eGFP;Fucci-G1* mice on day 0 and day 7. Scale bars, 100 μ m. **c**, Immunostaining of whisker HFs derived from E11.5 embryos on day 6 of ex vivo culture. Antibodies detected upper (NFATc1 $^+$ SOX9 $^+$ LHX2 $^+$) and lower (KRT15 $^+$ SOX9 $^+$ LHX2 $^+$) stem cell compartments, proliferative cells (Ki67 $^+$), sebaceous glands (SCD1 $^+$), hair matrix (CDH3 $^+$), dermal sheaths (SMA $^+$) and dermal papilla cells (SOX2 $^+$). Scale bars, 50 μ m. **d**, Immunostaining of day-6 ex vivo cultured whisker HFs derived from E11.5 embryos for hair cell layer markers shown in the left panel. Ex vivo developing whisker HFs had unique cellular layers characteristic of HFs, except for the medulla, which is formed in mature HFs. HS, hair shaft; IRS, inner root sheath; ORS, outer root sheath. Scale bars, 50 μ m.

Extended Data Fig. 3 Identification of the origin and lineage dynamics of HF epithelial cells by long-term live imaging.

a, Schema of epithelial cell subpopulations at the hair germ stage, which we defined for cell tracking. Magenta, IFE basal cells; red, basal cells located in the upper half of the HF; yellow, basal cells located in the lower half of the HF; blue, cells adjacent to the dermal papilla; green, suprabasal cells in the IFE or HF. **b**, Lineage tree reconstructed from tracking of a hair germ cell and its progeny. The *x* axis shows the duration of imaging. Lineage is colour-coded based on cell fate, and cell fate was identified based on the cell position in tissue. Scale bars, 50 μ m. **c**, Examples of lineage trees of tracked upper, lower and hair germ cells in Fig. 1a. **d, e**, HF development is accomplished by enlarging each earlier compartment longitudinally aligned in the follicle epithelium. Data of replicate whisker HFs related to Fig. 1a, b are shown. **d**, Snapshot images (top panels) and lineage tracking data (bottom panels) of long-term continuous imaging of whisker HF development from the hair germ to bulbous peg stage. Different epithelial lineages were longitudinally aligned as 3D cylindrical compartments in HFs, and prospective bulge SCs were located in the upper part of the HF as shown in Fig. 1a (replicate no. 1, represented in the main figure). Scale bars, 100 μ m. **e**, Cell fates of epithelial cells in the IFE, upper, lower, hair germ and inner regions of the hair germ stage. Cell fates at the bulbous peg stage are shown. **f**, Bar plot converted from stacked bar plot of Fig. 1b. Statistical analysis was performed by one-way ANOVA followed by Tukey's test. **g–i**, Different epithelial lineages are aligned in a concentric manner in the placode. Replicate whisker HFs related to Fig. 1c–e are shown in g–i. **g**, Snapshot images (top panels) and lineage tracking data (bottom panels) of long-term continuous imaging of whisker HF development from the placode stage to hair germ stage. Origin of prospective bulge SCs (red) was located at the periphery of the hair placode as shown in Fig. 1c (replicate no. 1, represented in the main figure). Scale bars, 50 μ m. **h**, Bee swarm plot showing the distances of cells from the placode centre. Different epithelial lineages were aligned in a concentric manner in the placode. Statistical analysis was performed by two-sided unpaired *t*-test. **i**, Fate of basal and suprabasal cells of the hair placode stage. Cell fates at the hair germ stage are shown. **j**, Summary of the developmental origins and lineage dynamics of HF epithelial cells. The

embryonic stage at which imaging started is indicated in each figure. Each value in the graph is the mean \pm s.d. from three independent experiments, one HF each. Numbers of analysed cell lineages are summarized in Supplementary Table 1. See also ‘Statistical analysis and reproducibility’ in Methods and Source Data.

Extended Data Fig. 4 Measurement of cell division angles in the developing epithelium.

In 3D live imaging data, morphology of the developing epithelium was changing constantly. Accordingly, the basement membrane zone was also bending, but not flat. Therefore, we calculated the cell division orientation relative to the basement membrane zone in the developing epithelium three-dimensionally as shown here. **a**, We first marked the dividing cells in the placode and surrounding IFE in live imaging data, based on chromosome condensation. Examples of a perpendicular (left panels) and horizontal division (middle panels) relative to the basement membrane zone, which were pseudo-coloured in blue; the mitotic spindle axis is indicated by a cyan line connecting the daughter-cell nuclei. The top panels are a planar view images of the epithelium, and the bottom panels are sagittal view images of the epithelium. The placode region in the epithelium was distinguished by accumulation of Fucci-G1 signals accompanied by condensation and cell cycle arrest of the underlying dermal cells, as shown by the dashed circle in the right panel. Scale bars, 20 μm . **b**, To extract positional information of the basement membrane zone, we next obtained the surface of the developing epithelium based on expression of *K14-H2B-eGFP* using the surface rendering function in Imaris. A surface object in Imaris was constructed as a mesh object consisting of triangles and vertex normal vectors. Then, based on the direction of the normal vectors, we cut the surface of the opposite side of the basement membrane zone (outer surface of the epithelium) and substituted the remaining dermis-side surface for the basement membrane zone. **c**, We calculated the 3D orientation of cell division to the basement membrane zone using x - y - z axis coordinates of the mitotic spindle axis and basement membrane zone. In brief, we first found the closest vertex and its associated normal unit vector on the dermis-side surface by calculating the distance between the centre of a mitotic spindle and each vertex. The cell division angle to the basement membrane

zone was then calculated from an inner product of the closest vertex normal unit vector and the unit vector corresponding to a mitotic spindle.

Extended Data Fig. 5 Placode cell fate is determined by cell position but not cell division orientation.

a, b, Bar plots were converted from the stacked bar plot in Fig. 2a, b, respectively. Statistical analysis was performed by one-way ANOVA followed by Tukey's test. **c**, Upper and lower daughter cells after perpendicular division in late placode basal layer are marked by LHX2, while the SOX9⁺ suprabasal nuclei are not labelled with LHX2. This suggests that upper daughter cells hold transcriptional similarity to the basal layer and remain in the pseudo-stratified basal layer. E14.5 dorsal HFs in embryonic skin tissue (not explants) were immunostained for SOX9 and LHX2. Cell division was identified by chromosome condensation. Dashed box shows magnified region (right panels). BM, basement membrane; DP, dermal papilla; U, upper daughter cell; L, lower daughter cell. Scale bars, 50 μ m. **d, e**, Localization of SOX9⁺ cells in HF placodes in vivo. E14.5 dorsal HFs (d) and E12.0 whisker HFs (e) in embryonic skin tissues (not explants) were immunostained for SOX9 and CDH3. Hair placodes were detected with CDH3 expression or Fucci-G1 probe fluorescence signals. SOX9 expressions were detected not only in flat suprabasal cells (cyan arrowheads) but also in basal cells (yellow arrowheads) located at the periphery of the hair placode. Scale bars, 50 μ m. **f**, Photographs of ex vivo cultured dorsal skin of E12.5 *K14-rtTA; TetO-H2B-eGFP; Fucci-G1* mice on days 0, 2, 3 and 10. Yellow open arrowheads and filled arrowheads indicate first-wave and second-wave hair placodes, respectively. Dashed box shows magnified region (right). Scale bars, 100 μ m. **g**, Immunostaining of dorsal HFs in day-9 ex vivo culture of E12.5 dorsal skin. The following tissue compartments were detected: bulge stem cells (NFATc1⁺SOX9⁺NPNT⁺KRT15⁺), sebaceous glands (LipidTOX⁺), hair matrix (CDH3⁺), dermal sheaths (SMA⁺), dermal papilla cells (SOX2⁺) and melanocyte (TRP2⁺). Scale bars, 50 μ m. **h**, Immunostaining of day-9 ex vivo cultured dorsal HFs derived from E12.5 embryos for hair cell layer markers shown in Extended Data Fig. 2d. Ex vivo developing dorsal HFs had distinct cellular layers characteristic of HFs except for the medulla,

which is formed in mature HFs. Scale bars, 50 µm. **i**, Lineage tracking data of long-term continuous imaging of dorsal HF development from the placode stage to the hair germ stage, which correspond to the bottom panels in Fig. [2c](#). Origin of prospective bulge SCs (red) was located at the periphery of the hair placode as observed in the whisker HF placode. Scale bars, 50 µm. **j**, Bee swarm plot of the distances of dorsal hair placode cells from the placode centre. HFs used for measurement were from cultured dorsal HFs of *K14-rtTA; TetO-H2B-eGFP; Fucci-G1* and *Sox9^{IRES-eGFP/+; R26-H2B-mCherry}* mice. Values were scaled based on the diameter of each placode. Different epithelial lineages were aligned in a concentric manner in the placode. Two-sided nested *t*-test was used. **k**, Fate of basal and suprabasal cells in the dorsal HF placode analysed in **i**. Cell fates at the hair germ stage are shown. Summarized data are shown in the left panel, and the data for corresponding replicate HFs are shown in the right panels. Two-sided Fisher's exact test was used. **l**, Stacked bar plots showing the lineage distribution of placode basal cells in the dorsal HF at the hair germ stage. Cells grouped in the black bar in **k** were examined. Summarized data are shown in the left panel, and the data for corresponding replicate HFs are shown in the right panel. **m–o**, Replicate HFs related to Fig. [2d–f](#) are shown in **m–o**. **m**, Fate of basal and suprabasal cells in pre-placodes of *Sox9-IRES-eGFP* reporter derived dorsal skin explants. Fate of GFP⁺ cells at hair placode stage are shown. GFP⁺ cell lineages were determined at hair germ stage. **n**, Fate of basal and suprabasal cells in placodes of *Sox9-IRES-eGFP* reporter-derived dorsal skin explants. Fate of GFP⁺ cells at the hair germ stage are shown. **o**, Lineage distribution of GFP⁺ basal cells at hair germ stage. Cells grouped in the black bar in **n** were examined. **p**, Lineage-tracing strategy of *Sox9⁺* cells in ex vivo cultured dorsal skin derived from E12.5 *Sox9^{creERt2/+; R26R-H2B-mCherry^{f/+; K14-H2B-eGFP}}* (top panel) and snapshot images of the culture (bottom panels). Yellow spots, one of tracked basal cell lineages; Cyan spots, one of tracked suprabasal cell lineages. 4-OHT, 4-hydroxytamoxifen. Scale bars, 50 µm. **q**, Fate of basal and suprabasal cells in the dorsal HF placode analysed by lineage-tracing with *Sox9-creER*. Fates of H2B–mCherry⁺ cells at the hair germ stage are shown. Summarized data are shown in the left panel, and the data for corresponding replicate HFs are shown in the right panels. Two-sided Fisher's exact test was used. **r**, Lineage distribution of H2B–mCherry⁺

basal cells at hair germ stage. Cells grouped in the black bar in **q** were examined. Summarized data are shown in the left panel, and the data for corresponding replicate HFs are shown in the right panels. Each value in the graph is the mean \pm s.d. from three independent experiments, one or two HF each. Numbers of analysed cell lineages are summarized in Supplementary Table 2. See also ‘Statistical analysis and reproducibility’ in Methods and Source Data.

[Source data](#)

[**Extended Data Fig. 6 Cell sorting of photo-converted developing whisker HF epithelial cells.**](#)

a, Photo-labelling of whisker HF epithelial cells in nKikGR mice at each embryonic stage. Scale bars, 50 μm . **b**, Single plane of E15.0 whisker HF showing the nKikGR signal intensities before and after the photo-conversion (Supplementary Video 9). Expression level of nKikGR varies between cells. There are two possible reasons for this: (1) the expression level of nKikGR varies for different cell types, and (2) the different mesenchymal tissue thickness of the explants around the whisker HFs affects the efficiency of detecting the fluorescent signals from the inside of the tissue. Despite this, the variation of nKikGR-green signal levels within the HF before photo-conversion closely correlates with the variation of nKikGR-red signal levels after photo-conversion, suggesting that the nKikGR signal was completely converted from green to red throughout the HF tissues (Supplementary Video 9). Scale bars, 50 μm . **c**, Experimental design for scRNA-seq of the developing whisker HF epithelium. **d**, Immunofluorescence staining of E14.0 whisker HF showed that the basal epithelial layer was marked by ITGA6 $^+$ CD31 $^-$ and that blood vessels in the mesenchyme were labelled by ITGA6 $^+$ CD31 $^+$ (arrowhead). Box shows magnified region (right). Scale bars, 50 μm . **e–g**, Isolation of photo-labelled whisker HF epithelial cells (E12.0–E17.0, DAPI $^-$ CD31 $^-$ ITGA6 $^+$ KikGR-red $^+$ cells; E11.5, DAPI $^-$ CD31 $^-$ ITGA6 $^+$ cells) by flow cytometry. **h–l**, Immunolocalization of ITGA6 in developing whisker HFs. Whisker HFs at E12.0 (**h**), E13.0 (**i**), E14.0 (**j**), E15.0 (**k**) and E17.0 (**l**) were stained with an antibody against ITGA6, and sections were counterstained with DAPI. ITGA6 was detected in all basal epithelial cells of developing whisker HFs.

Blood vessels in the dermis also were positive for ITGA6. Scale bars, 100 μ m.

Extended Data Fig. 7 Spatial and temporal reconstruction of scRNA-seq data of the developing whisker HF epithelium.

a, b, *t*-SNE plot visualizing scRNA-seq data for 1,614 single cells from developing whisker HFs (E11.5, 94 cells; E12.0, 276 cells; E13.0, 267 cells; E13.5, 181 cells; E14.0, 177 cells; E15.0, 350 cells; and E17.0, 269 cells). Cell populations were categorized by embryonic stage (**a**) and cell type (**b**). **c**, Violin plot showing the expression patterns of known lineage markers in each cluster. Colours refer to *t*-SNE clusters in **b**. **d**, Subclustering of whisker HF epithelial cells identified in **a–c**. *t*-SNE plot of 962 epithelial cells is coloured by embryonic stage. **e**, Low batch effects and high reproducibility of scRNA-seq data; scRNA-seq samples in this study consisted of cells from multiple batches: a plurality of plates and different dates and places of sampling, library preparation and sequencing. To investigate the batch effect caused by this technical handling, transcriptomes were divided into stages and projected onto the *t*-SNE plot corresponding to **d**. Grey spots in the *t*-SNE plot indicate all transcriptomes derived from E11.5–E17.0 epithelial cells. Cells derived from each stage were highlighted with different colours according to the batch of experiments. Cells from different batches were mixed stage-by-stage on the *t*-SNE plot and not clustered by batch. This suggests the low batch effects and high reproducibility of our scRNA-seq analysis. **f**, *t*-SNE plot in **d** is coloured by cluster annotations. **g**, Percentage cell cluster distribution per individual plate. Each plate derived from the same embryonic stage showed a similar distribution of the clusters. **h**, Heat map of the heterogeneity within and between clusters. **i**, Dot plot showing differentially expressed genes in each cluster identified in **f**. **j**, Expression of cell-type-specific marker genes projected onto the *t*-SNE plot in **d**. **k**, Expression of the marker genes projected onto the *t*-SNE plot are shown in the top panels, and the corresponding RNA ISH results are shown in the bottom panels. Grey spots in the *t*-SNE plot indicate all transcriptomes derived from E11.5–E17.0 epithelial cells. Only cells derived from E17.0 are highlighted and coloured according to relative expression levels of the markers. Brackets indicate the intended localization of ISH signals. Scale bars, 100 μ m.

Source data

Extended Data Fig. 8 In vivo expression patterns of representative genes in each cell cluster of E13.0–E17.0 whisker HFs.

Feature plots of characteristic differentially expressed genes in each cluster identified in Extended Data Fig. 7f are shown in the left panels. Feature plots divided by developmental stages of the whisker HFs (E13.0–E17.0) and the corresponding RNA ISH images are shown on the top and bottom right panels, respectively. Grey spots in the t-SNE plot indicate all transcriptomes derived from E11.5–E17.0 epithelial cells. Only cells derived from the indicated stage are highlighted and coloured according to relative expression levels of the indicated markers. Arrowheads indicate the intended localization of ISH signals. A cell cluster located at the lower part of the t-SNE plot (clusters 5 and 6) corresponded to the upper part of the HF, such as the infundibulum and junctional zone. A bulge SC marker (*Nfatc1*) was strongly expressed in cell clusters 7–12 located in the centre of the t-SNE plot. These clusters were divided into the upper and lower bulge regions, based on the expression pattern of each region marker (such as *Adamts20* and *Shisa2*). *Vdr* expression confirmed that clusters 7, 11 and 13 contained cells derived from the stalk region, the lower part of the HF. *Shh*-positive cells in cluster 14 were in the hair germ in vivo. These data indicated that cells were aligned from the bottom left to the top right on the t-SNE plot, reflecting the tissue architecture of the whisker HF. Scale bars, 100 µm.

Extended Data Fig. 9 Pseudospace analysis of scRNA-seq data derived from E12.0 placode cells.

a, In vivo expression patterns of representative genes in the pseudospace of E12.0 whisker HFs. Expression of the indicated marker genes projected onto the pseudospace are shown in the left panels, and the corresponding whole-mount RNA ISH results are shown in the right panels. Arrowheads indicate the intended localization of ISH signals. Scale bars, 100 µm. **b–e**, Expressions of indicated genes in an E14.5 primary dorsal HF placode were

detected with whole-mount RNAscope fluorescent ISH. A merged image (left) and individual images are shown. Scale bars, 50 µm. **f–j**, Expression of genes related to signalling pathways in pseudospace of the hair placode. Genes involved in WNT (**f**), TGF, BMP and activin (**g**), Hedgehog (**h**), FGF (**i**) and Notch signalling (**j**) were selected from the KEGG database and the expression of the genes is represented in a heat map. Direct target genes of WNT and β-catenin signalling, including *Axin2* and *Tcf4*, showed high expression at the placode centre but suppression towards the IFE. However, the expression of Notch, FGF and TGF and BMP target genes, including *Heyl*, Etv genes and *Id3*, was more broadly elevated from the placode centre to the periphery. SHH target genes *Igf2* and *Ccnd2* were highly expressed from the periphery to the IFE regions. Thus, the placode basal epithelium forms gradients of signalling activities from the placode centre to the periphery, and the placode periphery is characterized, in part, as a WNT^{low}BMP^{high} state, the characteristics of adult bulge SCs.

Extended Data Fig. 10 Reconstruction of epithelial lineage diversification and SC induction.

a, Timing of epithelial lineage divergence. Three-dimensional diffusion map showing pseudotemporally ordered whisker HF epithelial basal cells, related to Fig. [4c](#). Grey spots in the diffusion map indicate all transcriptomes derived from E11.5–E17.0 whisker HF epithelial basal cells. Cells derived from each stage are highlighted with different colours according to their embryonic stage. The arrow in the E12.0 diffusion map indicates the branching point of the hair germ lineage (branch 5). The open arrowhead in the E13.5 diffusion map indicates the branching point of infundibulum (branch 1), upper SCs (branch 2), lower SCs (branch 3) and stalk cells (branch 4). **b**, Cell clusters belonging to each trajectory are highlighted on the diffusion map (top panels) and t-SNE plot (bottom panels). Arrow and open arrowheads represent branching points. **c**, Expression of each lineage marker gene projected onto the diffusion map. **d**, RNA velocity field projected onto the t-SNE plot of epithelial cells (arrows represent the average RNA velocity). **e**, Selected terms of enrichment analysis associated with the gene categories identified in Fig. [4d](#). Only the gene list of gene cluster 6 raised no valid GO terms (*P* value <

0.03). **f**, HFSC signature genes and pSMAD1 targets in gene clusters 6, 9 and 10.

Supplementary information

Reporting Summary

Peer Review File

Supplementary Table 1

The detailed sample size information and analysed cell lineage numbers for Fig. 1 and Extended Data Fig. 3.

Supplementary Table 2

The detailed sample size information and analysed cell lineage numbers for Fig. 2 and Extended Data Fig. 5.

Supplementary Table 3

Information on scRNA-seq data used in this study.

Supplementary Table 4

List of resources and primers used for ISH probe synthesis.

Video 1 Time-lapse video of whisker HF development from the hair germ to bulbous peg stages with cell tracking data

Single plane time-lapse video of whisker HF development from the hair germ to bulbous peg stages with cell tracking data corresponding to Fig. 1a (replicate No. 1). Epithelial nuclei were visualised by *K14-rtTA; TetO-H2B-eGFP* and all nuclei were visualised by *R26-H2B-mCherry*.

[Video 2 Another time-lapse video of whisker HF development from the hair placode to bulbous peg stages](#)

Another single plane time-lapse video of whisker HF development from the hair placode to bulbous peg stages, related to Fig. 1a and corresponding to replicate No. 3 in Extended Data Fig. 3d and replicate No. 2 in Extended Data Fig. 3g. Epithelial nuclei were visualised by *K14-rtTA; TetO-H2B-eGFP* and G0/G1 phase nuclei were visualised by a Fucci-G1 probe (mKO2-hCdt1).

[Video 3 Time-lapse video of whisker HF development from the hair placode to hair germ stages](#)

Single plane time-lapse video of whisker HF development from the hair placode to hair germ stages, corresponding to Fig. 1c (replicate No. 1). Epithelial nuclei were visualised by *K14-rtTA; TetO-H2B-eGFP* and G0/G1 phase nuclei were visualised by Fucci-G1 probe (mKO2-hCdt1).

[Video 4 Video 3 with cell tracking data](#)

Supplementary Video 3 with cell tracking data, corresponding to Fig. 1c. Epithelial nuclei were visualised by *K14-rtTA; TetO-H2B-eGFP* and G0/G1 phase nuclei were visualised by Fucci-G1 probe (mKO2-hCdt1).

[Video 5 Time-lapse video showing cell tracking results of suprabasal cells at the placode stage](#)

Time-lapse video containing four representative clips showing cell tracking results of suprabasal cells at the placode stage. Tracked suprabasal cells, equivalent to SOX9⁺ suprabasal cells, did not contribute to the basal layer or HF formation. Tracked cells are marked by spots.

[Video 6 Time-lapse video showing cell tracking results of an upper daughter cell that remained in the basal layer after perpendicular cell division](#)

Time-lapse video containing four representative clips showing cell tracking results of an upper daughter cell that remained in the basal layer after perpendicular cell division. Tracked cells are marked by spots.

Video 7 Time-lapse video of dorsal HF development from the hair placode to hair peg stages

Single plane time-lapse video of dorsal HF development from the hair placode to hair peg stages, related to Extended Data Fig. 5i–l. Epithelial nuclei were visualised by *K14-rtTA; TetO-H2B-eGFP*.

Video 8 Another time-lapse video of dorsal HF development from the hair placode to hair peg stages

Single plane time-lapse video of dorsal HF development from the hair placode to hair peg stages, corresponding to Fig. 2c. *Sox9* expression was visualised by *Sox9-IRES-eGFP* reporter, and all nuclei were visualised by *R26-H2B-mCherry*.

Video 9 nKikGR signal intensities in E15.0 whisker HF before and after photo-conversion

Representative 3D video showing nKikGR signal intensities in an E15.0 whisker HF before and after photo-conversion. The photo-conversion occurs throughout the tissue.

Source data

Source Data Fig. 1

Source Data Fig. 2

Source Data Fig. 3

Source Data Fig. 4

[Source Data Extended Data Fig. 5](#)

[Source Data Extended Data Fig. 7](#)

Rights and permissions

[Reprints and Permissions](#)

About this article



Check for
updates

Cite this article

Morita, R., Sanzen, N., Sasaki, H. *et al.* Tracing the origin of hair follicle stem cells. *Nature* **594**, 547–552 (2021). <https://doi.org/10.1038/s41586-021-03638-5>

[Download citation](#)

- Received: 30 March 2020
- Accepted: 13 May 2021
- Published: 09 June 2021
- Issue Date: 24 June 2021
- DOI: <https://doi.org/10.1038/s41586-021-03638-5>

Comments

By submitting a comment you agree to abide by our [Terms](#) and [Community Guidelines](#). If you find something abusive or that does not comply with our terms or guidelines please flag it as inappropriate.

[Access through your institution](#)

[Change institution](#)

[Buy or subscribe](#)

Associated Content

[A 4D road map for the formation of hair follicles](#)

- Nivedita Saxena
- Michael Rendl

Advertisement

This article was downloaded by **calibre** from <https://www.nature.com/articles/s41586-021-03638-5>

| [Section menu](#) | [Main menu](#) |

Neutralizing antibody vaccine for pandemic and pre-emergent coronaviruses

[Download PDF](#)

- Article
- [Published: 10 May 2021](#)

Neutralizing antibody vaccine for pandemic and pre-emergent coronaviruses

- [Kevin O. Saunders](#) [ORCID: orcid.org/0000-0001-7399-7954](#)^{1,2,3,4},
- [Esther Lee](#)^{1,5},
- [Robert Parks](#)^{1,5},
- [David R. Martinez](#)⁶,
- [Dapeng Li](#)^{1,5},
- [Haiyan Chen](#)^{1,5},
- [Robert J. Edwards](#) [ORCID: orcid.org/0000-0003-4446-1194](#)^{1,5},
- [Sophie Gobeil](#) [ORCID: orcid.org/0000-0002-0057-2477](#)^{1,5},
- [Maggie Barr](#)^{1,5},
- [Katayoun Mansouri](#)^{1,5},
- [S. Munir Alam](#)^{1,5},
- [Laura L. Sutherland](#)^{1,5},
- [Fangping Cai](#)^{1,5},
- [Aja M. Sanzone](#)^{1,5},
- [Madison Berry](#)^{1,5},
- [Kartik Manne](#)^{1,5},
- [Kevin W. Bock](#) [ORCID: orcid.org/0000-0001-9454-0937](#)⁷,
- [Mahnaz Minai](#)⁷,
- [Bianca M. Nagata](#)⁷,
- [Anyway B. Kapingidza](#)^{1,5},
- [Mihai Azoitei](#)^{1,5},
- [Longping V. Tse](#) [ORCID: orcid.org/0000-0001-7582-8396](#)⁶,
- [Trevor D. Scobey](#)⁶,
- [Rachel L. Spreng](#) [ORCID: orcid.org/0000-0003-1254-0760](#)^{1,5},
- [R. Wes Rountree](#)^{1,5},

- [C. Todd DeMarco^{1,5}](#),
- [Thomas N. Denny^{1,5}](#),
- [Christopher W. Woods^{1,5,8}](#),
- [Elizabeth W. Petzold⁸](#),
- [Juanjie Tang⁹](#),
- [Thomas H. Oguin III^{1,5}](#),
- [Gregory D. Sempowski^{1,5}](#),
- [Matthew Gagne¹⁰](#),
- [Daniel C. Douek¹⁰](#),
- [Mark A. Tomai¹¹](#),
- [Christopher B. Fox¹²](#),
- [Robert Seder ORCID: orcid.org/0000-0003-3133-0849¹⁰](#),
- [Kevin Wiehe^{1,5}](#),
- [Drew Weissman¹³](#),
- [Norbert Pardi¹³](#),
- [Hana Golding⁹](#),
- [Surender Khurana ORCID: orcid.org/0000-0002-0593-7965⁹](#),
- [Priyamvada Acharya ORCID: orcid.org/0000-0002-0089-277X^{1,2}](#),
- [Hanne Andersen ORCID: orcid.org/0000-0003-1103-9608¹⁴](#),
- [Mark G. Lewis¹⁴](#),
- [Ian N. Moore⁷](#),
- [David C. Montefiori^{1,2}](#),
- [Ralph S. Baric ORCID: orcid.org/0000-0001-6827-8701⁶](#) &
- [Barton F. Haynes ORCID: orcid.org/0000-0002-7643-9023^{1,3,5}](#)

[Nature](#) volume 594, pages 553–559 (2021) [Cite this article](#)

- 64k Accesses
- 2128 Altmetric
- [Metrics details](#)

Subjects

- [Protein vaccines](#)
- [RNA vaccines](#)
- [SARS-CoV-2](#)
- [Viral infection](#)

Abstract

Betacoronaviruses caused the outbreaks of severe acute respiratory syndrome (SARS) and Middle East respiratory syndrome, as well as the current pandemic of SARS coronavirus 2 (SARS-CoV-2)^{1,2,3,4}. Vaccines that elicit protective immunity against SARS-CoV-2 and betacoronaviruses that circulate in animals have the potential to prevent future pandemics. Here we show that the immunization of macaques with nanoparticles conjugated with the receptor-binding domain of SARS-CoV-2, and adjuvanted with 3M-052 and alum, elicits cross-neutralizing antibody responses against bat coronaviruses, SARS-CoV and SARS-CoV-2 (including the B.1.1.7, P.1 and B.1.351 variants). Vaccination of macaques with these nanoparticles resulted in a 50% inhibitory reciprocal serum dilution (ID_{50}) neutralization titre of 47,216 (geometric mean) for SARS-CoV-2, as well as in protection against SARS-CoV-2 in the upper and lower respiratory tracts. Nucleoside-modified mRNAs that encode a stabilized transmembrane spike or monomeric receptor-binding domain also induced cross-neutralizing antibody responses against SARS-CoV and bat coronaviruses, albeit at lower titres than achieved with the nanoparticles. These results demonstrate that current mRNA-based vaccines may provide some protection from future outbreaks of zoonotic betacoronaviruses, and provide a multimeric protein platform for the further development of vaccines against multiple (or all) betacoronaviruses.

[Download PDF](#)

Main

SARS-CoV, SARS-CoV-2 and Middle East respiratory syndrome coronavirus (MERS-CoV) emerged from transmission events in which humans were infected with bat or camel coronaviruses^{5,6,7,8}. Betacoronaviruses that circulate in civets, bats and Malayan pangolins are genetically similar to SARS-CoV and SARS-CoV-2, and use human ACE2 as a receptor^{5,6,9,10,11}; these SARS-related coronaviruses have the potential to be transmitted to humans¹². Cross-neutralizing antibodies (cross-nAbs) that are capable of neutralizing multiple betacoronaviruses, and of preventing or treating betacoronavirus infection, have been isolated from humans infected with SARS-CoV^{13,14,15,16,17,18,19,20,21,22,23,24}, which provides proof-of-concept for the development of vaccines against members of the *Sarbecovirus* subgenus²⁵.

In mice, the induction of cross-nAbs through vaccination has previously been reported for coronavirus pseudoviruses^{26,27}. However, it is unknown whether the vaccination of primates with spike protein can elicit cross-nAbs against SARS-CoV, bat betacoronaviruses or SARS-CoV-2 escape viruses. One target of cross-nAbs is the receptor-binding domain (RBD) of the spike protein^{14,24,25}: for example, the antibody

DH1047 is a cross-nAb that targets the RBD and cross-neutralizes SARS-CoV, SARS-CoV-2 and bat coronaviruses¹⁵. RBD immunogenicity can be augmented by arraying multiple copies of the domain on nanoparticles, which mimics virus-like particles^{26,27,28,29}. We therefore designed a vaccine that comprised a 24-mer SARS-CoV-2 RBD nanoparticle conjugated to a ferritin scaffold. We constructed the RBD nanoparticle by expressing recombinant SARS-CoV-2 RBD with a C-terminal sortase A donor sequence, and by expressing a 24-subunit, self-assembling *Helicobacter pylori* ferritin with an N-terminal sortase A acceptor sequence³⁰. We then conjugated the RBD to ferritin nanoparticles using a sortase A reaction³⁰ (Fig. 1a, Extended Data Fig. 1). We used analytical size-exclusion chromatography and negative-stain electron microscopy to confirm that the RBD was conjugated to the surface of the ferritin nanoparticle (Fig. 1a, Extended Data Fig. 1b,c). The RBD sortase-A-conjugated nanoparticle (hereafter, RBD–scNP) bound to human ACE2 (the receptor for SARS-CoV-2) and to potent neutralizing SARS-CoV-2-specific RBD antibodies DH1041, DH1042, DH1043, DH1044 and DH1045¹⁵ (Fig. 1b). The cross-nAb DH1047 also bound to the RBD–scNP (Fig. 1b). The RBD–scNP lacked binding to SARS-CoV-2 spike antibodies that bound outside of the RBD (Fig. 1b).

Fig. 1: RBD–scNP elicits extremely high titres of SARS-CoV-2-pseudovirus neutralizing antibodies.

 **figure1**

a, SARS-CoV-2 RBD (blue and red)–*H. pylori* ferritin (grey) nanoparticle sortase (SrtA) conjugation. Model and two-dimensional class average of negative-stain electron microscopy (EM) of the resultant RBD–scNP are shown. **b**, Biolayer interferometry SARS-CoV-2 antibody and ACE2-receptor binding to RBD nanoparticles. nAbs, neutralizing antibodies; non-nAbs, non-neutralizing antibodies; non-nAbs IE, infection-enhancing non-neutralizing antibody; NTD, N-terminal

domain. Symbols represent values from three independent experiments; data are mean + s.e.m. **c**, Design of the cynomolgus macaque immunogenicity and challenge study. **d**, Macaque serum IgG binding titre as area-under-the-curve (AUC) of the \log_{10} -transformed curve ($\log(\text{AUC})$) to recombinant SARS-CoV-2 S-2P, RBD, NTD and fusion peptide. Group mean \pm s.e.m. are shown in **d**, **e** ($n = 5$ macaques). **e**, Plasma antibody blocking of SARS-CoV-2 S-2P binding to ACE2 and RBD neutralizing antibody DH1041. **f**, **g**, Dose-dependent serum neutralization of SARS-CoV-2 D614G pseudovirus infection of ACE2-expressing 293T cells (**f**) and neutralization ID₅₀ and ID₈₀ titres (**g**). Serum was examined after two immunizations. The mean value of duplicates is shown in **f**. **h**, SARS-CoV-2 D614G pseudovirus serum neutralization titre over time for individual macaques. **i**, Serum neutralization ID₅₀ titres from macaques immunized twice with RBD–scNP (blue) or S-2P mRNA-LNP (burgundy). ** $P = 0.0079$, two-tailed exact Wilcoxon test. $n = 5$ macaques. **j**, Serum neutralization titres for macaques immunized twice with RBD–scNP (blue) ($n = 5$ macaques) or humans with asymptomatic infection ($n = 34$ individuals) (A), symptomatic infection ($n = 71$ individuals) (S) or who were hospitalized ($n = 60$ individuals) (H). ** $P < 0.01$, two-tailed Wilcoxon test. Horizontal bars are the group geometric mean in **i**, **j**. Pre-vaccination serum or neutralizing antibody spiked serum were used as controls in **f**–**h**. **d**, **e**, **h**, Arrows, time of immunization.

[Source data](#)

[Full size image](#)

We immunized five cynomolgus macaques three times intramuscularly, four weeks apart, with 100 μg of RBD–scNP adjuvanted with 5 μg of the TLR7 and TLR8 agonist 3M-052 absorbed to 500 μg of alum³¹ (Fig. [1c](#), Extended Data Fig. [1d,e](#)). Immunizations were well-tolerated in macaques (Extended Data Fig. [2](#)). Immunization with RBD–scNP adjuvanted with 3M-052 and alum elicited binding IgG against both the SARS-CoV-2 RBD and the spike ectodomain stabilized by the introduction of two prolines (S-2P) (Fig. [1d](#)), but immunization with 3M-052 and alum alone did not (Extended Data Fig. [3a,b](#)). Boosting once maximally increased SARS-CoV-2 binding IgG titres (Fig. [1d](#)). ACE2 competitive-binding assays demonstrated the presence of ACE2-binding-site antibodies in the serum of vaccinated macaques (Fig. [1e](#)). Similarly, plasma antibodies blocked the binding of the ACE2-binding-site-focused, RBD-neutralizing antibody DH1041 (Fig. [1e](#)). We assessed the vaccine induction of neutralizing antibodies against a SARS-CoV-2 pseudovirus with an aspartic acid-to-glycine substitution at position 614 (D614G)³². Two RBD–scNP immunizations induced potent serum neutralizing antibodies, with ID₅₀ neutralization titres that ranged from 21,292 to 162,603 (Fig. [1f,g](#)). We compared these neutralizing antibody titres to those elicited by cynomolgus macaques that were immunized twice with 50 μg of nucleoside-modified mRNA encapsulated in lipid nanoparticles that encodes

transmembrane S-2P (S-2P mRNA-LNP). S-2P mRNA-LNP is analogous to COVID-19 vaccines that have been authorized for emergency use (Extended Data Fig. 1f). The serum neutralization titres against SARS-CoV-2 D614G pseudovirus that were elicited by RBD–scNP immunization were significantly higher than titres that were elicited by two immunizations with S-2P mRNA-LNP^{33,34} (group geometric mean ID₅₀ of 47,216 and 6,469, respectively; $P = 0.0079$ exact Wilcoxon test, $n = 5$ macaques for each vaccine) (Fig. 1i). When compared to natural human infection, RBD–scNP vaccination elicited higher ID₅₀ neutralization titres (Fig. 1j). RBD–scNP adjuvanted with 3M-052 and alum therefore elicits significantly higher neutralizing titres in macaques, compared to current vaccine platforms or natural human infection (Fig. 1i, j).

The SARS-CoV-2 variant B.1.1.7 is spreading globally, and has previously been suggested to have higher infectivity than the Wuhan-Hu-1 strain^{35,36}. B.1.351-lineage viruses are widespread in the Republic of South Africa^{36,37,38} and—along with the P.1 variant—are of concern owing to their neutralization-resistant phenotype, which is mediated by K417N, E484K and N501Y substitutions in the RBD³⁹. Each of these mutations is distal to the cross-nAb DH1047 binding site (owing to its long HCDR3 domain that is used to contact the RBD); however, the E484K substitution is within the binding site of the RBD neutralizing antibody DH1041¹⁵ (Fig. 2a, b). DH1041 binding to the SARS-CoV-2 RBD was therefore knocked out by the E484K substitution, but DH1047 binding to the RBD was unaffected by the K417N, E484K or N501Y substitutions (Fig. 2c, d, Extended Data Fig. 3).

Fig. 2: RBD–scNP elicits a higher titre of neutralizing antibodies against more transmissible or neutralization-resistant SARS-CoV-2 variants than does S-2P mRNA-LNP.

 **figure2**

a, b, The location of K417, E484 and N501 (spheres), which are mutated in the B.1.351 variant, are shown in the cryo-electron microscopy structures of the RBD neutralizing antibodies DH1041 (red) (**a**) and DH1047 (magenta) (**b**) bound to the RBD (grey) of spike trimers (Protein Data Bank codes (PDB) 7LAA and 7LD1)¹⁵. **c**, ACE2 receptor, DH1041 and DH1047 enzyme-linked immunosorbent assay (ELISA)

binding titre as log(AUC), for wild-type (WT) and mutant SARS-CoV-2 spike RBD monomers. **d**, Serum neutralization ID₅₀ (left) and ID₈₀ (right) titres for SARS-CoV-2 D614G and SARS-CoV-2 B.1.1.7 pseudoviruses from immunized macaques, in ACE2-expressing 293 cells. Symbols represent individual macaques; horizontal bars are group means. **P = 0.0079, two-tailed exact Wilcoxon test. n = 5 macaques. **e**, Fold decrease in neutralization potency in neutralization of SARS-CoV-2 B.1.1.7 pseudovirus relative to SARS-CoV-2 D614G pseudovirus. Fold change is shown for RBD–scNP-immunized and S-2P mRNA-LNP-immunized macaques on the basis of the ID₅₀ and ID₈₀ titres. Horizontal bars are the group mean. **f**, Vaccinated macaque serum neutralization ID₅₀ (left) and ID₈₀ titres (right) against SARS-CoV-2 WA-1 and B.1.351 pseudoviruses, in ACE2-expressing 293 cells. Symbols and horizontal bars are shown the same as in **d**. *P = 0.0159; **P = 0.0079, two-tailed exact Wilcoxon test. n = 5 macaques. **g**, Fold decrease in neutralization potency in neutralization of SARS-CoV-2 B.1.351 pseudovirus relative to SARS-CoV-2 WA-1 pseudovirus. Fold change is shown as in **e**. **h**, Vaccine-induced ID₅₀ (left) and ID₈₀ (right) neutralization titres of infection of ACE2- and TMPRSS2-expressing 293 cells by SARS-CoV-2 WA-1 or P.1 pseudovirus. Symbols and horizontal bars are as in **d**. *P = 0.0159; **P = 0.0079, two-tailed exact Wilcoxon test. n = 5 macaques. **i**, Fold decrease in neutralization potency (as shown in **e**) for SARS-CoV-2 P.1 pseudovirus relative to SARS-CoV-2 WA-1 pseudovirus.

[Source data](#)

[Full size image](#)

We determined whether immunization with RBD–scNP or S-2P mRNA-LNP elicited neutralizing antibodies against these particular SARS-CoV-2 variants. Serum from macaques vaccinated with RBD–scNP potently neutralized a pseudovirus bearing the D614G spike or the B.1.1.7 spike (Fig. [2d,e](#)). Similarly, S-2P mRNA-LNP immunization elicited equivalent titres of neutralizing antibodies against the B.1.1.7 and D614G variants, although titres were lower than with RBD–scNP immunization (Fig. [2d,e](#)). Serum from macaque immunized with RBD–scNP or S-2P mRNA-LNP neutralized SARS-CoV-2 WA-1, B.1.351 and P.1 pseudoviruses, with 80% inhibitory reciprocal serum dilution (ID₈₀) titres being more potent for the RBD–scNP group (Fig. [2f-i](#)). On average, the neutralization titres in the RBD–scNP group decreased by threefold against the B.1.351 or P.1 variants, whereas those of the S-2P mRNA-LNP group decreased by sixfold for B.1.351 and tenfold for P.1 (on the basis of ID₅₀ titres) (Fig. [2g,i](#)). Additionally, we observed that plasma IgG binding to SARS-CoV-2 spike after RBD–scNP and S-2P mRNA-LNP immunization was unaffected by mutations that have been observed in SARS-CoV-2 from Danish minks, as well as in the B.1.351, P.1 and B.1.1.7 strains^{[36,37,40](#)} (Extended Data Fig. [3](#)). In summary, both of the vaccines we tested elicited neutralizing antibodies that were unaffected by the

mutations in the B.1.1.7 strain. However, neutralizing antibodies elicited by RBD–scNP more potently neutralized the B.1.351 and P.1 virus strains than did neutralizing antibodies elicited with S-2P mRNA-LNP immunization.

SARS-related coronaviruses that circulate in humans and animals remain a threat for future outbreaks^{12,41,42}. We therefore examined the neutralization of SARS-CoV, the SARS-related group-2b bat coronavirus WIV-1 and the SARS-related bat coronavirus SHC014 by immune sera from macaques vaccinated with the RBD–scNP, S-2P mRNA-LNP or mRNA-LNP encoding monomeric RBD (RBD mRNA-LNP)^{6,9,41,42} (Extended Data Fig. 1e–g). After two immunizations, RBD–scNP, S-2P mRNA-LNP and RBD mRNA-LNP elicited neutralizing antibodies against SARS-CoV, WIV-1 and SHC014 (Fig. 3a, Extended Data Fig. 4). Neutralization was more potent for replication-competent SARS-CoV-2 virus compared to these three SARS-related viruses (Fig. 3a, Extended Data Fig. 4), and neutralization titres varied up to fourfold within the RBD–scNP group (Extended Data Fig. 4). Overall, RBD–scNP immunization elicited the highest neutralization titres (Fig. 3a, Extended Data Fig. 4). Modest increases in neutralization potency were gained by boosting a third time with RBD–scNP (Fig. 3b). Moreover, RBD–scNP immunization elicited cross-reactive plasma IgG against the spike proteins of SARS-CoV-2 and SARS-CoV, as well as those of the bat coronaviruses RaTG13 and SHC014 and the pangolin coronavirus GXP4L (Fig. 3c, Extended Data Fig. 5a,c). Binding antibody titres were high for these spike proteins, even in instances in which neutralization titres were low; this suggests that non-neutralizing antibodies contributed to binding titres. RBD–scNP-immune plasma IgG did not bind the spike protein from the four endemic human coronaviruses or MERS-CoV (Extended Data Fig. 5a,c). The lack of binding by plasma IgG to spike ectodomains of these latter five coronaviruses is consistent with RBD-sequence divergence among group 1, 2a, 2b and 2c coronaviruses (Fig. 3f, Extended Data Figs. 6, 7). The SARS-CoV-2 spike induced cross-nAbs against several group-2b SARS-related betacoronaviruses, with the highest titres being induced by RBD–scNP.

Fig. 3: Serum cross-neutralization of infections with SARS-related betacoronaviruses induced by RBD–scNP.

 figure3

a, Serum neutralization ID₅₀ titres from macaques immunized twice with RBD–scNP, S-2P mRNA-LNP or RBD mRNA-LNP for SARS-CoV, SARS-CoV-2 and SARS-related bat coronaviruses (WIV-1 and SHC014) infections. Symbols indicate individual macaques; black bars show the group geometric mean. Two-tailed exact Wilcoxon test, $n = 5$ or 8 macaques. **b**, Serum cross-neutralization ID₅₀ titres before (grey), or after two (light blue) or three (blue), RBD–scNP immunizations. Bars

represent the group geometric mean. **c**, Binding titre (log(AUC)), based on ELISA for the spike protein of human, bat (RaTG13 and SHC014) and pangolin (GXP4L) SARS-related betacoronaviruses, for plasma IgG from macaques immunized twice with RBD–scNP. ECD, ectodomain; S, spike. **d**, Structural comparison of the epitopes of SARS-CoV-2-specific neutralizing RBD antibody (DH1041) (red) (PDB 7LAA) and cross-neutralizing RBD antibody (DH1047) (magenta) (PDB 7LD1). Left, cartoon view of spike (green), RBD (grey) and receptor binding motif (RBM) (blue). Right, overlay of the RBDs of the two complexes from their respective cryo-electron microscopy structures. **e**, RBD coloured by conservation within group-2b betacoronaviruses. DH1047 epitope is shown in magenta outline. **f**, RBD sequence conservation. Heat map displaying pairwise amino acid sequence similarity for 57 representative betacoronaviruses. **g**, **h**, Plasma or serum antibody blocking of S-2P binding to ACE2 (grey) and DH1047 (navy blue). **g**, Plasma antibody inhibition of spike binding. SARS-CoV-2 S-2P (left) or SHC014 S-2P (right) blocking kinetics by serum from macaques immunized twice with RBD–scNP. Group mean \pm s.e.m. is shown. $n = 5$ macaques. Arrows, time of immunization. **h**, Blocking of SARS-CoV-2 S-2P binding to ACE2 (left) or DH1047 (right). Blocking activity by serum from macaques immunized twice with RBD–scNP or S-2P mRNA-LNP, and humans immunized twice with Pfizer BNT162b2 (BNT162b) or naturally infected with SARS-CoV-2 (convalescent). Each symbol represents an individual and filled bars indicate the group mean in **h**. Positivity threshold (dashed line) is greater than 20% in **h**.

[Source data](#)

[Full size image](#)

Immune sera from RBD–scNP-immunized macaques exhibited a cross-neutralizing profile similar to that of the cross-nAb DH1047. DH1047 bound with <0.02 nM affinity to monomeric SARS-CoV-2 RBD (Extended Data Fig. 5b), and bound the RBD–scNP (Fig. 1b). The cross-reactive DH1047 epitope is adjacent to the N terminus of the ACE2-binding site, which distinguishes the DH1047 antibody from dominant ACE2-binding-site-focused neutralizing antibodies such as DH1041¹⁵ (Fig. 3d), and the DH1047 epitope has high group-2b sequence conservation (Fig. 3e). Overall RBD sequences within betacoronavirus groups are more conserved than sequences from different groups (Fig. 3f, Extended Data Figs. 6, 7). We determined the presence of DH1047-like antibodies using DH1047 blocking assays. Plasma from all RBD–scNP-immunized macaques blocked the binding of ACE2 and DH1047 to SARS-CoV-2 S-2P (Fig. 3g, Extended Data Fig. 5d). The DH1047-blocking antibodies were cross-reactive, as they also potently blocked DH1047 binding to the S-2P of SHC014 (Fig. 3g). RBD–scNP immunization of macaques elicited higher magnitudes of DH1047-blocking antibodies than did S-2P mRNA-LNP; these magnitudes were also higher than those elicited by immunization of humans with the Pfizer BNT162b2 vaccine or SARS-CoV-2 infection in humans (Fig. 3h, Extended

Data Fig. 5d). ACE2 blocking was high in all groups (Fig. 3h). Whereas 5 out of 5 RBD–scNP-vaccinated macaques exhibited potent DH1047 serum blocking activity, 3 out of 4 immunized humans and 9 out of 22 humans who had recovered from COVID-19 had detectable serum DH1047 blocking activity (Fig. 3h). The DH1047-like antibody response was therefore weak and subdominant in naturally infected or immunized humans and S-2P mRNA-LNP-immunized macaques, but was a dominant macaque antibody response to RBD–scNP vaccination.

To determine vaccine protection against coronavirus infection, we challenged RBD–scNP-vaccinated or S-2P mRNA-LNP-primed and RBD–scNP-boosted macaques with 10^5 plaque-forming units of SARS-CoV-2 virus via the intratracheal and intranasal routes, after their last boost (Fig. 4a). Neutralizing antibodies were detectable in all macaques at two weeks after the final immunization (Fig. 3b, Extended Data Fig. 4b, c). We collected bronchoalveolar lavage (BAL) fluid two days after the challenge (Fig. 4a), and detected infectious SARS-CoV-2 in BAL fluid from 5 out of 6 unimmunized macaques, but none of the RBD–scNP or S-2P mRNA-LNP and RBD–scNP-immunized macaques (Fig. 4b). We quantified SARS-CoV-2 replication as the number of copies of envelope (*E*) and nucleocapsid (*N*) subgenomic RNA (sgRNA) in fluid from nasal swabs and BAL at two and four days after challenge (Fig. 4a). At two days after challenge, unimmunized macaques had an average of 1.3×10^5 and 1.2×10^4 copies per ml of *E* sgRNA in the nasal swab and BAL fluids, respectively (Fig. 4c, d). By contrast, all of the RBD–scNP-vaccinated macaques, and 4 out of 5 macaques vaccinated with S-2P mRNA-LNP and RBD–scNP, had undetectable levels of *E* sgRNA in the upper and lower respiratory tract (Fig. 4c, d). We sampled macaques again two days later, and found no detectable *E* sgRNA in the BAL or nasal swab samples from any of the vaccinated macaques (Fig. 4b, c). Similarly, 4 out of 5 RBD–scNP-vaccinated macaques had undetectable *N* sgRNA in BAL and nasal swab fluid; the exception had 234 copies per ml of *N* sgRNA, which was detected on day 2 in nasal swab fluid (Fig. 4e, f). Virus replication was undetectable in this macaque by the fourth day after challenge (Fig. 4e). Additionally, all but one of the macaques immunized with S-2P mRNA-LNP and RBD–scNP had undetectable *N* sgRNA in BAL or nasal swab samples (Fig. 4e, f). Moreover, we did not detect SARS-CoV-2 nucleocapsid antigen in the lung tissue of any of the vaccinated macaques, but detected this antigen in all of the control macaques (Fig. 4g, Extended Data Fig. 8). Haematoxylin and eosin staining of lung tissue showed a reduction in inflammation in immunized macaques compared to control macaques (Extended Data Fig. 8, Extended Data Table 1).

Fig. 4: RBD–scNP vaccination alone or as a boost can prevent virus replication in the upper and lower respiratory tract after intranasal and intratracheal SARS-CoV-2 challenge in macaques.

 **figure4**

a, Study design for intranasal and intratracheal challenge of macaques with SARS-CoV-2. Blue and burgundy arrows indicate the time points for RBD–scNP and S-2P mRNA-LNP immunizations, respectively. **b**, Infectious virus in macaque BAL fluid two days after challenge. LOD, limit of detection. **c–f**, Quantification of viral *E* gene

(**c**, **d**) or *N* gene (**e**, **f**) sgRNA in unimmunized (grey) and RBD–scNP-immunized (blue) macaques, and in macaques with a S-2P mRNA-LNP prime and RBD–scNP boost (burgundy). sgRNA in nasal swabs (**c**, **e**) and BAL fluid (**d**, **f**) was quantified two (left panels) and four (right panels) days after challenge. LOD for the assay is 150 copies per ml. Symbols and bars represent individual macaques and group mean, respectively. **g** Nucleocapsid immunohistochemistry of lung tissue sections at seven days after challenge. Left, representative image from 1 macaque from each group of 5 macaques is shown. Red arrows indicate site of antigen positivity. All images are shown at 10× magnification. Scale bars, 100 µm. Right, quantification of lung viral antigen positivity. In each panel, symbols represent individual macaques (group mean is shown as a black horizontal bar).

[Source data](#)

[Full size image](#)

Finally, when possible, we examined mucosal immunity to SARS-CoV-2 both before and after SARS-CoV-2 challenge (Extended Data Fig. 9). IgG from concentrated BAL bound to spike and blocked ACE2, DH1041 and DH1047 binding to spike (Extended Data Fig. 9b–d). Each response was higher in the BAL from macaques immunized three times with RBD–scNP, compared to macaques immunized two times with S-2P mRNA-LNP and boosted once with RBD–scNP (although the BAL was collected from each group at different time points). Unconcentrated nasal wash samples from macaques immunized with either RBD–scNP or a S-2P mRNA-LNP prime and RBD–scNP boost showed similar low levels of spike-binding IgG after challenge (Extended Data Fig. 9e). Nonetheless, RBD–scNP immunization elicited RBD-specific mucosal antibodies.

As three coronavirus epidemics have occurred in the past 20 years, there is a need to develop vaccines that are effective against all coronaviruses before the next pandemic²⁵. The epitopes of betacoronavirus cross-nAbs (such as DH1047) provide clear targets for vaccines that aim to protect against multiple coronaviruses^{13,14,15,43}. We have shown that immunization of macaques with RBD–scNP adjuvanted with 3M-052 and—to a lesser extent—S-2P mRNA-LNP induces cross-nAbs against multiple SARS-related human and bat betacoronaviruses. These results demonstrate that SARS-CoV-2 vaccination with either the RBD–scNP or S-2P mRNA-LNP vaccines (the latter of which are similar to vaccines that have already been authorized for use in humans) will probably elicit cross-nAbs, and have the potential to prevent future spillovers of group-2b betacoronaviruses from bats to humans^{12,26}.

The emergence of neutralization-resistant and highly infectious variants of SARS-CoV-2 continues to be a concern for vaccine efficacy. The RBD–scNP and S-2P mRNA-LNP immunizations elicited SARS-CoV-2 neutralizing antibodies against the

D614G, B.1.1.7, P.1 and B.1.351 strains of SARS-CoV-2. The neutralizing antibodies elicited by RBD–scNP and S-2P mRNA-LNP were of different specificities, as RBD–scNP-induced neutralizing antibodies showed a smaller reduction in neutralization potency across the different variants compared to S-2P mRNA-LNP immune sera. Our results are consistent with the previous demonstration that current COVID-19 vaccines have reduced efficacy against the B.1.351 SARS-CoV-2 variant^{[39](#),[44](#),[45](#),[46](#),[47](#),[48](#)}.

The RBD–scNP vaccine is a promising platform for the development of vaccines that target multiple coronaviruses for the following reasons. The RBD–scNP vaccine induced apparent sterilizing immunity in the upper respiratory tract, which has not been routinely achieved with SARS-CoV-2 vaccination in macaques^{[49](#),[50](#)}. Additionally, the high neutralization titres achieved by RBD–scNP vaccination bode well for an extended duration of protection. Despite the induction of high levels of antibody, we observed no evidence of increased immunopathology, inflammatory cytokines or virus replication indicative of vaccine-elicited antibody-dependent enhancement. This lack of in vivo infection enhancement is consistent with previous studies using SARS-CoV-2 monoclonal antibodies^{[15](#)}. 3M-052 adsorbed to alum is in clinical testing (NCT04177355), which generates a potential translational pathway for RBD–scNP adjuvanted with 3M-052. The RBD–scNP vaccine represents a platform for inducing high titres of protective antibodies against current human coronaviruses and their variants, and for producing vaccines that could prevent, rapidly temper or extinguish the next spillover of a coronavirus into humans.

Methods

The experiments were not randomized, and only the pathologists were blinded to group treatments during experiments and outcome assessment.

Animals, immunizations, and human samples

Rhesus and cynomolgus macaques were housed and treated in Association for Assessment and Accreditation of Laboratory Animal Care (AAALAC)-accredited institutions. The study protocol and all veterinarian procedures were approved by the Bioqual IACUC per a memorandum of understanding with the Duke IACUC, and were performed based on standard operating procedures. Macaques studied were housed and maintained in an AAALAC-accredited institution in accordance with the principles of the NIH. All studies were carried out in strict accordance with the recommendations in the Guide for the Care and Use of Laboratory Animals of the NIH in BIOQUAL. BIOQUAL is fully accredited by AAALAC and through OLAW, assurance number A-3086. All physical procedures associated with this work were done under anaesthesia to minimize pain and distress, in accordance with the

recommendations of the Weatherall report ‘The use of non-human primates in research.’ Teklad 5038 primate diet was provided once daily by macaque size and weight. The diet was supplemented with fresh fruit and vegetables. Fresh water was given ad libitum. All macaques were maintained in accordance with the Guide for the Care and Use of Laboratory Animals. mRNA-LNP was prepared as previously stated^{51,52}. Rhesus macaques ($n = 8$ macaques) were immunized intramuscularly twice with 50 µg of RBD mRNA-LNP. Cynomolgus macaques ($n = 5$ macaques) were immunized twice with 50 µg of S-2P mRNA-LNP (encoding the transmembrane spike protein stabilized with K986P and V987P mutations) and boosted once with 100 µg of RBD–scNP adjuvanted with 5 µg of 3M-052 aqueous formulation admixed with 500 µg of alum in PBS. An additional group of cynomolgus macaques ($n = 5$ macaques) were immunized in the right and left quadriceps with 100 µg of RBD–scNP adjuvanted with 5 µg of 3M-052 aqueous formulation admixed with 500 µg of Alum in PBS³¹. The mixture for immunization consisted of 250 µl of RBD–scNP mixed with 250 µl of 0.02 mg ml⁻¹ 3M-052 and 2 mg ml⁻¹ alum. Group sizes were selected such that statistical significance could be reached with between group nonparametric statistical comparisons. No other statistical methods were used to predetermine sample size. Macaques were on average 8 or 9 years old and ranged from 2.75 to 8 kg in body weight. Male and female macaques per group were balanced when availability permitted. Studies were performed unblinded. Macaques were evaluated by Bioqual veterinary staff before, during and after immunizations. In the macaques studied, complete blood counts and chemistries were obtained throughout the immunization regimen and no marked abnormalities were noted. Of the 10 cynomolgus macaques, there were no adverse events reported at injection sites. Over the course of the study, two cynomolgus macaques experienced slight weight loss. Two cynomolgus macaques showed a single incidence of poor appetite, with one additional cynomolgus macaque showing poor appetite intermittently throughout the study. Additionally, one macaque presented with an infected lymph node biopsy site that responded to appropriate veterinary treatment. Biospecimens were collected before challenge, and 2 and 4 days after challenge, as previously described¹⁵. Human samples were obtained with informed consent. All recruitment, sample collection and experimental procedures using human samples have been approved by the Duke Institutional Review Board.

SARS-CoV-2 intranasal and intratracheal challenge

All macaques were challenged at week 11 (3 weeks after last vaccination) through combined intratracheal (3.0 ml) and intranasal (0.5 ml per nostril) inoculation with an infectious dose of 10^5 plaque-forming units (PFU) of SARS-CoV-2 (2019-nCoV/USA-WA1/2020). The stock was generated at BIOQUAL (lot no. 030120-1030, 3.31×10^5 PFU ml⁻¹) from a p4 seed stock obtained from BEI Resources (NR-52281). The stock underwent deep sequencing to confirm homology with the WA1/2020 isolate. Virus was stored at -80 °C before use, thawed by hand and placed

immediately on wet ice. Stock was diluted to 2.5×10^4 PFU ml⁻¹ in PBS and vortexed gently for 5 s before inoculation. Nasal swabs, BAL, plasma and serum samples were collected seven days before, two days after and four days after challenge.

Unimmunized control cynomolgus macaques ($n = 5$) comprised macaques that had been infused with a 10 mg kg⁻¹ of a control antibody (CH65) and then 3 days later challenged with the same challenge dose and stock of SARS-CoV-2 as used in RBD–scNP-immunized macaques or S-2P mRNA-LNP and RBD–scNP-immunized macaques. Protection from SARS-CoV-2 infection was determined by quantitative PCR of SARS-CoV-2 subgenomic *E* and the more-sensitive *N* RNA (*E* or *N* sgRNA)³⁹ as stated in ‘sgRNA real-time PCR quantification’.

SARS-CoV-2 protein production

The coronavirus ectodomain DNA constructs were synthesized (Genscript), produced and purified as previously described⁵³. S-2P was stabilized by the introduction of 2 prolines at amino acid positions 986 and 987. Plasmids encoding S-2P and HexaPro⁵⁴ were transiently transfected in FreeStyle 293 cells (Thermo Fisher) using Turbo293 (SpeedBiosystems) or 293Fectin (ThermoFisher). All cells were tested monthly for mycoplasma. The constructs contained an HRV 3C-cleavable C-terminal twinStrepTagII-8×His tag. On day 6, cell-free culture supernatant was generated by centrifugation of the culture and filtering through a 0.8-μm filter. Protein was purified from filtered cell culture supernatants by StrepTactin resin (IBA) and by size-exclusion chromatography using Superose 6 column (GE Healthcare) in 10 mM Tris pH8, 150 mM NaCl or 2 mM Tris pH 8, 200 mM NaCl, 0.02% NaN₃. ACE2–Fc was expressed by transient transfection of Freestyle 293-F cells⁵³. ACE2–Fc was purified from cell culture supernatant by HiTrap protein A column chromatography and Superdex200 size-exclusion chromatography in 10 mM Tris pH8, 150 mM NaCl. SARS-CoV-2 NTD was produced as previously described⁵⁵. SARS-CoV-2 fusion peptide was synthesized (GenScript).

Sortase A conjugation of SARS-CoV-2 RBD to *H. pylori* ferritin nanoparticles

Wuhan strain SARS-CoV-2 RBD was expressed with a sortase A donor sequence LPETGG encoded at its C terminus. C-terminal to the sortase A donor sequence was an HRV-3C cleavage site, 8×His tag and a twin StrepTagII (IBA). The SARS-CoV-2 RBD was expressed in Freestyle 293 cells and purified by StrepTactin affinity chromatography (IBA) and Superdex200 size-exclusion chromatography as stated in ‘SARS-CoV-2 protein production’. *Helicobacter pylori* ferritin particles were expressed with a pentaglycine sortase A acceptor sequence encoded at its N terminus of each subunit. For affinity purification of ferritin particles, 6×His tags were

appended C-terminal to a HRV3C cleavage site. Ferritin particles with a sortase A N-terminal tag were buffer exchanged into 50 mM Tris, 150 mM NaCl, 5 mM CaCl₂, pH 7.5. Then, 180 µM SARS-CoV-2 RBD was mixed with 120 µM of ferritin subunits and incubated with 100 µM of sortase A overnight at room temperature. Following incubation, conjugated particles were isolated from free ferritin or free RBD by size-exclusion chromatography using a Superose6 16/60 column.

Biolayer interferometry binding assays

Binding was measured using an OctetRed 96 (ForteBio). Anti-human IgG capture (AHC) sensor tips (Forte Bio) were hydrated for at least 10 min in PBS. ACE2 and monoclonal antibodies were diluted to 20 µg ml⁻¹ in PBS and placed in black 96-well assay plate. The influenza antibody CH65 was used as the background reference antibody. The RBD nanoparticle was diluted to 50 µg ml⁻¹ in PBS and added to the assay plate. Sensor tips were loaded with antibody for 120 s. Subsequently, the sensor tips were washed for 60 s in PBS to remove unbound antibody. The sensor tips were incubated in a fresh well of PBS to establish baseline reading before being dipped into RBD–scNP to allow association for 400 s. To measure dissociation of the antibody–RBD–scNP complex, the tip was incubated in PBS for 600 s. At the end of dissociation, the tip was ejected and a new tip was attached to load another antibody. The data were analysed with Data Analysis HT v.12 (ForteBio). Background binding observed with CH65 was subtracted from all values. All binding curves were aligned to the start of association. The binding response at the end of the 400-s association phase was plotted in GraphPad Prism v.9.0.

Surface plasmon resonance assays

Surface plasmon resonance measurements of DH1047 antigen binding fragment (Fab) binding to monomeric SARS-CoV-2 RBD proteins were performed in HBS-EP+ running buffer using a Biacore S200 instrument (Cytiva). Assays were performed in the DHVI BIA Core Facility. The RBD was first captured via its twin-StrepTagII onto a Series S Streptavidin chip to a level of 300–400 resonance units. The antibody Fabs were injected at 0.5 to 500 nM over the captured spike proteins using the single cycle kinetics injection mode at a flow rate of 50 µl min⁻¹. Fab association occurred for 180 s followed by a dissociation of 360 s after the end of the association phase. At the end of the dissociation phase, the RBD was regenerated with a 30-s injection of glycine pH 1.5. Binding values were analysed with Biacore S200 Evaluation software (Cytiva). References included blank streptavidin surface along with blank buffer binding and was subtracted from DH1047 values to account for signal drift and non-specific protein binding. A 1:1 Langmuir model with a local R_{max} was used for curve fitting.

Binding rates and constants were derived from the curve. Representative results from two independent experiments are shown.

BAL plaque assay

SARS-CoV-2 plaque assays were performed in the Duke Regional Biocontainment biosafety level 3 (BSL3) Laboratory as previously described⁵⁶. Serial dilutions of BAL fluid were incubated with Vero E6 cells in a standard plaque assay^{57,58}. BAL and cells were incubated at 37 °C and 5% CO₂ for 1 h. At the end of the incubation, 1 ml of a viscous overlay (1:1 2× DMEM and 1.2% methylcellulose) was added to each well. Plates are incubated for four days. After fixation, staining and washing, plates were dried and plaques from each dilution of BAL sample were counted. Data are reported as PFU ml⁻¹ of BAL fluid. Samples were collected in virus transport medium from six unimmunized, SARS-CoV-2-challenged macaques for comparison to vaccinated macaques.

SARS-CoV-2 pseudovirus neutralization

For SARS-CoV-2(D614G) and SARS-CoV-2 B.1.1.7 pseudovirus neutralization assays, neutralization of SARS-CoV-2 spike-pseudotyped virus was performed by adapting a previously described infection assay with lentiviral vectors and infection in 293T/ACE2.MF (the cell line was provided by M. Farzan and H. Mu at Scripps). Cells were maintained in DMEM containing 10% FBS and 50 µg ml⁻¹ gentamicin. An expression plasmid encoding codon-optimized full-length spike of the Wuhan-1 strain (VRC7480) was provided by B. Graham and K. Corbett at the Vaccine Research Center, National Institutes of Health. The D614G substitution was introduced into VRC7480 by site-directed mutagenesis using the QuikChange Lightning Site-Directed Mutagenesis Kit from Agilent Technologies (210518). The mutation was confirmed by full-length spike gene sequencing. Pseudovirions were produced in HEK 293T/17 cells (ATCC, CRL-11268) by transfection using Fugene 6 (Promega, E2692). Pseudovirions for infection of 293T cells expressing ACE2 were produced by co-transfection with a lentiviral backbone (pCMV ΔR8.2) and firefly luciferase reporter gene (pHR' CMV Luc)⁵⁹. Culture supernatants from transfections were clarified of cells by low-speed centrifugation and filtration (0.45-µm filter) and stored in 1 ml aliquots at -80 °C.

For neutralization assays in 293T cells expressing ACE2, a pretitrated dose of virus was incubated with 8 serial threefold or fivefold dilutions of monoclonal antibodies in duplicate in a total volume of 150 µl for 1 h at 37 °C in 96-well flat-bottom poly-l-lysine-coated culture plates (Corning Biocoat). SARS-CoV-2 RBD neutralizing antibody DH1043 spiked into normal human serum was used as a positive control. Cells were suspended using TrypLE express enzyme solution (Thermo Fisher

Scientific) and immediately added to all wells (10,000 cells in 100 µl of growth medium per well). One set of eight control wells received cells + virus (virus control) and another set of eight wells received cells only (background control). After 66–72 h of incubation, medium was removed by gentle aspiration and 30 µl of Promega 1× lysis buffer was added to all wells. After a 10-min incubation at room temperature, 100 µl of Bright-Glo luciferase reagent was added to all wells. After 1–2 min, 110 µl of the cell lysate was transferred to a black/white plate (Perkin-Elmer). Luminescence was measured using a PerkinElmer Life Sciences, Model Victor2 luminometer.

To make WA-1, P.1 and B.1.351 SARS-CoV-2 pseudoviruses, human codon-optimized cDNA encoding SARS-CoV-2 spike glycoproteins of various strains were synthesized by GenScript and cloned into eukaryotic cell expression vector pcDNA 3.1 between the BamHI and XhoI sites. Pseudovirions were produced by co-transfection of Lenti-X 293T cells with psPAX2(gag/pol), pTrip-luc lentiviral vector and pcDNA 3.1 SARS-CoV-2-spike-deltaC19, using Lipofectamine 3000. The supernatants were collected at 48 h after transfection and filtered through 0.45-µm membranes and titrated using HEK293T cells that express ACE2 and TMPRSS2 protein (293-ACE2-TMPRSS2 cells).

For the neutralization assay, 50 µl of SARS-CoV-2 spike pseudovirions were pre-incubated with an equal volume of medium containing serum at varying dilutions at room temperature for 1 h, then virus-antibody mixtures were added to 293T cells expressing ACE2 (WA-1 and B.1.351 assays) or 293-ACE2-TMPRSS2 (WA-1 and P.1 assays) cells in a 96-well plate. After a 3-h incubation, the inoculum was replaced with fresh medium. Cells were lysed 24 h later, and luciferase activity was measured using luciferin. Controls included cell-only control, virus without any antibody control and positive control sera. Neutralization titres are the serum dilution (ID_{50} or ID_{80}) at which relative luminescence units (RLU) were reduced by 50% or 80%, respectively, compared to virus control wells after subtraction of background RLU.

Live virus neutralization assays

Full-length SARS-CoV-2, SARS-CoV, WIV-1 and RsSHC014 viruses were designed to express nanoluciferase (nLuc) and were recovered via reverse genetics as previously described^{60,61,62}. Virus titres were measured in Vero E6 USAMRIID cells, as defined by PFU ml⁻¹, in a 6-well plate format in quadruplicate biological replicates for accuracy. For the 96-well neutralization assay, Vero E6 USAMRID cells were plated at 20,000 cells per well the day previously in clear-bottom black-walled plates. Cells were inspected to ensure confluence on the day of assay. Serum samples were tested at a starting dilution of 1:20 and were serially diluted threefold up to nine dilution spots. Serially diluted serum samples were mixed in equal volume with diluted virus. Antibody–virus and virus-only mixtures were then incubated at 37 °C

with 5% CO₂ for 1 h. Following incubation, serially diluted sera and virus-only controls were added in duplicate to the cells at 75 PFU at 37 °C with 5% CO₂. After 24 h, cells were lysed, and luciferase activity was measured via Nano-Glo Luciferase Assay System (Promega) according to the manufacturer specifications. Luminescence was measured by a Spectramax M3 plate reader (Molecular Devices). Virus neutralization titres were defined as the sample dilution at which a 50% reduction in RLU was observed relative to the average of the virus control wells. Prebleed or unimmunized control macaque values were subtracted from WIV-1 neutralization titres, but all other viruses were not background-subtracted.

Biocontainment and biosafety

All work was performed with approved standard operating procedures for SARS-CoV-2 in a BSL3 facility conforming to requirements recommended in the Microbiological and Biomedical Laboratories, by the US Department of Health and Human Service, the US Public Health Service, and the US Center for Disease Control and Prevention and the NIH.

Plasma and mucosal IgG blocking of ACE2 binding

For ACE2 blocking assays, plates were coated with 2 µg ml⁻¹ recombinant ACE2 protein, then washed and blocked with 3% BSA in 1× PBS. While assay plates blocked, purified antibodies were diluted as stated in ‘Plasma and mucosal IgG ELISA binding assays’, only in 1% BSA with 0.05% Tween-20. In a separate dilution plate, S-2P was mixed with the antibodies at a final concentration equal to the half-maximal effective concentration at which spike binds to ACE2 protein. The mixture was allowed to incubate at room temperature for 1 h. Blocked assay plates were then washed and the antibody–spike mixture was added to the assay plates for a period of 1 h at room temperature. Plates were washed and a polyclonal rabbit serum against the same spike protein (S-2P expressed in Freestyle 293-F cells) was added for 1 h, washed and detected with goat anti rabbit-HRP (Abcam, ab97080) followed by TMB substrate. The extent to which antibodies were able to block the binding of the spike protein to ACE2 was determined by comparing the optical density (OD) of antibody samples at 450 nm to the OD of samples containing spike protein only with no antibody. The following formula was used to calculate the percentage of blocking: blocking % = (100 – (OD sample/OD of spike only) × 100).

Plasma and mucosal IgG blocking of RBD monoclonal antibody binding

Blocking assays for DH1041 and DH1047 were performed as stated in ‘Plasma and mucosal IgG blocking of ACE2 binding’, except plates were coated with either

DH1041 or DH1047 instead of ACE2.

Plasma and mucosal IgG ELISA binding assays

For ELISA binding assays of coronavirus spike antibodies, the antigen panel included SARS-CoV-2 spike S1 + S2 ECD (SINO, 40589-V08B1), SARS-CoV-2 S-2P⁵³, SARS-CoV-2 spike RBD from mammalian cell 293 (SINO, 40592- V08H), SARS-CoV-2 spike NTD–biotin, SARS-CoV-2 fusion peptide (FP), SARS-CoV spike protein delta (BEI, NR-722), SARS-CoV WH20 spike RBD (SINO, 40150-V08B2), SARS-CoV RBD, MERS-CoV spike S1 + S2 (SINO, 40069-V08B), pangolin GXP4L S-2P, Bat CoV-RaTG13 S-2P, and bat CoV-SHC014 S-2P.

For binding ELISA, 384-well ELISA plates were coated with 2 $\mu\text{g ml}^{-1}$ of antigens in 0.1 M sodium bicarbonate overnight at 4 °C. Plates were washed with PBS + 0.05% Tween 20 and blocked with assay diluent (PBS containing 4% (w/v) whey protein, 15% normal goat serum, 0.5% Tween-20, and 0.05% sodium azide) at room temperature for 1 h. Plasma or mucosal fluid were serially diluted threefold in superblock starting at a 1:30 dilution. Nasal fluid was started from neat and diluted 1:30, whereas BAL fluid was concentrated tenfold. To concentrate BAL, individual BAL aliquots from the same macaque and same time point were pooled in 3-kDa MWCO ultrafiltration tubes (Sartorius, VS2091). Pooled BAL was concentrated by centrifugation at 3,500 rpm for 30 min or until volume was reduced by a factor of 10. The pool was then aliquoted and frozen at –80 °C until its use in an assay. Purified monoclonal antibody samples were diluted to 100 $\mu\text{g ml}^{-1}$ and then serially diluted threefold in assay diluent. Samples were added to the antigen-coated plates, and incubated for 1 h, followed by washes with PBS-0.1% Tween 20. HRP-conjugated goat anti-human IgG secondary antibody or mouse anti-rhesus IgG secondary antibody (SouthernBiotech, 2040-05) was diluted to 1:10,000 and incubated at room temperature for 1 h. These plates were washed four times and developed with tetramethylbenzidine substrate (SureBlue Reserve- KPL). The reaction was stopped with 1 M HCl, and OD at 450 nm was determined.

sgRNA real-time PCR quantification

SARS-CoV-2 *E* gene and *N* gene subgenomic mRNAs were measured by one-step RT–qPCR adapted from previously described methods^{63, 64}. *E* and *N* genes were cloned into pCDNA3.1 and used as in vitro transcription templates. In vitro transcribed RNA was generated with the MEGAscript T7 Transcription Kit (ThermoFisher, AM1334) and purified with MEGAclear Transcription Clean-Up Kit (ThermoFisher, AM1908). Pure RNA was quantified and used as standards for qPCR. RNA extracted from animal samples was quantified using TaqMan Fast Virus 1-Step Master Mix (ThermoFisher, 4444432) and custom primers and probes targeting the *E* gene sgRNA (forward primer, 5'-CGATCTCTGTAGATCTGTTCTCE-3'; reverse primer, 5'-ATATTGCAGCAGTACGCACACA-3'; probe, 5'-FAM-ACACTAGCCATCCTACTGCGCTTCG-BHQ1-3') or the *N* gene sgRNA (forward primer, 5'-CGATCTCTGTAGATCTGTTCTC-3'; reverse primer, 5'-GGTGAACCAAGACGCAGTAT-3'; probe, 5'-FAM-TAACCCAGAATGGAGAACGCAGTG GG-BHQ1-3'). A QuantStudio 3 Real-Time PCR System (Applied Biosystems) or a StepOnePlus Real-Time PCR System (Applied Biosystems) was used for real-time PCR reactions. Cycle conditions were as follows: reverse transcription at 50 °C for 5 min, initial denaturation at 95 °C for 20 s, and 40 cycles of denaturation–annealing–extension at 95 °C for 15 s and 60 °C for 30 s. Standard curves were used to calculate *E* or *N* sgRNA in copies per ml. The LOD for both *E* and *N* sgRNA assays were 12.5 copies per reaction or 150 copies per ml of BAL, nasal swab or nasal wash.

Recombinant IgG production

Expi293-F cells were diluted to 2.5×10^6 cells per ml on the day of transfection. Cells were co-transfected with expifectamine and heavy and light chain expression plasmids. Enhancers were added 16 h after transfection. On day 5, the cell culture was cleared of cells by centrifugation, filtered and incubated with protein A beads overnight. The next day, the protein A resin was washed with Tris buffered saline and then added to a 25-ml column. The resin was washed again and then glacial acetic acid was used to elute antibody off of the protein A resin. The pH of the solution was neutralized with 1 M Tris pH 8. The antibody was buffer-exchanged into 25 mM sodium citrate pH 6 supplemented with 150 mM NaCl, 0.2-μm filtered and frozen at –80 °C.

Negative-stain electron microscopy

The RBD nanoparticle protein at about 1–5 mg ml⁻¹ concentration that had been flash-frozen and stored at -80 °C was thawed in an aluminium block at 37 °C for 5 min; then 1–4 µl of RBD nanoparticle was diluted to a final concentration of 0.1 mg ml⁻¹ into room-temperature buffer containing 150 mM NaCl, 20 mM HEPES pH 7.4, 5% glycerol and 7.5 mM glutaraldehyde. After 5 min of cross-linking, excess glutaraldehyde was quenched by adding sufficient 1 M Tris pH 7.4 stock to give a final concentration of 75 mM Tris and incubated for 5 min. For negative stain, carbon-coated grids (EMS, CF300-cu-UL) were glow-discharged for 20 s at 15 mA, after which a 5-µl drop of quenched sample was incubated on the grid for 10–15 s, blotted and then stained with 2% uranyl formate. After air drying, grids were imaged with a Philips EM420 electron microscope operated at 120 kV, at 82,000× magnification and images captured with a 2k × 2k CCD camera at a pixel size of 4.02 Å.

Processing of negative-stain images

The RELION 3.0 program was used for all negative-stain image processing. Images were imported, CTF-corrected with CTFFIND and particles were picked using a nanoparticle template from previous 2D class averages of nanoparticles alone. Extracted particle stacks were subjected to 2 or 3 rounds of 2D class averaging and selection to discard junk particles and background picks.

Betacoronavirus sequence analysis

Heat maps of amino acid sequence similarity were computed for a representative set of betacoronaviruses using the ComplexHeatmap package in R. In brief, 1,408 betacoronavirus sequences were retrieved from NCBI GenBank, aligned to the Wuhan-1 spike protein sequence and trimmed to the aligned region. The 1,408 spike sequences were then clustered using USEARCH⁶⁵ with a sequence identity threshold of 0.90, resulting in 52 clusters. We sampled one sequence from each cluster to generate a representative set of sequences. Five betacoronavirus sequences of interest

not originally included in the clustered set were added: SARS-CoV-2, GXP4L, bat coronavirus RaTG13, bat coronavirus SHC014 and bat coronavirus WIV-1. This resulted in a set of 57 representative spike sequences. Pairs of spike amino acid sequences were aligned using a global alignment and the BLOSUM62 scoring matrix. For RBD and NTD domain alignments, spike sequences were aligned to the Wuhan-1 spike protein RBD region (residues 330–521) and NTD region (residues 27–292), respectively, and trimmed to the aligned region. Phylogenetic tree construction of RBD sequences was performed with Geneious Prime 2020.1.2 using the neighbour joining method and default parameters. To map group-2b betacoronavirus sequence conservation onto the RBD structure, group-2b spike sequences were retrieved from GenBank and clustered using USEARCH⁶⁵ with a sequence identity threshold of 0.99, resulting in 39 clusters. For clusters of size >5, 5 spike sequences were randomly downsampled from each cluster. The resulting set of 73 sequences was aligned using MAFFT⁶⁶. Conservation scores for each position in the multiple sequence alignment were calculated using the trident scoring method⁶⁷ and computed using the MstatX program (<https://github.com/gcollet/MstatX>). The conservation scores were then mapped to the RBD domain coordinates (PDB 7LD1) and images rendered with PyMol version 2.3.5.

Histopathology

Lung specimen from macaques were fixed in 10% neutral-buffered formalin, processed and blocked in paraffin for histology analyses. All tissues were sectioned at 5 µm and stained with haematoxylin and eosin to assess histopathology. Stained sections were evaluated by a board-certified veterinary pathologist in a blinded manner. Sections were examined under light microscopy using an Olympus BX51 microscope and photographs were taken using an Olympus DP73 camera.

Immunohistochemistry

Staining for SARS-CoV-2 nucleocapsid antigen was performed by the Bond RX automated system with the Polymer Define Detection System (Leica) following the manufacturer's protocol. Tissue sections were dewaxed with

Bond Dewaxing Solution (Leica) at 72 °C for 30 min, then subsequently rehydrated with graded alcohol washes and 1× Immuno Wash (StatLab). Heat-induced epitope retrieval was performed using Epitope Retrieval Solution 1 (Leica) and by heating the tissue section to 100 °C for 20 min. A peroxide block (Leica) was applied for 5 min to quench endogenous peroxidase activity before applying the SARS-CoV-2 nucleocapsid antibody (1:2,000, GeneTex, GTX135357). Antibodies were diluted in Background Reducing Antibody Diluent (Agilent). The tissue was subsequently incubated with an anti-rabbit HRP polymer (Leica) and colorized with 3,3'-diaminobenzidine chromogen for 10 min. Slides were counterstained with haematoxylin.

Reagent authentication

Cell lines were received with a certificate of authentication certifying their identity. Cell identity was also confirmed by visualizing cell morphology and using flow cytometry to detect cell surface proteins. Cells were confirmed to be free of mycoplasma with monthly testing.

Statistics analysis

Data were plotted using Prism GraphPad 9.0. Wilcoxon rank-sum exact test was performed to compare differences between groups with *P* value <0.05, considered significant using SAS 9.4 (SAS Institute). No adjustments were made to the *P* values for multiple comparisons. The 50% and 80% inhibitory dilution (ID_{50} and ID_{80} , respectively) values were calculated using R statistical software (version 4.0.0). The R package ‘nplr’ was used to fit four-parameter logistic regression curves to the average values from duplicate experiments, and these fits were used to estimate the concentrations corresponding to 50% and 80% neutralization.

Reporting summary

Further information on research design is available in the [Nature Research Reporting Summary](#) linked to this paper.

Data availability

Data supporting the findings of this study are available within the Article and Supplementary Information. Any other relevant data are available from the corresponding authors upon reasonable request. [Source data](#) are provided with this paper.

References

1. 1.

Wang, C., Horby, P. W., Hayden, F. G. & Gao, G. F. A novel coronavirus outbreak of global health concern. *Lancet* **395**, 470–473 (2020).

[CAS](#) [PubMed](#) [PubMed Central](#) [Google Scholar](#)

2. 2.

Zaki, A. M., van Boheemen, S., Bestebroer, T. M., Osterhaus, A. D. & Fouchier, R. A. Isolation of a novel coronavirus from a man with pneumonia in Saudi Arabia. *N. Engl. J. Med.* **367**, 1814–1820 (2012).

[CAS](#) [PubMed](#) [Google Scholar](#)

3. 3.

Zhong, N. S. et al. Epidemiology and cause of severe acute respiratory syndrome (SARS) in Guangdong, People's Republic of China, in February, 2003. *Lancet* **362**, 1353–1358 (2003).

[CAS](#) [PubMed](#) [PubMed Central](#) [Google Scholar](#)

4. 4.

Zhu, N. et al. A novel coronavirus from patients with pneumonia in China, 2019. *N. Engl. J. Med.* **382**, 727–733 (2020).

[CAS](#) [PubMed](#) [PubMed Central](#) [Google Scholar](#)

5. 5.

Zhou, P. et al. A pneumonia outbreak associated with a new coronavirus of probable bat origin. *Nature* **579**, 270–273 (2020).

[ADS](#) [CAS](#) [PubMed](#) [PubMed Central](#) [Google Scholar](#)

6. 6.

Li, W. et al. Bats are natural reservoirs of SARS-like coronaviruses. *Science* **310**, 676–679 (2005).

[ADS](#) [CAS](#) [PubMed](#) [Google Scholar](#)

7. 7.

Olival, K. J. et al. Host and viral traits predict zoonotic spillover from mammals. *Nature* **546**, 646–650 (2017).

[ADS](#) [CAS](#) [PubMed](#) [PubMed Central](#) [Google Scholar](#)

8. 8.

Sabir, J. S. et al. Co-circulation of three camel coronavirus species and recombination of MERS-CoVs in Saudi Arabia. *Science* **351**, 81–84 (2016).

[ADS](#) [CAS](#) [PubMed](#) [Google Scholar](#)

9. 9.

Ge, X. Y. et al. Isolation and characterization of a bat SARS-like coronavirus that uses the ACE2 receptor. *Nature* **503**, 535–538 (2013).

[ADS](#) [CAS](#) [PubMed](#) [PubMed Central](#) [Google Scholar](#)

10. 10.

Guan, Y. et al. Isolation and characterization of viruses related to the SARS coronavirus from animals in southern China. *Science* **302**, 276–278 (2003).

[ADS](#) [CAS](#) [PubMed](#) [Google Scholar](#)

11. 11.

Xiao, K. et al. Isolation of SARS-CoV-2-related coronavirus from Malayan pangolins. *Nature* **583**, 286–289 (2020).

[ADS](#) [CAS](#) [PubMed](#) [Google Scholar](#)

12. 12.

Menachery, V. D., Graham, R. L. & Baric, R. S. Jumping species—a mechanism for coronavirus persistence and survival. *Curr. Opin. Virol.* **23**, 1–7 (2017).

[PubMed](#) [PubMed Central](#) [Google Scholar](#)

13. 13.

Pinto, D. et al. Cross-neutralization of SARS-CoV-2 by a human monoclonal SARS-CoV antibody. *Nature* **583**, 290–295 (2020).

[ADS](#) [CAS](#) [PubMed](#) [Google Scholar](#)

14. 14.

Wee, A. Z. et al. Broad neutralization of SARS-related viruses by human monoclonal antibodies. *Science* **369**, 731–736 (2020).

[ADS](#) [CAS](#) [PubMed](#) [PubMed Central](#) [Google Scholar](#)

15. 15.

Li, D. et al. The functions of SARS-CoV-2 neutralizing and infection-enhancing antibodies in vitro and in mice and nonhuman primates.

Preprint at <https://doi.org/10.1101/2020.12.31.424729> (2021).

16. 16.

Shi, R. et al. A human neutralizing antibody targets the receptor-binding site of SARS-CoV-2. *Nature* **584**, 120–124 (2020).

[ADS](#) [CAS](#) [PubMed](#) [Google Scholar](#)

17. 17.

Ju, B. et al. Human neutralizing antibodies elicited by SARS-CoV-2 infection. *Nature* **584**, 115–119 (2020).

[ADS](#) [CAS](#) [PubMed](#) [Google Scholar](#)

18. 18.

Robbiani, D. F. et al. Convergent antibody responses to SARS-CoV-2 in convalescent individuals. *Nature* **584**, 437–442 (2020).

[ADS](#) [CAS](#) [PubMed](#) [PubMed Central](#) [Google Scholar](#)

19. 19.

Zost, S. J. et al. Potently neutralizing and protective human antibodies against SARS-CoV-2. *Nature* **584**, 443–449 (2020).

[CAS](#) [PubMed](#) [PubMed Central](#) [Google Scholar](#)

20. 20.

Liu, L. et al. Potent neutralizing antibodies against multiple epitopes on SARS-CoV-2 spike. *Nature* **584**, 450–456 (2020).

[CAS](#) [PubMed](#) [Google Scholar](#)

21. 21.

Hansen, J. et al. Studies in humanized mice and convalescent humans yield a SARS-CoV-2 antibody cocktail. *Science* **369**, 1010–1014 (2020).

[ADS](#) [CAS](#) [PubMed](#) [PubMed Central](#) [Google Scholar](#)

22. 22.

Brouwer, P. J. M. et al. Potent neutralizing antibodies from COVID-19 patients define multiple targets of vulnerability. *Science* **369**, 643–650 (2020).

[ADS](#) [CAS](#) [PubMed](#) [PubMed Central](#) [Google Scholar](#)

23. 23.

Rogers, T. F. et al. Isolation of potent SARS-CoV-2 neutralizing antibodies and protection from disease in a small animal model. *Science* **369**, 956–963 (2020).

[ADS](#) [CAS](#) [PubMed](#) [PubMed Central](#) [Google Scholar](#)

24. 24.

Piccoli, L. et al. Mapping neutralizing and immunodominant sites on the SARS-CoV-2 spike receptor-binding domain by structure-guided high-resolution serology. *Cell* **183**, 1024–1042.e21 (2020).

[CAS](#) [PubMed](#) [PubMed Central](#) [Google Scholar](#)

25. 25.

Burton, D. R. & Walker, L. M. Rational vaccine design in the time of COVID-19. *Cell Host Microbe* **27**, 695–698 (2020).

[CAS](#) [PubMed](#) [PubMed Central](#) [Google Scholar](#)

26. 26.

Cohen, A. A. et al. Mosaic nanoparticles elicit cross-reactive immune responses to zoonotic coronaviruses in mice. *Science* **371**, 735–741 (2021).

[ADS](#) [CAS](#) [PubMed](#) [PubMed Central](#) [Google Scholar](#)

27. 27.

Ma, X. et al. Nanoparticle vaccines based on the receptor binding domain (RBD) and heptad repeat (HR) of SARS-CoV-2 elicit robust protective immune responses. *Immunity* **53**, 1315–1330.e9 (2020).

[CAS](#) [PubMed](#) [PubMed Central](#) [Google Scholar](#)

28. 28.

Bangaru, S. et al. Structural analysis of full-length SARS-CoV-2 spike protein from an advanced vaccine candidate. *Science* **370**, 1089–1094 (2020).

[ADS](#) [CAS](#) [PubMed](#) [PubMed Central](#) [Google Scholar](#)

29. 29.

Walls, A. C. et al. Elicitation of potent neutralizing antibody responses by designed protein nanoparticle vaccines for SARS-CoV-2. *Cell* **183**, 1367–1382.e17 (2020).

[CAS](#) [PubMed](#) [PubMed Central](#) [Google Scholar](#)

30. 30.

Saunders, K. O. et al. Targeted selection of HIV-specific antibody mutations by engineering B cell maturation. *Science* **366**, eaay7199 (2019).

[CAS](#) [PubMed](#) [PubMed Central](#) [Google Scholar](#)

31. 31.

Fox, C. B. et al. Adsorption of a synthetic TLR7/8 ligand to aluminum oxyhydroxide for enhanced vaccine adjuvant activity: a formulation approach. *J. Control. Release* **244** (Pt A), 98–107 (2016).

[CAS](#) [PubMed](#) [PubMed Central](#) [Google Scholar](#)

32. 32.

Korber, B. et al. Tracking changes in SARS-CoV-2 spike: evidence that D614G increases infectivity of the COVID-19 virus. *Cell* **182**, 812–827.e19 (2020).

[CAS](#) [PubMed](#) [PubMed Central](#) [Google Scholar](#)

33. 33.

Baden, L. R. et al. Efficacy and safety of the mRNA-1273 SARS-CoV-2 vaccine. *N. Engl. J. Med.* **384**, 403–416 (2021).

[CAS](#) [PubMed](#) [Google Scholar](#)

34. 34.

Polack, F. P. et al. Safety and efficacy of the BNT162b2 mRNA Covid-19 vaccine. *N. Engl. J. Med.* **383**, 2603–2615 (2020).

[CAS](#) [PubMed](#) [PubMed Central](#) [Google Scholar](#)

35. 35.

Galloway, S. E. et al. Emergence of SARS-CoV-2 B.1.1.7 lineage – United States, December 29, 2020–January 12, 2021. *MMWR Morb. Mortal. Wkly. Rep.* **70**, 95–99 (2021).

[CAS](#) [PubMed](#) [PubMed Central](#) [Google Scholar](#)

36. 36.

Leung, K., Shum, M. H., Leung, G. M., Lam, T. T. & Wu, J. T. Early transmissibility assessment of the N501Y mutant strains of SARS-CoV-2 in the United Kingdom, October to November 2020. *Euro Surveill.* **26**, 2002106 (2021).

37. 37.

Faria, N. R. et al. Genomic characterisation of an emergent SARS-CoV-2 lineage in Manaus: preliminary findings.

Virological <https://virological.org/t/genomic-characterisation-of-an-emergent-sars-cov-2-lineage-in-manaus-preliminary-findings/586> (2021).

38. 38.

Tegally, H. et al. Sixteen novel lineages of SARS-CoV-2 in South Africa. *Nat. Med.* **27**, 440–446 (2021).

[CAS](#) [PubMed](#) [Google Scholar](#)

39. 39.

Wibmer, C. K. et al. SARS-CoV-2 501Y.V2 escapes neutralization by South African COVID-19 donor plasma. *Nat. Med.* **27**, 622–625 (2021).

[CAS](#) [PubMed](#) [Google Scholar](#)

40. 40.

Lassaunière, R. et al. SARS-CoV-2 spike mutations arising in Danish mink and their spread to humans. https://files.ssi.dk/Mink-cluster-5-short-report_AFO2 (2021).

41. 41.

Menachery, V. D. et al. A SARS-like cluster of circulating bat coronaviruses shows potential for human emergence. *Nat. Med.* **21**, 1508–1513 (2015).

[CAS](#) [PubMed](#) [PubMed Central](#) [Google Scholar](#)

42. 42.

Menachery, V. D. et al. SARS-like WIV1-CoV poised for human emergence. *Proc. Natl Acad. Sci. USA* **113**, 3048–3053 (2016).

[ADS](#) [CAS](#) [PubMed](#) [PubMed Central](#) [Google Scholar](#)

43. 43.

Liu, H. et al. Cross-neutralization of a SARS-CoV-2 antibody to a functionally conserved site is mediated by avidity. *Immunity* **53**, 1272–1280.e5 (2020).

[CAS](#) [PubMed](#) [PubMed Central](#) [Google Scholar](#)

44. 44.

Muik, A. et al. Neutralization of SARS-CoV-2 lineage B.1.1.7 pseudovirus by BNT162b2 vaccine-elicited human sera. *Science* **371**, 1152–1153 (2021).

[ADS](#) [CAS](#) [PubMed](#) [PubMed Central](#) [Google Scholar](#)

45. 45.

Wu, K. et al. mRNA-1273 vaccine induces neutralizing antibodies against spike mutants from global SARS-CoV-2 variants. Preprint at <https://doi.org/10.1101/2021.01.25.427948> (2021).

46. 46.

Cele, S. et al. Escape of SARS-CoV-2 501Y.V2 variants from neutralization by convalescent plasma. Preprint at <https://doi.org/10.1101/2021.01.26.21250224> (2021).

47. 47.

Collier, D. et al. Sensitivity of SARS-CoV-2 B.1.1.7 to mRNA vaccine-elicited antibodies. *Nature* **593**, 136–141 (2021).

[ADS](#) [CAS](#) [PubMed](#) [Google Scholar](#)

48. 48.

Wang, Z. et al. mRNA vaccine-elicited antibodies to SARS-CoV-2 and circulating variants. *Nature*, **592**, 616–622 (2021).

[ADS](#) [CAS](#) [PubMed](#) [Google Scholar](#)

49. 49.

Yu, J. et al. DNA vaccine protection against SARS-CoV-2 in rhesus macaques. *Science* **369**, 806–811 (2020).

[ADS](#) [CAS](#) [PubMed](#) [PubMed Central](#) [Google Scholar](#)

50. 50.

Mercado, N. B. et al. Single-shot Ad26 vaccine protects against SARS-CoV-2 in rhesus macaques. *Nature* **586**, 583–588 (2020).

[ADS](#) [CAS](#) [PubMed](#) [PubMed Central](#) [Google Scholar](#)

51. 51.

Laczkó, D. et al. A single immunization with nucleoside-modified mRNA vaccines elicits strong cellular and humoral immune responses against SARS-CoV-2 in mice. *Immunity* **53**, 724–732.e7 (2020).

[PubMed](#) [PubMed Central](#) [Google Scholar](#)

52. 52.

Pardi, N. et al. Zika virus protection by a single low-dose nucleoside-modified mRNA vaccination. *Nature* **543**, 248–251 (2017).

[ADS](#) [CAS](#) [PubMed](#) [PubMed Central](#) [Google Scholar](#)

53. 53.

Wrapp, D. et al. Cryo-EM structure of the 2019-nCoV spike in the prefusion conformation. *Science* **367**, 1260–1263 (2020).

[ADS](#) [CAS](#) [PubMed](#) [PubMed Central](#) [Google Scholar](#)

54. 54.

Hsieh, C.-L. et al. Structure-based design of prefusion-stabilized SARS-CoV-2 spikes. *Science* **369**, 1501–1505 (2020).

[ADS](#) [CAS](#) [PubMed](#) [Google Scholar](#)

55. 55.

Zhou, T. et al. Structure-based design with tag-based purification and in-process biotinylation enable streamlined development of SARS-CoV-2 spike molecular probes. *Cell Rep.* **33**, 108322 (2020).

[CAS](#) [PubMed](#) [PubMed Central](#) [Google Scholar](#)

56. 56.

Berry, J. D. et al. Development and characterisation of neutralising monoclonal antibody to the SARS-coronavirus. *J. Virol. Methods* **120**, 87–96 (2004).

[CAS](#) [PubMed](#) [PubMed Central](#) [Google Scholar](#)

57. 57.

Coleman, C. M. & Frieman, M. B. Growth and quantification of MERS-CoV infection. *Curr. Protoc. Microbiol.* **37**, 15E.2.1–15.E.2.9 (2015).

[Google Scholar](#)

58. 58.

Kint, J., Maier, H. J. & Jagt, E. Quantification of infectious bronchitis coronavirus by titration in vitro and in ovo. *Methods Mol. Biol.* **1282**, 89–98 (2015).

[CAS](#) [PubMed](#) [Google Scholar](#)

59. 59.

Naldini, L., Blömer, U., Gage, F. H., Trono, D. & Verma, I. M. Efficient transfer, integration, and sustained long-term expression of the transgene in adult rat brains injected with a lentiviral vector. *Proc. Natl Acad. Sci. USA* **93**, 11382–11388 (1996).

[ADS](#) [CAS](#) [PubMed](#) [PubMed Central](#) [Google Scholar](#)

60. 60.

Yount, B. et al. Reverse genetics with a full-length infectious cDNA of severe acute respiratory syndrome coronavirus. *Proc. Natl Acad. Sci. USA* **100**, 12995–13000 (2003).

[ADS](#) [CAS](#) [PubMed](#) [PubMed Central](#) [Google Scholar](#)

61. 61.

Scobey, T. et al. Reverse genetics with a full-length infectious cDNA of the Middle East respiratory syndrome coronavirus. *Proc. Natl Acad. Sci. USA* **110**, 16157–16162 (2013).

[ADS](#) [CAS](#) [PubMed](#) [PubMed Central](#) [Google Scholar](#)

62. 62.

Hou, Y. J. et al. SARS-CoV-2 reverse genetics reveals a variable infection gradient in the respiratory tract. *Cell* **182**, 429–446.e14 (2020).

[CAS](#) [PubMed](#) [PubMed Central](#) [Google Scholar](#)

63. 63.

Wölfel, R. et al. Virological assessment of hospitalized patients with COVID-2019. *Nature* **581**, 465–469 (2020).

64. 64.

Yu, J. et al. DNA vaccine protection against SARS-CoV-2 in rhesus macaques. *Science* **369**, 806–811 (2020).

65. 65.

Edgar, R. C. Search and clustering orders of magnitude faster than BLAST. *Bioinformatics* **26**, 2460–2461 (2010).

[CAS](#) [PubMed](#) [PubMed Central](#) [Google Scholar](#)

66. 66.

Nakamura, T., Yamada, K. D., Tomii, K. & Katoh, K. Parallelization of MAFFT for large-scale multiple sequence alignments. *Bioinformatics* **34**, 2490–2492 (2018).

[CAS](#) [PubMed](#) [PubMed Central](#) [Google Scholar](#)

67. 67.

Valdar, W. S. Scoring residue conservation. *Proteins* **48**, 227–241 (2002).

[CAS](#) [PubMed](#) [Google Scholar](#)

[Download references](#)

Acknowledgements

We thank V. Gee-Lai, M. Deyton, C. McDanal, B. Watts and K. Cronin for technical assistance; E. Donahue for program management and assistance with manuscript preparation; P. J. C. Lin and Y. K. Tam from Acuitas Therapeutics for providing lipid nanoparticles; J. Harrison, A. Granados, A. Goode, A. Cook, A. Dodson, K. Steingrebe, B. Bart, L. Pessant, A. VanRy, D. Valentin, A. Strasbaugh and M. Cabus for assistance with macaque studies; and S. O'Connor and J. J. Baczenas at the Department of Pathology and Laboratory Medicine (University of Wisconsin-Madison) for sequencing support. The following reagent was deposited by the Centers for Disease Control and Prevention and obtained through BEI Resources, NIAID, NIH: SARS-CoV-2, isolate USA-WA1/2020, NR-52281. This work was supported by a grant from the State of North Carolina with funds from the federal CARES Act, by funds from NIH, NIAID, DAIDS grant AI142596 (B.F.H.), by support from the Ting Tsung & Wei Fong Chao Foundation (B.F.H.), by grant R01AI157155 (R.S.B.) and by grant U54 CA260543 (R.S.B.). This project was also supported by the North Carolina Policy Collaboratory at the University of North Carolina at Chapel Hill with funding from the North Carolina Coronavirus Relief Fund established and appropriated by the North Carolina General Assembly. This study was also supported by funding from an NIH F32 AI152296, a Burroughs Wellcome Fund Postdoctoral Enrichment Program Award, and was previously supported by an NIH NIAID T32 AI007151 (all three awarded to D.R.M.). COVID-19 sample processing was performed in the Duke Regional Biocontainment Laboratory, which received partial support for construction from the NIH/NIAD (UC6AI058607; G.D.S.) with support from a cooperative agreement with DOD/DARPA (HR0011-17-2-0069; G.D.S.).

Author information

Affiliations

1. Duke Human Vaccine Institute, Duke University School of Medicine, Durham, NC, USA

Kevin O. Saunders, Esther Lee, Robert Parks, Dapeng Li, Haiyan Chen, Robert J. Edwards, Sophie Gobeil, Maggie Barr, Katayoun Mansouri, S. Munir Alam, Laura L. Sutherland, Fangping Cai, Aja M.

Sanzone, Madison Berry, Kartik Manne, Anyway B.
Kapingidza, Mihai Azoitei, Rachel L. Spreng, R. Wes Rountree, C.
Todd DeMarco, Thomas N. Denny, Christopher W. Woods, Thomas H.
Oguin III, Gregory D. Sempowski, Kevin Wiehe, Priyamvada
Acharya, David C. Montefiori & Barton F. Haynes

2. Department of Surgery, Duke University, Durham, NC, USA

Kevin O. Saunders, Priyamvada Acharya & David C. Montefiori

3. Department of Immunology, Duke University School of Medicine,
Durham, NC, USA

Kevin O. Saunders & Barton F. Haynes

4. Department of Molecular Genetics and Microbiology, Duke University
School of Medicine, Durham, NC, USA

Kevin O. Saunders

5. Department of Medicine, Duke University School of Medicine,
Durham, NC, USA

Esther Lee, Robert Parks, Dapeng Li, Haiyan Chen, Robert J.
Edwards, Sophie Gobeil, Maggie Barr, Katayoun Mansouri, S. Munir
Alam, Laura L. Sutherland, Fangping Cai, Aja M. Sanzone, Madison
Berry, Kartik Manne, Anyway B. Kapingidza, Mihai Azoitei, Rachel
L. Spreng, R. Wes Rountree, C. Todd DeMarco, Thomas N.
Denny, Christopher W. Woods, Thomas H. Oguin III, Gregory D.
Sempowski, Kevin Wiehe & Barton F. Haynes

6. Department of Epidemiology, University of North Carolina at Chapel
Hill, Chapel Hill, NC, USA

David R. Martinez, Longping V. Tse, Trevor D. Scobey & Ralph S.
Baric

7. Infectious Disease Pathogenesis Section, Comparative Medicine
Branch, National Institute of Allergy and Infectious Diseases (NIAID),

National Institutes of Health (NIH), Bethesda, MD, USA

Kevin W. Bock, Mahnaz Minai, Bianca M. Nagata & Ian N. Moore

8. Center for Applied Genomics and Precision Medicine, Duke University Medical Center, Durham, NC, USA

Christopher W. Woods & Elizabeth W. Petzold

9. Division of Viral Products, Center for Biologics Evaluation and Research (CBER), Food and Drug Administration, Silver Spring, MD, USA

Juanjie Tang, Hana Golding & Surender Khurana

10. Vaccine Research Center, NIAID, NIH, Bethesda, MD, USA

Matthew Gagne, Daniel C. Douek & Robert Seder

11. Corporate Research Materials Lab, 3M Company, St Paul, MN, USA

Mark A. Tomai

12. Infectious Disease Research Institute, Seattle, WA, USA

Christopher B. Fox

13. Department of Medicine, University of Pennsylvania, Philadelphia, PA, USA

Drew Weissman & Norbert Pardi

14. BIOQUAL, Rockville, MD, USA

Hanne Andersen & Mark G. Lewis

Authors

1. Kevin O. Saunders

[View author publications](#)

You can also search for this author in [PubMed](#) [Google Scholar](#)

2. Esther Lee

[View author publications](#)

You can also search for this author in [PubMed](#) [Google Scholar](#)

3. Robert Parks

[View author publications](#)

You can also search for this author in [PubMed](#) [Google Scholar](#)

4. David R. Martinez

[View author publications](#)

You can also search for this author in [PubMed](#) [Google Scholar](#)

5. Dapeng Li

[View author publications](#)

You can also search for this author in [PubMed](#) [Google Scholar](#)

6. Haiyan Chen

[View author publications](#)

You can also search for this author in [PubMed](#) [Google Scholar](#)

7. Robert J. Edwards

[View author publications](#)

You can also search for this author in [PubMed](#) [Google Scholar](#)

8. Sophie Gobeil

[View author publications](#)

You can also search for this author in [PubMed](#) [Google Scholar](#)

9. Maggie Barr

[View author publications](#)

You can also search for this author in [PubMed](#) [Google Scholar](#)

10. Katayoun Mansouri

[View author publications](#)

You can also search for this author in [PubMed](#) [Google Scholar](#)

11. S. Munir Alam

[View author publications](#)

You can also search for this author in [PubMed](#) [Google Scholar](#)

12. Laura L. Sutherland

[View author publications](#)

You can also search for this author in [PubMed](#) [Google Scholar](#)

13. Fangping Cai

[View author publications](#)

You can also search for this author in [PubMed](#) [Google Scholar](#)

14. Aja M. Sanzone

[View author publications](#)

You can also search for this author in [PubMed](#) [Google Scholar](#)

15. Madison Berry

[View author publications](#)

You can also search for this author in [PubMed](#) [Google Scholar](#)

16. Kartik Manne

[View author publications](#)

You can also search for this author in [PubMed](#) [Google Scholar](#)

17. Kevin W. Bock

[View author publications](#)

You can also search for this author in [PubMed](#) [Google Scholar](#)

18. Mahnaz Minai

[View author publications](#)

You can also search for this author in [PubMed](#) [Google Scholar](#)

19. Bianca M. Nagata

[View author publications](#)

You can also search for this author in [PubMed](#) [Google Scholar](#)

20. Anyway B. Kapingidza

[View author publications](#)

You can also search for this author in [PubMed](#) [Google Scholar](#)

21. Mihai Azoitei

[View author publications](#)

You can also search for this author in [PubMed](#) [Google Scholar](#)

22. Longping V. Tse

[View author publications](#)

You can also search for this author in [PubMed](#) [Google Scholar](#)

23. Trevor D. Scobey

[View author publications](#)

You can also search for this author in [PubMed](#) [Google Scholar](#)

24. Rachel L. Spreng

[View author publications](#)

You can also search for this author in [PubMed](#) [Google Scholar](#)

25. R. Wes Rountree

[View author publications](#)

You can also search for this author in [PubMed](#) [Google Scholar](#)

26. C. Todd DeMarco

[View author publications](#)

You can also search for this author in [PubMed](#) [Google Scholar](#)

27. Thomas N. Denny

[View author publications](#)

You can also search for this author in [PubMed](#) [Google Scholar](#)

28. Christopher W. Woods

[View author publications](#)

You can also search for this author in [PubMed](#) [Google Scholar](#)

29. Elizabeth W. Petzold

[View author publications](#)

You can also search for this author in [PubMed](#) [Google Scholar](#)

30. Juanjie Tang

[View author publications](#)

You can also search for this author in [PubMed](#) [Google Scholar](#)

31. Thomas H. Oguin III

[View author publications](#)

You can also search for this author in [PubMed](#) [Google Scholar](#)

32. Gregory D. Sempowski

[View author publications](#)

You can also search for this author in [PubMed](#) [Google Scholar](#)

33. Matthew Gagne

[View author publications](#)

You can also search for this author in [PubMed](#) [Google Scholar](#)

34. Daniel C. Douek

[View author publications](#)

You can also search for this author in [PubMed](#) [Google Scholar](#)

35. Mark A. Tomai

[View author publications](#)

You can also search for this author in [PubMed](#) [Google Scholar](#)

36. Christopher B. Fox

[View author publications](#)

You can also search for this author in [PubMed](#) [Google Scholar](#)

37. Robert Seder

[View author publications](#)

You can also search for this author in [PubMed](#) [Google Scholar](#)

38. Kevin Wiehe

[View author publications](#)

You can also search for this author in [PubMed](#) [Google Scholar](#)

39. Drew Weissman

[View author publications](#)

You can also search for this author in [PubMed](#) [Google Scholar](#)

40. Norbert Pardi

[View author publications](#)

You can also search for this author in [PubMed](#) [Google Scholar](#)

41. Hana Golding

[View author publications](#)

You can also search for this author in [PubMed](#) [Google Scholar](#)

42. Surender Khurana

[View author publications](#)

You can also search for this author in [PubMed](#) [Google Scholar](#)

43. Priyamvada Acharya

[View author publications](#)

You can also search for this author in [PubMed](#) [Google Scholar](#)

44. Hanne Andersen

[View author publications](#)

You can also search for this author in [PubMed](#) [Google Scholar](#)

45. Mark G. Lewis

[View author publications](#)

You can also search for this author in [PubMed](#) [Google Scholar](#)

46. Ian N. Moore

[View author publications](#)

You can also search for this author in [PubMed](#) [Google Scholar](#)

47. David C. Montefiori

[View author publications](#)

You can also search for this author in [PubMed](#) [Google Scholar](#)

48. Ralph S. Baric

[View author publications](#)

You can also search for this author in [PubMed](#) [Google Scholar](#)

49. Barton F. Haynes

[View author publications](#)

You can also search for this author in [PubMed](#) [Google Scholar](#)

Contributions

K.O.S. and B.F.H. designed and managed the study, reviewed all data and wrote and edited the manuscript; D.W. and N.P. designed and produced the mRNA-LNPs; E.L., A.M.S., F.C., H.C. and A.B.K. expressed proteins; S.K., J.T., H.G., E.L., R.P., M. Barr, T.H.O. III, D.R.M., D.C.M., L.V.T., T.D.S., G.D.S. and R.S.B. carried out binding, virus plaque and neutralization assays; R.S.B. and D.R.M. prepared recombinant live viruses encoding nLuc; D.L., C.T.D., T.N.D., M.G. and D.C.D. designed or performed sgRNA or genomic RNA assays; R.J.E., S.G., P.A., K. Mansouri, K. Manne, M.A., M. Berry and K. W. performed structural or sequence analysis; S.M.A. performed surface plasmon resonance; L.L.S., M.G.L., H.A. and R.S. and performed or evaluated macaque studies; K.W.B., M.M., B.M.N. and I.N.M. performed histology and immunohistochemistry; C.W.W., E.W.P. and G.D.S. collected and annotated COVID-19 samples; M.A.T. selected and provided adjuvant; C.B.F. formulated 3M052 in alum; R.W.R. and R.L.S. performed statistical analyses; all authors edited and approved the manuscript.

Corresponding authors

Correspondence to [Kevin O. Saunders](#) or [Barton F. Haynes](#).

Ethics declarations

Competing interests

B.F.H. and K.O.S. have filed US patents regarding the nanoparticle vaccine, M.A.T. and the 3M company have US patents filed on 3M052, and C.B.F. and IDRI have filed patents on the formulation of 3M052 and alum. The 3M company had no role in the execution of the study, data collection or data interpretation. D.W. is named on US patents that describe the use of nucleoside-modified mRNA as a platform to deliver therapeutic proteins. D.W. and N.P. are also named on a US patent describing the use of nucleoside-modified mRNA in lipid nanoparticles as a vaccine platform. All other authors declare no competing interests.

Additional information

Peer review information *Nature* thanks Wolfgang Baumgärtner and the other, anonymous, reviewer(s) for their contribution to the peer review of this work. Peer reviewer reports are available.

Publisher's note Springer Nature remains neutral with regard to jurisdictional claims in published maps and institutional affiliations.

Extended data figures and tables

[Extended Data Fig. 1 Molecular and structural characterization of the RBD–scNP.](#)

a, Size-exclusion chromatography of RBD and ferritin sortase conjugation. The first peak shows conjugated protein. The second peak contains

unconjugated RBD. **b**, Analytical size-exclusion trace shows a homogenous nanoparticle preparation. **c**, Negative-stain electron microscopy image of RBD–scNP on a carbon grid. Inset shows a zoomed-in image of RBD–scNP. The zoomed image shows RBD molecules arrayed around the outside of the ferritin nanoparticle. A representative image from the 31 images taken of the micrograph to visualize 13,827 total particles is shown. **d**, Chemical structure of 3M-052. Alum formulation of 3M-052 was used to adjuvant RBD–scNP immunization. **e**, RBD–scNP immunization regimen used for vaccination of cynomolgus macaques ($n = 5$). Blue arrows indicate time points for intramuscular immunizations with RBD–scNP (100 μ g) adjuvanted with 3M-052 (5 μ g 3M-052 plus 500 μ g alum). BAL (orange arrows) and nasal swab (green arrows) fluids were collected 7 days before, 2 days after and 4 days after intratracheal and intranasal SARS-CoV-2 challenge (black arrow). **f**, S-2P mRNA-LNP prime and RBD–scNP boost vaccination of cynomolgus macaques ($n = 5$). Burgundy arrows indicate time points for S-2P mRNA-LNP immunization (50 μ g mRNA dose). Blue arrows are the same as in **a**. Macaques were challenged 9 weeks after RBD–scNP boost (week 17 of the study). BAL and nasal swab fluids were collected as in **a**. Macaques were challenged at week 17 (black arrow). **g**, RBD mRNA-LNP immunization of rhesus macaques ($n = 8$). Tan arrows indicate time points for RBD mRNA-LNP immunization (50 μ g mRNA dose). Blood was collected throughout each study as shown by red arrows in all panels.

[Source data](#)

Extended Data Fig. 2 Blood chemical analysis and blood cell counts in RBD–scNP- and S-2P mRNA-LNP-vaccinated macaques.

Each graph shows values for individual macaques before vaccination and 4 weeks after the RBD–scNP (week 8) or 6 weeks after the second S-2P mRNA-LNP immunization (week 10). RBD–scNP-immunized macaques are shown as blue symbols, and S-2P mRNA-LNP-immunized macaques are shown as red symbols. The reference range for each value is shown as grey shaded area for female macaques and cyan shaded area for male

macaques. Creatine kinase does not have a reference range indicated. Male macaques are shown as circles and female macaques are shown as triangles.

[Source data](#)

Extended Data Fig. 3 ACE2, RBD neutralizing antibody and post-vaccination macaque plasma IgG binding to SARS-CoV-2 spike variants.

a, b, Plasma IgG from macaques before immunization or after being immunized once with RBD–scNP adjuvanted with 3M-052 and alum (blue), RBD–scNP only (grey), or 3M-052 and alum only (white). Binding titres as log(AUC) were determined before (**a**) or two weeks after (**b**) a single immunization. Horizontal bars are the group mean. **c**, ACE2 receptor and cross-nAb DH1047 ELISA binding to SARS-CoV-2 spike ECD based on a Danish mink (H69/V70del/Y453F/D614G/I692V), B.1.351-like (K417N/E484K/N501Y/D614G) and B.1.1.7 (H69/V70del/Y144del/N501Y/A570D/D614G/P681H/T716I/S982A/D1118H) strains. Titres are shown as area under the log-transformed curve (log(AUC)). **d**, RBD–scNP- and S-2P mRNA-LNP-immunized macaque serum IgG ELISA binding to SARS-CoV-2 spike variants shown in **c**. Serum was tested after two immunizations. Horizontal bars are the group mean. **e**, ACE2 receptor (grey), cross-nAb DH1047 (navy) and ACE2-binding-site-targeting neutralizing antibody DH1041 (green) ELISA binding to SARS-CoV-2 spike RBD monomers. RBD variants contain a subset of mutations found in circulating B.1.351 and P.1 virus strains. Titres are shown as area under the log-transformed curve (log(AUC)). **f**, RBD–scNP- and S-2P mRNA-LNP-immunized macaque serum IgG ELISA binding to SARS-CoV-2 spike RBD variants shown in **e**. Serum was tested after two immunizations. Horizontal bars are the group mean.

[Source data](#)

Extended Data Fig. 4 Cross-nAbs are elicited by RBD–scNP and mRNA-LNP immunization.

a, Each row shows neutralization titre for an individual macaque immunized with one of the three immunogens. A reciprocal serum dilution titre of 87,480 is the upper limit of detection and 20 is the lower limit of detection for this assay. Titres are derived from a nonlinear regression curve fit to the average of duplicate measurements. **b, c**, Serum neutralization titres elicited by two S-2P mRNA-LNP immunizations were boosted by a subsequent RBD–scNP immunization. Serum neutralization of SARS-CoV-2 D614G (**b**) and SARS-CoV-2 B.1.1.7 (**c**) pseudovirus infection of ACE2-expressing 293 cells. Neutralization titres are ID₅₀ as reciprocal serum dilution for serum collected two weeks after the second (week 6) and third immunization (week 10). Each symbol connected by a line represents the titre for an individual macaque before and after RBD–scNP immunization. Normal human serum spiked with DH1043 was used as a positive control.

[Source data](#)

Extended Data Fig. 5 Cross-reactive plasma antibody responses elicited by RBD–scNP immunization in macaques.

a, Plasma IgG from macaques immunized twice with RBD–scNP binds to spike from human, bat and pangolin SARS-related coronavirus spike in ELISA, but not endemic human coronaviruses or MERS-CoV. **b**, Determination of DH1047 Fab binding kinetics to RBD monomer by surface plasmon resonance. Each curve shows a different concentration of DH1047 Fab. Binding kinetics are shown to the right from a 1:1 model fit. **c**, Time course of vaccinated macaque plasma IgG binding to human, bat and pangolin coronavirus spike protein by ELISA. Each curve indicates the binding titre for an individual macaque. Arrows indicate immunization time points. **d**, Unimmunized macaque plasma antibody blocking of SARS-CoV-2 S-2P (left) and SHC014 (middle) binding to ACE2, RBD neutralizing antibody DH1041 and RBD cross-nAb DH1047. Right, blocking activity in the serum of humans immunized with Pfizer BNT162b2 vaccine ($n = 4$). Each symbol represents an individual human or macaque. Bars indicate group mean \pm s.e.m.

[Source data](#)

Extended Data Fig. 6 Multiple sequence alignment of spike protein from a representative set of group 2b betacoronaviruses.

SARS-CoV-2 Wuhan-1 spike protein numbering is shown. CD, connecting domain; CH, central helix; FP, fusion peptide; HR1, heptad repeat 1; HR2, heptad repeat 2; S1/S2, SARS-CoV-2 furin cleavage site; TM, transmembrane domain. ACE2 contact positions in SARS-CoV-2 (calculated from PDB coordinates 6MOJ and 6LZG) are highlighted in dark red.

Extended Data Fig. 7 Sequence conservation among SARS-related betacoronaviruses, MERS-CoV and endemic human coronaviruses.

a, b Sequence similarity of RBD (**a**) and spike protein (**b**) for representative betacoronaviruses. Heat maps displaying pairwise amino acid sequence similarity for 57 representative betacoronaviruses. Dark blue shading indicates high sequence similarity. **c**, List of viruses used for alignments in **a, b** and Fig. [3f](#). **d**, Phylogenetic tree of representative betacoronavirus RBD sequences. Group 2b betacoronaviruses of interest are shown highlighted in red. Branch length units are substitutions per site.

Extended Data Fig. 8 Histology and immunohistochemistry of lung tissue collected seven days after SARS-CoV-2 WA-1 intratracheal and intranasal challenge.

a–c, Macaques were immunized thrice with RBD–scNP (**a**), twice with S-2P mRNA-LNP and once with RBD–scNP (**b**) or not immunized (**c**). Each column shows results from an individual macaque. The macaque identification number is shown above each column. Haematoxylin and eosin stain of lung sections are shown on the top row, with nucleocapsid immunohistochemistry shown on the bottom row for each macaque. Red arrows indicate site of antigen positivity. All images are shown at 10 \times magnification. Scale bars, 100 μ m.

Extended Data Fig. 9 Mucosal SARS-CoV-2 IgG responses in BAL and nasal wash fluids before and after SARS-CoV-2 challenge.

a, ELISA binding titres for SARS-CoV-2-specific IgG in 10× BAL fluid from macaques immunized with (blue symbols, left column) RBD–scNP three times or S-2P mRNA-LNP twice and RBD–scNP once (red symbols, left column). Day –7 BAL fluid was collected at week 10 or 16 for the RBD–scNP-alone group or the S-2P mRNA-LNP and RBD–scNP group, respectively. Group mean ± s.e.m. are shown ($n = 5$ macaques). **b–d**, The 10× BAL fluid blocking of ACE2, RBD neutralizing antibody DH1041 and cross-nAb DH1047 binding to SARS-CoV-2 D614G stabilized spike ectodomain. A black horizontal bar indicates the group mean blocking percentage. Blocking above 20% (above the dashed line) is considered positive. **e**, Neat nasal wash fluid from RBD–scNP-immunized or S-2P mRNA-LNP- and RBD–scNP-immunized macaques. Day –7 nasal wash fluid was collected at week 16 and 2 and 4 days after challenge for the S-2P mRNA-LNP and RBD–scNP group. Nasal wash fluid was unavailable for the RBD–scNP group before challenge, but was collected 2 and 4 days after the week-11 challenge. Group mean ± s.e.m. is shown ($n = 5$).

[Source data](#)

Extended Data Table 1 Scoring of haematoxylin and eosin staining and immunohistochemistry of macaque lung tissue collected seven days after challenge

[Full size table](#)

Supplementary information

[Reporting Summary](#)

[Peer Review File](#)

Source data

[Source Data Fig. 1](#)

[Source Data Fig. 2](#)

[Source Data Fig. 3](#)

[Source Data Fig. 4](#)

[Source Data Extended Data Fig. 1](#)

[Source Data Extended Data Fig. 2](#)

[Source Data Extended Data Fig. 3](#)

[Source Data Extended Data Fig. 4](#)

[Source Data Extended Data Fig. 5](#)

[Source Data Extended Data Fig. 9](#)

Rights and permissions

[Reprints and Permissions](#)

About this article



Check for
updates

Cite this article

Saunders, K.O., Lee, E., Parks, R. *et al.* Neutralizing antibody vaccine for pandemic and pre-emergent coronaviruses. *Nature* **594**, 553–559 (2021).

<https://doi.org/10.1038/s41586-021-03594-0>

[Download citation](#)

- Received: 07 February 2021
- Accepted: 29 April 2021
- Published: 10 May 2021
- Issue Date: 24 June 2021
- DOI: <https://doi.org/10.1038/s41586-021-03594-0>

Comments

By submitting a comment you agree to abide by our [Terms](#) and [Community Guidelines](#). If you find something abusive or that does not comply with our terms or guidelines please flag it as inappropriate.

[Download PDF](#)

Associated Content

Collection

[Coronavirus](#)

Advertisement

This article was downloaded by **calibre** from <https://www.nature.com/articles/s41586-021-03594-0>

MARK4 controls ischaemic heart failure through microtubule detyrosination
[Download PDF](#)

- Article
- [Published: 26 May 2021](#)

MARK4 controls ischaemic heart failure through microtubule detyrosination

- [Xian Yu¹](#) ✉¹,
- [Xiao Chen²](#) ✉¹,
- [Mamta Amrute-Nayak³](#),
- [Edward Allgeyer](#) ORCID: orcid.org/0000-0002-2187-4423^{4,5},
- [Aite Zhao⁶](#),
- [Hannah Chenoweth¹](#),
- [Marc Clement¹](#),
- [James Harrison¹](#),
- [Christian Doreth¹](#),
- [George Sirinakis](#) ORCID: orcid.org/0000-0002-4762-422X^{4,5},
- [Thomas Krieg](#) ORCID: orcid.org/0000-0002-5192-580X⁷,
- [Huiyu Zhou⁸](#),
- [Hongda Huang⁹](#),
- [Kiyotaka Tokuraku](#) ORCID: orcid.org/0000-0002-7747-4808¹⁰,
- [Daniel St Johnston](#) ORCID: orcid.org/0000-0001-5582-3301^{4,5},
- [Ziad Mallat](#) ORCID: orcid.org/0000-0003-0443-7878^{1,11} &
- [Xuan Li](#) ORCID: orcid.org/0000-0002-0754-3011¹

[Nature](#) volume **594**, pages 560–565 (2021) [Cite this article](#)

- 9654 Accesses
- 855 Altmetric
- [Metrics details](#)

Subjects

- [Cardiomyopathies](#)
- [Heart failure](#)
- [Kinases](#)
- [Microtubules](#)
- [Phosphorylation](#)

Abstract

Myocardial infarction is a major cause of premature death in adults. Compromised cardiac function after myocardial infarction leads to chronic heart failure with systemic health complications and a high mortality rate¹. Effective therapeutic strategies are needed to improve the recovery of cardiac function after myocardial infarction. More specifically, there is a major unmet need for a new class of drugs that can improve cardiomyocyte contractility, because inotropic therapies that are currently available have been associated with high morbidity and mortality in patients with systolic heart failure^{2,3} or have shown a very modest reduction of risk of heart failure⁴. Microtubule detyrosination is emerging as an important mechanism for the regulation of cardiomyocyte contractility⁵. Here we show that deficiency of microtubule-affinity regulating kinase 4 (MARK4) substantially limits the reduction in the left ventricular ejection fraction after acute myocardial infarction in mice, without affecting infarct size or cardiac remodelling. Mechanistically, we provide evidence that MARK4 regulates cardiomyocyte contractility by promoting phosphorylation of microtubule-associated protein 4 (MAP4), which facilitates the access of vasohibin 2 (VASH2)—a tubulin carboxypeptidase—to microtubules for the detyrosination of α -tubulin. Our results show how the detyrosination of microtubules in cardiomyocytes is finely tuned by MARK4 to regulate cardiac inotropy, and identify MARK4 as a promising therapeutic target for improving cardiac function after myocardial infarction.

[Download PDF](#)

Main

Myocardial infarction—the main cause of ischaemic heart disease and chronic heart failure—is a serious ischaemic syndrome in which the blood supply to the heart is blocked, thus causing substantial death of myocardial cells and loss of function in the remaining viable cells⁶. Microtubule detyrosination, which is associated with desmin at force-generating sarcomeres⁵, is upregulated in failing hearts of patients with ischaemic cardiomyopathy^{5,7} and hypertrophic cardiomyopathies^{5,7,8}, and suppression of microtubule detyrosination improves contractility in failing cardiomyocytes⁷. VASH1 or VASH2, coupled to a small vasohibin-binding protein (SVBP), forms tubulin carboxypeptidases (TCPs) that are capable of tubulin detyrosination^{9,10}.

Depletion of VASH1 increases the speed of contraction and relaxation in failing human cardiomyocytes¹¹. Structural and biophysical studies have suggested that VASH interacts with the C-terminal tail of α -tubulin^{12,13,14}. However, the regulatory mechanisms of this system are still poorly understood.

Microtubule stability is regulated by microtubule-associated proteins (MAPs), including classical MAPs such as MAP2, MAP4 and tau¹⁵. MAP4 is expressed in cardiomyocytes and the level of MAP4 significantly increases in human hearts with cardiomyopathy⁷. MAP4 dephosphorylation on the microtubule network has previously been described in a feline model of pressure-overload cardiac hypertrophy¹⁶, but the relationship between MAP4 phosphorylation and microtubule detyrosination has not been examined. MARK4 is an evolutionarily conserved serine-threonine kinase^{17,18} that is known to phosphorylate MAPs including tau, MAP2 and MAP4, on KXGS motifs within their microtubule-binding repeats^{19,20,21}. The phosphorylation of MAPs triggered by MARK induces conformational changes that alter the association of MAPs with microtubules, and thereby regulates microtubule dynamics^{19,20,21}. MARK4 is expressed in the heart²⁰; however, the role of MARK4 in the cardiomyocyte has not been studied. Here we examined whether MARK4 regulates the function of the failing cardiomyocyte through modulation of microtubule detyrosination.

Function of *Mark4*^{−/−} hearts after myocardial infarction

To evaluate the effect of MARK4 in the setting of ischaemic heart disease, we used a mouse model of permanent left anterior descending coronary artery ligation to induce a large myocardial infarction^{22,23} (Extended Data Fig. 1a). We detected *Mark4* mRNA (Fig. 1a) and MARK4 protein (Fig. 1b) expression in the heart tissues, peaking between day 3 and day 5 after myocardial infarction (Fig. 1a–c). MARK4 was almost exclusively detected in the cytoskeleton-enriched insoluble fraction of the whole-heart extracts (Fig. 1b) and was localized in cardiomyocytes (Fig. 1c and Extended Data Fig. 2a). MARK4-deficient mice (*Mark4*^{−/−}) displayed a remarkable preservation of left ventricular ejection fraction (LVEF), which was 63.6% ($\pm 5.8\%$) higher compared with their wild-type littermate controls on the first week after left anterior descending coronary artery ligation (Fig. 1d), without any alteration in cardiac remodelling (Supplementary Table 1). Notably, infarct scar size was similar between the two groups of mice (Fig. 1e), indicating that the substantial difference in cardiac function between wild-type and *Mark4*^{−/−} mice was not attributable to differences in the size of viable cardiac tissues.

Fig. 1: MARK4 deficiency preserves cardiac function after myocardial infarction without altering the size of the scar.

 **figure1**

a, Expression of *Mark4* mRNA in heart samples from wild-type hearts, baseline hearts (BL; hearts without myocardial infarction) and from hearts obtained at the indicated days (1, 3, 5 and 7 days) after myocardial infarction (MI) was analysed using real-time PCR. $n = 5$ at baseline, $n = 6$ mice per time point at 1, 3 and 5 days after myocardial infarction and $n = 5$ mice at 7 days after myocardial infarction. **b**, Western blots of wild-type hearts after myocardial infarction. Expression of MARK4 in the insoluble cytoskeletal fractions (with desmin as marker) and GAPDH in corresponding soluble cytosolic fractions is shown. $n = 3$ mice at each time point. **c**, Representative immunohistochemistry staining of MARK4 in wild-type mice at baseline or after myocardial infarction. Isotype IgG was used as control. Scale bar, 50 μm . **d**, Assessment of LVEF in *Mark4*^{-/-} mice ($n = 7$) and their littermate controls (*Mark4*^{+/+}) ($n = 7$) at baseline, and 1, 2 and 4 weeks after myocardial infarction. **e**, Scar size at week 4 after myocardial infarction. Scale bar, 2 mm. **a**, **d**, **e**, Data are mean \pm s.e.m. One-way analysis of variance (ANOVA) with Bonferroni post hoc correction (**a**); two-way ANOVA with Bonferroni post hoc correction for multiple comparisons (**d**); two-tailed unpaired Student's *t*-test (**e**). *P* values are indicated.

[Source data](#)

[Full size image](#)

MARK4 regulates cardiac contractility

We found that the protective effect of MARK4 deficiency on the preservation of cardiac function was already apparent at 24 h after myocardial infarction (Fig. 2a and Extended Data Fig. 1b), despite a similar extent of myocardial injury, shown by comparable serum levels of cardiac troponin I (Fig. 2b) and a comparable infarct size analysed by triphenyltetrazolium chloride staining (Fig. 2c), in *Mark4*^{-/-} and wild-type mice. MARK4 has previously been shown to regulate NLRP3 activation in macrophages^{24,25}, which could affect the outcome of a post-ischaemic injury given the role of the NLRP3 inflammasome in this setting^{26,27}. However, MARK4 deficiency

did not significantly alter local and systemic inflammatory responses to myocardial injury at day 3 after myocardial infarction (Extended Data Fig. 2b and Supplementary Table 2) when the preservation of the LVEF was already evident in *Mark4*^{-/-} mice (Extended Data Fig. 2c). Moreover, bone marrow transfer of *Mark4*^{-/-} haematopoietic cells into wild-type mice (Extended Data Fig. 1c; validation in Extended Data Fig. 3a, b) did not improve cardiac function after myocardial infarction in comparison with the transfer of wild-type bone marrow cells (Fig. 2d), indicating that the protective effect of MARK4 deficiency after myocardial infarction could not be explained by the role of MARK4 in haematopoietic cells. By contrast, using an inducible conditional deletion of *Mark4* in cardiomyocytes (*Mark4* conditional knockout (cKO)) (Extended Data Fig. 1d; validation in Extended Data Fig. 3c), we found a substantial preservation of LVEF in *Mark4* cKO mice after myocardial infarction, which was 56.8% (\pm 6.2%) higher compared with littermate control mice at day 1 after myocardial infarction (Fig. 2e). The protective effect seen in *Mark4* cKO mice started as early as the first day after myocardial infarction and lasted until the end of the observation at four weeks after myocardial infarction (Fig. 2e). Notably, *Mark4* cKO mice had a reduction of only 4.3% (\pm 3.8%) in LVEF at day 1 after myocardial infarction, compared with a reduction of 37.9% (\pm 5.5%) in the control mice (Fig. 2e), without any difference in infarct size (Extended Data Fig. 3e). The data further show that the remaining, viable MARK4-deficient cardiomyocytes affect contractile function. Collectively, our data demonstrate that cardiomyocyte-expressed MARK4 has an intrinsic role in the control of cardiac function after myocardial infarction.

Fig. 2: MARK4 expression in cardiomyocytes regulates cardiac contractile function after myocardial infarction.

figure2

a–c, *Mark4*^{-/-} mice ($n = 5$) and their littermate controls (*Mark4*^{+/+}, $n = 5$) at day 1 (D1) after myocardial infarction. **a**, LVEF. **b**, **c**, Circulating cardiac troponin I (cTnI) levels (**b**) and infarct size (**c**) at 24 h after myocardial infarction are shown. cardiac troponin I measurements at baseline were used as controls. Scale bar, 2 mm. **d**, Assessment of LVEF in chimeric mice ($n = 8$ wild-type recipients of *Mark4*^{+/+} bone marrow (BM) donors; $n = 6$ wild-type recipients of *Mark4*^{-/-} bone marrow donors) at the indicated time points. **e**, Assessment of LVEF at the indicated time points after

conditional *Mark4* knockout using tamoxifen (Tm) in *Myh6-mcm^{+/−};Mark4^{fl/fl}* (also known as *αMHC-mcm^{+/−};Mark4^{fl/fl}*) mice ($n = 6$) (*Myh6* encodes the cardiomyocyte-specific marker *αMHC*). Tamoxifen-injected *Myh6-mcm^{+/−}* and *Mark4^{fl/fl}* littermate mice were used as controls ($n = 6$). **f–i**, Contractility assay of single primary cardiomyocytes isolated at baseline or at day 3 after myocardial infarction in the following groups: baseline, *Mark4^{+/+}* mice ($n = 4$ mice, $n = 45$ cardiomyocytes examined over 4 independent experiments); baseline, *Mark4^{−/−}* mice ($n = 3$ mice, $n = 45$ cardiomyocytes examined over 3 independent experiments); myocardial infarction, *Mark4^{+/+}* mice ($n = 5$ mice, $n = 54$ cardiomyocytes examined over 5 independent experiments); and myocardial infarction, *Mark4^{−/−}* mice ($n = 6$ mice, $n = 57$ cardiomyocytes examined over 6 independent experiments). **f**, Correlation between LVEF (measured at day 1 after myocardial infarction) and sarcomere peak shortening. **g**, Sarcomere peak shortening. **h, i**, Pooled data of contraction (**h**) and relaxation (**i**) velocity. **a–e**, Data are mean \pm s.e.m. **g–i**, Violin plots show lines at the median (solid) and quartiles (dashed). Two-tailed unpaired *t*-test (**a–c**); two-way ANOVA with Bonferroni post hoc correction for multiple comparisons (**d, e, g–i**). *P* values are indicated.

[Source data](#)

[Full size image](#)

To examine the effect of MARK4 on cardiomyocyte function, we subjected freshly isolated primary cardiomyocytes²⁸ from wild-type and *Mark4^{−/−}* mice to a single-cell contractility assay using an electrical stimulator (Fig. [2f–i](#)). We found that sarcomere peak shortening of isolated cardiomyocytes strongly correlated with the in vivo LVEF (Fig. [2f](#)), indicating that the contraction of isolated cardiomyocyte measured ex vivo reflects LVEF assessed in vivo (Figs. [1d](#), [2a, e](#)). At baseline, wild-type and MARK4-deficient cardiomyocytes had similar levels of resting sarcomere length (Extended Data Fig. [4a, b](#)), sarcomere peak shortening and contraction and relaxation velocities (Fig. [2g–i](#)), an observation that is consistent with the absence of a difference in LVEF between wild-type and *Mark4^{−/−}* mice before myocardial infarction (Fig. [1d](#)). After myocardial infarction, wild-type cardiomyocytes displayed markedly reduced sarcomere shortening (decreased by $22.5\% \pm 3.7\%$) (Fig. [2g](#) and Extended Data Fig. [4c](#)), with slower relaxation velocity (decreased by $25.2\% \pm 4.4\%$) (Fig. [2i](#) and Extended Data Fig. [4e](#)), compared with cardiomyocytes isolated from wild-type mice without myocardial infarction. Notably, although no difference in resting sarcomere length was observed between *Mark4^{−/−}* and wild-type cardiomyocytes after myocardial infarction (Extended Data Fig. [4b](#)), *Mark4^{−/−}* cardiomyocytes displayed a greater level of sarcomere shortening (increased by $36.0\% \pm 6.0\%$) (Fig. [2g](#) and Extended Data Fig. [4d](#)) together with a greater velocity during both the contraction (increased by $42.0\% \pm 6.9\%$) and relaxation (increased by $46.7\% \pm 7.5\%$) phases (Fig.

[2h, i](#) and Extended Data Fig. [4f](#)) compared with wild-type cardiomyocytes. Upstream changes in the influx of calcium (Ca^{2+}) through excitation–contraction coupling could contribute to the contractile alterations; however, we did not observe any significant difference in Ca^{2+} transients between electrically stimulated $\text{Mark4}^{-/-}$ and wild-type cardiomyocytes at baseline or at day 3 after myocardial infarction (Extended Data Fig. [4g–m](#)). These data demonstrate that MARK4 deficiency substantially improves both contractile and relaxation functions of cardiomyocytes after myocardial infarction.

MARK4 alters microtubule detyrosination

Detyrosinated microtubules represent tunable, compression-resistant elements that impair cardiac function in failing hearts in humans.[5,7](#) We confirmed that the level of detyrosinated α -tubulin was significantly higher in cardiomyocytes isolated from ischaemic hearts compared with cardiomyocytes isolated from mice that received a sham operation, in contrast to the remaining cell pool (immune cells, fibroblasts and endothelial cells), which did not display a change in α -tubulin detyrosination (Extended Data Fig. [2d, e](#)). Previous data indicated that MARK4 affects the posttranslational detyrosination and polyglutamylation of microtubules in ciliated cells.[29](#) Therefore, we hypothesized that MARK4 deficiency may affect microtubule detyrosination in cardiomyocytes after myocardial infarction. We found a significantly lower level of detyrosinated microtubules in whole-heart tissue extracts (Fig. [3a, b](#)), and in isolated cardiomyocytes (together with reduced polyglutamylated microtubules) (Fig. [3e–g](#) and Extended Data Fig. [2f, g](#)) of $\text{Mark4}^{-/-}$ mice compared with littermate wild-type controls after myocardial infarction. In the absence of MARK4, we observed a reduced ratio of α -tubulin in the soluble fraction versus its level in the insoluble fraction (Fig. [3c](#)), indicating a reduced percentage of free tubulin without MARK4. Notably, we found that the level of tubulin detyrosination inversely correlated with LVEF (Fig. [3d](#)), suggesting that the MARK4-dependent modulation of microtubule detyrosination has an important role in controlling cardiac function after myocardial infarction.

Fig. 3: MARK4 regulates cardiomyocyte contractility by promoting microtubule detyrosination.

 **figure3**

a–d, Western blots of whole-heart extraction from mice at day 3 after myocardial infarction, in soluble and insoluble fractions. dTyr-tub, detyrosinated α -tubulin; α -tub, α -tubulin. **a**, Representative western blots. **b**, Ratio of detyrosinated α -tubulin over total α -tubulin in the following groups: myocardial infarction, soluble fraction, $Mark4^{+/+}$ mice ($n = 20$); myocardial infarction, soluble fraction, $Mark4^{-/-}$ mice ($n = 17$); myocardial infarction, insoluble fraction, $Mark4^{+/+}$ mice ($n = 8$); and myocardial infarction, insoluble fraction $Mark4^{-/-}$ mice ($n = 8$). **c**, Ratio of α -tubulin in the soluble fraction over α -tubulin in the insoluble fraction ($n = 8$ mice per group). **d**, Correlation between LVEF and the ratio of detyrosinated α -tubulin/ α -tubulin in $Mark4^{-/-}$ ($n = 9$) and control mice ($n = 12$). **e–g**, Confocal images of isolated cardiomyocytes at day 3 after myocardial infarction. **e**, Representative images. Scale bar, 20 μ m. **f**, **g**, Percentage of detyrosinated α -tubulin or total α -tubulin area per cell (**f**) and ratio of detyrosinated α -tubulin/total α -tubulin ($n = 3$ mice, $n = 15$ cardiomyocytes per group) (**g**). **h–j**, Adenovirus (Adv)-mediated overexpression (OE) of TTL in primary cardiomyocytes isolated from $Mark4^{-/-}$ or control mice at day 3 after myocardial infarction, with overexpression of a null virus as controls. Contractility assay of single cardiomyocytes in the following groups: myocardial infarction, Adv-Null, $Mark4^{+/+}$ mice ($n = 3$ mice, $n = 75$ cardiomyocytes examined over 3 independent experiments); myocardial infarction, Adv-TTL, $Mark4^{+/+}$ mice ($n = 3$ mice, $n = 69$ cardiomyocytes examined over 3 independent experiments); myocardial infarction, Adv-Null, $Mark4^{-/-}$ mice ($n = 3$ mice, $n = 74$ cardiomyocytes examined over 3 independent experiments); and myocardial infarction, Adv-TTL, $Mark4^{-/-}$ mice ($n = 3$ mice, $n = 73$ cardiomyocytes examined over 3 independent experiments). **h**, Sarcomere peak shortening. Pooled data of contraction (**i**) and relaxation (**j**) velocity. **h–j**, Violin plots show lines at the median (solid) and quartiles (dashed). **b**, **c**, **f**, **g**, Data are mean \pm s.e.m. Two-tailed unpaired *t*-test (**b**, **c**, **f**, **g**); two-tailed correlation test (**d**); two-way ANOVA with Bonferroni post hoc correction for multiple comparisons (**h–j**). *P* values are indicated.

[Source data](#)

[Full size image](#)

To further address the hypothesis that MARK4 deficiency improves cardiomyocyte contractility through its influence on microtubule detyrosination, we used a genetic approach to overexpress tubulin tyrosine ligase (TTL) using an adenovirus system (Extended Data Fig. 5a–c) to reverse the effect of TCP³⁰ (Fig. 3h–j). TTL overexpression robustly improved peak shortening (Fig. 3h and Extended Data Fig. 5d) and increased the velocity of both contraction and relaxation (Fig. 3i,j and Extended Data Fig. 5g) of failing wild-type cardiomyocytes⁷. However, overexpression of TTL could not further improve peak shortening (Fig. 3h and Extended Data Fig. 5e) and contractile velocities of *Mark4*^{−/−} cardiomyocytes after myocardial infarction (Fig. 3i,j and Extended Data Fig. 5h), which is consistent with the already low level of detyrosinated microtubules in *Mark4*^{−/−} cardiomyocytes. We further confirmed these data using a pharmacological approach with parthenolide to inhibit microtubule detyrosination^{5,7} (Extended Data Fig. 5j–s). Taken together, our data show that MARK4 regulates cardiac inotropic function through its effect on microtubule detyrosination in cardiomyocytes.

MARK4 directs VASH2 access to microtubules

Detyrosination of α-tubulin preferentially occurs on polymerized microtubules³¹. Apart from binding to VASH, the C-terminal tubulin tails of polymerized microtubules are also important for MAP binding^{32,33}. MAP4 bound to the C-terminal tubulin tail along the protofilament stabilizes the longitudinal contacts of the microtubule, and this interaction can affect other microtubule-binding partners such as the motor protein kinesin-1³³. MARK4, as a kinase, is expected to phosphorylate MAP4 at its KXGS motifs (including S941 and S1073 in human MAP4, or S914 and S1046 in mouse MAP4) within its microtubule-binding repeats^{19,20} (Extended Data Fig. 6a) and alter MAP4-binding status on the protofilament (Extended Data Fig. 6b). We therefore hypothesized that MARK4—by modifying MAP4 phosphorylation—may affect VASH accessibility to the C-terminal α-tubulin tail and therefore influence microtubule detyrosination. As such, we used an in vitro microtubule co-sedimentation assay. Both MAP4 (Extended Data Fig. 6c,d) and VASH2–SVBP (Extended Data Fig. 6e,f) were able to incrementally bind to polymerized microtubules when incremental amounts were separately applied in the assays, which is consistent with the results of previous studies^{12,33}. Notably, we found that VASH2–SVBP bound to polymerized microtubules gradually decreased in the presence of incremental amounts of previously bound MAP4 (with four microtubule-binding repeats (4R-MAP4)) (Fig. 4a,b). Therefore, these results support the hypothesis that the level of MAP4 occupancy on the polymerized microtubules influences the level of access of VASH2 to the microtubule protofilaments.

Fig. 4: MARK4 controls microtubule detyrosination through MAP4 phosphorylation to facilitate VASH2 access to microtubules.

 figure4

a, b, Representative gel image of VASH2–SVBP (3 μ M) binding to polymerized microtubules (MTs) (5 μ M) in the presence of different amounts of 4R-MAP4 (1–4 μ M) in a microtubule co-sedimentation assay (**a**) and quantification of the binding (**b**). $n = 3$ independent experiments per group. **c–e,** Subcellular fractionations of *Mark4*^{−/−} or control cardiomyocytes isolated after myocardial infarction. **c,** Representative western blots of the fractions from CEB or PEB derived from the same experiment. **d,** Quantification of the levels of pMAP4(S1046) in CEB, pMAP4(S914) in PEB and VASH2 in PEB ($n = 6$ mice per group, blots were processed in parallel). **e,** Correlation between VASH2 level in the PEB fraction and pMAP4 levels. **f, g,** Stimulated emission depletion images of VASH2 and α -tubulin in *Mark4*^{−/−} or control cardiomyocytes isolated from mice after myocardial infarction. **f,** Representative images. Scale bar, 2 μ m. **g,** Pearson correlation coefficient (PCC) of VASH2 and α -tubulin signals, percentage of VASH2 signals on the polymerized microtubules, percentage of VASH2 signals off the polymerized microtubules in the *Mark4*^{+/+} myocardial infarction group ($n = 6$ mice, $n = 38$ cardiomyocytes examined over 3 independent experiments) and *Mark4*^{−/−} myocardial infarction group ($n = 6$ mice, $n = 47$ cardiomyocytes examined over 3 independent experiments). **b, d, g,** Data are mean \pm s.e.m. One-way ANOVA (**b**); two-tailed unpaired *t*-test (**d, g**); two-tailed correlation test (**e**). *P* values are indicated.

[Source data](#)

[Full size image](#)

To confirm this hypothesis *in vivo*, we performed biochemical subcellular fractionation on primary cardiomyocytes isolated from non-ischaemic and ischaemic hearts of wild-type and *Mark4*^{−/−} mice using a commercial kit, which we have validated (Extended Data Fig. [7a, b](#)). We first confirmed that MAP4 was expressed in the cardiomyocytes and that the level of MAP4 was higher after myocardial infarction (Extended Data Fig. [7c](#)), a result consistent with data showing that MAP4 levels

significantly increase in hearts of individuals with cardiomyopathies⁷. MAP4 was detected in its S914 phosphorylated form ((pMAP4(S914); S914 is located within the KXGS motif)) in the pellet extraction buffer (PEB) and also in its S1046 form (pMAP4(S1046); S1046 is located within the KXGS motif) in the cytosolic extraction buffer (CEB) (Extended Data Fig. 7c–e). Knocking down MAP4 using small hairpin RNA (shRNA) in isolated cardiomyocytes after myocardial infarction led to increased VASH2 levels in the PEB fraction, which was confirmed by both western blot and immunocytochemistry (Extended Data Fig. 7f–i); these results are in line with the results of an in vitro microtubule co-sedimentation assay (Fig. 4a, b). VASH2 was detected as a specific band (validated by specific knockdown using shRNA) (Extended Data Fig. 8a) of around 50 kDa in the PEB fraction (Extended Data Fig. 8a, b), which is higher than its theoretical molecular weight of 40 kDa and presumably due to the formation of a stable complex with SVBP, because the addition of a denaturing agent (urea) reduced its size to around 40 kDa (Extended Data Fig. 8b). After myocardial infarction, pMAP4(S914) was detected in a 110 kDa form in the PEB fraction whereas pMAP4(S1046) was detected in a 220 kDa form in the CEB fraction (Fig. 4c and Extended Data Fig. 7c). MAP4 was detected as giant puncta in the cytosol of cardiomyocytes isolated after myocardial infarction, and these puncta were barely present at baseline (Extended Data Fig. 8c, d). pMAP4(S1046) (in the CEB fraction) formed oligomerized structures (at 440 kDa or higher) as revealed by native gel analysis (Extended Data Fig. 8e, f), and these pMAP4(S1046) oligomers could be further reduced to the 220 kDa form in the presence of urea as revealed by denaturing gel analysis (Extended Data Fig. 8g). The data suggest that MAP4 phosphorylation at S1046 is associated with its presence as oligomers or giant puncta in the cytosol in situ. Our results are consistent with a structural model, in which S914 is within the weak binding site of the microtubule-binding repeat of MAP4 to the microtubules, whereas S1046 is within the strong anchor point of the microtubule-binding repeat of MAP4 to the microtubules³³ (Extended Data Fig. 6b), so that phosphorylation at S1046 leads to the detachment of MAP4 from polymerized microtubules and accumulation in the cytosol. Accordingly, a higher level of pMAP4(S1046) was strongly and positively correlated with increased VASH2 levels in the PEB fraction (there was also a weaker correlation between pMAP4(S914) levels and VASH2 levels in the PEB fraction) (Extended Data Fig. 7c, e) in wild-type cardiomyocytes, indicating an association between pMAP4 (phosphorylated at S941 and S1046) and VASH2 levels on the polymerized microtubules. Notably, levels of pMAP4(S914) and pMAP4(S1046) were substantially reduced in *Mark4*^{-/-} cardiomyocytes after myocardial infarction (Fig. 4c, d), confirming that S914 and S1046 of MAP4 are substrate sites of the MARK4 kinase. Reduced levels of pMAP4(S1046) in the CEB fraction and pMAP4(S914) in the PEB fraction correlated well with a reduced level of VASH2 in the PEB fraction ($r^2 = 0.6165, P = 0.0025$; $r^2 = 0.4529, P = 0.0165$, respectively) (Fig. 4c–e), with a stronger association between pMAP4(S1046) and VASH2. In addition, we found that VASH2 levels were positively correlated with

desmin levels in the PEB fraction (Extended Data Fig. 8*h–j*), supporting previous data that detyrosinated microtubules are positively correlated with desmin levels in cardiomyocytes⁵. In summary, our results suggest that MARK4 kinase, through phosphorylation of MAP4 at S914 and S1046, changes the status of MAP4 to allow VASH2 access to the polymerized microtubule for its TCP activity.

To further confirm the causal effect of MARK4 on VASH2 localization, we overexpressed MARK4 in primary cardiomyocytes, which caused the appearance of pMAP4(S1046) (Extended Data Fig. 9*a–c*) and giant MAP4 puncta in the cytosol (Extended Data Fig. 9*d,e*) and led to increased VASH2 levels in the PEB fraction (Extended Data Fig. 9*a–c*). By using stimulated emission depletion super-resolution microscopy³⁴, we found a strong localization of VASH2 on the polymerized microtubules in primary cardiomyocytes isolated from wild-type hearts after myocardial infarction compared with samples isolated from wild-type hearts at baseline (Extended Data Fig. 10*a,b*). Total VASH2 levels were comparable between *Mark4*^{−/−} and *Mark4*^{+/+} cardiomyocytes after myocardial infarction (Extended Data Fig. 10*c,d*). However, there was a significant reduction in the association between VASH2 and polymerized microtubules in *Mark4*^{−/−} compared with wild-type cardiomyocytes (Fig. 4*f,g*). In conclusion, our results demonstrate that MARK4 regulates microtubule detyrosination by phosphorylating MAP4 and controlling VASH2 accessibility to the microtubules (Extended Data Fig. 10*e*).

Discussion

Detyrosinated microtubules interfere with the contractile function of cardiomyocytes from failing hearts in humans⁷, and targeting the regulatory mechanism that controls microtubule detyrosination could represent a new inotropic strategy for improving cardiac function. We show that MARK4 has an important role in the alteration of cardiomyocyte contractility through the modulation of microtubule detyrosination in the ischaemic heart. It will be interesting to examine whether this protective effect of MARK4 inactivation on cardiac function after myocardial infarction is sustained in the very long term (several months after myocardial infarction) without inducing any harmful side effects, and whether MARK4 inhibition can improve contractile function in the setting of non-ischaemic heart failure. Furthermore, the marked improvement in relaxation kinetics in the absence of MARK4 raises the possibility of a potential beneficial effect of MARK4 inhibition in the setting of heart failure with preserved ejection fraction, an increasingly common cardiac syndrome that is associated with high morbidity and mortality. The molecular and structural mechanisms of MARK4 coupled with MAP4 and VASH2–SVBP in modifying microtubule detyrosination will need to be investigated in other settings such as mitosis, where regulation of detyrosinated microtubules has important pathophysiological relevance^{9,35}, and the

differential role of other TCPs (for example, VASH1) will need to be studied further in future.

Methods

Data reporting

The experiments were randomized when possible, and the investigators were blinded to allocation during experiments and outcome assessment when possible (further information on randomization and blinding is available in the Nature Research Reporting Summary linked to this Article).

Mice

All in vivo experiments using mice were approved by the UK Home Office and were performed under PPL PA4BDF775. All mice were on a C57BL/6 background and housed under standard temperature (18–23 °C) and humidity (40–60%), with a 12-h light–dark cycle. *Mark4*^{−/−} mice were provided by Y. Shi²⁴ and Mutant Mouse Resource and Research Center; *Myh6-mcm*^{+/−} Cre mice were originally from the Jackson Laboratory (Cre was expressed under mouse cardiac-specific α-myosin heavy chain promoter (α-MHC; Myh6)); *Mark4*^{f/f} mice were from Taconic Biosciences. *Myh6-mcm*^{+/−} Cre mice were crossed with *Mark4*^{f/f} mice to generate *Myh6-mcm*^{+/-cre;Mark4}^{f/f} mice. The Cre-mediated excision of floxed *Mark4* alleles was induced by treatment with tamoxifen dissolved in corn oil by intraperitoneal injection at 20 mg kg^{−1} body weight per day for 5 consecutive days.

Left anterior descending coronary artery ligation model

Permanent left anterior descending (LAD) coronary artery ligation was performed on mice as previously described^{22,23} with minor modifications. Mice, at 8–10 weeks of age, were anaesthetized using ketamine at 100 mg kg^{−1} body weight and xylazine at 10 mg kg^{−1} body weight by intraperitoneal injection, and then intubated and ventilated with air (supplemented with oxygen) using a small-animal respirator. A thoracotomy was performed in the fourth left intercostal space. The left ventricle was visualized and the pericardial sac was ruptured to expose the LAD coronary artery. The LAD was permanently ligated using a 7-0 Prolene suture. The suture was passed approximately 2 mm below the tip of the left auricle. Marked colour changes of the ischaemic area and ECG changes were monitored as an indication of successful coronary artery occlusion. The thoracotomy was closed with 6-0 Prolene sutures. Sham-operated mice underwent the same procedure without coronary artery ligation. The endotracheal tube was removed once spontaneous respiration resumed, and the mice were placed in a

warm recovery cage maintained at 37 °C until they were completely awake. At the indicated time points in the experimental timeline, the mice were euthanized by CO₂ asphyxiation and the tissues were subsequently collected for analysis.

Bone marrow transplants

Eight-to-ten-week-old C57BL/6 mice were maintained overnight with Baytril (Bayer) before irradiation with two doses of 5.5 Gy (separated by 4 h) followed by reconstitution with 1 × 10⁷ sex-matched donor bone marrow cells. Mice were randomly assigned to receive the *Mark4*^{-/-} or *Mark4*^{+/+} bone marrow. Mice were then maintained on Baytril for a 4-week recovery period before performing LAD ligation.

Echocardiography

Transthoracic echocardiography was performed on all mice using Vevo 3100 with a MX400 linear array transducer (VisualSonics), 30 MHz. Mice were anaesthetized with 2–3% isoflurane and kept warm on a heated platform (37 °C). The chest hairs were removed using depilatory cream and a layer of acoustic coupling gel was applied to the thorax. After alignment in the transverse B-mode with the papillary muscles, cardiac function was measured on M-mode images. Echocardiography data were collected using VisualSonics Vevo 3100 and analysed using Vevo LAB3.1.1.

Histological analysis

Whole hearts were excised at different time point after LAD ligation, rinsed in PBS and fixed with 4% PFA overnight at 4 °C. Fixed tissues were thoroughly washed in PBS, and then immersed in 30% sucrose. Tissues were embedded and sectioned by a cryostat into 10-µm thick slices, which started at the apex and ended at the suture ligation site. Masson's trichrome staining was performed to determine scar size. Scar size was calculated as the total infarct circumference divided by the total left ventricle circumference. Some hearts were excised at 24 h after myocardial infarction and quickly sliced into four 1.0-mm thick sections perpendicular to the long axis of the heart. The sections were then incubated with 1% triphenyltetrazolium chloride (TTC, Sigma) for 15 min at 37 °C and digitally photographed. To analyse the infarct size at 24 h after myocardial infarction, the TTC-stained area and TTC-negative area (infarcted myocardium) were measured using ImageJ (v.2.0). Myocardial infarct size was expressed as a percentage of the total left ventricle area. Images were obtained using a Leica DM6000 B microscope, collected using LAS AF software (2.4.0 build 6254) and analysed using ImageJ (v.2.0).

Tissue immunohistochemistry

Whole hearts were excised, quickly washed in PBS and flash-frozen. Tissues were then embedded and cryo-sectioned. Slices were fixed in pre-chilled methanol for 10 min at -20°C . After washing with PBST (0.1% Tween-20 in 1× PBS), slices were incubated with 3% H₂O₂ (in PBS) for 10 min, and then with blocking buffer (5% BSA in PBST) for 1 h at room temperature. The primary antibody against MARK4 (Abcam, ab124267, used at 1:200) or rabbit IgG isotype control (Novus Biologicals, NB810-56910, used at 1:1,000) was used overnight at 4°C . Extensive washing steps were performed to remove nonspecific antibody binding. Slices were incubated with the biotinylated secondary antibody (Abcam, ab6720, used at 1:800) for 1 h at room temperature. Reagents A and B from the Avidin-Biotin Complex kit (VECTOR, PK-4000) were diluted and added to the slides. The slides were stained with ImmPACT DAB peroxidase substrate (VECTOR, SK-4105) and counterstained with haematoxylin. Images were obtained using a Leica DM6000 B microscope, collected using LAS AF software (2.4.0 build 6254) and analysed using ImageJ (v.2.0) analyse tools.

Microtubule co-sedimentation assay

Lyophilized porcine brain tubulin (T240) was purchased from Cytoskeleton. Recombinant proteins of 4R-MAP4 and VASH2–SVBP were previously described^{12,33}. Desiccated tubulin was reconstituted in the microtubule polymerization buffer to 10 mg ml⁻¹. To generate polymerized microtubules, tubulin was diluted to 2 mg ml⁻¹ in the polymerization buffer (80 mM K-PIPES, pH 6.8, 1 mM MgCl₂, 1 mM EGTA and 1 mM DTT), supplemented with 5% glycerol and 1 mM GTP at 37°C for 30 min, and then stabilized by incubating with 2.5 μM taxol at 37°C for 15 min. The taxol-stabilized microtubules were centrifuged over a cushion buffer (polymerization buffer with 40% glycerol) at 131,700g at 37°C for 15 min to remove the free tubulin. The pellet was resuspended in the polymerization buffer with 1 μM taxol. Taxol influenced the association of 4R-MAP4 with the microtubules in our assay. 4R-MAP4 association was facilitated when taxol was completely excluded from the buffer. The microtubules without taxol were susceptible to depolymerization if stored at room temperature. In these conditions, the polymerized microtubules were maintained at 37°C throughout the experiment. For the co-sedimentation assay, the microtubules were mixed with various concentrations of 4R-MAP4 (1–6 μM) and VASH2–SVBP (1–4 μM) in the polymerization buffer. In the competition experiments, the microtubules were incubated with specified 4R-MAP4 concentrations (1–4 μM) for 10 min, followed by addition of a constant amount of VASH2–SVBP (3 μM) with further incubation for 10 min. Subsequently, the reaction mixture was centrifuged using a TLA120.2 rotor at 55,000 rpm for 15 min. The pellet fraction containing the microtubules and bound proteins was resuspended in the loading buffer. The samples were loaded on a 10% SDS–PAGE gel and stained with colloidal Coomassie blue dye

(ThermoFisher). The experiments were repeated at least three times. The band intensities were analysed using ImageJ (v.2.0).

Mouse cardiomyocyte isolation

Preparation of cardiomyocytes was accomplished as previously described²⁸. In brief, mice were anaesthetized and the chest was opened to expose the heart. the descending aorta was cut and the heart was immediately flushed by injection of 7 ml EDTA buffer into the right ventricle. The ascending aorta was clamped and the heart was transferred to a 60-mm dish containing fresh EDTA buffer. Digestion was achieved by sequential injection of 10 ml EDTA buffer (NaCl, 130 mM; KCl, 5 mM; NaH₂PO₄, 0.5 mM; HEPES, 10 mM; glucose, 10 mM; BDM, 10 mM; taurine, 10 mM; EDTA, 5 mM; pH to 7.8), 3 ml perfusion buffer (NaCl, 130 mM; KCl, 5 mM; NaH₂PO₄, 0.5 mM; HEPES, 10 mM; glucose, 10 mM; BDM, 10 mM; taurine, 10 mM; MgCl₂, 1 mM; pH to 7.8) and 30–50 ml collagenase buffer (collagenase 2, 0.5 mg ml⁻¹; collagenase 4, 0.5 g ml⁻¹; protease XIV, 0.05 mg ml⁻¹; made fresh and diluted in perfusion buffer) into the left ventricle. The left ventricle was then separated and gently pulled into 1-mm pieces using forceps. Cellular dissociation was completed by gentle trituration, and enzyme activity was inhibited by addition of 5 ml stop buffer (perfusion buffer containing 5% sterile FBS). The cell suspension was passed through a 100-μm filter. Cells underwent four sequential rounds of gravity settling, using three intermediate calcium reintroduction buffers (buffer 1, 75% perfusion buffer with 25% culture medium; buffer 2, 50% perfusion buffer with 50% culture medium; buffer 3, 25% perfusion buffer with 75% culture medium; culture medium comprised 0.1% BSA, 1% ITS, 10 mM BDM, 1% CD lipid and 5% penicillin–streptomycin in M199) to gradually restore the calcium concentration to physiological levels.

Primary cardiomyocyte culture and adenoviral transduction

Adenoviral vectors including pAdeno-SV40-GFP-Blank vector (Adv-null), pAdeno-Ttl-SV40-GFP vector (Adv-Ttl) (NM_027192.2) and pAdeno-Mark4-SV40-GFP vector (Adv-Mark4) (NM_172279.1) were purchased from Applied Biological Materials. Adenoviral vector pAV[shRNA]-EGFP-U6>mMap4 (*Map4* shRNA target sequence: AGAGTGGACTATCCGGATTAT), adenoviral vector pAV[shRNA]-EGFP-U6>mVash2 (*Vash2* shRNA target sequence: GAGAACCTTGCTATCAAAT) and adenoviral vector pAV[shRNA]-EGFP-U6>Scramble were purchased from VectorBuilder. Six-well plates or coverslips were coated with laminin at a final concentration of 5 μg ml⁻¹ in PBS overnight at 4 °C. The wells were washed and air-dried for 10 min before plating cells. After collecting the cells by gravity settling and calcium re-introduction, the final cardiomyocyte pellets were resuspended in 2 ml culture medium and 2 ml pre-equilibrated plating medium (0.1% FBS, 10 mM BDM

and 5% penicillin–streptomycin in M199) for culture. After incubation for 1 h, the cell medium was changed with pre-equilibrated culture medium and adenovirus vectors were administered at 5×10^6 PFU ml⁻¹. After co-culture with virus for 8 h, fresh culture medium was used to wash and replace the old culture medium containing the virus. Cells were either used for the contractility assay and western blotting immediately after the medium change (in the experiments of overexpression of TTL), or collected at 48 h after transduction (in the experiments of *Mark4* overexpression, *Map4* shRNA and *Vash2* shRNA) for the subsequent assays.

Cardiomyocyte contractility assay

Sarcomere shortening and relaxation were measured in freshly isolated left ventricular cardiomyocytes of mouse hearts using the integrated IonOptix contractility/photometry system. Cardiomyocytes were maintained in normal Tyrode's solution (NaCl, 140 mM; MgCl₂, 0.5 mM; NaH₂PO₄, 0.33 mM; HEPES, 5 mM; glucose, 5.5 mM; CaCl₂, 1 mM; KCl, 5 mM; NaOH, pH to 7.4) at room temperature, electrically stimulated at 2 Hz using a field stimulator, and changes in sarcomere length were recorded. Basal and peak sarcomere length, maximum departure and return velocities and time to peak were measured. All measurements were performed at room temperature. For parthenolide (PTL) experiments, cardiomyocytes were treated with 10 µM PTL (Sigma P0667) or vehicle at room temperature in normal Tyrode's solution for 1 h before contractility measurements, and the vehicle—dimethyl sulfoxide (DMSO)—diluted in the same way was applied as control. All measurements were performed at room temperature within 4 h. Data were collected and analysed using IonWizard 7.4.

Calcium measurements

Measurement of intracellular calcium was performed in freshly isolated left ventricular cardiomyocytes using the integrated IonOptix contractility/photometry system. Cardiomyocytes were loaded with 1 µM Fura-2-AM for 20 min (protected from light) and then washed to allow de-esterification for 20 min. Cells were then rinsed with normal Tyrode's solution. Cells were stimulated at 2 Hz using a field stimulator with dual excitation (at 360 and 380 nm), and emission light was collected at 510 nm. Changes in calcium transients were recorded using IonOptix software. All of the cells analysed were beating. All measurements were performed at room temperature within 4 h. Data were collected and analysed using IonWizard 7.4.

Immunofluorescence and image acquirement

Cardiomyocytes were fixed with pre-chilled methanol for 10 min, then washed twice using PBST (0.1% Tween-20 in 1× PBS) with 5-min intervals. Cells were blocked for 1 h at room temperature with blocking buffer (5% BSA in PBST) and incubated with primary antibodies overnight at 4 °C. The primary antibodies were: detyrosinated α -tubulin (Abcam, ab48389, used at 1:200), α -tubulin (CST, 3873S, used at 1:200), MARK4 (Abcam, ab124267, used at 1:200), APC anti-mouse CD45 (BioLegend, 103112, used at 1:200) and rabbit IgG isotype control (Novus Biologicals, NB810-56910, used at 1:2,000). The cells were then washed with PBST and incubated with secondary antibody for 1 h at room temperature. The secondary antibodies were: AF488 donkey anti-rabbit IgG (Invitrogen, A21206, used at 1:200), AF647 goat anti-mouse IgG (Invitrogen, A21236, used at 1:200), AF647 goat anti-rat IgG (Invitrogen, A21247, used at 1:200). DAPI (Sigma, 10236276001, used at 1:1,000) was used. Confocal images were obtained using a Leica SP5 confocal laser scanning microscope, collected using LAS AF software (2.7.3.9723) and analysed using ImageJ (v.2.0) analyse tools.

Stimulated emission depletion imaging and image analysis

Cardiomyocytes on coverslips were fixed with 100% methanol for 15 min at room temperature and then washed three times with PBS (5-min intervals). Cells were blocked with buffer (5% BSA and 0.2% Triton X-100 in PBS) for 30 min, then incubated with primary antibodies (diluted in blocking buffer) overnight at 4 °C. The primary antibodies were VASH2 (Abcam, ab224723, used at 1:200), MAP4 (Abcam, ab245578, used at 1:200) and α -tubulin (CST, 3873S, used at 1:200). The cells were washed three times using wash buffer (0.05% Triton X-100 in PBS) at room temperature, then incubated with the secondary antibody for 1 h at room temperature. The secondary antibodies were: Atto-594 goat anti-rabbit IgG (Sigma, 77671, used at 1:500) and Atto-647N goat anti-mouse IgG (Sigma, 50185, used at 1:500). Cells were then washed three times in wash buffer. Cells were fixed (3% paraformaldehyde and 0.1% glutaraldehyde diluted in PBS) followed by three washes in PBS. The coverslips were then mounted on the slide.

Stimulated emission depletion (STED) imaging was carried out on a custom multicolour system with three pulsed excitation lines, one fixed depletion line, fast 16 kHz beam scanning and gated detection centred around an Olympus IX83 microscope base. This system uses identical hardware, and a closely matched optical arrangement, to a previously described system³⁴. In brief, two-colour STED imaging was performed sequentially. Images were acquired with a 100 \times oil-immersion objective lens (Olympus, UPLSAPO 100XO/PSF). Fields of view between 23 and 27 μm^2 were imaged with a 1,024 \times 1,024 image format and an approximately 20 nm pixel size. Excitation powers were between 15 and 30 μW at the microscope side port and the STED depletion power was approximately 120 mW at the microscope side

port. Fast, 16 kHz, unidirectional beam scanning with blanking was used to minimize light exposure. Each line of an image was scanned 850 times, resulting in an image acquisition time of approximately 54 s per colour. STED image data were collected with a custom program written in National Instrument (NI) LabVIEW 2014 64-bit, NI FPGA Module and NI Vision Development Module.

MAP4 oligomerized puncta (with a diameter longer than 400 nm) were measured and calculated using ImageJ (v.2.0). The number of puncta was normalized against the cell area of each image.

For the acquired images, a dynamic thresholding algorithm was used for the image analysis. Images were converted into HSV colour images (C) with information of hue (h), saturation (s) and value (v). $C(i,j)$ was assumed as a non-background image pixel, N was the total number of non-background image pixels, H was image height and W was image width. The average of all the non-background image pixels was calculated as $\langle k = \text{hspace}\{-1\text{pt}\} \mathop{\sum} \limits_{i=1}^H \mathop{\sum} \limits_{j=1}^W C(i,j) \text{hspace}\{-1\text{pt}\} \rangle / N$. The following three thresholds were applied to discriminate signals: $h = [0, 180]$; $s = [0, 43]$; $v = [k + 30, 220]$. A Gaussian filter $((f(x) = \frac{1}{2\pi\sigma^2} e^{-\frac{(x-x_0)^2}{2\sigma^2}}))$, a two-dimensional convolution operator, was used to remove noise. For the VASH2 signals, the Gaussian filter with a kernel of 3×3 was used for image denoising. For the linear microtubule signals, the Gaussian filter with a kernel of 5×5 was used for image denoising when $k \geq 35$ and a kernel of 3×3 was applied when $k < 35$. The total numbers of VASH2 (v) and α -tubulin (t) pixels were calculated. The total number of overlapping image pixels (o) between VASH2 and tubulin was calculated as VASH2 signals on the microtubules, and $(1 - o)/v$ was calculated as VASH2 signals off the microtubules. The Pearson correlation coefficient $((\rho_{X,Y} = \frac{\text{cov}(X,Y)}{\sigma_X \sigma_Y}))$ between VASH2 signals and tubulin signals was calculated. Automatic image processing was coded using a custom algorithm in Python v.3.7.8.

Subcellular fractionations of the primary cardiomyocytes

Subcellular fractionations of primary cardiomyocytes were performed according to the manufacturer's instructions (Pierce, 87790). In brief, cells were incubated with CEB, which selectively permeabilizes the cell membrane for 10 min at 4 °C with gentle mixing. Cells were centrifuged for 5 min at 500g and supernatants were collected. The cytoskeletal binding proteins were isolated in the PEB.

Subcellular fractionations of primary cardiomyocytes were also obtained using a conventional method. Primary mouse cardiomyocytes were isolated and homogenized in pre-warmed (37 °C) microtubule-stabilizing buffer (PIPES, 80 mM; MgCl₂, 1 mM;

EGTA, 1 mM; 0.5% Triton X-100; 10% glycerol; GTP, 0.5 mM; Halt protease inhibitor cocktail from Thermo Fisher Scientific 1862209; pH to 6.8) using a Dounce homogenizer. The homogenates were centrifuged at 100,000g for 15 min at room temperature. The supernatants were collected as the free-tubulin fraction as F1, and the pellets were dissolved in the microtubule-destabilizing buffer (Tris-HCl, 20 mM; NaCl, 150 mM; 1% Triton X-100; CaCl₂, 10 mM; Halt protease inhibitor cocktail from Thermo Fisher Scientific 1862209; pH to 7.4) for further incubation on ice for 1 h to depolymerize the microtubules. The dissolved lysates were centrifuged at 12,000g for 15 min at 4 °C. The pellets were incubated with 150 units of micrococcal nuclease (100 units μl^{-1} , Thermo Fisher Scientific, 88216) in microtubule-destabilizing buffer for 15 min at room temperature, and then centrifuged at 12,000g for 5 min at 4 °C to remove the nuclear debris. The collected pellets were dissolved in 2× SDS buffer (4% SDS; 20% glycerol; Tris-HCl, 0.25 M; pH to 6.5). The dissolved lysates were then centrifuged at 14,000g for 5 min at 4 °C. The supernatants were collected as F2 (extraction from the stable pellet fraction) and the residual pellets were kept.

Western blotting

The heart tissues were grounded thoroughly with a mortar and pestled in liquid nitrogen. Tissue powder was lysed using Triton lysis buffer (20 mM Tris-HCl, pH to 7.5; 150 mM NaCl; 1 mM Na₂EDTA; 1 mM EGTA; 1% Triton X-100; 1 mM Na₃VO₄; 5 mM NaF; protease inhibitor cocktail (ThermoFisher, 1862209)). The supernatant (soluble fraction) was collected, and the pellets (insoluble fraction) were dissolved in 8 M urea (Figs. 1b, 3a, d; $n = 12$ mice in the *Mark4*^{+/+} myocardial infarction group and $n = 9$ mice in the *Mark4*^{-/-} myocardial infarction group used for Fig. 3b). For some experiments ($n = 8$ mice per group used for Fig. 3b, c), heart tissues were homogenized in the lysis buffer (0.1 M PIPES pH to 6.8; 2 mM EGTA; 0.1 mM EDTA; 0.5 mM MgCl₂; 20% glycerol; 0.1% Triton X-100; protease inhibitor cocktail (ThermoFisher, 1862209)) and incubated for 30 min at 37 °C. After centrifugation (21,100g for 5 min), the supernatants were collected as the soluble fraction, and the pellets were dissolved in buffer (RIPA buffer (CST, 9806); 0.8% SDS; and protease inhibitor cocktail (ThermoFisher, 1862209)) and collected as the insoluble fraction. The protein concentration was determined using a BCA protein assay kit (ThermoFisher, 23235). Molecular mass markers (ThermoFisher, LC5603 and LC5925) were used. Supernatant samples were prepared in NuPAGE LDS sample buffer (Invitrogen) and run on NuPAGE 4–12% Bis-Tris gels (Invitrogen). Pellet samples were prepared in Tris-glycine SDS sample buffer (Invitrogen) and run on Novex 4–20% Tris-glycine gels (Invitrogen). All samples were blotted onto a PVDF membrane after electrophoresis. The following primary antibodies were used in the experiments: MARK4 (CST, 4834S, used at 1:1,000), GAPDH (CST, 5174S, used at

1:1,000), desmin (R&D, AF3844, used at 1:1,000), detyrosinated α -tubulin (Abcam, ab48389, used at 1:200), polyglutamylated α -tubulin (AdipoGen, AG-20B-0020-C100, used at 1:1,000), acetylated α -tubulin (Santa Cruz Biotechnology, sc23950, used at 1:1,000), α -tubulin (CST, 3873S, used at 1:200). After antibody detection, membranes were revealed with ECL. Quantification of the western blot bands was performed using ImageJ (v.2.0).

For the fractionation assay, equal amounts of total protein (20 μ g) from each fraction were used for western blot. The DC protein assay kit (Bio-Rad, 5000111) was used to measure protein concentrations. Across different gels, equal amounts of a molecular mass marker (ThermoFisher, LC5603) were loaded in each gel. Samples were run on NuPAGE 4–12% Bis-Tris gels (Invitrogen) and blotted onto a PVDF membrane.

Some samples of the CEB fraction from the fractionation assay were prepared for native gel analysis. Samples were processed in Tris-glycine native sample buffer (ThermoFisher, LC2673) before loading without heating or addition of any reducing reagent. Samples were loaded on a 3–8% NuPAGE Tris-acetate gel (ThermoFisher, EA0375BOX) for electrophoresis in Tris-glycine native running buffer (Tris-base, 25 mM; glycine, 192 mM; pH to 8.3). Native molecular marker (ThermoFisher, LC0725) was used. After electrophoresis, proteins were transferred to a PVDF membrane by transfer buffer (Bicine, 25mM; Bis-Tris, 25 mM; EDTA, 1 mM; pH to 7.2).

Some samples from the fractionation assay were prepared with a denaturing treatment by adding urea. Urea (0 M, 2 M, 4 M or 8 M) was added to the samples as indicated. A micro-BCA protein assay kit (ThermoFisher, 23235) was used to measure protein concentrations if urea was added to the samples. Samples were then processed in Tris-glycine SDS sample buffer (ThermoFisher, LC2676) and reducing reagent (10% 2-mercaptoethanol). A 4–20% Tris-glycine gel (ThermoFisher, EC6026BOX) was used for electrophoresis in Tris-glycine SDS running buffer (Tris-base, 25 mM; glycine, 192 mM; 0.1% SDS; pH to 8.3). After electrophoresis, proteins were transferred to PVDF membrane by transfer buffer (Tris-base, 12 mM; glycine, 96 mM; pH to 8.3).

The primary antibodies used for fractionation assays were: detyrosinated α -tubulin (Abcam, ab48389, used at 1:1,000), α -tubulin (CST, 3873S, used at 1:1,000), TTL (Proteintech, 13618-1-AP, used at 1:1,000), VASH1 (Abcam, ab199732, used at 1:1,000), VASH2 (Abcam, ab224723, used at 1:1,000), pMAP4(S1073) (Abnova, PAB15916, used at 1:1,000), MAP4 (Abcam, ab245578, used at 1:1,000), pMAP4(S941) (Abcam, ab56087, used at 1:1,000), GAPDH (CST, 5174S, used at 1:1,000), desmin (R&D, AF3844, used at 1:1,000). Membranes were revealed with ECL. Quantification of western blot bands was performed using ImageJ (v.2.0). The band density was normalized in two steps: (1) the density of the targeted band was first normalized against the density of the loading molecular mass marker band (norm 1);

(2) the value of norm 1 was internally normalized against the average value of norm 1 of the control group (norm 2). The finalized value (norm 2) was used to compare the fold changes against the value of the control groups across different gels. desmin was used as a marker for the pellet fraction, and GAPDH was used as a marker for the cytosolic fraction. Coomassie-blue-stained gels loaded with the same amounts of proteins as used in western blotting experiments or Ponceau-S-stained membranes after the transfer step were used to confirm equal loading. All of the immunoblots, gels and membranes associated with the data presented in the figures and extended data figures are provided (Supplementary Fig. 1).

Heart tissue digestion and flow cytometry

Hearts were collected and the left ventricle was isolated, minced with fine scissors and subjected to enzymatic digestion solution (RPMI 1640, collagenase D (0.2 mg ml⁻¹, Roche), dispase (1 U ml⁻¹, StemCell Technologies) and DNase I (0.2 mg ml⁻¹, Sigma)) for 45 min at 37 °C. Cells were collected, filtered through a 40-μm nylon mesh and washed with PBS with 2.5% v/v fetal bovine serum. Cell suspensions were incubated with a Zombie Aqua Fixable Viability Kit (Biolegend, 423102, used at 1:1,000) for 20 min at room temperature and washed with PBS. Cells were then stained with fluorescently labelled anti-mouse antibodies, including APC anti-mouse CD45 (Biolegend, 103112, used at 1:100), AF488 anti-mouse CD11b (Biolegend, 101217, used at 1:100), Pacific blue anti-mouse Ly6G (Biolegend, 127612, used at 1:100), PE anti-mouse F4/80 (Biolegend, 123110, used at 1:100), PECY7 anti-mouse CD11c (Biolegend, 117318, used at 1:100), Brilliant Violet 605 anti-mouse CD3 (Biolegend, 100237, used at 1:100) and FITC anti-mouse CD19 (Biolegend, 553785, used at 1:100), diluted in staining buffer for 30 min at 4 °C in the presence of 24G2 Fc receptor blocker (obtained from the Division of Immunology, Department of Pathology, University of Cambridge), before extensive washing. The cytometric acquisition was performed on a LSR II Fortessa (BD biosciences). Cell analysis was done using BD FACSDiva Software 6.0 and FlowJo software (v.10).

Real-time PCR

For gene expression analysis, RNA from heart tissues or separated cardiomyocytes was isolated using an RNAeasy mini kit (Qiagen). Reverse transcription was performed using a QuantiTect reverse-transcription kit (Qiagen). qRT–PCR was performed with SYBR Green qPCR mix (Eurogentec) using the Roche LightCycler 480II. Primer sequences are as follows: *Mark4* (forward 5'-GGACACGCATGGCACATTG-3'; reverse 5'-GCAGGAAGCGATAGAGTTCCG-3'); *Vash2* (forward 5'-GCCTTCCTGGCTAACGCCCTC-3'; reverse 5'-CCCTGTGTGGTTGTATTGTAGAG-3'); *Hprt* (forward 5'-TCAGTCAACGGGGACATAAA-3'; reverse 5'-GGGGCTGTACTGCTTAACCAG-

3'); *Rpl4* (forward 5'-CCGTCCCCTCATATCGGTGTA-3'; reverse 5'-GCATAGGGCTGTCTGTTGTTT-3'); *Rpl13a* (forward 5'-AGCCTACCAGAAAGTTGCTTAC-3'; reverse 5'-GCTTCTTCTTCGATAGTGCATC-3'). The average of three housekeeping genes (*Hprt*, *Rpl4* and *Rpl13a*) was used as reference for qPCR gene expression analysis.

Measurement of cardiac troponin I and inflammatory cytokines

Serum was collected within 24 h after myocardial infarction or at day 3 after myocardial infarction. Measurements of the cardiac injury biomarker (collected within 24 h) and cytokines (collected at day 3 after myocardial infarction) were performed by the core biochemical assay laboratory of Cambridge University Hospitals.

Statistics and reproducibility

All values in the text and figures are presented as mean \pm s.e.m. of independent experiments with given n sizes. No statistical methods were used to predetermine sample size. Statistical analysis was performed with Prism v.7.05 (GraphPad) and Excel (Microsoft Excel 2102). Violin plots were created with Prism v.9.1.0 (216) (GraphPad). Data were tested for normality using a Kolmogorov–Smirnov test. Group comparisons were analysed using two-tailed analyses. Comparisons of three or more groups were analysed using one-way (one variable) or two-way (two variables) ANOVA followed by the Bonferroni post hoc correction for multiple comparisons when appropriate. $P < 0.05$ was considered statistically significant.

Data in Figs. 1b, c, 3a and Extended Data Figs. 2a, 5a, 7b, 8a, b are representative of three independent experiments. Data in Extended Data Fig. 8e–g are representative of two independent experiments.

Reporting summary

Further information on research design is available in the [Nature Research Reporting Summary](#) linked to this paper.

Data availability

All of the associated raw data presented in this paper are available from the corresponding author upon request. [Source data](#) are provided with this paper.

Code availability

Custom STED microscope control software used for data collection can be accessed at <https://github.com/Gurdon-Super-Res-Lab/STED-Control>, and a customized algorithm used for STED image analysis is available at https://github.com/zhaoaite/dynamic_thresholding_algorithm.

References

1. 1.

Murray, C. J. & Lopez, A. D. Measuring the global burden of disease. *N. Engl. J. Med.* **369**, 448–457 (2013).

[CAS](#) [Article](#) [Google Scholar](#)

2. 2.

Packer, M. et al. Effect of oral milrinone on mortality in severe chronic heart failure. *N. Engl. J. Med.* **325**, 1468–1475 (1991).

[CAS](#) [Article](#) [Google Scholar](#)

3. 3.

Cohn, J. N. et al. A dose-dependent increase in mortality with vesnarinone among patients with severe heart failure. *N. Engl. J. Med.* **339**, 1810–1816 (1998).

[CAS](#) [Article](#) [Google Scholar](#)

4. 4.

Teerlink, J. R. et al. Cardiac myosin activation with omecamtiv mecarbil in systolic heart failure. *N. Engl. J. Med.* **384**, 105–116 (2021).

[CAS](#) [Article](#) [Google Scholar](#)

5. 5.

Robison, P. et al. Detyrosinated microtubules buckle and bear load in contracting cardiomyocytes. *Science* **352**, aaf0659 (2016).

[Article](#) [Google Scholar](#)

6. 6.

Anderson, J. L. & Morrow, D. A. Acute myocardial infarction. *N. Engl. J. Med.* **376**, 2053–2064 (2017).

[CAS](#) [Article](#) [Google Scholar](#)

7. 7.

Chen, C. Y. et al. Suppression of detyrosinated microtubules improves cardiomyocyte function in human heart failure. *Nat. Med.* **24**, 1225–1233 (2018).

[CAS](#) [Article](#) [Google Scholar](#)

8. 8.

Schuldt, M. et al. Proteomic and functional studies reveal detyrosinated tubulin as treatment target in sarcomere mutation-induced hypertrophic cardiomyopathy. *Circ. Heart Fail.* **14**, e007022 (2021).

[CAS](#) [Article](#) [Google Scholar](#)

9. 9.

Aillaud, C. et al. Vasohibins/SVBP are tubulin carboxypeptidases (TCPs) that regulate neuron differentiation. *Science* **358**, 1448–1453 (2017).

[ADS](#) [CAS](#) [Article](#) [Google Scholar](#)

10. 10.

Nieuwenhuis, J. et al. Vasohibins encode tubulin detyrosinating activity. *Science* **358**, 1453–1456 (2017).

[ADS](#) [CAS](#) [Article](#) [Google Scholar](#)

11. 11.

Chen, C. Y. et al. Depletion of vasohibin 1 speeds contraction and relaxation in failing human cardiomyocytes. *Circ. Res.* **127**, e14–e27 (2020).

[CAS](#) [PubMed](#) [Google Scholar](#)

12. 12.

Wang, N. et al. Structural basis of tubulin detyrosination by the vasohibin–SVBP enzyme complex. *Nat. Struct. Mol. Biol.* **26**, 571–582 (2019).

[CAS Article](#) [Google Scholar](#)

13. 13.

Li, F., Hu, Y., Qi, S., Luo, X. & Yu, H. Structural basis of tubulin detyrosination by vasohibins. *Nat. Struct. Mol. Biol.* **26**, 583–591 (2019).

[CAS Article](#) [Google Scholar](#)

14. 14.

Zhou, C., Yan, L., Zhang, W. H. & Liu, Z. Structural basis of tubulin detyrosination by VASH2/SVBP heterodimer. *Nat. Commun.* **10**, 3212 (2019).

[ADS Article](#) [Google Scholar](#)

15. 15.

Ramkumar, A., Jong, B. Y. & Ori-McKenney, K. M. Remapping the microtubule landscape: how phosphorylation dictates the activities of microtubule-associated proteins. *Dev. Dyn.* **247**, 138–155 (2018).

[CAS Article](#) [Google Scholar](#)

16. 16.

Chinnakkannu, P. et al. Site-specific microtubule-associated protein 4 dephosphorylation causes microtubule network densification in pressure overload cardiac hypertrophy. *J. Biol. Chem.* **285**, 21837–21848 (2010).

[CAS Article](#) [Google Scholar](#)

17. 17.

Doerflinger, H., Benton, R., Shulman, J. M. & St Johnston, D. The role of PAR-1 in regulating the polarised microtubule cytoskeleton in the *Drosophila* follicular epithelium. *Development* **130**, 3965–3975 (2003).

[CAS Article](#) [Google Scholar](#)

18. 18.

Goldstein, B. & Macara, I. G. The PAR proteins: fundamental players in animal cell polarization. *Dev. Cell* **13**, 609–622 (2007).

[CAS](#) [Article](#) [Google Scholar](#)

19. 19.

Illenberger, S. et al. Phosphorylation of microtubule-associated proteins MAP2 and MAP4 by the protein kinase p110^{mark}. Phosphorylation sites and regulation of microtubule dynamics. *J. Biol. Chem.* **271**, 10834–10843 (1996).

[CAS](#) [Article](#) [Google Scholar](#)

20. 20.

Trinczek, B., Brajenovic, M., Ebneth, A. & Drewes, G. MARK4 is a novel microtubule-associated proteins/microtubule affinity-regulating kinase that binds to the cellular microtubule network and to centrosomes. *J. Biol. Chem.* **279**, 5915–5923 (2004).

[CAS](#) [Article](#) [Google Scholar](#)

21. 21.

Drewes, G., Ebneth, A. & Mandelkow, E. M. MAPs, MARKs and microtubule dynamics. *Trends Biochem. Sci.* **23**, 307–311 (1998).

[CAS](#) [Article](#) [Google Scholar](#)

22. 22.

Zouggari, Y. et al. B lymphocytes trigger monocyte mobilization and impair heart function after acute myocardial infarction. *Nat. Med.* **19**, 1273–1280 (2013).

[CAS](#) [Article](#) [Google Scholar](#)

23. 23.

Pell, V. R. et al. Ischemic preconditioning protects against cardiac ischemia reperfusion injury without affecting succinate accumulation or oxidation. *J. Mol. Cell. Cardiol.* **123**, 88–91 (2018).

[ADS](#) [CAS](#) [Article](#) [Google Scholar](#)

24. 24.

Li, X. et al. MARK4 regulates NLRP3 positioning and inflammasome activation through a microtubule-dependent mechanism. *Nat. Commun.* **8**, 15986 (2017).

[ADS](#) [CAS](#) [Article](#) [Google Scholar](#)

25. 25.

Clement, M. et al. MARK4 (microtubule affinity-regulating kinase 4)-dependent inflammasome activation promotes atherosclerosis—brief report. *Arterioscler. Thromb. Vasc. Biol.* **39**, 1645–1651 (2019).

[CAS](#) [Article](#) [Google Scholar](#)

26. 26.

Toldo, S. & Abbate, A. The NLRP3 inflammasome in acute myocardial infarction. *Nat. Rev. Cardiol.* **15**, 203–214 (2018).

[CAS](#) [Article](#) [Google Scholar](#)

27. 27.

Baldrighi, M., Mallat, Z. & Li, X. NLRP3 inflammasome pathways in atherosclerosis. *Atherosclerosis* **267**, 127–138 (2017).

[CAS](#) [Article](#) [Google Scholar](#)

28. 28.

Ackers-Johnson, M. et al. A simplified, Langendorff-free method for concomitant isolation of viable cardiac myocytes and nonmyocytes from the adult mouse heart. *Circ. Res.* **119**, 909–920 (2016).

[CAS](#) [Article](#) [Google Scholar](#)

29. 29.

Kuhns, S. et al. The microtubule affinity regulating kinase MARK4 promotes axoneme extension during early ciliogenesis. *J. Cell Biol.* **200**, 505–522 (2013).

[CAS](#) [Article](#) [Google Scholar](#)

30. 30.

Szyk, A., Deaconescu, A. M., Piszczeck, G. & Roll-Mecak, A. Tubulin tyrosine ligase structure reveals adaptation of an ancient fold to bind and modify tubulin. *Nat. Struct. Mol. Biol.* **18**, 1250–1258 (2011).

[CAS](#) [Article](#) [Google Scholar](#)

31. 31.

Arce, C. A. & Barra, H. S. Release of C-terminal tyrosine from tubulin and microtubules at steady state. *Biochem. J.* **226**, 311–317 (1985).

[CAS](#) [Article](#) [Google Scholar](#)

32. 32.

Kellogg, E. H. et al. Near-atomic model of microtubule–tau interactions. *Science* **360**, 1242–1246 (2018).

[ADS](#) [CAS](#) [Article](#) [Google Scholar](#)

33. 33.

Shigematsu, H. et al. Structural insight into microtubule stabilization and kinesin inhibition by tau family MAPs. *J. Cell Biol.* **217**, 4155–4163 (2018).

[CAS](#) [Article](#) [Google Scholar](#)

34. 34.

Bottanelli, F. et al. Two-colour live-cell nanoscale imaging of intracellular targets. *Nat. Commun.* **7**, 10778 (2016).

[ADS](#) [CAS](#) [Article](#) [Google Scholar](#)

35. 35.

Barisic, M. et al. Microtubule detyrosination guides chromosomes during mitosis. *Science* **348**, 799–803 (2015).

[ADS](#) [CAS](#) [Article](#) [Google Scholar](#)

[Download references](#)

Acknowledgements

The work is supported by a British Heart Foundation (BHF) fellowship grant (FS/14/28/30713) to X.L., an Isaac Newton Trust grant (18.40u) to X.L. and Cambridge BHF Centre of Research Excellence grants (RE/13/6/30180 and RE/18/1/34212) to X.L. X.Y. was supported by a Royal Society Newton Advanced Fellowship grant (NA140277) and is supported by BHF grants (FS/14/28/30713, RE/18/1/34212). Z.M. is supported by BHF chair grant (CH/10/001/27642) and the NIHR Cambridge Biomedical Research Centre. M.A.-N. is supported by German Research Foundation (Deutsche Forschungsgemeinschaft (DFG)) (AM 507/1-1). G.S., E.A. and D.S.J. are supported by a Wellcome Trust collaborative award (203285), a Wellcome Principal Research Fellowship (207496) and core support from the Wellcome Trust (203144) and Cancer Research UK (A24823). The work of H.Z. is supported in part by a Royal Society Newton Advanced Fellowship grant (NA160342). We thank staff at the phenotyping hub and biochemical assay laboratory of Cambridge University Hospitals; staff at the Phenomics Laboratory and Anne McLaren Building of Cambridge University; B. Prosser for sharing protocols and discussion; M. Zhang for advice on echography data; M. A. Ackers-Johnson from R. Foo's laboratory for technical advice on isolating and culturing primary mouse cardiomyocytes; S. Ozanne and L. Pantaleao for access and training of ultracentrifuge use; D. Pavlovic for advice on IonOptix; C. Huang for advice on calcium measurements; T. Zhao for his intellectual discussion and reading the manuscript; and X. Luo, who passed away due to COVID-19 during the outbreak in Wuhan, for her support of this project.

Author information

Author notes

1. These authors contributed equally: Xian Yu, Xiao Chen

Affiliations

1. Department of Medicine, Cardiovascular Division, University of Cambridge, Addenbrooke's Hospital, Cambridge, UK

Xian Yu, Hannah Chenoweth, Marc Clement, James Harrison, Christian Doreth, Ziad Mallat & Xuan Li

2. Department of Cardiology, Union Hospital, Tongji Medical College, Huazhong University of Science and Technology, Wuhan, China

Xiao Chen

3. Department of Molecular and Cell Physiology, Hannover Medical School, Hannover, Germany

Mamta Amrute-Nayak

4. The Gurdon Institute, University of Cambridge, Cambridge, UK

Edward Allgeyer, George Sirinakis & Daniel St Johnston

5. Department of Genetics, University of Cambridge, Cambridge, UK

Edward Allgeyer, George Sirinakis & Daniel St Johnston

6. College of Computer Science and Technology, Qingdao University, Shandong, China

Aite Zhao

7. Department of Medicine, Experimental Medicine and Immunotherapeutics Division, University of Cambridge, Addenbrooke's Hospital, Cambridge, UK

Thomas Krieg

8. School of Informatics, University of Leicester, Leicester, UK

Huiyu Zhou

9. Department of Biology, Southern University of Science and Technology, Shenzhen, China

Hongda Huang

10. Muroran Institute of Technology, Muroran, Japan

Kiyotaka Tokuraku

11. Université de Paris, Institut National de la Santé et de la Recherche Médicale, U970, PARCC, Paris, France

Ziad Mallat

Authors

1. Xian Yu

[View author publications](#)

You can also search for this author in [PubMed](#) [Google Scholar](#)

2. Xiao Chen

[View author publications](#)

You can also search for this author in [PubMed](#) [Google Scholar](#)

3. Mamta Amrute-Nayak

[View author publications](#)

You can also search for this author in [PubMed](#) [Google Scholar](#)

4. Edward Allgeyer

[View author publications](#)

You can also search for this author in [PubMed](#) [Google Scholar](#)

5. Aite Zhao

[View author publications](#)

You can also search for this author in [PubMed](#) [Google Scholar](#)

6. Hannah Chenoweth

[View author publications](#)

You can also search for this author in [PubMed](#) [Google Scholar](#)

7. Marc Clement

[View author publications](#)

You can also search for this author in [PubMed](#) [Google Scholar](#)

8. James Harrison

[View author publications](#)

You can also search for this author in [PubMed](#) [Google Scholar](#)

9. Christian Doreth

[View author publications](#)

You can also search for this author in [PubMed](#) [Google Scholar](#)

10. George Sirinakis

[View author publications](#)

You can also search for this author in [PubMed](#) [Google Scholar](#)

11. Thomas Krieg

[View author publications](#)

You can also search for this author in [PubMed](#) [Google Scholar](#)

12. Huiyu Zhou

[View author publications](#)

You can also search for this author in [PubMed](#) [Google Scholar](#)

13. Hongda Huang

[View author publications](#)

You can also search for this author in [PubMed](#) [Google Scholar](#)

14. Kiyotaka Tokuraku

[View author publications](#)

You can also search for this author in [PubMed](#) [Google Scholar](#)

15. Daniel St Johnston

[View author publications](#)

You can also search for this author in [PubMed](#) [Google Scholar](#)

16. Ziad Mallat

[View author publications](#)

You can also search for this author in [PubMed](#) [Google Scholar](#)

17. Xuan Li

[View author publications](#)

You can also search for this author in [PubMed](#) [Google Scholar](#)

Contributions

X.Y., X.C., M.A.-N., A.Z., H.Z. and X.L. designed the experiments. X.Y., X.C., M.A.-N., E.A., A.Z., H.C., M.C., J.H. and X.L. performed the experiments. X.Y., X.C., M.A.-N., H.C., A.Z., H.Z. and X.L. analysed the data. X.Y. performed all of the *in vivo* experiments using mouse models and contractility assays, and wrote the relevant Methods section. X.C. performed the primary cardiomyocyte isolation, fractionation, real-time PCR, western blotting and imaging experiments. M.A.-N. performed *in vitro* microtubule co-sedimentation assay, analysed the data and wrote the relevant Methods section. E.A. configured the custom STED system, performed STED imaging and wrote the relevant Methods section. G.S. provided assistance for STED imaging. A.Z. and H.Z. wrote the STED image analytic code, analysed STED data and wrote the relevant Methods section. H.C. assisted with tissue collection, performed tissue sectioning and staining assays, and optimized some of the experimental conditions. M.C. assisted with part of the tissue collection, staining and analysis. J.H. provided some technical supports on mouse experiments. C.D., H.C. and X.L. performed the initial test. H.H. and K.T. provided recombinant proteins. T.K. provided initial training for the LAD model. D.S.J. provided the super-resolution imaging platform. Z.M. independently had the idea and supported the initiation of the project (the mouse *in vivo* work was performed under the Procedure Project Licence of Z.M.). X.Y., X.C., Z.M. and X.L. interpreted the data for important intellectual contents. X.L. conceived idea, designed and initiated the project, established the collaboration, supervised the project, and wrote the manuscript. All authors reviewed and edited the manuscript.

Corresponding author

Correspondence to [Xuan Li](#).

Ethics declarations

Competing interests

The authors declare no competing interests.

Additional information

Peer review information *Nature* thanks Leslie Leinwand and the other, anonymous, reviewer(s) for their contribution to the peer review of this work.

Publisher's note Springer Nature remains neutral with regard to jurisdictional claims in published maps and institutional affiliations.

Extended data figures and tables

Extended Data Fig. 1 Timeline of experimental design.

a, Timeline of the experimental design for Fig. [1d, e](#). Investigation of the effect of total MARK4 deficiency on cardiac function using the model of LAD coronary artery ligation to induce myocardial infarction. Echocardiography (Echo) and histological analyses were performed at the indicated time points. **b**, Timeline of the experimental design for Fig. [2a–c](#). Investigation of the effect of total MARK4 deficiency on cardiac function at 24 h after myocardial infarction. Echocardiography, circulating cardiac troponin and histological analyses were performed at the indicated time point. **c**, Timeline of the experimental design for Fig. [2d](#) and Extended Data Fig. [3a, b](#). Investigation of the effect of MARK4 expression in haematopoietic cells on cardiac function using the LAD ligation model. BM, bone marrow; BMT, bone marrow transplantation. Echocardiography analysis was performed at the indicated time points. **d**, Timeline of the experimental design for Fig. [2e](#) and Extended Data Fig. [3c–e](#). Investigation of the effect of MARK4 expression in cardiomyocytes on cardiac function using the LAD ligation model. Tm, tamoxifen. *Mark4* cKO, *Mark4* conditional knockout mice. Echocardiography analysis was performed at the indicated time points.

Extended Data Fig. 2 MARK4 expression, α-tubulin posttranslational modifications and changes in the

inflammatory response after myocardial infarction.

a, Representative confocal images of primary cardiomyocytes (CMs) isolated from *Mark4*^{-/-} or control mice at baseline or at day 3 after myocardial infarction. Scale bar, 20 µm. **b**, Levels of pro-inflammatory cytokines at day 3 after myocardial infarction ($n = 6$ per group). **c**, LVEF at day 3 after myocardial infarction ($n = 4$ per group). **d**, **e**, Western blots of detyrosinated α-tubulin in cell lysates of cardiomyocytes isolated from wild-type mice at day 3 after myocardial infarction or post-sham surgery (S), with the lysates of the remaining cells from the same hearts used as control. **d**, Representative western blots. **e**, Ratio of detyrosinated α-tubulin over total α-tubulin quantified using western blot data from biologically independent samples. Sham group, $n = 4$ mice; myocardial infarction group, $n = 5$ mice. **f**, **g**, Western blots of cell lysates from the isolated cardiomyocytes of *Mark4*^{-/-} or control mice at day 3 after myocardial infarction to detect detyrosinated α-tubulin, polyglutamylated α-tubulin (Polyglu-tub), acetylated α-tubulin (Ace-tub) and α-tubulin. **f**, Representative western blots. **g**, Ratio of detyrosinated α-tubulin, polyglutamylated α-tubulin or acetylated α-tubulin over total α-tubulin quantified using western blot data from biologically independent samples ($n = 3$ mice per group). **b**, The box bounds represent the 25th and 75th percentiles, the middle line shows the median, the whiskers show the minimum and maximum, and individual replicates are shown as circles. **c**, **e**, **g**, Data are mean ± s.e.m. **b**, **c**, **e**, **g**, Two-tailed unpaired *t*-tests were used; *P* values are indicated.

[Source data](#)

Extended Data Fig. 3 Validation of the mouse models for MARK4 selective expression in either haematopoietic cells or cardiomyocytes.

a, **b**, Confirmation of MARK4 deficiency in CD45⁺ cells of chimeric wild-type mice reconstituted with bone marrow (BM) cells from *Mark4*^{-/-} mice (strategy is shown in Extended Data Fig. [1c](#)). **a**, Representative image with arrows pointing to CD45⁺ cells in the infarct area. Scale bars, 20 µm (**a**). **b**,

Quantification of the percentage of MARK4⁺ cells (green) within CD45⁺ cells (red). $n = 3$ mice per group. **c**, Confirmation of *Mark4* deletion in cardiomyocytes (strategy is shown in Extended Data Fig. 1d). Real-time PCR of *Mark4* level in primary cardiomyocytes isolated from *Myh6-mcm*^{+/−}; *Mark4*^{f/f} (also known as α MHC-*mcm*^{+−}; *Mark4*^{f/f}) ($n = 4$) and control mice ($n = 3$) at day 7 after the last tamoxifen injection. **d**, Assessment of LVEF of a different group (compared with Fig. 2e) of *Mark4* cKO and control mice ($n = 6$ per group) at day 1 after myocardial infarction. **e**, Infarct size at 24 h after myocardial infarction ($n = 6$ per group). Scale bar, 2 mm. **b–e**, Data are mean ± s.e.m.; two-tailed unpaired *t*-test; *P* values are indicated.

[Source data](#)

[Extended Data Fig. 4 The effect of MARK4 deficiency on sarcomere length, peak shortening, velocity and calcium transients in cardiomyocytes before and after myocardial infarction.](#)

a–f, Contractility assay of single primary cardiomyocytes isolated at baseline or at day 3 after myocardial infarction from the following groups: *Mark4*^{+/+} baseline ($n = 4$ mice, $n = 45$ cardiomyocytes examined over 4 independent experiments), *Mark4*^{−−} baseline ($n = 3$ mice, $n = 45$ cardiomyocytes examined over 3 independent experiments), *Mark4*^{+/+} myocardial infarction ($n = 5$ mice, $n = 54$ cardiomyocytes examined over 5 independent experiments) and *Mark4*^{−−} myocardial infarction ($n = 6$ mice, $n = 57$ cardiomyocytes examined over 6 independent experiments). **a**, Colour denotation of samples. **b**, Resting sarcomere length. **c**, **d**, Average sarcomere shortening traces were compared. **e**, **f**, Average velocity traces (dSL/dT). **g–m**, Calcium influx assay on single cardiomyocytes isolated from *Mark4*^{−−} or control mice at baseline or at day 3 after myocardial infarction in the following groups: *Mark4*^{+/+} baseline group ($n = 2$ mice, $n = 34$ cardiomyocytes examined over 2 independent experiments), *Mark4*^{−−} baseline group ($n = 2$ mice, $n = 33$ cardiomyocytes examined over 2 independent experiments), *Mark4*^{+/+} myocardial infarction group ($n = 4$ mice, $n = 65$ cardiomyocytes examined over 4 independent experiments)

and $Mark4^{-/-}$ myocardial infarction group ($n = 3$ mice, $n = 58$ cardiomyocytes examined over 3 independent experiments). **g**, Basal Ca^{2+} level. **h**, Amplitude level of Ca^{2+} transients. **i**, Ca^{2+} release speed during contraction. **j**, Ca^{2+} reuptake speed during contraction. **k**, Ca^{2+} elevation time. **l**, Ca^{2+} reuptake time. **m**, Traces of Ca^{2+} kinetic curves. **b**, **g–l**, The box bounds represent the 25th and 75th percentiles, the middle line shows the median, the whiskers show the minimum and maximum, and individual cardiomyocytes are shown as circles. **b**, **g–l**, Two-way ANOVA with Bonferroni post hoc correction for multiple comparisons; P values are indicated.

[Source data](#)

[Extended Data Fig. 5 The effect of TTL overexpression, or PTL treatment, on contractility of \$Mark4^{-/-}\$ cardiomyocytes after myocardial infarction.](#)

a–i, Adenovirus (Adv)-mediated overexpression (o.e.) of TTL in cardiomyocytes isolated from $Mark4^{-/-}$ or control $Mark4^{+/+}$ mice at day 3 after myocardial infarction, with overexpression of a null vector as control (Ctrl). **a**, Representative western blot. **b–i**, Contractility assay of single cardiomyocytes with overexpression in the following groups: $Mark4^{+/+}$ myocardial infarction Adv-Null ($n = 3$ mice, $n = 75$ cardiomyocytes examined over 3 independent experiments), $Mark4^{+/+}$ myocardial infarction Adv-TTL ($n = 3$ mice, $n = 69$ cardiomyocytes examined over 3 independent experiments), $Mark4^{-/-}$ myocardial infarction Adv-Null ($n = 3$ mice, $n = 74$ cardiomyocytes examined over 3 independent experiments) and $Mark4^{-/-}$ myocardial infarction Adv-TTL ($n = 3$ mice, $n = 73$ cardiomyocytes examined over 3 independent experiments). **b**, Colour denotation of samples. **c**, Resting sarcomere length. **d–f**, Average sarcomere shortening traces. **g–i**, Average velocity traces ($d\text{SL}/dT$). **j–s**, Contractility assay of single cardiomyocytes isolated at day 3 after myocardial infarction with the following treatments: $Mark4^{+/+}$ myocardial infarction DMSO ($n = 3$ mice, $n = 46$ cardiomyocytes examined over 3 independent experiments), $Mark4^{+/+}$ myocardial infarction PTL ($n = 3$ mice, $n = 67$ cardiomyocytes

examined over 3 independent experiments), *Mark4*^{-/-} myocardial infarction DMSO ($n = 3$ mice, $n = 55$ cardiomyocytes examined over 3 independent experiments) and *Mark4*^{-/-} myocardial infarction PTL ($n = 3$ mice, $n = 64$ cardiomyocytes examined over 3 independent experiments). **j**, Colour denotation of samples. **k**, Resting sarcomere length. **l**, Sarcomere peak shortening. **m–o**, Average sarcomere shortening traces. **p**, Pooled data of contraction velocity and relaxation velocity. **q–s**, Average velocity traces (dSL/dT). **c, k, l, p**, The box bounds represent the 25th and 75th percentiles, the middle line shows the median, the whiskers show the minimum and maximum and individual cardiomyocytes are shown as circles. **c, k, l, p**, Two-way ANOVA test with Bonferroni post hoc correction for multiple comparisons; P values are indicated.

[Source data](#)

Extended Data Fig. 6 The association of MAP4 or VASH2 with polymerized microtubules.

a, Protein sequence alignment between human MAP4 (NP002366) and mouse MAP4 (NP001192259). KXGS motifs (highlighted with red frames) within the tubulin-binding repeats (highlighted with yellow, brown, dark brown and purple frames) of MAP4 are MARK4 substrate sites. S941 of human MAP4 (S914 of mouse MAP4) and S1073 of human MAP4 (S1046 of mouse MAP4) are conserved phosphorylation sites within the KXGS motifs. **b**, Schematic illustration of the possible association between MAP4 and microtubules before or after MARK4-dependent phosphorylation. Unphosphorylated MAP4 binds to microtubules. After MARK4-dependent phosphorylation of S914 of mouse MAP4 at the microtubule weak binding site, MAP4 makes allosteric changes. After MARK4-dependent phosphorylation of S1046 of mouse MAP4 at the microtubule anchor site, MAP4 detaches from microtubules. **c**, Representative gel image of 4R-MAP4 (1–4 μ M) binding to the polymerized microtubules (5 μ M) in a microtubule co-sedimentation assay. **d**, Quantification of the binding shown in **c**. $n = 7$ samples examined over 3 independent experiments (1 μ M); $n = 4$ samples examined over 3 independent experiments (2 μ M); $n = 6$ samples examined over 3 independent experiments (3 μ M); $n = 3$ samples examined over 3 independent experiments (4 μ M). **e**, Representative gel image of

VASH2–SVBP (0.5–2 μ M) binding to the polymerized microtubules (2.5 μ M) in a microtubule co-sedimentation assay. |**f**, Quantification of the binding shown in **e**. $n = 7$ samples examined over 5 independent experiments (0.5 μ M); $n = 7$ samples examined over 5 independent experiments (1 μ M); $n = 4$ samples examined over 3 independent experiments (1.5 μ M); $n = 4$ samples examined over 3 independent experiments (2 μ M). **d, f**, Data are mean \pm s.e.m.; one-way ANOVA; P values are indicated.

Extended Data Fig. 7 Association of VASH2 with microtubules in cardiomyocytes before and myocardial infarction, and the effect of MAP4 knockdown.

a, Subcellular fractionation of primary cardiomyocytes isolated from mice at baseline or after myocardial infarction. Western blotting of the fractions from CEB or PEB. **b**, Representative western blots of the free-tubulin fraction (F1) and extraction from the stable pellet fraction (F2) obtained using a conventional fractionation method. **c–e**, Western blots of CEB or PEB fractions of wild-type (WT) cardiomyocytes at baseline or after myocardial infarction. **c**, Representative western blots (derived from the same experiment). **d**, Quantification of pMAP4(S1046) in CEB, pMAP4(S914) in PEB and VASH2 levels in PEB ($n = 5$ mice at baseline, $n = 6$ mice after myocardial infarction, blots were processed in parallel). **e**, Correlation between VASH2 level in the PEB fraction and pMAP4 levels. **f–i**, Wild-type cardiomyocytes after myocardial infarction transduced with adenovirus-mediated *Map4* or control shRNA. **f**, Representative western blots of CEB or PEB fraction, and Coomassie-stained gels loaded with the same amounts of proteins. **g**, Quantification of VASH2 levels in PEB ($n = 3$ mice examined over 3 experiments per group). **h, i**, STED images of VASH2 and α -tubulin in the cardiomyocytes after knocking down MAP4. **h**, Representative images. Scale bar, 2 μ m. **i**, Pearson correlation coefficient of VASH2 and α -tubulin signals, percentage of VASH2 signals on the polymerized microtubules and percentage of VASH2 signals off the polymerized microtubules, in the following groups: control shRNA ($n = 2$ mice, $n = 35$ cardiomyocytes examined over 2 independent experiments) and *Map4* shRNA ($n = 2$ mice, $n = 27$ cardiomyocytes examined over 2

independent experiments). **d, g, i**, Data are mean \pm s.e.m.; two-tailed unpaired *t*-test. **e**, Two-tailed correlation test. *P* values are indicated.

[Source data](#)

Extended Data Fig. 8 The status of VASH2 and MAP4 in cardiomyocytes before and after myocardial infarction.

a, Subcellular fractionation of wild-type cardiomyocytes, isolated from mice after myocardial infarction and transduced with adenovirus-mediated *Vash2* or control shRNA. Representative western blots of fraction in PEB, with the same membrane stained with Ponceau S. **b**, Representative western blot of PEB extractions denatured in the presence or absence of urea from cardiomyocytes after myocardial infarction. **c, d**, STED images of MAP4 and α -tubulin in cardiomyocytes of *Mark4*^{−/−} or control mice at baseline or after myocardial infarction. **c**, Representative images. Oligomerized puncta are indicated within the square frames. Scale bar, 2 μ m. **d**, Quantification of the presence of the MAP4 oligomerized puncta in the following groups: *Mark4*^{+/+} baseline ($n = 2$ mice, $n = 22$ cardiomyocytes examined over 2 independent experiments), *Mark4*^{+/+} myocardial infarction ($n = 2$ mice, $n = 26$ cardiomyocytes examined over 2 independent experiments) and *Mark4*^{−/−} myocardial infarction ($n = 2$ mice, $n = 21$ cardiomyocytes examined over 2 independent experiments). **e, f**, Western blot of native gels loaded with samples in CEB of cardiomyocytes isolated at baseline or after myocardial infarction. **e**, The presence of pMAP4(S1046) and total MAP4 is indicated. **f**, Coomassie-stained native gel loaded with the same amounts of proteins as used in **e**. **g**, Western blot of the CEB fraction denatured in the presence of urea, with a Coomassie-stained denaturing gel loaded with the same amounts of protein. **h**, Western blot of fractions in PEB of cardiomyocytes isolated from *Mark4*^{−/−} or control mice after myocardial infarction, with a Coomassie-stained gel loaded with the same amounts of proteins. **i**, Quantification of VASH2 and desmin levels in PEB fraction ($n = 4$ mice per group). **j**, Correlation between desmin and VASH2 levels in PEB. **d, i**, Data are mean \pm s.e.m.; two-tailed unpaired *t*-test. **j**, Two-tailed correlation test. *P* values are indicated.

[Source data](#)

Extended Data Fig. 9 MARK4 overexpression regulates MAP4 phosphorylation, and the presence of MAP4 oligomers in the cytosolic fraction.

a–c, Subcellular fractionation of wild-type cardiomyocytes transduced with adenovirus to overexpress *Mark4* or a null control. **a**, Representative western blots of fractions in CEB or PEB (derived from the same experiment). **b**, Quantification of pMAP4(S1046) in CEB and VASH2 level in PEB ($n = 5$ mice per group, blots were processed in parallel). **c**, Correlation between VASH2 level in the PEB fraction and pMAP4 levels. **d, e**, STED images of MAP4 and α -tubulin in wild-type cardiomyocytes at baseline transduced with adenovirus to overexpress *Mark4* or a null control. **d**, Representative images. Scale bar, 2 μ m. **e**, Quantification of MAP4 oligomerized puncta in the following groups: overexpression of control ($n = 2$ mice, $n = 20$ cardiomyocytes examined over 2 independent experiments) and overexpression of *Mark4* ($n = 2$ mice, $n = 24$ cardiomyocytes examined over 2 independent experiments). **d, e**, Data are mean \pm s.e.m.; two-tailed unpaired *t*-test. **c**, Two-tailed correlation test. *P* values are indicated.

[Source data](#)

Extended Data Fig. 10 VASH2 status in cardiomyocytes before and after myocardial infarction, and the schematic summary of the results.

a, b, STED images of VASH2 and α -tubulin in wild-type cardiomyocytes at baseline or after myocardial infarction. **a**, Representative images. Scale bar, 2 μ m. **b**, Pearson correlation coefficient of VASH2 and α -tubulin signals, percentage of VASH2 signals on the polymerized microtubules and percentage of VASH2 signals off the microtubules in the following groups: wild-type baseline ($n = 4$ mice, $n = 38$ cardiomyocytes examined over 2 independent experiments) and wild-type myocardial infarction ($n = 38$ cardiomyocytes of $n = 6$ mice, $n = 38$ cardiomyocytes examined over 3 independent experiments). **c**, Real-time PCR of cardiomyocytes after myocardial infarction from the following groups: *Mark4*^{+/+} myocardial

infarction ($n = 5$ mice) and $\text{Mark4}^{-/-}$ myocardial infarction ($n = 6$ mice). **d**, Quantification of VASH2 mean fluorescence intensity (MFI) within the cell area (region of interest (ROI)) using the STED images from the following groups: $\text{Mark4}^{+/+}$ myocardial infarction ($n = 6$ mice, $n = 38$ cardiomyocytes examined over 3 independent experiments) and $\text{Mark4}^{-/-}$ myocardial infarction ($n = 6$ mice, $n = 47$ cardiomyocytes examined over 3 independent experiments). **b–d**, Data are mean \pm s.e.m.; two-tailed unpaired *t*-test. *P* values are indicated. **e**, A working model for the MARK4-dependent regulation of microtubule detyrosination after myocardial infarction. After ischaemic injury, increased MARK4 phosphorylates MAP4 at its KXGS motifs. Phosphorylated MAP4 either changes its conformation on the polymerized microtubules or detaches itself from the polymerized microtubules to form oligomerized MAP4 structures in the cytosol. The phosphorylation of MAP4 by MARK4 allows for space access of VASH2 to the polymerized microtubules, thereby promoting α -tubulin detyrosination. As a consequence, the increased level of detyrosinated microtubules causes a reduction in the contractile function of the cardiomyocyte.

[Source data](#)

Supplementary information

[Supplementary Figures](#)

This file contains Supplementary Figs 1-2. Supplementary Fig. 1 contains immunoblots, and loading controls (Coomassie stained gels and Ponceau S stained membranes) associated with the data presented in the Figures and Extended Data Figures. Supplementary Fig. 2 shows the gating strategy for infiltrating immune cells post-myocardial infarction.

[Reporting Summary](#)

[Supplementary Table 1](#)

The effect of MARK4 deficiency on cardiac parameters after myocardial infarction (MI). M-mode echocardiography was acquired at baseline, and

week 1 (W1), week 2 (W2), week 4 (W4) post-myocardial infarction (MI). All statistical tests were Two-way ANOVA with Bonferroni post-hoc correction for multiple comparisons. All data are mean \pm s.e.m. P>0.05 is considered statistically non-significant.

Supplementary Table 2

The effect of MARK4 deficiency on immune cells infiltrating the hearts after myocardial infarction (MI). Immune cells were collected from hearts at day 3 post-MI or post-sham surgery. Data were analyzed using unpaired *t*-test (two-tailed), and presented as mean \pm s.e.m. P>0.05 is considered statistically non-significant.

Source data

Source Data Fig. 1

Source Data Fig. 2

Source Data Fig. 3

Source Data Fig. 4

Source Data Extended Data Fig. 2

Source Data Extended Data Fig. 3

Source Data Extended Data Fig. 4

Source Data Extended Data Fig. 5

Source Data Extended Data Fig. 7

Source Data Extended Data Fig. 8

Source Data Extended Data Fig. 9

Source Data Extended Data Fig. 10

Rights and permissions

Reprints and Permissions

About this article



Check for
updates

Cite this article

Yu, X., Chen, X., Amrute-Nayak, M. *et al.* MARK4 controls ischaemic heart failure through microtubule detyrosination. *Nature* **594**, 560–565 (2021). <https://doi.org/10.1038/s41586-021-03573-5>

Download citation

- Received: 15 December 2019
- Accepted: 21 April 2021
- Published: 26 May 2021
- Issue Date: 24 June 2021
- DOI: <https://doi.org/10.1038/s41586-021-03573-5>

Comments

By submitting a comment you agree to abide by our [Terms](#) and [Community Guidelines](#). If you find something abusive or that does not comply with our terms or guidelines please flag it as inappropriate.

[Download PDF](#)

Advertisement

This article was downloaded by **calibre** from <https://www.nature.com/articles/s41586-021-03573-5>

| [Section menu](#) | [Main menu](#) |

- Article
- [Published: 02 June 2021](#)

Hepatic stellate cells suppress NK cell-sustained breast cancer dormancy

- [Ana Luísa Correia](#) [ORCID: orcid.org/0000-0003-2414-0131](#)^{1,2,3},
- [Joao C. Guimaraes](#) [ORCID: orcid.org/0000-0002-1664-472X](#)⁴ nAff11,
- [Priska Auf der Maur](#) [ORCID: orcid.org/0000-0002-9059-8979](#)^{1,3},
- [Duvini De Silva](#)^{1,2} nAff11,
- [Marcel P. Trefny](#) [ORCID: orcid.org/0000-0001-6755-7899](#)¹,
- [Ryoko Okamoto](#)^{1,2,3} nAff12,
- [Sandro Bruno](#)² nAff13,
- [Alexander Schmidt](#) [ORCID: orcid.org/0000-0002-3149-2381](#)⁵,
- [Kirsten Mertz](#) [ORCID: orcid.org/0000-0002-3074-6925](#)⁶,
- [Katrin Volkmann](#)^{1,3},
- [Luigi Terracciano](#)⁷,
- [Alfred Zippelius](#) [ORCID: orcid.org/0000-0003-1933-8178](#)^{1,8},
- [Marcus Vetter](#)^{8,9,10},
- [Christian Kurzeder](#)^{9,10},
- [Walter Paul Weber](#)^{3,10} &
- [Mohamed Bentires-Alj](#) [ORCID: orcid.org/0000-0001-6344-1127](#)^{1,2,3}

[Nature](#) volume 594, pages 566–571 (2021) [Cite this article](#)

- 15k Accesses
- 244 Altmetric

- [Metrics details](#)

Subjects

- [Breast cancer](#)
- [Cancer microenvironment](#)

Abstract

The persistence of undetectable disseminated tumour cells (DTCs) after primary tumour resection poses a major challenge to effective cancer treatment^{1,2,3}. These enduring dormant DTCs are seeds of future metastases, and the mechanisms that switch them from dormancy to outgrowth require definition. Because cancer dormancy provides a unique therapeutic window for preventing metastatic disease, a comprehensive understanding of the distribution, composition and dynamics of reservoirs of dormant DTCs is imperative. Here we show that different tissue-specific microenvironments restrain or allow the progression of breast cancer in the liver—a frequent site of metastasis⁴ that is often associated with a poor prognosis⁵. Using mouse models, we show that there is a selective increase in natural killer (NK) cells in the dormant milieu. Adjuvant interleukin-15-based immunotherapy ensures an abundant pool of NK cells that sustains dormancy through interferon- γ signalling, thereby preventing hepatic metastases and prolonging survival. Exit from dormancy follows a marked contraction of the NK cell compartment and the concurrent accumulation of activated hepatic stellate cells (aHSCs). Our proteomics studies on liver co-cultures implicate the aHSC-secreted chemokine CXCL12 in the induction of NK cell quiescence through its cognate receptor CXCR4. CXCL12 expression and aHSC abundance are closely correlated in patients with liver metastases. Our data identify the interplay between NK cells and aHSCs as a master switch of cancer dormancy, and suggest that therapies aimed at normalizing the NK cell pool might succeed in preventing metastatic outgrowth.

Access options

[Subscribe to Journal](#)

Get full journal access for 1 year

\$199.00

only \$3.90 per issue

[Subscribe](#)

All prices are NET prices.

VAT will be added later in the checkout.

Tax calculation will be finalised during checkout.

Rent or Buy article

Get time limited or full article access on ReadCube.

from \$8.99

[Rent or Buy](#)

All prices are NET prices.

Additional access options:

- [Log in](#)
- [Access through your institution](#)
- [Learn about institutional subscriptions](#)

Fig. 1: NK cells sustain breast cancer dormancy in the liver.

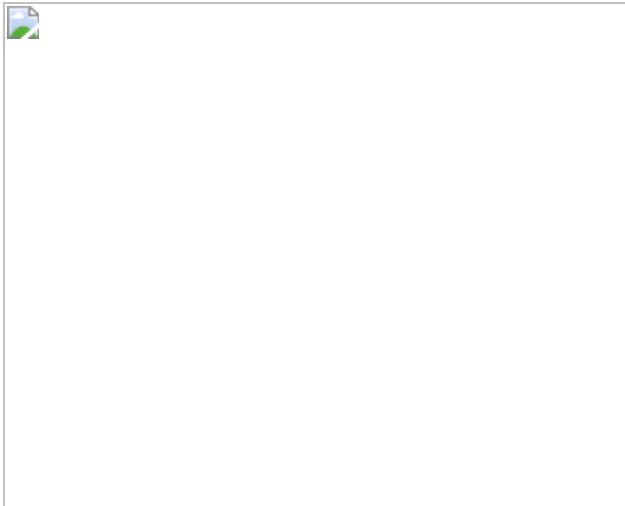


Fig. 2: NK cells sustain dormancy through IFN γ .

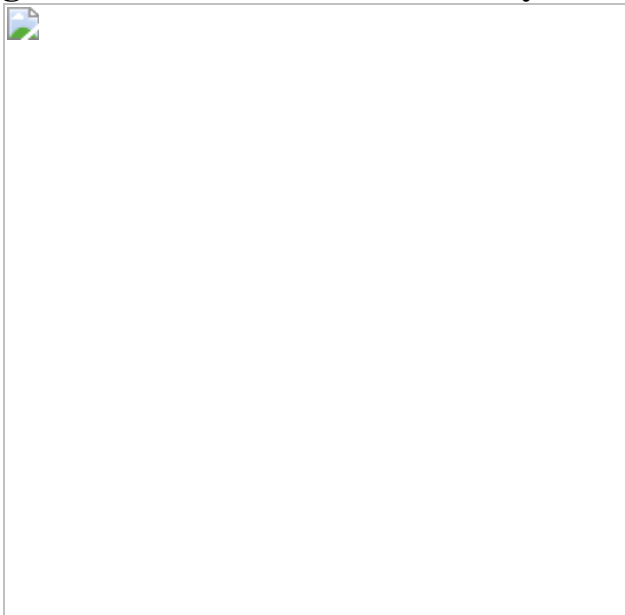


Fig. 3: aHSCs steer NK cell depletion and promote liver metastasis.

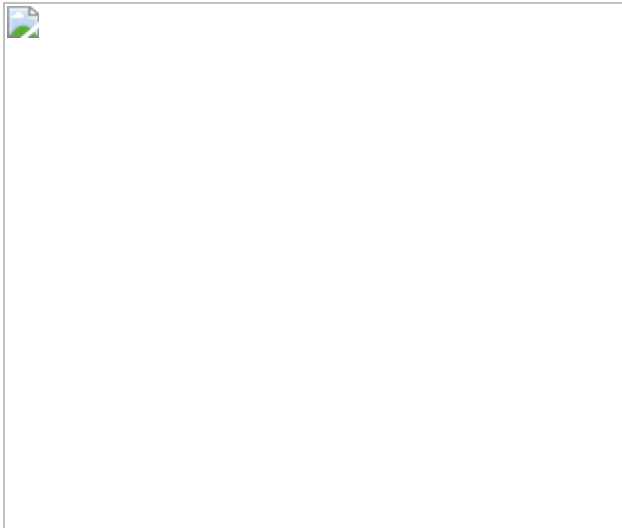
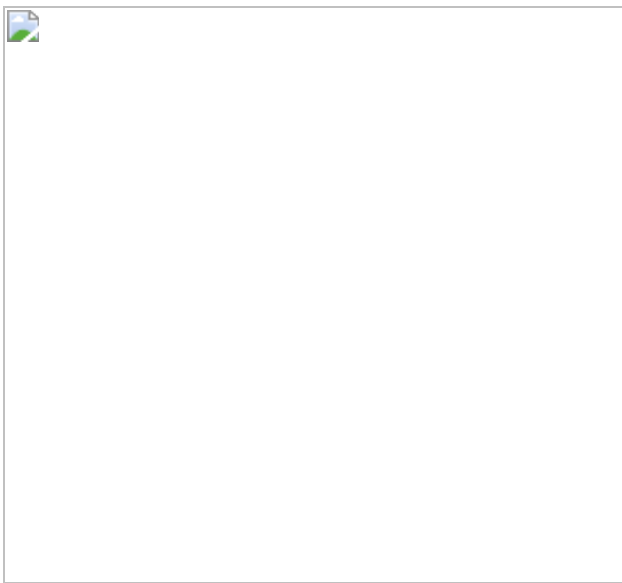


Fig. 4: CXCL12 mediates hepatic stellate cell-induced quiescence in NK cells.



Data availability

All mass spectrometry raw data files have been deposited to the ProteomeXchange Consortium via the PRIDE⁶⁰ partner repository with the data set identifier PXD015426. The mRNA sequencing data have been deposited in the Sequence Read Archive (SRA) database under BioProject accession number [PRJNA576660](#). [Source data](#) are provided with this paper.

Code availability

The source code to replicate genomics and image analysis presented in this study is available from Zenodo at <https://doi.org/10.5281/zenodo.4570079>.

References

1. 1.

Chambers, A. F., Groom, A. C. & MacDonald, I. C. Dissemination and growth of cancer cells in metastatic sites. *Nat. Rev. Cancer* **2**, 563–572 (2002).

[CAS](#) [PubMed](#) [Google Scholar](#)

2. 2.

Polzer, B. & Klein, C. A. Metastasis awakening: the challenges of targeting minimal residual cancer. *Nat. Med.* **19**, 274–275 (2013).

[CAS](#) [Google Scholar](#)

3. 3.

Sosa, M. S., Bragado, P. & Aguirre-Ghiso, J. A. Mechanisms of disseminated cancer cell dormancy: an awakening field. *Nat. Rev. Cancer* **14**, 611–622 (2014).

[CAS](#) [PubMed](#) [PubMed Central](#) [Google Scholar](#)

4. 4.

Disibio, G. & French, S. W. Metastatic patterns of cancers: results from a large autopsy study. *Arch. Pathol. Lab. Med.* **132**, 931–939 (2008).

[Google Scholar](#)

5. 5.

Diamond, J. R., Finlayson, C. A. & Borges, V. F. Hepatic complications of breast cancer. *Lancet Oncol.* **10**, 615–621 (2009).

[Google Scholar](#)

6. 6.

Cote, R. J. et al. Monoclonal antibodies detect occult breast carcinoma metastases in the bone marrow of patients with early stage disease. *Am. J. Surg. Pathol.* **12**, 333–340 (1988).

[CAS](#) [Google Scholar](#)

7. 7.

Schlimok, G. et al. Micrometastatic cancer cells in bone marrow: in vitro detection with anti-cytokeratin and in vivo labeling with anti-17-1A monoclonal antibodies. *Proc. Natl Acad. Sci. USA* **84**, 8672–8676 (1987).

[ADS](#) [CAS](#) [PubMed](#) [PubMed Central](#) [Google Scholar](#)

8. 8.

Braun, S. et al. A pooled analysis of bone marrow micrometastasis in breast cancer. *N. Engl. J. Med.* **353**, 793–802 (2005).

[CAS](#) [Google Scholar](#)

9. 9.

Cote, R. J., Rosen, P. P., Lesser, M. L., Old, L. J. & Osborne, M. P. Prediction of early relapse in patients with operable breast cancer by detection of occult bone marrow micrometastases. *J. Clin. Oncol.* **9**, 1749–1756 (1991).

[CAS](#) [Google Scholar](#)

10. 10.

Janni, W. et al. Persistence of disseminated tumor cells in the bone marrow of breast cancer patients predicts increased risk for relapse—a European pooled analysis. *Clin. Cancer Res.* **17**, 2967–2976 (2011).

[Google Scholar](#)

11. 11.

Klein, C. A. Cancer progression and the invisible phase of metastatic colonization. *Nat. Rev. Cancer* **20**, 681–694 (2020).

[CAS](#) [Google Scholar](#)

12. 12.

Risson, E., Nobre, A. R., Maguer-Satta, V. & Aguirre-Ghiso, J. A. The current paradigm and challenges ahead for the dormancy of disseminated tumor cells. *Nat. Cancer* **1**, 672–680 (2020).

[Google Scholar](#)

13. 13.

Correia, A. L. & Bissell, M. J. The tumor microenvironment is a dominant force in multidrug resistance. *Drug Resist. Updat.* **15**, 39–49 (2012).

[CAS](#) [PubMed](#) [PubMed Central](#) [Google Scholar](#)

14. 14.

Ghajar, C. M. et al. The perivascular niche regulates breast tumour dormancy. *Nat. Cell Biol.* **15**, 807–817 (2013).

[CAS](#) [PubMed](#) [PubMed Central](#) [Google Scholar](#)

15. 15.

Oskarsson, T. et al. Breast cancer cells produce tenascin C as a metastatic niche component to colonize the lungs. *Nat. Med.* **17**, 867–874 (2011).

[CAS](#) [PubMed](#) [PubMed Central](#) [Google Scholar](#)

16. 16.

Oki, T. et al. A novel cell-cycle-indicator, mVenus-p27K⁻, identifies quiescent cells and visualizes G0–G1 transition. *Sci. Rep.* **4**, 4012 (2014).

[PubMed](#) [PubMed Central](#) [Google Scholar](#)

17. 17.

Cabezas-Wallscheid, N. et al. Vitamin A–retinoic acid signaling regulates hematopoietic stem cell dormancy. *Cell* **169**, 807–823 (2017).

[CAS](#) [Google Scholar](#)

18. 18.

Ren, D. et al. Wnt5a induces and maintains prostate cancer cells dormancy in bone. *J. Exp. Med.* **216**, 428–449 (2019).

[CAS](#) [PubMed](#) [PubMed Central](#) [Google Scholar](#)

19. 19.

Sosa, M. S. et al. NR2F1 controls tumour cell dormancy via SOX9- and RAR β -driven quiescence programmes. *Nat. Commun.* **6**, 6170 (2015).

[ADS](#) [CAS](#) [Google Scholar](#)

20. 20.

Albrengues, J. et al. Neutrophil extracellular traps produced during inflammation awaken dormant cancer cells in mice. *Science* **361**, eaao4227 (2018).

[PubMed](#) [PubMed Central](#) [Google Scholar](#)

21. 21.

Coffelt, S. B. et al. IL-17-producing $\gamma\delta$ T cells and neutrophils conspire to promote breast cancer metastasis. *Nature* **522**, 345–348 (2015).

[ADS](#) [CAS](#) [PubMed](#) [PubMed Central](#) [Google Scholar](#)

22. 22.

Wculek, S. K. & Malanchi, I. Neutrophils support lung colonization of metastasis-initiating breast cancer cells. *Nature* **528**, 413–417 (2015).

[ADS](#) [CAS](#) [PubMed](#) [PubMed Central](#) [Google Scholar](#)

23. 23.

Lee, J. W. et al. Hepatocytes direct the formation of a pro-metastatic niche in the liver. *Nature* **567**, 249–252 (2019).

[ADS](#) [CAS](#) [PubMed](#) [PubMed Central](#) [Google Scholar](#)

24. 24.

Nielsen, S. R. et al. Macrophage-secreted granulin supports pancreatic cancer metastasis by inducing liver fibrosis. *Nat. Cell Biol.* **18**, 549–560 (2016).

[CAS](#) [PubMed](#) [PubMed Central](#) [Google Scholar](#)

25. 25.

Limberis, M. P., Bell, C. L. & Wilson, J. M. Identification of the murine firefly luciferase-specific CD8 T-cell epitopes. *Gene Ther.* **16**, 441–447 (2009).

[CAS](#) [Google Scholar](#)

26. 26.

Stripecke, R. et al. Immune response to green fluorescent protein: implications for gene therapy. *Gene Ther.* **6**, 1305–1312 (1999).

[CAS](#) [Google Scholar](#)

27. 27.

Waldmann, T. A. The biology of interleukin-2 and interleukin-15: implications for cancer therapy and vaccine design. *Nat. Rev. Immunol.* **6**, 595–601 (2006).

[CAS](#) [Google Scholar](#)

28. 28.

Malladi, S. et al. Metastatic latency and immune evasion through autocrine inhibition of WNT. *Cell* **165**, 45–60 (2016).

[CAS](#) [PubMed](#) [PubMed Central](#) [Google Scholar](#)

29. 29.

Barrow, A. D. et al. Natural killer cells control tumor growth by sensing a growth factor. *Cell* **172**, 534–548 (2018).

[CAS](#) [Google Scholar](#)

30. 30.

Tsuchida, T. & Friedman, S. L. Mechanisms of hepatic stellate cell activation. *Nat. Rev. Gastroenterol. Hepatol.* **14**, 397–411 (2017).

[CAS](#) [Google Scholar](#)

31. 31.

Brown, Z. J., Heinrich, B. & Greten, T. F. Mouse models of hepatocellular carcinoma: an overview and highlights for immunotherapy research. *Nat. Rev. Gastroenterol. Hepatol.* **15**, 536–554 (2018).

[CAS](#) [Google Scholar](#)

32. 32.

Taub, R. Liver regeneration: from myth to mechanism. *Nat. Rev. Mol. Cell Biol.* **5**, 836–847 (2004).

[CAS](#) [Google Scholar](#)

33. 33.

Bleul, C. C., Fuhlbrigge, R. C., Casasnovas, J. M., Aiuti, A. & Springer, T. A. A highly efficacious lymphocyte chemoattractant, stromal cell-derived factor 1 (SDF-1). *J. Exp. Med.* **184**, 1101–1109 (1996).

[CAS](#) [Google Scholar](#)

34. 34.

Müller, A. et al. Involvement of chemokine receptors in breast cancer metastasis. *Nature* **410**, 50–56 (2001).

[ADS](#) [Google Scholar](#)

35. 35.

Sugiyama, T., Kohara, H., Noda, M. & Nagasawa, T. Maintenance of the hematopoietic stem cell pool by CXCL12–CXCR4 chemokine

signaling in bone marrow stromal cell niches. *Immunity* **25**, 977–988 (2006).

[CAS](#) [Google Scholar](#)

36. 36.

Price, T. T. et al. Dormant breast cancer micrometastases reside in specific bone marrow niches that regulate their transit to and from bone. *Sci. Transl. Med.* **8**, 340ra73 (2016).

[Google Scholar](#)

37. 37.

Orimo, A. et al. Stromal fibroblasts present in invasive human breast carcinomas promote tumor growth and angiogenesis through elevated SDF-1/CXCL12 secretion. *Cell* **121**, 335–348 (2005).

[CAS](#) [Google Scholar](#)

38. 38.

Stange, D. E. et al. Expression of an *ASCL2* related stem cell signature and *IGF2* in colorectal cancer liver metastases with 11p15.5 gain. *Gut* **59**, 1236–1244 (2010).

[CAS](#) [Google Scholar](#)

39. 39.

Robinson, D. R. et al. Integrative clinical genomics of metastatic cancer. *Nature* **548**, 297–303 (2017).

[ADS](#) [CAS](#) [PubMed](#) [PubMed Central](#) [Google Scholar](#)

40. 40.

López-Soto, A., Gonzalez, S., Smyth, M. J. & Galluzzi, L. Control of metastasis by NK cells. *Cancer Cell* **32**, 135–154 (2017).

[Google Scholar](#)

41. 41.

Schreiber, R. D., Old, L. J. & Smyth, M. J. Cancer immunoediting: integrating immunity's roles in cancer suppression and promotion. *Science* **331**, 1565–1570 (2011).

[ADS](#) [CAS](#) [Google Scholar](#)

42. 42.

Koebel, C. M. et al. Adaptive immunity maintains occult cancer in an equilibrium state. *Nature* **450**, 903–907 (2007).

[ADS](#) [CAS](#) [Google Scholar](#)

43. 43.

Khoo, W. H. et al. A niche-dependent myeloid transcriptome signature defines dormant myeloma cells. *Blood* **134**, 30–43 (2019).

[CAS](#) [Google Scholar](#)

44. 44.

Alspach, E., Lussier, D. M. & Schreiber, R. D. Interferon γ and its important roles in promoting and inhibiting spontaneous and therapeutic cancer immunity. *Cold Spring Harb. Perspect. Biol.* **11**, a028480 (2019).

[CAS](#) [PubMed](#) [PubMed Central](#) [Google Scholar](#)

45. 45.

Burke, J. D. & Young, H. A. IFN- γ : a cytokine at the right time, is in the right place. *Semin. Immunol.* **43**, 101280 (2019).

[CAS](#) [PubMed](#) [PubMed Central](#) [Google Scholar](#)

46. 46.

Sahai, E. et al. A framework for advancing our understanding of cancer-associated fibroblasts. *Nat. Rev. Cancer* **20**, 174–186 (2020).

[CAS](#) [PubMed](#) [PubMed Central](#) [Google Scholar](#)

47. 47.

Barkan, D. et al. Metastatic growth from dormant cells induced by a Col-I-enriched fibrotic environment. *Cancer Res.* **70**, 5706–5716 (2010).

[CAS](#) [PubMed](#) [PubMed Central](#) [Google Scholar](#)

48. 48.

Fearon, D. T. The carcinoma-associated fibroblast expressing fibroblast activation protein and escape from immune surveillance. *Cancer Immunol. Res.* **2**, 187–193 (2014).

[CAS](#) [Google Scholar](#)

49. 49.

Feig, C. et al. Targeting CXCL12 from FAP-expressing carcinoma-associated fibroblasts synergizes with anti-PD-L1 immunotherapy in pancreatic cancer. *Proc. Natl Acad. Sci. USA* **110**, 20212–20217 (2013).

[ADS](#) [CAS](#) [PubMed](#) [PubMed Central](#) [Google Scholar](#)

50. 50.

Joyce, J. A. & Fearon, D. T. T cell exclusion, immune privilege, and the tumor microenvironment. *Science* **348**, 74–80 (2015).

[ADS](#) [CAS](#) [Google Scholar](#)

51. 51.

Dull, T. et al. A third-generation lentivirus vector with a conditional packaging system. *J. Virol.* **72**, 8463–8471 (1998).

[CAS](#) [PubMed](#) [PubMed Central](#) [Google Scholar](#)

52. 52.

Liu, H. et al. Cancer stem cells from human breast tumors are involved in spontaneous metastases in orthotopic mouse models. *Proc. Natl Acad. Sci. USA* **107**, 18115–18120 (2010).

[ADS](#) [CAS](#) [PubMed](#) [PubMed Central](#) [Google Scholar](#)

53. 53.

Hoffmann, S. et al. Fast mapping of short sequences with mismatches, insertions and deletions using index structures. *PLOS Comput. Biol.* **5**, e1000502 (2009).

[MathSciNet](#) [PubMed](#) [PubMed Central](#) [Google Scholar](#)

54. 54.

Love, M. I., Huber, W. & Anders, S. Moderated estimation of fold change and dispersion for RNA-seq data with DESeq2. *Genome Biol.* **15**, 550 (2014).

[PubMed](#) [PubMed Central](#) [Google Scholar](#)

55. 55.

MacParland, S. A. et al. Single cell RNA sequencing of human liver reveals distinct intrahepatic macrophage populations. *Nat. Commun.* **9**, 4383 (2018).

[ADS](#) [PubMed](#) [PubMed Central](#) [Google Scholar](#)

56. 56.

Zhou, J. et al. Liver-resident NK cells control antiviral activity of hepatic T cells via the PD-1–PD-L1 axis. *Immunity* **50**, 403–417 (2019).

[CAS](#) [Google Scholar](#)

57. 57.

Subramanian, A. et al. Gene set enrichment analysis: a knowledge-based approach for interpreting genome-wide expression profiles. *Proc. Natl Acad. Sci. USA* **102**, 15545–15550 (2005).

[ADS](#) [CAS](#) [PubMed](#) [PubMed Central](#) [Google Scholar](#)

58. 58.

Ahrné, E. et al. Evaluation and improvement of quantification accuracy in isobaric mass tag-based protein quantification experiments. *J. Proteome Res.* **15**, 2537–2547 (2016).

[Google Scholar](#)

59. 59.

Glatter, T. et al. Large-scale quantitative assessment of different in-solution protein digestion protocols reveals superior cleavage efficiency of tandem Lys-C/trypsin proteolysis over trypsin digestion. *J. Proteome Res.* **11**, 5145–5156 (2012).

[CAS](#) [Google Scholar](#)

60. 60.

Vizcaíno, J. A. et al. 2016 update of the PRIDE database and its related tools. *Nucleic Acids Res.* **44**, D447–D456 (2016).

[Google Scholar](#)

[Download references](#)

Acknowledgements

We thank the following: T. Oki and T. Kitamura for providing the pMXs-IRES-puro/mVenus-p27K⁻ vector; A. Bottos and N. E. Hynes for providing the pFU-Luc2-tdTomato vector; H. Kohler, T. Lopes, L. Raeli and E. Traunecker for assistance with FACS; T. Roloff, K. Hirschfeld, P. Demougin and C. Beisel for genomic library preparation and mRNA sequencing; the sciCORE team for their maintenance of the High Performance Computing facility at the University of Basel; S. Eppenberger-Castori for support on selecting the paired liver biopsies; S. Bichet, A. Bogucki, D. Calabrese and M-M. Coissieux for assistance with immunohistochemical staining; M. Ritter, S. D. Soysal and B.T. Preca for writing ethical permits; members of the Bentires-Alj laboratory for advice and discussion; and N. E. Hynes and S. Eppenberger-Castori for critically reading the manuscript. We also thank all the patients who donated tissues and blood to this study. A.L.C. was supported by an EMBO long-term postdoctoral fellowship (ALTF 1107-2014) and the research fund for excellent junior researchers from the University of Basel. J.C.G. was supported by a SystemsX.ch Transitional Postdoctoral Fellowship (grant 51FSP0_157344) and a Novartis University of Basel Excellence Scholarship for Life Sciences. Research in the Bentires-Alj laboratory is supported by the Swiss Initiative for Systems Biology-SystemsX, the European Research Council (ERC advanced grant 694033 STEM-BCPC), the Swiss National Science Foundation, Novartis, the Krebsliga Beider Basel, the Swiss Cancer League, the Swiss Personalized Health Network (Swiss Personalized Oncology driver project) and the Department of Surgery of the University Hospital Basel.

Author information

Author notes

1. Joao C. Guimaraes & Duvini De Silva

Present address: F. Hoffmann-La Roche AG, Basel, Switzerland

2. Ryoko Okamoto

Present address: Department of Biosystems Science and Engineering,
ETH Zürich, Basel, Switzerland

3. Sandro Bruno

Present address: Novartis Institutes for BioMedical Research, Basel,
Switzerland

Affiliations

1. Department of Biomedicine, University of Basel, Basel, Switzerland

Ana Luísa Correia, Priska Auf der Maur, Duvini De Silva, Marcel P. Trefny, Ryoko Okamoto, Katrin Volkmann, Alfred Zippelius & Mohamed Bentires-Alj

2. Friedrich Miescher Institute for Biomedical Research, Basel,
Switzerland

Ana Luísa Correia, Duvini De Silva, Ryoko Okamoto, Sandro Bruno & Mohamed Bentires-Alj

3. Department of Surgery, University Hospital Basel, Basel, Switzerland

Ana Luísa Correia, Priska Auf der Maur, Ryoko Okamoto, Katrin Volkmann, Walter Paul Weber & Mohamed Bentires-Alj

4. Computational and Systems Biology, Biozentrum, University of Basel,
Basel, Switzerland

Joao C. Guimaraes

5. Proteomics Core Facility, Biozentrum, University of Basel, Basel,
Switzerland

Alexander Schmidt

6. Institute of Pathology Liestal, Cantonal Hospital Basel-Land, Liestal,
Switzerland

Kirsten Mertz

7. Institute of Pathology, University Hospital Basel, Basel, Switzerland

Luigi Terracciano

8. Department of Medical Oncology, University Hospital Basel, Basel,
Switzerland

Alfred Zippelius & Marcus Vetter

9. Gynecologic Cancer Center, University Hospital Basel, Basel,
Switzerland

Marcus Vetter & Christian Kurzeder

10. Breast Center, University of Basel and University Hospital Basel,
Basel, Switzerland

Marcus Vetter, Christian Kurzeder & Walter Paul Weber

Authors

1. Ana Luísa Correia

[View author publications](#)

You can also search for this author in [PubMed](#) [Google Scholar](#)

2. Joao C. Guimaraes

[View author publications](#)

You can also search for this author in [PubMed](#) [Google Scholar](#)

3. Priska Auf der Maur

[View author publications](#)

You can also search for this author in [PubMed](#) [Google Scholar](#)

4. Duvini De Silva

[View author publications](#)

You can also search for this author in [PubMed](#) [Google Scholar](#)

5. Marcel P. Trefny

[View author publications](#)

You can also search for this author in [PubMed](#) [Google Scholar](#)

6. Ryoko Okamoto

[View author publications](#)

You can also search for this author in [PubMed](#) [Google Scholar](#)

7. Sandro Bruno

[View author publications](#)

You can also search for this author in [PubMed](#) [Google Scholar](#)

8. Alexander Schmidt

[View author publications](#)

You can also search for this author in [PubMed](#) [Google Scholar](#)

9. Kirsten Mertz

[View author publications](#)

You can also search for this author in [PubMed](#) [Google Scholar](#)

10. Katrin Volkmann

[View author publications](#)

You can also search for this author in [PubMed](#) [Google Scholar](#)

11. Luigi Terracciano

[View author publications](#)

You can also search for this author in [PubMed](#) [Google Scholar](#)

12. Alfred Zippelius

[View author publications](#)

You can also search for this author in [PubMed](#) [Google Scholar](#)

13. Marcus Vetter

[View author publications](#)

You can also search for this author in [PubMed](#) [Google Scholar](#)

14. Christian Kurzeder

[View author publications](#)

You can also search for this author in [PubMed](#) [Google Scholar](#)

15. Walter Paul Weber

[View author publications](#)

You can also search for this author in [PubMed](#) [Google Scholar](#)

16. Mohamed Bentires-Alj

[View author publications](#)

You can also search for this author in [PubMed](#) [Google Scholar](#)

Contributions

A.L.C. conceived the study, conducted experiments, analysed and interpreted data and wrote the manuscript. J.C.G. contributed to experimental design, and conducted all analyses and data interpretation related to mRNA sequencing. P.A.d.M. designed and performed experiments related to CRISPR-mediated knockout of *Cxcr4*, and assisted with animal experiments. D.D.S. performed many experiments involving flow cytometry, and analysed and interpreted the resulting data. M.P.T. helped design and perform experiments related to NK cell-mediated cytotoxicity. R.O. assisted with animal experiments. S.B. performed experiments to harmonize nutritional requirements and assemble different cell types in the liver co-cultures. A.S. conducted proteomics experiments, and analysed and interpreted the resulting data. K.M. performed immunohistochemistry and analysed NK cell frequency on liver biopsies. K.V. conducted image acquisitions on the CQ1 Benchtop High-Content Analysis System. L.T. provided patient materials and assisted in analysing HSC frequency on liver biopsies. A.Z., M.V., W.P.W. and C.K. provided patient material. M.B.-A. conceived the study. All authors read and provided feedback on the manuscript.

Corresponding authors

Correspondence to [Ana Luísa Correia](#) or [Mohamed Bentires-Alj](#).

Ethics declarations

Competing interests

A.L.C., P.A.d.M., M.P.T., R.O., A.S., K.M., K.V., L.T., M.V. and C.K. declare no competing interests. J.C.G. and D.D.S. are employees of F. Hoffmann–La Roche. S.B. is an employee of Novartis. A.Z. received honoraria from Bristol-Myers Squibb, Merck Sharp & Dohme, Hoffmann–La Roche, NBE Therapeutics, Secarna, ACM Pharma and Hookipa. A.Z. maintains non-commercial research agreements with Hoffmann–La Roche. A.Z. maintains further non-commercial research agreements with NBE Therapeutics, Secarna, ACM Pharma, Hookipa and BeyondSpring. M.B.-A. owns equities in and receives laboratory support and compensation from

Novartis, and serves as consultant for Basilea. Outside of the submitted work, W.P.W. received research support from Takeda Pharmaceuticals International paid to the Swiss Group for Clinical Cancer Research (SAKK) and personal honoraria from Genomic Health. Support for meetings was paid to his institution from Sandoz, Genomic Health, Medtronic, Novartis Oncology, Pfizer and Eli Lilly.

Additional information

Peer review information *Nature* thanks Eric Vivier and the other, anonymous, reviewer(s) for their contribution to the peer review of this work.

Publisher's note Springer Nature remains neutral with regard to jurisdictional claims in published maps and institutional affiliations.

Extended data figures and tables

[Extended Data Fig. 1 Expression profiling of breast DTCs and stroma from dormant and metastatic milieus reveals the determinants of progression of breast cancer in the liver.](#)

a, Principal component analysis (PCA) of cycling and quiescent DTCs in the MDA-MB-231 model. Transcriptional profiles cluster on the basis of cell cycle state. The dots in the plot represent DTCs isolated from different liver parts ($n = 11$ cycling, $n = 13$ quiescent; data combine three independent experiments). **b**, Scatter plot of mRNA expression levels (library-normalized mRNA counts) in cycling and quiescent DTCs. Shown are mean expression values for each transcript in each cell cycle state ($n = 11$ cycling, $n = 13$ quiescent). mRNAs significantly upregulated or downregulated (that is, $\log_2(\text{mRNA counts in cycling DTCs}/\text{mRNA counts in quiescent DTCs}) > 1$ and $\text{FDR} < 0.01$) in cycling DTCs are shown in red or blue, respectively. The dashed line indicates equal abundances in the two different conditions. **c, d**, GSEA comparing gene-expression data from quiescent (**c**) and cycling (**d**) DTCs. **e**, PCA of dormancy and metastasis stroma. Transcriptional profiles cluster on the basis of disease stage. The

dots in the plot represent stroma isolated from different liver parts ($n = 17$ dormancy, $n = 12$ metastasis). **f**, Scatter plot of mRNA expression levels (library-normalized mRNA counts) in metastasis and dormancy stroma. Shown are mean expression values for each transcript in each stroma ($n = 12$ metastasis, $n = 17$ dormancy). mRNAs significantly upregulated or downregulated ($\log_2(\text{mRNA counts in metastasis stroma}/\text{mRNA counts in dormancy stroma}) > 1$ and $\text{FDR} < 0.01$) in metastasis stroma are shown in red or blue, respectively. The dashed line indicates equal abundances in the two different conditions. **g**, GSEA comparing gene-expression data from metastasis and dormancy liver stroma. **h**, Heat map depicting the hierarchical clustering of standard-score-normalized (z -score) expression level of NK cell markers⁵⁵ across stroma ($n = 12$ metastasis, $n = 17$ dormancy). **i**, Mean \pm s.e.m. mRNA fold change (\log_2 -transformed) of NK cell markers in metastasis ($n = 12$) compared to dormancy ($n = 17$) stroma samples. Multiple-test-corrected P values for two-tailed Wald tests comparing the fold change between metastasis and dormancy samples are depicted above each dot (* $P < 0.05$, *** $P < 0.001$). **j**, Violin plot showing the distribution of the median standard-score normalized (z -score) expression level of NK cell markers across metastasis and dormancy stroma ($n = 12$ metastasis, $n = 17$ dormancy). Solid and dashed horizontal lines depict the median and the upper and lower quartiles, respectively. Shown is the P value for the two-tailed nonparametric Mann–Whitney U test. In **c**, **d**, **g**, P values were calculated by one-tailed comparisons of the empirical ES of a gene set to a null distribution of ESs derived from permuting the gene set, and then adjusted for multiple-hypotheses testing (that is, FDR).

Source data

Extended Data Fig. 2 NK cells are specifically enriched in liver dormancy milieus.

a, Flow cytometry quantification of the frequency (top) and number (bottom) of different immune cell subsets in liver parts isolated from the MDA-MB-231 model ($n = 11$ no tumour, $n = 17$ dormancy, $n = 20$ metastasis; data combine three independent experiments). **b**, **c**, Histological characterization of the dormant 4T07 (**b**) and metastatic 4T1 (**c**) models.

Left, representative H&E-stained liver lobes. Scale bars, 2 mm. Right, examples (corresponding to i–vi from the left images) of scattered Ki67[−] quiescent DTCs (indicated by arrowheads), and liver metastases (surrounded by a dashed coloured line). Scale bars, 30 µm. **d**, Quantification of metastatic foci in livers of 4T07 and 4T1 models, normalized to the liver lobe area analysed ($n = 10$ 4T07, $n = 10$ 4T1; mean ± s.d.; two-tailed nonparametric Mann–Whitney U test). **e**, Flow cytometry quantification of the frequency (top) and number (bottom) of different immune cell populations in livers from dormant 4T07 and metastatic 4T1 models ($n = 10$ no tumour, $n = 10$ 4T07, $n = 10$ 4T1; data combine two independent experiments). **f**, Flow cytometry quantification of the frequency of NK and T cells, as well as T cell-activated populations, in liver sub-microenvironments from the metastatic 4T1 model ($n = 10$ no tumour, $n = 10$ dormancy, $n = 10$ metastasis; data combine two independent experiments). In **a**, **e**, **f**, mean ± s.d.; two-tailed nonparametric Kruskal–Wallis test with Dunn’s multiple comparison post-hoc test.

[Source data](#)

Extended Data Fig. 3 Both conventional and liver-resident NK cells decrease during metastatic progression.

a, The gene signature of NK cells alone—but not that of conventional NK (cNK) cells or liver-resident NK (LrNK) cells—can reliably distinguish dormancy and metastasis in the liver. Violin plots show the distribution of the median standard-score normalized (z -score) expression level of NK cell (left), cNK cell (middle) and LrNK cell (right) markers across stroma ($n = 12$ metastasis, $n = 17$ dormancy). Solid and dashed horizontal lines depict the median and the upper and lower quartiles, respectively. Shown is the P value for the two-tailed nonparametric Mann–Whitney U test. **b**, **c**, cNK and LrNK cells are similarly represented within the NK compartment across different hepatic milieus. Flow cytometry quantification of the number per gram of liver (**b**) or the frequency within the NK cell compartment (**c**) of cNK cells ($CD49b^+CD49a^-TRAIL^-$) and LrNK cells ($CD49b^-CD49a^+TRAIL^+$) in liver parts isolated from the MDA-MB-231 model ($n = 6$ no tumour, $n = 12$ dormancy, $n = 9$ metastasis; data combine

two independent experiments; mean \pm s.d.; two-tailed nonparametric Kruskal–Wallis test with Dunn’s multiple comparison post-hoc test).

[Source data](#)

Extended Data Fig. 4 Normalizing the NK cell pool prevents hepatic metastases.

a, Flow cytometry quantification of NK cell frequency in mice treated with IgG, anti-GM1, PBS or IL-15. Left, MDA-MB-231 model ($n = 8$ IgG, $n = 10$ anti-GM1, $n = 8$ PBS, $n = 10$ IL-15; data combine two independent experiments). Right, 4T1 model ($n = 4$ IgG, $n = 5$ anti-GM1, $n = 5$ PBS, $n = 5$ IL-15). **b**, Bioluminescence imaging 10 weeks after MDA-MB-231 tumour resection. **c**, **d**, Quantification of metastatic foci (**c**) and metastatic area (**d**) in livers of mice treated with IgG, anti-GM1, PBS or IL-15, normalized to the liver lobe area analysed. Left, MDA-MB-231 model ($n = 8$ IgG, $n = 10$ anti-GM1, $n = 8$ PBS, $n = 10$ IL-15; data combine two independent experiments). Right, 4T1 model ($n = 5$ IgG, $n = 10$ anti-GM1, $n = 6$ PBS, $n = 10$ IL-15). **e**, Experimental design for examining the effects of NK cell depletion on the 4T07 model. **f**, Sustained NK cell depletion reactivates dormant 4T07 DTCs in the liver. Arrowheads indicate single Ki67[−] quiescent DTCs. Coloured line delineates a metastasis. Scale bars, 30 μ m. **g**, Quantification of liver metastatic foci after NK cell depletion in the 4T07 model, normalized to the liver lobe area analysed ($n = 10$ IgG, $n = 10$ anti-GM1). **h**, Quantification of scattered quiescent DTCs in livers of mice treated with IgG, anti-GM1, PBS or IL-15, normalized to the liver lobe area analysed ($n = 8$ IgG, $n = 10$ anti-GM1, $n = 8$ PBS, $n = 10$ IL-15; data combine two independent experiments). **i**, Expression of IL-15R α in MDA-MB-231, 4T07 and 4T1 cells assessed by western blotting. ERK2 was used as a loading control. For gel source data, see Supplementary Fig. 1 ($n = 3$ experiments). **j**, Histogram of IL-15R α measured by antibody-based staining and flow cytometry in MDA-MB-231, 4T07 and 4T1 cells. **k**, Quantification of the relative percentages of quiescent (Tomato⁺mVenus⁺) and cycling (Tomato⁺mVenus[−]) cancer cells after 24 h of treatment with IL-15 shows no effect on cell population ratios ($n = 3$ independent experiments). **l–n**, Flow cytometry quantification of T cell frequency (**l**) and activation (**m**, **n**) in livers from 4T1-injected mice treated

with PBS or IL-15 ($n = 5$ PBS, $n = 5$ IL-15). In **a, c, d, g, h, k–n**, mean \pm s.d.; two-tailed nonparametric Mann–Whitney U test.

[Source data](#)

Extended Data Fig. 5 Quiescent DTCs are not intrinsically resistant to recognition and killing by NK cells.

a, b, Mean \pm s.e.m. mRNA fold change (log₂-transformed) of NK cell activating (**a**) and inhibitory (**b**) ligands in cycling ($n = 11$) compared to quiescent DTCs ($n = 13$). Multiple-test-corrected P values for two-tailed Wald tests comparing the fold change between cycling and quiescent DTCs are depicted above each dot (* $P < 0.05$, ** $P < 0.01$, *** $P < 0.001$). **c**, Schematic of experiment to test the sensitivity of cycling and quiescent DTCs to NK cell-mediated cytotoxicity. Human MDA-MB-231 or mouse 4T07 and 4T1 cancer cells co-expressing Tomato and mVenus-p27K[−] were co-cultured with NK cells derived from human blood or mouse livers, and assayed for cytolysis. **d**, NK cells kill DTCs regardless of their cell-cycle stage. The percentage of specifically killed cycling and quiescent cancer cells was calculated for different effector:target (E:T) ratios. For 4T07 and 4T1, $n = 3$ pooled mice per experiment, data combine three independent experiments; for MDA-MB-231, $n = 4$ healthy donors; mean \pm s.d.; two-tailed nonparametric Mann–Whitney U test.

[Source data](#)

Extended Data Fig. 6 Transcriptional landscape of NK cells from dormant, metastatic and tumour-free liver milieus.

a, b, GSEA comparing gene expression data from dormancy (**a**) and tumour-free (**b**) liver NK cells ($n = 10$ no tumour, $n = 17$ dormancy). **c, d**, GSEA comparing gene-expression data from metastasis (**c**) and tumour-free (**d**) liver NK cells ($n = 10$ no tumour, $n = 7$ metastasis). **e**, GSEA comparing gene-expression data from metastasis and dormancy liver NK cells ($n = 17$ dormancy, $n = 7$ metastasis). In **a–e**, one-tailed comparisons of the ES of a gene set to a null distribution of ESs derived from permuting the gene set,

and then adjusted for multiple-hypotheses testing (that is, FDR). **f**, Flow cytometry quantification of liver TNF⁺ NK cells. Left, liver parts from the MDA-MB-231 model ($n = 6$ no tumour, $n = 12$ dormancy, $n = 9$ metastasis; data combine two independent experiments). Right: livers from dormant 4T07 and metastatic 4T1 models ($n = 12$ no tumour, $n = 12$ 4T07, $n = 12$ 4T1; data combine two independent experiments; mean \pm s.d.; two-tailed nonparametric Mann–Whitney U test.). **g**, GSEA of the Hallmark ‘IFN γ response’ pathway in DTCs ($n = 11$ cycling, $n = 13$ quiescent). NES, normalized enrichment score. **h**, Mean \pm s.e.m. mRNA fold change (\log_2 -transformed) of members of the IFN γ signalling pathway in cycling ($n = 11$) compared to quiescent DTCs ($n = 13$). Multiple-test-corrected P values for two-tailed Wald tests comparing the fold change between cycling and quiescent DTCs are depicted above each dot (* $P < 0.05$, ** $P < 0.01$, *** $P < 0.001$).

[Source data](#)

[Extended Data Fig. 7 aHSCs mediate NK cell depletion and promote liver metastasis.](#)

a, Mean \pm s.e.m. mRNA fold change (\log_2 -transformed) of aHSC markers in metastasis ($n = 12$) compared to dormancy ($n = 17$). Multiple-test-corrected P values for two-tailed Wald tests comparing the fold change between metastasis and dormancy are depicted above each dot (* $P < 0.05$, *** $P < 0.001$). **b**, Violin plot showing the distribution of the median z -score expression level of aHSC markers across liver stroma ($n = 12$ metastasis, $n = 17$ dormancy). Solid and dashed horizontal lines depict the median and the upper and lower quartiles, respectively; two-tailed nonparametric Mann–Whitney U test. **c**, Quantification of α -SMA⁺ aHSCs after NK cell modulation. Left, MDA-MB-231 model ($n = 8$ IgG, $n = 10$ anti-GM1, $n = 8$ PBS, $n = 10$ IL-15; data combine two independent experiments). Right, 4T1 model ($n = 5$ IgG, $n = 10$ anti-GM1, $n = 6$ PBS, $n = 10$ IL-15). **d**, Bioluminescence imaging six weeks after tumour resection. **e**, Quantification of bioluminescence shows no changes in lung metastatic burden ($n = 10$ oil, $n = 16$ CCl₄; data combine two independent

experiments). In **c**, **e**, mean \pm s.d.; two-tailed nonparametric Mann–Whitney *U* test.

[Source data](#)

Extended Data Fig. 8 Activation of HSCs shrinks the NK cell compartment even in the absence of tumour cells.

a, Representative micrographs of α -SMA⁺ aHSCs and collagen deposition in livers from non-tumour-bearing NOD-SCID mice that were treated with oil or CCl₄ for one or six weeks. Scale bars, 30 μ m. **b**, **c**, Flow cytometry quantification of NK cell frequency (**b**) and proliferation (**c**) in livers from non-tumour-bearing NOD-SCID mice that were treated with oil or CCl₄ for one or six weeks (for each time point, $n = 10$ oil, $n = 10$ CCl₄; data combine two independent experiments; mean \pm s.d.; two-tailed nonparametric Mann–Whitney *U* test).

[Source data](#)

Extended Data Fig. 9 CXCL12 limits the proliferation of NK cells from healthy donors and patients with breast cancer with liver metastases.

a, *t*-distributed stochastic neighbour embedding (t-SNE) plot showing the relative expression of CXCR4 on different liver cell types based on 8,444 human liver cells previously sequenced⁵⁵. Each dot represents a single cell, and cells are coloured from lowest (yellow) to highest (purple) expression. **b**, Histogram of CXCR4 measured by flow cytometry on human NK-92 cells. **c**, Exogenous CXCL12 increases the number of G0–G1 resting NK-92 cells, but it has no effect on NK cell viability ($n = 5$ independent experiments; mean \pm s.d.; two-tailed nonparametric Kruskal–Wallis test with Dunn’s multiple comparison post-hoc test). **d**, Schematic of experiments to test the effect of CXCL12 on blood-derived NK cells purified from healthy donors and patients with breast cancer (BC) with liver metastases. NK cells labelled with CellTrace Violet (CTV) were primed with IL-2 and IL-15, and then expanded with IL-2 in the presence of

CXCL12 alone or combined with IL-15 until assessed for division profile. **e**, Representative histogram of the NK cell division profile of a healthy donor. **f**, Quantification of the division index (that is, the average number of cell divisions a cell has undergone) of blood-derived NK cells from healthy donors (left, $n = 6$) and patients with breast cancer with liver metastases (right, $n = 6$) after treatment with CXCL12 alone or combined with IL-15. C1–C3 correspond to different concentrations of recombinant CXCL12 ($C1 = 0.02 \mu\text{g ml}^{-1}$, $C2 = 0.2 \mu\text{g ml}^{-1}$ and $C3 = 2 \mu\text{g ml}^{-1}$). Mean \pm s.d.; two-tailed nonparametric Kruskal–Wallis test with Dunn’s multiple comparison post-hoc test. **g**, Experimental schematic to assess the effects of aHSC-secreted CXCL12 on liver NK cells. Mouse NK cells were treated with conditioned medium (CM) from liver-derived aHSCs in the presence of a function-blocking antibody against CXCL12 or a control IgG, and G0–G1 resting cells were quantified after EdU incorporation. **h**, Flow cytometry quantification of quiescent Ki67[−] NK cells in mouse liver milieus ($n = 6$ no tumour, $n = 12$ dormancy, $n = 9$ metastasis; data combine two independent experiments; mean \pm s.d.; nonparametric two-tailed Kruskal–Wallis test with Dunn’s multiple comparison post-hoc test). **i**, Proliferation of CXCR4⁺ NK cells from metastatic milieus ($n = 9$ metastasis; mean \pm s.d.; nonparametric Mann–Whitney *U* test).

[Source data](#)

[Extended Data Fig. 10 CXCR4 expression confers DTCs with a proliferative advantage but is not required for outgrowth.](#)

a, Experimental design for testing the influence of aHSC-secreted CXCL12 on cancer cell proliferation. Co-cultures of hepatocytes and sparsely seeded cancer cells were exposed to recombinant CXCL12 protein or conditioned medium (CM) from aHSCs alone or in combination with anti-CXCL12, anti-CXCR4, control IgG or a CXCR4 inhibitor, and the number of cancer cells was analysed by flow cytometry. **b**, Quantification of the number of cancer cells in different liver-like milieus shows that CXCL12–CXCR4 signalling induces cancer cell proliferation (for each cell line, $n = 5$ independent experiments). **c**, Scheme of *Cxcr4* sites targeted by single-guide RNAs to generate 4T1 *Cxcr4*-KO cells. **d**, Genotyping of clonally derived cells obtained through CRISPR–Cas9 targeting of *Cxcr4*. Coloured

lanes represent clones selected and pooled as 4T1 *Cxcr4* wild type (*Cxcr4*-WT) and 4T1 *Cxcr4*-KO lines ($n = 1$ PCR per clone; selected clones were also confirmed by sequencing). bp, base pair. **e**, Experimental design for assessing the requirement of CXCR4 for liver metastasis. **f**, Representative H&E-stained livers from 4T1 *Cxcr4*-WT and 4T1 *Cxcr4*-KO lines injected in BALB/c immunocompetent mice. Arrowheads and coloured lines indicate metastases. Scale bars, 2 mm. **g**, Quantification of liver metastatic foci in livers of oil- and CCl₄-treated mice normalized to the liver lobe area analysed ($n = 6$ WT oil, $n = 9$ WT CCl₄, $n = 8$ KO oil, $n = 11$ KO CCl₄). **h**, Quantification of metastatic area in livers of oil- and CCl₄-treated mice, normalized to the liver lobe area analysed ($n = 6$ WT oil, $n = 9$ WT CCl₄, $n = 8$ KO oil, $n = 11$ KO CCl₄). In **b**, **g**, **h**, mean \pm s.d.; two-tailed nonparametric Mann–Whitney *U* test.

Source data

Extended Data Fig. 11 Activated hepatic stellate cells and CXCL12 accumulate in patients with liver metastases.

a, Staining of NK cells (CD3[−]CD57⁺) and aHSCs (α -SMA⁺) in paired metastases and normal adjacent tissues in liver biopsies from patients with breast cancer. Arrowheads indicate HSCs (top) and NK cells (bottom). Scale bars, 30 μ m. **b**, Correlation between aHSCs and NK cells in paired metastases and normal adjacent tissues in liver biopsies from patients with breast cancer ($n = 34$ paired biopsies; Fisher’s exact test). **c**, Staining of NK cells (CD3[−]CD57⁺) and aHSCs (α -SMA⁺) in liver biopsies from patients with breast cancer with chronic liver disease but no metastases. Arrowheads indicate HSCs (top) and NK cells (bottom). Scale bars, 30 μ m. **d**, Correlation between aHSCs and NK cells in liver biopsies from patients with breast cancer with chronic liver disease but no metastases ($n = 35$ biopsies; Fisher’s exact test). **e**, Heat map depicting the hierarchical clustering of standard-score-normalized (*z*-score) expression level of aHSC markers⁵⁵ across normal and metastatic liver samples from patients with colon cancer³⁸ ($n = 5$ normal livers, $n = 18$ liver metastases). **f**, Violin plot showing the distribution of the *z*-score expression level of aHSC markers across human healthy livers ($n = 5$) and liver metastases ($n = 18$). Solid and

dashed horizontal lines depict the median and the upper and lower quartiles, respectively. Shown is the P value for the two-sided nonparametric Mann–Whitney U test. **g**, Heat map depicting the hierarchical clustering of z -score expression level of NK cell markers⁵⁵ across healthy livers ($n = 5$) and liver metastases ($n = 18$) from patients with colon cancer³⁸. **h**, Violin plot showing the distribution of the z -score expression level of NK markers across human healthy livers ($n = 5$) and liver metastases ($n = 18$). Solid and dashed horizontal lines depict the median and the upper and lower quartiles, respectively. Two-sided nonparametric Mann–Whitney U test. **i**, Scatter plot of median standard-score-normalized (z -score) expression level of HSC markers and *CXCL12* expression across human liver metastases ($n = 134$). The Pearson correlation coefficient (R) and respective P value are also shown. The dashed line indicates the linear regression between the two estimates. FPKM, fragments per kilobase per million mapped reads.

[Source data](#)

Supplementary information

[Supplementary Figures](#)

This file contains Supplementary Figures 1-2, which show the uncropped blots and the gating strategy used to quantify liver immune cell subsets in main and Extended Data figures.

[Reporting Summary](#)

[Supplementary Table 1](#)

Differential gene expression analysis between metastasis and dormancy liver stroma. mRNA expression levels (library normalized mRNA counts) in metastasis compared to dormancy stroma ($n = 12$ metastases, $n = 17$ dormancy). Multiple test corrected P -values for two-tailed Wald tests comparing fold-changes between metastasis and dormancy.

[Supplementary Table 2](#)

Differential gene expression analysis between metastasis and dormancy liver NK cells. mRNA expression levels (library normalized mRNA counts) in metastasis compared to dormancy NK cells ($n = 9$ metastases, $n = 12$ dormancy). Multiple test corrected P -values for two-tailed Wald tests comparing fold-changes between metastasis and dormancy.

Supplementary Table 3

Proteomic analysis of aHSCs and hepatocytes secretome. Proteomic analysis of aHSCs and hepatocytes (Heps) secretome ($n = 3$ CM_aHSCs, $n = 3$ CM_Heps, normalized by $n = 3$ control growth medium; Bayes-moderated t-statistics, P values corrected for multiple testing using the Benjamini-Hochberg method).

Supplementary Table 4

Details on antibodies, cytokines and inhibitors used in this study.

Supplementary Table 5

Details on crRNA and genotyping primers used for CRISPR mediated knockout of CXCR4.

Source data

Source Data Fig. 1

Source Data Fig. 2

Source Data Fig. 3

Source Data Fig. 4

Source Data Extended Data Fig. 1

[Source Data Extended Data Fig. 2](#)

[Source Data Extended Data Fig. 3](#)

[Source Data Extended Data Fig. 4](#)

[Source Data Extended Data Fig. 5](#)

[Source Data Extended Data Fig. 6](#)

[Source Data Extended Data Fig. 7](#)

[Source Data Extended Data Fig. 8](#)

[Source Data Extended Data Fig. 9](#)

[Source Data Extended Data Fig. 10](#)

[Source Data Extended Data Fig. 11](#)

Rights and permissions

[Reprints and Permissions](#)

About this article



Check for
updates

Cite this article

Correia, A.L., Guimaraes, J.C., Auf der Maur, P. *et al.* Hepatic stellate cells suppress NK cell-sustained breast cancer dormancy. *Nature* **594**, 566–571

(2021). <https://doi.org/10.1038/s41586-021-03614-z>

[Download citation](#)

- Received: 16 December 2019
- Accepted: 04 May 2021
- Published: 02 June 2021
- Issue Date: 24 June 2021
- DOI: <https://doi.org/10.1038/s41586-021-03614-z>

Comments

By submitting a comment you agree to abide by our [Terms](#) and [Community Guidelines](#). If you find something abusive or that does not comply with our terms or guidelines please flag it as inappropriate.

[Access through your institution](#)

[Change institution](#)

[Buy or subscribe](#)

Associated Content

[Natural killer cells lull tumours into dormancy](#)

- Noella Lopes
- Eric Vivier

Advertisement

| [Section menu](#) | [Main menu](#) |

- Article
- [Published: 09 June 2021](#)

Concerted cutting by Spo11 illuminates meiotic DNA break mechanics

- [Dominic Johnson](#) ORCID: orcid.org/0000-0001-7464-0893^{1 na1},
- [Margaret Crawford](#)^{1 na1},
- [Tim Cooper](#)¹,
- [Corentin Claeys Bouuaert](#) ORCID: orcid.org/0000-0001-5801-7313^{2,3},
- [Scott Keeney](#) ORCID: orcid.org/0000-0002-1283-6417²,
- [Bertrand Llorente](#)⁴,
- [Valerie Garcia](#) ORCID: orcid.org/0000-0002-4941-0989^{1,4} &
- [Matthew J. Neale](#) ORCID: orcid.org/0000-0002-6453-1877¹

[Nature](#) volume 594, pages 572–576 (2021) [Cite this article](#)

- 2821 Accesses
- 31 Altmetric
- [Metrics details](#)

Subjects

- [DNA recombination](#)
- [Double-strand DNA breaks](#)
- [Enzyme mechanisms](#)

Abstract

Genetic recombination arises during meiosis through the repair of DNA double-strand breaks (DSBs) that are created by Spo11, a topoisomerase-like protein^{1,2}. Spo11 DSBs form preferentially in nucleosome-depleted regions termed hotspots^{3,4}, yet how Spo11 engages with its DNA substrate to catalyse DNA cleavage is poorly understood. Although most recombination events are initiated by a single Spo11 cut, here we show in *Saccharomyces cerevisiae* that hyperlocalized, concerted Spo11 DSBs separated by 33 to more than 100 base pairs also form, which we term ‘double cuts’. Notably, the lengths of double cuts vary with a periodicity of 10.5 base pairs, which is conserved in yeast and mice. This finding suggests a model in which the orientation of adjacent Spo11 molecules is fixed relative to the DNA helix—a proposal supported by the in vitro DNA-binding properties of the Spo11 core complex. Deep sequencing of meiotic progeny identifies recombination scars that are consistent with repair initiated from gaps generated by adjacent Spo11 DSBs. Collectively, these results revise our present understanding of the mechanics of Spo11-DSB formation and expand on the original concepts of gap repair during meiosis to include DNA gaps that are generated by Spo11 itself.

Access options

Subscribe to Journal

Get full journal access for 1 year

\$199.00

only \$3.90 per issue

[Subscribe](#)

All prices are NET prices.

VAT will be added later in the checkout.

Tax calculation will be finalised during checkout.

Rent or Buy article

Get time limited or full article access on ReadCube.

from \$8.99

[Rent or Buy](#)

All prices are NET prices.

Additional access options:

- [Log in](#)
- [Access through your institution](#)
- [Learn about institutional subscriptions](#)

Fig. 1: Spo11-DC formation during meiosis in *S. cerevisiae*.

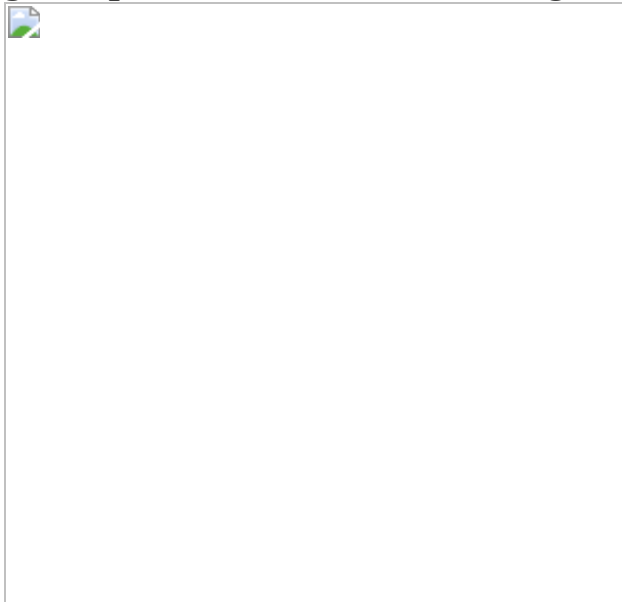


Fig. 2: Identification of Spo11-DCs within Spo11-oligo libraries.

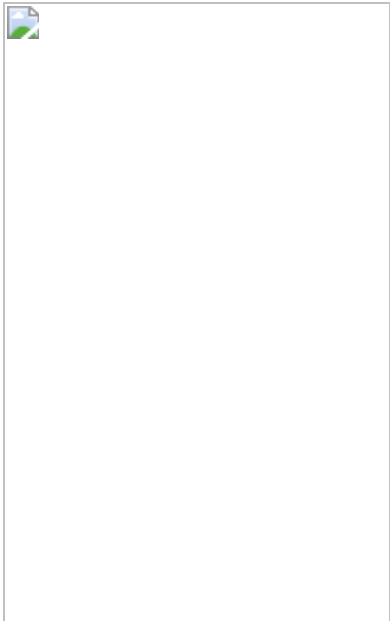


Fig. 3: Spo11-DC-induced gap repair in *S. cerevisiae*.

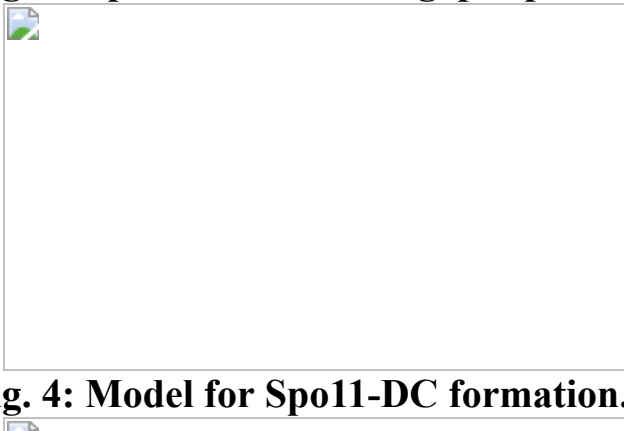


Fig. 4: Model for Spo11-DC formation.

Data availability

Raw *S. cerevisiae* and mouse Spo11-oligo FASTQ data were obtained from published archives [GSE84696](#) and [GSE84689](#), respectively. Nucleotide-resolution maps generated by paired-end Bowtie2 alignment are provided in the Supplementary Information. For mice, the maps used here were generated from the following biological samples: wild type, [GSM2247728](#); *Atm*^{-/-}, [GSM2247731](#). FASTQ files used for mapping HR patterns in *S. cerevisiae* SK1 × S288c F₁ hybrid octads in *msh2Δ*; *tellΔmsh2Δ*; and

mlh1Δmsh2Δ, *mlh3Δmsh2Δ* and *exo1Δmsh2Δ* are deposited in the NCBI Sequence Read Archive (SRA) with accession numbers [PRJNA479661](#); [PRJNA480956](#); and [PRJNA393087¹⁹](#), respectively. Additional data are included in the [Supplementary Data](#). [Source data](#) are provided with this paper.

References

1. 1.

Keeney, S., Giroux, C. N. & Kleckner, N. Meiosis-specific DNA double-strand breaks are catalyzed by Spo11, a member of a widely conserved protein family. *Cell* **88**, 375–384 (1997).

[CAS](#) [PubMed](#) [Google Scholar](#)

2. 2.

Bergerat, A. et al. An atypical topoisomerase II from Archaea with implications for meiotic recombination. *Nature* **386**, 414–417 (1997).

[ADS](#) [CAS](#) [PubMed](#) [Google Scholar](#)

3. 3.

Pan, J. et al. A hierarchical combination of factors shapes the genome-wide topography of yeast meiotic recombination initiation. *Cell* **144**, 719–731 (2011).

[CAS](#) [PubMed](#) [PubMed Central](#) [Google Scholar](#)

4. 4.

Lange, J. et al. The landscape of mouse meiotic double-strand break formation, processing, and repair. *Cell* **167**, 695–708 (2016).

[CAS](#) [PubMed](#) [PubMed Central](#) [Google Scholar](#)

5. 5.

Neale, M. J., Pan, J. & Keeney, S. Endonucleolytic processing of covalent protein-linked DNA double-strand breaks. *Nature* **436**, 1053–1057 (2005).

[ADS](#) [CAS](#) [PubMed](#) [PubMed Central](#) [Google Scholar](#)

6. 6.

Garcia, V., Phelps, S. E. L., Gray, S. & Neale, M. J. Bidirectional resection of DNA double-strand breaks by Mre11 and Exo1. *Nature* **479**, 241–244 (2011).

[ADS](#) [CAS](#) [PubMed](#) [PubMed Central](#) [Google Scholar](#)

7. 7.

Fowler, K. R., Sasaki, M., Milman, N., Keeney, S. & Smith, G. R. Evolutionarily diverse determinants of meiotic DNA break and recombination landscapes across the genome. *Genome Res.* **24**, 1650–1664 (2014).

[CAS](#) [PubMed](#) [PubMed Central](#) [Google Scholar](#)

8. 8.

Choi, K. et al. Nucleosomes and DNA methylation shape meiotic DSB frequency in *Arabidopsis thaliana* transposons and gene regulatory regions. *Genome Res.* **28**, 532–546 (2018).

[CAS](#) [PubMed](#) [PubMed Central](#) [Google Scholar](#)

9. 9.

Cannavo, E. & Cejka, P. Sae2 promotes dsDNA endonuclease activity within Mre11-Rad50-Xrs2 to resect DNA breaks. *Nature* **514**, 122–125 (2014).

[ADS](#) [CAS](#) [PubMed](#) [Google Scholar](#)

10. 10.

Garcia, V., Gray, S., Allison, R. M., Cooper, T. J. & Neale, M. J. Tel1^{ATM}-mediated interference suppresses clustered meiotic double-strand-break formation. *Nature* **520**, 114–118 (2015).

[ADS](#) [CAS](#) [PubMed](#) [PubMed Central](#) [Google Scholar](#)

11. 11.

Mohibullah, N. & Keeney, S. Numerical and spatial patterning of yeast meiotic DNA breaks by Tel1. *Genome Res.* **27**, 278–288 (2017).

[CAS](#) [PubMed](#) [PubMed Central](#) [Google Scholar](#)

12. 12.

Zhang, L., Kim, K. P., Kleckner, N. E. & Storlazzi, A. Meiotic double-strand breaks occur once per pair of (sister) chromatids and, via Mec1/ATR and Tel1/ATM, once per quartet of chromatids. *Proc. Natl Acad. Sci. USA* **108**, 20036–20041 (2011).

[ADS](#) [CAS](#) [PubMed](#) [PubMed Central](#) [Google Scholar](#)

13. 13.

Joyce, E. F. et al. *Drosophila* ATM and ATR have distinct activities in the regulation of meiotic DNA damage and repair. *J. Cell Biol.* **195**, 359–367 (2011).

[CAS](#) [PubMed](#) [PubMed Central](#) [Google Scholar](#)

14. 14.

Lange, J. et al. ATM controls meiotic double-strand-break formation. *Nature* **479**, 237–240 (2011).

[ADS](#) [CAS](#) [PubMed](#) [PubMed Central](#) [Google Scholar](#)

15. 15.

Carballo, J. A. et al. Budding yeast ATM/ATR control meiotic double-strand break (DSB) levels by down-regulating Rec114, an essential component of the DSB-machinery. *PLoS Genet.* **9**, e1003545 (2013).

[CAS](#) [PubMed](#) [PubMed Central](#) [Google Scholar](#)

16. 16.

Liu, J., Wu, T. C. & Lichten, M. The location and structure of double-strand DNA breaks induced during yeast meiosis: evidence for a covalently linked DNA-protein intermediate. *EMBO J.* **14**, 4599–4608 (1995).

[CAS](#) [PubMed](#) [PubMed Central](#) [Google Scholar](#)

17. 17.

Claeys Bouuaert, C. et al. Structural and functional characterization of the Spo11 core complex. *Nat. Struct. Mol. Biol.* **28**, 92–102 (2021).

[CAS](#) [PubMed](#) [Google Scholar](#)

18. 18.

Martini, E. et al. Genome-wide analysis of heteroduplex DNA in mismatch repair-deficient yeast cells reveals novel properties of meiotic recombination pathways. *PLoS Genet.* **7**, e1002305 (2011).

[CAS](#) [PubMed](#) [PubMed Central](#) [Google Scholar](#)

19. 19.

Marsolier-Kergoat, M. C., Khan, M. M., Schott, J., Zhu, X. & Llorente, B. Mechanistic view and genetic control of DNA recombination during meiosis. *Mol. Cell* **70**, 9–20 (2018).

[CAS](#) [PubMed](#) [Google Scholar](#)

20. 20.

Kulkarni, D. S. et al. PCNA activates the Mut γ endonuclease to promote meiotic crossing over. *Nature* **586**, 623–627 (2020).

[ADS](#) [CAS](#) [PubMed](#) [Google Scholar](#)

21. 21.

Cannavo, E. et al. Regulation of the MLH1-MLH3 endonuclease in meiosis. *Nature* **586**, 618–622 (2020).

[ADS](#) [CAS](#) [PubMed](#) [Google Scholar](#)

22. 22.

Szostak, J. W., Orr-Weaver, T. L., Rothstein, R. J. & Stahl, F. W. The double-strand-break repair model for recombination. *Cell* **33**, 25–35 (1983).

[CAS](#) [PubMed](#) [Google Scholar](#)

23. 23.

Diaz, R. L., Alcid, A. D., Berger, J. M. & Keeney, S. Identification of residues in yeast Spo11p critical for meiotic DNA double-strand break formation. *Mol. Cell. Biol.* **22**, 1106–1115 (2002).

[CAS](#) [PubMed](#) [PubMed Central](#) [Google Scholar](#)

24. 24.

Prieler, S. et al. Spo11 generates gaps through concerted cuts at sites of topological stress. *Nature*, <https://doi.org/10.1038/s41586-021-03632-x> (2021).

25. 25.

Noll, M. Internal structure of the chromatin subunit. *Nucleic Acids Res.* **1**, 1573–1578 (1974).

[CAS](#) [PubMed](#) [PubMed Central](#) [Google Scholar](#)

26. 26.

Gittens, W. H. et al. A nucleotide resolution map of Top2-linked DNA breaks in the yeast and human genome. *Nat. Commun.* **10**, 4846 (2019).

[ADS](#) [PubMed](#) [PubMed Central](#) [Google Scholar](#)

27. 27.

Prieler, S., Penkner, A., Borde, V. & Klein, F. The control of Spo11's interaction with meiotic recombination hotspots. *Genes Dev.* **19**, 255–269 (2005).

[CAS](#) [PubMed](#) [PubMed Central](#) [Google Scholar](#)

28. 28.

Panizza, S. et al. Spo11-accessory proteins link double-strand break sites to the chromosome axis in early meiotic recombination. *Cell* **146**, 372–383 (2011).

[CAS](#) [PubMed](#) [Google Scholar](#)

29. 29.

Kugou, K. et al. Rec8 guides canonical Spo11 distribution along yeast meiotic chromosomes. *Mol. Biol. Cell* **20**, 3064–3076 (2009).

[CAS](#) [PubMed](#) [PubMed Central](#) [Google Scholar](#)

30. 30.

Li, J., Hooker, G. W. & Roeder, G. S. *Saccharomyces cerevisiae* Mer2, Mei4 and Rec114 form a complex required for meiotic double-strand break formation. *Genetics* **173**, 1969–1981 (2006).

[CAS](#) [PubMed](#) [PubMed Central](#) [Google Scholar](#)

31. 31.

Kee, K., Protacio, R. U., Arora, C. & Keeney, S. Spatial organization and dynamics of the association of Rec102 and Rec104 with meiotic chromosomes. *EMBO J.* **23**, 1815–1824 (2004).

[CAS](#) [PubMed](#) [PubMed Central](#) [Google Scholar](#)

32. 32.

Kumar, R., Bourbon, H. M. & de Massy, B. Functional conservation of Mei4 for meiotic DNA double-strand break formation from yeasts to mice. *Genes Dev.* **24**, 1266–1280 (2010).

[CAS](#) [PubMed](#) [PubMed Central](#) [Google Scholar](#)

33. 33.

Claeys Bouuaert, C. et al. DNA-driven condensation assembles the meiotic DNA break machinery. *Nature* **592**, 144–149 (2021).

34. 34.

Lukaszewicz, A., Lange, J., Keeney, S. & Jasins, M. De novo deletion mutations at recombination hotspots in mouse germlines. Preprint at <https://doi.org/10.1101/2020.06.23.168138> (2020).

35. 35.

Crawford, M., Cooper, T. J., Marsolier-Kergoat, M.-C., Llorente, B. & Neale, M. J. Separable roles of the DNA damage response kinase Mec1^{ATR} and its activator Rad24^{RAD17} within the regulation of meiotic recombination. Preprint at <https://doi.org/10.1101/496182> (2018).

36. 36.

Johnson, D., Allison, R. M., Cannavo, E., Cejka, P. & Neale, M. Removal of Spo11 from meiotic DNA breaks in vitro but not in vivo by tyrosyl DNA phosphodiesterase 2. Preprint at <https://doi.org/10.1101/527333> (2019).

37. 37.

Xu, L. & Kleckner, N. Sequence non-specific double-strand breaks and interhomolog interactions prior to double-strand break formation at a meiotic recombination hot spot in yeast. *EMBO J.* **14**, 5115–5128 (1995).

[CAS](#) [PubMed](#) [PubMed Central](#) [Google Scholar](#)

38. 38.

Kane, S. M. & Roth, R. Carbohydrate metabolism during ascospore development in yeast. *J. Bacteriol.* **118**, 8–14 (1974).

[CAS](#) [PubMed](#) [PubMed Central](#) [Google Scholar](#)

39. 39.

Cortes Ledesma, F., El Khamisy, S. F., Zuma, M. C., Osborn, K. & Caldecott, K. W. A human 5'-tyrosyl DNA phosphodiesterase that repairs topoisomerase-mediated DNA damage. *Nature* **461**, 674–678 (2009).

[ADS](#) [PubMed](#) [Google Scholar](#)

40. 40.

Cao, L., Alani, E. & Kleckner, N. A pathway for generation and processing of double-strand breaks during meiotic recombination in *S. cerevisiae*. *Cell* **61**, 1089–1101 (1990).

[CAS](#) [PubMed](#) [Google Scholar](#)

41. 41.

Alani, E., Padmore, R. & Kleckner, N. Analysis of wild-type and *rad50* mutants of yeast suggests an intimate relationship between meiotic chromosome synapsis and recombination. *Cell* **61**, 419–436 (1990).

[CAS](#) [PubMed](#) [Google Scholar](#)

42. 42.

Furuse, M. et al. Distinct roles of two separable in vitro activities of yeast Mre11 in mitotic and meiotic recombination. *EMBO J.* **17**, 6412–6425 (1998).

[CAS](#) [PubMed](#) [PubMed Central](#) [Google Scholar](#)

43. 43.

Moreau, S., Ferguson, J. R. & Symington, L. S. The nuclease activity of Mre11 is required for meiosis but not for mating type switching, end joining, or telomere maintenance. *Mol. Cell. Biol.* **19**, 556–566 (1999).

[CAS](#) [PubMed](#) [PubMed Central](#) [Google Scholar](#)

44. 44.

Blat, Y., Protacio, R. U., Hunter, N. & Kleckner, N. Physical and functional interactions among basic chromosome organizational features govern early steps of meiotic chiasma formation. *Cell* **111**, 791–802 (2002).

[CAS](#) [PubMed](#) [Google Scholar](#)

45. 45.

Acquaviva, L. et al. The COMPASS subunit Spp1 links histone methylation to initiation of meiotic recombination. *Science* **339**, 215–218 (2013).

[ADS](#) [CAS](#) [PubMed](#) [Google Scholar](#)

46. 46.

Sommermeyer, V., Béneut, C., Chaplais, E., Serrentino, M. E. & Borde, V. Spp1, a member of the Set1 complex, promotes meiotic DSB formation in promoters by tethering histone H3K4 methylation sites to chromosome axes. *Mol. Cell* **49**, 43–54 (2013).

[CAS](#) [PubMed](#) [Google Scholar](#)

[Download references](#)

Acknowledgements

We thank S. Yamada and N. Mohibullah for help accessing and analysing the mouse and yeast Spo11-oligo datasets, M.-C. Marsolier-Kergoat for sharing Python scripts, J. Carballo and M. Lichten for sharing *S. cerevisiae* strains containing relevant constructs (*tel1Δ::hphNT2* and *sae2Δ::kanMX6*, respectively), K. Caldecott and A. Oliver for sharing recombinant TDP2 and R. Allison for critical reading of the manuscript. D.J., V.G., T.C. and M.J.N. were supported by an ERC Consolidator Grant (311336), the BBSRC (BB/M010279/1), the Wellcome Trust (200843/Z/16/Z) and a Career Development Award from the Human Frontier Science Program (CDA00060/2010). B.L. and V.G. were supported by the ANR-13-BSV6-0012-01 and ANR-16-CE12-0028-01 grants from the Agence Nationale de la Recherche and a grant from the Fondation ARC pour la Recherche sur le Cancer (PJA20181207756). Work in the S.K. laboratory was supported by the Howard Hughes Medical Institute. Memorial Sloan Kettering core facilities are supported by grant P30 CA008748 from the National Institutes of Health.

Author information

Author notes

1. These authors contributed equally: Dominic Johnson, Margaret Crawford

Affiliations

1. Genome Damage and Stability Centre, University of Sussex, Brighton, UK

Dominic Johnson, Margaret Crawford, Tim Cooper, Valerie Garcia & Matthew J. Neale

2. Howard Hughes Medical Institute, Memorial Sloan Kettering Cancer Center, New York, NY, USA

Corentin Claeys Bouuaert & Scott Keeney

3. Louvain Institute of Biomolecular Science and Technology, Louvain-la-Neuve, Belgium

Corentin Claeys Bouuaert

4. Cancer Research Centre of Marseille, CNRS, Inserm, Institut Paoli-Calmettes, Aix-Marseille Université, Marseille, France

Bertrand Llorente & Valerie Garcia

Authors

1. Dominic Johnson

[View author publications](#)

You can also search for this author in [PubMed](#) [Google Scholar](#)

2. Margaret Crawford

[View author publications](#)

You can also search for this author in [PubMed](#) [Google Scholar](#)

3. Tim Cooper

[View author publications](#)

You can also search for this author in [PubMed](#) [Google Scholar](#)

4. Corentin Claeys Bouuaert

[View author publications](#)

You can also search for this author in [PubMed](#) [Google Scholar](#)

5. Scott Keeney

[View author publications](#)

You can also search for this author in [PubMed](#) [Google Scholar](#)

6. Bertrand Llorente

[View author publications](#)

You can also search for this author in [PubMed](#) [Google Scholar](#)

7. Valerie Garcia

[View author publications](#)

You can also search for this author in [PubMed](#) [Google Scholar](#)

8. Matthew J. Neale

[View author publications](#)

You can also search for this author in [PubMed](#) [Google Scholar](#)

Contributions

M.J.N. and V.G. conceived the project and prepared the manuscript. D.J., V.G., C.C.B. and M.J.N. performed physical analysis of Spo11-DCs. M.C. prepared and analysed whole-genome recombination maps with B.L. advising on mechanistic interpretation. T.C. and M.J.N. mapped and analysed Spo11-oligo library data. C.C.B. and S.K. contributed protein biochemistry and provided critical mechanistic interpretations. All authors helped to write the manuscript.

Corresponding authors

Correspondence to [Valerie Garcia](#) or [Matthew J. Neale](#).

Ethics declarations

Competing interests

The authors declare no competing interests.

Additional information

Peer review information *Nature* thanks Bernard de Massy and the other, anonymous, reviewer(s) for their contribution to the peer review of this work. Peer reviewer reports are available.

Publisher's note Springer Nature remains neutral with regard to jurisdictional claims in published maps and institutional affiliations.

Extended data figures and tables

[Extended Data Fig. 1 Spo11-DC sizing, quantification and genetic analysis.](#)

a–h, Immunoprecipitated *S. cerevisiae* Spo11-oligos and Spo11-DCs isolated from meiotic extracts of the indicated mutants (at 5 h, or indicated number of hours, after induction of meiosis) were radiolabelled with chain-terminating 3'-dATP using terminal transferase and separated on 19% denaturing PAGE following digestion with proteinase K. Where indicated, samples were also treated with mammalian TDP2³⁹, which removes the residual Spo11 peptide that is left after proteinase K treatment³⁶, thereby permitting accurate estimation of the Spo11-DC oligo length. In the absence of TDP2 digestion, the residual 5'-linked Spo11 peptide retards the migration of Spo11-oligos and Spo11-DCs by the equivalent of around 6–8 nt (**b–d, g**). A 10-nt ladder (also radiolabelled with 3'-dATP) is included

in each gel to permit accurate sizing. Spo11-DCs arose in *tel1Δ* cells in the presence and absence of *SAE2* (**a**, **b**, **h**). Spo11-DCs also arose independently of single or dual mutations in the MRX complex (*rad50S*, *mre11^{H125N}*, *mre11^{D56N}*) that abrogate endonuclease activity^{1,5,6,40,41,42,43} (**c**), and were abolished by homozygous mutation of the Spo11 active site (*spo11^{Y135F}*) (**d**). Loading normalization was not performed on samples in **c**, therefore differences in Spo11-DC abundance do not convey information. In **c**, **d**, Spo11-DCs were not treated with TDP2, leading to slower migration. In **e**, **f**, representative 4-h lane traces of sequencing gels shown in Fig. **1c** are shown using two modes of background subtraction (top and middle), with the resulting maximum, minimum and mid Spo11-DC quantifications (bottom). Shaded areas in top panels are the area being quantified. Shaded areas in lower quantification data show the range between maximum and minimum, as indicated in the figure. Quantified average mid-values are reported in Fig. **1d** (minimum–maximum range of 8–25%). Further quantification details are provided in Methods.

SPO11/spo11^{Y135F} heterozygous diploids (**g**) display an altered Spo11-DC oligo size distribution (biological duplicate lanes of each are presented alongside averaged intensity trace). **h**, Analysis of Spo11-oligo and Spo11-DC intermediates at hourly time points during meiotic prophase in the absence of Tell1.

Source data

Extended Data Fig. 2 Biased sequence composition around Spo11-DC 5' ends.

Spo11-oligos¹¹ isolated from the indicated *S. cerevisiae* strains were remapped using paired-end Bowtie2 alignment. **a**, Size distribution of total Spo11-oligos in wild-type and *tel1Δ* strains. Periodic peaks in the distribution are indicated, including a subtle shoulder at 33 nt, consistent with the Spo11-DC sizes detected on gels. **b**, Top, cartoon depicting Spo11 dimer staggered cuts; bottom, mean nucleotide composition surrounding the Spo11 cleavage site ([Methods](#)). Population-averaged features of Spo11 cleavage sites include preferred cleavage 3' to a C nucleotide and flanking A/T skews^{3,26}. **c–e**, Nucleotide composition of Spo11-oligos of the

indicated size was computed for each base position, revealing a Spo11 signature at both ends (**d**), or a Spo11 signature at the 5' end plus a Mre11 signature at the 3' end (**c, e**). **f–i**, Spo11-DCs were filtered out from total Spo11-oligo libraries based on overlapping molecules sharing 5' and 3' coordinates with a precise 2-nt offset (**f**). The theoretical dyad axis of each Spo11 dimer (at each end of the molecule) is indicated. Owing to the rotational symmetry of cleavage, the distance between such dyad axes is identical to the filtered oligo length. **g**, Ratio of filtered to total Spo11-oligos plotted as a function of molecule length. Because molecules of less than 30-nt length were not detected on Spo11-oligo gels in *sae2Δ*, we infer that the retention of some molecules that are smaller than 30 nt is due to the fortuitous artefactual overlap of canonical Spo11-oligos (around 27 nt). Such filtered molecules were therefore excluded from all bioinformatic analyses. **h**, The mean nucleotide composition of filtered Spo11-oligos of the indicated size (the sizes presented are peaks in the filtered size distribution) was computed for each base position and plotted relative to the inferred dyad axis of cleavage of the leftmost Spo11 DSB, revealing signature nucleotide skews characteristic of Spo11 at both the 5' and the 3' ends. No base skews were observed in the central regions of each molecule, arguing against a major influencer of Spo11-DC formation being localized DNA bending, which is expected to be favoured by an AT-rich base composition. **i**, The percentage of the total Spo11-oligo library in the filtered (Spo11-DC) fraction is plotted for the indicated size ranges. As defined, Spo11-DCs make up around 4.6% and 7.9% of the total pool of Spo11-oligos in wild-type and *tel1Δ* strains, respectively, consistent with the *tel1Δ*-dependent increase measured by our physical analysis. In absolute terms, these values are presumably lower than our gel-based estimates owing to size selection during library preparation, the stringency of the filtering, and inaccuracies in quantifying Spo11-DCs on gels, which we estimate make up less than 1% of the total cellular Spo11 protein ([Methods](#)). **j**, In vitro DNA mobility shift assay as described¹⁷. Spo11 core complex (Spo11, Rec102, Rec104 and Ski8) was incubated with dsDNA substrate of different lengths with a 2-nt TA overhang on both ends. On the basis of previous experiments¹⁷, the robust supershift observed at around 3 nM is interpreted to indicate double-end binding by the Spo11 core complex. Quantification is provided in Fig. [2d](#). Although the in vitro assay involves heterotetrameric Spo11 complexes (that is, a Spo11 core-complex

monomer), we assume that similar binding characteristics will take place in vivo involving octameric complexes (that is, Spo11 core-complex dimers).

[Source data](#)

Extended Data Fig. 3 Spo11-DC composition of *S. cerevisiae* DSB hotspots in wild-type and *tel1Δ* yeast.

a, Percentage of total Spo11-oligos and filtered Spo11-DCs that arise within annotated DSB hotspots. Overall, nearly all (95%) of the Spo11-DCs map within hotspots—more so than total Spo11-oligos (86%)—suggesting that Spo11-DCs are more prevalent where Spo11 activity is strongest. **b**, Percentage of total Spo11-oligos that are Spo11-DCs, plotted for every hotspot ($n = 3,910$). Although the proportion of Spo11-DCs within each hotspot varied widely from less than 0.1% to more than 10% of the Spo11-oligo signal, the majority (86%) of hotspots displayed a Spo11-DC proportion of at least 1%, and about one fifth (18%) of hotspots displayed a Spo11-DC proportion of over 5%. In *tel1Δ*, the fraction of hotspots falling into these categories increased to 94% and 47%, respectively, consistent with the median fraction of Spo11-DCs per hotspot being about 1.7-fold greater. P value by two-tailed Kruskal–Wallis H -test. **c, d**, Quantitative correlation between filtered Spo11-DC frequency (**c**), or percentage of Spo11-DCs within each hotspot (**d**), and total Spo11-oligo frequency for all DSB hotspots, in wild-type (left) and *tel1Δ* (right) yeast. Although Spo11-DC frequency correlated positively with total Spo11-oligo counts, the relationship was nonlinear, such that Spo11-DCs were observed disproportionately more frequently within the strongest hotspots. **e**, Comparison between *tel1Δ* and wild type of the percentage of total Spo11-oligo signal within each hotspot that is classified as a Spo11-DC. These ratios are stratified on the x axis by the Spo11-DC frequency in wild-type cells, and ratios are coloured to indicate those hotspots in which the proportion of Spo11-DCs is at least twofold increased (red) or twofold decreased (blue) in *tel1Δ* relative to wild type. Although Spo11-DCs were globally more frequent in *tel1Δ* compared to wild type, this relationship was not uniform across all hotspots.

Extended Data Fig. 4 Fine-scale patterns of *S. cerevisiae* Spo11-DCs within DSB hotspots.

a, Spo11-DC arcs link the 5' ends of overlapping Franklin- and Rosalind-strand filtered reads. For all bioinformatic analyses, only overlapping read pairs of lengths greater than 30 nt are considered because this is the minimum length of Spo11-DCs detected physically (Fig. 1c). We believe that enrichment of some shorter overlapping pairs arises from the artefactual overlap of canonical oligos (less than 30-nt length) within dense hotspot regions. **b–e**, Arc diagram depiction of Spo11-DCs mapped across example hotspots encompassing strong (**b**), narrow (**c**), and wide (**d**) classes, presented as in Fig. 2e,f. Top, unfiltered strand-specific Spo11-oligos (Franklin strand, red; Rosalind strand, blue). Arcs (grey-scale-frequency-weighted) link the 5' ends of each Spo11-DC. Bottom, smoothed unfiltered strand-specific Spo11-oligos, overlaid with frequency histograms of Spo11-DC midpoints (grey). The left flanks of Spo11-DC peaks are enriched for Franklin-strand hits, whereas the right flanks are enriched for Rosalind-strand hits. This relationship was visualized most easily at narrow, low-frequency hotspots in which the patterns of Spo11-DCs were less complex. In **e**, wild-type and *tel1Δ* data are compared for the same hotspots. Although *TEL1* deletion does have subtle effects on the pattern and abundance of both Spo11-oligos and Spo11-DCs, it did not alter the asymmetric pattern of Spo11-oligo strand disparity that is associated with regions of preferential Spo11-DC formation. In all plotted Spo11-oligo and Spo11-DC maps, Rosalind-strand signals are shifted by 1 bp to the left so that differences between the abundance of F- and R-mapping reads at individual cleavage sites can be more directly compared.

Extended Data Fig. 5 Global analysis of strand disparities at Spo11-DC termini in *S. cerevisiae* wild-type and *tel1Δ* cells.

a, Explanatory cartoon for the calculation of Spo11-DC strand ratio and strand-ratio differential (left/right). See [Methods](#) for further details. **b–g**, Strand ratios of Spo11-oligos at Spo11-DC sites in wild-type (**b**, **c**) and *tel1Δ* (**d–g**) cells. Average strand-specific Spo11-oligo signal (**b**, **f**), and strand ratio (**c**, **g**), centred on the strongest Spo11-DC midpoint within

every DSB hotspot ($n = 3,910$). Strand ratio (Franklin/Rosalind total Spo11-oligo HPM) was computed at the left and right 5' end of every unique Spo11-DC molecule (**a**), stratified by length. Strand-ratio differential (**c, g**) indicates the fold difference in the ratios when comparing the left and right 5' ends of each Spo11-DC molecule. The relationships described above were unchanged after *TEL1* deletion, suggesting that the Spo11-oligo patterns are an intrinsic feature of sites at which Spo11-DCs are generated, and are not subject to regulation by Tel1. **h**, Explanatory cartoon for strand-ratio calculation for all Spo11-oligos. **i, j**, Strand ratio (Franklin/Rosalind total Spo11-oligo HPM) was computed at the 5' end of all observed (unfiltered) Franklin- or Rosalind-strand Spo11-oligos (**h**). Unlike at Spo11-DC sites (**b, f**), bulk Spo11-oligos, across all sites, display no net strand disparity in either wild-type (**i**) or *tel1Δ* (**j**) strains. In all plotted Spo11-oligo and Spo11-DC maps, Rosalind-strand signals are shifted by 1 bp to the left so that differences between the abundance of Franklin- and Rosalind-mapping reads at individual cleavage sites can be more directly compared. When considering all Spo11-oligo sites (**h–j**), some degree of strand disparity is a feature of most Spo11-oligo sites (it is a continuum of skew in both directions—some sites are skewed towards Franklin, some towards Rosalind, and some have little or no skew), but, when considered in aggregate, bulk Spo11-oligo sites have no net skew towards Franklin or Rosalind regardless of which strand the Spo11-oligo is considered. By contrast, sites at which we detect Spo11-DC formation (**a–g**; which is only a subset of all the sites onto which Spo11-oligos are mapped) display an asymmetric average skew within the total Spo11-oligo Franklin and Rosalind reads, with the left end of Spo11-DCs being sites at which the total Spo11-oligo pool is skewed towards Franklin and the right end sites at which the total Spo11-oligo pool is skewed towards Rosalind. Notably, this analysis uses the total Spo11-oligo pool, not just Spo11-DC molecules. Thus, the pattern of skews is a global feature of the entire Spo11-oligo pool at sites that form Spo11-DCs, and is not a feature that is observed at all Spo11-oligo sites. We interpret these observations to mean that sites at which Spo11-DCs form are different, being disproportionately sites of biased strand disparity. Owing to their low abundance at any particular site, removing Spo11-DCs from the total pool of Franklin and Rosalind reads has no effect on the strand disparity observed. Finally, consistent with these interpretations, we have found that the degree of disparity at any given site

is not predictive of Spo11-DC abundance at that site, further indicating that Spo11-DC formation is not the cause of the disparity. Instead, locations of strand disparity and Spo11-DC are correlated in position, probably because they are influenced by similar properties of DSB hotspots (that is, a proposed Spo11 platform) (Fig. 4). Thus, overall, we conclude that asymmetric strand disparity is not unique to specific hotspots, nor to specific mutants, nor caused by Spo11-DCs, but is, instead, an intrinsic feature of the meiotic recombination process that informs the mechanism of Spo11-DSB formation.

Extended Data Fig. 6 Fine-scale analysis of SPO11-DCs within mouse DSB hotspots.

Mouse SPO11-oligo libraries⁴ were remapped using paired-end Bowtie2 alignment. **a, b**, SPO11-oligo length distribution of the entire library (**a**), or after applying the 2-bp overlap filter (**b**) as in upper cartoon in Fig. 2a. Filtering was less efficient than in yeast ([Methods](#)), retaining numerous molecules of less than 30-nt length that, based on our analysis in yeast, are likely to be a filtering artefact. Therefore, as for *S. cerevisiae*, SPO11-DCs are defined as filtered molecules of greater than 30 nt in length. Filtering retains weak peaks in *Atm*^{−/−} that display an approximately 10-bp periodicity. **c**, Percentage of total SPO11-oligos that are SPO11-DCs on the basis of overlap filtering, plotted for every hotspot in which filtered Spo11-DCs were detected ($n = 1,831$ in wild-type mice; $n = 8,010$ in *Atm*^{−/−} mice). *P* value by two-tailed Kruskal–Wallis *H*-test. **d**, Total *Atm*^{−/−} SPO11-oligos were filtered into two size classes then aggregated around approximately 21,000 hotspot centres revealing a strand-specific disparity for SPO11-oligos greater than 30 nt. **e–h**, Representative arc diagrams of SPO11-DCs (grey-scale-frequency-weighted arcs) in wild-type and *Atm*^{−/−} mice at four different hotspots in chromosomes 11 (**e**), 10 (**f**), 8 (**g**) and 5 (**h**) relative to total strand-specific SPO11-oligos (top, raw; bottom, smoothed; red, Franklin strand; blue, Rosalind strand). The percentage of total SPO11-oligos that are SPO11-DCs is indicated. Unlike in *Atm*^{−/−} mice, SPO11-DCs in wild-type mice often did not coincide with strong SPO11-oligo signals, suggesting that some may arise from additional artefacts of the filtering.

Extended Data Fig. 7 Categorization of *S. cerevisiae* meiotic recombination events containing short 6:2 segments.

a, Summary of the frequency of each subclassification event type for the indicated strains. Only events containing 6:2 segments of 30 to 150 bp in length were considered. Category-A events are compatible with gap repair because flanking heteroduplex DNA patterns are in *trans* orientation, whereas category B events are incompatible because the flanking heteroduplex DNA patterns are in *cis* orientation. Category-C events lack the flanking heteroduplex DNA patterns necessary to assign the event. Events were separated into those with a single or multiple such 6:2 segments. Fractions of total events for each subtype were not calculated for multi events because they frequently contain more than one sub-type. **b–g**, Example event sub-classifications. Genotype calls were made at each marker (vertical line). Adjacent segments of the same genotype are joined with horizontal bars (red or blue) to aid visualization of patterns. Each horizontal bar is a sequenced haplotype from one meiotic octad. 6:2 segments are indicated in pale blue. Event limits are indicated by beige (crossover) or pink (noncrossover) bars. Orientation of 5' and 3' strands are indicated in instances in which it was possible to obtain phasing information from noncrossover *trans* events within the event, or from events elsewhere in the octad (see [Methods](#) for further details). In **c**, a second segment of 6:2 segregation was not considered because the minimum length is more than 1.2 kb. **h**, Relationship between Spo11-DC size and the probability of it overlapping at least one SNP. To estimate probable detection rates of theoretical Spo11-DCs of varying size, sliding windows of increasing size were moved across the reference genome, and the number of genetic markers within each window was recorded for each position. As examples, on average, Spo11-DCs of 30 bp and 150 bp in size will be detected only 15% and 50% of the time, respectively. Owing to the non-uniform distribution of both Spo11 DSBs and genetic markers—in particular the slightly greater density of polymorphisms within intergenic regions in which Spo11 DSBs most often arise—the probability of detection may be slightly greater than that estimated from the genome-wide polymorphism density. **i**, Quantification of recombination event types in *tel1Δmsh2Δ* based on categories presented in Fig. [3b,c](#). Relative proportions of category A–C were unchanged when compared to wild type,

but a greater number of events containing 6:2 segments of greater than 150 bp were observed. **j**, **k**, \log_2 -transformed ratio of observed Spo11-oligo (**j**) or Spo11-DC (**k**) density within each 6:2 segment divided by the Spo11-oligo or Spo11-DC density within the entire event, in $msh2\Delta$, for each category. Although these analyses broadly agree with each other, the absence of Spo11-DCs in many of the category-B and -C segments prevented their analysis, artefactually inflating both their global ratio and decreasing the difference when compared to category A (which overlaps with both Spo11-oligos and Spo11-DCs). **l–n**, *TEL1* deletion has no effect on the association between recombination patterns containing 6:2 segments and Spo11-DSB activity. **l**, Fraction of 6:2 segments overlapping hotspots in $tel1\Delta msh2\Delta$, as for Fig. 3f. **m**, \log_2 ratio of observed Spo11-oligo density within each 6:2 segment divided by the Spo11-oligo density within the entire event, in $tel1\Delta msh2\Delta$, for each category, as for **j**. Unlike deletion of *MLH1*, *MLH3* and *EXO1* (Fig. 3e), deletion of *TEL1* had no effect on the relative frequencies of 6:2 segments within categories A–C (**n**). In (**j**, **k**, **m**), *P* values by two-tailed Kruskal–Wallis *H*-test. Individual data points are shown overlaid with box indicating median plus first and third quartiles, and whiskers indicating 1.5 \times the interquartile range. In **l**, **n**, whiskers indicate 95% confidence intervals. In **l**, *P* value by two-tailed Z-test of proportions. In **i**, **l**, **m**, 2,159 events were analysed across 10 biologically independent meiotic samples. In **j**, **k**, 1,643 events were analysed across 9 biologically independent meiotic samples.

[Extended Data Fig. 8 Cartoon to explain mapped strand disparity and Tel1-insensitive Spo11-DC formation.](#)

a, Model to account for observed strand bias. Mre11-dependent 3'→5' exonuclease activity is shown relative to the covalent attachment of Spo11 to 5' DNA ends. We hypothesize that Spo11-oligos and Spo11-DCs that formed within the axis-associated Spo11 platform (grey area) are protected from Mre11 nuclease activity and are therefore efficiently mapped (long Spo11-oligos), whereas efficient resection in the flanking regions leads to shorter Spo11-oligos that are not mapped. We assume that because the position and frequency of such hotspot–axis interactions will vary from one hotspot to another—and from one cell to another—this will contribute to

the substantial variations in position and abundance of both Spo11-oligos and Spo11-DCs within hotspot regions. Although it is formally possible that the disparity can alternatively arise from less (rather than more) efficient resection flanking the platform area—leading to unprocessed DSB ends, and thereby a paucity of Spo11-oligo reads in these locations—we consider this unlikely because it would require there to be a high frequency of persistent unresected DSBs, something which is not observed in wild-type cells. **b**, In *S. cerevisiae*, Tel1 has no greater effect on Spo11-DC formation than on global DSB formation (Fig. 1d), yet efficiently inhibits DSB formation between adjacent hotspots¹⁰. Therefore, we propose that DSBs arise concordantly within a DSB-active hotspot region (top cartoon)—creating Spo11-DCs—before Tel1 can act to inhibit their formation. Such hotspot activation is likely to arise through the proposed tethering of nucleosome-depleted hotspot DNA to the pro-DSB axis components^{28,44,45,46} (bottom). These interactions will enable the formation of both single Spo11 DSBs and/or Spo11-DCs at the tethered locus, either of which will cause Tel1 activation. Once activated, Tel1 inhibits DSB formation at hotspots within the rest of the tethered loop¹⁰, and at any axis-associated DSB hotspots within adjacent loop regions. Such inhibition may arise through direct inhibition and/or destabilization of Spo11 and/or other pro-DSB axis components such as Rec114–Mer2–Mei4 (RMM), and/or inhibition of hotspot–axis interactions^{10,11,15}.

Extended Data Table 1 Strains used in this study

[Full size table](#)

Supplementary information

[Reporting Summary](#)

[Peer Review File](#)

[Supplementary Data](#)

This file contains Supplementary Data.

Source data

[Source Data Fig. 1](#)

[Source Data Extended Data Fig. 1](#)

[Source Data Extended Data Fig. 2](#)

Rights and permissions

[Reprints and Permissions](#)

About this article



Check for
updates

Cite this article

Johnson, D., Crawford, M., Cooper, T. *et al.* Concerted cutting by Spo11 illuminates meiotic DNA break mechanics. *Nature* **594**, 572–576 (2021). <https://doi.org/10.1038/s41586-021-03389-3>

[Download citation](#)

- Received: 06 March 2020
- Accepted: 24 February 2021
- Published: 09 June 2021
- Issue Date: 24 June 2021
- DOI: <https://doi.org/10.1038/s41586-021-03389-3>

Comments

By submitting a comment you agree to abide by our [Terms](#) and [Community Guidelines](#). If you find something abusive or that does not comply with our terms or guidelines please flag it as inappropriate.

[Access through your institution](#)

[Change institution](#)

[Buy or subscribe](#)

Advertisement

This article was downloaded by **calibre** from <https://www.nature.com/articles/s41586-021-03389-3>

| [Section menu](#) | [Main menu](#) |

- Article
- [Published: 09 June 2021](#)

Spo11 generates gaps through concerted cuts at sites of topological stress

- [Silvia Prieler¹ na1](#),
- [Doris Chen](#) [ORCID: orcid.org/0000-0001-8835-0280¹ na1](#),
- [Lingzhi Huang¹](#),
- [Elisa Mayrhofer](#) [ORCID: orcid.org/0000-0002-4613-8131¹ nAff2](#),
- [Soma Zsótér¹ nAff3](#),
- [Magdalena Vesely¹](#),
- [Jean Mbognning¹ nAff4](#) &
- [Franz Klein](#) [ORCID: orcid.org/0000-0001-7204-1432¹](#)

[Nature](#) volume 594, pages 577–582 (2021) [Cite this article](#)

- 2819 Accesses
- 1 Citations
- 134 Altmetric
- [Metrics details](#)

Subjects

- [Chromatin immunoprecipitation](#)
- [DNA recombination](#)
- [Eukaryote](#)

- [Meiosis](#)

Abstract

Meiotic recombination is essential for chromosome segregation at meiosis and fertility. It is initiated by programmed DNA double-strand breaks (DSBs) introduced by Spo11, a eukaryotic homologue of an archaeal topoisomerase (Topo VIA)¹. Here we describe previously uncharacterized Spo11-induced lesions, 34 to several hundred base pair-long gaps, which are generated by coordinated pairs of DSBs termed double DSBs. Isolation and genome-wide mapping of the resulting fragments with single base-pair precision revealed enrichment at DSB hotspots but also a widely dispersed distribution across the genome. Spo11 prefers to cut sequences with similarity to a DNA-bending motif², which indicates that bendability contributes to the choice of cleavage site. Moreover, fragment lengths have a periodicity of approximately $(10.4n + 3)$ base pairs, which indicates that Spo11 favours cleavage on the same face of underwound DNA. Consistently, double DSB signals overlap and correlate with topoisomerase II-binding sites, which points to a role for topological stress and DNA crossings in break formation, and suggests a model for the formation of DSBs and double DSBs in which Spo11 traps two DNA strands. Double DSB gaps, which make up an estimated 20% of all initiation events, can account for full gene conversion events that are independent of both Msh2-dependent heteroduplex repair^{3,4} and the MutL γ endonuclease⁴. Because non-homologous gap repair results in deletions, and ectopically re-integrated double DSB fragments result in insertions, the formation of double DSBs is a potential source of evolutionary diversity and pathogenic germline aberrations.

Access options

Subscribe to Journal

Get full journal access for 1 year

\$199.00

only \$3.90 per issue

[Subscribe](#)

All prices are NET prices.

VAT will be added later in the checkout.

Tax calculation will be finalised during checkout.

Rent or Buy article

Get time limited or full article access on ReadCube.

from \$8.99

[Rent or Buy](#)

All prices are NET prices.

Additional access options:

- [Log in](#)
- [Access through your institution](#)
- [Learn about institutional subscriptions](#)

Fig. 1: Discovery and characterization of chromosomal fragments formed by closely spaced meiotic DSBs.

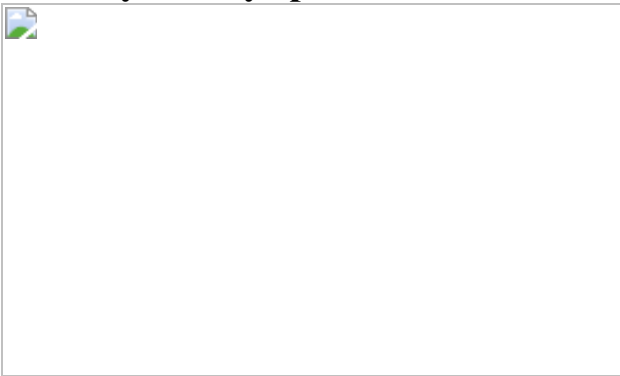


Fig. 2: Spo11 prefers a DNA-bending motif at periodic distances.

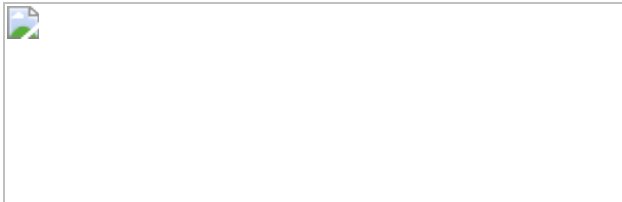
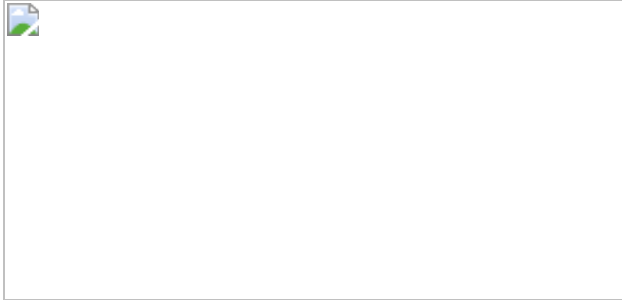


Fig. 3: Overlap and correlation of (d)DSB signals with Top2 peaks.



Fig. 4: Gaps at sites of Msh2/MutL γ -independent full gene conversions.



Data availability

Protec-seq and ChIP-seq data have been deposited in the Gene Expression Omnibus (GEO) database as [GSE171046](#) SuperSeries, with SubSeries [GSE171042](#) (dDSB) and [GSE169760](#) (Top2). [Source data](#) are provided with this paper.

Code availability

Essential scripts are available at GitHub repository
https://github.com/FranzKlein-lab/dDSB_tools.

References

1. 1.

Bergerat, A. et al. An atypical topoisomerase II from Archaea with implications for meiotic recombination. *Nature* **386**, 414–417 (1997).

[ADS](#) [CAS](#) [PubMed](#) [Google Scholar](#)

2. 2.

El-Deiry, W. S., Kern, S. E., Pietenpol, J. A., Kinzler, K. W. & Vogelstein, B. Definition of a consensus binding site for p53. *Nat. Genet.* **1**, 45–49 (1992).

[CAS](#) [PubMed](#) [Google Scholar](#)

3. 3.

Martini, E. et al. Genome-wide analysis of heteroduplex DNA in mismatch repair-deficient yeast cells reveals novel properties of meiotic recombination pathways. *PLoS Genet.* **7**, e1002305 (2011).

[CAS](#) [PubMed](#) [PubMed Central](#) [Google Scholar](#)

4. 4.

Marsolier-Kergoat, M. C., Khan, M. M., Schott, J., Zhu, X. & Llorente, B. Mechanistic view and genetic control of DNA recombination during meiosis. *Mol. Cell* **70**, 9–20 (2018).

[CAS](#) [PubMed](#) [Google Scholar](#)

5. 5.

Keeney, S., Giroux, C. N. & Kleckner, N. Meiosis-specific DNA double-strand breaks are catalyzed by Spo11, a member of a widely conserved protein family. *Cell* **88**, 375–384 (1997).

[CAS](#) [PubMed](#) [Google Scholar](#)

6. 6.

Robert, T. et al. The TopoVIB-like protein family is required for meiotic DNA double-strand break formation. *Science* **351**, 943–949 (2016).

[ADS](#) [CAS](#) [PubMed](#) [Google Scholar](#)

7. 7.

Vrielynck, N. et al. A DNA topoisomerase VI-like complex initiates meiotic recombination. *Science* **351**, 939–943 (2016).

[ADS](#) [CAS](#) [PubMed](#) [Google Scholar](#)

8. 8.

Liu, J., Wu, T. C. & Lichten, M. The location and structure of double-strand DNA breaks induced during yeast meiosis: evidence for a covalently linked DNA-protein intermediate. *EMBO J.* **14**, 4599–4608 (1995).

[CAS](#) [PubMed](#) [PubMed Central](#) [Google Scholar](#)

9. 9.

Keeney, S. & Kleckner, N. Covalent protein-DNA complexes at the 5' strand termini of meiosis-specific double-strand breaks in yeast. *Proc. Natl Acad. Sci. USA* **92**, 11274–11278 (1995).

[ADS](#) [CAS](#) [PubMed](#) [PubMed Central](#) [Google Scholar](#)

10. 10.

Neale, M. J., Pan, J. & Keeney, S. Endonucleolytic processing of covalent protein-linked DNA double-strand breaks. *Nature* **436**, 1053–1057 (2005).

[ADS](#) [CAS](#) [PubMed](#) [PubMed Central](#) [Google Scholar](#)

11. 11.

Hunter, N. in *Homologous recombination* (eds Aguilera, A. & Rotshtein, R.) 1–62 (Springer-Verlag, 2007).

12. 12.

Mimitou, E. P., Yamada, S. & Keeney, S. A global view of meiotic double-strand break end resection. *Science* **355**, 40–45 (2017).

[ADS](#) [CAS](#) [PubMed](#) [PubMed Central](#) [Google Scholar](#)

13. 13.

Pan, J. et al. A hierarchical combination of factors shapes the genome-wide topography of yeast meiotic recombination initiation. *Cell* **144**, 719–731 (2011).

[CAS](#) [PubMed](#) [PubMed Central](#) [Google Scholar](#)

14. 14.

Lichten, M. & Goldman, A. S. Meiotic recombination hotspots. *Annu. Rev. Genet.* **29**, 423–444 (1995).

[CAS](#) [PubMed](#) [Google Scholar](#)

15. 15.

Mohibullah, N. & Keeney, S. Numerical and spatial patterning of yeast meiotic DNA breaks by Tel1. *Genome Res.* **27**, 278–288 (2017).

[CAS](#) [PubMed](#) [PubMed Central](#) [Google Scholar](#)

16. 16.

Borde, V. et al. Histone H3 lysine 4 trimethylation marks meiotic recombination initiation sites. *EMBO J.* **28**, 99–111 (2009).

[CAS](#) [PubMed](#) [Google Scholar](#)

17. 17.

Zhu, X. & Keeney, S. High-resolution global analysis of the influences of bas1 and ino4 transcription factors on meiotic DNA break distributions in *Saccharomyces cerevisiae*. *Genetics* **201**, 525–542 (2015).

[CAS](#) [PubMed](#) [PubMed Central](#) [Google Scholar](#)

18. 18.

Sommermeyer, V., Beneut, C., Chaplais, E., Serrentino, M. E. & Borde, V. Spp1, a member of the set1 complex, promotes meiotic dsb formation in promoters by tethering histone h3k4 methylation sites to chromosome axes. *Mol. Cell* **49**, 43–54 (2012).

[PubMed](#) [Google Scholar](#)

19. 19.

Lichten, M. Meiotic chromatin: the substrate for recombination initiation. *Genome Dyn. Stab.* **3**, 165–128 (2008).

[Google Scholar](#)

20. 20.

Buhler, C., Borde, V. & Lichten, M. Mapping meiotic single-strand DNA reveals a new landscape of DNA double-strand breaks in *Saccharomyces cerevisiae*. *PLoS Biol.* **5**, e324 (2007).

[PubMed](#) [PubMed Central](#) [Google Scholar](#)

21. 21.

Garcia, V., Gray, S., Allison, R. M., Cooper, T. J. & Neale, M. J. Tel1(ATM)-mediated interference suppresses clustered meiotic double-strand-break formation. *Nature* **520**, 114–118 (2015).

[ADS](#) [CAS](#) [PubMed](#) [PubMed Central](#) [Google Scholar](#)

22. 22.

Zhang, L., Kim, K. P., Kleckner, N. E. & Storlazzi, A. Meiotic double-strand breaks occur once per pair of (sister) chromatids and, via Mec1/ATR and Tel1/ATM, once per quartet of chromatids. *Proc. Natl Acad. Sci. USA* **108**, 20036–20041 (2011).

[ADS](#) [CAS](#) [PubMed](#) [PubMed Central](#) [Google Scholar](#)

23. 23.

Wu, T. C. & Lichten, M. Factors that affect the location and frequency of meiosis-induced double-strand breaks in *Saccharomyces cerevisiae*. *Genetics* **140**, 55–66 (1995).

[CAS](#) [PubMed](#) [PubMed Central](#) [Google Scholar](#)

24. 24.

Fan, Q. Q., Xu, F., White, M. A. & Petes, T. D. Competition between adjacent meiotic recombination hotspots in the yeast *Saccharomyces cerevisiae*. *Genetics* **145**, 661–670 (1997).

[CAS](#) [PubMed](#) [PubMed Central](#) [Google Scholar](#)

25. 25.

Xu, L. & Kleckner, N. Sequence non-specific double-strand breaks and interhomolog interactions prior to double-strand break formation at a meiotic recombination hot spot in yeast. *EMBO J.* **14**, 5115–5128 (1995).

[CAS](#) [PubMed](#) [PubMed Central](#) [Google Scholar](#)

26. 26.

Ohta, K., Wu, T. C., Lichten, M. & Shibata, T. Competitive inactivation of a double-strand DNA break site involves parallel

suppression of meiosis-induced changes in chromatin configuration. *Nucleic Acids Res.* **27**, 2175–2180 (1999).

[CAS](#) [PubMed](#) [PubMed Central](#) [Google Scholar](#)

27. 27.

McKie, S. J., Maxwell, A. & Neuman, K. C. Mapping DNA topoisomerase binding and cleavage genome wide using next-generation sequencing techniques. *Genes (Basel)* **11**, E92 (2020).

[Google Scholar](#)

28. 28.

Spitzner, J. R. & Muller, M. T. A consensus sequence for cleavage by vertebrate DNA topoisomerase II. *Nucleic Acids Res.* **16**, 5533–5556 (1988).

[CAS](#) [PubMed](#) [PubMed Central](#) [Google Scholar](#)

29. 29.

Buhler, C., Lebbink, J. H., Bocs, C., Ladenstein, R. & Forterre, P. DNA topoisomerase VI generates ATP-dependent double-strand breaks with two-nucleotide overhangs. *J. Biol. Chem.* **276**, 37215–37222 (2001).

[CAS](#) [PubMed](#) [Google Scholar](#)

30. 30.

Gittens, W. H. et al. A nucleotide resolution map of Top2-linked DNA breaks in the yeast and human genome. *Nat. Commun.* **10**, 4846 (2019).

[ADS](#) [PubMed](#) [PubMed Central](#) [Google Scholar](#)

31. 31.

Jang, Y. et al. Selection of DNA cleavage sites by topoisomerase II results from enzyme-induced flexibility of DNA. *Cell Chem. Biol.* **26**, 502–511 (2019).

[CAS](#) [PubMed](#) [PubMed Central](#) [Google Scholar](#)

32. 32.

Murakami, H. & Nicolas, A. Locally, meiotic double-strand breaks targeted by Gal4BD-Spo11 occur at discrete sites with a sequence preference. *Mol. Cell. Biol.* **29**, 3500–3516 (2009).

[CAS](#) [PubMed](#) [PubMed Central](#) [Google Scholar](#)

33. 33.

Claeys Bouuaert, C. et al. Structural and functional characterization of the Spo11 core complex. *Nat. Struct. Mol. Biol.* **28**, 92–102 (2021).

[CAS](#) [PubMed](#) [Google Scholar](#)

34. 34.

Tokino, T. et al. p53 tagged sites from human genomic DNA. *Hum. Mol. Genet.* **3**, 1537–1542 (1994).

[CAS](#) [PubMed](#) [Google Scholar](#)

35. 35.

Nagaich, A. K. et al. p53-induced DNA bending and twisting: p53 tetramer binds on the outer side of a DNA loop and increases DNA twisting. *Proc. Natl Acad. Sci. USA* **96**, 1875–1880 (1999).

[ADS](#) [CAS](#) [PubMed](#) [PubMed Central](#) [Google Scholar](#)

36. 36.

Lam, I. & Keeney, S. Nonparadoxical evolutionary stability of the recombination initiation landscape in yeast. *Science* **350**, 932–937 (2015).

[CAS](#) [PubMed](#) [PubMed Central](#) [Google Scholar](#)

37. 37.

Carballo, J. A. et al. Budding yeast ATM/ATR control meiotic double-strand break (DSB) levels by down-regulating Rec114, an essential component of the DSB-machinery. *PLoS Genet.* **9**, e1003545 (2013).

[CAS](#) [PubMed](#) [PubMed Central](#) [Google Scholar](#)

38. 38.

Hu, B. et al. Biological chromodynamics: a general method for measuring protein occupancy across the genome by calibrating ChIP-seq. *Nucleic Acids Res.* **43**, e132 (2015).

[PubMed](#) [PubMed Central](#) [Google Scholar](#)

39. 39.

Liu, L. F. & Wang, J. C. Supercoiling of the DNA template during transcription. *Proc. Natl Acad. Sci. USA* **84**, 7024–7027 (1987).

[ADS](#) [CAS](#) [PubMed](#) [PubMed Central](#) [Google Scholar](#)

40. 40.

Achar, Y. J., Adhil, M., Choudhary, R., Gilbert, N. & Foiani, M. Negative supercoil at gene boundaries modulates gene topology. *Nature* **577**, 701–705 (2020).

[ADS](#) [CAS](#) [PubMed](#) [Google Scholar](#)

41. 41.

Wendorff, T. J. & Berger, J. M. Topoisomerase VI senses and exploits both DNA crossings and bends to facilitate strand passage. *eLife* **7**, e31724 (2018).

[PubMed](#) [PubMed Central](#) [Google Scholar](#)

42. 42.

Zechiedrich, E. L. & Osheroff, N. Eukaryotic topoisomerases recognize nucleic acid topology by preferentially interacting with DNA crossovers. *EMBO J.* **9**, 4555–4562 (1990).

[CAS](#) [PubMed](#) [PubMed Central](#) [Google Scholar](#)

43. 43.

Heldrich, J., Sun, X., Vale-Silva, L. A., Markowitz, T. E. & Hochwagen, A. Topoisomerases modulate the timing of meiotic DNA breakage and chromosome morphogenesis in *Saccharomyces cerevisiae*. *Genetics* **215**, 59–73 (2020).

[CAS](#) [PubMed](#) [PubMed Central](#) [Google Scholar](#)

44. 44.

Schwacha, A. & Kleckner, N. Interhomolog bias during meiotic recombination: meiotic functions promote a highly differentiated interhomolog-only pathway. *Cell* **90**, 1123–1135 (1997).

[CAS](#) [PubMed](#) [Google Scholar](#)

45. 45.

Johnson, D. et al. Concerted cutting by Spo11 illuminates meiotic DNA break mechanics. *Nature* <https://doi.org/10.1038/s41586-021-03389-3> (2021).

46. 46.

Fowler, K. R., Sasaki, M., Milman, N., Keeney, S. & Smith, G. R. Evolutionarily diverse determinants of meiotic DNA break and recombination landscapes across the genome. *Genome Res.* **24**, 1650–1664 (2014).

[CAS](#) [PubMed](#) [PubMed Central](#) [Google Scholar](#)

47. 47.

Tiemann-Boege, I., Schwarz, T., Striedner, Y. & Heissl, A. The consequences of sequence erosion in the evolution of recombination hotspots. *Phil. Trans. R. Soc. Lond. B* **372**, 20160462 (2017).

[Google Scholar](#)

48. 48.

Lukaszewicz, A., Lange, J., Keeney, S. & Jasins, M. De novo deletion mutations at recombination hotspots in mouse germlines. Preprint at <https://doi.org/10.1101/2020.06.23.168138> (2020).

49. 49.

Xaver, M., Huang, L., Chen, D. & Klein, F. Smc5/6-Mms21 prevents and eliminates inappropriate recombination intermediates in meiosis. *PLoS Genet.* **9**, e1004067 (2013).

[PubMed](#) [PubMed Central](#) [Google Scholar](#)

50. 50.

Gao, R. et al. Proteolytic degradation of topoisomerase II (Top2) enables the processing of Top2-DNA and Top2-RNA covalent complexes by tyrosyl-DNA-phosphodiesterase 2 (TDP2). *J. Biol. Chem.* **289**, 17960–17969 (2014).

[CAS](#) [PubMed](#) [PubMed Central](#) [Google Scholar](#)

51. 51.

Cortes Ledesma, F., El Khamisy, S. F., Zuma, M. C., Osborn, K. & Caldecott, K. W. A human 5'-tyrosyl DNA phosphodiesterase that repairs topoisomerase-mediated DNA damage. *Nature* **461**, 674–678 (2009).

[ADS](#) [PubMed](#) [Google Scholar](#)

52. 52.

Mendoza, M. A., Panizza, S. & Klein, F. Analysis of protein-DNA interactions during meiosis by quantitative chromatin immunoprecipitation (qChIP). *Methods Mol. Biol.* **557**, 267–283 (2009).

[CAS](#) [PubMed](#) [Google Scholar](#)

53. 53.

Haruki, H., Nishikawa, J. & Laemmli, U. K. The anchor-away technique: rapid, conditional establishment of yeast mutant phenotypes. *Mol. Cell* **31**, 925–932 (2008).

[CAS](#) [PubMed](#) [Google Scholar](#)

54. 54.

Yue, J. X. et al. Contrasting evolutionary genome dynamics between domesticated and wild yeasts. *Nat. Genet.* **49**, 913–924 (2017).

[CAS](#) [PubMed](#) [PubMed Central](#) [Google Scholar](#)

55. 55.

Sedlazeck, F. J., Rescheneder, P. & von Haeseler, A. NextGenMap: fast and accurate read mapping in highly polymorphic genomes. *Bioinformatics* **29**, 2790–2791 (2013).

[CAS](#) [PubMed](#) [Google Scholar](#)

56. 56.

Brar, G. A. et al. High-resolution view of the yeast meiotic program revealed by ribosome profiling. *Science* **335**, 552–557 (2012).

[ADS](#) [CAS](#) [PubMed](#) [Google Scholar](#)

57. 57.

Cheng, Z. et al. Pervasive, coordinated protein-level changes driven by transcript isoform switching during meiosis. *Cell* **172**, 910–923 (2018).

[CAS](#) [PubMed](#) [PubMed Central](#) [Google Scholar](#)

58. 58.

Duroc, Y. et al. Concerted action of the MutL β heterodimer and Mer3 helicase regulates the global extent of meiotic gene conversion. *eLife* **6**, e21900 (2017).

[PubMed](#) [PubMed Central](#) [Google Scholar](#)

59. 59.

Poplin, R. et al. Scaling accurate genetic variant discovery to tens of thousands of samples. Preprint at <https://doi.org/10.1101/201178> (2017).

60. 60.

McKenna, A. et al. The Genome Analysis Toolkit: a MapReduce framework for analyzing next-generation DNA sequencing data. *Genome Res.* **20**, 1297–1303 (2010).

[CAS](#) [PubMed](#) [PubMed Central](#) [Google Scholar](#)

61. 61.

Pedregosa, F. et al. Scikit-learn: machine learning in Python. *JMLR* **12**, 2826–2830 (2011).

[MathSciNet](#) [MATH](#) [Google Scholar](#)

62. 62.

Benjamini, Y. & Speed, T. P. Summarizing and correcting the GC content bias in high-throughput sequencing. *Nucleic Acids Res.* **40**, e72 (2012).

[CAS](#) [PubMed](#) [PubMed Central](#) [Google Scholar](#)

63. 63.

Mancera, E., Bourgon, R., Brozzi, A., Huber, W. & Steinmetz, L. M. High-resolution mapping of meiotic crossovers and non-crossovers in yeast. *Nature* **454**, 479–485 (2008).

[ADS](#) [CAS](#) [PubMed](#) [PubMed Central](#) [Google Scholar](#)

64. 64.

Panizza, S. et al. Spo11-accessory proteins link double-strand break sites to the chromosome axis in early meiotic recombination. *Cell* **146**, 372–383 (2011).

[CAS](#) [PubMed](#) [Google Scholar](#)

65. 65.

Claeys Bouuaert, C. et al. DNA-driven condensation assembles the meiotic DNA break machinery. *Nature* **592**, 144–149 (2021).

[ADS](#) [CAS](#) [PubMed](#) [Google Scholar](#)

66. 66.

Mosconi, F., Allemand, J. F., Bensimon, D. & Croquette, V. Measurement of the torque on a single stretched and twisted DNA using magnetic tweezers. *Phys. Rev. Lett.* **102**, 078301 (2009).

[ADS](#) [PubMed](#) [Google Scholar](#)

67. 67.

Lipfert, J., Kerssemakers, J. W., Jager, T. & Dekker, N. H. Magnetic torque tweezers: measuring torsional stiffness in DNA and RecA-DNA filaments. *Nat. Methods* **7**, 977–980 (2010).

[CAS](#) [PubMed](#) [Google Scholar](#)

[Download references](#)

Acknowledgements

We thank S. Zich and M. Galova for technical assistance, S. Keeney and K. Nasmyth for sharing strains, P. Schloegelhofer, N. Kleckner, M. Xaver, J. Marko, J. Roca for stimulating discussions, and N. Kleckner, M. Xaver, C. Campbell for comments on the manuscript. We thank M. Neale for discussing results ahead of publication. Furthermore, we thank A. v. Haeseler and the Center for Integrative Bioinformatics of Vienna (CIBIV) for hosting D. C. and providing the computer cluster infrastructure. This work was funded by SFB grant F34 and by DK W1238-B20 from the Austrian Science Foundation.

Author information

Author notes

1. Elisa Mayrhofer

Present address: Austrian Research Institute for Chemistry and Technology, Microbiology and Cell Culture, Vienna, Austria

2. Soma Zsótér

Present address: Humboldt University of Berlin, IRI Life Sciences, Berlin, Germany

3. Jean Mbogning

Present address: McGill University, Department of Pharmacology and Therapeutics, Montréal, Canada

4. These authors contributed equally: Silvia Prieler, Doris Chen

Affiliations

1. Max Perutz Labs Vienna, University of Vienna, Department of Chromosome Biology, Vienna, Austria

Silvia Prieler, Doris Chen, Lingzhi Huang, Elisa Mayrhofer, Soma Zsótér, Magdalena Vesely, Jean Mbogning & Franz Klein

Authors

1. Silvia Prieler

[View author publications](#)

You can also search for this author in [PubMed](#) [Google Scholar](#)

2. Doris Chen

[View author publications](#)

You can also search for this author in [PubMed](#) [Google Scholar](#)

3. Lingzhi Huang

[View author publications](#)

You can also search for this author in [PubMed](#) [Google Scholar](#)

4. Elisa Mayrhofer

[View author publications](#)

You can also search for this author in [PubMed](#) [Google Scholar](#)

5. Soma Zsótér

[View author publications](#)

You can also search for this author in [PubMed](#) [Google Scholar](#)

6. Magdalena Vesely

[View author publications](#)

You can also search for this author in [PubMed](#) [Google Scholar](#)

7. Jean Mbognign

[View author publications](#)

You can also search for this author in [PubMed](#) [Google Scholar](#)

8. Franz Klein

[View author publications](#)

You can also search for this author in [PubMed](#) [Google Scholar](#)

Contributions

S.P. developed Protec-seq, performed most of the experiments, and co-wrote the manuscript. D.C. developed and performed most of the bioinformatic analyses and visualizations, and co-wrote the manuscript. L.H. found first evidence of dDSB fragments and performed the Top2 ChIP-seq experiments. E.M. helped developing Protec-seq and contributed experiments; J.M. made the initial finding of Top2 at DSB hotspots; S.Z. and M.V. generated strains, constructs and Western blots. F.K. supervised the research, performed and contributed to computational analyses, and wrote the manuscript. All authors discussed experiments and results and commented on the manuscript.

Corresponding author

Correspondence to [Franz Klein](#).

Ethics declarations

Competing interests

The authors declare no competing interests.

Additional information

Peer review information *Nature* thanks Bernard de Massy and the other, anonymous, reviewer(s) for their contribution to the peer review of this work. Peer review reports are available.

Publisher's note Springer Nature remains neutral with regard to jurisdictional claims in published maps and institutional affiliations.

Extended data figures and tables

[Extended Data Fig. 1 DNA fragments released in meiosis are characterized with single-nucleotide precision.](#)

a, In a *rad50S* mutant about one-third of the dDSB fragments are robustly resistant to all Exo V concentrations analysed. qPCR of dDSB signals at the YCR047 hotspot (dark blue) or the YCR011 cold region (light blue) using primer pairs PP7 (248 bp) or PP2 (130 bp), respectively (blue bars represent mean values, error bars denote s.d. of three independent experiments, black dots indicate individual values). Digests were performed at 37 °C except for one negative control (4 °C). **b**, dDSB signals peak during DSB formation in wild-type synchronized meiotic cultures. qPCR as in **a** (mean and s.d. of two independent experiments are shown, individual values are represented as circles and diamonds). Signals were depleted in the untagged control, the catalytically inactive *spo11^{Y135F}* mutant and the DSB formation-impaired *rec102Δ* mutant. **c–e**, Internal quality controls show single-nucleotide precision and striking signal-to-noise ratio of Protec-seq. **c**, Diagram explaining the Spo11 signature and the representation of dDSB fragments as arcs. A strong break site produces dDSB fragments in both orientations

(grey and green) with a 1-nt offset between Watson (W) and Crick (C) 5' ends reflecting the 2-nt overhang produced by Spo11⁸ (Spo11 signature). Differently oriented fragments arise from independent cleavage events at different rates. Thus fragments originating at the same break site but ending at opposite sides may show different depths (dDSB asymmetry). **d**, ‘Cut site fingerprints’ demonstrate single-nucleotide precision in Protec-seq. Cut site fingerprints are single-nucleotide resolution patterns with a window of a few nucleotides around a dominant, isolated Watson signal. Inaccurate determination of 5' ends would result in a spill over from the dominant signal. Left, averaged fingerprint from 11 cut sites on the Watson strand selected for strength and isolation, with Crick signals serving as independent readout. Watson signals are depicted as filled columns with positive values (percentage of the dominant Watson signal), Crick signals as empty columns with negative values (percentage of the dominant Crick signal). Right, filled and empty columns as in the left panel, but averaged over eight different experiments, involving six different mutant backgrounds at the same cut site (chromosome IV, 824,137). **e**, Genome-wide detection of the Spo11 signature for assessment of the Protec-seq accuracy. Quantification of the Watson–Crick offset for strong and isolated peaks (Methods) show a high percentage of the 1-nt Watson–Crick offset in the dDSB samples. Wild-type ($n = 3,272$), *tel1Δ rec114-8A* ($n = 3,726$), *mre11S* ($n = 1,155$), *rad50S* ($n = 1,947$), *coml/sae2Δ* ($n = 1,674$), and for comparison Spo11-oligos ($n = 1,964$, derived from ref. ¹⁵) are shown (n denotes the number of peaks that fulfil the selection criteria). **f**, The architecture of dDSB hotspots is well conserved across resection mutants and the *tel1Δ* checkpoint mutant. Arcs represent dDSB fragments at a hotspot around 824,100 on chromosome IV, with grey shades corresponding linearly to the fragment depths. Plots in the bottom right show dDSB fragments starting at a single position (116,869, chromosome IV) for wild-type and *rad50S* strains. Orange bars represent Spo11-oligo 5' ends. All samples are from t_4 .

[Source data](#)

[**Extended Data Fig. 2 Protec-seq results in robust and high quality DSB maps.**](#)

a, Biological repeats as well as samples with similar phenotype show high correlation at 10-nt resolution. 5' end log₂-transformed counts are shown. The corresponding Pearson correlation coefficients (R) are indicated in the bottom right corner of the scatter plots. The compared samples and time points are indicated at the left and bottom axes. Top right, to test whether the differences between *rad50S* and wild-type are mainly due to differential degradation, sub-samples of *rad50S* dDSB fragments were selected according to the dDSB length distribution of wild-type cells. The resulting improvement of R from 0.88 (for unselected *rad50S* versus wild-type dDSB) to 0.93 supports this assumption. **b**, Positional overlaps of dDSB 5' ends with Spo11-oligo 5' ends with 1 nt tolerance. OO, both dDSB fragments ends overlap; ON, one end overlaps; NN, both ends do not overlap. Filled bars represent total fragment counts as a percentage of the total; empty bars represent deduplicated counts. The last panel shows the percentages of the Spo11-oligo sample overlapping with wild-type dDSB (O, overlap; N, no overlap). All samples are from 4 h in SPM (t_4). **c**, dDSB fragment and Spo11-oligo profiles from chromosome III. Genome-wide Pearson correlation coefficients with the wild-type t_4 profile at a resolution of 10 nt are indicated on the right side of each panel. **d**, Left, frequency of (d)DSB sites of certain depths (log₁₀ bins) as a percentage of total recovered break sites. Right, the frequency of (d)DSBs of certain depths (log₁₀ bins) as a percentage of total (d)DSBs. The depths are binned into 1, 2–10, 11–100, 101–1000, 10³+1–10⁴, 10⁴+1–10⁵. All samples are from t_4 .

[Source data](#)

Extended Data Fig. 3 Preference of Spo11 for a DNA-bending motif at periodic distances.

a, Spo11 cleavage preference and internal GC accumulation in *S. cerevisiae* as in Fig. [2a](#), but for 64-nt dDSB fragments (wild-type, t_4 ; $n = 164,104$, with n being the number of independently identified fragments of a given length). The GC content of 47.8% is lower than for the 34-nt fragments (57.9%), but markedly above the genome average (38.3%). The GC enrichment is not caused by preferential resistance to degradation (data not shown), or by preferential PCR amplification, as the enrichment is robust

against deduplication, and GC-rich DNA is known to be underrepresented in over-amplified libraries⁶². Separate analysis of the 5' and the 3' ends of dDSB fragments reveals an asymmetry of base preferences relative to the cleavage axes. The nucleotide preferences inside the fragment (at positions 1, 2 and 13 relative to the cleavage axes) are stronger than their counterparts that flank the dDSB fragment (at positions -1, -2 and -13). All features are robust to deduplication (data not shown). **b, c**, Cleavage preference and internal GC accumulation in *S. kudriavzevii* for dDSB fragment lengths of 64 nt (**b**; 50.4% GC, $n = 12,004$) and 34 nt (**c**; 59.4% GC, $n = 853$) are very similar to their counterparts in *S. cerevisiae*. Preferential excision of GC-rich sequences could help to limit GC accumulation at yeast hotspots⁶³. **d**, In *tel1Δ rec114-8A* double mutants, the periodicity of dDSB fragment lengths was detectable for up to 335 nt. Peak lengths are indicated by pink bars and numbers on the top; valleys are indicated by blue bars. Peaks and valleys were called automatically by a custom algorithm after smoothing with bandwidth = 3 and resolution = 1 (R ‘ksmooth’). **e**, *S. kudriavzevii com1/sae2Δt₆* displays a similar distribution of dDSB fragment lengths as *S. cerevisiae* resection mutants and the same $10.4n + 3$ nt periodicity as all *S. cerevisiae* dDSB samples. **f**, Quantification of dDSB signal from ref. ¹⁵ (gel separation). Left, on the basis of their length distribution, signals are interpreted either as DSB oligonucleotides (dark blue, A1) or dDSB fragments (cyan, A2). Right, diagram illustrating the rationale for estimation of the dDSB fraction F . Each single DSB is represented by two oligonucleotides, one (approximately 30 bp) gives rise to the A1 signal, the other one (14 bp long) is not visible on this gel. dDSB fragments smaller than 70 bp produce two long oligonucleotides with periodic lengths and two with Spo11-oligo lengths that can contribute to the 30-nt peak (A1) (Methods). **g**, Periodicity does not require nucleosomes. The length periodicity is observed with dDSB fragments lying with both ends in nucleosome-occupied (NN) or in nucleosome-depleted (DD) regions. The nucleosome map is derived from ref. ¹³ (Methods). **h**, Table of peak fragment lengths <108 bp averaged from 21 dDSB samples of various genetic background, resulting in a mean peak to peak distance of 10.4 ± 0.36 nt and helix lengths ranging from 11.33 bp (for 34-nt long fragments) to 10.7 bp (for 107 nt).

Source data

Extended Data Fig. 4 Top2 ChIP-seq profiles indicate accumulation of topological stress at hotspots at the time of DSB formation.

a, (d)DSB 5' ends located within ± 1 kb of TSSs from assembled transcripts from previously published RNA-seq data of 3–6 h of meiosis ($n = 7,913$), stratified by downstream high (H), medium (M) and low (L) transcriptional stress (expression level times length). Wild-type dDSB, *rad50S* dDSB, Spo11-oligos, and *spo11^{Y135F}* dDSB are shown. The corresponding Spearman correlation coefficients (rho) are shown. **b**, dDSB signals of *rad50S* (left) and *spo11^{Y135F}* (right) located within ± 1 kb of a Top2 peak ($n = 10,689$; from Top2 ChIP-seq experiment at t_4 , with depth >100) were stratified into 12 groups according to the corresponding Top2 peak intensities. The Spearman correlation coefficients (rho) are indicated. **c**, Examples of calibrated Top2 ChIP-seq signals accumulating at several kilobase-wide hotspot clusters. Top2 t_4 (dark green), untagged control (grey), Spo11-oligos (orange bars), Watson transcripts and open-reading frames (ORFs) (black), Crick transcripts and ORFs (green) are shown. **d**, Top2–Myc peaks at TSSs, stratified by high, medium and low transcriptional stress (expression level times length). From left to right: all TSS ($n = 7,913$), divergent ($n = 3,930$), tandem ($n = 2,109$) and convergent sites ($n = 3,900$). The corresponding Spearman correlation coefficients (rho) are shown. **e**, Typical examples of Top2 occupancy at divergent, tandem or convergent sites with corresponding DSB signals. Colour labels as in **c**.

[Source data](#)

Extended Data Fig. 5 Analyses of dDSB lifespan.

a, Specific and complete nuclear depletion of Rec104 within 30 min by the ‘anchor away’ technique⁵³. In situ staining of wild-type cells at $t_{4.5}$ stained with an anti-haemagglutinin (HA) antibody to visualize Rec104-FRB–HA3. The left two panels show nuclei stained either with DAPI or anti-HA antibody in yeast cells without rapamycin, and Rec104 is localized in the nucleus. The right two panels are as in the left two panels, but after the addition of rapamycin ($1 \mu\text{g ml}^{-1}$) for 30 min. Rec104 is in the cytoplasm

and nuclei are visibly depleted of Rec104 (blue arrows). The experiment was repeated six times with $n = 100$ nuclei inspected. **b**, Spo11 is retained in the nucleus during the anchor-away technique. In situ staining of Rec104-FRB-HA3 with an anti-HA antibody (red), Spo11–Myc18 (green) or DAPI (cyan) in *rad50S* cells without rapamycin (left) or with rapamycin added at t_4 for 30 min (right). The experiment was repeated six times with $n = 100$ nuclei inspected. **c**, dDSB fragments from wild-type cells with one end at a single position (399,594) on chromosome VII before (grey) and after (red) 30 min of DSB inhibition by Rec104 depletion. Almost all fragments greater than 100 bp are lost, whereas fragments smaller than 70 bp persist. **d**, Length-independent decay of dDSB fragments in *rad50S* Rec104-FRB-HA3 cells. The fold change of (calibrated) fragment length levels 60 min versus 0 min without rapamycin (dark cyan), 30 min versus 0 min plus rapamycin (light violet), and 60 min versus 0 min plus rapamycin (dark violet) are shown. For one ratio (60 min versus 0 min minus rapamycin), the joint fragment depths are shown to indicate the sample number per length (light grey). A fold change of one indicates stability; a fold change of 0.5 indicates a half-life of 30 min. Fragments with disfavoured lengths ('valleys') are slightly less stable overall.

[Source data](#)

[**Extended Data Fig. 6 dDSB fragments reveal preferential gap formation at sites of Msh2-independent full gene conversions.**](#)

a, Raw data of publicly available S288C/SK1 hybrid octads were re-aligned to the parental reference genomes and re-analysed to create a high-precision and high-confidence recombination event map, with focus on full gene conversions ('6:2' events) (Methods, Supplementary Table 4). Average number of crossover (CO), non-crossover (NCO) and double crossover (dCO) events of *msh2Δ* (four octads with on average 211.8 ± 32.8 events), *msh2Δ mutLyΔ* (four octads, 189.0 ± 8.8 events), and *msh2Δ exo1Δ* (two octads, 148.5 ± 29.0) octads are depicted by doughnut plots, in which the outer ring represents all events, and the inner circle denotes the 6:2-containing events (with a radius proportional to their fraction). Among 6:2 events, crossovers are markedly overrepresented in *msh2Δ* mutants ($P = 4.3 \times 10^{-12}$), but not in *msh2Δ mutLyΔ* double mutants ($P = 0.54$

Fisher's exact test) as the Mut γ -independent full gene conversion events show an only slightly enhanced tendency for crossovers (29.1% of 6:2 versus 25.5% of total events). Because the preferential association of 6:2 events with crossovers disappears when Mut γ is defective, the crossover-associated 6:2 events seem to be generated by the Mut γ pathway, not by dDSBs. Deletion of another Mut γ component, Exo1, in conjunction with Msh2, yields even fewer full gene conversion events (14.8%), because it also affects the early stages in both DSB and dDSB processing, including the interhomologue bias⁴⁴, and thus affects 6:2 formation from all pathways. **b, c**, As in Fig. 4f, g, but with *msh2Δ* octad data. Msh2-independent 6:2 events ($n = 349$ from four octads) have significantly higher dDSB (gap) coverage than randomly distributed events. In **b**, the cumulative fraction of Msh2-independent 6:2 events is plotted against the number of identified gaps that completely overlap them. Plots based on gap distributions from (left to right) wild-type, *rad50S* and *spo11Y135F* strains are shown. Results from distributing 6:2 events 1,000× randomly are included (light blue dots). Values above random indicate a positive correlation between the incidences of 6:2 events and gap probabilities. P values were determined by Wilcoxon rank test and Bonferroni multiple-test correction. In **c**, the dDSB fragment coverage of wild-type (top) and *rad50S* (bottom) strains per observed or 1,000× randomly distributed (light blue) 6:2 events are plotted. Median values of wild-type and *rad50S* were significantly different from random (Mood's median test, $P = 7.0 \times 10^{-14}$ and 4.6×10^{-30} , respectively). The central lines indicate the median, the boxes indicate the interquartile range, and whiskers span maximally 1.5 times the interquartile range.

[Source data](#)

[Extended Data Fig. 7 Spo11 sets up a topological trap for DNA crossings.](#)

As mounting evidence stresses similarities between the Spo11 complex and type IIB topoisomerases^{1,33,41} our 'topological trap' model strives to explain how Spo11 induces (d)DSBs at DNA crossings. To explain the encounter between the complex and a DNA crossing, we suggest that Spo11

traps a second strand in the tip of bent DNA, a principle that if corroborated, could explain how type II topoisomerases arrive at crossings in general. **a**, When axis-anchored⁶⁴ Spo11 encounters a DNA strand (G-segment, grey), the tethering of the G-strand to the presumed Mer2, Mei4, Rec114 dependent condensate⁶⁵ forms a physical barrier, which can capture an additional strand. Spo11 bends the DNA at the binding site, but does not cleave the DNA. This will draw a second strand (T-segment, brown) into the tip of the bend, and provoke the formation of a DNA crossing. After the arrival of the second strand (T-segment), Spo11 undergoes a conformational change, and entraps both strands. This movement accompanies the cleavage reaction as for topoisomerase VI⁴¹, which results in the breakage of both single strands of the G-segment, setting the T-segment free. **b**, If the G-segment interacts with two or more Spo11 complexes before it encounters a T-strand, the formation of a gap and the corresponding release of a dDSB fragment can occur. Spo11 prefers motifs that mediate DNA bending in defined angles³⁵. Two such bending angles will add up to form a flat U-shape (second panel from top), only if these bending motifs are in phase, resulting in cleavage products of periodic length. DNA between the two tethering Spo11 complexes is in close proximity to the condensate—an additional constraint that may cause the observed GC preference in short fragments. The ensuing steps are completely analogous to single DSB formation in **a**, with one additional requirement. A dDSB will only occur when a T-strand crosses both G-strand tethers. As shown in the second and third panel, it is important that the T-strand enters below both G-strand arms, which triggers the conformational change of the Spo11 complexes to clamp down the crossings and cleave the G-segment in a concerted fashion. If the T-segment crosses below one, but above the other, grey arm, only a single crossing is trapped and the structure resolves with a single DSB. The two DNA crossings between the G- and T-strands generate the dDSB irrespective of how many Spo11 complexes tether the G segment. Because of the torsional stiffness of DNA at that scale, measured by the twist persistence length, phosphodiester bonds are presented at the same angle to Spo11 at periodic distances (top panel in **b**). The twist persistence length for dsDNA ranges from 120 to 300 bp, increasing with the stress acting on DNA^{66,67}. These numbers are in good agreement with the maximal range (around 335 bp) over which we could detect periodicity (Extended Data Fig. 3d).

Extended Data Table 1 Genomic distribution of (d)DSBs

[Full size table](#)

Extended Data Table 2 Yeast strains used in this study

[Full size table](#)

Extended Data Table 3 Primers and synthetic DNA templates used in this study

[Full size table](#)

Supplementary information

Supplementary Information

This file contains Supplementary Discussions 1-3.

Reporting Summary

41586_2021_3632_MOESM3_ESM.txt

Supplementary Table 1 *S. cer.* SK1 ASM205788v1 gene annotation (gtf format). Sequence data were downloaded from SGD (R64-2-1, version 17.1. 2017, with non-coding and other features) and the Ensembl database (release 98, R64-1-1), and subsequently re-aligned and merged.

41586_2021_3632_MOESM4_ESM.txt

Supplementary Table 2 *S. cer.* SK1 ASM205788v1 transcript annotation as obtained from re-alignment and assembly of RNA-seq data from GEO GSE34082 and GSE108778, including transcript start sites, lengths and expression levels from 3 hrs – 6 hrs after initiation of meiosis.

41586_2021_3632_MOESM5_ESM.txt

Supplementary Table 3 *S. cer.* SK1 ASM205788v1 Spo11-oligo map, wild type t4. Raw data was downloaded from GEO GSE84696 (SRR3942949, replicate 2), re-processed and re-aligned (unique alignments only). 5'-end counts of Watson and Crick strands are reported separately.

Supplementary Table 4

Genotype and recombination event predictions with *S. cer.* ASM205788v1 and R64 coordinates for S288C/SK1 hybrid octads with *msh2Δ* (4 octads; raw data from SRA accession SRP075437), *msh2Δ/mlh1Δ* or *msh2Δ/mlh3Δ*, and *msh2Δ/exo1Δ* (2 octads each; SRP111430) background. Data for each octad (in total 10) are presented in separate Excel sheets.

Peer Review File

Source data

Source Data Fig. 2

Source Data Fig. 3

Source Data Fig. 4

Source Data Extended Data Fig. 1

Source Data Extended Data Fig. 2

Source Data Extended Data Fig. 3

Source Data Extended Data Fig. 4

Source Data Extended Data Fig. 5

Source Data Extended Data Fig. 6

Rights and permissions

Reprints and Permissions

About this article



Cite this article

Prieler, S., Chen, D., Huang, L. *et al.* Spo11 generates gaps through concerted cuts at sites of topological stress. *Nature* **594**, 577–582 (2021). <https://doi.org/10.1038/s41586-021-03632-x>

[Download citation](#)

- Received: 05 March 2020
- Accepted: 11 May 2021
- Published: 09 June 2021
- Issue Date: 24 June 2021
- DOI: <https://doi.org/10.1038/s41586-021-03632-x>

Further reading

- [Concerted cutting by Spo11 illuminates meiotic DNA break mechanics](#)
 - Dominic Johnson
 - , Margaret Crawford
 - , Tim Cooper
 - , Corentin Claeys Bouuaert
 - , Scott Keeney
 - , Bertrand Llorente
 - , Valerie Garcia

◦ & Matthew J. Neale

Nature (2021)

Comments

By submitting a comment you agree to abide by our [Terms](#) and [Community Guidelines](#). If you find something abusive or that does not comply with our terms or guidelines please flag it as inappropriate.

[Access through your institution](#)

[Change institution](#)

[Buy or subscribe](#)

Advertisement

This article was downloaded by **calibre** from <https://www.nature.com/articles/s41586-021-03632-x>

| [Section menu](#) | [Main menu](#) |

- Article
- [Published: 16 June 2021](#)

Structures of G_i-bound metabotropic glutamate receptors mGlu2 and mGlu4

- [Shuling Lin](#)^{1,2 na1},
- [Shuo Han](#) ORCID: [orcid.org/0000-0003-0760-0183](#)^{3 na1},
- [Xiaoqing Cai](#)^{1,4 na1},
- [Qiuxiang Tan](#)¹,
- [Kexiu Zhou](#)^{1,2,5},
- [Dejian Wang](#)^{2,3},
- [Xinwei Wang](#)^{1,2},
- [Juan Du](#)⁶,
- [Cuiying Yi](#)³,
- [Xiaojing Chu](#)¹,
- [Antao Dai](#)^{1,4},
- [Yan Zhou](#)^{1,4},
- [Yan Chen](#)⁷,
- [Yu Zhou](#)^{2,3},
- [Hong Liu](#)^{2,3,5},
- [Jianfeng Liu](#) ORCID: [orcid.org/0000-0002-0284-8377](#)^{8,9},
- [Dehua Yang](#) ORCID: [orcid.org/0000-0003-3028-3243](#)^{1,2,4},
- [Ming-Wei Wang](#) ORCID: [orcid.org/0000-0001-6550-9017](#)^{1,2,4,5,7,10},
- [Qiang Zhao](#) ORCID: [orcid.org/0000-0001-6251-6676](#)^{2,3,11} &
- [Beili Wu](#) ORCID: [orcid.org/0000-0002-1936-0909](#)^{1,2,5,6}

- 2963 Accesses
- 1 Citations
- 50 Altmetric
- [Metrics details](#)

Subjects

- [Cryoelectron microscopy](#)
- [G protein-coupled receptors](#)

Abstract

The metabotropic glutamate receptors (mGlu_s) have key roles in modulating cell excitability and synaptic transmission in response to glutamate (the main excitatory neurotransmitter in the central nervous system)¹. It has previously been suggested that only one receptor subunit within an mGlu homodimer is responsible for coupling to G protein during receptor activation². However, the molecular mechanism that underlies the asymmetric signalling of mGlu_s remains unknown. Here we report two cryo-electron microscopy structures of human mGlu2 and mGlu4 bound to heterotrimeric G_i protein. The structures reveal a G-protein-binding site formed by three intracellular loops and helices III and IV that is distinct from the corresponding binding site in all of the other G-protein-coupled receptor (GPCR) structures. Furthermore, we observed an asymmetric dimer interface of the transmembrane domain of the receptor in the two mGlu–G_i structures. We confirmed that the asymmetric dimerization is crucial for receptor activation, which was supported by functional data; this dimerization may provide a molecular basis for the asymmetric signal transduction of mGlu_s. These findings offer insights into receptor signalling of class C GPCRs.

Access options

[Subscribe to Journal](#)

Get full journal access for 1 year

\$199.00

only \$3.90 per issue

[Subscribe](#)

All prices are NET prices.

VAT will be added later in the checkout.

Tax calculation will be finalised during checkout.

Rent or Buy article

Get time limited or full article access on ReadCube.

from \$8.99

[Rent or Buy](#)

All prices are NET prices.

Additional access options:

- [Log in](#)
- [Access through your institution](#)
- [Learn about institutional subscriptions](#)

Fig. 1: Overall structures of mGlu2–G_{i1} and mGlu4–G_{i3} complexes.

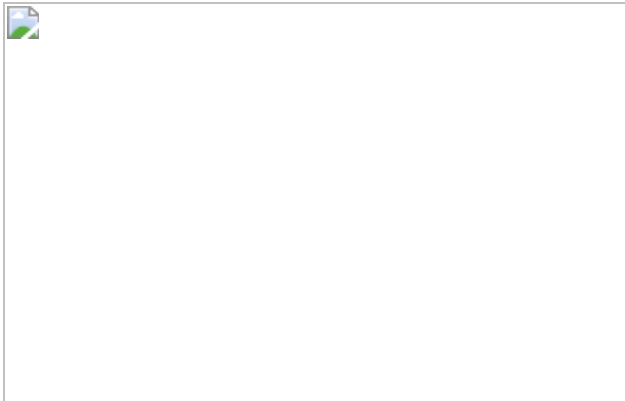


Fig. 2: G_i recognition pattern of mGlu2 and mGlu4, and PAM binding mode in mGlu2.

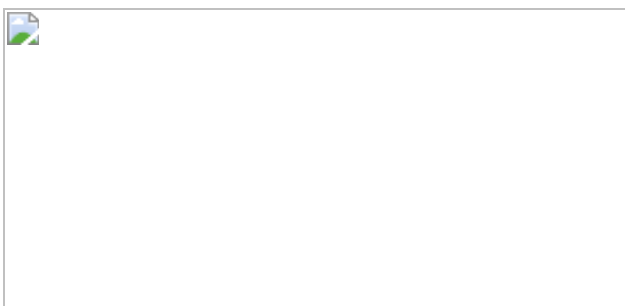


Fig. 3: Asymmetric dimerization of mGlu2 and mGlu4.

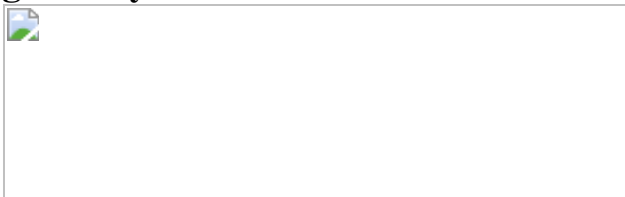
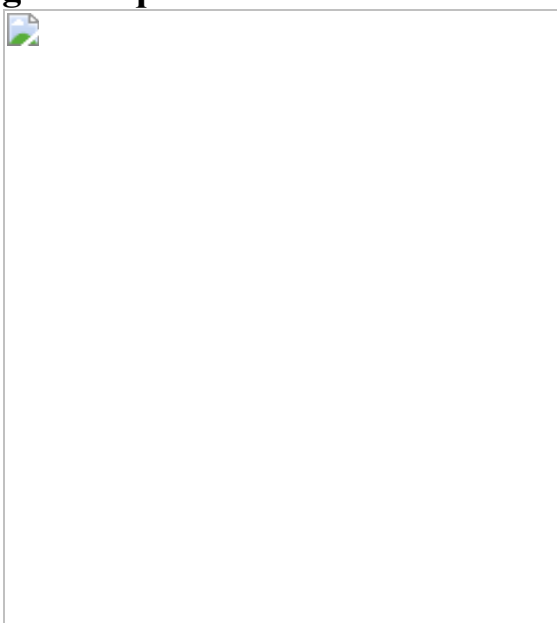


Fig. 4: Sequential conformational changes of mGlu2.



Data availability

Atomic coordinates and cryo-EM density maps for the structures of mGlu2–G_{i1} and mGlu4–G_{i3} complexes have been deposited in the PDB under identification codes [7E9G](#) and [7E9H](#), respectively, and in the Electron Microscopy Data Bank under accession codes [EMD-31031](#) and [EMD-31032](#), respectively. The uncropped gels shown in Extended Data Figs. [1b](#), [i](#), [5u](#) are displayed in Supplementary Fig. [1](#). The database used in this study includes PDB 3SN6, 4OR2, 4OO9, 4XAQ, 4XAS, 5CNI, 5CNJ, 6DDE, 6LMK, 6LML, 6N51, 6N52 and 6OT0.

References

1. 1.

Niswender, C. M. & Conn, P. J. Metabotropic glutamate receptors: physiology, pharmacology, and disease. *Annu. Rev. Pharmacol. Toxicol.* **50**, 295–322 (2010).

[CAS](#) [PubMed](#) [PubMed Central](#) [Google Scholar](#)

2. 2.

Hlavackova, V. et al. Evidence for a single heptahelical domain being turned on upon activation of a dimeric GPCR. *EMBO J.* **24**, 499–509 (2005).

[CAS](#) [PubMed](#) [PubMed Central](#) [Google Scholar](#)

3. 3.

Kniazeff, J. et al. Closed state of both binding domains of homodimeric mGlu receptors is required for full activity. *Nat. Struct. Mol. Biol.* **11**, 706–713 (2004).

[CAS](#) [PubMed](#) [Google Scholar](#)

4. 4.

Tateyama, M., Abe, H., Nakata, H., Saito, O. & Kubo, Y. Ligand-induced rearrangement of the dimeric metabotropic glutamate receptor 1 α . *Nat. Struct. Mol. Biol.* **11**, 637–642 (2004).

[CAS](#) [PubMed](#) [Google Scholar](#)

5. 5.

Matsushita, S., Nakata, H., Kubo, Y. & Tateyama, M. Ligand-induced rearrangements of the GABA_B receptor revealed by fluorescence resonance energy transfer. *J. Biol. Chem.* **285**, 10291–10299 (2010).

[CAS](#) [PubMed](#) [PubMed Central](#) [Google Scholar](#)

6. 6.

Rasmussen, S. G. et al. Crystal structure of the β_2 adrenergic receptor–Gs protein complex. *Nature* **477**, 549–555 (2011).

[ADS](#) [CAS](#) [PubMed](#) [PubMed Central](#) [Google Scholar](#)

7. 7.

Zhang, Y. et al. Cryo-EM structure of the activated GLP-1 receptor in complex with a G protein. *Nature* **546**, 248–253 (2017).

[ADS](#) [CAS](#) [PubMed](#) [PubMed Central](#) [Google Scholar](#)

8. 8.

Monn, J. A. et al. Design, synthesis, and pharmacological characterization of (+)-2-aminobicyclo[3.1.0]hexane-2,6-dicarboxylic acid (LY354740): a potent, selective, and orally active group 2 metabotropic glutamate receptor agonist possessing anticonvulsant and anxiolytic properties. *J. Med. Chem.* **40**, 528–537 (1997).

[CAS](#) [PubMed](#) [Google Scholar](#)

9. 9.

Kang, H. J. et al. Selectivity and evolutionary divergence of metabotropic glutamate receptors for endogenous ligands and G proteins coupled to phospholipase C or TRP channels. *J. Biol. Chem.* **289**, 29961–29974 (2014).

[CAS](#) [PubMed](#) [PubMed Central](#) [Google Scholar](#)

10. 10.

Cid, J. M. et al. Discovery of 1-butyl-3-chloro-4-(4-phenyl-1-piperidinyl)-(1*H*)-pyridone (JNJ-40411813): a novel positive allosteric modulator of the metabotropic glutamate 2 receptor. *J. Med. Chem.* **57**, 6495–6512 (2014).

[CAS](#) [PubMed](#) [Google Scholar](#)

11. 11.

Jones, C. K. et al. The metabotropic glutamate receptor 4-positive allosteric modulator VU0364770 produces efficacy alone and in combination with l-DOPA or an adenosine 2A antagonist in preclinical rodent models of Parkinson’s disease. *J. Pharmacol. Exp. Ther.* **340**, 404–421 (2012).

[CAS](#) [PubMed](#) [PubMed Central](#) [Google Scholar](#)

12. 12.

Scholler, P. et al. Allosteric nanobodies uncover a role of hippocampal mGlu2 receptor homodimers in contextual fear consolidation. *Nat. Commun.* **8**, 1967 (2017).

[ADS](#) [PubMed](#) [PubMed Central](#) [Google Scholar](#)

13. 13.

Koehl, A. et al. Structural insights into the activation of metabotropic glutamate receptors. *Nature* **566**, 79–84 (2019).

[ADS](#) [CAS](#) [PubMed](#) [PubMed Central](#) [Google Scholar](#)

14. 14.

Monn, J. A. et al. Synthesis and pharmacological characterization of C4-disubstituted analogs of 1*S*,2*S*,5*R*,6*S*-2-aminobicyclo[3.1.0]hexane-2,6-dicarboxylate: identification of a potent, selective metabotropic glutamate receptor agonist and determination of agonist-bound human mGlu2 and mGlu3 amino terminal domain structures. *J. Med. Chem.* **58**, 1776–1794 (2015).

[ADS](#) [CAS](#) [PubMed](#) [Google Scholar](#)

15. 15.

Monn, J. A. et al. Synthesis and pharmacological characterization of C4-(thiotriazolyl)-substituted-2-aminobicyclo[3.1.0]hexane-2,6-dicarboxylates. Identification of (1*R*,2*S*,4*R*,5*R*,6*R*)-2-amino-4-(1*H*-1,2,4-triazol-3-ylsulfanyl)bicyclo[3.1.0]hexane-2,6-dicarboxylic acid (LY2812223), a highly potent, functionally selective mGlu2 receptor agonist. *J. Med. Chem.* **58**, 7526–7548 (2015).

[ADS](#) [CAS](#) [PubMed](#) [Google Scholar](#)

16. 16.

Du, J. et al. Structures of human mGlu2 and mGlu7 homo- and heterodimers. *Nature* <https://doi.org/10.1038/s41586-021-03641-w> (2021).

17. 17.

Shaye, H. et al. Structural basis of the activation of a metabotropic GABA receptor. *Nature* **584**, 298–303 (2020).

[ADS](#) [CAS](#) [PubMed](#) [PubMed Central](#) [Google Scholar](#)

18. 18.

Mao, C. et al. Cryo-EM structures of inactive and active GABA_B receptor. *Cell Res.* **30**, 564–573 (2020).

[CAS](#) [PubMed](#) [Google Scholar](#)

19. 19.

Francesconi, A. & Duvoisin, R. M. Role of the second and third intracellular loops of metabotropic glutamate receptors in mediating dual signal transduction activation. *J. Biol. Chem.* **273**, 5615–5624 (1998).

[CAS](#) [PubMed](#) [Google Scholar](#)

20. 20.

Chang, W., Chen, T. H., Pratt, S. & Shoback, D. Amino acids in the second and third intracellular loops of the parathyroid Ca²⁺-sensing receptor mediate efficient coupling to phospholipase C. *J. Biol. Chem.* **275**, 19955–19963 (2000).

[CAS](#) [PubMed](#) [Google Scholar](#)

21. 21.

Dixon, A. S. et al. NanoLuc complementation reporter optimized for accurate measurement of protein interactions in cells. *ACS Chem. Biol.* **11**, 400–408 (2016).

[CAS](#) [PubMed](#) [Google Scholar](#)

22. 22.

Qiao, A. et al. Structural basis of G_s and G_i recognition by the human glucagon receptor. *Science* **367**, 1346–1352 (2020).

[ADS](#) [CAS](#) [PubMed](#) [Google Scholar](#)

23. 23.

Flock, T. et al. Universal allosteric mechanism for G α activation by GPCRs. *Nature* **524**, 173–179 (2015).

[ADS](#) [CAS](#) [PubMed](#) [PubMed Central](#) [Google Scholar](#)

24. 24.

Pin, J. P., Galvez, T. & Prézeau, L. Evolution, structure, and activation mechanism of family 3/C G-protein-coupled receptors. *Pharmacol. Ther.* **98**, 325–354 (2003).

[CAS](#) [PubMed](#) [Google Scholar](#)

25. 25.

Lundström, L. et al. Pharmacological and molecular characterization of the positive allosteric modulators of metabotropic glutamate receptor 2. *Neuropharmacology* **111**, 253–265 (2016).

[PubMed](#) [Google Scholar](#)

26. 26.

Pérez-Benito, L. et al. Molecular switches of allosteric modulation of the metabotropic glutamate 2 receptor. *Structure* **25**, 1153–1162.e4 (2017).

[PubMed](#) [Google Scholar](#)

27. 27.

Wu, H. et al. Structure of a class C GPCR metabotropic glutamate receptor 1 bound to an allosteric modulator. *Science* **344**, 58–64 (2014).

[ADS](#) [CAS](#) [PubMed](#) [PubMed Central](#) [Google Scholar](#)

28. 28.

Doré, A. S. et al. Structure of class C GPCR metabotropic glutamate receptor 5 transmembrane domain. *Nature* **511**, 557–562 (2014).

[ADS](#) [PubMed](#) [Google Scholar](#)

29. 29.

Rovira, X. et al. Overlapping binding sites drive allosteric agonism and positive cooperativity in type 4 metabotropic glutamate receptors. *FASEB J.* **29**, 116–130 (2015).

[CAS](#) [PubMed](#) [Google Scholar](#)

30. 30.

Gregory, K. J. et al. Identification of specific ligand-receptor interactions that govern binding and cooperativity of diverse modulators to a common metabotropic glutamate receptor 5 allosteric site. *ACS Chem. Neurosci.* **5**, 282–295 (2014).

[CAS](#) [PubMed](#) [PubMed Central](#) [Google Scholar](#)

31. 31.

Fukuda, J. et al. Identification of a novel transmembrane domain involved in the negative modulation of mGluR1 using a newly discovered allosteric mGluR1 antagonist, 3-cyclohexyl-5-fluoro-6-methyl-7-(2-morpholin-4-ylethoxy)-4*H*-chromen-4-one. *Neuropharmacology* **57**, 438–445 (2009).

[CAS](#) [PubMed](#) [Google Scholar](#)

32. 32.

Xue, L. et al. Major ligand-induced rearrangement of the heptahelical domain interface in a GPCR dimer. *Nat. Chem. Biol.* **11**, 134–140 (2015).

[CAS](#) [PubMed](#) [Google Scholar](#)

33. 33.

Huang, S. et al. Interdomain movements in metabotropic glutamate receptor activation. *Proc. Natl Acad. Sci. USA* **108**, 15480–15485 (2011).

[ADS](#) [CAS](#) [PubMed](#) [PubMed Central](#) [Google Scholar](#)

34. 34.

Hlavackova, V. et al. Sequential inter- and intrasubunit rearrangements during activation of dimeric metabotropic glutamate receptor 1. *Sci. Signal.* **5**, ra59 (2012).

[PubMed](#) [Google Scholar](#)

35. 35.

Kang, Y. et al. Cryo-EM structure of human rhodopsin bound to an inhibitory G protein. *Nature* **558**, 553–558 (2018).

[ADS](#) [CAS](#) [PubMed](#) [PubMed Central](#) [Google Scholar](#)

36. 36.

García-Nafría, J., Nehmé, R., Edwards, P. C. & Tate, C. G. Cryo-EM structure of the serotonin 5-HT_{1B} receptor coupled to heterotrimeric G_o. *Nature* **558**, 620–623 (2018).

[ADS](#) [PubMed](#) [PubMed Central](#) [Google Scholar](#)

37. 37.

Mastronarde, D. N. Automated electron microscope tomography using robust prediction of specimen movements. *J. Struct. Biol.* **152**, 36–51 (2005).

[PubMed](#) [Google Scholar](#)

38. 38.

Zheng, S. Q. et al. MotionCor2: anisotropic correction of beam-induced motion for improved cryo-electron microscopy. *Nat. Methods* **14**, 331–332 (2017).

[CAS](#) [PubMed](#) [PubMed Central](#) [Google Scholar](#)

39. 39.

Zhang, K. Gctf: real-time CTF determination and correction. *J. Struct. Biol.* **193**, 1–12 (2016).

[ADS](#) [CAS](#) [PubMed](#) [PubMed Central](#) [Google Scholar](#)

40. 40.

Zivanov, J. et al. New tools for automated high-resolution cryo-EM structure determination in RELION-3. *eLife* **7**, e42166 (2018).

[PubMed](#) [PubMed Central](#) [Google Scholar](#)

41. 41.

Pettersen, E. F. et al. UCSF Chimera—a visualization system for exploratory research and analysis. *J. Comput. Chem.* **25**, 1605–1612 (2004).

[CAS](#) [Google Scholar](#)

42. 42.

Arnold, K., Bordoli, L., Kopp, J. & Schwede, T. The SWISS-MODEL workspace: a web-based environment for protein structure homology modelling. *Bioinformatics* **22**, 195–201 (2006).

[CAS](#) [PubMed](#) [Google Scholar](#)

43. 43.

Emsley, P. & Cowtan, K. Coot: model-building tools for molecular graphics. *Acta Crystallogr. D* **60**, 2126–2132 (2004).

[Google Scholar](#)

44. 44.

Adams, P. D. et al. PHENIX: a comprehensive Python-based system for macromolecular structure solution. *Acta Crystallogr. D* **66**, 213–221 (2010).

[CAS](#) [PubMed](#) [PubMed Central](#) [Google Scholar](#)

45. 45.

Chen, V. B. et al. MolProbity: all-atom structure validation for macromolecular crystallography. *Acta Crystallogr. D* **66**, 12–21 (2010).

[CAS](#) [PubMed](#) [Google Scholar](#)

46. 46.

Monnier, C. et al. Trans-activation between 7TM domains: implication in heterodimeric GABA_B receptor activation. *EMBO J.* **30**, 32–42 (2011).

[ADS](#) [CAS](#) [PubMed](#) [Google Scholar](#)

47. 47.

Kato, H. E. et al. Conformational transitions of a neurotensin receptor 1–G_{i1} complex. *Nature* **572**, 80–85 (2019).

[CAS](#) [PubMed](#) [PubMed Central](#) [Google Scholar](#)

48. 48.

Kingston, A. E. et al. LY341495 is a nanomolar potent and selective antagonist of group II metabotropic glutamate receptors. *Neuropharmacology* **37**, 1–12 (1998).

[CAS](#) [PubMed](#) [Google Scholar](#)

[Download references](#)

Acknowledgements

The cryo-EM studies were performed at the electron microscopy facility of Shanghai Institute of Materia Medica (SIMM), Chinese Academy of Sciences. We thank Q. Wang from SIMM for cryo-EM data collection and Q. Wang from ShanghaiTech University for help with cryo-EM data processing. This work was supported by the National Science Foundation of China grants 31825010 (B.W.), 81872915 and 82073904 (M.-W.W.), and 81773792 and 81973373 (D.Y.), National Key R&D Program of China 2018YFA0507000 (B.W., Q.Z. and M.-W.W.), CAS Strategic Priority Research Program XDB37030100 (B.W. and Q.Z.) and National Science & Technology Major Project of China – Key New Drug Creation and Manufacturing Program 2018ZX09735–001 (M.-W.W.) and 2018ZX09711002–002–005 (D.Y.).

Author information

Author notes

1. These authors contributed equally: Shuling Lin, Shuo Han, Xiaoqing Cai

Affiliations

1. CAS Key Laboratory of Receptor Research, Shanghai Institute of Materia Medica, Chinese Academy of Sciences, Shanghai, China

Shuling Lin, Xiaoqing Cai, Qiuxiang Tan, Kexiu Zhou, Xinwei Wang, Xiaojing Chu, Antao Dai, Yan Zhou, Dehua Yang, Ming-Wei Wang & Beili Wu

2. University of Chinese Academy of Sciences, Beijing, China

Shuling Lin, Kexiu Zhou, Dejian Wang, Xinwei Wang, Yu Zhou, Hong Liu, Dehua Yang, Ming-Wei Wang, Qiang Zhao & Beili Wu

3. State Key Laboratory of Drug Research, Shanghai Institute of Materia Medica, Chinese Academy of Sciences, Shanghai, China

Shuo Han, Dejian Wang, Cuiying Yi, Yu Zhou, Hong Liu & Qiang Zhao

4. The National Center for Drug Screening, Shanghai Institute of Materia Medica, Chinese Academy of Sciences, Shanghai, China

Xiaoqing Cai, Antao Dai, Yan Zhou, Dehua Yang & Ming-Wei Wang

5. School of Life Science and Technology, ShanghaiTech University, Shanghai, China

Kexiu Zhou, Hong Liu, Ming-Wei Wang & Beili Wu

6. School of Pharmaceutical Science and Technology, Hangzhou Institute for Advanced Study, University of Chinese Academy of Sciences, Hangzhou, China

Juan Du & Beili Wu

7. School of Pharmacy, Fudan University, Shanghai, China

Yan Chen & Ming-Wei Wang

8. Key Laboratory of Molecular Biophysics of MOE, International Research Center for Sensory Biology and Technology of MOST, College of Life Science and Technology, Huazhong University of Science and Technology, Wuhan, China

Jianfeng Liu

9. Bioland Laboratory (Guangzhou Regenerative Medicine and Health Guangdong Laboratory), Guangzhou, China

Jianfeng Liu

10. School of Basic Medical Sciences, Fudan University, Shanghai, China

Ming-Wei Wang

11. Zhongshan Branch, Institute of Drug Discovery and Development, Chinese Academy of Sciences, Zhongshan, China

Qiang Zhao

Authors

1. Shuling Lin

[View author publications](#)

You can also search for this author in [PubMed](#) [Google Scholar](#)

2. Shuo Han

[View author publications](#)

You can also search for this author in [PubMed](#) [Google Scholar](#)

3. Xiaoqing Cai

[View author publications](#)

You can also search for this author in [PubMed](#) [Google Scholar](#)

4. Qiuxiang Tan

[View author publications](#)

You can also search for this author in [PubMed](#) [Google Scholar](#)

5. Kexiu Zhou

[View author publications](#)

You can also search for this author in [PubMed](#) [Google Scholar](#)

6. Dejian Wang

[View author publications](#)

You can also search for this author in [PubMed](#) [Google Scholar](#)

7. Xinwei Wang

[View author publications](#)

You can also search for this author in [PubMed](#) [Google Scholar](#)

8. Juan Du

[View author publications](#)

You can also search for this author in [PubMed](#) [Google Scholar](#)

9. Cuiying Yi

[View author publications](#)

You can also search for this author in [PubMed](#) [Google Scholar](#)

10. Xiaojing Chu

[View author publications](#)

You can also search for this author in [PubMed](#) [Google Scholar](#)

11. Antao Dai

[View author publications](#)

You can also search for this author in [PubMed](#) [Google Scholar](#)

12. Yan Zhou

[View author publications](#)

You can also search for this author in [PubMed](#) [Google Scholar](#)

13. Yan Chen

[View author publications](#)

You can also search for this author in [PubMed](#) [Google Scholar](#)

14. Yu Zhou

[View author publications](#)

You can also search for this author in [PubMed](#) [Google Scholar](#)

15. Hong Liu

[View author publications](#)

You can also search for this author in [PubMed](#) [Google Scholar](#)

16. Jianfeng Liu

[View author publications](#)

You can also search for this author in [PubMed](#) [Google Scholar](#)

17. Dehua Yang

[View author publications](#)

You can also search for this author in [PubMed](#) [Google Scholar](#)

18. Ming-Wei Wang

[View author publications](#)

You can also search for this author in [PubMed](#) [Google Scholar](#)

19. Qiang Zhao

[View author publications](#)

You can also search for this author in [PubMed](#) [Google Scholar](#)

20. Beili Wu

[View author publications](#)

You can also search for this author in [PubMed](#) [Google Scholar](#)

Contributions

S.L. developed the protein expression and purification procedures, prepared the protein samples for cryo-EM, performed signalling assays and helped with manuscript preparation. S.H. prepared cryo-samples, collected cryo-EM data and performed cryo-EM data processing and analysis, model building and structure refinement. X. Cai, A.D., Yan Zhou and Y.C. developed and performed NanoBiT assays. Q.T. helped with signalling assays and negative-stain electron microscopy data acquisition and analysis. K.Z. and X.W. helped with protein preparation and signalling assays. D.W. performed crosslinking assays and helped with manuscript preparation. J.D. helped with data analysis. C.Y. and X. Chu expressed the proteins. Yu Zhou and H.L. provided the mGlu2 PAM, and helped with data analysis and interpretation. J.L. helped with data analysis and interpretation, and edited the manuscript. D.Y. and M.-W.W. oversaw the NanoBiT assay, helped with data analysis and interpretation, and edited the manuscript. Q.Z. and B.W. initiated the project, planned and analysed experiments, supervised the research and wrote the manuscript with input from all co-authors.

Corresponding authors

Correspondence to [Ming-Wei Wang](#) or [Qiang Zhao](#) or [Beili Wu](#).

Ethics declarations

Competing interests

The authors declare no competing interests.

Additional information

Peer review information *Nature* thanks Karen Gregory, Guillaume Lebon and the other, anonymous, reviewer(s) for their contribution to the peer review of this work.

Publisher's note Springer Nature remains neutral with regard to jurisdictional claims in published maps and institutional affiliations.

Extended data figures and tables

Extended Data Fig. 1 Sample preparation and cryo-EM processing of the mGlu2–G_{i1} and mGlu4–G_{i3} complexes.

a–g, Results of the mGlu2–G_{i1} complex. **a**, Comparison of protein samples of the wild-type mGlu2 (WT) and the mGlu2 construct (including truncation of the C-terminal residues V826–L872 and introduction of mutation S601A) used to solve the mGlu2–G_{i1} structure. The curves of SEC of the purified protein samples show higher protein yield of the construct (red) than the WT (black). **b**, Analytical SEC and SDS–PAGE (Coomassie blue stain) of the purified complex. Four independent experiments were performed with similar results. Results from a representative experiment are shown. For gel source data, see Supplementary Fig. 1. **c**, Representative cryo-EM image from four independent experiments with similar results. **d**, Two-dimensional averages. **e**, Gold-standard Fourier shell correlation (FSC) curve for the local refinement of the TMDs and G_{i1}, showing a resolution of 3.5 Å. **f**, Gold-standard FSC curve for the local refinement of the ECDs, showing a resolution of 3.1 Å. **g**, Composite cryo-EM map coloured according to local resolution (in Å). **h–n**, Results of the mGlu4–G_{i3} complex. **h**, Comparison of protein samples of the mGlu4–G_{i1} and mGlu4–G_{i3} complexes. The SEC curves of the purified protein samples show better protein homogeneity of the mGlu4–G_{i3} complex (red) than the mGlu4–G_{i1} complex (black). **i**, Analytical SEC and SDS–PAGE (Coomassie blue stain) of the purified complex. Six independent experiments were performed with similar results. Results from a representative experiment are shown. For gel source data, see Supplementary Fig. 1. **j**, Representative cryo-EM image from four independent experiments with similar results. **k**, Two-

dimensional averages. **I**, Gold-standard FSC curve, showing an overall resolution of 4.0 Å. **m**, Gold-standard FSC curve for the local refinement of the ECDs, showing a resolution of 3.1 Å. **n**, Composite cryo-EM map coloured according to local resolution (in Å).

Extended Data Fig. 2 Cryo-EM processing workflow of mGlu2–Gi1 and mGlu4–Gi3 complexes.

a, Data processing workflow of mGlu2–Gi₁. **b**, Angular distribution of the ECDs, and TMDs and Gi₁ reconstructions, in mGlu2–Gi₁. **c**, Data processing workflow of mGlu4–Gi₃. **d**, Angular distribution of the ECDs, and mGlu4 and Gi₃ reconstructions, in mGlu4–Gi₃.

Extended Data Fig. 3 Cryo-EM density maps of the mGlu2–Gi1 and mGlu4–Gi3 structures.

a, mGlu2–Gi₁. **b**, mGlu4–Gi₃. Cryo-EM density maps and models of the two structures are shown for helices III, V and VI and ICL1, ICL2 and ICL3 in the mGlu_G subunit, helices I, VI and VII in the mGlu_{free} subunit, Gα_i αN helix and α5 helix, and ligands LY354740, JNJ-40411813 and L-SOP. The models are shown as sticks and coloured blue (mGlu2_G), cyan (mGlu2_{free}), orange (mGlu4_G), yellow (mGlu4_{free}), green (Gα_i), magenta (JNJ-40411813), red (LY354740) and purple (L-SOP). The density maps are coloured grey.

Extended Data Fig. 4 Structural comparison with other GPCR structures and binding modes of Gi and PAM.

a, Comparison of VFT conformation. The VFT domains in the Gi-bound structures of mGlu2 and mGlu4 as well as previously published structures of agonist-bound mGlu5 (PDB code 6N51) and mGlu2 VFT bound to LY354740 (PDB code 4XAO) are shown in cartoon representation and coloured blue, orange, pink and grey, respectively. The agonists in these structures are shown as sticks. **b**, Comparison of agonist binding mode. The

agonists in the structures of mGlu2–G_{i1}, mGlu4–G_{i3}, mGlu5, mGlu2 VFT–LY354740, mGlu2 VFT–LY2934747 (PDB code 4XAS), mGlu2 VFT–glutamate (PDB code 5CNI) and mGlu2 VFT–LY2812223 (PDB code 5CNJ) are shown as sticks with blue, orange, pink, grey, red, green and cyan carbons, respectively. Only the receptors in the mGlu2–G_{i1} and mGlu4–G_{i3} structures are shown for clarity. **c**, Conformations of CRD and ECL2 in the mGlu2–G_{i1} and mGlu4–G_{i3} complexes. The two subunits in the mGlu2–G_{i1} structure are coloured blue and cyan, respectively. The two subunits in the mGlu4–G_{i3} structure are coloured orange and yellow, respectively. The cryo-EM maps are coloured grey. **d**, Comparison of the TMD helical bundles in the structures of mGlu2–G_{i1} (mGlu2_G), mGlu4–G_{i3} (mGlu4_G), inactive mGlu2 (mGlu2_{inactive}) and inactive mGlu5 (mGlu5_{inactive}; PDB code 6N52). **e**, Structural comparison of the TMDs in the mGlu2–G_{i1} structure. **f**, Structural comparison of the TMDs in the mGlu4–G_{i3} structure. **g**, Binding pocket for the C terminus of Gα_i α5 helix in mGlu2. The receptor is shown in blue cartoon and surface representations in an intracellular view. The Gα_i α5 helix is shown in green cartoon representation. **h**, Binding pocket for the C terminus of Gα_i α5 helix in mGlu4. The receptor is shown in orange cartoon and surface representations in an intracellular view. **i**, A hypothetical dual-G_i-binding model of mGlu2. The TMDs of the mGlu2 dimer are shown as blue and cyan cartoon, respectively. The two G_i proteins are displayed as green and grey surface, respectively. The panel shows that the two G_i proteins form a clash if both mGlu2 subunits bind to G_i. The clash is highlighted by a red circle. **j**, Comparison of the positions of the C terminus of Gα α5 helix in some G-protein-bound GPCR structures. The mGlu2–G_{i1} and mGlu4–G_{i3} structures and the previously determined structures of β₂AR–Gs, μOR–G_i, GCGR–G_s, GCGR–G_i and SMO–G_i (PDB codes 3SN6, 6DDE, 6LMK, 6LML and 6OT0, respectively) are coloured blue, orange, dark red, yellow, magenta, pink and cyan, respectively. Only the helical bundle of the receptors and Gα α5 helix are shown for clarity. The Gα α5 helices in the structures are highlighted by a red dashed box. The red arrow indicates the shift of the α5 C terminus in the G_i-bound mGlu structures relative to the

other known GPCR–G protein structures. **k**, Comparison of the G_i binding pose in mGlu2 and a class A GPCR. The structures of mGlu2– G_{i1} and μ OR– G_i are shown in blue and yellow cartoon representation, respectively. The G_i proteins in the two structures are also shown as surface. The red arrow indicates the movement of the G_i protein in the mGlu2– G_{i1} structure relative to the μ OR– G_i structure. **l**, Comparison of allosteric modulator binding sites in mGlus. The receptors in the mGlu2– G_{i1} structure and the previously determined structures of mGlu1 TMD–FITM and mGlu5 TMD–mavoglurant (PDB codes 4OR2 and 4OO9, respectively) are shown in cartoon representation and coloured blue, dark red and light gold, respectively. The allosteric modulators JNJ-40411813, FITM and mavoglurant are shown as sticks and coloured magenta, dark red and light gold, respectively. **m**, **n**, Comparison of the cryo-EM maps of the PAM-binding site in the mGlu2_G (**m**) and mGlu2_{free} (**n**) subunits. The mGlu2_G and mGlu2_{free} subunits are coloured blue and cyan, respectively. The PAM JNJ-40411813 is shown as magenta sticks. The residues within the PAM-binding pocket are shown as sticks. The cryo-EM maps are coloured grey. **o**, Comparison of binding modes between the PAM and NAM in mGlu2. The receptors in the structures of mGlu2– G_{i1} and mGlu2 TMD–NAM563¹⁶ are coloured blue and grey, respectively. The PAM JNJ-40411813 and NAM NAM563 are shown as magenta and yellow sticks, respectively. The residue W773^{6.50} that forms a close contact with the PAM and NAM in the structures is shown as sticks. The red arrows indicate the rotamer conformational change of W773^{6.50} and downward shift of helix VI in the mGlu2_G subunit of the mGlu2– G_{i1} complex relative to the NAM-bound inactive structure. **p**, Comparison of the mGlu2– G_{i1} and mGlu2 TMD–NAM563 structures. The two subunits in the mGlu2– G_{i1} structure are coloured blue and cyan, respectively. The mGlu2 TMD–NAM563 structure¹⁶ is in grey. The residues I771^{6.48} in the mGlu2_G subunit and L800^{7.38} and V804^{7.42} in the mGlu2_{free} subunit that form contacts are shown as sticks. The residue I771^{6.48} in the mGlu2 TMD–NAM563 structure is also shown as sticks. The red arrow indicates the movement of helix VI in the G_i -bound structure relative to the inactive structure.

Extended Data Fig. 5 G_i activation, signalling and crosslinking assays of mGlu2 and mGlu4.

a, e, i, LY354740-induced IP accumulation assay of wild-type mGlu2 (WT) and mutants of the mGlu2 residues involved in G_i binding. **b, f, j**, LY354740-induced G_i activation assay of WT mGlu2 and mutants of the mGlu2 residues involved in G_i binding using NanoBiT. **c, g, k**, Glutamate- and VU0364770-induced IP accumulation assay of WT mGlu4 and mutants of the mGlu4 residues involved in G_i binding. **d, h, l**, Glutamate- and VU0364770-induced G_i activation assay of WT mGlu4 and mutants of the mGlu4 residues involved in G_i binding using NanoBiT. **m, q**, JNJ-40411813-induced IP accumulation assay of WT mGlu2 and mutants of the mGlu2 residues involved in JNJ-40411813 binding. **n–p**, LY354740-induced IP accumulation assay of WT mGlu2 and mutants of the mGlu2 residues involved in dimerization. **r–t**, Glutamate- and VU0364770-induced IP accumulation assay of WT mGlu4 and mutants of the mGlu4 residues involved in dimerization. Data are mean ± s.e.m. from at least five independent experiments performed in technical triplicate (IP accumulation) or duplicate (NanoBiT). Extended Data Tables 2, 4 provide detailed numbers of independent experiments (*n*) and statistical evaluation of the IP accumulation data. Extended Data Table 3 provides detailed numbers of independent experiments (*n*) and statistical evaluation of the NanoBiT data. **u**, Crosslinking of the mGlu2 mutants C121A/P778^{6,55}C and C121A/V796^{7,34}C as well as C121A/Y781^{6,58}C and C121A/W567^{1,39}C with (+) or without (–) pre-incubation with the agonist LY354740. The WT receptor and the C121A mutant were evaluated in parallel as controls. Three independent experiments were performed with similar results. Results from a representative experiment are shown. For gel source data, see Supplementary Fig. 1. **v**, Basal activity of the WT mGlu2 and mutants of residues involved in asymmetric dimerization. The IP accumulation assays were performed in parallel with the measurement of the IP production using the cells transfected only with the chimeric G α protein G α_{q19} as a control. The basal activity was calculated by subtracting the IP production measured in the control for the WT receptor and all the mutants and is shown as per cent of the activity of the C121A mutant. The basal

activity was substantially reduced by adding the orthosteric antagonist LY341495 (ref. [48](#)). Data are mean \pm s.e.m. (bars) with individual data points shown (dots). The numbers of independent experiments (n) performed in technical triplicate are shown in the parentheses.

*** $P < 0.0001$ by one-way analysis of variance (ANOVA) followed by Dunnett's post-test, compared with the basal activity of C121A (WT, $P = 0.9994$; WT–LY341495, F747C–H815C, R750C–H815C, I771C–V804C, L774C–L800C, P778C–V796C and Y781C–W567C, $P < 0.0001$).

#The mutation C121A was introduced in both subunits for all the mutants.

Protein expression levels of the mGlu2 mutants at the cell surface were determined in parallel by flow cytometry with an anti-Flag antibody (Sigma, 1:100 diluted in TBS + 4% BSA) and reported as per cent compared to the C121A mutant (% of C121A) from at least three independent measurements performed in technical duplicate: WT, 103 ± 1 ; F747C–H815C, 115 ± 5 ; R750C–H815C, 106 ± 5 ; I771C–V804C, 90 ± 3 ; L774C–L800C, 96 ± 10 ; P778C–V796C, 102 ± 7 ; Y781C–W567C, 88 ± 1 .

Extended Data Fig. 6 Sequence alignment of the TMDs in the human mGlus and GABA_B.

Colours represent the similarity of residues: red background, identical; red text, strongly similar. The mGlu2 residues that are involved in G_i binding are indicated by red arrows. The mGlu2 residues that mediate dimerization in the mGlu2– G_{i1} structure are indicated by green arrows, and labelled with 'G' (in mGlu2_G) and/or 'f' (in mGlu2_{free}). The alignment was generated using UniProt (<http://www.uniprot.org/align/>) and the graphic was prepared on the ESPript 3.0 server (<http://escript.ibcp.fr/ESPript/cgi-bin/ESPript.cgi>).

Extended Data Table 1 Cryo-EM data collection, refinement and validation statistics

[Full size table](#)

Extended Data Table 2 IP accumulation assays of wild-type and mutant mGlus using the chimeric $G\alpha$ protein $G\alpha_{q19}$

[Full size table](#)

Extended Data Table 3 G_i activation assays of wild-type and mutant mGlus using NanoBiT

[Full size table](#)

Extended Data Table 4 PAM- and agonist-induced IP accumulation assays of wild-type and mutant mGlu2 using the chimeric G α protein G α_{q19}

[Full size table](#)

Supplementary information

[Supplementary Figure](#)

Uncropped blots for Extended Data Figures 1 and 5.

[Reporting Summary](#)

Rights and permissions

[Reprints and Permissions](#)

About this article



Check for
updates

Cite this article

Lin, S., Han, S., Cai, X. *et al.* Structures of G_i-bound metabotropic glutamate receptors mGlu2 and mGlu4. *Nature* **594**, 583–588 (2021). <https://doi.org/10.1038/s41586-021-03495-2>

[Download citation](#)

- Received: 25 September 2020
- Accepted: 25 March 2021
- Published: 16 June 2021
- Issue Date: 24 June 2021
- DOI: <https://doi.org/10.1038/s41586-021-03495-2>

Further reading

- **Structures of human mGlu2 and mGlu7 homo- and heterodimers**
 - Juan Du
 - , Dejian Wang
 - , Hongcheng Fan
 - , Chanjuan Xu
 - , Linhua Tai
 - , Shuling Lin
 - , Shuo Han
 - , Qiuxiang Tan
 - , Xinwei Wang
 - , Tuo Xu
 - , Hui Zhang
 - , Xiaojing Chu
 - , Cuiying Yi
 - , Peng Liu
 - , Xiaomei Wang
 - , Yu Zhou
 - , Jean-Philippe Pin
 - , Philippe Rondard
 - , Hong Liu
 - , Jianfeng Liu
 - , Fei Sun
 - , Beili Wu

◦ & Qiang Zhao

Nature (2021)

Comments

By submitting a comment you agree to abide by our [Terms](#) and [Community Guidelines](#). If you find something abusive or that does not comply with our terms or guidelines please flag it as inappropriate.

[Access through your institution](#)

[Change institution](#)

[Buy or subscribe](#)

Advertisement

This article was downloaded by **calibre** from <https://www.nature.com/articles/s41586-021-03495-2>

| [Section menu](#) | [Main menu](#) |

- Article
- [Published: 16 June 2021](#)

Structures of human mGlu2 and mGlu7 homo- and heterodimers

- [Juan Du](#)^{1,2,3 na1},
- [Dejian Wang](#)^{1,4 na1},
- [Hongcheng Fan](#)^{4,5 na1},
- [Chanjuan Xu](#) ORCID: orcid.org/0000-0002-5640-1896^{6 na1},
- [Linhua Tai](#)^{4,5 na1},
- [Shuling Lin](#)^{2,4 na1},
- [Shuo Han](#) ORCID: orcid.org/0000-0003-0760-0183¹,
- [Qixiang Tan](#)²,
- [Xinwei Wang](#)^{2,4},
- [Tuo Xu](#)^{1,4},
- [Hui Zhang](#)^{2,4},
- [Xiaojing Chu](#)²,
- [Cuiying Yi](#)¹,
- [Peng Liu](#)⁶,
- [Xiaomei Wang](#)⁶,
- [Yu Zhou](#)^{1,4},
- [Jean-Philippe Pin](#) ORCID: orcid.org/0000-0002-1423-345X⁷,
- [Philippe Rondard](#) ORCID: orcid.org/0000-0003-1134-2738⁷,
- [Hong Liu](#) ORCID: orcid.org/0000-0003-3685-6268^{1,3,4,8},
- [Jianfeng Liu](#) ORCID: orcid.org/0000-0002-0284-8377^{6,9},
- [Fei Sun](#) ORCID: orcid.org/0000-0002-0351-5144^{4,5,9,10},
- [Beili Wu](#) ORCID: orcid.org/0000-0002-1936-0909^{2,3,4,8} &
- [Qiang Zhao](#) ORCID: orcid.org/0000-0001-6251-6676^{1,4,11}

- 3024 Accesses
- 40 Altmetric
- [Metrics details](#)

Subjects

- [Cryoelectron microscopy](#)
- [G protein-coupled receptors](#)

Abstract

The metabotropic glutamate receptors (mGlus) are involved in the modulation of synaptic transmission and neuronal excitability in the central nervous system¹. These receptors probably exist as both homo- and heterodimers that have unique pharmacological and functional properties^{2,3,4}. Here we report four cryo-electron microscopy structures of the human mGlu subtypes mGlu2 and mGlu7, including inactive mGlu2 and mGlu7 homodimers; mGlu2 homodimer bound to an agonist and a positive allosteric modulator; and inactive mGlu2–mGlu7 heterodimer. We observed a subtype-dependent dimerization mode for these mGlus, as a unique dimer interface that is mediated by helix IV (and that is important for limiting receptor activity) exists only in the inactive mGlu2 structure. The structures provide molecular details of the inter- and intra-subunit conformational changes that are required for receptor activation, which distinguish class C G-protein-coupled receptors from those in classes A and B. Furthermore, our structure and functional studies of the mGlu2–mGlu7 heterodimer suggest that the mGlu7 subunit has a dominant role in controlling dimeric association and G-protein activation in the heterodimer. These insights into mGlu homo- and heterodimers highlight the complex landscape of mGlu dimerization and activation.

Access options

Subscribe to Journal

Get full journal access for 1 year

\$199.00

only \$3.90 per issue

[Subscribe](#)

All prices are NET prices.

VAT will be added later in the checkout.

Tax calculation will be finalised during checkout.

Rent or Buy article

Get time limited or full article access on ReadCube.

from \$8.99

[Rent or Buy](#)

All prices are NET prices.

Additional access options:

- [Log in](#)
- [Access through your institution](#)
- [Learn about institutional subscriptions](#)

Fig. 1: Maps and structures of mGlu2 and mGlu7.

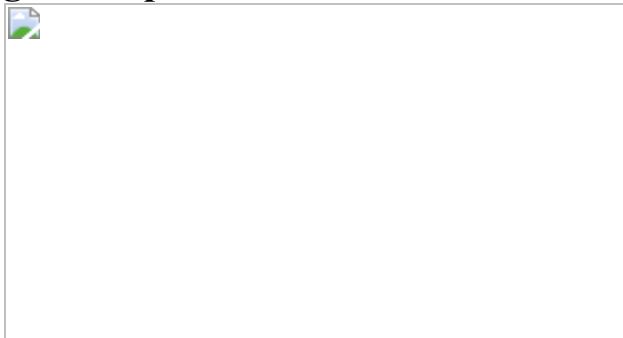


Fig. 2: Structures of inactive mGlus.

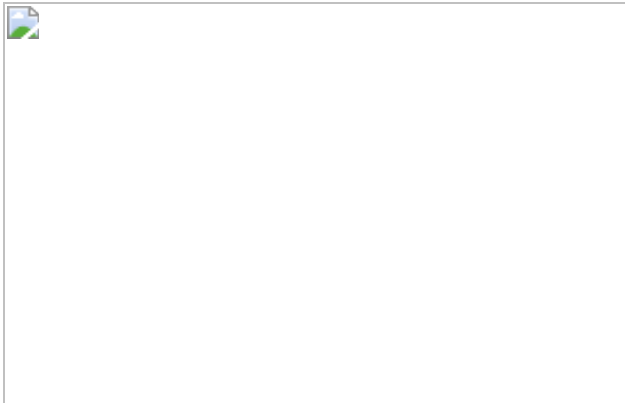
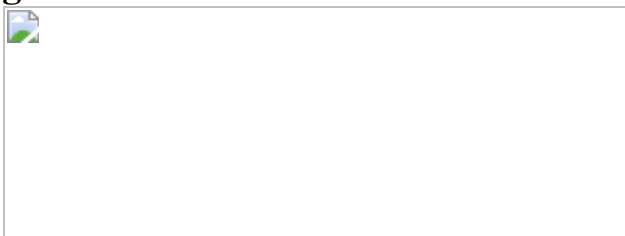


Fig. 3: Structure and activation of the mGlu2–mGlu7 heterodimer.



Data availability

Atomic coordinates and cryo-EM density maps for the structures of inactive mGlu2, agonist- and PAM-bound mGlu2, inactive mGlu7 and inactive mGlu2–mGlu7 have been deposited in the PDB under accession codes [7EPA](#), [7EPB](#), [7EPC](#) and [7EPD](#), respectively, and in the Electron Microscopy Data Bank under accession codes [EMD-31235](#), [EMD-31236](#), [EMD-31237](#) and [EMD-31238](#), respectively. Atomic coordinates for the structures of mGlu2 TMD–NAM563 and mGlu2 TMD–NAM597 have been deposited in the PDB under accession codes [7EPE](#) and [7EPF](#), respectively. The uncropped gels shown in Extended Data Fig. [1r,u](#) are displayed in Supplementary Fig. [1](#). Any other relevant data are available from the corresponding authors upon reasonable request.

References

1. 1.

Niswender, C. M. & Conn, P. J. Metabotropic glutamate receptors: physiology, pharmacology, and disease. *Annu. Rev. Pharmacol.*

Toxicol. **50**, 295–322 (2010).

[CAS](#) [PubMed](#) [PubMed Central](#) [Google Scholar](#)

2. 2.

Levitz, J. et al. Mechanism of assembly and cooperativity of homomeric and heteromeric metabotropic glutamate receptors. *Neuron* **92**, 143–159 (2016).

[CAS](#) [PubMed](#) [PubMed Central](#) [Google Scholar](#)

3. 3.

Kniazeff, J., Prézeau, L., Rondard, P., Pin, J. P. & Goudet, C. Dimers and beyond: the functional puzzles of class C GPCRs. *Pharmacol. Ther.* **130**, 9–25 (2011).

[CAS](#) [PubMed](#) [Google Scholar](#)

4. 4.

Pin, J. P. & Bettler, B. Organization and functions of mGlu and GABA_B receptor complexes. *Nature* **540**, 60–68 (2016).

[ADS](#) [CAS](#) [PubMed](#) [Google Scholar](#)

5. 5.

Bungard, C. J. et al. Quinoline carboxamide and quinoline carbonitrile derivatives as mGluR2-negative allosteric modulators, compositions, and their use. International Patent Application WO 2013/066736 A1 (2013).

6. 6.

Suzuki, G. et al. In vitro pharmacological characterization of novel isoxazolopyridone derivatives as allosteric metabotropic glutamate receptor 7 antagonists. *J. Pharmacol. Exp. Ther.* **323**, 147–156 (2007).

[CAS](#) [PubMed](#) [Google Scholar](#)

7. 7.

Monn, J. A. et al. Design, synthesis, and pharmacological characterization of (+)-2-aminobicyclo[3.1.0]hexane-2,6-dicarboxylic acid (LY354740): a potent, selective, and orally active group 2 metabotropic glutamate receptor agonist possessing anticonvulsant and anxiolytic properties. *J. Med. Chem.* **40**, 528–537 (1997).

[CAS](#) [PubMed](#) [Google Scholar](#)

8. 8.

Cid, J. M. et al. Discovery of 1-butyl-3-chloro-4-(4-phenyl-1-piperidinyl)-(1*H*)-pyridone (JNJ-40411813): a novel positive allosteric modulator of the metabotropic glutamate 2 receptor. *J. Med. Chem.* **57**, 6495–6512 (2014).

[CAS](#) [PubMed](#) [Google Scholar](#)

9. 9.

Scholler, P. et al. Allosteric nanobodies uncover a role of hippocampal mGlu2 receptor homodimers in contextual fear consolidation. *Nat. Commun.* **8**, 1967 (2017).

[ADS](#) [PubMed](#) [PubMed Central](#) [Google Scholar](#)

10. 10.

Arasappan, A. et al. Tetrahydronaphthyridine derivatives as mGluR2-negative allosteric modulators, compositions, and their use. International Patent Application WO 2016/029454 A1 (2016).

11. 11.

Koehl, A. et al. Structural insights into the activation of metabotropic glutamate receptors. *Nature* **566**, 79–84 (2019).

[ADS](#) [CAS](#) [PubMed](#) [PubMed Central](#) [Google Scholar](#)

12. 12.

Chappell, M. D. et al. Discovery of (1*S*,2*R*,3*S*,4*S*,5*R*,6*R*)-2-amino-3-[(3,4-difluorophenyl)sulfanyl methyl]-4-hydroxy-bicyclo[3.1.0]hexane-2,6-dicarboxylic acid hydrochloride (LY3020371·HCl): a potent, metabotropic glutamate 2/3 receptor antagonist with antidepressant-like activity. *J. Med. Chem.* **59**, 10974–10993 (2016).

[CAS](#) [PubMed](#) [Google Scholar](#)

13. 13.

Xue, L. et al. Major ligand-induced rearrangement of the heptahelical domain interface in a GPCR dimer. *Nat. Chem. Biol.* **11**, 134–140 (2015).

[CAS](#) [PubMed](#) [Google Scholar](#)

14. 14.

Gutzeit, V. A. et al. Conformational dynamics between transmembrane domains and allosteric modulation of a metabotropic glutamate receptor. *eLife* **8**, e45116 (2019).

[CAS](#) [PubMed](#) [PubMed Central](#) [Google Scholar](#)

15. 15.

Huang, S. et al. Interdomain movements in metabotropic glutamate receptor activation. *Proc. Natl Acad. Sci. USA* **108**, 15480–15485 (2011).

[ADS](#) [CAS](#) [PubMed](#) [PubMed Central](#) [Google Scholar](#)

16. 16.

Hlavackova, V. et al. Sequential inter- and intrasubunit rearrangements during activation of dimeric metabotropic glutamate receptor 1. *Sci. Signal.* **5**, ra59 (2012).

[PubMed](#) [Google Scholar](#)

17. 17.

Lin, S. et al. Structures of G_i-bound metabotropic glutamate receptors mGlu2 and mGlu4. *Nature* <https://doi.org/10.1038/s41586-021-03495-2> (2021).

18. 18.

Wu, H. et al. Structure of a class C GPCR metabotropic glutamate receptor 1 bound to an allosteric modulator. *Science* **344**, 58–64 (2014).

[ADS](#) [CAS](#) [PubMed](#) [PubMed Central](#) [Google Scholar](#)

19. 19.

Doré, A. S. et al. Structure of class C GPCR metabotropic glutamate receptor 5 transmembrane domain. *Nature* **511**, 557–562 (2014).

[ADS](#) [PubMed](#) [Google Scholar](#)

20. 20.

Habrian, C. H. et al. Conformational pathway provides unique sensitivity to a synaptic mGluR. *Nat. Commun.* **10**, 5572 (2019).

[ADS](#) [CAS](#) [PubMed](#) [PubMed Central](#) [Google Scholar](#)

21. 21.

Liu, J. et al. Allosteric control of an asymmetric transduction in a G protein-coupled receptor heterodimer. *eLife* **6**, e26985 (2017).

[PubMed](#) [PubMed Central](#) [Google Scholar](#)

22. 22.

Saugstad, J. A., Kinzie, J. M., Mulvihill, E. R., Segerson, T. P. & Westbrook, G. L. Cloning and expression of a new member of the l-2-amino-4-phosphonobutyric acid-sensitive class of metabotropic glutamate receptors. *Mol. Pharmacol.* **45**, 367–372 (1994).

[CAS](#) [PubMed](#) [Google Scholar](#)

23. 23.

Francesconi, A. & Duvoisin, R. M. Role of the second and third intracellular loops of metabotropic glutamate receptors in mediating dual signal transduction activation. *J. Biol. Chem.* **273**, 5615–5624 (1998).

[CAS](#) [PubMed](#) [Google Scholar](#)

24. 24.

Olsen, R. H. J. et al. TRUPATH, an open-source biosensor platform for interrogating the GPCR transducerome. *Nat. Chem. Biol.* **16**, 841–849 (2020).

[CAS](#) [PubMed](#) [PubMed Central](#) [Google Scholar](#)

25. 25.

Fegan, A., White, B., Carlson, J. C. & Wagner, C. R. Chemically controlled protein assembly: techniques and applications. *Chem. Rev.* **110**, 3315–3336 (2010).

[CAS](#) [PubMed](#) [Google Scholar](#)

26. 26.

Huang, X. et al. Amorphous nickel titanium alloy film: a new choice for cryo electron microscopy sample preparation. *Prog. Biophys. Mol. Biol.* **156**, 3–13 (2020).

[CAS](#) [PubMed](#) [Google Scholar](#)

27. 27.

Mastronarde, D. N. Automated electron microscope tomography using robust prediction of specimen movements. *J. Struct. Biol.* **152**, 36–51 (2005).

[PubMed](#) [Google Scholar](#)

28. 28.

Scheres, S. H. RELION: implementation of a Bayesian approach to cryo-EM structure determination. *J. Struct. Biol.* **180**, 519–530 (2012).

[CAS](#) [PubMed](#) [PubMed Central](#) [Google Scholar](#)

29. 29.

Zhang, K. Gctf: real-time CTF determination and correction. *J. Struct. Biol.* **193**, 1–12 (2016).

[ADS](#) [CAS](#) [PubMed](#) [PubMed Central](#) [Google Scholar](#)

30. 30.

Bepler, T. et al. Positive-unlabeled convolutional neural networks for particle picking in cryo-electron micrographs. *Nat. Methods* **16**, 1153–1160 (2019).

[CAS](#) [PubMed](#) [PubMed Central](#) [Google Scholar](#)

31. 31.

Punjani, A., Rubinstein, J. L., Fleet, D. J. & Brubaker, M. A. cryoSPARC: algorithms for rapid unsupervised cryo-EM structure determination. *Nat. Methods* **14**, 290–296 (2017).

[CAS](#) [PubMed](#) [Google Scholar](#)

32. 32.

Ramlaul, K., Palmer, C. M., Nakane, T. & Aylett, C. H. S. Mitigating local over-fitting during single particle reconstruction with SIDESPLITTER. *J. Struct. Biol.* **211**, 107545 (2020).

[PubMed](#) [PubMed Central](#) [Google Scholar](#)

33. 33.

Kaur, S. et al. Local computational methods to improve the interpretability and analysis of cryo-EM maps. *Nat. Commun.* **12**, 1240 (2021).

[ADS](#) [CAS](#) [PubMed](#) [PubMed Central](#) [Google Scholar](#)

34. 34.

Pettersen, E. F. et al. UCSF Chimera—a visualization system for exploratory research and analysis. *J. Comput. Chem.* **25**, 1605–1612 (2004).

[CAS](#) [Google Scholar](#)

35. 35.

Zheng, S. Q. et al. MotionCor2: anisotropic correction of beam-induced motion for improved cryo-electron microscopy. *Nat. Methods* **14**, 331–332 (2017).

[CAS](#) [PubMed](#) [PubMed Central](#) [Google Scholar](#)

36. 36.

Emsley, P., Lohkamp, B., Scott, W. G. & Cowtan, K. Features and development of Coot. *Acta Crystallogr. D* **66**, 486–501 (2010).

[CAS](#) [PubMed](#) [PubMed Central](#) [Google Scholar](#)

37. 37.

Adams, P. D. et al. PHENIX: a comprehensive Python-based system for macromolecular structure solution. *Acta Crystallogr. D* **66**, 213–221 (2010).

[CAS](#) [PubMed](#) [PubMed Central](#) [Google Scholar](#)

38. 38.

Chen, V. B. et al. MolProbity: all-atom structure validation for macromolecular crystallography. *Acta Crystallogr. D* **66**, 12–21 (2010).

[CAS](#) [PubMed](#) [Google Scholar](#)

39. 39.

Chun, E. et al. Fusion partner toolchest for the stabilization and crystallization of G protein-coupled receptors. *Structure* **20**, 967–976 (2012).

[CAS](#) [PubMed](#) [PubMed Central](#) [Google Scholar](#)

40. 40.

Caffrey, M. & Cherezov, V. Crystallizing membrane proteins using lipidic mesophases. *Nat. Protocols* **4**, 706–731 (2009).

[CAS](#) [PubMed](#) [Google Scholar](#)

41. 41.

Otwinowski, Z. & Minor, W. Processing of X-ray diffraction data collected in oscillation mode. *Methods Enzymol.* **276**, 307–326 (1997).

[CAS](#) [PubMed](#) [Google Scholar](#)

42. 42.

McCoy, A. J. et al. Phaser crystallographic software. *J. Appl. Crystallogr.* **40**, 658–674 (2007).

[CAS](#) [PubMed](#) [PubMed Central](#) [Google Scholar](#)

43. 43.

Vagin, A. A. et al. REFMAC5 dictionary: organization of prior chemical knowledge and guidelines for its use. *Acta Crystallogr. D* **60**, 2184–2195 (2004).

[PubMed](#) [Google Scholar](#)

44. 44.

Smart, O. S. et al. Exploiting structure similarity in refinement: automated NCS and target-structure restraints in BUSTER. *Acta Crystallogr. D* **68**, 368–380 (2012).

[CAS](#) [PubMed](#) [PubMed Central](#) [Google Scholar](#)

45. 45.

Jalan-Sakrikar, N. et al. Identification of positive allosteric modulators VU0155094 (ML397) and VU0422288 (ML396) reveals new insights into the biology of metabotropic glutamate receptor 7. *ACS Chem. Neurosci.* **5**, 1221–1237 (2014).

[CAS](#) [PubMed](#) [Google Scholar](#)

[Download references](#)

Acknowledgements

The cryo-EM studies were performed at the Center for Biological Imaging (CBI) (<http://cbi.ibp.ac.cn>), Institute of Biophysics, Chinese Academy of Sciences and the electron microscopy facility of Shanghai Institute of Materia Medica (SIMM), Chinese Academy of Sciences. We thank B. Zhu, X. Huang, X. Li, L. Chen and X. Niu from CBI and Q. Wang from SIMM for their help with cryo-EM data collection. The synchrotron radiation experiments were performed at the BL41XU of SPring-8 with approval of the Japan Synchrotron Radiation Research Institute (proposal no. 2019A2543, 2019B2543, 2019A2541 and 2019B2541). We thank the beamline staff members K. Hasegawa, N. Mizuno, T. Kawamura and H. Murakami of the BL41XU for help with X-ray data collection. We thank Merck for providing the mGlu2 NAMs NAM563 and NAM597. This work was supported by the National Key R&D Program of China 2018YFA0507000 (Q.Z., B.W. and J.L.), National Science Foundation of China grants 31825010 (B.W.), 31830020 (F.S.) and 81720108031 (J.L.), CAS Strategic Priority Research Programs XDB37030100 (Q.Z. and B.W.) and XDB37040102 (F.S.), Agence Nationale de la Recherche, ANR 18-CE11-0004-01 and Fondation Recherche Médicale (DEQ20170336747) (J.-P.P.), and ANR-15-CE18-0020-01, CNRS PRC no. 1403 and Inserm IRP BrainSignal (P.R.).

Author information

Author notes

1. These authors contributed equally: Juan Du, Dejian Wang, Hongcheng Fan, Chanjuan Xu, Linhua Tai, Shuling Lin

Affiliations

1. State Key Laboratory of Drug Research, Shanghai Institute of Materia Medica, Chinese Academy of Sciences, Shanghai, China

Juan Du, Dejian Wang, Shuo Han, Tuo Xu, Cuiying Yi, Yu Zhou, Hong Liu & Qiang Zhao

2. CAS Key Laboratory of Receptor Research, Shanghai Institute of Materia Medica, Chinese Academy of Sciences, Shanghai, China

Juan Du, Shuling Lin, Qiuxiang Tan, Xinwei Wang, Hui Zhang, Xiaojing Chu & Beili Wu

3. School of Pharmaceutical Science and Technology, Hangzhou Institute for Advanced Study, University of Chinese Academy of Sciences, Hangzhou, China

Juan Du, Hong Liu & Beili Wu

4. University of Chinese Academy of Sciences, Beijing, China

Dejian Wang, Hongcheng Fan, Linhua Tai, Shuling Lin, Xinwei Wang, Tuo Xu, Hui Zhang, Yu Zhou, Hong Liu, Fei Sun, Beili Wu & Qiang Zhao

5. National Laboratory of Biomacromolecules, National Center of Protein Science-Beijing, CAS Center for Excellence in Biomacromolecules, Institute of Biophysics, Chinese Academy of Sciences, Beijing, China

Hongcheng Fan, Linhua Tai & Fei Sun

6. Key Laboratory of Molecular Biophysics of MOE, International Research Center for Sensory Biology and Technology of MOST, College of Life Science and Technology, Huazhong University of Science and Technology, Wuhan, China

Chanjuan Xu, Peng Liu, Xiaomei Wang & Jianfeng Liu

7. Institut de Génomique Fonctionnelle (IGF), Université de Montpellier, CNRS, INSERM, Montpellier, France

Jean-Philippe Pin & Philippe Rondard

8. School of Life Science and Technology, ShanghaiTech University,
Shanghai, China

Hong Liu & Beili Wu

9. Bioland Laboratory (Guangzhou Regenerative Medicine and Health
Guangdong Laboratory), Guangzhou, China

Jianfeng Liu & Fei Sun

10. Center for Biological Imaging, Institute of Biophysics, Chinese
Academy of Sciences, Beijing, China

Fei Sun

11. Zhongshan Branch, Institute of Drug Discovery and Development,
Chinese Academy of Sciences, Zhongshan, China

Qiang Zhao

Authors

1. Juan Du

[View author publications](#)

You can also search for this author in [PubMed](#) [Google Scholar](#)

2. Dejian Wang

[View author publications](#)

You can also search for this author in [PubMed](#) [Google Scholar](#)

3. Hongcheng Fan

[View author publications](#)

You can also search for this author in [PubMed](#) [Google Scholar](#)

4. Chanjuan Xu

[View author publications](#)

You can also search for this author in [PubMed](#) [Google Scholar](#)

5. Linhua Tai

[View author publications](#)

You can also search for this author in [PubMed](#) [Google Scholar](#)

6. Shuling Lin

[View author publications](#)

You can also search for this author in [PubMed](#) [Google Scholar](#)

7. Shuo Han

[View author publications](#)

You can also search for this author in [PubMed](#) [Google Scholar](#)

8. Qiuxiang Tan

[View author publications](#)

You can also search for this author in [PubMed](#) [Google Scholar](#)

9. Xinwei Wang

[View author publications](#)

You can also search for this author in [PubMed](#) [Google Scholar](#)

10. Tuo Xu

[View author publications](#)

You can also search for this author in [PubMed](#) [Google Scholar](#)

11. Hui Zhang

[View author publications](#)

You can also search for this author in [PubMed](#) [Google Scholar](#)

12. Xiaojing Chu

[View author publications](#)

You can also search for this author in [PubMed](#) [Google Scholar](#)

13. Cuiying Yi
[View author publications](#)

You can also search for this author in [PubMed](#) [Google Scholar](#)

14. Peng Liu
[View author publications](#)

You can also search for this author in [PubMed](#) [Google Scholar](#)

15. Xiaomei Wang
[View author publications](#)

You can also search for this author in [PubMed](#) [Google Scholar](#)

16. Yu Zhou
[View author publications](#)

You can also search for this author in [PubMed](#) [Google Scholar](#)

17. Jean-Philippe Pin
[View author publications](#)

You can also search for this author in [PubMed](#) [Google Scholar](#)

18. Philippe Rondard
[View author publications](#)

You can also search for this author in [PubMed](#) [Google Scholar](#)

19. Hong Liu
[View author publications](#)

You can also search for this author in [PubMed](#) [Google Scholar](#)

20. Jianfeng Liu
[View author publications](#)

You can also search for this author in [PubMed](#) [Google Scholar](#)

21. Fei Sun

[View author publications](#)

You can also search for this author in [PubMed](#) [Google Scholar](#)

22. Beili Wu

[View author publications](#)

You can also search for this author in [PubMed](#) [Google Scholar](#)

23. Qiang Zhao

[View author publications](#)

You can also search for this author in [PubMed](#) [Google Scholar](#)

Contributions

J.D. developed the protein expression and purification procedures of mGlu2, prepared the mGlu2 protein samples for cryo-EM and crystallization, solved the crystal structures of mGlu2 TMD–NAMs, performed the IP accumulation assay and helped with manuscript preparation. D.W. developed the protein expression and purification procedures of mGlu7, prepared the mGlu7 protein sample for cryo-EM, performed model building and structure refinement of the homodimers, and helped with the IP accumulation assay and manuscript preparation. H.F. performed the cryo-EM studies of the mGlu2 homodimers. C.X. performed crosslinking, calcium release and FRET assays. L.T. performed the cryo-EM studies of the mGlu7 homodimer. S.L. developed the protein expression and purification procedures of the mGlu2–mGlu7 heterodimer, prepared the mGlu2–mGlu7 protein sample for cryo-EM, and performed model building and structure refinement of the heterodimer. S.H. performed the cryo-EM studies of the mGlu2–mGlu7 heterodimer. Q.T. performed the BRET assay. Xinwei Wang and T.X. helped with protein preparation and functional assays. H.Z. collected the crystal diffraction data. X.C. and C.Y. expressed the proteins. P.L. and Xiaomei Wang helped with crosslinking and calcium release assays. J.-P.P. and P.R. helped with data analysis and interpretation,

and edited the manuscript. Y.Z. and H.L. provided mGlu2 ligands for structural and functional studies. J.L. oversaw crosslinking, calcium release and FRET assays, helped with data analysis and interpretation, and edited the manuscript. F.S. oversaw the cryo-EM studies of mGlu2 and mGlu7 homodimers, helped with data analysis and interpretation, and edited the manuscript. B.W. and Q.Z. initiated the project, planned and analysed experiments, supervised the research and wrote the manuscript with input from all co-authors.

Corresponding authors

Correspondence to [Hong Liu](#) or [Jianfeng Liu](#) or [Fei Sun](#) or [Beili Wu](#) or [Qiang Zhao](#).

Ethics declarations

Competing interests

The authors declare no competing interests.

Additional information

Peer review information *Nature* thanks Karen J. Gregory, Tracy Josephs and the other, anonymous, reviewer(s) for their contribution to the peer review of this work.

Publisher's note Springer Nature remains neutral with regard to jurisdictional claims in published maps and institutional affiliations.

Extended data figures and tables

[Extended Data Fig. 1 Optimization and characterization of mGlu2 and mGlu7 homo- and heterodimers.](#)

a, Comparison of the mGlu2 homodimers with different C-terminal truncations. The curves of size-exclusion chromatography (SEC) of purified protein samples show higher yield and better homogeneity for the protein with the C-terminal residues V826–L872 truncated. **b**, Comparison of the mGlu7 homodimers with different C-terminal truncations. The SEC curves of purified protein samples show higher yield and better homogeneity for the protein with the C-terminal residues K860–I915 truncated. **c**, Comparison of the mGlu2 homodimers with different mutations. The SEC curves of purified protein samples show higher yield for the mutant N655^{3.52}Y/H815^{7.53}Y (construct 1, used to determine the inactive mGlu2 structure). **d**, Comparison of the mGlu7 homodimers with different mutations. The SEC results of purified protein samples show higher yield for the mutant N678^{3.52}Y/G722^{4.52}I/I775^{5.59}F/P789^{6.38}Y (construct 2, used to determine the inactive mGlu7 structure). **e**, LY354740-induced IP accumulation assay of wild-type (WT) mGlu2 and mutants. The IP accumulation data are mean ± s.e.m. from at least three independent experiments performed in technical triplicate (same for below). The numbers of independent experiments (*n*) are shown in the parentheses (same for below). Surface expression levels of the mutants are reported as per cent compared to the wild type from at least three independent measurements performed in duplicate (% of WT): N655^{3.52}Y, 112 ± 29; H815^{7.53}Y, 56 ± 10; S601A, 88 ± 13; C-truncation (V826–L872), 53 ± 3. **f**, Inhibition of LY354740-induced IP accumulation of wild-type mGlu2 and mutants by NAM563. **g**, Glutamate-induced IP accumulation assay of wild-type mGlu7 and mutants in the presence of VU0422288. Surface expression levels of the mutants (% of WT): N678^{3.52}Y, 200 ± 25; G722^{4.52}I, 144 ± 14; I775^{5.59}F, 136 ± 13; P789^{6.38}Y, 129 ± 12; C-truncation (K860–I915), 110 ± 10. **h**, Inhibition of glutamate-induced IP accumulation of wild-type mGlu7 and mutants by MMPIP. **i**, LY354740-induced G_i activation of wild-type mGlu2 and mutants measured by the BRET assay. The BRET data are mean ± s.e.m. from at least three independent experiments performed in technical duplicate (same for below). **j**, Glutamate-induced G_i activation of wild-type mGlu7 and mutants in the presence of VU0422288 measured by the BRET assay. **k**, Ligand screening for the inactive mGlu2 homodimer. The SEC curves show that the NAM563-bound mGlu2 has higher yield and better homogeneity compared to the apo receptor and LY341495-bound

mGlu2. **I**, Ligand screening for the inactive mGlu7 homodimer. The SEC curves show that the NAM MMPIP-bound mGlu7 has higher yield and better homogeneity compared to the apo receptor and the receptor bound to other ligands. **m**, Inhibition of LY354740-induced IP accumulation of wild-type mGlu2 by NAM563 or NAM597. **n**, Comparison of wild-type mGlu2 and construct 3 (used to determine the agonist- and PAM-bound mGlu2 structure). The SEC curves of purified protein samples show higher yield and better homogeneity for construct 3. **o**, JNJ-40411813-induced IP accumulation assay of wild-type mGlu2 and mutants. **p**, JNJ-40411813-induced G_i activation of wild-type mGlu2 and mutants measured by the BRET assay. **q**, Ligand screening for the agonist- and PAM-bound mGlu2 homodimer. The SEC curves show higher yield for the agonist- or PAM-bound receptor than the apo protein. **r**, Nu-PAGE and western blot results of the mGlu2–mGlu7 heterodimer. Double staining (anti-His for His-tagged mGlu2 and anti-Strep for Strep-tagged mGlu7) confirms the existence of mGlu2–mGlu7 heterodimer. Three independent experiments were performed with similar results. Results from a representative experiment are shown. For gel source data, see Supplementary Fig. [1](#). **s**, **t**, Glutamate-induced IP accumulation of wild-type mGlu2 and mutants. Extended Data Table [3](#) provides detailed independent experiment numbers (*n*), statistical evaluation and expression level. **u**, Crosslinking of the mGlu2 mutants C121A/L698^{4.51}C, C121A/V699^{4.52}C and C121A/V782^{6.59}C–C121A/V789^{7.27}C with (+) or without (–) preincubation with the agonist LY354740 and PAM JNJ-40411813 or the antagonist LY341495 and NAM Ro64-5299. The mutant C121A/V782^{6.59}C–C121A/V789^{7.27}C was tested using an optimized GABA_B quality control system, in which the C-terminal tails of the two mGlu2 subunits were replaced by the modified C1 and C2 domains of GABA_{B1} and GABA_{B2}, respectively, to only allow the mGlu2 dimers containing the C1–C2 dimer to reach the cell surface^{[15](#)}. The wild-type and mutant C121A were tested in parallel as controls. Three independent experiments were performed with similar results. Results from a representative experiment are shown. For gel source data, see Supplementary Fig. [1](#). **v**, LY354740-induced IP accumulation assay of mGlu2 in the presence of the oxidant CuP. Surface expression levels of the mGlu2 mutants are reported as per cent compared to the wild type from at least three independent measurements performed in duplicate (% of WT):

C121A, 100 ± 6 ; C121A/L698^{4.51}C, 84 ± 11 ; C121A/V699^{4.52}C, 92 ± 9 . **w**, LY354740-induced IP accumulation assay of the mGlu2 mutants in the CRD. Extended Data Table 3 provides detailed statistical evaluation and expression level. **x**, Glutamate-induced IP accumulation assay of wild-type mGlu7 and mutants in the presence of VU0422288. Extended Data Table 3 provides detailed statistical evaluation and expression level. **y**, LY354740-induced IP accumulation assay of mGlu2 mutants in the CRD and ECL2. Extended Data Table 3 provides detailed independent experiment numbers (*n*), statistical evaluation and expression level. **z**, JNJ-40411813-induced IP accumulation assay of wild-type mGlu2 and the mutant in ECL2. **aa**, Crosslinking of the mGlu2–mGlu7 mutants C121A/D174C (mGlu2)–C136A/R191C (mGlu7) and C121A/S176C (mGlu2)–C136A/R191C (mGlu7). The crosslinking studies were carried out using the GABA_B C1–C2 quality control system that allows cell surface targeting of the heterodimer only²¹. The wild-type heterodimer and mutant C121A (mGlu2)–C136A (mGlu7) were tested in parallel as controls. Four independent experiments were performed with similar results. Results from a representative experiment are shown. For gel source data, see Supplementary Fig. 1.

Extended Data Fig. 2 Cryo-EM processing and 3D reconstruction workflow.

a–f, Results of the inactive mGlu2 homodimer. **a**, Processing workflow. **b**, Representative cryo-EM image from four independent experiments with similar results. **c**, Two-dimensional averages. **d**, Cryo-EM map coloured according to local resolution (in Å). **e**, Gold-standard Fourier shell correlation (FSC) curve showing an overall resolution at 3.6 Å. **f**, Cross-validation of model to cryo-EM density map. FSC curves for the final model versus the final map and half maps are shown in black, red and green, respectively. **g–l**, Results of the inactive mGlu7 homodimer. **g**, Processing workflow. **h**, Representative cryo-EM image from five independent experiments with similar results. **i**, Two-dimensional averages. **j**, Cryo-EM map coloured according to local resolution (in Å). **k**, Gold-standard FSC curves showing an overall resolution at 4.0 Å and a resolution at 3.6 Å for the extracellular domains (ECDs). **l**, Cross-validation of model

to cryo-EM density map. **m–r**, Results of the agonist- and PAM-bound mGlu2 homodimer. **m**, Processing workflow. **n**, Representative cryo-EM image from three independent experiments with similar results. **o**, Two-dimensional averages. **p**, Cryo-EM map coloured according to local resolution (in Å). **q**, Gold-standard FSC curve showing an overall resolution at 3.1 Å. **r**, Cross-validation of model to cryo-EM density map. **s–x**, Results of the inactive mGlu2–mGlu7 heterodimer. **s**, Processing workflow. **t**, Representative cryo-EM image from four independent experiments with similar results. **u**, Two-dimensional averages. **v**, Cryo-EM map coloured according to local resolution (in Å). **w**, Gold-standard FSC curves showing an overall resolution at 3.9 Å and a resolution at 3.5 Å for the extracellular domains. **x**, Cross-validation of model to cryo-EM density map.

Extended Data Fig. 3 Cryo-EM density maps of mGlu2 and mGlu7 homo- and heterodimers.

The models are shown as cartoon and sticks. The density maps are coloured grey. **a**, Map and model of the inactive mGlu2 structure shown for all transmembrane helices, B and C helices in VFTs, CRDs and inter-subunit disulfide bond. The model is coloured blue (molecule A) and grey (molecule B). **b**, Map and model of the inactive mGlu7 structure shown for all transmembrane helices, B and C helices in VFTs, CRDs and inter-subunit disulfide bond. The model is coloured orange (molecule A) and yellow (molecule B). **c**, Map and model of the agonist- and PAM-bound mGlu2 structure shown for all transmembrane helices, B and C helices in VFTs, LY354740, DN13, CRDs and inter-subunit disulfide bond. The model is coloured blue (molecule A) and grey (molecule B). **d**, Map and model of the inactive mGlu2–mGlu7 structure shown for all transmembrane helices, B and C helices in VFTs, CRDs, inter-subunit disulfide bond and some non-conserved residues in the two subunits that aided modelling. The model is coloured blue (mGlu2) and orange (mGlu7).

Extended Data Fig. 4 VFT and CRD conformations in mGlus.

a, Comparison of inter-subunit disulfide bonds in the inactive mGlu2 and mGlu7 homo- and heterodimers. The structures of inactive mGlu2

homodimer, mGlu7 homodimer and mGlu2–mGlu7 heterodimer are shown in cartoon representation. The disulfide bonds are shown as yellow sticks. The inter-subunit disulfide bonds are highlighted by a red dashed box. **b**, Comparison of inter-subunit disulfide bonds in the inactive mGlu2 and agonist- and PAM-bound mGlu2. The structures of inactive mGlu2 homodimer and agonist- and PAM-bound mGlu2 homodimer are shown in cartoon representation. **c**, Comparison of VFT conformations in inactive mGlu structures. The structures of inactive mGlu2, inactive mGlu5 (PDB code 6N52), inactive mGlu7, apo mGlu2 VFT (PDB code 5KZN) and LY3020371 (antagonist)-bound mGlu2 VFT (PDB code 5KZQ) are shown in cartoon representation. **d**, Comparison of the VFTs in the inactive structures of mGlu2, mGlu5 and mGlu7. The structures are shown in a side view. The C α atoms of the mGlu2 residue C234 and its counterparts in mGlu5 and mGlu7 are shown as spheres. The green arrow indicates the shift of the VFT in the mGlu5 structure compared to that in the mGlu2 and mGlu7 structures. **e**, Comparison of the CRDs in the inactive structures of mGlu2, mGlu5 and mGlu7. The structures are shown in both side and extracellular views. The C α atoms of the mGlu2 residue C540 and its counterparts in mGlu5 and mGlu7 are shown as spheres. The distance between the C α atoms of the cysteine residues in each structure is indicated by a dashed line and coloured blue (mGlu2), magenta (mGlu5) or orange (mGlu7). The red arrow indicates the movement of the CRDs in mGlu5 and mGlu7 relative to that in mGlu2. **f**, Comparison of VFT conformations in agonist-bound mGlu structures. The structures of LY354740- and JNJ-40411813-bound mGlu2, l-quisqualate- and CDPPB-bound mGlu5 (PDB code 6N51), LY354740-bound mGlu2 VFT (PDB code 4XAQ) and glutamate-bound mGlu2 VFT (PDB code 5CNI) are shown in cartoon representation and coloured blue, magenta, red and light gold, respectively. **g**, Comparison of the CRDs in the agonist- and PAM-bound mGlu2 and mGlu5 structures. The structures are shown in both side and extracellular views. **h**, Interactions between the CRDs in the agonist- and PAM-bound mGlu2 structure. The residues that are involved in dimerization are shown as blue and grey sticks, respectively. The disulfide bonds are shown as yellow sticks. **i**, Comparison of VFT conformations in the inactive mGlu2 and mGlu7 homo- and heterodimers. **j**, VFT dimer interface in the inactive mGlu2–mGlu7 heterodimer structure. The residues that are involved in dimerization are shown as sticks.

Extended Data Fig. 5 Sequence alignment of the TMDs of human mGlus.

Colours represent the similarity of residues: red background, identical; red text, strongly similar. The red arrows indicate the positions with mutations in the inactive mGlu2 and mGlu7 structures (2, mGlu2; 7, mGlu7). The mGlu2 residues that are involved in TMD dimerization in the inactive mGlu2 structure are indicated by green arrows. The conserved residues with the modified Ballesteros–Weinstein numbers for class C GPCRs 1.50, 2.50, 3.50, 4.50, 5.50, 6.50 and 7.50 are indicated by black arrows. The alignment was generated using UniProt (<http://www.uniprot.org/align/>) and the graphic was prepared on the ESPript 3.0 server (<http://escript.ibcp.fr/ESPript/cgi-bin/ESPript.cgi>).

Extended Data Fig. 6 Inter- and intra-subunit interactions upon mGlu2 activation and NAM-binding sites in mGlus.

a, Interactions between the CRD and ECL2 in the agonist- and PAM-bound mGlu2 and mGlu5 structures. The structures of agonist- and PAM-bound mGlu2 and mGlu5 (PDB code 6N51) are shown in cartoon representation and coloured blue and pink, respectively. The residues that potentially form interactions between the CRD and ECL2 are shown as sticks. **b**, Comparison of the helical bundles in the agonist- and PAM-bound structures of mGlu2 and mGlu5. The mGlu2 residues V782^{6.59} and V789^{7.27} that are involved in dimerization are shown as sticks. The red arrows indicate the movement of each helix in the mGlu2 structure relative to the mGlu5 structure. **c**, Crystal structures of mGlu2 TMD–NAMs. The receptor is coloured cyan. The NAMs NAM563 and NAM597 are shown as sticks and coloured yellow and magenta, respectively. The mGlu2 residues that form interactions with the NAMs are shown as cyan sticks (middle panels). The ligand electron densities are contoured at 1.0σ from an $|2F_o| - |F_c|$ map, and coloured grey (bottom panels). **d**, Comparison of ligand-binding sites in mGlus and class A GPCRs. The ligands in the crystal structures of mGlu2 TMD–NAM563, mGlu1 TMD–FITM (PDB code 4OR2), mGlu5 TMD–mavoglurant (PDB code 4OO9), β_2 AR–carazalol (PDB code 2RH1), M2–AF-DX384 (PDB code 5ZKB) and D3R–

eticlopride (PDB code 3PBL) are shown as sticks. Only the receptor in the mGlu2 TMD–NAM563 structure is shown in cyan cartoon representation for clarity. **e**, Comparison of the helical bundles in the inactive and active structures of mGlu2. The helical bundles in the structures of mGlu2 TMD–NAM563, inactive mGlu2, agonist- and PAM-bound mGlu2, and the G_i-free (free) and G_i-bound (G) subunits in the mGlu2–G_i complex (PDB code 7E9G) are shown in an intracellular view. **f**, Comparison of helix VI in the mGlu2 TMD–NAM563 and mGlu2–G_i structures. The red arrow indicates the downward shift of helix VI in the G_i-bound subunit of the mGlu2–G_i complex relative to the mGlu2 TMD–NAM563 structure and the G_i-free subunit in the G_i-bound structure. **g**, Comparison of the W^{6.50} conformation in the inactive and active mGlu2 structures. The mGlu2 TMD–NAM563 structure and the G_i-bound subunit in the mGlu2–G_i structure are coloured cyan and dark red, respectively. The residue W773^{6.50} in the two structures and the residues that form interactions with W773^{6.50} in the mGlu2 TMD–NAM563 structure are shown as sticks. The red arrow indicates the rotamer conformational change of W773^{6.50} in the active structure relative to the inactive structure. **h**, Comparison of the ionic locks in the inactive and active mGlu2 structures. The mGlu2 TMD–NAM563 structure is coloured cyan. The G_i-bound subunit and G_i protein in the mGlu2–G_i structure are coloured dark red and green, respectively. The residues K653^{3.50}, R656^{3.53}, E754 and E758^{6.35} that form ionic interactions in the inactive structure are shown as sticks in both structures. The ionic interactions in the inactive structure are shown as red dashed lines and the interaction between R656^{3.53} and Gα_i in the active structure is shown as a blue dashed line.

Extended Data Fig. 7 tr-FRET and functional assays of mGlu2 and mGlu7 homo- and heterodimers.

a, Validation of mGlu2–mGlu7 heterodimer and construct used for structure determination by tr-FRET assay. The signals were measured using the N-terminal HA and Flag tags in each subunit. In each panel, cartoons illustrating the dimer compositions are shown at the bottom. Data are mean ± s.e.m. (bars) from three independent experiments performed in technical triplicate with individual data points shown (dots). **b**, Cell surface

expression of homo- and heterodimers quantified by ELISA. Data were calculated as the fold of mock. Data are mean \pm s.e.m. (bars) from three independent experiments performed in technical triplicate with individual data points shown (dots). **c–g**, Calcium release assays of mGlu2–mGlu7 heterodimer. Data are mean \pm s.e.m. from at least three independent experiments performed in technical triplicate and correspond to the peak response. The numbers of independent experiments (n) are shown in parentheses. **c, e, f**, LY354740-induced calcium release of wild-type mGlu2–mGlu7 heterodimer and mutants. **d, g**, L-AP4-induced calcium release of wild-type mGlu2–mGlu7 heterodimer and mutants. **h, G_i**, activation of mGlu2–mGlu7(F784S) in the presence of LY354740, LY354740 + mGlu2 PAM (JNJ-40411813) or LY354740 + mGlu7 NAM (MMPIP, ADX71743 or MDIP) measured by the BRET assay. Data are mean \pm s.e.m. from at least three independent experiments performed in technical duplicate. The numbers of independent experiments (n) are shown in the parentheses.

Extended Data Table 1 Cryo-EM data collection, refinement and validation statistics

[Full size table](#)

Extended Data Table 2 Data collection and structure refinement statistics of mGlu2 TMD–NAM563 and mGlu2 TMD–NAM597 complexes

[Full size table](#)

Extended Data Table 3 IP accumulation assays of wild-type and mutant mGlus using a chimeric G α protein G α_{q19}

[Full size table](#)

Supplementary information

[Supplementary Figure](#)

This file contains the raw uncropped gels for Extended Data Figure 1.

[Reporting Summary](#)

Rights and permissions

[Reprints and Permissions](#)

About this article



Check for
updates

Cite this article

Du, J., Wang, D., Fan, H. *et al.* Structures of human mGlu2 and mGlu7 homo- and heterodimers. *Nature* **594**, 589–593 (2021).
<https://doi.org/10.1038/s41586-021-03641-w>

[Download citation](#)

- Received: 02 November 2020
- Accepted: 13 May 2021
- Published: 16 June 2021
- Issue Date: 24 June 2021
- DOI: <https://doi.org/10.1038/s41586-021-03641-w>

Comments

By submitting a comment you agree to abide by our [Terms](#) and [Community Guidelines](#). If you find something abusive or that does not comply with our terms or guidelines please flag it as inappropriate.

[Access through your institution](#)

[Change institution](#)

[Buy or subscribe](#)

Advertisement

This article was downloaded by **calibre** from <https://www.nature.com/articles/s41586-021-03641-w>

| [Section menu](#) | [Main menu](#) |

Structural basis of GABA_B receptor–G_i protein coupling

[Download PDF](#)

- Article
- Open Access
- [Published: 28 April 2021](#)

Structural basis of GABA_B receptor–G_i protein coupling

- [Cangsong Shen](#)^{1,2,3 na1},
- [Chunyou Mao](#) ORCID: orcid.org/0000-0001-5349-8592^{2,3,4 na1},
- [Chanjuan Xu](#) ORCID: orcid.org/0000-0002-5640-1896^{1,5 na1},
- [Nan Jin](#)^{1,2,3 na1},
- [Huibing Zhang](#) ORCID: orcid.org/0000-0003-3025-0185^{2,3,4},
- [Dan-Dan Shen](#) ORCID: orcid.org/0000-0001-8757-4602^{2,3,4},
- [Qingya Shen](#) ORCID: orcid.org/0000-0001-6602-7116^{2,3,4},
- [Xiaomei Wang](#)¹,
- [Tingjun Hou](#)⁶,
- [Zhong Chen](#) ORCID: orcid.org/0000-0003-4755-9357⁷,
- [Philippe Rondard](#) ORCID: orcid.org/0000-0003-1134-2738⁸,
- [Jean-Philippe Pin](#) ORCID: orcid.org/0000-0002-1423-345X⁸,
- [Yan Zhang](#) ORCID: orcid.org/0000-0003-2189-0244^{2,3,4,9} &
- [Jianfeng Liu](#) ORCID: orcid.org/0000-0002-0284-8377^{1,5}

Nature volume 594, pages 594–598 (2021) [Cite this article](#)

- 9894 Accesses
- 40 Altmetric
- [Metrics details](#)

Subjects

- [Cryoelectron microscopy](#)
- [G protein-coupled receptors](#)

- [Membrane structure and assembly](#)

Abstract

G-protein-coupled receptors (GPCRs) have central roles in intercellular communication^{1,2}. Structural studies have revealed how GPCRs can activate G proteins. However, whether this mechanism is conserved among all classes of GPCR remains unknown. Here we report the structure of the class-C heterodimeric GABA_B receptor, which is activated by the inhibitory transmitter GABA, in its active form complexed with G_{i1} protein. We found that a single G protein interacts with the GB2 subunit of the GABA_B receptor at a site that mainly involves intracellular loop 2 on the side of the transmembrane domain. This is in contrast to the G protein binding in a central cavity, as has been observed with other classes of GPCR. This binding mode results from the active form of the transmembrane domain of this GABA_B receptor being different from that of other GPCRs, as it shows no outside movement of transmembrane helix 6. Our work also provides details of the inter- and intra-subunit changes that link agonist binding to G-protein activation in this heterodimeric complex.

[Download PDF](#)

Main

GPCRs are essential elements that are involved in cell–cell communication and represent major targets for therapeutic drugs¹. Recent structural studies have provided important information on how GPCRs can act as nucleotide-exchange factors that allow the release of GDP from the inactive G protein, and then the activation of these proteins upon GTP binding². Several previous structures of activated GPCR–G protein complexes have revealed a similar mode of action for each^{3,4,5,6}. Despite differences in the interaction mode of G proteins for various class-A, -B and -F GPCRs, in all previously characterized interactions the C-terminal extremity of the G α subunit engages with a cavity on the intracellular side of the receptor that results from the opening of this domain owing to the movement of transmembrane helix (TM) 6 relative to TM3^{5,7}.

Compared to other classes of GPCRs that can be activated in a monomeric form, class-C GPCRs are mandatory dimers⁸ that are composed of two identical or similar subunits^{9,10,11}. These dimers may activate only one G protein at a time^{10,11}, but the molecular basis of this asymmetric mode of action remains unknown. Among the class-C GPCRs that are activated by the neurotransmitter GABA, the GABA_B receptor

(hereafter referred to as GABA_B) is an attractive drug target for the treatment of brain diseases¹². GABA_B is composed of two distinct subunits: GB1 (to which agonists bind) and GB2 (which is responsible for G-protein activation)^{9,13,14}. Each subunit is composed of an extracellular Venus flytrap (VFT) domain and a transmembrane domain (TMD)^{10,15}. The structure of this receptor has recently been solved in a number of states, including apo, antagonist-bound, agonist-bound, and agonist- and positive allosteric modulator (PAM)-bound^{11,16,17,18}. Although these studies have helped to identify the conformational changes in subunits that are associated with ligand binding, it remains unclear at the atomic level how this heterodimeric GPCR activates G proteins.

Here we report the cryo-electron microscopy (cryo-EM) structure of the agonist- and PAM-bound form of the GABA_B in complex with the G protein G_{i1} at 3.5 Å resolution. Our results reveal a mode of G-protein coupling that differs from those that have previously been reported for GPCRs of other classes; our structures reveal that small movements of TM3 and TM5 lead to changes in the intracellular loops (ICLs) that offer a binding site for the G protein on the side of the GB2 subunit of GABA_B. These data also help to refine models that describe how agonist binding in the VFT domain of GB1 leads to the activation of the TMD of GB2, and how small molecules can act as PAMs.

Overall architecture of GABA_B-G_i complex

Using a modified version of a previously established protocol¹¹ (Extended Data Fig. 1), we assembled the GABA_B-G_{i1} complex by incubating purified GABA_B with G_{i1} in the presence of the agonist baclofen and the PAM *R,S*-5,7-di-tert-butyl-3-hydroxy-3-trifluoromethyl-3*H*-benzofuran-2-one (BHFF)¹⁹ (Fig. 1a,b). Our cryo-EM analysis indicated that the binding of G_{i1} to GABA_B was flexible, and the consensus refinement map exhibited poor density in the G protein (Extended Data Fig. 2). The flexible conformations of G_{i1} bound to GABA_B in a similar pocket, but were rotated within an angle of up to 46° (Extended Data Fig. 3, Supplementary Videos 1, 2). To obtain detailed structural information, we subjected the individual structures of G_{i1} and GABA_B to local reconstruction, and produced improved G_{i1} and the GABA_B maps at a resolution of 3.4 Å and 3.3 Å, respectively (Extended Data Figs. 2, 4). These maps were combined on the basis of the consensus refinement map, and provided a rational structural framework for analyses of G-protein coupling (Fig. 1a,b, Extended Data Table 1).

Fig. 1: Cryo-EM structure of GABA_B-G_i complex.



a, b, Cryo-EM map (**a**) and model (**b**) of the baclofen- and BHFF-bound GABA_B-G_{i1} complex.

[Full size image](#)

Our determined structure of the GABA_B-G_{i1} complex assumes an overall architecture that is similar to the previously reported low-resolution GABA_B-G_{i1} structure in the B2a state¹¹ (Extended Data Fig. 5a). The agonist- and PAM-G_{i1}-bound GABA_B exhibited a conformation similar to that of the agonist- and PAM-bound GABA_B (Protein Data Bank code (PDB) 6UO8) with a root mean squared deviation of 2.3 Å, in which the TMDs adopted a TM6-TM6 interface and the TMD of subunit GB2 showed an outward shift at the intracellular ends of TM3 and TM5. We did not observe conformation changes of TM3 and TM5 in the agonist-bound states (PDB 6UO9) (Extended Data Fig. 5b). Our structure shows that G_{i1} binds to a shallow cavity that is formed by the ICLs of GB2, which provides a structural basis for understanding the distinct mode of G_{i1} coupling to GABA_B.

Asymmetric activation of GABA_B

In the GABA_B-G_{i1} complex, there is no obvious opening of a central cavity on the intracellular side of the TMDs of either GB1 or GB2 (Fig. 2a, Extended Data Fig. 6a). Using the TMD of GB1 in agonist-bound GABA_B (PDB 6UO9) as a reference, the TMDs of GB1 remained unchanged but the TMDs of GB2 did not overlap well (a root mean squared deviation of 4.8 Å) (Fig. 2a). However, we observed only local environmental differences between two forms when the GB2 TMD alone was aligned (Extended Data Fig. 6a). The GB2 TMD underwent an anticlockwise rotation relative to GB1 upon binding to a PAM and/or G protein (Fig. 2a). Therefore, interactions with the PAM and G protein may induce further structural rearrangements to agonist-bound GABA_B. GB1 Y810^{6.44} (superscript numbers refer to the GPCRdb numbering scheme) and GB2 Y697^{6.44} had rotamer changes and formed a hydrogen bond with GB2 N689^{6.45} and GB1 N811^{6.45}, respectively (Extended Data Fig. 6b,c). The resulting TM6-TM6 interaction was critical for G-protein coupling but did not lead to a conformational change of TM6 relative to the rest of the GB2 TMD.

Fig. 2: Asymmetric activation of GABA_B.

 **figure2**

a, Side, extracellular, and intracellular views of the superposed structures of the agonist-bound (PDB 6UO9) and the agonist- and PAM-G_i-bound (agonist/PAM-bound) GABA_B, aligned by the TMD of GB1. **b**, Conformational changes of the TMD of GB2 between antagonist-bound (PDB 7C7S) and agonist- and PAM-G_i-bound structure. **c**, Magnified views of the critical residue F568, the bulky side chain of which undergoes a substantial rotation upon activation and causes the TM3 shifting. **d**, Baclofen-induced IP1 accumulation of wild-type (WT) and F568A-mutant GABA_B using the chimeric G α protein G α_{qi9} . Data are mean \pm s.e.m. from six independent

experiments, performed in technical triplicate. **e**, Magnified views of the ‘ionic lock’ located in the cytoplasmic TMD of GB2. **f**, Baclofen-induced IP1 accumulation of wild-type GABA_B and several forms of GABA_B with substitutions in the ionic lock region using Gα_{q19}. Data are mean ± s.e.m. from at least three independent experiments, performed in technical triplicate.

[Source data](#)

[Full size image](#)

Intra-subunit conformational changes within the TMDs were located in the intracellular half of TM3 and the entire TM5 of GB2 (Fig. [2b](#)). TM5 moved 4 Å towards TM3, and F568^{3.44} rotated away from TM5 by about 65° to avoid potential spatial clashes (which is likely to be a critical origin for the 20°- rotation of the cytoplasmic end of TM3) (Fig. [2c](#)). Mutation of F568^{3.44} to alanine largely impaired GABA_B-induced G_i coupling (Fig. [2d](#), Extended Data Fig. [6d](#)), which suggests that the bulky side chain of F568^{3.44} is essential for GB2 activation. The intracellular tip of TM3 was farther away from TM5, and was further stabilized by three critical charged residues that may help to accommodate G protein (Fig. [2b,e](#)). This is consistent with a previous study^{[20](#)} that identified residues of TM3 (K572^{3.50} and R575^{3.53}) and TM6 (D688^{6.35}) of GB2, all of which are conserved among class-C GPCRs. Similar to class-A GPCRs (in which a D/ERY motif constitutes an ionic lock that stabilizes the inactive state)^{[21](#)}, K574^{3.50} and D688^{6.35} of GB2 form an ionic lock in the inactive state and become weaker owing to inward movement of TM3 upon receptor activation. K574^{3.50} turned to N520^{2.39} of GB2 to form an additional ionic interaction (Fig. [2e](#)). Substitution of these residues with alanine or oppositely charged amino acids impaired or abolished agonist-induced receptor activity (Fig. [2f](#), Extended Data Fig. [6e](#)). The intra-subunit conformational changes of GB2 TMD led to asymmetric activation of GABA_B through binding and activation of a single G protein.

Specificity of GABA_B-G_i coupling

In the GB2 subunit, the three ICLs and the intracellular tip of TM3 form a shallow pocket for the G protein (Fig. [3a](#), Extended Data Fig. [7a](#)). The ICL2 of GB2 establishes extensive interactions with the α₅ helix and the two linker regions (β₂-β₃ and α_N-β₁) in Gα_{i1} (Fig. [3b](#)). There are potential salt bridges between lysine residues in this ICL2 (K586, K589 and K590) and acidic residues in α_N (E28) and the linker region in β₂-β₃ (D193) in Gα_{i1}. ICL1 and ICL3 were away from the G protein and participated only in the recognition of the C-terminal ‘hook-like’ region of Gα_i (Fig. [3c](#)).

Fig. 3: GABA_B-G_i coupling and G-protein selectivity.

 figure3

a, The G_{i1} binding pocket in GABA_B, which is mainly formed by three intracellular loops of GB2. GB2, green; Gα_{i1}, yellow. **b, c**, Detailed interactions of the ICL2 and

TM3 of GB2 with G α _i (**b**), and of ICL1 and ICL3 with G α _i (**c**). **d**, Baclofen-induced IP1 accumulation using G α _{qi9}. Bars represent differences in calculated E_{\max} and basal activity or potency (pEC₅₀) for each mutant as a percentage of the maximum in wild type. Data are mean \pm s.e.m. from at least three independent experiments, performed in technical triplicate and analysed using one-way analysis of variance with Dunnett's multiple comparison test to determine significance (compared with wild type). ND, not determined; NS, not significant. **e**, The C^{G.H5.23} and G^{G.H5.24} residues in the C-terminal α 5 helix of G α _i are involved in the selective coupling between GABA_B and G α _i protein. The α 5-helix structures of G_s (PDB 5VAI), G_q (PDB 6WHA) and the GABA_B-bound G α _i were aligned. **f**, **g**, Effect of C^{G.H5.23} (**f**) and G^{G.H5.24} (**g**) mutations in G α _i on GABA_B-G α _i coupling using NanoBiT G-protein dissociation assay. Data are mean \pm s.e.m. from at least three independent experiments.

[Source data](#)

[Full size image](#)

Given the flexibility of G α _{i1} engagement to the receptor, we subjected residues of GABA_B within 6 Å of the GABA_B-G α _{i1} interface to mutagenesis and functional analyses (Fig. 3d, Extended Data Fig. 7b–g, Supplementary Table 1). Substitutions of residues with alanine in the intracellular tip of TM3 and entire ICL2 of GB2 led to a substantial 20–75% reduction in maximal responses (E_{\max}) (Fig. 3d). Most mutants in the ICL2 showed decreased basal activity compared with wild type. Among them, M587A, K590A and I592A decreased the agonist potency (half-maximal effective concentration (EC₅₀)) by 6–22 fold, which highlights the essential role of ICL2 in GB2-G α _{i1} coupling (consistent with previous studies²²). Substitutions in ICL1 (S515A) or TM3 (R577A and I581W) abolished GABA_B-induced production of inositol monophosphate (IP1). Substitutions in TM3 (V578A, I581A, F582A and N584A) and in ICL3 (L686A) decreased the agonist potency by 9–32 fold, which indicates that ICL1, ICL3 and TM3 are involved in the recognition of G α _{i1}.

GABA_B predominantly couples to G α _{i/o} subtypes of G protein²³. The C-terminal 5–9 residues of the α ₅ helix of G protein have previously been found to be the key determinants for G-protein-coupling specificity^{24,25}. The α ₅ helix of G α _{i1} contributed 62% (533 Å²) of the interaction surface with GABA_B (Extended Data Fig. 7a). Sequence alignment of G α _s, G α _q, G α ₁₃ and G α _i showed four nonidentical amino acids among the final five C-terminal residues (G.H5.22–G.H5.26)²⁶ (Fig. 3e, Extended Data Fig. 7h). We mutated these four residues in G α _{i1} to the corresponding residues of

$\text{G}\alpha_s$, $\text{G}\alpha_q$ and $\text{G}\alpha_{13}$. Substitution mutations of C351^{G.H5.23} (superscript codes refer to common $\text{G}\alpha$ numbering system) or G352^{G.H5.24}—but not L353^{G.H5.22} or F354^{G.H5.25}—impaired GABA_B-induced G-protein signalling, which suggests an essential role for C351^{G.H5.23} and a partial involvement of G352^{G.H5.24} in the specificity of G_i coupling (Fig. 3f,g, Extended Data Fig. 7i,j), consistent with previous data²⁵. The overall structure was similar in the backbone of the α_5 helix to that in different G proteins, but $\text{G}\alpha_s$ and $\text{G}\alpha_q$ possess a tyrosine instead of cysteine in $\text{G}\alpha_i$ G.H5.23, which may lead to potential steric hindrance with the ICL2 of GB2 (Fig. 3e). When replacing C351^{G.H5.23} or G352^{G.H5.24} with a bulky tryptophan to create clashes with ICL2, we observed decreased GABA_B-induced G_i signalling, whereas the substitution of C351^{G.H5.23} with alanine led to no obvious signalling loss (Fig. 3f,g). The specificity of recognition of the α_5 helix of G_{i1} by GABA_B confirmed the importance of ICL2 in the selective activation of G_i .

Distinct G_i binding model of GABA_B

G_{i1} binding to GABA_B forms a smaller interface (856 \AA^2) than in the class-A cannabinoid receptor 1 ($1,155 \text{ \AA}^2$), class-B glucagon receptor (905 \AA^2), or class-F smoothened receptor ($1,060 \text{ \AA}^2$) (Extended Data Fig. 8). The α_5 helices coupled to class-A, -B and -F GPCRs through nearly the same intracellular cavity that reached the same depth into the TMDs of the receptor, whereas the α_5 of G_i coupled to GABA_B inserts around 10 \AA less deeply (Fig. 4a, Extended Data Fig. 8). Consequently, the C-terminal end of the α_5 of $\text{G}\alpha_i$ did not penetrate into a central cavity (which we term pocket^R), but rather into a cavity located at the periphery (Fig. 4b,c). The extended ICL2 inserted into a G-protein pocket (which we term pocket^G) that comprised the α_5 helix, the linker region in β_2 – β_3 and the linker region of α_N – β_1 (Fig. 4c). The GABA_B-bound G_{i1} adopted open conformations, showing a notable separation of Ras and helical domains and the displacement of the α_5 helix away from GDP-binding sites (Fig. 4d). Compared with other G_{i1} structures in the GPCR– G_i complexes, GABA_B-activated G protein retained all of the expected conformational features of an activated G protein, except for a 25° upward rotation along the α_N domain that was due to the distinct interactions with ICL2 of GABA_B (Fig. 4e). Collectively, these results suggest that the GABA_B adopts a distinct mode of G-protein coupling compared to class-A, -B and -F GPCRs.

Fig. 4: Distinct G_i binding model of GABA_B.

 **figure4**

a, b, Orientations of the α 5 helix in G_i protein when coupling to GABA_B, cannabinoid receptor 1 (CB1) (class A), glucagon receptor (GCR) (class B) and smoothened (SMO) (class F). Structures were aligned by the TMDs; only the TMD of GB2 is shown, for clarity. GABA_B-bound, yellow; CB1-bound α 5, PDB 6N4B; GCR-bound α 5, PDB 6LML; SMO-bound α 5, PDB 6OT0. **c**, Schematics of the two types of pocket that are involved in G-protein recognition. GABA_B, green; monomeric GPCR, blue; G_i , yellow. **d**, Superposition of GABA_B-bound G_{i1} with the GDP-bound G_{i1} . GDP-bound G_{i1} , PDB 1GP2. **e**, Structural comparison of the GABA_B-bound G_{i1} with CB1-, GCR- and SMO-bound G_{i1} . G proteins are coloured as in **a, b**.

[Full size image](#)

Discussion

Our cryo-EM structure of the GABA_B- G_i complex stabilized with an agonist and a PAM reveals an asymmetric activation process in which a single G protein interacts with GB2. It also reveals a distinct mode of G-protein activation, as the $G\alpha$ C-terminal end interacts with a shallow groove that involves TM3 and the ICLs of GB2 (Extended Data Fig. 9) rather than with a central pocket that results from TM6 movement (as

observed with other GPCRs)^{5,7}. Consistent with the PAM-binding site being located at the TM6 interface between the subunits, no outward movement of TM6 is observed in the GABA_B–Gi complex. Despite this different mode of activation, the activated G protein retained all of the expected conformational changes (as observed with the other classes of GPCR)^{5,27,28}. This binding mode explains the G_i selectivity of the GABA_B, and is supported by numerous mutations within the ICLs and the G protein^{22,25,29}. The similar determinants that are involved in G-protein recognition, the conservation of ICL2^{30,31} and the similar mode of activation of these dimeric receptors suggest that there may be a similar coupling mechanism in the other class-C GPCRs.

The agonist- and PAM–G_i-bound GABA_B structure was almost identical to that observed with the agonist and PAM without G_i (Extended Data Fig. 5b), which indicates that the G protein has no additional effect on the conformation of the receptor. This also suggests that the PAM has an effect similar to that of the G protein on the conformation of GB2. Although an agonist-bound GABA_B–Gi complex will be informative in clarifying this issue, we have not been able to obtain such a complex that is stable enough for cryo-EM analysis.

Our observations demonstrate how agonist binding in the VFT domain of GB1 can allosterically control activation of the TMD of GB2. Our results show that a closed VFT domain of GB1 leads to a new positioning of the VFT domain of GB2 that is associated with the bending of this subunit and the movement of the TMDs one relative to the other, which leads to a change from TM5 to TM6 as the dimer interface (Extended Data Fig. 9a, b). This probably corresponds to the first activation step, as previously reported in mGlus^{32,33}. The addition of a PAM (with or without the G protein) leads to a second movement of the two TMDs with a closer apposition of GB2 on GB1 that creates the PAM-binding site and leads to a change in the bending of the GB2 subunit (Extended Data Fig. 9e–g). This bending is associated with a slight change in the conformation of ICL2 and a movement of TM3 relative to TM5 in GB2 only, which opens the shallow cavity in which the C-terminal end of the G protein binds (Fig. 2b). This model highlights the intra-GB2-subunit conformational changes that result from the closing of the VFT domain of GB1 and the contact between the TM6s as being the essential route for the allosteric interaction between the agonist-binding site and the G-protein-activating site.

Taken together, our observations provide structural information for the asymmetric activation of a dimeric GABA_B, which may also apply to other class-C receptors. Our results also reveal that—despite a different binding mode compared to other GPCRs—activated GABA_B leads to an almost identical conformational change in the G_a protein that allows the receptor to act as a guanine nucleotide-exchange factor.

Methods

No statistical methods were used to predetermine sample size. The experiments were not randomized, and investigators were not blinded to allocation during experiments and outcome assessment.

Constructs

To facilitate expression and purification, human GABA_B with the haemagglutinin (HA) signal peptide—including GB1a (UniProt: Q9UBS5) and GB2 (UniProt: O75899)—were cloned into the pEG BacMam vector³⁴. An 8× histidine tag and 3C protease cleavage site were inserted at the C terminus of the GB1a (residues 15–919) subunit, and a Flag epitope tag (DYKDDDD) and a 2× GSG linker were added to the N terminus of the GB2 (residues 42–819) subunit. GABA_B and G_{i1} mutants were generated using site-directed mutagenesis. All the constructs were confirmed by sequencing.

Expression and purification of scFv16

scFv16 was expressed and purified as previously described³⁵. In brief, the 6×histidine-tagged scFv16 was expressed in secreted form in *Trichoplusia ni* Hi5 insect cells for 48 h using the Bac-to-Bac system. The expressed scFv16 was purified using a Ni-NTA resin. The C-terminal 6×His tag of the Ni-NTA eluent was cleaved by 3C protease and further purified by gel filtration chromatography using a Superdex 200 column. Finally, the purified scFv16 was concentrated and stored at –80 °C until further use.

Expression and purification of heterotrimeric G_{i1}

Heterotrimeric G_{i1} was expressed and purified as previously described³⁵. In brief, the dominant-negative Gα_{i1} (S47N, G203A, E245A and A326S) and human β1γ2 subunits (β1–8×His tag) were co-expressed in Hi5 insect cells for 48 h using the Bac-to-Bac system. The cells were collected and lysed with a buffer containing 10 mM HEPES (pH 7.5), 100 μM MgCl₂ and 10 μM GDP. The cell membrane was collected by centrifugation and heterotrimeric G_{i1} was extracted in a buffer containing 1% sodium cholate. The supernatant was purified by Ni-NTA column and the detergent was exchanged with *n*-dodecyl-β-d-maltoside (Anatrace) on a column. Afterward, G_{i1} was mixed with a 1.2 molar excess of scFv16 and further purified by Superdex 200 column. Finally, the G_{i1}–scFv16 complex was concentrated and flash-frozen in liquid nitrogen until further use.

Formation of the GABA_B–G_{i1}–scFv16 complex

The GB1 and GB2 plasmids mixed with PEI 25 K at a 3:0.5:0.5 ratio of PEI to GB1 and GB2 plasmid (w/w) were added to HEK293F cells when the density reached about 2.8 million per ml. Seventeen hours after infection, sodium butyrate was added at a final concentration of 10 mM and the cells were grown for another 3 days at 30 °C before being collected¹¹. The collected cells were solubilized for 3 h at 4 °C in a buffer containing 0.5% (w/v) lauryl maltose neopentyl glycol (Anatrace) and 0.1% (w/v) cholesteryl hemisuccinate (Anatrace). After centrifugation at 30,000g for 30 min, the GABA_B was purified by Ni-NTA column and M1 anti-Flag affinity resin. The GABA_B was further concentrated and mixed with a 1.3 molar excess of G_{i1}–scFv16 complex in the presence of 100 μM baclofen and 50 μM BHFF. The sample was incubated at 25 °C for 1 h, followed by the addition of 0.2 U ml⁻¹ apyrase for an additional 1.5-h incubation at 24 °C³⁶. Finally, the sample was purified using a Superose 6 Increase column (GE Healthcare) to acquire a homogeneous GABA_B receptor–G_{i1} complex. The entire purification procedure was accomplished in 12 h, followed by immediate verification to acquire a stable and fresh sample for structural determination.

Cryo-EM grid preparation and data collection

To prepare cryo-EM grids, 3.0 μl of the purified baclofen- and BHFF-activated GABA_B–G_{i1} complex at 1.8 mg ml⁻¹ was applied onto the glow-discharged holey carbon grids (Quantifoil, R1.2/1.3, 300 mesh). The grids were blotted for 3.0 s with a blot force of 3 at 4 °C, 100% humidity, and then plunge-frozen in liquid ethane using Vitrobot Mark IV (Thermo Fischer Scientific). Cryo-EM data collection was performed on a Titan Krios at 300 kV accelerating voltage in the Center of Cryo-Electron Microscopy (Zhejiang University). Micrographs were recorded using a Gatan K2 Summit Detector in counting mode with a pixel size of 1.014 Å using SerialEM software³⁷. Image stacks were obtained at a dose rate of about 8.0 electrons per Å² per second with a defocus ranging from −1.0 to −2.5 μm. The total exposure time was 8 s, and 40 frames were recorded per micrograph. A total of 13,843 movies were collected for the GABA_B–G_{i1} complex.

Cryo-EM data processing

Image stacks for the GABA_B–G_{i1} complex were subjected to beam-induced motion correction using MotionCor2³⁸. Contrast transfer function parameters for non-dose-weighted micrographs were determined by Gctf³⁹. Cryo-EM data processing was performed using Relion 3.1⁴⁰ and CryoSPARC 2.15⁴¹. Template-based particle selection yielded 5,889,932 particle projections using Relion. The projections were

imported to CryoSPARC for 2D classification to discard poorly defined particles. The selected particle projections were further subjected to ab initio reconstruction and heterogeneous refinement in CryoSPARC. The well-defined subsets accounting for 1,366,533 particles were re-extracted for further processing in Relion. Three-dimensional classification showed that G_{i1} predominantly bound to GB2, however, a small subset (112,338 particles) was also found to interact with GB1. To sort out conformational uniform particles for 3D reconstruction, these projections were subjected to 3D classification with a mask on the TMD–G_{i1}, producing one good subset that accounted for 362,826 particles. Further 3D classifications focusing the alignment on the G_{i1} produced two good subsets, which accounted for 275,089 particles that were subsequently subjected to 3D refinement, contrast transfer function refinement and Bayesian polishing. The overall refinement of GABA_B–G_{i1} generated a map with an indicated global resolution of 3.5 Å at a Fourier shell correlation of 0.143. To further improve the map quality of the complex (especially for G_{i1}), local 3D reconstruction focusing on the GABA_B receptor and G_{i1} was performed using the partial signal subtracted particles in Relion. The local refinement maps for the GABA_B and G_{i1} showed a global resolution of 3.3 Å and 3.4 Å, respectively, which were combined on the basis of the global refinement map using ‘vop maximum’ command in UCSF Chimera⁴². This composite map of the GABA_B–G_{i1} complex was used for subsequent model building and analysis. Global and local resolution was determined using the Bsoft 2.0.7 package⁴³ with half maps as input maps.

Model building and refinement

The model of the active GABA_B (PDB 7C7Q)¹¹ was used to generate the initial template of the GABA_B. The atomic coordinates of G_{i1} and scFv16 from the structure of the human cannabinoid receptor 2–G_{i1} complex (PDB 6PT0)³⁶ were used to generate the initial template of the G_{i1}–scFv16 complex. Models of GABA_B and G_{i1}–scFv16 were docked into the electron microscopy density map using UCSF Chimera⁴². Agonist and PAM coordinates and geometry restraints were generated using a phenix.elbow⁴⁴. The docked model was subjected to flexible fitting using Rosetta⁴⁵ and was further rebuilt in Coot⁴⁵ and real-space-refined in Rosetta⁴⁵ and Phenix⁴⁴. The final refinement statistics were validated using the module ‘comprehensive validation (cryo-EM)’ in Phenix. The goodness-of-fit of the model to the map was determined using a global model-versus-map Fourier shell correlation. The refinement statistics are provided in [Supplementary Information](#) and Extended Data Table 1. Structural figures were created using UCSF Chimera⁴² and the UCSF Chimera X package⁴⁶.

Enzyme-linked immunosorbent assay

The cell-surface expression of the receptor subunits was detected using an enzyme-linked immunosorbent assay (ELISA). In brief, HEK293T cells were plated in each well of a 6-well plate at a concentration of 0.3 million per ml (2 ml per well). Plasmid transfection was performed with a mixture of 200 ng $\text{G}\alpha_{i1}$ -lgb1, 500 ng $\text{G}\gamma$ -smb1t, 500 ng $\text{G}\beta$, 200 ng GABA_B wild type (HA-GB1 and Flag-GB2) or mutants using Lipofectamine 2000 (Thermo Fisher Scientific) in 200 μl of Opti-MEM (Thermo Fisher Scientific). The Flag- and HA-tagged subunits were cotransfected into HEK293T cells and plated in a 96-well plate with a white transparent bottom. HEK293T cells were fixed with 4% paraformaldehyde and blocked with 10% fetal bovine serum (FBS). Bound antibodies coupled to horseradish peroxidase were detected by luminescence using SuperSignal ELISA Femto Maximum Sensitivity substrate (ThermoFisher Scientific), and luminescence was measured using a luminescence microplate reader (Tecan).

IP1 accumulation assay

IP1 accumulation was measured using the IP-One HTRF kit (PerkinElmer, CisBio Bioassays). Transfected HEK293 cells were seeded in a 96-well plate, and 24 h after transfection, cells were treated with baclofen diluted in stimulation buffer in a Cisbio kit for 30 min at 37 °C. Then, cryptate-labelled anti-IP1 monoclonal antibody and d2-labelled IP1 in lysis buffer were added to the wells. After 1 h of incubation at room temperature, the plates were read in PHERAstar FS with excitation at 337 nm and emission at 620 and 665 nm. The accumulation of IP1 was calculated according to a standard dose-response curve.

NanoBiT-G-protein dissociation assay

G-protein activation was detected using a Nanobit-G protein dissociation assay⁴⁷. The transfection system was the same as that used in the ELISA. After 1 day of transfection, cells in the 6-well plate were digested and resuspended in complete medium DMEM (5% FBS, 1% antibiotic) and plated in 96-well flat-bottomed white microplates. After 24 h, the cells were washed twice with D-PBS and incubated in 40 μl of 5 μM coelenterazine H (Promega) solution diluted with 0.01% BSA- and 5 mM HEPES (pH 7.4)-containing HBSS (assay buffer) for 2 h at room temperature. Baseline luminescence was measured using a luminescent microplate reader (Tecan). The test compound (5×, diluted in the assay buffer) was added to the cells (10 μl) and incubated for 3–5 min at room temperature before the second measurement. The ligand-induced signal ratio was normalized to the baseline luminescence, and fold-

change signals over vehicle treatment were used to show the G-protein dissociation response.

Statistical analysis

Statistical analyses were performed on at least three individual datasets and analysed using GraphPad Prism software. Bars represent differences in the calculated agonist potency (pEC_{50}), maximum agonist response (E_{max}) and basal activity for each mutant relative to the wild-type receptor. Data are mean \pm s.e.m. from at least three independent experiments, performed in triplicates. ND, not determined. * $P < 0.05$, ** $P < 0.01$, *** $P < 0.001$, **** $P < 0.0001$ (one-way analysis of variance (ANOVA) followed by Dunnett's test, compared with the response of the wild type). For dose–response experiments, data were normalized and analysed using nonlinear curve fitting for the log (agonist) versus response (three parameters) curves.

Reporting summary

Further information on research design is available in the [Nature Research Reporting Summary](#) linked to this paper.

Data availability

The cryo-EM density map and corresponding atomic coordinate of the GABA_B–G_{i1} complex have been deposited in the Electron Microscopy Data Bank and PDB under the accession codes [EMD-31049](#) and [7EB2](#), respectively. All data analysed in this study are included in this Article and its [Supplementary Information](#). Any other relevant data are available from the corresponding authors upon reasonable request. [Source data](#) are provided with this paper.

References

1. 1.

Hauser, A. S., Attwood, M. M., Rask-Andersen, M., Schiöth, H. B. & Gloriam, D. E. Trends in GPCR drug discovery: new agents, targets and indications. *Nat. Rev. Drug Discov.* **16**, 829–842 (2017).

[CAS](#) [PubMed](#) [PubMed Central](#) [Google Scholar](#)

2. 2.

Gilman, A. G. G proteins: transducers of receptor-generated signals. *Annu. Rev. Biochem.* **56**, 615–649 (1987).

[CAS](#) [PubMed](#) [Google Scholar](#)

3. 3.

Rasmussen, S. G. et al. Crystal structure of the $\beta 2$ adrenergic receptor–Gs protein complex. *Nature* **477**, 549–555 (2011).

[ADS](#) [CAS](#) [PubMed](#) [PubMed Central](#) [Google Scholar](#)

4. 4.

Kang, Y. et al. Cryo-EM structure of human rhodopsin bound to an inhibitory G protein. *Nature* **558**, 553–558 (2018).

[ADS](#) [CAS](#) [PubMed](#) [PubMed Central](#) [Google Scholar](#)

5. 5.

Qi, X. et al. Cryo-EM structure of oxysterol-bound human Smoothened coupled to a heterotrimeric G_i. *Nature* **571**, 279–283 (2019).

[ADS](#) [CAS](#) [PubMed](#) [PubMed Central](#) [Google Scholar](#)

6. 6.

Velazhahan, V. et al. Structure of the class D GPCR Ste2 dimer coupled to two G proteins. *Nature* **589**, 148–153 (2021).

[ADS](#) [CAS](#) [PubMed](#) [Google Scholar](#)

7. 7.

Hilger, D. et al. Structural insights into differences in G protein activation by family A and family B GPCRs. *Science* **369**, eaba3373 (2020).

[CAS](#) [PubMed](#) [PubMed Central](#) [Google Scholar](#)

8. 8.

Kniazeff, J., Prézeau, L., Rondard, P., Pin, J. P. & Goudet, C. Dimers and beyond: the functional puzzles of class C GPCRs. *Pharmacol. Ther.* **130**, 9–25 (2011).

[CAS](#) [PubMed](#) [Google Scholar](#)

9. 9.

Kaupmann, K. et al. GABA_B-receptor subtypes assemble into functional heteromeric complexes. *Nature* **396**, 683–687 (1998).

[ADS](#) [CAS](#) [PubMed](#) [Google Scholar](#)

10. 10.

Pin, J. P. & Bettler, B. Organization and functions of mGlu and GABA_B receptor complexes. *Nature* **540**, 60–68 (2016).

[ADS](#) [CAS](#) [PubMed](#) [Google Scholar](#)

11. 11.

Mao, C. et al. Cryo-EM structures of inactive and active GABA_B receptor. *Cell Res.* **30**, 564–573 (2020).

[CAS](#) [PubMed](#) [Google Scholar](#)

12. 12.

Bettler, B., Kaupmann, K., Mosbacher, J. & Gassmann, M. Molecular structure and physiological functions of GABA_B receptors. *Physiol. Rev.* **84**, 835–867 (2004).

[CAS](#) [PubMed](#) [Google Scholar](#)

13. 13.

Jones, K. A. et al. GABA_B receptors function as a heteromeric assembly of the subunits GABA_BR1 and GABA_BR2. *Nature* **396**, 674–679 (1998).

[ADS](#) [CAS](#) [PubMed](#) [Google Scholar](#)

14. 14.

White, J. H. et al. Heterodimerization is required for the formation of a functional GABA_B receptor. *Nature* **396**, 679–682 (1998).

[ADS](#) [CAS](#) [PubMed](#) [Google Scholar](#)

15. 15.

Chun, L., Zhang, W. H. & Liu, J. F. Structure and ligand recognition of class C GPCRs. *Acta Pharmacol. Sin.* **33**, 312–323 (2012).

[CAS](#) [PubMed](#) [PubMed Central](#) [Google Scholar](#)

16. 16.

Park, J. et al. Structure of human GABA_B receptor in an inactive state. *Nature* **584**, 304–309 (2020).

[ADS](#) [CAS](#) [PubMed](#) [PubMed Central](#) [Google Scholar](#)

17. 17.

Papasergi-Scott, M. M. et al. Structures of metabotropic GABA_B receptor. *Nature* **584**, 310–314 (2020).

[ADS](#) [CAS](#) [PubMed](#) [PubMed Central](#) [Google Scholar](#)

18. 18.

Shaye, H. et al. Structural basis of the activation of a metabotropic GABA receptor. *Nature* **584**, 298–303 (2020).

[ADS](#) [CAS](#) [PubMed](#) [PubMed Central](#) [Google Scholar](#)

19. 19.

Koek, W., Cheng, K. & Rice, K. C. Discriminative stimulus effects of the GABA_B receptor-positive modulator rac–BHFF: comparison with GABA_B receptor agonists and drugs of abuse. *J. Pharmacol. Exp. Ther.* **344**, 553–560 (2013).

[CAS](#) [PubMed](#) [PubMed Central](#) [Google Scholar](#)

20. 20.

Binet, V. et al. Common structural requirements for heptahelical domain function in class A and class C G protein-coupled receptors. *J. Biol. Chem.* **282**, 12154–12163 (2007).

[CAS](#) [PubMed](#) [Google Scholar](#)

21. 21.

Gether, U. Uncovering molecular mechanisms involved in activation of G protein-coupled receptors. *Endocr. Rev.* **21**, 90–113 (2000).

[CAS](#) [PubMed](#) [Google Scholar](#)

22. 22.

Havlickova, M. et al. The intracellular loops of the GB2 subunit are crucial for G-protein coupling of the heteromeric γ -aminobutyrate B receptor. *Mol. Pharmacol.* **62**, 343–350 (2002).

[CAS](#) [PubMed](#) [Google Scholar](#)

23. 23.

Tu, H. et al. GABA_B receptor activation protects neurons from apoptosis via IGF-1 receptor transactivation. *J. Neurosci.* **30**, 749–759 (2010).

[CAS](#) [PubMed](#) [PubMed Central](#) [Google Scholar](#)

24. 24.

Conklin, B. R., Farfel, Z., Lustig, K. D., Julius, D. & Bourne, H. R. Substitution of three amino acids switches receptor specificity of G_q α to that of G_i α . *Nature* **363**, 274–276 (1993).

[ADS](#) [CAS](#) [PubMed](#) [Google Scholar](#)

25. 25.

Franek, M. et al. The heteromeric GABA-B receptor recognizes G-protein α subunit C-termini. *Neuropharmacology* **38**, 1657–1666 (1999).

[CAS](#) [PubMed](#) [Google Scholar](#)

26. 26.

Vroeling, B. et al. GPCRDB: information system for G protein-coupled receptors. *Nucleic Acids Res.* **39**, D309–D319 (2011).

[CAS](#) [PubMed](#) [Google Scholar](#)

27. 27.

Krishna Kumar, K. et al. Structure of a signaling cannabinoid receptor 1–G protein complex. *Cell* **176**, 448–458.e12 (2019).

[CAS](#) [PubMed](#) [Google Scholar](#)

28. 28.

Qiao, A. et al. Structural basis of G_s and G_i recognition by the human glucagon receptor. *Science* **367**, 1346–1352 (2020).

[ADS](#) [CAS](#) [PubMed](#) [Google Scholar](#)

29. 29.

Duthey, B. et al. A single subunit (GB2) is required for G-protein activation by the heterodimeric GABA_B receptor. *J. Biol. Chem.* **277**, 3236–3241 (2002).

[CAS](#) [PubMed](#) [Google Scholar](#)

30. 30.

Havlickova, M. et al. The second intracellular loop of metabotropic glutamate receptors recognizes C termini of G-protein α-subunits. *J. Biol. Chem.* **278**, 35063–35070 (2003).

[CAS](#) [PubMed](#) [Google Scholar](#)

31. 31.

Gomeza, J. et al. The second intracellular loop of metabotropic glutamate receptor 1 cooperates with the other intracellular domains to control coupling to G-proteins. *J. Biol. Chem.* **271**, 2199–2205 (1996).

[CAS](#) [PubMed](#) [Google Scholar](#)

32. 32.

Hlavackova, V. et al. Sequential inter- and intrasubunit rearrangements during activation of dimeric metabotropic glutamate receptor 1. *Sci. Signal.* **5**, ra59 (2012).

[PubMed](#) [Google Scholar](#)

33. 33.

Grushevskyi, E. O. et al. Stepwise activation of a class C GPCR begins with millisecond dimer rearrangement. *Proc. Natl Acad. Sci. USA* **116**, 10150–10155 (2019).

[CAS](#) [PubMed](#) [PubMed Central](#) [Google Scholar](#)

34. 34.

Goehring, A. et al. Screening and large-scale expression of membrane proteins in mammalian cells for structural studies. *Nat. Protocols* **9**, 2574–2585 (2014).

[CAS](#) [PubMed](#) [Google Scholar](#)

35. 35.

Koehl, A. et al. Structure of the μ -opioid receptor–G_i protein complex. *Nature* **558**, 547–552 (2018).

[ADS](#) [CAS](#) [PubMed](#) [PubMed Central](#) [Google Scholar](#)

36. 36.

Xing, C. et al. Cryo-EM structure of the human cannabinoid receptor CB2–G_i signaling complex. *Cell* **180**, 645–654.e13 (2020).

[CAS](#) [PubMed](#) [Google Scholar](#)

37. 37.

Schorb, M., Haberbosch, I., Hagen, W. J. H., Schwab, Y. & Mastronarde, D. N. Software tools for automated transmission electron microscopy. *Nat. Methods* **16**, 471–477 (2019).

[CAS](#) [PubMed](#) [PubMed Central](#) [Google Scholar](#)

38. 38.

Zheng, S. Q. et al. MotionCor2: anisotropic correction of beam-induced motion for improved cryo-electron microscopy. *Nat. Methods* **14**, 331–332 (2017).

[CAS](#) [PubMed](#) [PubMed Central](#) [Google Scholar](#)

39. 39.

Zhang, K. Gctf: real-time CTF determination and correction. *J. Struct. Biol.* **193**, 1–12 (2016).

[ADS](#) [CAS](#) [PubMed](#) [PubMed Central](#) [Google Scholar](#)

40. 40.

Scheres, S. H. Processing of structurally heterogeneous cryo-EM data in RELION. *Methods Enzymol.* **579**, 125–157 (2016).

[CAS](#) [PubMed](#) [Google Scholar](#)

41. 41.

Punjani, A., Rubinstein, J. L., Fleet, D. J. & Brubaker, M. A. cryoSPARC: algorithms for rapid unsupervised cryo-EM structure determination. *Nat. Methods* **14**, 290–296 (2017).

[CAS](#) [PubMed](#) [Google Scholar](#)

42. 42.

Pettersen, E. F. et al. UCSF Chimera—a visualization system for exploratory research and analysis. *J. Comput. Chem.* **25**, 1605–1612 (2004).

[CAS](#) [Google Scholar](#)

43. 43.

Heymann, J. B. Single particle reconstruction and validation using Bsoft for the map challenge. *J. Struct. Biol.* **204**, 90–95 (2018).

[PubMed](#) [PubMed Central](#) [Google Scholar](#)

44. 44.

Adams, P. D. et al. PHENIX: a comprehensive Python-based system for macromolecular structure solution. *Acta Crystallogr. D* **66**, 213–221 (2010).

[CAS](#) [PubMed](#) [PubMed Central](#) [Google Scholar](#)

45. 45.

Emsley, P. & Cowtan, K. Coot: model-building tools for molecular graphics. *Acta Crystallogr D* **60**, 2126–2132 (2004).

[Google Scholar](#)

46. 46.

Goddard, T. D. et al. UCSF ChimeraX: meeting modern challenges in visualization and analysis. *Prot. Sci.* **27**, 14–25 (2018).

[CAS](#) [Google Scholar](#)

47. 47.

Kato, H. E. et al. Conformational transitions of a neuropeptidergic receptor 1–G_{i1} complex. *Nature* **572**, 80–85 (2019).

[CAS](#) [PubMed](#) [PubMed Central](#) [Google Scholar](#)

[Download references](#)

Acknowledgements

The cryo-EM data were collected at the Cryo-Electron Microscopy Center of Zhejiang University with the technical support from S. Chang. Protein purification were performed at the Protein Facilities (Zhejiang University School of Medicine) with the support of C. Ma. This project was supported by Ministry of Science and Technology (2019YFA050880 to Y.Z., 2018YFA0507003 to J.L.), the National Natural Science Foundation of China Grant (81922071 to Y.Z. and 81720108031, 81872945, 31721002 to J.L.), Zhejiang Province Natural Science Fund for Excellent Young Scholars (LR19H31000 to Y.Z.); the Fondation pour la Recherche Médicale (DEQ20170336747, to J.-P.P.) and the Agence Nationale pour la Recherche (ANR 18-CE11-0004-01 to J.-P.P.). J.-P.P. and P.R. were supported by the Centre National de la Recherche Scientifique (CNRS, PICS no. 07030; PRC no. 1403), the Institut National de la Santé et de la Recherche Médicale (INSERM) and the Program Hubert Curien (PHC) Cai Yuanpei from the Ministère Français des Affaires Etrangères.

Author information

Author notes

1. These authors contributed equally: Cangsong Shen, Chunyou Mao, Chanjuan Xu, Nan Jin

Affiliations

1. ZJU-HUST Joint Laboratory of Cellular Signaling, Key Laboratory of Molecular Biophysics of MOE, International Research Center for Sensory Biology and Technology of MOST, College of Life Science and Technology, Huazhong University of Science and Technology (HUST), Wuhan, China

Cangsong Shen, Chanjuan Xu, Nan Jin, Xiaomei Wang & Jianfeng Liu

2. Department of Biophysics and Department of Pathology of Sir Run Run Shaw Hospital, Zhejiang University School of Medicine, Hangzhou, China

Cangsong Shen, Chunyou Mao, Nan Jin, Huibing Zhang, Dan-Dan Shen, Qingya Shen & Yan Zhang

3. Liangzhu Laboratory, Zhejiang University Medical Center, Hangzhou, China

Cangsong Shen, Chunyou Mao, Nan Jin, Huibing Zhang, Dan-Dan Shen, Qingya Shen & Yan Zhang

4. Zhejiang Provincial Key Laboratory of Immunity and Inflammatory Diseases, Hangzhou, China

Chunyou Mao, Huibing Zhang, Dan-Dan Shen, Qingya Shen & Yan Zhang

5. Bioland Laboratory, Guangzhou Regenerative Medicine and Health Guangdong Laboratory, Guangzhou, China

Chanjuan Xu & Jianfeng Liu

6. Innovation Institute for Artificial Intelligence in Medicine of Zhejiang University, College of Pharmaceutical Sciences, Zhejiang University, Hangzhou, China

Tingjun Hou

7. Key Laboratory of Neuropharmacology and Translational Medicine of Zhejiang Province, Zhejiang Chinese Medical University, Hangzhou, China

Zhong Chen

8. Institut de Génomique Fonctionnelle (IGF), Université de Montpellier, CNRS, INSERM, 34094, Montpellier, France

Philippe Rondard & Jean-Philippe Pin

9. MOE Frontier Science Center for Brain Research and Brain-Machine Integration, Zhejiang University School of Medicine, Hangzhou, China

Yan Zhang

Authors

1. Cangsong Shen

[View author publications](#)

You can also search for this author in [PubMed](#) [Google Scholar](#)

2. Chunyou Mao

[View author publications](#)

You can also search for this author in [PubMed](#) [Google Scholar](#)

3. Chanjuan Xu

[View author publications](#)

You can also search for this author in [PubMed](#) [Google Scholar](#)

4. Nan Jin

[View author publications](#)

You can also search for this author in [PubMed](#) [Google Scholar](#)

5. Huibing Zhang

[View author publications](#)

You can also search for this author in [PubMed](#) [Google Scholar](#)

6. Dan-Dan Shen

[View author publications](#)

You can also search for this author in [PubMed](#) [Google Scholar](#)

7. Qingya Shen

[View author publications](#)

You can also search for this author in [PubMed](#) [Google Scholar](#)

8. Xiaomei Wang
[View author publications](#)

You can also search for this author in [PubMed](#) [Google Scholar](#)

9. Tingjun Hou
[View author publications](#)

You can also search for this author in [PubMed](#) [Google Scholar](#)

10. Zhong Chen
[View author publications](#)

You can also search for this author in [PubMed](#) [Google Scholar](#)

11. Philippe Rondard
[View author publications](#)

You can also search for this author in [PubMed](#) [Google Scholar](#)

12. Jean-Philippe Pin
[View author publications](#)

You can also search for this author in [PubMed](#) [Google Scholar](#)

13. Yan Zhang
[View author publications](#)

You can also search for this author in [PubMed](#) [Google Scholar](#)

14. Jianfeng Liu
[View author publications](#)

You can also search for this author in [PubMed](#) [Google Scholar](#)

Contributions

Y.Z. and J.L. conceived and supervised the whole project; C.S. designed the constructs, and expressed and purified the GABA_B-G_{i1} complex; C.M. prepared the cryo-EM grids, collected the cryo-EM data, and performed cryo-EM map calculation and model building; C.S., C.M. and C.X. designed the constructs for functional assays; C.S., C.X. and N.J. generated the constructs of mutants; C.X. and X.W. performed the

IP1 functional experiments; N.J. performed the NanoBiT cellular functional assays with assistance of H.Z. and Q.S.; D.-D.S. evaluated the sample by negative-stain electron microscopy; C.S., C.M., C.X. and N.J. prepared the figures; C.S., C.M. and C.X. participated in manuscript writing; P.R. and J.-P.P. participated in the interpretation of the data and the preparation of the manuscript; T.H. and Z.C. helped to improve the manuscript; J.-P.P., Y.Z. and J.L. wrote the manuscript with inputs from all the authors.

Corresponding authors

Correspondence to [Jean-Philippe Pin](#) or [Yan Zhang](#) or [Jianfeng Liu](#).

Ethics declarations

Competing interests

The authors declare no competing interests.

Additional information

Peer review information *Nature* thanks Martin Lohse and the other, anonymous, reviewer(s) for their contribution to the peer review of this work.

Publisher's note Springer Nature remains neutral with regard to jurisdictional claims in published maps and institutional affiliations.

Extended data figures and tables

[Extended Data Fig. 1 Purification of the GABA_B-G_{i1} complex.](#)

a Pharmacology of wild-type GABA_B and the purification construct (EM) in a baclofen-mediated NanoBiT-G-protein dissociation assay. Data are mean ± s.e.m. from four independent experiments, performed in technical triplicate. **b**, Flow chart of the purification steps for the GABA_B-G_{i1} complex. GABA_B was expressed in HEK293F cells. Heterotrimeric G_{i1} and scFv16 were expressed in Hi5 cells. **c–e**, Size-exclusion chromatography profile (**c**), SDS-PAGE gel (**d**) and the negative-staining electron microscopy analysis (**e**) of the purified GABA_B-G_{i1} complex.

[Source data](#)

Extended Data Fig. 2 Cryo-EM data processing of the GABA_B-G_i complex.

a, Representative cryo-EM micrograph (from 13,483 movies) and 2D class averages (from 16 classes) of the GABA_B-G_{i1} complex. **b**, Flow chart of cryo-EM data processing. **c**, Gold-standard Fourier shell correlation curves of the globally refined GABA_B-G_{i1} complex and the locally refined GABA_B and G_{i1}.

Extended Data Fig. 3 Flexibility analysis of GABA_B-G_{i1} coupling.

a, Multibody refinement and principal component analysis of the relative orientations of GABA_B and G_{i1}. The GABA_B-G_{i1} consensus map and the body masks of GABA_B and G_{i1} are shown. **b**, Contribution of individual eigenvectors to the total variance in rotation and translation between GABA_B and G_{i1}. The first and second eigenvectors explain more than 50% of the variance observed and are highlighted in red. **c**, Histograms of the amplitudes along the first and second eigenvectors. **d**, Motion represented by the first and second eigenvectors.

Extended Data Fig. 4 Analysis of the quality of the cryo-EM map.

a, Global fitting of the GABA_B-G_{i1} structure into the composite cryo-EM density map. **b**, Fourier shell correlation curves of the model versus the map. **c**, Cryo-EM densities and the fitted atomic models are shown. GB1 in red; GB2 in green; Gα_{i1} in yellow; baclofen in magenta; BHFF in blue.

Extended Data Fig. 5 Structural comparisons of the determined GABA_B-G_i complex with the previously reported low-resolution B2a state GABA_B-G_i complex, the agonist-bound, and the agonist- and PAM-bound GABA_B.

a, Structural comparison between the low-resolution GABA_B-G_i complex in B2a state (grey) and this study determined GABA_B-G_i structure (green). **b**, Structural comparisons of the G_i-bound GABA_B (ago/PAM-G_i) (green) with the agonist-bound (ago) (PDB 6UO9) (grey) and agonist- and PAM-bound GABA_B (ago/PAM) (PDB 6UO8) (blue).

Extended Data Fig. 6 Intra-subunit conformational changes of the TMD of GB2 upon activation.

a, Overlay of the structures of the TMD of GB2 in antagonist-bound (antago) (PDB 7C7S) (yellow), agonist-bound (ago) (PDB 6UO9) (sky blue), and agonist- and PAM-G_i-bound (ago/PAM-G_i) (green) states. **b, c**, Overlay of the different states of the TM6 of GB1 (antago, grey; ago/PAM-G_i, red) (**b**) and the TM6 of GB2 (antago, yellow; ago, blue; ago/PAM-G_i, green) (**c**). **d, e**, NanoBiT G-protein dissociation assay of GABA_B with alterations of the residues that are involved in activation. Data are mean ± s.e.m. from at least three independent experiments, performed in technical triplicate.

[Source data](#)

Extended Data Fig. 7 G_i activation and signalling assays.

a, Interface of GABA_B and G_{i1} protein. GB2, green; G_{i1}, yellow. The interaction interface between GB2 and G_{i1} is in red. **b–e**, Agonist-induced IP1 accumulation assay of the wild-type and the G_{i1}-binding-pocket mutant GABA_B. **f, g**, E_{max} and basal activity for each mutant relative to wild type, detected by IP1 accumulation assay and presented as dot plots. Data are mean ± s.e.m. from at least three independent experiments, performed in technical triplicate and analysed using one-way ANOVA with Dunnett's multiple comparison test to determine significance (compared with wild type). **h**, Sequence alignment of the final five residues in the α5 helix among different Gα proteins. **i, j**, NanoBiT G-protein dissociation assay of the D350^{G.H5.22} (**i**) and F354^{G.H5.26} (**j**) mutant G_{i1}. Data points in **b–g, i, j** are mean ± s.e.m. from at least three independent experiments, performed in technical triplicate.

[Source data](#)

Extended Data Fig. 8 Comparison of the G_i binding pocket among class-A, -B, -C and -F GPCRs.

a–c, Parallel comparisons of the G_i binding pocket between the GABA_B and class-A CB1 (**a**), class-B GCGR (**b**) and class-F SMO (**c**) receptors. Four structures were aligned by the class-A TMD as a reference, as in Fig. 2. A comparison of the indicated two receptors is shown. Colours for α5 are: GABA_B-bound, yellow; CB1-bound (PDB 6N4B), orange-red; GCGR-bound (PDB 6LML), sky blue; and SMO-bound (PDB 6OT0), magenta.

Extended Data Fig. 9 Proposed model of GABA_B activation.

a–d, Schematic of the essential steps for GABA_B activation. **e**, Comparison of the relative bending of GB2 subunit in the agonist- and PAM–G_i-bound (ago/PAM–G_i) (green), the agonist-bound (ago) (PDB 6UO9) (blue), and antagonist-bound (antago) (PDB 7C7S) (yellow) when aligned on the GB2 VFT. **f**, The transmembrane domain rearrangement of GABA_B during activation. The antagonist-bound (antago) (PDB 7C7S) (yellow), agonist-bound (ago) (PDB 6UO9) (blue), and the agonist- and PAM–G_i-bound (ago/PAM–G_i) (green) structures of the TMD of GABA_B were aligned by the TMB of GB1. **g**, PAM binding in agonist- and PAM–G_i-bound GABA_B (ago/PAM–G_i).

Extended Data Table 1 Cryo-EM data collection, model refinement and validation statistics

[Full size table](#)

Supplementary information

[Supplementary Information](#)

This file contains Supplementary Fig. 1 (the uncropped gels) and Supplementary Table 1.

[Reporting Summary](#)

[Video 1](#)

The relative motion of GABA_B and G_{i1} represented by the first eigenvector from the principal component analysis.

[Video 2](#)

The relative motion of GABA_B and G_{i1} represented by the second eigenvector from the principal component analysis.

Source data

[Source Data Fig. 2](#)

[Source Data Fig. 3](#)

[Source Data Extended Data Fig. 1](#)

[Source Data Extended Data Fig. 6](#)

[Source Data Extended Data Fig. 7](#)

Rights and permissions

Open Access This article is licensed under a Creative Commons Attribution 4.0 International License, which permits use, sharing, adaptation, distribution and reproduction in any medium or format, as long as you give appropriate credit to the original author(s) and the source, provide a link to the Creative Commons license, and indicate if changes were made. The images or other third party material in this article are included in the article's Creative Commons license, unless indicated otherwise in a credit line to the material. If material is not included in the article's Creative Commons license and your intended use is not permitted by statutory regulation or exceeds the permitted use, you will need to obtain permission directly from the copyright holder. To view a copy of this license, visit <http://creativecommons.org/licenses/by/4.0/>.

[Reprints and Permissions](#)

About this article



Check for
updates

Cite this article

Shen, C., Mao, C., Xu, C. *et al.* Structural basis of GABA_B receptor–G_i protein coupling. *Nature* **594**, 594–598 (2021). <https://doi.org/10.1038/s41586-021-03507-1>

[Download citation](#)

- Received: 14 January 2021
- Accepted: 29 March 2021
- Published: 28 April 2021
- Issue Date: 24 June 2021

- DOI: <https://doi.org/10.1038/s41586-021-03507-1>

Comments

By submitting a comment you agree to abide by our [Terms](#) and [Community Guidelines](#). If you find something abusive or that does not comply with our terms or guidelines please flag it as inappropriate.

[Download PDF](#)

Advertisement

This article was downloaded by **calibre** from <https://www.nature.com/articles/s41586-021-03507-1>

| [Section menu](#) | [Main menu](#) |